Proceedings of the

International Conference on the Structure and the Interactions of the Photon

including the
18th International Workshop on Photon-Photon Collisions

and the
International Workshop on High Energy Photon Linear Colliders

PHOTON09

May 11-15, 2009
Hamburg, Germany

Editors: Olaf Behnke, Markus Diehl, Thomas Schörner-Sadenius, Georg Steinbrück
Verlag Deutsches Elektronen-Synchrotron

Impressum

Proceedings of the International Conference on the Structure and the Interactions of the Photon

including the
18th International Workshop on Photon-Photon Collisions

and the
International Workshop on High Energy Photon Linear Colliders

(PHOTON09)

May 11-15, 2009, Hamburg, Germany

Conference homepage
`http://photon09.desy.de`

Slides and online proceedings at
`https://indico.desy.de/conferenceDisplay.py?confId=1407`

Editors:
Olaf Behnke, Markus Diehl, Thomas Schörner-Sadenius, Georg Steinbrück
January 2010
DESY-PROC-2009-03
ISBN 978-3-935702-33-1
ISSN 1435-8077

Published by
Verlag Deutsches Elektronen-Synchrotron
Notkestraße 85
22607 Hamburg
Germany

Committees and Support

Local Organizing Committee

Olaf Behnke (DESY), Markus Diehl (DESY), Thomas Schörner-Sadenius (DESY), Georg Steinbrück (Hamburg U.)

International Advisory Committee

S. Brodsky (SLAC, Stanford, and IPPP, Durham), J. Engelen (NIKHEF, Amsterdam), V. Fadin (INP Novosibirsk), J. H. Field (Geneva U.), A. Finch (Lancaster U.), I. Ginzburg (IM Novosibirsk), M. Greco (INFN, Rome), J. Gronberg (LLNL Livermore), J. Gunion (UC Davis), K. Hagiwara (KEK, Tsukuba), R.-D. Heuer (CERN, Geneva), F. Kapusta (LPNHE, Paris), U. Karshon (Weizmann I., Rehovot), M. N. Kienzle-Focacci (Geneva U.), R. Klanner (Hamburg U.), M. Klasen (LPSC, Grenoble), M. Krawczyk (Warsaw U.), E. Laenen (NIKHEF, Amsterdam), K. Moenig (DESY Zeuthen), G. Pancheri (INFN, Frascati), M. Risse (Wuppertal U.), A. de Roeck (CERN, Geneva), S. Soeldner-Rembold (Manchester U.), Y. Sakai (KEK, Tsukuba), T. Takahashi (Hiroshima U.), V. I. Telnov (INP, Novosibirsk), S. Uehara (KEK, Tsukuba), M. Velasco (Northwestern U.), S.-S. Yu (FNAL), P. Zerwas (DESY and RWTH Aachen), F. Zomer (LAL Orsay)

Supported by

Deutsche Forschungsgemeinschaft, Deutsches Elektronen-Synchrotron DESY, Universität Hamburg

Preface

The Photon 2009 conference took place at DESY in Hamburg, Germany, from May 11 - 15, 2009, and was attended by 104 participants. The Photon conference series is unique in focusing on the role of the photon in particle physics. Two distinct areas are covered: on one side the properties and interactions of the photon in elementary particle physics, and on the other side the physics and technology for a future photon collider, where electroweak precision measurements as well as searches for physics beyond the Standard Model of particle physics could be performed.
An important aspect of the conference is bringing theorists and experimentalists together, which was reflected in sessions co-organized by members of both communities and a well-balanced program. In all sessions, new theoretical developments and results from completed and running experiments were shown, as well as studies for future experiments like the Large Hadron Collider (LHC) or future linear colliders. The conference program was complemented by two sessions that recognized DESY as host institute: in a special colloquium entitled “Highlights of HERA”, two speakers summarized key results of the HERA experiments. In a session on “Research with photons at DESY”, two speakers outlined the activities at DESY in the area of photon science. This kind of session, in which other aspects of photon physics are covered, thus extending the core topic of the conference, is part of the tradition of this conference series.
We feel that the Photon 2009 conference successfully covered a wide range of topics, all following the leitmotiv of “the photon in elementary particle physics”. We thank the participants for an interesting conference with lively discussions, and the session convenors for their invaluable help in shaping the conference program.
It is a pleasure to thank Marion Bierhahn, Antje Brandes, Antje Daum, Michaela Grimm, Iris Kerkhoff, Ramona Matthes and Andrea Schrader for their tireless support before and during the conference. We thank Kirsten Sachs and Maren Stein for their help in preparing these proceedings, and Julia Grebenyuk for taking the conference photo. We acknowledge a grant from the Deutsche Forschungsgemeinschaft (DFG). Finally, we are grateful to the DESY directorate for financial support and for the hospitality extended to the participants of this conference.

The local organizing committee
Olaf Behnke, Markus Diehl, Thomas Schörner-Sadenius, Georg Steinbrück

Contents

Chapter 1

Electroweak and New Physics

Convenors:

M. Mühlleitner (Annecy) and K. Piotrzowski (Louvain-la-Neuve)

Search for New Physics with Photons and Exclusive Z Production at the Tevatron

Dan Krop on behalf of the CDF and DØ Collaborations

Enrico Fermi Institute, University of Chicago, Chicago, Illinois 60637

DOI: http://dx.doi.org/10.3204/DESY-PROC-2009-03/Krop

We report the results of searches for non-standard model phenomena in photon final states and a search for exclusive Z boson production. These searches use data from $p\bar{p}$ collisions at $\sqrt{s} = 1.96$ TeV collected with the CDF and DØ detectors at the Fermilab Tevatron corresponding to $1.0 - 4.2$ fb^{-1} of integrated luminosity. No disagreement of data with standard model predictions is observed. We report limits on the parameters of several models including anomalous triple gauge couplings, large extra dimensions, fermiophobic Higgs models, and supersymmety.

1 Introduction

The standard model (SM) of particle physics [1] has been remarkably successful at predicting the details of almost all observed high energy physics processes. However, because the predicted high energy behavior of the SM becomes unphysical at an interaction energy of a few TeV we know that new physical phenomena are required. In this document we present the results of searches for phenomena that are beyond the standard model (BSM) using final states containing photons. The data used for these searches are obtained with the CDF and DØ detectors at the Fermilab Tevatron, where protons collide with antiprotons at $\sqrt{s} = 1.96$ TeV. Additionally, we present a search for exclusive Z production where the p and $\bar{p}$ emerge from the collision intact. The CDF and DØ detectors are described in detail in Refs. [2] and [3], respectively.

2 Exclusive Z production

The CDF collaboration has performed a search for the exclusive production of Z bosons decaying to a $\mu^+\mu^-$ or e^+e^- pair and a measurement of the cross section for exclusive $\mu^+\mu^-$ and e^+e^- production with dilepton invariant mass $M_{ll} > 40$ GeV and $|\eta_l| < 4$[1]. The analysis requires two

[1] We use a cylindrical coordinate system in which ϕ is the azimuthal angle, r is the radius from the nominal beam line, and z points in the proton beam direction. The transverse $(r-\phi)$ plane is perpendicular to the z axis. Transverse momentum and energy are the respective projections of momentum measured in the tracking system and energy measured in the calorimeter system onto the $r-\phi$ plane, and are defined as $p_T = p\sin\theta$ and $E_T = E\sin\theta$. Here, θ is the polar angle measured with respect to the interaction vertex. Missing $\mathrm{E_T}$ ($\vec{\not\!\!E}_T$) is defined by $\vec{\not\!\!E}_T = -\sum_i E_T^i \hat{n}_i$, where i is the calorimeter tower number for $|\eta| < 3.6$, and $\hat{n}_i$ is a unit vector perpendicular to the beam axis and pointing at the i^{th} tower. The pseudorapidity η is defined as $-\ln(\tan(\theta/2))$, where θ is measured with respect to the origin of the detector. We define the magnitude $\not\!\!E_T = |\vec{\not\!\!E}_T|$. We use the convention that "momentum" refers to pc and "mass" to mc^2.

oppositely-charged leptons of the same flavor with $M_{ll} > 40$ GeV and $p_T^l > 20$ GeV. For the exclusive Z search, a subsample is selected with $82 < M_{ll} < 98$ GeV and $p_T^l > 25$ GeV. Events containing additional tracks or energy deposition in any calorimeter above that expected from noise are rejected. Events are also rejected if any beam shower counter (BSC) has hits above threshold[2]. The acceptance for reconstructing exclusive dilepton events is calculated using the LPAIR [6] Monte Carlo (MC) event generator while the corresponding acceptance for exclusive Z production is obtained from PYTHIA [7]. The detector response to these events is simulated with GEANT [8]. No events pass the exclusive $Z \to l^+l^-$ selection criteria and we therefore set an upper limit on the cross section of exclusive Z production at the Tevatron of $\sigma_{excl}(Z) < 0.96$ pb at 95% confidence level (C.L.). Eight exclusive dilepton events are observed with an estimated background of 1.45 ± 0.61 events. Figure 1 shows the dilepton invariant mass distribution of these events as well as the LPAIR prediction. The cross section for exclusive dilepton production in the region $M_{ll} > 40$ GeV is found to be $\sigma_{obs} = 0.24^{+0.13}_{-0.10}$ pb, which is in good agreement with the LPAIR prediction of 0.256 pb.

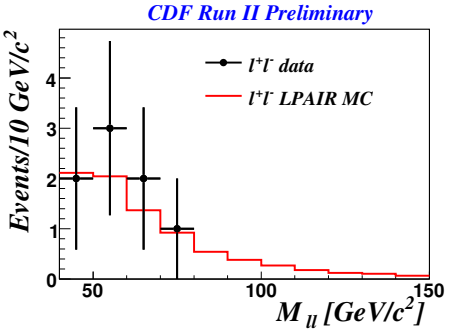

Figure 1: The CDF exclusive Z production search: the dilepton invariant mass distribution observed and the LPAIR prediction with the GEANT simulation scaled to account for acceptance and luminosity.

3 Searches in the $\gamma \not\!\!E_T$ final state

The $\gamma \not\!\!E_T$ channel is useful both as a test of SM parameters, through the $Z\gamma \to \nu\bar{\nu}\gamma$ process, and to search for BSM processes that contain a photon where the missing energy is associated with some new, undetected particle.

The DØ collaboration performs a measurement of the $Z\gamma \to \nu\bar{\nu}\gamma$ cross section and searches for anomalous triple gauge couplings [9] using 3.6 fb^{-1} of data. It also searches [10] for pairs of close-by leptons in the $\gamma \not\!\!E_T$ final state and sets limits on SUSY models containing "dark" sectors inspired by possible dark matter signals in cosmic ray detection experiments [11] using 4.1 fb^{-1} of data. Finally, both DØ [12] and CDF [13] search for large extra dimensions (LED) [14] that would leave a $\gamma \not\!\!E_T$ signature in the detector through the emission of an undetected Kaluza-Klein graviton (G_{KK}), $q\bar{q} \to \gamma G_{KK}$.

[2]The BSC consists of scintillation counters located along the beam pipe at high pseudorapidities, $3.6 < |\eta| < 7.4$.

3.1 Triple gauge coupling

The SM has no tree-level $Z\gamma\gamma$ or $ZZ\gamma$ couplings, leading to a small cross section for $Z\gamma$ production. The presence of such couplings in BSM theories can enhance the yield, especially at higher values of photon E_T. Anomalous couplings can be parametrized using a set of eight complex parameters $h_i^V (i = 1, \ldots, 4; V = Z, \gamma)$ of the form $h_i^V = h_{i0}/(1 + \hat{s}/\Lambda^2)^n$ [15]. The DØ collaboration sets limits on the real part of the anomalous coupling, $Re(h_{i0}^V)$, referred to as ATGC in the following.

The analysis requires one photon candidate with $E_T > 90$ GeV and $|\eta| < 1.1$ and missing transverse energy of $\not\!\!E_T > 70$ GeV. Events containing jets with $E_T > 15$ GeV, any muon, and additional electromagnetic objects with $E_T > 15$ GeV are rejected. Furthermore, to suppress non-collision backgrounds, a pointing algorithm [16] is used to reconstruct the photon trajectory. The z position of the interaction vertex predicting by the pointing algorithm must be within 10 cm of the chosen reconstructed primary vertex. 51 events are observed with a background prediction, excluding $Z\gamma \to \nu\bar{\nu}\gamma$, of $17.3 \pm 0.6(\text{stat.}) \pm 2.3(\text{syst.})$. The cross section of $Z\gamma$ production multiplied by the branching fraction of the Z into neutrinos is thus measured to be (32 ± 9) fb with a significance of 5.1σ. This agrees well with the SM prediction of 39 ± 4 fb.

To test for the presence of a BSM signal, the observed photon E_T spectrum is compared with that expected from the SM. Figure 2 shows this spectrum. No excess over backgrounds predictions is observed. Using this distribution and Poisson statistics, limits of $|h_{30}^\gamma| < 0.033$, $|h_{40}^\gamma| < 0.0017$, $|h_{30}^Z| < 0.033$, and $|h_{40}^Z| < 0.0017$ are set at 95% C.L.

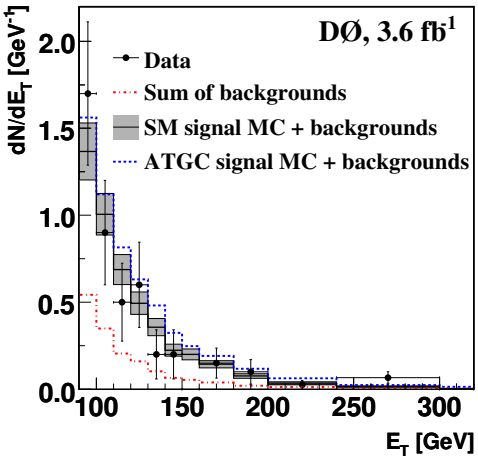

Figure 2: The DØ $\gamma\not\!\!E_T$ triple gauge coupling search: Photon E_T spectrum in data (solid circles), the sum of MC signal and backgrounds (dash-dot line), and for the ATGC prediction with $h_{30}^\gamma = 0.09$ and $h_{40}^\gamma = 0.005$ (dashed line). The shaded band corresponds to the ± 1 s.d. total uncertainty on the predicted sum of the SM signal and background.

3.2 Dark photons

The DØ dark photon analysis searches for events with a photon, large $\not\!\!E_T$, and two close-by leptons as indicated by the example diagram on the left side of Fig. 3. The $\gamma\not\!\!E_T$ base

sample is selected by requiring a photon with $E_T > 30$ GeV and $\not\!\!E_T > 20$ GeV. Dark photons candidates are formed by selecting pairs of oppositely charged tracks that are close-by spatially, $\Delta R < 0.2$, and originate from the same point along the beamline, $|\Delta z| < 2$ cm. The QCD background is suppressed by requiring that no track has its azimuthal angle aligned with the photon, $0.4 < \Delta\phi_{\gamma,track} < 2.74$. For electron pair candidates, the calorimeter depositions are expected to overlap, so the dark photon candidate is required to match an electromagnetic cluster with $E_T > 10$ GeV, $EM_{frac} > 97\%$, and $\mathcal{I} < 0.1$[3]. No evidence for a peak in the dilepton mass spectrum is observed. A modified version of the SUSYHT [17] generator is used along with PYTHIA [7] and GEANT [8] to generate the signal hypotheses in the dilepton mass spectrum. Limits are then set from the dilepton mass spectrum using a log-likelihood ratio (LLR) statistic method [18]. These limits are interpreted in terms of the branching fraction of the neutralino into the dark photon, $\mathcal{B} = Br(\tilde{\chi}_1^0 \rightarrow \gamma_D \tilde{X})$. The right side of Fig. 3 shows the chargino mass limit as a function of $\mathcal{B}$ for three representative dark photon masses. For dark photon masses of 0.2, 0.782, and 1.5 GeV chargino masses of 230, 142, and 200 GeV are excluded at the 95% C.L., respectively.

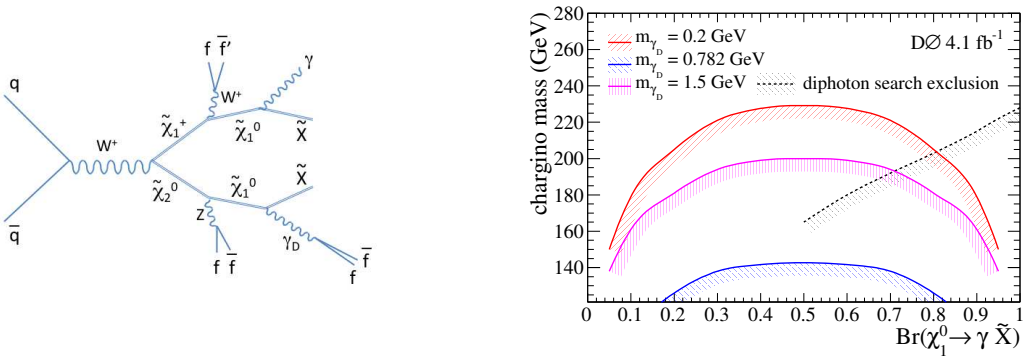

Figure 3: The DØ dark photon search. On the left: One of the diagrams giving rise to a photon, dark photon (γ_D), and large $\not\!\!E_T$ due to escaping darkinos ($\tilde{X}$). On the right: The dependence of the excluded chargino masses on the branching ratio of the neutralino into a photon are given for dark photon masses of 0.2, 0.782, and 1.5 GeV. The black contour corresponds to the exclusion from a previous diphoton search [19].

3.3 Large extra dimensions

The CDF and DØ $\gamma\not\!\!E_T$ LED searches use data corresponding to 2.0 fb^{-1} and 2.7 fb^{-1} of $p\bar{p}$ collisions, respectively. The analyses require one central photon with $E_T > 90$ GeV and $\not\!\!E_T > 50(70)$ GeV for CDF(DØ). Events with additional high p_T tracks or jets are removed. The DØ analysis uses the photon pointing technique mentioned above to reduce non-collision backgrounds. The CDF analysis requires the photon to be in time with the $p\bar{p}$ collision and uses topological variables to reduce these backgrounds. Neither analysis observes a significant

[3]The electromagnetic fraction, EM_{frac}, is defined as the fraction of total energy of the cluster deposited in the EM section of the calorimeter. The calorimeter isolation, $\mathcal{I}$, is defined as $\mathcal{I} = [E_{tot}(0.4) - E_{EM}(0.2)]/E_{EM}(0.2)$. The 0.2 and 0.4 refer to radius of the cone in ΔR which is used to calculate the energy of the cluster.

excess in the data over the expected SM contribution. CDF observes 40 events with an expected background of 46.3 ± 3.0 events and DØ observes 51 versus an expected background of 49.9 ± 4.1. CDF reports lower limits on the fundamental Planck scale, M_D, of 1080–900 GeV for $n_d = 2$–6 at 95% C.L while DØ obtains limits of 970–804 GeV for $n_d = 2$–8, where n_d refers to the number of extra dimensions.

4 Searches in the $\gamma\gamma$ final state

The diphoton channel is used by DØ in an LED search [20] and by both CDF [21] and DØ [22] in fermiophobic Higgs searches. DØ uses data corresponding to 1.1 fb^{-1} of $p\bar{p}$ collisions for the LED search and 4.2 fb^{-1} for the fermiophobic Higgs search. CDF uses data corresponding to 3.0 fb^{-1} of collisions for its fermiophobic Higgs search.

4.1 Large extra dimensions

The DØ diphoton LED search selection requires two EM objects, each having $E_T > 25$ GeV and being both in the central EM calorimeter ($|\eta| < 1.1$) or one in the central and one in the forward EM calorimeter ($1.5 < |\eta| < 2.4$). Because no track selection is made, the analysis combines the dielectron and diphoton channels. The normalization of the QCD background is obtained by fitting M_{diEM} in the range of $60 - 140$ GeV, where no LED signal is expected, to a combination of SM $ee/\gamma\gamma$ and QCD shapes, with the QCD shape being obtained from a dataset where an EM object fails shower profile requirements. No discrepancy from the backgrounds prediction is observed and lower limits on M_S[4] at the 95% C.L. are set: 1.62 TeV using the GRW [23] formalism and $2.09 - 1.29$ TeV using the HLZ [24] formalism for $n_d = 2 - 7$.

4.2 Fermiophobic Higgs

The SM branching fraction for a low mass Higgs boson in the diphoton final state, $Br(h \to \gamma\gamma)$, has a maximal value of approximately 0.2% for Higgs boson masses of about 120 GeV. In so-called "fermiophobic" Higgs models, $Br(h \to \gamma\gamma)$ is enhanced [25]. CDF selects photons having $E_T > 15$ GeV and requires them to be either both central ($|\eta| < 1.05$) or one to be central and one forward ($1.2 < |\eta| < 2.8$). DØ selects two central ($|\eta| < 1.1$) photons with $E_T > 20$ GeV. CDF requires $p_T(\gamma\gamma) > 75$ GeV and DØ selects $p_T(\gamma\gamma) > 35$ GeV. The DØ analysis uses an artificial neural network (ANN) [26] to reduce the contribution from jets misidentified as photons and a matrix background subtraction method [27] to obtain detailed estimates of γ+jet and di-jet backgrounds. After no excess is observed in the diphoton mass distribution, this distribution is used to set limits on fermiophobic Higgs models using a modified frequentist approach [18, 28]. CDF also observes no excess in the diphoton mass spectrum and approximates the background via a fit to a smooth curve; limits are set using a binned-likelihood method and Poisson fluctuation of the $M_{\gamma\gamma}$ bin contents. Figure 4 shows $M_{\gamma\gamma}$ distributions from both analsyes. DØ(CDF) obtains a limit of $M(h_f) > 102.5(106)$ GeV at 95% C.L.

[4] M_S is the ultraviolet cutoff of the sum over Kaluza-Klein states, also called the "effective Planck scale"

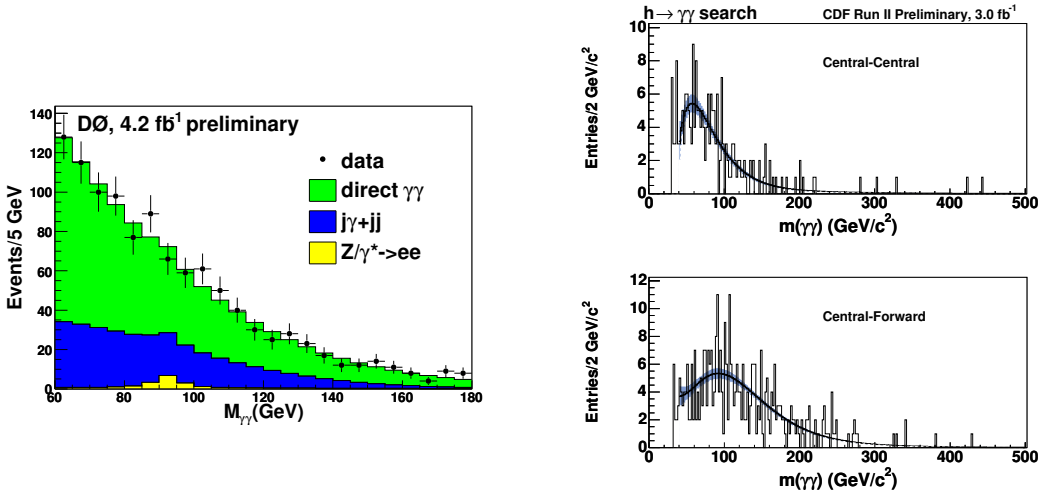

Figure 4: Fermiophobic Higgs searches: Invariant mass distributions of diphoton candidates for the DØ search on the left and the CDF search on the right. CDF plots the central-central and central-forward diphoton candidates separately and has the results of fits to a smooth curve overlaid on the distributions.

5 Searches for supersymmetry in the $\gamma\gamma \not\!\!E_T$ final state

The CDF and DØ collaborations have searched for gauge-mediated supersymmetry breaking (GMSB) [29] in 2.6 and 1.1 fb^{-1} of $p\bar{p}$ collisions, respectively. In GMSB, the next-to-lightest supersymmetric particle $\tilde{\chi}_1^0$ may decay to a gravitino via $\tilde{\chi}_1^0 \to \tilde{G}\gamma$. Pair production of massive SUSY particles would result in a final state with two photons and large $\not\!\!E_T$ due to the undetected gravitino. Both analyses consider the minimal Snowmass Slope SPS 8 [30] GMSB model to quote results as a function of $\tilde{\chi}_1^0$ mass and lifetime. DØ(CDF) requires two central photons with $E_T > 25(13)$ GeV. To reduce the bias of the $\not\!\!E_T$ measurement arising from mismeasurement of the jet transverse momentum, DØ requires the highest E_T jet to be separated from the $\not\!\!E_T$ by no more than 2.5 radians. CDF requires $\Delta\phi(\gamma_1, \gamma_2) < \pi - 0.15$, H_T[5] > 200 GeV, and $\not\!\!E_T$ significance[6] > 3. DØ uses the photon pointing algorithm to suppress non-collision backgrounds while CDF achieves this suppression by requiring the photon candidates to be in time with the $p\bar{p}$ collision and by using topological variables. After all selections, DØ observes 3 events with $\not\!\!E_T > 60$ GeV with a background expectation of 1.6 ± 0.4 events. CDF observes no events with a background expectation of 1.23 ± 0.38. 95% C.L. limits of $m(\tilde{\chi}_1^0) > 125$ GeV and $m(\tilde{\chi}_1^0) > 149$ GeV are obtained from DØ and CDF for $\tau(\tilde{\chi}_1^0) = 0$, respectively.

[5] H_T is defined as the scalar sum p_T of all identified objects in the event

[6] $\not\!\!E_T$ significance is defined as $-\log(\mathcal{P})$, where $\mathcal{P}$ is the probability form $\not\!\!E_T$ drawn from the expected mismeasured $\not\!\!E_T$ distribution to be equal to or larger than the observed $\not\!\!E_T$

6 Signature-based searches with photons

Motivated by the unknown nature of possible BSM signals in the Tevatron dataset, the CDF collaboration presents search analyses which test whether a particular signature is consistent with SM predictions and do not set limits on specific exotic models. Two of these so-called "signature-based" searches are presented: an analysis of the $l\gamma b\not{E}_T$ final state [33] and an analysis of the $\gamma bj\not{E}_T$ final state [34].

6.1 The $l\gamma b\not{E}_T$ final state

The $l\gamma b\not{E}_T$ analysis requires events with a central γ candidate having $E_T > 10$ GeV, a central electron or muon with $E_T > 20$ GeV, $\not{E}_T > 20$ GeV, and a b-tagged[7] jet with $E_T > 15$ GeV. Events passing these requirements form a "base" sample. A second search is constructed to enhance the contribution of $t\bar{t}\gamma$ events by additionally requiring $H_T > 200$ GeV and $N(\text{jets}) > 3$. 28 events are observed in the base sample with a corresponding SM background prediction of $31.0^{+4.1}_{-3.9}$ events. In the enhanced sample, 16 events are observed with a background prediction of $11.2^{+2.3}_{-2.1}$ events. The probability that non-$t\bar{t}\gamma$ backgrounds produce 16 or more events is calculated to be 1%. Assuming this excess to be due to SM $t\bar{t}\gamma$ production, the $t\bar{t}\gamma$ cross section is calculated to be $\sigma_{t\bar{t}\gamma} = 0.15 \pm 0.08$ pb.

6.2 The $\gamma bj\not{E}_T$ final state

The event selections for the $\gamma bj\not{E}_T$ analysis are as follows: one central photon with $E_T > 25$ GeV, two jets with $|\eta| < 2.0$ and E_T at least one of which must be b-tagged, $\not{E}_T > 25$ GeV, $\Delta R > 0.4$ for any two objects in the event, and $\Delta\phi(\not{E}_T, \text{jet}) > 0.3$ for any jet. The CDF collaboration observes 617 events while the SM prediction is $607 \pm 74(\text{stat.}) \pm 86(\text{syst.})$; no deviation from the SM prediction is observed. The consistency of the distributions of 11 kinematic variables with the SM prediction is tested by using the Kolmogorov-Smirnoff (KS) test; the probability that the SM hypothesis is consistent with the observed distributions range from $7 - 99\%$, again indicating agreement with the SM hypothesis. Finally, 11 additional selections are applied to enhance any possible signals on the tails of kinematic distribution. No deviation from the SM hypothesis is observed in any of these additional selections.

7 Conclusions

The CDF and DØ collaborations have a far-reaching program to search for new physics in photon final states. No significant deviation from the SM has yet been observed in data corresponding to between $1 - 4.2$ fb^{-1} of $p\bar{p}$ collisions. However, none of the results presented in this document utilize more than half of the expected full dataset from the Tevatron by the end of Run II. As more data is collected, we expect to see many interesting results from both experiments.

[7] A b-tagging algorithm identifies jets containing b hadrons through the presence of a b-hadron decay vertex displaced from the beam line [35].

Acknowledgements

The author acknowledges and thanks the CDF exotic and DØ new phenomena group conveners for their helpful suggestions to improve the presentation of these results and Yuri Gershtein for his helpful explanation of the dark photon result.

References

[1] S.L. Glashow, Nucl. Phys. **22**, 588 (1961); S. Weinberg, Phys. Rev. Lett. **19**, 1264 (1967);

[2] D. E. Acosta *et al.* [CDF Collaboration], Phys. Rev. D **71**, 052003 (2005).

[3] V. M. Abazov *et al.* [D0 Collaboration], Nucl. Instrum. Meth. A **565**, 463 (2006).

[4] T. Aaltonen *et al.* [CDF Collaboration], Phys. Rev. Lett. **102**, 222002 (2009).

[5] L. Motyka and G. Watt, Phys. Rev. D **78**, 014023 (2008).

[6] J. A. M. Vermaseren, Nucl. Phys. B **229**, 347 (1983); S. P. Baranov, O. Duenger, H. Shooshtari, and J. A. M. Vermaseren, *In *Hamburg 1991, Proceedings, Phyiscs at HERA, vol. 3* 1478-1482 (see HIGH ENERGY PHYSICS INDEX 30 (1992) No. 12988).*

[7] T. Sjostrand *et al.*, Comput. Phys. Commun. **135**, 238 (2001).

[8] R. Brun and F. Carminati, CERN Program Library Long Writeup, W5013 (1993) [unpublished].

[9] V. M. Abazov *et al.* [D0 Collaboration], Phys. Rev. Lett. **102**, 201802 (2009).

[10] V. M. Abazov *et al.* [D0 Collaboration], FERMILAB-PUB-09-229-E, arXiv:0905.1478v2 [hep-ex], (2009).

[11] N. Arkani-Hamed, D. P. Finkbeiner, T. R. Slatyer and N. Weiner, Phys. Rev. D **79**, 015014 (2009); N. Arkani-Hamed and N. Weiner, JHEP **0812**, 104 (2008);

[12] E. Carrera [D0 Collaboration], arXiv:0180.1331 [hep-ex].

[13] T. Aaltonen *et al.* [CDF Collaboration], Phys. Rev. Lett. **101**, 181602 (2008).

[14] N. Arkani-Hamed, S. Dimopoulos, and G. R. Dvali, Phys. Lett. B **429**, 263 (1998).

[15] U. Baur and E. Berger, Phys. Rev. D **47**, 4889 (1993).

[16] S. Keisisoglou, Brown University, Ph.D. Thesis, FERMILAB-THESIS-2004-44, UMI-31-74625 (2004).

[17] A. Djouadi, M. M. Muehlleitner, M. Spira, Acta Phys. Pol. B 38, 635 (2007).

[18] T. Junk, Nucl. Instrum. Methods A **434**, 435 (1999); A. Read, CERN 2000-005 (200).

[19] V. M. Abazov *et al.* [D0 Collaboration], Phys. Lett. B **659**, 856 (2008).

[20] V. M. Abazov *et al.* [D0 Collaboration], Phys. Rev. Lett. **102**, 051501 (2009).

[21] T. Aaltonen *et al.* [CDF Collaboration], FERMILAB-PUB-09-218-E, arXiv:0905.0413 [hep-ex] (2009).

[22] V. M. Abazov *et al.* [D0 Collaboration], D0 Note 5880-CONF (2009).

[23] G. Giudice, R. Rattazzi, and J. Wells Nucl. Phys. B **544**, 3 (1999).

[24] T. Han, J. Lykken, and R. Zhang, Phys. Rev. D **59** 105006 (1999).

[25] S. Mrenna and J. D. Wells, Phys. Rev. D **63**, 015006 (2001).

[26] C. Peterson, T. Rognvaldsson, and L. Lonnblad, Lund University Preprint LU-TP 93-29.

[27] Y. Liu, Ph.D Thesis, FERMILAB-THESIS-2004-37 (2004).

[28] W. Fisher, FERMILAB-TM-2836-E (2007).

[29] S. Ambrosiano, G. L. Kane, G. D. Kribs, S. P. Martin, and S. Mrenna, Phys. Rev. D **54**, 5395 (1996); C. H. Chen and J. F. Gunion, Phys. Rev. D **58**, 075005 (1998).

[30] B. C. Allanach *et al.*, Eur. Phys. J. C **25**, 113 (2002).

[31] V. M. Abazov *et al.* [D0 Collaboration], Phys. Lett. B **659**, 856 (2008)

[32] T. Aaltonen *et al.* [CDF Collaboration], CDF Note 9625 (2008).

[33] T. Aaltonen *et al.* [CDF Collaboration], FERMILAB-PUB-09-280-E, arXiv:0906.0518 [hep-ex] (2009).

[34] T. Aaltonen *et al.* [CDF Collaboration], FERMILAB-PUB-09-221-E, arXiv:0905.0231 [hep-ex] (2009).

[35] D. Acosta *et al.* [CDF Collaboration] Phys. Rev. D **71**, 052003 (2005); C. Neu, FERMILAB-CONF-06-162-E (2006).

Standard Models Tests and Searches with Photons at the LHC

Suen Hou, on behalf of the ATLAS and CMS collaborations
Institute of Physics, Academia Sinica, Nankang, Taipei, Taiwan

DOI: http://dx.doi.org/10.3204/DESY-PROC-2009-03/Hou

We report on the sensitivity of the LHC experiments to the Standard Model predictions for $W\gamma$ and $Z\gamma$ productions in pp collisions with final states containing electrons, muons and photons. The studies use detector simulation data at $\sqrt{s} = 14$ TeV including calibration and alignment corrections. The results show that the cross-section measurements of $W\gamma$, and $Z\gamma$ can be established with significance better than 5 sigma for the first 0.1 fb^{-1} of integrated luminosity. The sensitivities to anomalous triple gauge boson couplings is also estimated. The measurements can be significantly improved with 1 fb^{-1} of data over the results from the Tevatron.

1 Introduction

The Large Hadron Collider (LHC) is built for finding possible evidence of the Higgs boson and new physics beyond the Standard Model. Two general purpose experiments, ATLAS [1] and CMS [2], have been constructed to study proton-proton collisions at a center of mass energy of 14 TeV. Measurements of electroweak interactions shall be accurate and the data samples will be used as reference for calibration of detector response of leptons, photons and jets. Detection of photons in the final states is important for many analyses such as the searches for Higgs bosons, supersymmetry, and precision measurements of Standard Model processes. The diboson production of $W\gamma$ and $Z\gamma$ probes triple gauge boson couplings (TGC) of $WW\gamma$, $ZZ\gamma$ and $Z\gamma\gamma$ vertices, and therefore the non-Abelian structure of the Standard Model [3]. Charged TGCs of $WW\gamma$ and WWZ are predicted, while those involving only neutral gauge bosons (Z, γ) are absent at tree-level, and the higher order corrections are at the 10^{-4} level [4]. If there will be contributions of anomalous couplings, the signature would be obtained for enhanced production cross-sections particularly at high transverse momentum of the bosons. Indication of new physics is explored by measuring deviations of these distributions to theoretical predictions.

In this report we first discuss measurements of W and Z bosons in leptonic decays to electrons and muons. Detection of W and Z associated with a photon is studied with Monte Carlo samples applying full detector layout for realistic understanding of the event selection. The sensitivities to anomalous triple gauge couplings are determined.

2 Leptonic W and Z decays

The LHC provides a new energy domain for exploration beyond LEP and Tevatron. The measurements described here will be dominated by uncertainties in the electroweak sector of the Standard Model. Study of leptonic decays of W and Z bosons will be the first to be exploited. These processes have large production cross sections and the theoretical understanding is very advanced to next-to-leading order (NLO). Their experimental signatures are very clean, in particular for $Z \to ll$, and will be extensively used for detector calibration and tuning of Monte Carlo simulation.

Events of $Z \to e^+e^-$ and $\mu^+\mu^-$ are triggered by high p_T leptons. The typical event selection requires finding a pair of oppositely charged leptons above a p_T threshold in a mass interval adjacent to the Z mass in the fiducial volume of the detector (typically $|\eta| < 2.5$, limited by the tracking detectors). The invariant mass spectra of the CMS study [5] for $Z \to e^+e^-$, expected for 10 pb^{-1}, is plotted in Figure 1. $W^\pm \to e^\pm\nu$ or $\mu^\pm\nu$ events are selected similarly with a single lepton trigger, finding an isolated high p_T lepton with large missing energy, and the transverse mass consistent with the W. The transverse mass distribution of the ATLAS analysis [6] is shown in Figure 1 for $W^\pm \to \mu^\pm\nu$ expected for an integrated luminosity of 50 pb^{-1}. The large statistics of signal events suggest that the cross section measurements will be dominated by systematic errors. An overall uncertainty of about 5% can be achieved with 50 pb^{-1} in the W channels, mainly due to background uncertainty. The precision for Z channels is expected for 3% with the uncertainty coming from the lepton selection [6]. These values will be reduced with more stringent selections when the available data statistics increases. The theoretical uncertainty from modeling the parton density functions (PDF) has the effect on absolute normalization, and is estimated to be $6-7\%$ [7]. The uncertainty on luminosity, typically obtained by measuring forward elastic scattering, is estimated to be 10% at the beginning

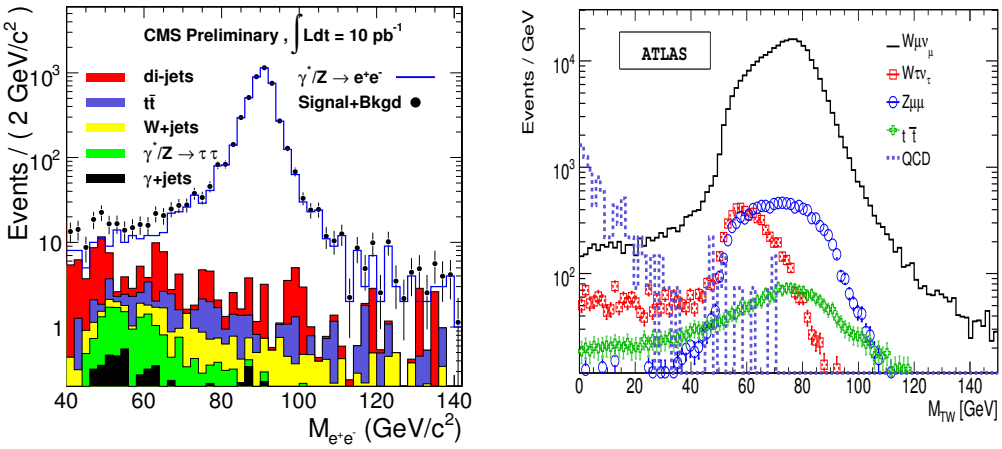

Figure 1: Left: Invariant mass distribution in the $Z \to \mu\mu$ channel as expected in CMS for an integrated luminosity of 10 pb^{-1} [5]. Right: Transverse mass distribution in the $W \to \mu\nu$ events channel as expected in ATLAS for an integrated luminosity of 50 pb^{-1} [6].

of data taking.

3 W and Z production associated with a photon

Both ATLAS and CMS collaborations have carried out studies on diboson events with leptons and photons in the final states for the production cross sections and the sensitivity to anomalous triple gauge boson couplings. The tree-level Feynman diagrams for production of a W or a Z boson accompanied with a photon are shown in Figure 2. The diagrams of $WW\gamma$, $ZZ\gamma$ and $Z\gamma\gamma$ coupling vertices are also illustrated. At LHC the energy will be seven times higher than at the Tevatron, the LHC sensitivity to anomalous couplings is expected to be improved by orders of magnitude. Comparison of the production cross-sections are listed in Table 1.

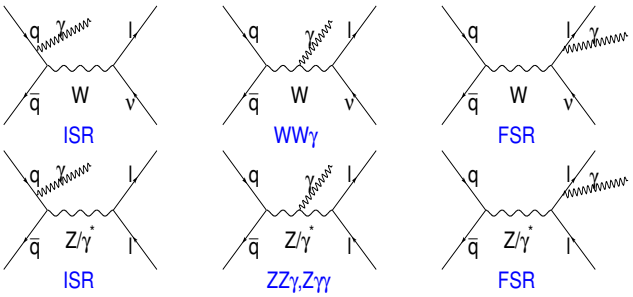

Figure 2: The Standard Model tree-level diagrams for $W\gamma$ and $Z\gamma$ productions at hadron colliders.

Selections for $W\gamma$ and $Z\gamma$ events have profited from the clean signals of the leptonic final states and by the well established identification of W and Z bosons. The $W\gamma$ candidates are inclusive $e^{\pm}\gamma$ and $\mu^{\pm}\gamma$ events having one electron or muon observed with the absence of the oppositely charged lepton of the same flavor. The neutrino from W decay escapes detection and introduces a large transverse energy imbalance. Signal events of interest are those with a photon of initial state radiation (ISR) or of the $WW\gamma$ coupling. The $WW\gamma$ coupling introduces a destructive interference with the ISR diagram, and leads to cancellation of $W\gamma$ production with *zero amplitude* at $\cos\theta_{\bar{q},\gamma} = \pm 1/3$, where $\theta_{\bar{q},\gamma}$ is the photon scattering angle to the incoming anti-quarks.

Mode	$\sqrt{s} = 1.96$ TeV	$\sqrt{s} = 14$ TeV
$W^{\pm}\gamma$	19.3	451
$Z\gamma$	4.74	219

Table 1: The Standard Model total cross-sections (pb) calculated to NLO [8] for $W\gamma$ and $Z\gamma$ with $E_T^{\gamma} > 7$ GeV and $\Delta R(\ell, \gamma) > 0.7$.

Events with a photon of final state radiation (FSR) are considered as background. A FSR photon can be distinguished by its low p_T and small angle to the lepton from which it is radiated, and in addition, by the invariant masses of the photon with observable particles. Illustrated in Figure 3 (left) are the transverse mass distributions of the CMS study [9] for signal events with a ISR (or $WW\gamma$) photon and background of radiative W decays with a FSR photon. The radiative W decays are distinguishable for having transverse mass distributed around the W boson mass. Contribution of anomalous TGC are searched for events with a high transverse mass or a high p_T photon, in which the background is dominated by inclusive $W + jets$ events with jet remnants like π^0 faking photons. Fake photons are suppressed by requiring isolation and subdetector measurements of the photon shower profiles.

Selection of $W\gamma$ events has been studied with a cut-based method by CMS and a Boosted

Decision Tree (BDT) algorithm [10] by ATLAS. The event triggers are evaluated with realistic detector simulations. The BDT selection requires a low $p_T(\gamma)$ threshold of 10 GeV to optimize event yield for early LHC running. The expectations for 1 fb^{-1} of data, at 65% signal efficiency, are 1604 (2166) events for the electron (muon) channels, and the corresponding background are 1180 (1340) events, respectively [6].

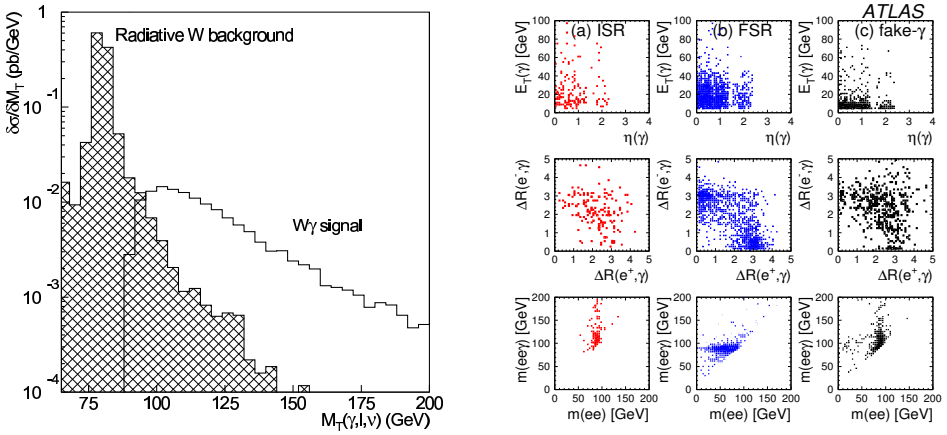

Figure 3: Left: Transverse mass $M_T(l,\nu,\gamma)$ of $W\gamma$ events with a ISR (or $WW\gamma$) photon or of radiative W decays with a FSR photon (hatched) [9]. Right: Distributions of $Z(ee)\gamma$ event variables for signal with an ISR photon, and backgrounds with a FSR or a fake photon [6].

The $Z\gamma$ candidates are selected for inclusive $e^+e^-\gamma$ and $\mu^+\mu^-\gamma$ events with an ISR photon. The Monte Carlo used does not include $ZZ\gamma$ nor $Z\gamma\gamma$ vertices as neutral TGCs are forbidden at tree-level. The Z boson is reconstructed using the pair of most energetic leptons of the same flavor with opposite charges. Sources of background are inclusive Z production with a FSR photon radiated by a Z decay lepton ($Z \to l^+l^-\gamma$); and inclusive $Z + jets$ with a fake photon reconstructed.

Distributions of $Z\gamma$ signal and background events are shown in Figure 3 (right) for some of the event variables. The invariant mass distributions of the lepton-pair and photon are distinguishable for radiative Z decays with $m(l^+l^-\gamma)$ consists with the Z mass. The opening angles of the photon to leptons provide additional selection for FSR photons. Events with fake photons resemble the signal in the invariant mass and angular distributions. The ATLAS study has conducted a BDT algorithm to optimize $Z\gamma$ selection from background with a fake photon. The expected number of events for 1 fb^{-1} of data, at 67% signal efficiency, are 367 (751) events for electron (muon) channels with 187 (429) background events, respectively.

Unlike the $W\gamma$ measurement which suffers under the undetected neutrino, all observables in the $Z\gamma$ measurement are fully determined, and the cross section measurement is thus complementary to $W\gamma$ for the contribution of $WW\gamma$ coupling. $W\gamma$ and $Z\gamma$ are two of the diboson processes having large production cross sections. With the initial LHC running of an integrated luminosity of 0.1 fb^{-1}, hundreds of selected events are expected and the detection significance will be greater than 10 σ.

4 Sensitivity to anomalous couplings

A signature for anomalous triple gauge boson couplings is an increased cross-section with respect to the Standard Model prediction, especially at high vector boson p_T. The effective Lagrangian for TGCs is formulated assuming Lorentz and electromagnetic gauge invariance. The $WW\gamma$ coupling that attributes to $W\gamma$ production is parameterized with two parameters, κ_γ and λ_γ, and the Standard Model values are $\Delta\kappa_\gamma \equiv \kappa_\gamma - 1 = 0$, and $\lambda_\gamma = 0$ [11]. The neutral $ZZ\gamma$ and $Z\gamma\gamma$ couplings in $Z\gamma$ production are parameterized with eight parameters, h^V_{i0} ($i = 1...4$, and $V = Z, \gamma$). CP invariance and parity conservation forbids h^V_{10} and h^V_{20}, and the Standard Model values at tree-level are all zero.

With anomalous coupling, the diboson production amplitudes grow with energy. This is avoided by scaling the TGC parameters with a form factor, e.g. $\Delta\kappa(\hat{s}) = \Delta\kappa/(1 + \hat{s}/\Lambda^2)^n$ [12], where $\sqrt{\hat{s}}$ is the invariant mass of the vector-boson pair and $\Delta\kappa(0)$ is the coupling value in the low energy limit. The cutoff parameter, Λ, is the mass scale where the new phenomenon responsible for the anomalous couplings would be directly observable. The value is chosen such that the extracted limit from data for a certain diboson production process is less than the unitarity limit. With 0.1-1.0 fb^{-1} of integrated luminosity at early LHC running, Λ values of 2-3 TeV are used.

The photon transverse energy in $W\gamma$ and $Z\gamma$ productions is the most sensitive variable to anomalous couplings and is directly measurable. The sensitivity to anomalous TGCs is obtained by comparing the measured production cross-section and the photon $p_T(\gamma)$ distribution to models with anomalous TGCs. The Monte Carlo generator of Baur *et al.* [8] is used to compute differential cross sections over a grid of points in the parameter space. Distributions of the fully simulated Standard Model events are re-weighted by the generator calculations of $d\sigma(TGC)/d\sigma_{SM}$. A binned likelihood fitting procedure on the photon transverse energy $E_{\rm T}(\gamma)$ spectra is followed to extract the 95% C.L. intervals of TGC parameters. The production of $W\gamma$ events involves exclusively the $WW\gamma$ triple gauge coupling. The one and two-dimensional limits extracted for $\Delta\kappa_\gamma$ and λ_γ are shown in Figure 4 for $p_T(\gamma)$ distribution of the ATLAS

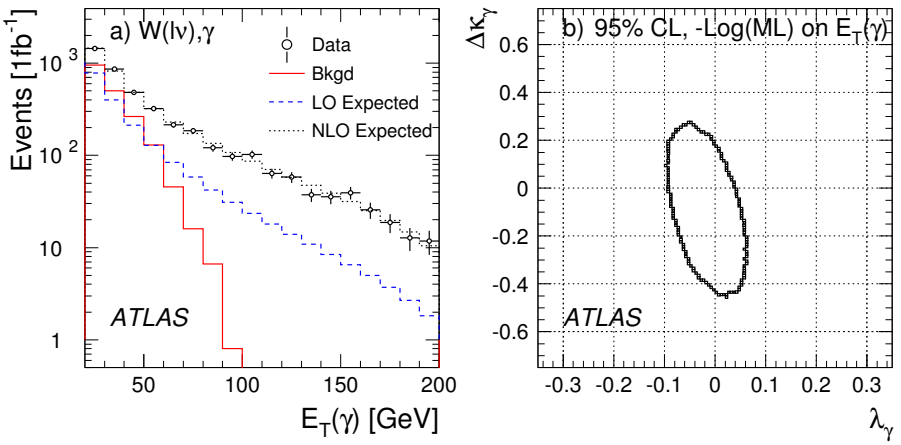

Figure 4: The photon transverse energy distributions of $W(l\nu)\gamma$ ($l = e, \mu$) events, and the 95 % confidence contour extracted in the $\Delta\kappa_\gamma$, λ_γ parameter space ($\Lambda = 2$ TeV) for 1 fb^{-1} of data [6].

study [6]. The signal expectations at the tree-level and NLO are plotted as the dashed and dotted lines. The 95% confidence contour obtained is plotted in the $\Delta\kappa_\gamma$, λ_γ parameter space. The sensitivities to λ_γ and $\Delta\kappa_\gamma$ for 1, 10 and 30 fb^{-1} are listed in Table 2.

Anomalous $ZZ\gamma$ and $Z\gamma\gamma$ couplings would enhance the event rates in the large $p_T(\gamma)$ region. This is shown in Figure 5 for the $p_T(\gamma)$ distributions with a non-zero h_{40}^Z, and the dependence on the Λ scale is illustrated for $\Lambda = 2$ and 3 TeV. The sensitivity to anomalous couplings is studied by CMS [13] for two of the CP conserving parameters, h_{30}^Z and h_{40}^Z, with several Λ scales. The binned likelihood fits have been conducted for the $p_T(\gamma)$ distributions normalized to 10 and 100 fb^{-1} of data. The confidence contours of 68%, 90% and 95% with $\Lambda =$ 3 TeV are shown in Figure 5. The one dimensional limits obtained are listed in Table 3.

	1 fb^{-1}	10 fb^{-1}	30 fb^{-1}
$\Delta\kappa_\gamma$	[-0.43, 0.20]	[-0.26, 0.07]	[-0.11,0.05]
λ_γ	[-0.09, 0.04]	[-0.05, 0.02]	[-0.02,0.01]

Table 2: One dimensional limits (95% C.L.) for $WW\gamma$ coupling with $\Lambda = 2$ TeV [6].

Λ (TeV)		10 fb^{-1}	100 fb^{-1}
2	$h_{30}^Z(10^{-3})$	[-5.2, 5.2]	[-2.4, 2.2]
	$h_{40}^Z(10^{-5})$	[-6.4, 6.8]	[-2.9, 3.2]
3	$h_{30}^Z(10^{-3})$	[-2.3, 2.3]	[-1.5, 1.5]
	$h_{40}^Z(10^{-5})$	[-1.9, 1.8]	[-0.97, 0.85]
6	$h_{30}^Z(10^{-3})$	[-1.2, 1.3]	[-0.65, 0.64]
	$h_{40}^Z(10^{-5})$	[-0.42, 0.40]	[-0.18, 0.17]

Table 3: One dimensional limits (95% C.L.) for CP-conserving TGC parameters h_{30}^Z and h_{40}^Z in $Z\gamma$ production [13].

Both ATLAS and CMS have demonstrated significantly higher sensitivities to anomalous TGCs than those reported by the LEP and Tevatron experiments [14, 15]. The confidence intervals for parameters in $W\gamma$ and $Z\gamma$ productions are expected to be improved with 1 fb^{-1} of the early running data.

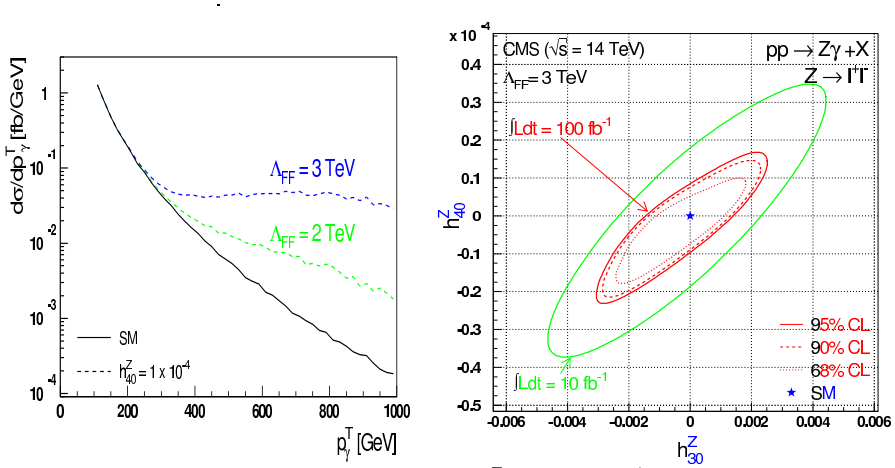

Figure 5: Left: photon p_T of $Z\gamma$ production with $h_{40}^Z = 1 \times 10^{-4}$ and $\Lambda = 2$ and 3 TeV. Right: the sensitivity contours in the h_{30}^Z, h_{40}^Z parameter space obtained with $\Lambda = 3$ TeV for 10 and 100 fb^{-1} of data [13].

5 Summary

Detailed data analyses are being eagerly pursued for the LHC start up. Studies of inclusive W and Z events are among the most urgent for measurements of Standard Model physics in a much extended kinematic region. Diboson events of $W^{\pm}\gamma$ and $Z\gamma$ signals will be established in leptonic channels with the initial statistics of 0.1 fb^{-1}. Measurement of high p_T photons will be sensitive to anomalous coupling which leads to indications of new physics phenomena. Confidence intervals on anomalous couplings are expected to be significantly improved with respect to the present values.

References

[1] ATLAS Collab., JINST 3 S08003 (2008).

[2] CMS Collab., JINST 3 S08004 (2008).

[3] J. Ellison and J. Wudka, Annu. Rev. Nucl. Part. Sci. **48**, 33 (1998), and references therein.

[4] A. Barroso *et al.*, Z Phys. **C28**, 149 (1985);

[5] CMS Collab., CERN-LHCC-2006-021; CMS PAS EWK-08-005 (2008); CMS PAS EWK-07-002 (2008).

[6] ATLAS Collab., CERN-OPEN-2008-020, arXiv:0901.0512.

[7] J. Alcoraz, CMS Collab., CMS NOTE 2006/082.

[8] U. Baur, T. Han and J. Ohnemus, Phys. Rev., **D50**, 1917 (1994); Phys. Rev., **D51**, 3381 (1995); Phys. Rev., **D53**, 1098 (1996); Phys. Rev., **D57**, 2823 (1998).

[9] C.K. Mackay, P.R. Hobson, CMS Note 2001/056.

[10] H.-J. Yang *et al.*, Nucl. Instr. and Meth. **A 555** 370 (2005); Nucl. Instr. and Meth. **A 543** 577 (2005); Nucl. Instr. and Meth. **A 574** 342 (2007).

[11] F. Larios, M.A. Perez, G. Tavares-Velasco, J.J. Toscano, Phys. Rev. **D63**, 113014 (2001);
U. Baur and D. Zeppenfeld, Phys. Lett. **B201**, 383 (1988);
K. Hagiwara , R.D. Peccei, D. Zeppenfeld and K.Hikasa Nucl Phys **B282** 253 (1987);
K. J. F. Gaemers and G.J. Gounaris Z Phys **C1** (1979) 259.

[12] T. G. Rizzo Phys. Rev. **D32** 43 (1985);
U. Baur, E. Berger, Phys. Rev. **D47** 4889 (1993).

[13] Th. Müller, D. Neuberger, W.H. Thümmel, CMS Note 2000/017.

[14] ALEPH Collab., Phys. Lett. **B 614** 7 (2005);
DELPHI Collab., Eur. Phys. J. **C 51** 525 (2007).

[15] D0 Collab., Phys. Rev. Lett. **100** 241805 (2008);
D0 Collab., Phys. Lett. **B 653** 378 (2007);
CDF Collab., Phys. Rev. Lett. **94** 041803 (2005).

Photoproduction of Single Top at LHC

Vincent Lemaitre, Jérôme de Favereau, Sverine Ovyn, Krzysztof Piotrzkowski

Center for Particle Physics and Phenomenology (CP3)
Université catholique de Louvain
Chemin du cyclotron 2, 1348 Louvain-la-Neuve, Belgium

DOI: http://dx.doi.org/10.3204/DESY-PROC-2009-03/Lemaitre

High-energy photon-proton interactions at the LHC offer interesting possibilities for the study of the electroweak sector up to TeV scales and searches for processes beyond the Standard Model. In particular, after 10 fb-1, the analysis of W associated single top photoproduction events can provide a sensitivity to $|V_{tb}|$ comparable to the one obtained using the standard single top production in pp collisions. Study of photoproduction at the LHC provides also an ideal framework for observing anomalous productions of single top induced by Flavour-Changing Neutral Currents.

1 Introduction

A significant fraction of pp collisions at the LHC will involve (quasi-real) photon interactions occurring at energies well beyond the electroweak energy scale [1]. The LHC can therefore be considered to some extend as a high-energy photon-proton collider. In a recent paper [2], several studies of high energy photon interactions at the LHC were reported. In particular, it is shown that a large variety of $pp(\gamma g/q \to X)pY$ processes have sizable cross section and could therefore be studied during the very low and low luminosity phases of LHC. Interestingly, the SM inclusive photoproduction cross section of top quark reaches 2.5 pb and the fraction of single top to top quark pair cross sections is close to one. This large ratio offers an interesting framework for the studies of top properties which can only be addressed from single top production mechanism such as the CKM $|V_{tb}|$ matrix element. Probing possible anomalous photoproduction of single top via flavour-changing neutral currents (FCNC) is also particularly relevant at the LHC since the expected cross section calculated with the present limits on the anomalous couplings $k_{tq\gamma}$ is close to 10 pb.

2 Tagging photoproduction

Tagging is essential for the extraction of high energy photon-induced interactions from the large parton-parton interactions. Photon-induced interactions are characterised by a large pseudo-rapidity region completely devoid of any hadronic activity. This region is usually called *large rapidity gap* (LRG).

2.1 Very low luminosity phase ($< 10^{33}$ cm^{-2}s^{-1})

The number of extra interactions per beam crossing (*pile-up*) is negligible at very low luminosity. Thanks to the colour flow in *pp* interactions between the proton remnant and the hard hadronic final states, a simple way to suppress generic *pp* interactions is to require LRGs by looking at the energy measured in the forward detector containing the minimum forward activity (between $3 < |\eta| < 5$), denoted as E^{FCal}. For a maximal allowed energy of 50 GeV, a typical reduction factor of 10^{-3} and 10^{-2} for a parton-parton $t\bar{t}$ and Wj production is expected, respectively. A total integrated luminosity of 1 fb^{-1} for such no *pile-up* condition seems to be a realistic assumption. The rejection can be further improved by using an exclusivity condition requiring no additional tracks (*i.e.* excluding isolated leptons and jet cones) with $p_T > 0.5$ GeV/c and $1 < \eta < 2.5$ in the hemisphere where the rapidity gap is present. It should be pointed out that this condition can also be used during the higher luminosity phases if proper vertex determination is possible. The efficiency of rapidity gap and exclusivity conditions for signal processes drops roughly by a factor of two while the reduction factors for parton-parton reactions are better than 10^{-3}.

2.2 Low luminosity phase

When event *pile-up* increase to much, the LRG technique cannot be used, and the exclusivity condition alone cannot reduce partonic backgrounds to a level that allows proper signal extraction. Therefore, in addition to the exclusivity condition, the use of *very forward detectors* (VFD) to detect the escaping proton is mandatory in order to retain *pp* background low. However, VFDs cannot provide a total rejection of the partonic processes because of the presence of single diffractive events in the *pile-up*. Hence, the overall event mimics well a photoproduction event. The probability of such accidental coincidences provides directly the rejection power of VFDs. For instance, the case for which VFD stations would be put at 220 m and 420 m from the interaction point has been computed and provides rejection factors of 11 and 5.6 for a luminosity of 10^{33} cm^{-2} s^{-1} and 2×10^{33} cm^{-2} s^{-1}, respectively.

3 Cross section and event simulation

All cross sections and event samples used in this analysis have been obtained using the adapted MadGraph/MadEvent [4, 5] and CalcHEP [6] programs (except for some induced proton-proton induced backgrounds where Alpgen was used). Cross sections are therefore calculated at Leading order and do not include any survival probability factor. In order to take into account the effect of jet algorithms and the efficiency of event selection under realistic experimental conditions, the generated events were passed: (1) to PYTHIA 6.227 [7] and (2) a fast simulation of a typical LHC multi-purpose detector.

The detector response simulation is performed using Delphes assuming geometrical acceptance of sub-detectors and their finite energy resolutions. The default card provided to simulate the CMS detector has been used and the jets are reconstructed using the MidPointCone algorithm with a cone radius of $\Delta R = 0.7$. A proper simulation of the proton propagation in the LHC beamline performed using HECTOR [11], shows that using detectors stations at 220 m and 420 m from the IP, one selects events for which the proton has lost between 20 GeV and 800 GeV. Magnetic field was also taken into account when evaluating the forward energy deposits. The transverse missing energy is calculated from the calorimetric towers. When heavy

flavour tagging is required, a tagging efficiency of 40% , 10%, and 1% has been applied for b-, c-, and light- jets respectively.

Another possible background source not simulated in this analysis is the Inelastic photoproduction, in which the proton having emitted a photon does not survive the interaction. It should be stressed that Inelastic photoproduction would actually increase the cross section of both signal and photon-induced backgrounds.

4 W associated single top photoproduction

Photoproduction of single top is dominated by t-channel amplitudes when the top quark is produced in association with a W boson (Fig. 1). These amplitudes are all proportional to the CKM $|V_{tb}|$ matrix element.

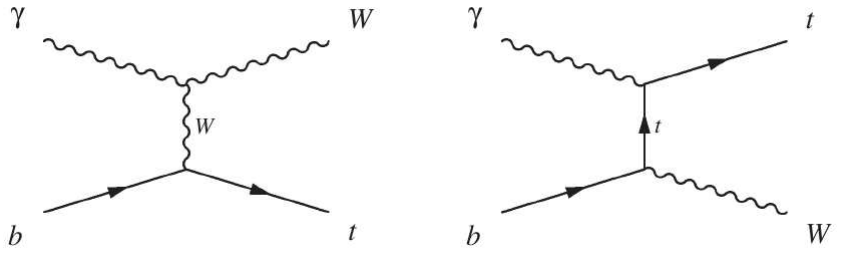

Figure 1: Diagrams for the dominant contribution to the SM production of single top quark.

The $pp(\gamma q \to Wt)pY$ process results in a final state of two on-shell W bosons and a b quark. The studied topologies are ℓbjj for the semi-leptonic decay of the two W bosons and $\ell\ell b$ for the di-leptonic decay, where $\ell = e,\ \mu$ or τ. The cross sections times branching ratios of these final states are 440 fb and 104 fb respectively. The dominant irreducible background of both channels is expected to stem from the $t\bar{t}$ production, where a jet misses the acceptance region. Other backgrounds are $Wb\bar{b}q'$, $Wjjj$ and WWq' processes produced either from photon-proton interactions, or from proton-proton interactions. Their cross sections including the branching ratio into the desired topology are summarised in Tab. 1.

4.1 Signal selection

For the semi-leptonic final state, the following "acceptance cuts" are applied: one isolated lepton with $p_T^\ell > 20$ GeV/c; exactly 3 jets with $p_T^j > 30$ GeV/c. Lepton isolation requires that there is no other charged particles with $p_T > 2$ GeV/c within a cone of $\Delta R < 0.5$ around the lepton. Partonic backgrounds are reduced by requiring the E^{FCal} condition with a cut value of 30 GeV as well as the exclusivity condition (γp cuts).Moreover, exactly one of the three jets must be identified as a b-jet (b-tagged). In addition, the invariant mass of the two non b-tagged jets must satisfy $|m_W - m_{jj}| < 20$ GeV/c^2 and the scalar sum of the visible particles must be smaller than 230 GeV/c ("Final cuts").

After this selection, the final cross section times branching ratio for the signal is reduced to 5.6 fb, against 5.2 fb for the backgrounds, 52 % of which comes from partonic processes. The

Process		$\sigma\times$ Br [fb]	sample size
$\gamma p \rightarrow$	$t\bar{t}(2\ell)$	159.1	200 k
	$t\bar{t}(1\ell)$	671.8	179 k
	$WWq'(2\ell)$	62.5	70 k
	$Wjjj$	2793.0	50 k
	$Wb\bar{b}q'$	55.2	10 k
$pp \rightarrow$	$t\bar{t}(2\ell)$	77.7×10^3	130 k
	$t\bar{t}(1\ell)$	328×10^3	390 k
	$W2j$	2.4×10^6	830 k
	$W3j$	6.9×10^5	264 k
	$W4j$	1.7×10^5	105 k
	$Wb\bar{b}j$	2.7×10^5	120 k
	tj	6.7×10^3	100 k
	$WWj(2\ell)$	5.2×10^3	100 k

Table 1: Background processes used in the semi-leptonic and di-leptonic channels. Cross-sections include generation cuts of $p_T > 1$ GeV/c for q' and $p_T > 10$ GeV/c for jets. Branching ratios quoted in parenthesis are also taken into account. The $W2j$, $W3j$ and $W4j$ have been generated using Alpgen with a minimal p_T^{cut} on the jets of 20 GeV/c. Branching ratio of the W boson into leptons (e, μ or τ) is taken into account.

$t\bar{t} \rightarrow \ell\ell bb$ topology is also taken into account in the backgrounds. Details are given in Tab. 2. The visible cross sections obtained using the expected rejection of 11 for the low luminosity phase $\mathcal{L} = 10^{33}$ cm^{-2} s^{-1} are also shown. In this case, the large number of partonic events is mainly due to $pp \rightarrow W$jets events.

σ [fb]		signal	γp backgrounds	pp backgrounds
Production		440.6	3.6×10^3	74×10^6
Acceptance cuts		39.1	152.5	126×10^3
γp cuts	Very low $\mathcal{L}$	27.4	90.7	127.1
	Low $\mathcal{L}$	27.4	85.5	873.7
Final cuts	Very low $\mathcal{L}$	5.6	2.4	2.8
	Low $\mathcal{L}$	5.6	2.2	18.6

Table 2: List and effect on the visible cross-section of all applied cuts on the $\gamma p \rightarrow Wt \rightarrow \ell\nu jjb$ events and their relevant photon-induced and proton-induced backgrounds. Very low luminosity refer to $\mathcal{L} < 10^{33}$ cm^{-2} s^{-1} and Low luminosity refers to $\mathcal{L} = 10^{33}$ cm^{-2} s^{-1}.

The procedure to select the di-leptonic topology is simpler: it requires two isolated lepton with $p_T > 20$ GeV/c; one b-tagged jet with $p_T^b > 30$ GeV/c and no additional jets with $p_T^j > 30$ GeV/c. The same rapidity gap and exclusivity condition as in the semi-leptonic topology are applied. Signal cross section times branching ration for this topology is 5.9 fb after cuts, for a background cross section of 3.1 fb with less than 40 % of partonic contribution (32%). Details are in Tab. 3. During the phase of low luminosity, using forward proton taggers, event if the number of partonic event is less important than for the semi-leptonic case, the signal to

background ratio decreases from 1.6 to 0.4.

σ [fb]		signal	$t\bar{t}$		WWq'	
			γp	pp	γp	pp
Production		104.3	159.1	77×10^3	62.5	5×10^3
Acceptance cuts		15.6	10.5	3.4×10^3	4.2	486
γp cuts	Very low $\mathcal{L}$	14.3	4.9	1.8	4.0	0.6
	Low $\mathcal{L}$	12.8	4.8	24.0	3.4	4.2
Final cuts	Very low $\mathcal{L}$	5.9	2.0	0.8	0.1	0.2
	Low $\mathcal{L}$	5.0	1.9	9.1	0.1	1.1

Table 3: List and effect on the visible cross-section of all applied cuts on the $\gamma p \to Wt \to \ell\nu\ell\nu b$ events and their relevant photon-induced and proton-induced backgrounds. Very low luminosity refer to $\mathcal{L} < 10^{33}$ cm^{-2} s^{-1} and Low luminosity refers to $\mathcal{L} = 10^{33}$ cm^{-2} s^{-1}.

4.2 Systematic errors

When no estimate on the theoretical uncertainties is found in the literature for photon-proton cross sections, a conservative attitude was adopted in taking the same uncertainty as for the corresponding partonic process. Partonic cross sections after cuts are considered to be known to the 2 % level as the cross section without application of the E^{FCal} and exclusivity conditions can be measured directly and the error on the effect of these cuts is computed separately. The most relevant detector systematics are expected to be the uncertainties on the Jet Energy Scale (JES), the number of reconstructed tracks in order to apply the exclusivity condition and the energy measurement in the forward calorimeter. The uncertainty due to JES is expected to be 5% for jets with $p_T < 30$ GeV/c, 3% for jets with $p_T > 50$ GeV/c and a linear interpolation between these two boundaries. The systematic uncertainty due to the exclusivity condition is estimated by moving the track reconstruction efficiency, fixed to 90 % by default, to 85% and 95%. Finally, the cut on the energy in the forward calorimeter of the gap side has been moved by 10 % upwards and downwards in order to have an idea of the E^{FCal} condition uncertainty. The b-tagging uncertainty is taken as $\pm$5%, while the error on mis-tagging is assumed to be 10%. The uncertainty due to luminosity is expected to be 5%.

All systematic errors between the different samples have been assumed to be 100% correlated and are therefore applied simultaneously on all samples except for the theoretical errors. The different error sources are supposed to be uncorrelated and are therefore added quadratically. For both topologies, the error is dominated by the rapidity gap and exclusivity cuts uncertainties on the pp induced backgrounds.

4.3 Results

A simple propagation of errors shows that the relative uncertainty on the measured cross section is given by the following formula :

$$\frac{\Delta\sigma_{obs}}{\sigma_{obs}} = \frac{\Delta\varepsilon}{\varepsilon} \oplus \frac{\Delta L}{L} \oplus \left[\frac{B}{S}\right] \frac{\Delta B}{B} \oplus \left[\frac{B}{S} + 1\right] \frac{\Delta N}{N},$$

where $\Delta\varepsilon$, ΔL and ΔB are the systematic errors estimates on the signal selection efficiency, the luminosity and the background cross section respectively and ΔN is the statistical error on the observed number of events. The uncertainties obtained for the di-leptonic and the semi-leptonic topologies after an integrated luminosity of 10 fb^{-1} are summarised in Tab. 4. Comparing these errors on the cross section to the expected one from parton-parton interactions, 10 % in the *t-channel*, 31 % in the *s-channel*, 25.8 % for the di-leptonic and 22.6 % for the semi-leptonic topologies in the *tW-channel* [8] using the same integrated luminosity, we can conclude that photoproduction is at least competitive with partonic-based studies and that the combination of both studies could lead to significant improvement of the error.

Error	Di-leptonic [%]		Semi-leptonic [%]	
$\mathcal{L}$	Very low	Low	Very low	Low
$\frac{\Delta\varepsilon}{\varepsilon}$	5.0	5.02	9.2	9.1
$\frac{\Delta L}{L}$	5.0	5.0	5.0	5.0
$\left[\frac{B}{S}\right]\frac{\Delta B}{B}$	10.3	25.9	19.5	68.1
$\left[\frac{B}{S}+1\right]\frac{\Delta N}{N}$	16.4	26.2	9.7	29.1
total	20.6	37.6	27.9	74.8

Table 4: Contributions to the total cross-section measurement error.

Taking into account a 5% uncertainty on the theoretical total single top cross section,the expected error on the measurement of $|V_{tb}|$ is 14.3% for the semi-leptonic channel and 10.7% for the di-leptonic one after 10 fb^{-1} of integrated luminosity. Assuming the same integrated luminosity during the low luminosity phase of the LHC ($\mathcal{L} = 10^{33}$ cm^{-2} s^{-1}) the two obtained values are respectively 37.5% and 19.0%.

5 Anomalous single top photoproduction

FCNC appear in many extensions of the Standard Model, such as two Higgs-doublet models or R-Parity violating supersymmetry. Such a FCNC transition can occur in the process of single top photoproduction via anomalous couplings, as shown on Fig. 2. The effective Lagrangian for these anomalous coupling can be written as [9]:

$$\mathcal{L} = iee_t\bar{t}\ \frac{\sigma_{\mu\nu}q^\nu}{\Lambda}\ k_{tu\gamma}uA^\mu + iee_t\bar{t}\ \frac{\sigma_{\mu\nu}q^\nu}{\Lambda}\ k_{tc\gamma}cA^\mu + h.c.,$$

where $\sigma^{\mu\nu}$ is defined as $(\gamma^\mu\gamma^\nu - \gamma^\nu\gamma^\mu)/2$, q^ν being the photon 4-vector and Λ an arbitrary scale, conventionally taken as the top mass. The anomalous couplings $k_{tu\gamma}$ and $k_{tc\gamma}$ are real and positive such that the cross section takes the form

$$\sigma_{pp\to t} = \alpha_u\ k^2_{tu\gamma} + \alpha_c\ k^2_{tc\gamma}.$$

The computed α parameters obtained using CalcHEP are $\alpha_u = 368$ pb and $\alpha_c = 122$ pb. The present best upper limit on $k_{tu\gamma}$ is around 0.14, depending on the top mass [10] while the anomalous coupling $k_{tc\gamma}$ has not been probed yet.

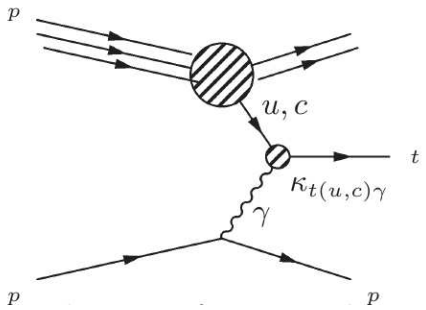

Figure 2: Main diagram for FCNC production of single top.

The studied final state consists in one hard lepton and missing transverse energy issued from the W boson coming from the top quark decay, which produced as well a b quark. The dominant background processes for this final state come from events with one W boson and one jet mis-tagged as a b-jet. We assumed no contribution of genuine b-jets since its cross section is three orders of magnitude lower than the cross section of the Wc topology. Backgrounds cross sections and sample sizes are given in Tab. 5.

Process	σ [fb]	sample size
$\gamma p \rightarrow Wj$	41.6×10^3	100 k
Wc	11.5×10^3	100 k
$pp \rightarrow Wj$	77.3×10^6	100 k
Wc	8.8×10^6	100 k
Diffractive W	1.3×10^6	100 k

Table 5: Background processes used for the analysis of the anomalous top photoproduction. Cross-sections include the branching ratio of the W boson to electron or muon and generation cuts of $p_T > 10$ GeV/c for leptons and $p_T > 20$ GeV/c for jets (j=u,d,s,and g).

5.1 Signal selection

Preselection cuts require the presence of exactly one jet with $p_T > 45$ GeV/c, one isolated lepton with $p_T > 20$ GeV/c, and a transverse missing energy above 15 GeV. These cuts designed to reject pp interactions in the scheme of zero pile-up conditions are applied with a maximum allowed energy in the forward hemisphere of 20 GeV. An event is selected if the only allowed jet is tagged as a b-jet and a top candidate is also reconstructed from the W-boson and the "b-jet" with a mass between 140 GeV and 210 GeV.

In order to extend this study in presence of event *pile-up*, the use of the E^{FCal} selection cut is replaced by the tagging of the escaping proton by VFDs as described in section 2. As stated before, the reduction of the partonic background is less effective than the one obtained in zero *pile-up* condition. However, another advantage of the VFD is that, considering a well designed reconstruction algorithm, the energy loss of the proton that hits the VFD can be determined and

used to improve the selection of photoproduction processes. An additional cut is therefore used that reconstructs the top quark longitudinal momentum both from the central event and from the proton energy loss. The difference between these two values allows to distinguish between photoproduction events for which they are close, and partonic events for which the distance between them is distributed randomly.

5.2 Systematic errors

The same systematic uncertainties as in the case of the SM single top study have been estimated. Once again, the rapidity gap and exclusivity condition account for the most important part of it. In the case of low luminosities (corresponding here to $\mathcal{L} = 2 \times 10^{33}$ cm^{-2} s^{-1}) for which the VFDs where used, no systematic error is assumed on this tagging. The detail of all errors for both scenario's are given on Tab. 6. Signal systematics stay unaffected by the scenario change, as the error due to the LRG requirement is negligible. The uncertainty on the diffractive cross section has been set to 50%.

Error	signal (%)	Background (%)				
		$\gamma p \to Wj$	$\gamma p \to Wc$	$pp \to Wj$	$pp \to Wc$	Diffr. W
JES	1.6	2.0	3.0	4.0	3.1	-
Exclusivity	1.0	1.0	1.0	10.0	10.0	-
LRG	0.0	0.0	0.0	20.0	20.0	-
Luminosity	5.0	5.0	5.0	5.0	5.0	-
b-tagging	5.0	10.0	5.0	10.0	5.0	-
Theoretical	5.0	5.0	5.0	2.0	2.0	50
total	8.9			18.6		

Table 6: Systematic errors on signal and backgrounds at very low luminosity.

5.3 Results

Using the LRG requirement for an integrated luminosity of 1 fb^{-1}, one gets the following number of events (for $k_{tu\gamma} = 0.15$, $k_{tc\gamma} = 0$) : 129 signal events, 13.2 background events from photoproduction, 10 events from pp induced backgrounds and 12 diffractive events. The corresponding expected 95% C.L. limit for the anomalous couplings are: $k_{tu\gamma} < 0.024$, $k_{tc\gamma} < 0.039$. These limits can be further improved by a factor two when collecting a few then of inverse femptobarns at low luminosity regime.

6 Conclusions and prospects

Top quark photoproduction cross section is large and, in particular, the Wt associated production can be studied with a much better signal to noise ratio as the corresponding process induced by generic pp collisions. This process could permits, for instance, to extract $|V_{tb}|$ with a similar accuracy but with an error which is dominated by the statistical error.

Photoproduction at LHC can probe electroweak and BSM theories at c.m.s energy up to 2 TeV with sizable cross sections. For instance, anomalous single top photoproduction has a similar sensitivity to anomalous FCNC couplings than analyses based on rare top decays.

However, the studies presented in this paper will be refined when full detector simulation will be used, providing a better estimate of the systematic errors. Also, studying the influence of diffractive backgrounds on $|V_{tb}|$ is an important part of the work to be done, as well as the evaluation of the contribution of inelastic photon emissions to both signal and backgrounds.

References

[1] K. Piotrzkowski, Phys. Rev. D**63**, (2001) 071502.

[2] J. de Favereau et al, to be published

[3] The CMS Collaboration, J. Phys. G**34** (2007) 1237-1240.

[4] J. Alwall et al., JHEP**09**, (2007) 028.

[5] T. Stelzer and W.F. Long, Phys.Commun.**81**, (1994) 357-371.

[6] A. Pukhov, Nucl. Inst. Meth A**502**, (2003) 596-598.

[7] T. Sjöstrand et al., Comput. Phys. Commun. **135**, (2001) 238.

[8] The CMS Collaboration, J. Phys. G**34** (2007) 1227-1237.

[9] T. Han and J.L. Hewett, Phys. Rev. D**60**, (1999) 074015.

[10] S. Chekanov et al., Phys. Lett. B**559**, (2003) 153-170.

[11] J. de Favereau de Jeneret, X. Rouby, K. Piotrzkowski, JINST 2 P09005, arXiv:0707.1198v1 [physics.acc-ph] (CP3-07-13).

Two-Photon Exclusive Production of Supersymmetric Pairs at the LHC

Nicolas Schul

Center for Particle Physics and Phenomenology (CP3), Université catholique de Louvain, 1348 Louvain-la-Neuve, Belgium

DOI: http://dx.doi.org/10.3204/DESY-PROC-2009-03/Schul

The two-photon production of charged supersymmetric pairs at the LHC has a unique signature of two leptons, large missing energy and two forward scattered protons. For low-mass supersymmetric scenarios, significant cross–sections are predicted for the MSSM. Proton kinematics information from very forward detectors (VFD) would allow for a precise mass reconstruction of right-handed sleptons and the LSP. For high luminosity runs, the probability to have accidental coincidence within central and very forward detectors increases although it can be reduced applying exclusivity conditions.

1 $\gamma\gamma$ physics at the LHC

In addition to the usual parton-parton interactions, a significant fraction of the *pp* collisions at the LHC will also involve photon-interactions. The available relative luminosity reaches 1% for photon-photon centre-of-mass energies $W_{\gamma\gamma} > 23$ GeV and still 0.1% for $W_{\gamma\gamma} > 225$ GeV [1]. Among the whole photon interactions at the LHC, the study of pair production of charged particles, including supersymmetric particles, is one of the most interesting cases since the QCD background is suppressed.

Exclusive two-photon interactions at the LHC provide clean detection conditions thanks to striking experimental signatures in absence of proton remnants: two very forward scattered protons, remaining intact after photon-exchange, and large rapidity gaps in the forward regions due to the exchange of a colorless object.

2 Detection of exclusive supersymmetric pairs

In $\gamma\gamma$ collisions, the production and decay mechanisms for low mass supersymmetry are simple and without decay chain problems. Also two-photon pair productions of left- and right-handed sleptons ($\tilde{e}_L^+$, $\tilde{\mu}_L^+$, $\tilde{e}_R^+$ $\tilde{\mu}_R^+$), staus ($\tilde{\tau}_1^+$, $\tilde{\tau}_2^+$), charginos ($\tilde{\chi}_1^+$, $\tilde{\chi}_2^+$) and charged Higgs bosons (H^+) have significant cross-sections of femtobarn-level. As an example for a low-mass supersymmetric scenario, the LM1 benchmark point in the mSugra theory [2] is used in the following discussion. The total cross-section for sparticle pair production is 2.23 fb in that specific model, the major contribution to signal being the two-photon production of scalars $\tilde{\ell}_R^+\tilde{\ell}_R^-$ ($m(\tilde{\ell}_R^+) =$ 118 GeV) and fermions $\tilde{\chi}_1^+\tilde{\chi}_1^-$ ($m(\tilde{\chi}_1^+) = 178$ GeV) as it is shown in Table 1. The Lightest

Supersymmetric Particle (LSP) is the first neutralino in that model ($m(\tilde{\chi}_1^0) = 96$ GeV). Details on model parameters and on mass spectrum can be found in [3].

Assuming a general multi-pupose LHC detector as CMS or ATLAS and full-set of dedicated very forward detectors to tag photon-interaction [4, 5], event selection requires very clean dileptonic final states:

- two isolated leptons of opposite charge,
- two scattered protons,
- large missing energy from the non-detection of ν and $\tilde{\chi}_1^0$,
- acoplanarity.

The only irreducible background process for this topology is the two-photon production of W pairs with fully leptonic decay. Indeed, two-photon production of lepton pairs $pp(\gamma\gamma \to \ell^+\ell^-)pp$ is easily suppressed using a cut on E_{miss} or accoplanarity. Exclusive WW production has a larger cross-section, around 108 fb.

Processes	σ [fb]	$\sigma_{acc}^{2p^+}$ [fb]	σ_{ana} [fb]
$\gamma\gamma \to \tilde{\ell}_R^+\tilde{\ell}_R^-$	0.798	0.445	0.357
$\gamma\gamma \to \tilde{\ell}_L^+\tilde{\ell}_L^-$	0.183	0.093	0.073
$\gamma\gamma \to \tilde{\tau}_i^+\tilde{\tau}_i^-$	0.604	0.001	0.001
$\gamma\gamma \to \tilde{\chi}_i^+\tilde{\chi}_i^-$	0.642	0.021	0.015
$\gamma\gamma \to H^+H^-$	0.004	/	/
$\gamma\gamma \to W^+W^-$	108.5	1.463	0.168

Table 1: Cross-sections of exclusive signal processes for production (σ), after applying central and forward detector acceptance cuts ($\sigma_{acc}^{2p^+}$) and after applying analysis cuts (σ_{ana}). '*acc*' includes same flavour leptons and τ-lepton tag; '*ana*' means $W_{miss} > 194$ GeV, $W_{\gamma\gamma} > 236$ GeV, $\Delta(\eta) < 2.1$, $\Delta(R) < 3.2$, $P_T^{miss} > 5$ GeV, $W_{lep} \notin [87\text{ GeV}; 95\text{ GeV}]$.

The two leptons must fall in the acceptance of the detector:

$$p_T(\mu^\pm) > 7 \text{ GeV}, \qquad p_T(e^\pm) > 10 \text{ GeV}, \qquad |\eta(\ell^\pm)| < 2.5 \tag{1}$$

while the protons are assumed to produce a hit in one very forward detector (VFD) if [6]:

$$\begin{aligned} 900 \text{ GeV} < E_\gamma < 120 \text{ GeV} \quad &\text{for 420m forward stations,} \\ 120 \text{ GeV} < E_\gamma < 20 \text{ GeV} \quad &\text{for 220m forward stations,} \end{aligned} \tag{2}$$

for a distance from the beam to the active edge taken as 4mm and 2mm respectively. An energy resolution $\sigma_{E_\gamma} = \max(\frac{E_\gamma}{100}, 1.5 \text{ GeV})$ is simulated on each detected proton.

Various possibilities to reduce the exclusive WW background based on kinematic variables are applied as cuts on the spatial distance ΔR, acoplanarity difference $\Delta\phi$, invariant dilepton mass W_{lep}, ... using the information of the central objects [3]. In case of low $\tan(\beta)$ models, another efficient way to reduce by a factor 2 the WW contribution is to select only same flavour dileptonic final states, as it is requested in this analysis. Also, lepton from tau decay can be tagged and rejected on a displaced vertex position veto.

The cross-sections after acceptance cuts (including same flavour requirement and τ-lepton tag) are 0.56 fb and 1.46 fb for the SUSY signal and the WW background respectively, as detailed in Table 1.

3 Precise mass reconstruction

The detection of the two scattered forward protons and the associated measurement of the photon energies give an unique and precise tool to reconstruct the initial conditions of the event. The two-photon invariant mass $W_{\gamma\gamma} = 2\sqrt{E_{\gamma_1} E_{\gamma_2}}$ and the missing mass W_{miss} (reconstructed

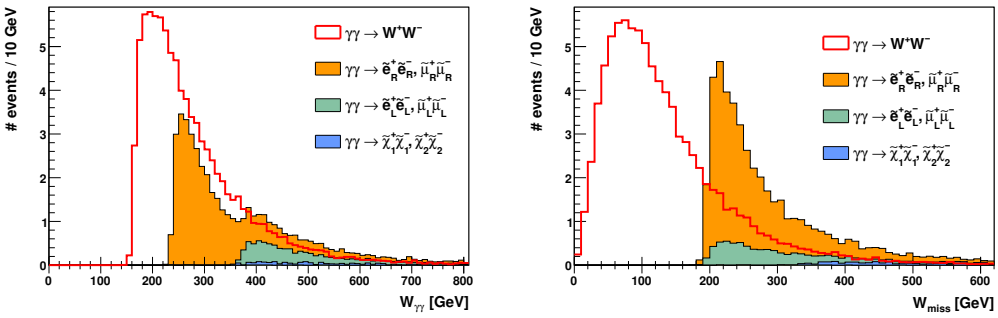

Figure 1: Distributions of the two-photon invariant mass $W_{\gamma\gamma}$ (left) and the missing mass W_{miss} (right) for the inetgarted luminosity L = 100 fb^{-1}. The background distribution of WW pairs is shown separately. Both are computed for events with 2 opposite charge same flavour leptons and 2 protons passing the acceptance cuts (1) and (2) only.

from $E_{miss} = E_{\gamma_1} + E_{\gamma_2} - E_{\ell_1} - E_{\ell_2}$ and similary for P_{miss}) distributions are shown in Figure 1, cumulatively for the signal, and separately for the background. The $W_{\gamma\gamma}$ distribution reflects the SUSY mass spectrum with two peaks due to the production thresholds of right slepton pairs (around 250 GeV) and left slepton pairs (around 400 GeV). Similary the W_{miss} distribution starts at about twice the mass of the LSP for the signal, whereas for the background the missing energy distribution starts at zero and peaks at around 70 GeV. Both distributions can be used to perform a mass edge study and extract the mass of $\tilde{\ell}^+_R$, $\tilde{\ell}^+_L$ and $\tilde{\chi}^0_1$. It should be stressed that the sleptons mass determination depends only on the VFD energy resolution and not on the ones for the central detectors. Also, since the energies and momenta of leptons are well reconstructed in the central detector, the uncertainty on the LSP mass determination is mainly dominated by photon energy resolutions.

Furthermore, combination of both information on the two-photon mass and the missing mass allows to measure the mass of the light $\tilde{\mu}_R$ and $\tilde{e}_R$ using the empirical quantity [3]:

$$(2m_{reco})^2 = W^2_{\gamma\gamma} - \left([W^2_{miss} - 4m^2_{\tilde{\chi}^0_1}]^{1/2} + [W^2_{lep} - 4m^2_{lep}]^{1/2} \right)^2 \qquad (3)$$

The only input is this method is the mass value of the LSP, which can be taken from the mass edge study on W_{miss}. The distribution after an integrated luminosity of 100 fb^{-1} is shown on Figure 2. A narrow peak centered on $2 * m_{reco} = 236$ GeV $= 2 \times 118$ GeV, allows for an event-by-event determination of the $\tilde{e}^{\pm}_R$ and $\tilde{\mu}^{\pm}_R$ mass with few GeV resolution.

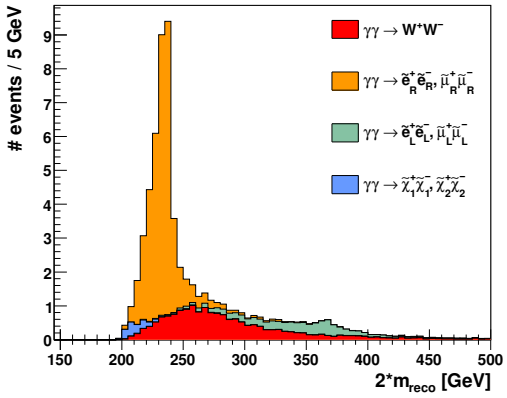

Figure 2: Cumulative distributions of the reconstructed mass $2 * m_{reco}$ for an integrated luminosity of L = 100 fb^{-1} assuming no pile-up.

4 Accidental coincidence background

In order to be sensitive to the femtobarn-level cross-sections of the exclusive SUSY pair production, this analysis has to be performed at designed LHC luminosity, when multiple interactions per bunch crossing (pile-up events) become significant. Assuming a total inelastic cross-section of 80mb and a collision frequency of 40 MHz, the number of overlap events per collision is distributed according to a Poisson distribution with

- for low luminosity $\mathcal{L} = 2 \times 10^{33} cm^{-2} s^{-1}$, $\langle N \rangle = 5.1$,
- for high luminosity $\mathcal{L} = 10^{34} cm^{-2} s^{-1}$, $\langle N \rangle = 25.4$.

At these luminosities, the large number of overlap events leads to high probability to get accidental coincidence background when the dileptonic event detected in the central detector and the two forward proton detected in the VFD do not come from the same vertex [5, 7].

4.1 Accidental proton hits

The total inelastic cross section at the LHC is expected to be roughtly 80mb [8] with:

- Single diffraction:

Processes corresponding to $pp \to pX$ or $pp \to Xp$, simulated with MUSB(92) or MUSB(93) respectively in Pythia [9]. The associated cross-section is 14mb. Efficiencies to detect a scattered proton in a VFD are $\epsilon_{FP240} \simeq 15\%$ and $\epsilon_{F420} \simeq 12\%$. This is the dominant component of accidental proton hit for both distances.

- Double diffraction:

Processes corresponding to $pp \to XY$, simulated with MUSB(94) in Pythia. The associated cross-section is 10mb. Efficiencies to detect a scattered proton in a VFD are $\epsilon_{FP240} \simeq 1.3\%$

and $\epsilon_{FP420} \simeq 0$.

• Non-diffractive inelastic events:
Processes corresponding to $pp \to X$,simulated with MUSB(95) in Pythia (also called low p_T production). The associated cross-section is 55mb. Efficiencies to detect a scattered proton in a VFD are $\epsilon_{FP240} = 0.5\%$ and $\epsilon_{FP420} \simeq 0$.

Effect of multiple interactions per collision is simulated by superimposing N extra events, with N following the Poisson distribution, and distributing the vertices along a gaussian with 48.2mm width [10]. The associated probability to have two accidental proton hits per collision (one on each side of the interaction point) is calculated to be 1.16% for low and 21.54% for high luminosity on average.

4.2 Dileptons from inclusive processes

The considered inclusive processes with dileptonic final states, likely to mimic an exclusive SUSY signature if VFD hits match, are the inclusive $W^+W^- \to \ell^+\ell^-\nu$'s, $ZZ \to \ell^+\ell^- + jets$ and the Drell-Yan $Z/\gamma* \to \ell^+\ell^-$ processes, for which cross-sections for productions and after applying acceptance cuts (1) and (2) are quoted in Table 2 and have to be compared with numbers in Table 1 for the SUSY signal.

Processes		σ [fb]	$\sigma_{acc}^{2p^+}$ [fb]	$\sigma_{ana+excl}$ [fb]
WW^a	Low lumi	7.4×10^3	11.47	1.3×10^{-3}
	High lumi	"	213.23	24.0×10^{-3}
ZZ	Low lumi	1.1×10^4	10.64	0.4×10^{-3}
	High lumi	"	197.85	6.8×10^{-3}
$\gamma^*/Z^{a,b}$	Low Lumi	1.3×10^7	2.4×10^4	1.13
	High lumi	"	4.5×10^5	20.94

Table 2: Cross-sections of inclusive background processes for production (σ), after applying central and forward acceptance cuts ($\sigma_{acc}^{2p^+}$) and after applying analysis and exclusivity conditions ($\sigma_{ana+excl}$) (see section 5). MC generation cut : ^{a}: leptonic decay only; ^{b}: for $\sqrt{\hat{s}} > 14$ GeV. The conditions for '*acc*' and '*ana*' are the same as in Table 1. *excl* means no extra track associated to the $\ell^+\ell^-$ vertex with $p_T > 0.5$ GeV.

As the dominant component is the inclusive Drell-Yan process, the analysis selection includes cuts on p_T^{miss} and on W_{lep}, both calculated from the lepton kinematic information in order to reduce the '$\gamma*$ part' and the 'Z part' of the spectrum respectively. We set $P_T^{miss} > 5$ GeV and $W_{lep} \notin [87\text{ GeV}; 95\text{ GeV}]$.

5 Exclusivity conditions

Accidental coincidence background, mainly composed by collisions with one inclusive Drell-Yan event and two single diffractive events, can be reduced at higher level trigger stage using kinematic constraints as consistency between the central and the forward systems in rapidity and

mass. It can be further reduced using the fact that in general the number of tracks associated to the dilepton vertex is much smaller in exclusive events than in generic collisions.

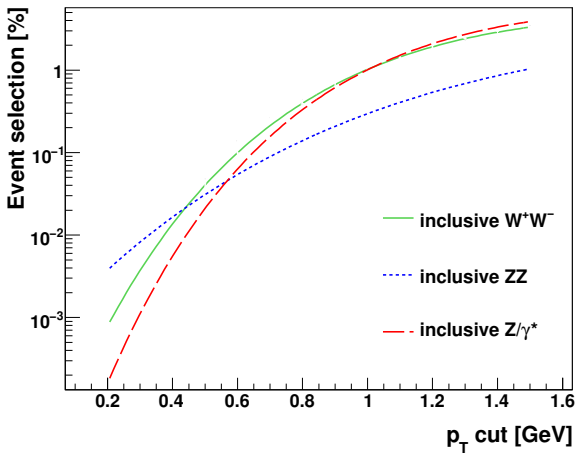

Figure 3: Background selection for 'no extra track with $p_T > p_{T,cut}$' condition

For illustration, the inefficiency due to track-based exclusive conditions is shown in Figure 3 as a function of the minimum p_T value for track reconstruction. Using the high performance of the central tracking detector to reconstruct tracks even at low p_T [11], one can request an extra track with $p_T > 0.5$ GeV associated to the $\ell^+\ell^-$ vertex. This provides a reduction factor around 2500 for inclusive WW, 3000 for inclusive ZZ and 4500 for Drell-Yan production. However, it has to be emphasized that these reduction factor are strongly dependent on the Multiple Parton Interaction model used, and then have large uncertainty of factor 2.

The effect of the accidental coincidence background with track-based exclusivity conditions is shown in Figure 4 for low and high luminosities. For the lower one, the inclusive background remains at an acceptable level, so that $\tilde{e}^{\pm}_R$ and $\tilde{\mu}^{\pm}_R$ masses could still be reconstructed with a few GeV resolution. However, in case of high luminosity, the probability to have a central dileptonic event accidentally associated

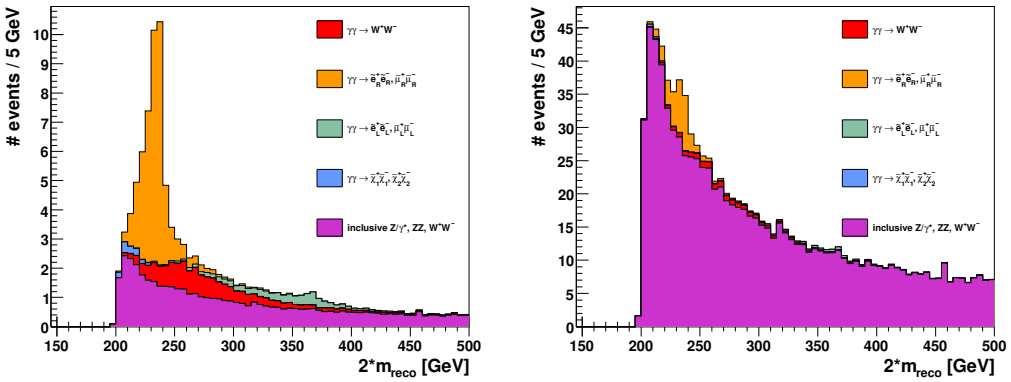

Figure 4: Cumulative distributions of the reconstructed mass $2 * m_{reco}$ for the integrated luminosity L = 100 fb^{-1} assuming low (left) and high (right) pile-up conditions. Track-based exclusivity conditions are applied.

to VFD hits is so large that the signal peak from exclusive supersymmetric pairs is hidden. In this context, precise time-of-flight detectors with few pico-second resolution have to be installed in association to the proton detector aiming to measure the relative time of arrival of protons in the VFD leg and reconstruct the proton-proton vertex [5, 12].

6 Conclusions

Photon-photon interactions provide novel, unique and complementary physics in the search of supersymmetric low mass models at the LHC, thanks to extra kinematical information obtained using the VFD. Even though the detection of low mass sparticles would be achieved earlier in nominal proton-proton collisions, the main interest lies in the capabilities for a reconstruction with a few GeV resolution of the LSP and the charged light scalars ($\tilde{e}_R$ and $\tilde{\mu}_R$) masses.

Unfortunately, in the harsh environment of the LHC, pile-up events will cause accidental coincidence background (an inclusive dilepton event associated to two accidental proton hits) which will degrade the SUSY detection potential.

At low luminosity, the use of strong track-based exclusivity conditions allows for a large reduction of the accidental background, and few GeV resolution on mass reconstruction is still expected. However, at high luminosity, the number of extra interactions per collisions is so high that no SUSY signal peak could be observed anymore. Fast timing detector, with $\mathcal{O}$(10ps) time resolution are then mandatory for the proton-proton vertices.

Acknowledgments

This work is supported by the Belgian Federal Office for Scientific, Technical and Cultural Affairs through the Interuniversity Attraction Pole P6/11.

References

[1] T. Pierzchala and K. Piotrzkowski, Nucl.Phys.Proc.Suppl.**179-180** 257 (2008), arXiv:0807.1121 [hep-ph].

[2] M. Battaglia *et al.*, Eur.Phys.J. **C33** 273 (2004).

[3] N. Schul and K. Piotrzkowski, Nucl.Phys.Proc.Suppl.**179-180** 289 (2008), arXiv:0806.1097 [hep-ph].

[4] K. Piotrzkowski, Phys. Rev. **D63** 071502 (2001), arXiv:hep-ex/0009065.
K. Piotrzkowski, arXiv:hep-ex/0201027.

[5] The FP420 collaboration, arXiv:0806.0302 [hep-ex].

[6] J. de Favereau de Jeneret, X. Rouby and K. Piotrzkowski, JINST2:P09005 (2007) arXiv:0707.1198 [physics.acc-ph].

[7] B. Cox, F. Loebinger and A. Pilkington, JHEP0710:090 (2007), arXiv:0709.3035 [hep-ph].

[8] V. Khose, A. Martin, M. Ryskin, arXiv:0906.4876v1 [hep-ph].

[9] T. Sjstrand *et al.*, Comput. Phys. Commun. **135** 238 (2001).

[10] S. White, arXiv:0707.1500 [hep-ex].

[11] The CMS collaboration, JINST3:S08004 (2008).

[12] L. Bonnet *et al.*, ActaPhys.Polon.B38:477 (2007), arXiv:hep-ph/0703320.

Constraints on Supersymmetric Models from $b \to s\gamma$

Farvah Mahmoudi

Laboratoire de Physique Corpusculaire de Clermont-Ferrand (LPC), Université Blaise Pascal, CNRS/IN2P3, 63177 Aubière Cedex, France

DOI: http://dx.doi.org/10.3204/DESY-PROC-2009-03/Mahmoudi

Flavor physics constraints on supersymmetric models and in particular those from $b \to s\gamma$ transitions are discussed. These rare transitions provide valuable information in the quest for new physics and are complementary to the direct searches. The contributions of supersymmetric particles in the inclusive branching ratio in $B \to X_s\gamma$ as well as the isospin symmetry violation in $B \to K^*\gamma$ decay mode are investigated. The model parameters are adopted from the minimal supersymmetric extension of the Standard Model (MSSM) with minimal flavor violation.

1 Introduction

Rare B decays are very sensitive to new physics effects and can play an important role in disentangling different scenarios. The transition which is most often discussed in this context is the flavor changing neutral current process $b \to s\gamma$. Since this transition occurs first at one-loop level in the SM, the new physics contributions can be of comparable magnitude.

The penguin loops here involve W boson in the Standard Model, and in addition loops from charged Higgs boson, chargino, neutralino and gluino for the MSSM as presented in Figs. 1 and 2. The contribution of neutralino and gluino loops is negligible in minimal flavor violating scenarios. Charged Higgs loop always adds constructively to the SM penguin. Thus, this observable is an effective tool to probe the 2HDM scenario. Chargino loops however can add constructively or destructively. If the interference is positive, it results in a great enhancement in the BR($b \to s\gamma$), which becomes therefore a powerful observable.

In the following, we present an overview of two observables in $b \to s\gamma$ transitions, namely the inclusive branching ratio of $B \to X_s\gamma$ and isospin asymmetry in the exclusive decay of $B \to K^*\gamma$.

The calculation of $b \to s\gamma$ observables begins with introducing an effective Hamiltonian

$$\mathcal{H}_{eff} = -\frac{4G_F}{\sqrt{2}} V_{ts}^* V_{tb} \sum_{i=1}^{8} C_i(\mu) O_i(\mu) \tag{1}$$

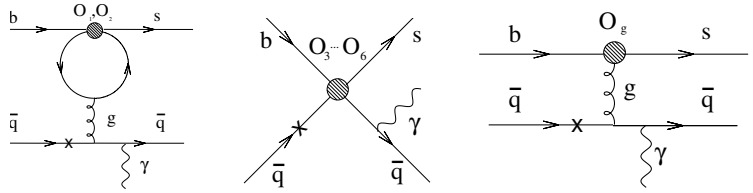

Figure 1: Example of diagrams contributing to $B \to X_s\gamma$.

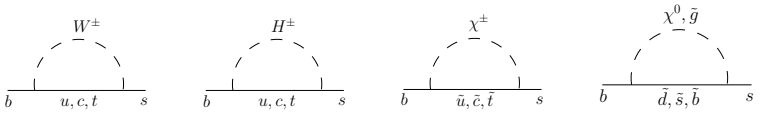

Figure 2: Loops involved in $b \to s\gamma$ transitions.

where G_F is the Fermi coupling constant, V_{ij} are elements of the CKM matrix, $O_i(\mu)$ are the relevant operators and $C_i(\mu)$ are the corresponding Wilson coefficients evaluated at the scale μ. The operators O_i can be listed as follows

$$\begin{aligned}
O_1 &= (\bar{s}\gamma_\mu T^a P_L c)(\bar{c}\gamma^\mu T^a P_L b) \,, \\
O_2 &= (\bar{s}\gamma_\mu P_L c)(\bar{c}\gamma^\mu P_L b) \,, \\
O_3 &= (\bar{s}\gamma_\mu P_L b)\sum_q (\bar{q}\gamma^\mu q) \,, \\
O_4 &= (\bar{s}\gamma_\mu T^a P_L b)\sum_q (\bar{q}\gamma^\mu T^a q) \,, \\
O_5 &= (\bar{s}\gamma_{\mu_1}\gamma_{\mu_2}\gamma_{\mu_3} P_L b)\sum_q (\bar{q}\gamma^{\mu_1}\gamma^{\mu_2}\gamma^{\mu_3} q) \,, \\
O_6 &= (\bar{s}\gamma_{\mu_1}\gamma_{\mu_2}\gamma_{\mu_3} T^a P_L b)\sum_q (\bar{q}\gamma^{\mu_1}\gamma^{\mu_2}\gamma^{\mu_3} T^a q) \,, \\
O_7 &= \frac{e}{16\pi^2}\,[\bar{s}\sigma^{\mu\nu}(m_s P_L + m_b P_R) b]\, F_{\mu\nu} \,, \\
O_8 &= \frac{g}{16\pi^2}\,[\bar{s}\sigma^{\mu\nu}(m_s P_L + m_b P_R) T^a b]\, G^a_{\mu\nu} \,,
\end{aligned} \tag{2}$$

The presence of SUSY particles does not introduce new operators in the list, however, the Wilson coefficients C_i receive additional contributions from virtual sparticles.

2 Inclusive Branching ratio

The branching ratio of $B \to X_s\gamma$ can be written as [1]

$$\mathcal{B}[\bar{B} \to X_s\gamma]_{E_\gamma > E_0} = \mathcal{B}[\bar{B} \to X_c e\bar{\nu}]_{\rm exp} \left|\frac{V_{ts}^* V_{tb}}{V_{cb}}\right|^2 \frac{6\alpha_{\rm em}}{\pi C}\,[P(E_0) + N(E_0)] \tag{3}$$

with

$$C = \left|\frac{V_{ub}}{V_{cb}}\right|^2 \frac{\Gamma[\bar{B} \to X_c e\bar{\nu}]}{\Gamma[\bar{B} \to X_u e\bar{\nu}]} \,. \tag{4}$$

$P(E_0)$ and $N(E_0)$ denote respectively the perturbative and non perturbative contributions, where E_0 is a cut on the photon energy. The numerical values of C, $\mathrm{BR}(\bar{B} \to X_c e \bar{\nu})_{\mathrm{exp}}$ and E_0 can be found in [1].

Following [1], we can expand $P(E_0)$ as

$$P(E_0) = P^{(0)}(\mu_b) + \alpha_s(\mu_b)\left[P_1^{(1)}(\mu_b) + P_2^{(1)}(E_0,\mu_b)\right] \quad (5)$$

$$+ \alpha_s^2(\mu_b)\left[P_1^{(2)}(\mu_b) + P_2^{(2)}(E_0,\mu_b) + P_3^{(2)}(E_0,\mu_b)\right] + \mathcal{O}\left(\alpha_s^3(\mu_b)\right) \quad (6)$$

where P_i's are related to the Wilson coefficients. The latest combined experimental value for this branching ratio is reported by the Heavy Flavor Averaging Group (HFAG) [2]:

$$\mathcal{B}[\bar{B} \to X_s\gamma] = (3.52 \pm 0.25) \times 10^{-4}\,, \quad (7)$$

to be compared to the SM predicted value [9]:

$$\mathcal{B}[\bar{B} \to X_s\gamma] = (3.11 \pm 0.22) \times 10^{-4}\,. \quad (8)$$

The accuracy of the experimental and theoretical values, as well as the slight shift between the central values, make this observable particularly interesting to constrain new physics parameters, and especially in the MSSM where the new contributions can lead to very different predictions.

3 Isospin asymmetry

The isospin asymmetry in $B \to K^*\gamma$ decays is defined as:

$$\Delta_{0-} = \frac{\Gamma(\bar{B}^0 \to \bar{K}^{*0}\gamma) - \Gamma(B^- \to K^{*-}\gamma)}{\Gamma(\bar{B}^0 \to \bar{K}^{*0}\gamma) + \Gamma(B^- \to K^{*-}\gamma)}\ . \quad (9)$$

and similarly Δ_{0+} is defined as the charge conjugate of this equation. The isospin asymmetry has been measured experimentally by Babar [3] and Belle [4]:

$$\Delta_{0-} = +0.029 \pm 0.019(\mathrm{stat.}) \pm 0.016(\mathrm{syst.}) \pm 0.018(R^{+/0}) \quad \text{(Babar)}\,, \quad (10)$$

$$\Delta_{0+} = +0.012 \pm 0.044(\mathrm{stat.}) \pm 0.026(\mathrm{syst.}) \quad \text{(Belle)}\,. \quad (11)$$

Calculating the isospin asymmetry, while considering the supersymmetric contributions, and comparing the results with the above experimental data allows us to establish very tight constraints on the SUSY parameters [5, 6].

Using the QCD factorization and following the method of [7], one can show that the isospin symmetry breaking, Δ_{0-}, can be written as:

$$\Delta_{0-} = \mathrm{Re}(b_d - b_u)\ , \quad (12)$$

where the coefficients b_q reads:

$$b_q = \frac{12\pi^2 f_B\, Q_q}{\bar{m}_b\, T_1^{B\to K^*}\, a_7^c}\left(\frac{f_{K^*}^{\perp}}{\bar{m}_b}\, K_1 + \frac{f_{K^*} m_{K^*}}{6\lambda_B m_B}\, K_{2q}\right)\ . \quad (13)$$

In this formula, the coefficients a_7^c, K_1 and K_{2q} can be written in function of the Wilson coefficients C_i at scale μ_b. The other parameters are described in [5].

Calculating the expected isospin asymmetry from Eqs. (1.2) and (1.3), and confronting the results to the combined experimental limits of (1.4) and (1.5) allow us to establish limits on the supersymmetry parameters.

4 Constraints

We explore the constraints from isospin asymmetry and branching ratio, while scanning over parts of the parameter spaces of different supersymmetric models such as the minimal supergravity (mSUGRA) model and the non universal Higgs mass (NUHM) framework, as well as the Anomaly Mediated Supersymmetry Breaking (AMSB) and the Gauge Mediated Supersymmetry Breaking (GMSB) models.
The results presented here, for both the inclusive branching ratio and the isospin asymmetry have been calculated using SuperIso v2.5 [8, 9]. The SUSY mass spectrum, as well as the couplings and the mixing matrices, are generated using SOFTSUSY 2.0.18 [10]. The constraints are presented in Fig. 3, where severe restrictions on the allowed parameter space regions for the aforementioned models are obtained.

In Fig. 4 we present a comparison between the constraints obtained by different flavor observables (both tree-level and one-loop induced) for fixed values of $m_0 = m_{1/2} = \mu = 500$ GeV and $A_0 = 0$. We show the results in the plane $[\tan\beta, m_A]$, for $m_A > 200$ GeV. The regions excluded by $b \to s\gamma$ observables are displayed in red for the isospin asymmetry and in blue for the branching ratio [5, 6]. The region excluded by $\mathrm{BR}(\mathrm{D_s^\pm} \to \tau^\pm\nu)$ is depicted in yellow. The green area represents the region excluded by $\mathrm{BR}(\mathrm{B}^\pm \to \tau^\pm\nu)$, the violet region by $\mathrm{BR}(\mathrm{B_s^0} \to \mu^+\mu^-)$, the light blue region by $K^\pm \to \mu^\pm\nu$, and the orange area by $\mathrm{BR}(\mathrm{B} \to \mathrm{D}\tau\nu)$ [11]. To obtain the constraints presented in this figure the input values of [9] are used. It is important to remember that the constraints can be subject to uncertainties, in particular from decay constants and CKM matrix elements. To obtain the constraint from $\mathrm{BR}(\mathrm{D_s^\pm} \to \tau^\pm\nu)$ the central value $m_s/m_c = 0.08$ is used [12]. Finally, the black region in the figure represents the region excluded by the direct searches at colliders [13].

5 Conclusions

We have shown that the flavor changing neutral current process $b \to s\gamma$ provides valuable observables for constraining the MSSM parameter space. Many other flavor physics observables can also be of great interest for the search of new physics, and they will prove to be powerful tools when combined with the future LHC data. The SuperIso package provides the possibility to explore the supersymmetry parameter space using many flavor observables and for different scenarios.

Acknowledgements

I would like to thank the organizers of PHOTON 2009 for their invitation and for the interesting conference.

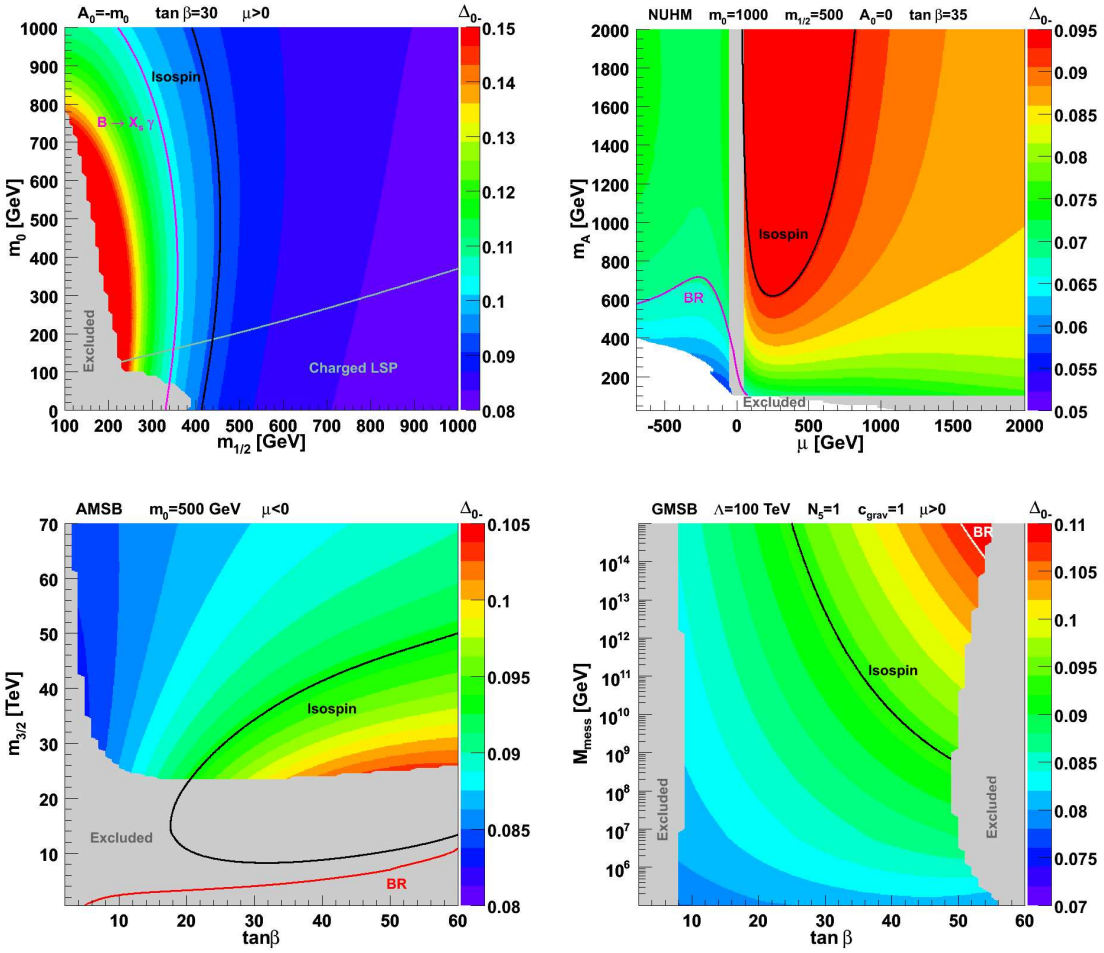

Figure 3: Constraints on the SUSY parameter space from $b \to s\gamma$ branching ratio and isospin asymmetry. The colors correspond to the intensity of isospin asymmetry. The upper left plot shows the constraints in mSUGRA parameter plane $(m_{1/2}, m_0)$ with $\mu > 0$ for $\tan\beta = 30$ and for $A_0 = 0$; the upper right plot shows the constraints in NUHM parameter plane (μ, m_A) for $m_0 = 1000$ GeV, $m_{1/2} = 500$ GeV, $\tan\beta = 35$ and $A_0 = 0$; the lower left plot illustrate the constraints in AMSB parameter plane $(m_{3/2}, \tan\beta)$ for $m_0 = 500$ GeV and $\mu < 0$; and the lower right shows the constraints in GMSB parameter plane $(M_{mess}, \tan\beta)$ for $\Lambda = 100$ TeV, $N_5 = 1$, $c_{grav} = 1$ and $\mu > 0$.

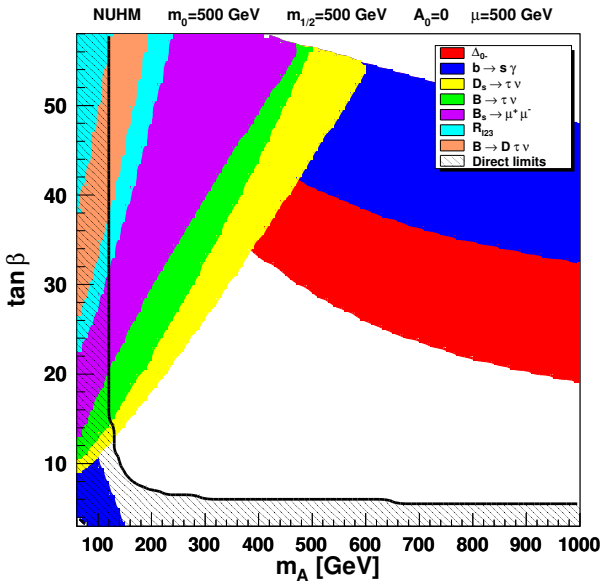

Figure 4: Constraints in NUHM $(m_A, \tan\beta)$ parameter plane. The contours are superimposed in the order given in the legend and are excluded at 95% C.L.

References

[1] M. Misiak and M. Steinhauser, Nucl. Phys. B**764**, 62 (2007) [hep-ph/0609241].

[2] E. Barberio *et al.* [Heavy Flavor Averaging Group], arXiv:0808.1297 [hep-ex].

[3] B. Aubert *et al.* [BABAR Collaboration], arXiv:0808.1915 [hep-ex].

[4] M. Nakao *et al.* [BELLE Collaboration], 112001 (2004) [hep-ex/0402042].

[5] M.R. Ahmady and F. Mahmoudi, Phys. Rev. D**75**, 015007 (2007) [hep-ph/0608212].

[6] F. Mahmoudi, JHEP **0712**, 026 (2007) [arXiv:0710.3791].

[7] A. Kagan and M. Neubert, Phys. Lett. B**539**, 227 (2002) [hep-ph/0110078].

[8] F. Mahmoudi, Comput. Phys. Commun. **178**, 745 (2008) [arXiv:0710.2067], http://superiso.in2p3.fr .

[9] F. Mahmoudi, arXiv:0808.3144 [hep-ph].

[10] B.C. Allanach, Comput. Phys. Commun. **143**, 305 (2002) [hep-ph/0104145].

[11] D. Eriksson, F. Mahmoudi and O. Stål, JHEP **0811**, 035 (2008) [arXiv:0808.3551].

[12] A.G. Akeroyd and F. Mahmoudi, JHEP **0904**, 121 (2009) [arXiv:0902.2393].

[13] C. Amsler *et al.* [Particle Data Group], Phys. Lett. B**667**, 1 (2008).

Anomalous Gauge Couplings in Photon-Photon Interactions at the LHC

Émilien Chapon, Oldřich Kepka, Christophe Royon

IRFU-SPP, CEA Saclay, 91191 cedex Gif-sur-Yvette, France

DOI: http://dx.doi.org/10.3204/DESY-PROC-2009-03/Chapon

We show that the expected sensitivity to triple and quartic gauge couplings at the LHC with the ATLAS or the CMS detector, in photon-photon interactions, can be improved by 3 orders of magnitude with respect to LEP results. In particular we study anomalous $WW\gamma$, $WW\gamma\gamma$ and $ZZ\gamma\gamma$ couplings.

We first present the results obtainable with early data (10 to 100 pb^{-1}). We discuss finally the sensitivity reached with higher integrated luminosity (30 fb^{-1} and more) using the forward proton detectors foreseen for an upgrade of the ATLAS/CMS detector.

1 Introduction

A lot of new physics analyses at the LHC need a significant amount of data to be carried out. Nevertheless, even with early data, some new results are achievable, for example on anomalous gauge couplings in photon induced processes. A dramatic improvement on the current knowledge of those anomalous couplings is possible even with very few data (from 10 pb^{-1}).

2 Two-photon interactions and anomalous couplings

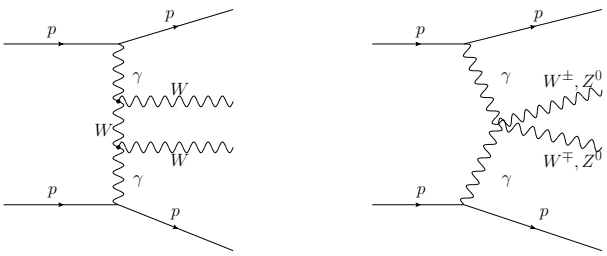

Figure 1: Feynman diagrams for the signal (triple gauge couplings on the left, quartic on the right)

The process we studied is $pp \to p(\gamma\gamma)p \to ppWW$ (see Figure 1). In this photon-induced process, the two photons interact through the exchange of a virtual W, giving a pair of Ws in

the final state. The main particularity of this process is that nothing else is produced in the central detectors, and we only detect the products of the decay of the Ws, namely two leptons (including taus if they decay leptonically) as we only studied the leptonic channel.

Even though we would have had more statistics, we did not consider the case when the Ws decay hadronically. In this case one would have to face the high QCD background and thus a more refine analysis would be needed. The protons loose little transverse momentum and fly into the beam pipe, they are therefore left undetected (unless forward proton detectors are installed at ATLAS or CMS, e.g. ATLAS Forward Physics detectors: see below). So we have a very clean signature for our events: only two reconstructed leptons in the central detectors *and nothing else*.

2.1 W pair production through two-photon interaction

The cross section of this process in the Standard Model is well known, since it is a pure Quantum Electrodynamics process. This cross section is $\sigma_{pp\to ppWW} = 95.6\,\text{fb}$ at $\sqrt{s} = 14\,\text{TeV}$, $\sigma_{pp\to ppWW} = 62\,\text{fb}$ at $\sqrt{s} = 10\,\text{TeV}$ ($\alpha_{EM} = 1/137$).

In our study we used the equivalent photon approximation (Budnev flux), which predicts exchanges of quasi-real (low virtuality Q^2) photons whose energy can be substantially large. In particular we can have a high missing mass $M_{\gamma\gamma} = \sqrt{s\xi_1\xi_2}$ (where ξ is the momentum fraction loss of the proton). Therefore photon interactions allow to probe new physics even at the terascale.

2.2 Anomalous couplings

We studied two types of effective Lagrangians of anomalous gauge couplings extending the Standard Model. The first one corresponds to quartic couplings.

$$\begin{aligned}
\mathcal{L}_6^0 &= \frac{-e^2}{8}\frac{a_0^W}{\Lambda^2}F_{\mu\nu}F^{\mu\nu}W^{+\alpha}W^-_\alpha - \frac{e^2}{16\cos^2\Theta_W}\frac{a_0^Z}{\Lambda^2}F_{\mu\nu}F^{\mu\nu}Z^\alpha Z_\alpha,\\
\mathcal{L}_6^C &= \frac{-e^2}{16}\frac{a_C^W}{\Lambda^2}F_{\mu\alpha}F^{\mu\beta}(W^{+\alpha}W^-_\beta + W^{-\alpha}W^+_\beta) - \frac{e^2}{16\cos^2\Theta_W}\frac{a_C^Z}{\Lambda^2}F_{\mu\alpha}F^{\mu\beta}Z^\alpha Z_\beta.
\end{aligned}$$

Anomalous $WW\gamma\gamma$ couplings are parametrised by dimensionless parameters a_0^W and a_C^W, and anomalous $ZZ\gamma\gamma$ couplings by a_0^Z and a_C^Z. We studied the effect of each of these parameters independently, varying only one while the other ones were set to their Standard Model value: 0.

The second Lagrangian, corresponding to triple couplings, reads:

$$\mathcal{L}/ig_{WW\gamma} = \left(W^\dagger_{\mu\nu}W^\mu A^\nu - W_{\mu\nu}W^{\dagger\mu}A^\nu\right) + (1+\Delta\kappa^\gamma)\,W^\dagger_\mu W_\nu A^{\mu\nu}. + \frac{\lambda^\gamma}{M_W^2}W^\dagger_{\rho\mu}W^\mu_\nu A^{\nu\rho}$$

Similarly, the parameters λ^γ and $\Delta\kappa^\gamma$ are 0 in the Standard Model, and were studied independently. See [1] for a study of these couplings at the LHC.

2.3 Signal and backgrounds

The signal we study is characterised by two high-p_T leptons reconstructed in the central detector, and the absence of any other reconstructed object or energy flow. We have a very clear

signature for the signal and we can easily reject potential inclusive backgrounds, such as inclusive W pair production. Of course, this is only true at low luminosity: otherwise, electronic pile-up and multiple interactions will add additional activity in the central detector.

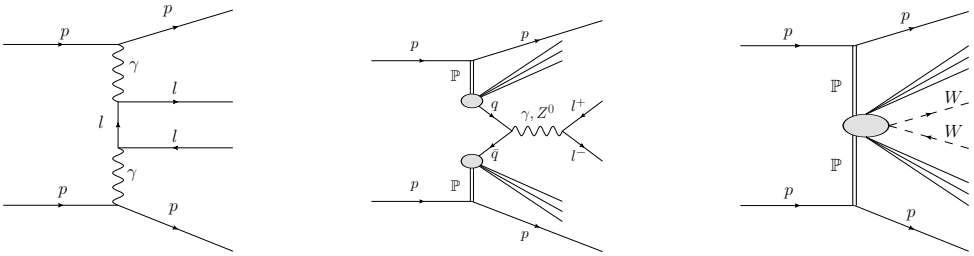

Figure 2: Feynman diagrams for the different background processes.

The backgrounds taken into account for this study are the following (see diagrams on Figure 2):

Non-diffractive W pairs: completely suppressed by requiring two rapidity gaps (regions of the detector devoid of energy) and at most two tracks (not shown).

Dilepton production through photon exchange: suppressed by asking at least one lepton with $p_T > 160\,\text{GeV}$ and missing transverse energy $> 20\,\text{GeV}$.

Dilepton production through pomeron exchange: suppressed by the same cuts as above and by the cut on the number of tracks.

W pair through pomeron exchange: low background, mainly suppressed by the cut on tracks.

All those processes (except inclusive production of W pairs) were generated using Forward Physics Monte Carlo (FPMC) [2], a generator based on Herwig, dedicated to the study of forward physics processes. The matrix elements were generated with CompHEP [3]. The events were then reconstructed with ATLFast++ [4], a ROOT standalone package that performs a fast simulation of the ATLAS detector in a parametrised way.

3 Sensitivity using low integrated luminosity at the LHC

In this part, we studied the expected sensitivity on anomalous couplings with a low integrated luminosity at the LHC ($10-100\,\text{pb}^{-1}$ depending on the LHC running scenario), without pile-up and with proton-proton collisions at $\sqrt{s} = 10\,\text{TeV}$.

3.1 Event Selection

The event selection is as follows:

2 reconstructed leptons with $p_T > 10\,\text{GeV}$ where a 'reconstructed lepton' is an electron or a muon. Tau lepton reconstruction was not taken into account: therefore final states involving a tau lepton are kept if the tau decayed leptonically, but not if the tau decayed hadronically.

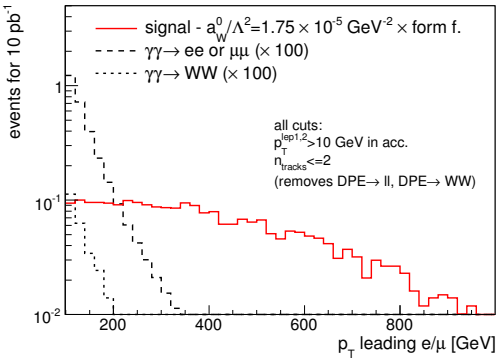

Figure 3: Leading lepton p_T spectrum of the signal and different backgrounds, after all cuts.

Exclusivity In practise, we required that the event does not contain any other reconstructed object than the two reconstructed leptons. This means at most two tracks, no unused calorimeter cluster, and no other reconstructed object (muon, electron, jet or photon). With real data, one would also have to ask for two rapidity gaps[1], one on each side of the detector. This exclusivity requirement is important to reject non-diffractive events, whose production cross section is much higher but in which the proton remnants lead to a large energy flow in the forward region. It also allows to reject processes involving double pomeron exchange, in which the pomeron remnants lead to additional energy flow and higher number of tracks.

1 lepton with $p_T > 160\,\text{GeV}$ With this requirement, we suppress most of the dilepton background. Indeed, this background produces mostly low-p_T leptons, whereas our signal produces much higher p_T leptons, especially with anomalous couplings which mostly enhance the cross section at high $M_{\gamma\gamma}$.

Missing transverse energy $> 20\,\text{GeV}$ This cut further suppresses the dilepton background. The final state for the signal is two leptons and two neutrinos, which leads to a much higher MET than the dilepton background, which does not produce any neutrino (except in the case of a tau decay, but the corresponding cross section is low).

Such event selection has a moderate effect on the signal, and it cuts almost all the background (see Figure 3). The main background, as seen on this plot, is two-photon dilepton production.

3.2 Results

The expected results are presented in Table 1. We see that we can gain a factor 1 000 with respect to the current limits from the OPAL collaboration [5] from as little as $10\,\text{pb}^{-1}$ of data. No similar study has been performed so far at the Tevatron, but the expected sensitivity would be one order of magnitude better than the present LEP limits.

[1] A rapidity gap is a section of the detector, in pseudo-rapidity η, with no deposited energy (with respect to the expected noise). The detailed study of rapidity gaps requires the use of the full detector simulation and is not possible with fast simulation. Nevertheless it is reasonable to assume that the rapidity gap requirement suppresses all of the inclusive background but keeps all of the signal.

Couplings	OPAL limits [GeV^{-2}]	Limits @ 10 TeV [GeV^{-2}]		Limit @ 2 TeV [GeV^{-2}]
		$\mathcal{L} = 10\,\text{pb}^{-1}$	$\mathcal{L} = 100\,\text{pb}^{-1}$	$\mathcal{L} = 100\,\text{pb}^{-1}$
a_0^W/Λ^2	[-0.020, 0.020]	1.41×10^{-5}	4.52×10^{-6}	7×10^{-4}
a_C^W/Λ^2	[-0.052, 0.037]	5.44×10^{-5}	1.68×10^{-5}	2.6×10^{-3}
a_0^Z/Λ^2	[-0.007, 0.023]	1.05×10^{-4}	3.30×10^{-5}	4.25×10^{-3}
a_C^Z/Λ^2	[-0.029, 0.029]	4.54×10^{-4}	1.23×10^{-4}	1.5×10^{-2}

Table 1: Sensitivity at low luminosity

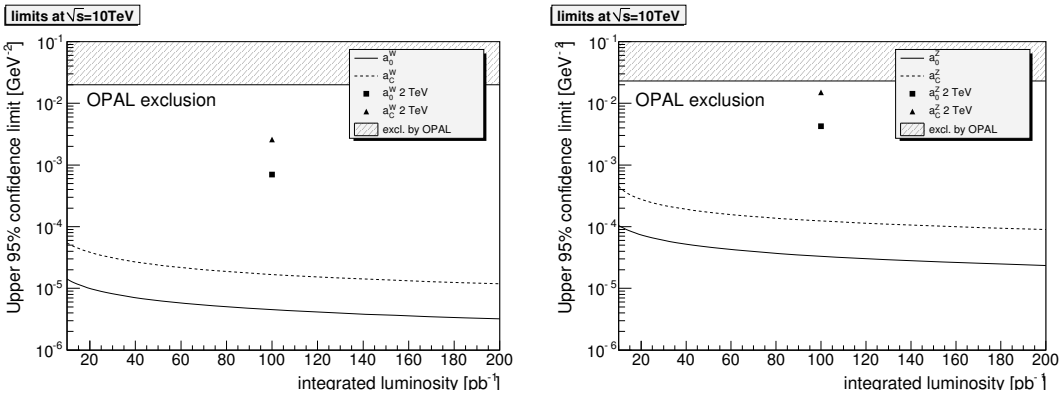

Figure 4: Upper 95% C.L. confidence limits on a_0^W and a_C^W (*left*) and a_0^Z and a_C^Z (*right*). The exclusion from the OPAL collaboration and the estimated limits at 2 TeV are also represented.

NB: the effective Lagrangians as such violate the unitarity at high energy. If we introduce a form-factor ($a \to \frac{a}{1+W_{\gamma\gamma}^2/\Lambda^2}$ where we set $\Lambda = 2\,\text{TeV}$) the actual limits are about 5-6 times worse.

We also studied anomalous $\gamma\gamma ZZ$ couplings (see results in Table 1), which were also implemented in our model. The analysis is much simpler in this case, since the corresponding process ($pp \to ppZZ$ through photon exchange) is forbidden in the Standard Model. The gain of sensitivity is this time of 2 orders of magnitude on the sensitivity from the OPAL collaboration.

Once again, we limit ourselves to the pure leptonic channel, with both Zs decaying to two leptons. To select the events, we required at least 3 reconstructed leptons (or at least 2 of the same generation and sign, e.g. $\mu^+\mu^+$) with $p_T > 10\,\text{GeV}$, at most 4 tracks, and no reconstructed jet.

4 Sensitivity using high integrated luminosity at the LHC

This part of the study, now assuming collisions at 14 TeV, comprises high luminosity runs, with multiple interactions per bunch crossing and pile-up. These will spoil the rapidity gaps on which we relied at low luminosity, and we can no longer use them.

Nevertheless, we use the forward detectors to select the exclusive events with forward protons in the final state. They are currently under development by the AFP collaboration [8], foreseen to be installed at 220 and 420 meters on both sides of the CMS and/or ATLAS detectors. These detectors, installed in the LHC tunnel very close to the beam, will detect diffracted protons

with an acceptance on the momentum fraction loss of the proton of $0.0015 < \xi < 0.15$.

To reject the inclusive background, we now ask for two deflected protons to be tagged in those detectors. In practice, it will be necessary to check that these tagged protons come from the main vertex, which will actually be possible with the picosecond time of flight detectors enabling to associate the tagged proton with a vertex in the central detector.

Other changes in the cuts are necessary, mainly because we suppose now a higher integrated luminosity (at least a few tens of fb^{-1}). Therefore we are sensitive to smaller values of the anomalous parameters, but we have more background events.

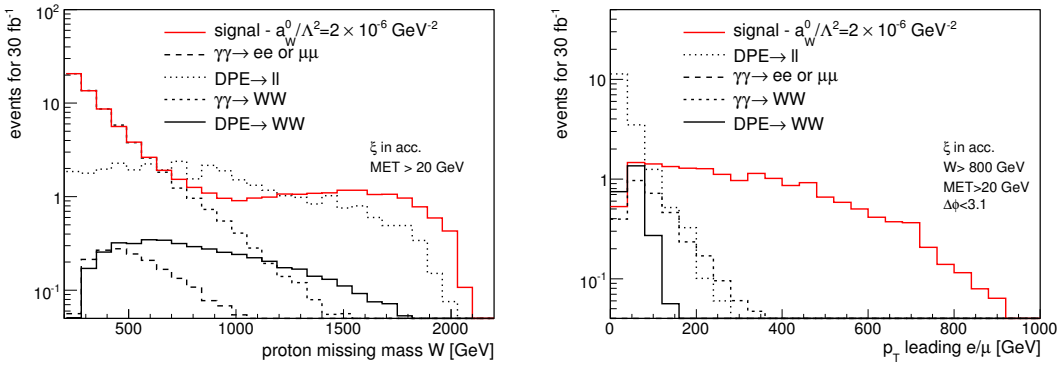

Figure 5: *Left:* W distribution for signal and background. *Right:* p_T distribution of the leading lepton.

The new event selection, motivated by the higher luminosity and the pile-up background, is as follows:

2 reconstructed leptons with $p_T > 10\,\text{GeV}$;

2 tagged protons $(0.0015 < \xi_{1,2} < 0.15)$**, coming from the same vertex** ;

1 lepton with $p_T > 160\,\text{GeV}$;

Missing mass $M_{\gamma\gamma} = \sqrt{s\xi_1\xi_2} > 800\,\text{GeV}$ (This cut enhances the signal / noise ratio, because anomalous couplings only enhance the cross section at high missing mass, as we can see on the left plot of Figure 5.);

Angle difference between the two leptons $\Delta\phi < 3.13$ (This further suppresses the dilepton background (especially from $\gamma\gamma$ interaction), for which the leptons are emitted back-to-back.);

Missing transverse energy $> 20\,\text{GeV}$.

The main remaining backgrounds after these cuts are the double pomeron exchange dilepton production, and the standard model two-photon W pair production, as seen on the right plot of Figure 5.

The expected limits in this scenario are presented in Table 2. We see that we gain an additional factor about 10 with respect to the limits presented in Table 1. The form-factor introduced in Section 3.2 has a smaller impact here, it changes the limits by about a factor 2.

Couplings	Limits from LEP [GeV^{-2}]	Limits @ 14 TeV $\mathcal{L} = 30\,\mathrm{fb}^{-1}$	Limits @ 14 TeV $\mathcal{L} = 200\,\mathrm{fb}^{-1}$
a_0^W/Λ^2	$[-0.020, 0.020]$	$2.3 \times 10^{-6}\,\mathrm{GeV}^{-2}$	$1.5 \times 10^{-6}\,\mathrm{GeV}^{-2}$
a_C^W/Λ^2	$[-0.052, 0.037]$	$8.7 \times 10^{-6}\,\mathrm{GeV}^{-2}$	$5.5 \times 10^{-6}\,\mathrm{GeV}^{-2}$
λ^γ	[-0.098, 0.101]	[-0.033,0.026]	[-0.024,0.017]
$\Delta\kappa^\gamma$	[-0.044, 0.047]	[-0.034,0.029]	[-0.013,0.012]

Table 2: Sensitivity at high luminosity

5 Conclusion

We studied anomalous $WW\gamma$, $WW\gamma\gamma$ and $ZZ\gamma\gamma$ couplings, considering not only the photon-induced backgrounds but also double pomeron exchange ones, and we found that dilepton production through double pomeron exchange is one of the dominant backgrounds to this study.

With that, we showed that even with only $10\,\mathrm{pb}^{-1}$ of data at the LHC, we can set limits more than 2 orders of magnitude better (form-factor taken into account) than the ones from the OPAL collaboration. With $30\,\mathrm{fb}^{-1}$, and thanks to the AFP proton taggers, we can even reach an additional factor 10 of improvement, leading to a total improvement by factor of 10 000 for $WW\gamma\gamma$ couplings and 1 000 for $ZZ\gamma\gamma$ couplings.

6 Acknowledgements

We would like to thank Tomasz Pierzchała and Krzysztof Piotrzkowski that kindly provided us the CompHEP implementation of the quartic gauge Lagrangians.

References

[1] O. Kepka and C. Royon, Phys. Rev. **D78** 073005 (2008);
T. Pierzchała and K. Piotrzkowski, arXiv:hep-ph/0807.1121v1 (2008);
E. Chapon, O. Kepka and C. Royon, to be submitted (2009).

[2] Forward Physics Monte Carlo, `http://cern.ch/fpmc`.

[3] CompHEP, `http://comphep.sinp.msu.ru/`.

[4] ATLFast++ package for ROOT, `http://root.cern.ch/root/Atlfast.html`.

[5] OPAL Collaboration, Phys. Rev. **D70** 032005 (2004).

[6] V.M. Abazov *et al.* [DØ Collaboration], Phys.Rev.Lett.**100**:241805,2008 (2008).

[7] J. Alcaraz *et al.* [ALEPH Collaboration], arXiv:hep-ex/0612034 (2006).

[8] C. Royon [RP220 Collaboration], arXiv:physics.ins-det/0706.1796 (2007);
M.G. Albrow *et al.* [AF420 R&D Collaboration], arXiv:hep-ex/0806.0302 (2008).

Physics at a $\gamma\gamma$ Collider

Klaus Mönig

DESY, Platanenallee 6, 15738 Zeuthen, Germany

DOI: http://dx.doi.org/10.3204/DESY-PROC-2009-03/Moenig

A $\gamma\gamma$-collider is a possible extension of an e^+e^- linear collider. The physics case of such a machine will be reviewed and compared to the one of the e^+e^- mode of the machine.

1 Introduction

At a linear collider beams are used only once so that it is possible to "convert" an electron beam into a photon beam by colliding it with an intense laser a few millimetres in front of the interaction point [1, 2, 3]. The high energy photons follow the electron flight direction so that the focusing of the beams works as in the e^+e^- mode. Using one or two lasers the machine can be used as an eγ or $\gamma\gamma$ collider. If the appropriate laser wavelength is chosen the photon beam has an energy of up to 80% of the energy of the incoming electron beam. Figure 1 (left) shows the photon energy spectrum for the different choices of the electron and laser polarisation. To achieve a high peak at maximal energy the helicity of the electron and laser beams must be opposite. Figure 1 (right) shows the resulting beam polarisation for the different cases. The setup that give the best energy spectrum also results in a large and stable polarisation in the high energy peak. Since only the product of the electron and laser polarisation matters the γ-beam polarisation can be varied by flipping both helicities simultaneously and the longitudinal angular momentum of the $\gamma\gamma$ system can be dominantly $J_z = 0$ or $J_z = 2$. In reality the spectrum gets distorted by two effects. To reach a high conversion probability the laser energy must be high which leads to non linear effects distorting the high energy peak. In addition there is a high chance that electrons interact a second time with a laser photon giving rise to a large peak at low energies. The resulting spectrum is shown in Fig. 2 [3].

In addition to circular polarisation also linear polarisation is possible at a photon collider. In this case the laser must be polarised linearly resulting in a less peaked energy spectrum. The linear polarisation in the high energy beam is on the 30% level, the simultaneous circular polarisation around 80%. The luminosity of a photon collider in the high energy part is around 10% of the e^+e^- luminosity for identical beam parameters. Due to the missing beam-beam effects the beams can be squeezed stronger so that a luminosity of $\mathcal{L}_{\gamma\gamma} \approx 0.3\mathcal{L}_{e^+e^-}$ seems possible.

Charged particles at the photon collider are produced via t-channel exchange which leads to a well known cross section proportional to Q^4. Especially for particles with unit charge they are typically one order of magnitude larger than in e^+e^-. Neutral particles like the Higgs can only be produced via loop diagrams, nevertheless the cross sections can be significant.

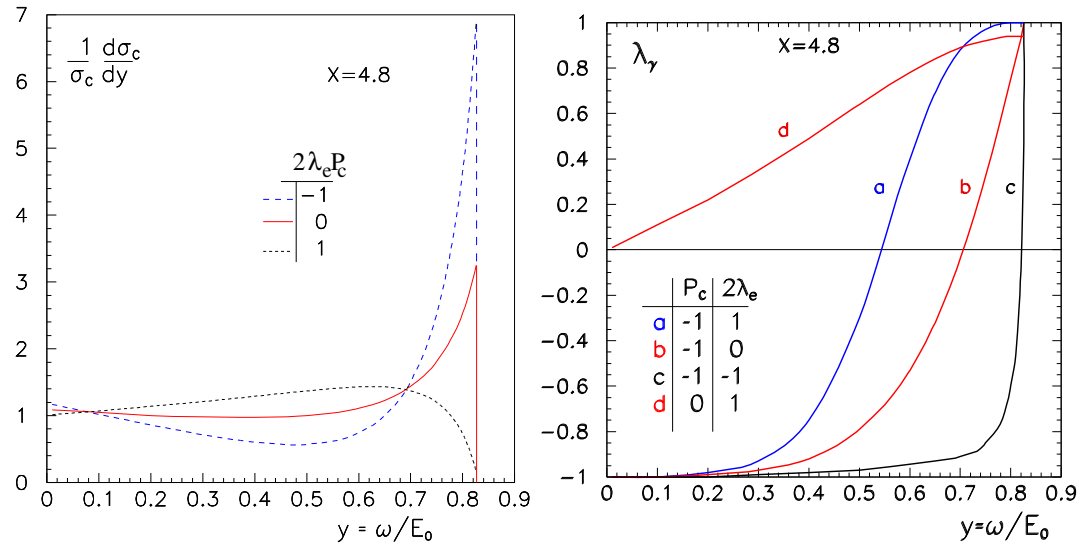

Figure 1: Left: normalised photon energy spectrum from Compton scattering for different electron and laser polarisation; right: photon circular polarisation for different electron and laser polarisation. Because of parity conservation in Compton scattering the missing combinations can be obtained from the shown ones by flipping all involved helicities [2].

2 Higgs Physics

Higgses are produced at the photon collider mainly by the loop graph shown in Fig. 3. All charged particles that couple to the Higgs contribute. In the Standard Model the cross section is dominated by the top-quark and the W-boson and there is a large sensitivity of the production cross section to new heavy charged particles coupling to the Higgs. At the photon collider the Higgs must be identified in a channel with a large branching ratio like $H \to b\bar{b}$ or $H \to W^+W^-$ and the observable $\Gamma(H \to \gamma\gamma) \times BR(H \to X\overline{X})$ is measured. For a light Higgs $BR(H \to b\bar{b})$ can be measured with a precision of around 2% in the e^+e^- mode [5]. For $m_H = 120\,\mathrm{GeV}$ about 10000 events per year will be produced at the photon collider. For Higgs production $J_z = 0$ is needed. For this polarisation state fermion pair production is suppressed by a factor m^2/s so that the background is manageable. Because of the Q^4-dependence of the background cross section a good b-tagging, especially b-c separation, is mandatory.

Detailed MC studies including all experimental and theoretical effects exist [6, 7]. The final mass spectrum is shown in Fig. 4 (left). $\Gamma(H \to \gamma\gamma) \times BR(H \to b\bar{b})$ can be measured with a precision of better than 2%. Combining with the $BR(H \to b\bar{b})$ measurement from the e^+e^- mode [5] this leads to a measurement of the coupling $g_{H\gamma\gamma}$ of around 1.5%.

For a heavier Higgs the decay mode $H \to W^+W^-$ must be used. This mode has the disadvantage of a much larger Standard Model background. However the interference with the $\gamma\gamma \to W^+W^-$ amplitude can also be used to measure the phase of the coupling [8]. The reconstructed WW mass spectrum is shown in Fig. 4 (right). Figure 5 (left) shows the possible precision of $\Gamma(H \to \gamma\gamma)$ as a function on m_H. For relatively light Higgses the precision is similar as in the $b\bar{b}$-mode. Figure 5 (right) shows the predicted change in $\Gamma(H \to \gamma\gamma) \times BR(H \to WW)$

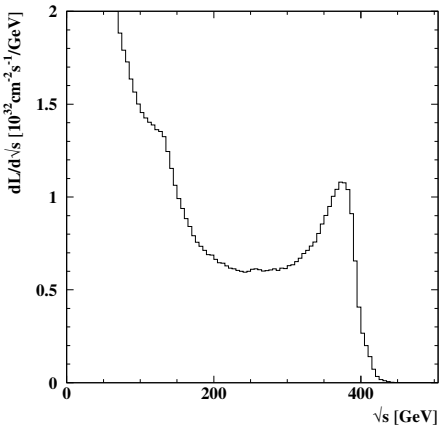

Figure 2: Luminosity spectrum for $\sqrt{s}_{ee} = 500\,\text{GeV}$ including non-linear effects and multiple interactions calculated with CAIN [4].

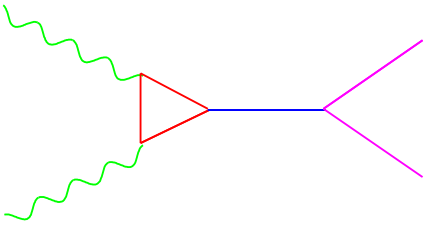

Figure 3: Feynman-graph for Higgs production at the photon collider.

and in the phase of the coupling for a 2HDM model. It can be seen that the phase brings additional information to distinguish the model from the SM or to measure model parameters.

For supersymmetric Higgses the photon collider has a real discovery window. If the A is significantly heavier than the Z the A, H and $H^{\pm}$ are almost mass degenerate and the ZZH and ZZA couplings vanish. The relevant production modes in e^+e^- are thus $e^+e^- \to HA$ and $e^+e^- \to H^+H^-$ and the mass reach is $\sqrt{s}/2$ [5]. For medium $\tan\beta$ and $m_A > 200$GeV also the LHC cannot detect the supersymmetric Higgses [9]. At the photon collider the loop induced s-channel production still works and the mass reach remains $0.8\sqrt{s}_{ee}$. Detailed studies show that the H and A can be reconstructed (see Fig. 6, left) and that it can bee identified with 5σ in at most two years of running (Fig. 6, right) [10].

Another possibility at the linear collider is the use of linear beam polarisation. With a linearly polarised laser a linear beam polarisation of around 30% can be achieved. As can be seen from Fig. 1 this leads, however, to s smaller circular polarisation and a less peaked energy spectrum. With linear beam polarisation a CP-even Higgs will only be produced if the polarisation direction of the two beams is parallel while for CP-odd states it must be orthogonal. A 3-year run has been simulated running for one year each at maximal linear polarisation with parallel and orthogonal direction and for one year with maximal circular polarisation [11]. Figure 7 (left) shows the mass spectrum for mass-degenerate H,A with linear polarisation. Due to the smaller circular polarisation the background is much higher than in Fig. 6. Figure 7

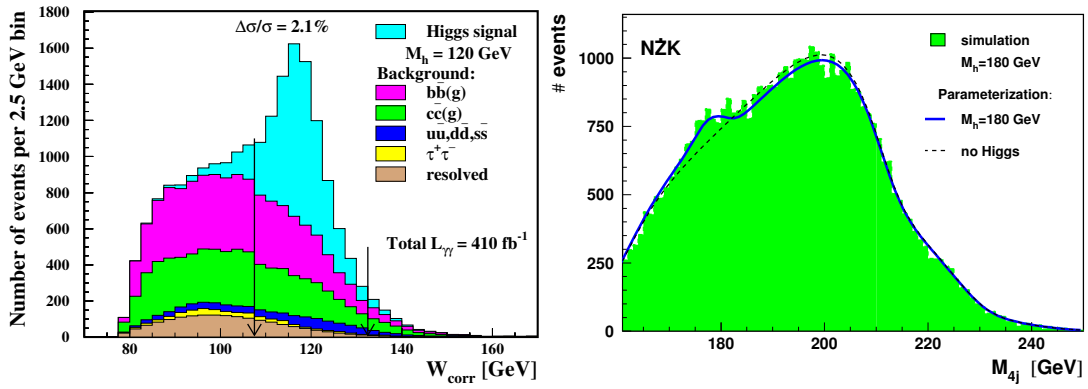

Figure 4: Possible reconstructed mass spectrum for $\gamma\gamma \to H \to b\overline{b}$ (left) [6] and $\gamma\gamma \to H \to WW$ (right) [8].

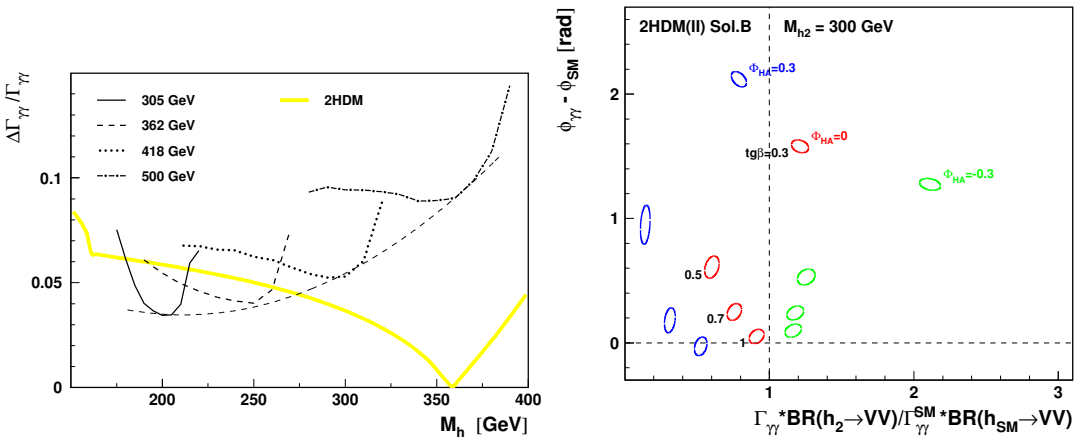

Figure 5: Left: relative precision of $\Gamma_{\gamma\gamma}$ for $H \to WW$ as a function of m_H; right: prediction for the change of $\Gamma_{\gamma\gamma} \times BR(H \to WW)$ and the phase of the coupling for different parameters in a 2HDM model [8].

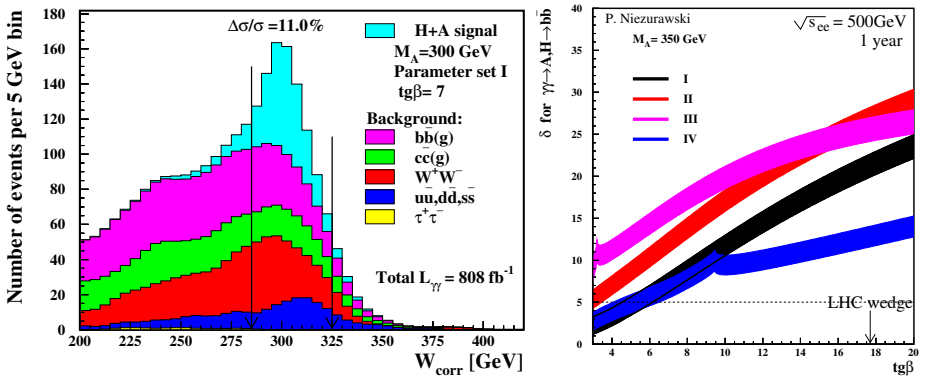

Figure 6: Left: mass spectrum for H, A production at a photon collider; right: H,A discovery range for one year of running at the photon collider. The parameters are defined in [10].

(right) shows the possible cross section measurements for pure CP states. In the case of one pure state, CP can be established with 5σ. If the H and A are mass-degenerate the two cross sections can be measured separately with a 20% precision.

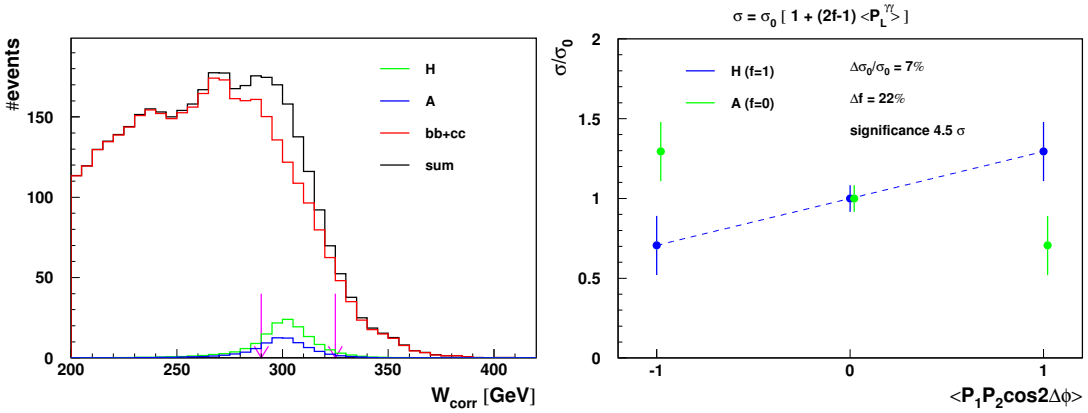

Figure 7: Left: reconstructed mass spectrum for $\gamma\gamma \to H, A \to b\bar{b}$ with linear polarisation; right: possible cross section measurement for $\gamma\gamma \to H \to b\bar{b}$ and $\gamma\gamma \to A \to b\bar{b}$ with one year each on maximal linear polarisation with parallel and orthogonal orientation and one year with zero linear and maximal circular polarisation [11].

The photon collider might also have the possibility to measure $\tan\beta$ [12]. The coupling of the τ to the H and A is proportional to $\tan\beta$ and Higgses can be produced via $\tau\tau$-fusion ($\gamma\gamma \to A\tau^+\tau^-$, $H\tau^+\tau^-$). The cross section is in the fb range (see Fig. 8) so that $\mathcal{O}(100)$ events per year are expected allowing to measure $\tan\beta$ to a few percent [12]. However an experimental study to estimate the reconstruction efficiency and backgrounds is still missing.

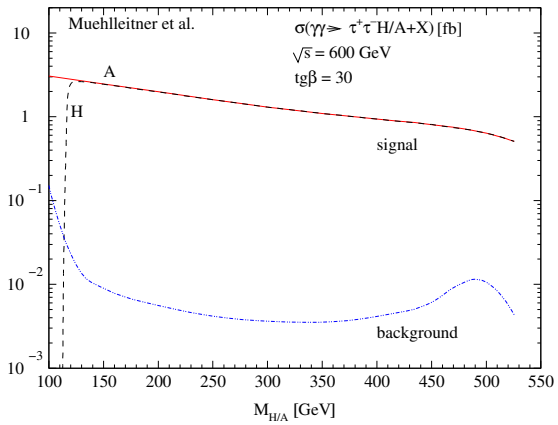

Figure 8: Cross section of the process $\gamma\gamma \to A\tau^+\tau^-$, $H\tau^+\tau^-$ as a function of the A,H mass [12].

3 Supersymmetry

In $\gamma\gamma$ superpartners are produced in pairs so that the reach is somewhat lower than in e^+e^-. However there is a possible discovery window in eγ using the process $e\gamma \to \tilde{e}_r\tilde{\chi}_1^0$. The mass reach for this process is $m(\tilde{e}_r) + m(\tilde{\chi}_1^0) < 0.9\sqrt{s}_{ee}$ which might be larger than the e^+e^- reach for slepton pair production ($0.5\sqrt{s}_{ee}$) if the mass difference $\tilde{e}_r - \tilde{\chi}_1^0$ is large. One needs right handed electrons to produce the $\tilde{e}_r$ which simultaneously reduces the single-W background that otherwise would be huge. An experimental simulation indicates that this channel can indeed be identified at an eγ collider [13]. The resulting mass spectrum is shown in Fig. 9 (left).

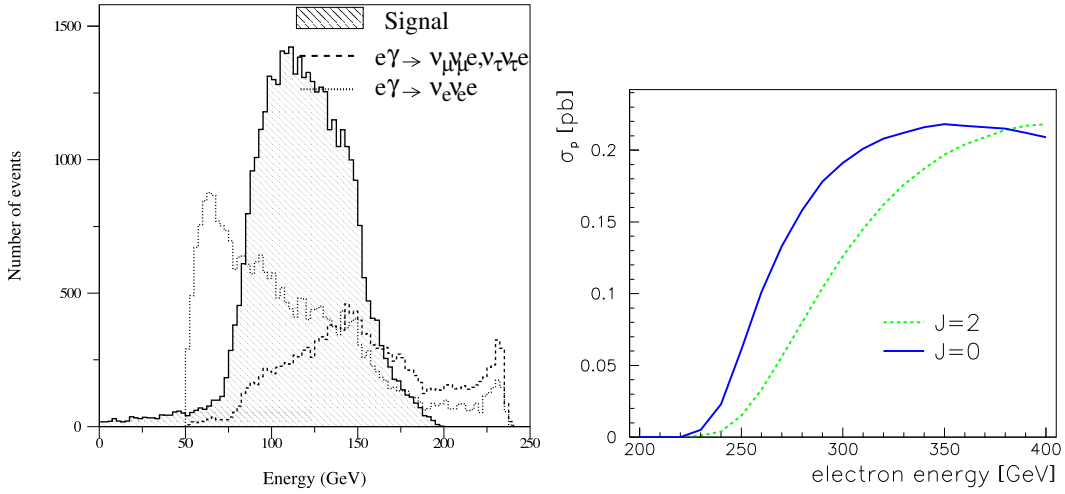

Figure 9: Left: mass spectrum for $e\gamma \to \tilde{e}_r\tilde{\chi}_1^0$ and corresponding backgrounds after cuts [13]; right: effective cross section for $\gamma\gamma \to \tilde{\chi}_1^+\tilde{\chi}_1^-$ for the two beam polarisation sates [14].

In the $\gamma\gamma$-mode all charged superpartners are produced in pairs. The cross sections are large, however the background, typically WW-production, is large as well. The cross sections can be calculated reliably in QED so that the measured event rates are directly proportional to the decay branching ratios. Figure 9 (right) shows the effective cross section[1] of the process $\gamma\gamma \to \tilde{\chi}_1^+\tilde{\chi}_1^- \to W^+W^-\tilde{\chi}_1^0\tilde{\chi}_1^0 \to q\bar{q}q\bar{q}\tilde{\chi}_1^0\tilde{\chi}_1^0$ for a SUSY scenario with $m_{\tilde{\chi}_1^\pm} = 180\,\text{GeV}$, $m_{\tilde{\chi}_1^0} = 96\,\text{GeV}$ and $BR(\tilde{\chi}_1^\pm \to \tilde{\chi}_1^0 W^\pm) = 26\%$ [14]. At $\sqrt{s}_{ee} = 600\,\text{GeV}$ this results in 8000 signal events per year. With an efficiency of 24% and a purity of 11% a measurement of $\frac{\Delta BR(\tilde{\chi}_1^\pm \to \tilde{\chi}_1^0 W)}{BR(\tilde{\chi}_1^\pm \to \tilde{\chi}_1^0 W)} = 3.5\%$ is possible. In the SUSY fits for ILC [15] this result improves the precision of $\tan\beta$ by more than a factor two. However no decay-mode sensitive variables from e^+e^- have been included in the fit up to now.

4 Coupling measurements

The photon-collider is only sensitive to the coupling of charged particles to photons, which has, however, the advantage that there are no ambiguities between the couplings to Z-bosons and photons. The monopole coupling (charge) is given by electromagnetic gauge invariance so that higher order couplings are accessible in the measurements. The best studied case is the γWW couplings which can be measured in $\gamma\gamma \to WW$ and $e\gamma \to \nu_e W$ [16, 17]. The cross section is large ($\sim 80\,\text{pb}$), however there is no sensitivity enhancement due to gauge cancellations. Because of the unknown longitudinal momentum the WW-system can only be fully reconstructed if both W-bosons decay hadronically. However, with symmetric beams the polar angle ambiguity $\theta \leftrightarrow \pi - \theta$, that arises because the W-charge cannot be measured, does not matter. In the $\gamma\gamma$-mode both polarisation states are sensitive to the triple gauge couplings. The J=0 state is, however, problematic since the luminosity cannot be measured accurately. Figure 10 compares the sensitivities to κ_γ and λ_γ at the different machines. For κ_γ, which is the more interesting coupling because of the lower mass dimension, the e^+e^--mode of the ILC is the by far most sensitive possibility. For λ_γ the $\gamma\gamma$ and $e\gamma$ modes are more sensitive than e^+e^-, however the LHC has a similar potential.

5 Conclusions

Depending on the physics scenario the photon collider can be an important addition to the e^+e^--mode of the ILC. For the interpretation of the data from the photon collider and for the final decision if the photon collider should be built data from e^+e^- are needed, so the the $\gamma\gamma$ mode should run after e^+e^-. This is also technically the preferred solution because the photon collider is more challenging with respect to the beam parameters and more difficult to set up. To exploit fully the physics case of the photon collider also the highest possible beam energy is needed.

For these reasons it is important that the design of the ILC includes the photon collider as an option that can run with maximum luminosity after or interleaved with the e^+e^- mode.

[1] The effective cross section is obtained by folding the $\gamma\gamma \to \tilde{\chi}_1^+\tilde{\chi}_1^-$ cross section with the luminosity spectrum.

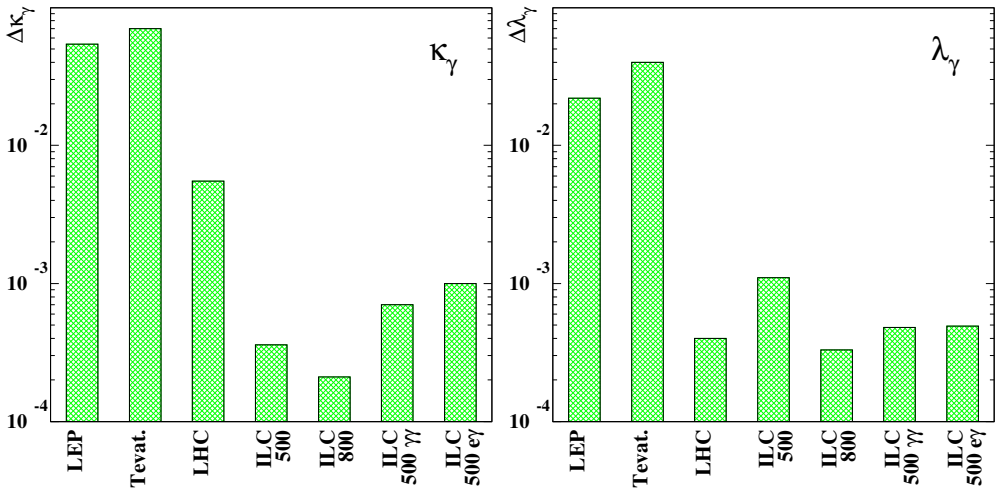

Figure 10: Sensitivity to κ_γ and λ_γ at the different machines [3].

References

[1] I. F. Ginzburg, G. L. Kotkin, V. G. Serbo, and V. I. Telnov *JETP Lett.* **34** (1981) 491–495.

[2] ECFA/DESY Photon Collider Working Group , B. Badelek *et al.*, "TESLA Technical Design Report, Part VI, Chapter 1: Photon collider at TESLA.". DESY-01-011E.

[3] F. Bechtel *et al. Nucl. Instrum. Meth.* **A564** (2006) 243–261, arXiv:physics/0601204.

[4] P. Chenand, T. Ohgaki, T. Takahashi, A. Spitkovsky, and K. Yokoya *Nucl.Instr.Meth.* **A397** (1997) 458–464.

[5] A. Djouadi *et al.* arXiv:0709.1893 [hep-ph].

[6] P. Niezurawski arXiv:hep-ph/0507004.

[7] K. Monig and A. Rosca *Eur. Phys. J.* **C57** (2008) 535–540, arXiv:0705.1259 [hep-ph].

[8] P. Niezurawski, A. F. Zarnecki, and M. Krawczyk arXiv:hep-ph/0307175.

[9] ATLAS Collaboration, Physics TDR, CERN-LHCC-99-14 and CERN-LHCC-99-15.

[10] P. Niezurawski, A. F. Zarnecki, and M. Krawczyk *Acta Phys. Polon.* **B37** (2006) 1187–1191.

[11] A. F. Zarnecki, P. Niezurawski, and M. Krawczyk arXiv:0710.3843 [hep-ph].

[12] S. Y. Choi *et al. Phys. Lett.* **B606** (2005) 164–172, arXiv:hep-ph/0404119.

[13] I. Alvarez Illan and K. Mönig, "Selectron production in $e\gamma$ collisions at a linear collider.". LC-PHSM-2005-002.

[14] G. Klamke and K. Moenig *Eur. Phys. J.* **C42** (2005) 261, arXiv:hep-ph/0503191.

[15] P. Bechtle, K. Desch, W. Porod, and P. Wienemann hep-ph/0511006.

[16] K. Mönig and J. Sekaric *Eur. Phys. J.* **C38** (2005) 427–436, hep-ex/0410011.

[17] K. Mönig and J. Sekaric hep-ex/0507050.

Higgs Physics at e^+e^- and Photon Colliders

Michael Spira

Paul Scherrer Institut, CH–5232 Villigen PSI, Switzerland

DOI: http://dx.doi.org/10.3204/DESY-PROC-2009-03/Spira

The search for Higgs bosons is one of the most important motivations for future linear e^+e^- and photon colliders. In this contribution the major aspects of Higgs physics of the Standard Model and its minimal supersymmetric extension at these two collider types will be reviewed. In particular the measurements of Higgs masses, quantum numbers and couplings via their production and decay processes at a linear e^+e^- collider will be shortly summarized. Ongoing developments of Higgs boson production via $\gamma\gamma$ fusion and their impact on coupling and parameter measurements will be discussed in detail.

1 Introduction

The Standard Model (SM) predicts the existence of one scalar Higgs boson which constitutes the remainder of electroweak symmetry breaking by means of the Higgs mechanism [1]. The requirement of a weakly interacting SM with a stable vacuum state at the electroweak ground state up to the scale of Grand Unified Theories (GUT), i.e. $\mathcal{O}(10^{16})$ GeV, constrains the Higgs mass to be between 130 and 190 GeV, while lowering this cutoff to the TeV scale enlarges the allowed Higgs mass range to about 50 – 800 GeV [2]. In all experiments this particle has escaped detection so far. The direct search in the LEP2 experiments via the process $e^+e^- \to ZH$ yields a lower bound of 114.4 GeV on the Higgs mass [3]. Electroweak fits to the precision observables at LEP, SLC and the Tevatron colliders yield an upper limit of the Standard Model Higgs mass of about 186 GeV at 95% CL [4].

Due to the hierarchy problem in the context of Grand Unified Theories supersymmetric (SUSY) extensions of the SM are considered as the most attractive solutions. The minimal supersymmetric extension of the SM (MSSM) requires the existence of five elementary Higgs bosons, two neutral CP-even (scalar) bosons h, H, one neutral CP-odd (pseudoscalar) boson A and two charged bosons $H^\pm$. At lowest order all couplings and masses of the MSSM Higgs sector are fixed by two independent input parameters, which are generally chosen as $\tan\beta = v_2/v_1$, the ratio of the two vacuum expectation values $v_{1,2}$, and the pseudoscalar Higgs mass M_A. Including the one-loop and dominant two-loop cor-

Φ		g_u^Φ	g_d^Φ	g_V^Φ
SM	H	1	1	1
MSSM	h	$\cos\alpha/\sin\beta$	$-\sin\alpha/\cos\beta$	$\sin(\beta-\alpha)$
	H	$\sin\alpha/\sin\beta$	$\cos\alpha/\cos\beta$	$\cos(\beta-\alpha)$
	A	$1/\tan\beta$	$\tan\beta$	0

Table 1: MSSM Higgs couplings to SM particles relative to SM Higgs couplings.

rections the upper bound on the light scalar Higgs mass is $M_h \lesssim 135$ GeV [5]. More recent first three-loop results confirm this upper bound within less than 1 GeV [6]. The couplings of the various Higgs bosons to fermions and gauge bosons depend on mixing angles α and β, which are defined by diagonalizing the neutral and charged Higgs mass matrices. They are collected in Table 1 relative to the SM Higgs couplings. For large values of $\tan\beta$ the down-type Yukawa couplings are strongly enhanced, while the up-type Yukawa couplings are suppressed. This feature causes the dominance of bottom-Yukawa-coupling induced processes for large values of $\tan\beta$ at present and future colliders as Higgs decays into bottom quarks and Higgs bremsstrahlung off bottom quarks at hadron and e^+e^- colliders. Moreover, Higgs boson production via gluon fusion $gg \to h, H, A$ is dominated by the bottom-loop contributions for large $\tan\beta$.

Once the Higgs boson of the SM will be found at the LHC, its properties have to be analyzed. However, at the LHC only ratios of Higgs couplings can be determined in the intermediate mass range in a model-independent way. The expected accuracies for the ratios of the various decay channels are displayed in Fig. 1 [7] which implies that a first insight into the fundamental rule $g_i/g_j = m_i/m_j$ for various particles $i, j = W, Z, \tau, b$ can be obtained. For Higgs masses above about 200 GeV the total Higgs decay width can be measured at the LHC with an accuracy down to $\mathcal{O}(10\%)$ for larger Higgs masses, while it is too small to be extracted from the invariant mass peak for smaller Higgs masses [8].

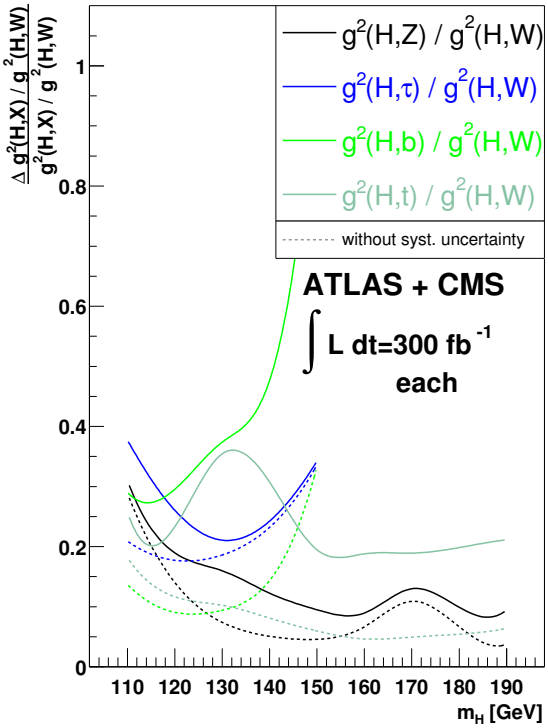

Figure 1: Expected accuracies in measurements of ratios of Higgs couplings at the LHC [7].

A similar situation is expected to emerge for the supersymmetric Higgs bosons of the MSSM in regions where several decay modes of the Higgs particles can be detected. For large values of $\tan\beta$ this fundamental MSSM parameter can be measured with an accuracy at the level of 10% [8]. However, within the MSSM there is a large region for intermediate values of $\tan\beta$ and moderate to large values of the pseudoscalar mass M_A, where the LHC will discover the light scalar Higgs particle h only. Since in this region the light scalar is SM-like it cannot be distinguished from the Higgs boson of the SM. None of the heavier Higgs particles can be seen at the LHC in this wedge region.

2 Higgs Physics at the ILC

Higgs boson production at the ILC proceeds analogously to the LEP collider, i.e. via Higgs-strahlung $e^+e^- \to ZH$ and WW/ZZ–fusion $e^+e^- \to \nu_e\bar{\nu}_e/e^+e^- + H$. The SM Higgs boson can be discovered up to about 70% of the c.m. energy. The Higgs-strahlung process provides the potential to reconstruct the Higgs mass purely from the recoil mass due to the monoenergetic Z boson in the final state and thus independently of the Higgs decay mode. This offers a precise measurement of the Higgs boson mass with an accuracy of 40-80 MeV as is shown in Fig. 2. Moreover, the Higgs boson coupling to the Z boson can be determined in a model-independent manner [9]. This opens the way to a model-independent

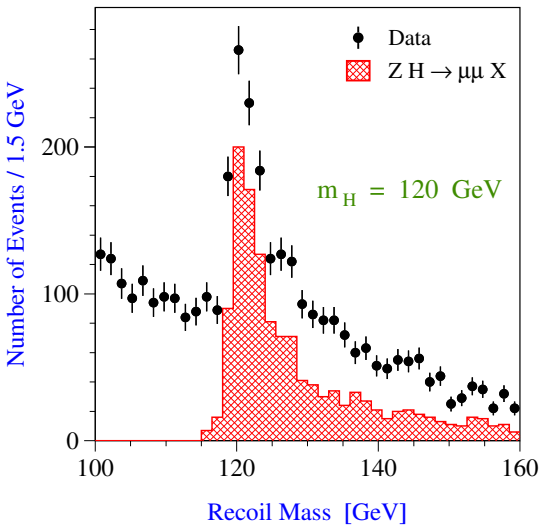

Figure 2: The $\mu^+\mu^-$ recoil mass distribution in the process $e^+e^- \to HZ \to X\mu^+\mu^-$ for $M_H = 120$ GeV and $\int \mathcal{L} = 500 fb^{-1}$ at $\sqrt{s} = 350$ GeV. The dots with error bars are Monte Carlo simulations of the Higgs signal and the background. The shaded histogram represents the signal only. Ref. [9].

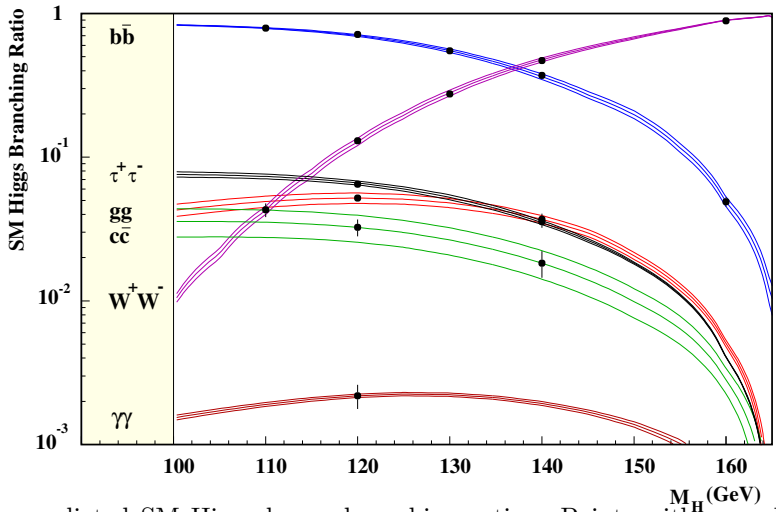

Figure 3: The predicted SM Higgs boson branching ratios. Points with error bars show the expected experimental accuracy, while the lines show the estimated parametric uncertainties on the SM predictions. Ref. [9].

measurement of the branching ratios of several Higgs boson decay modes with high accuracy. The results of these studies are displayed in Fig. 3 [9]. These measurements can then be used to determine the corresponding Higgs couplings to bottom and charm quarks, τ leptons as well as to W^+W^-, gg and $\gamma\gamma$ pairs down to the per-cent level in several cases. This completes the picture of the first studies at the LHC with much higher accuracy and with much more model independence.

The angular distribution of the Z/H particles in the Higgs-strahlung process can be used to determine the spin and parity of the Higgs particle as can be inferred from the left plot of Fig. 4. The generic angular distributions of scalar and pseudoscalar Higgs-strahlung differ significantly between each other and from the background of Z boson pair production $e^+e^- \to ZZ$. This can be used to determine the admixture of a pseudoscalar component to the scalar SM Higgs matrix element at the per-cent level [9].

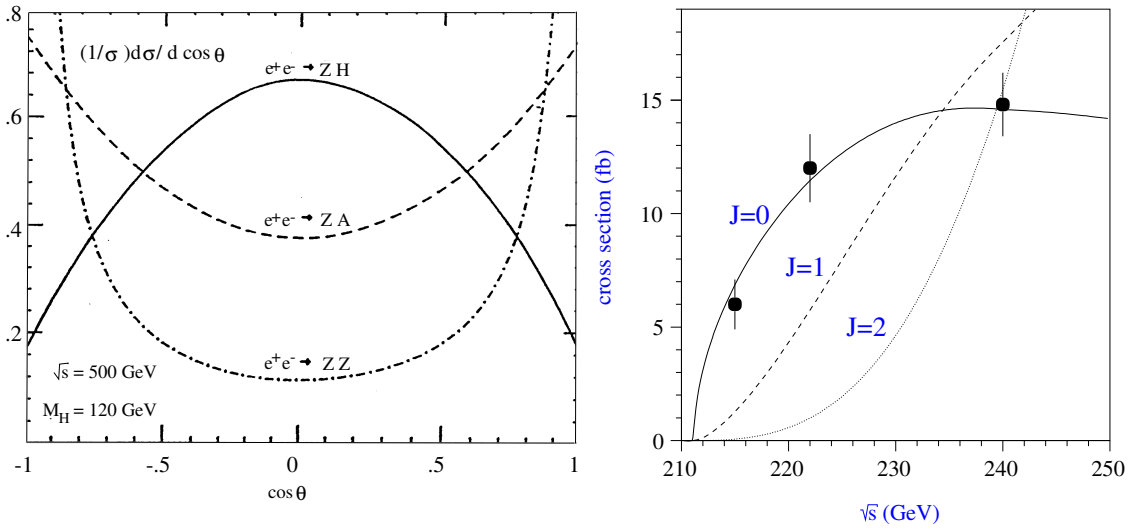

Figure 4: Left: Angular distribution of Z/H bosons in Higgs-strahlung, compared with the production of pseudoscalar particles and the ZZ background final states. Ref. [10]. Right: Threshold excitation of Higgs-strahlung which discriminates spin=0 from other assignments, Ref. [11].

A different method to determine the spin of the Higgs particle is provided by a threshold scan in the Higgs-strahlung process. The theoretical threshold behaviour of particles with different integer spin quantum numbers is shown in the right plot of Fig. 4. The data points reflect the expected accuracies that can be reached at the ILC by a threshold scan [11]. In contrast to the LHC the spin and $\mathcal{CP}$ quantum numbers of the Higgs boson can be uniquely determined at the ILC.

Higgs boson pair production via double Higgs-strahlung $e^+e^- \to ZHH$ and the WW-fusion processes $e^+e^- \to \nu_e\bar{\nu}_e HH$ are sensitive to the trilinear Higgs coupling λ_{HHH}. A measurement of this coupling exhibits the first step towards an experimental measurement of the Higgs potential. This constitutes a crucial test of electroweak symmetry breaking in the Higgs sector. Although the sensitivity of the processes above to λ_{HHH} is quite limited, the experimental accuracy at the ILC with energies up to the TeV range allows a measurement down to the 10%

level in the intermediate Higgs mass range [12] as is shown in Fig. 5.

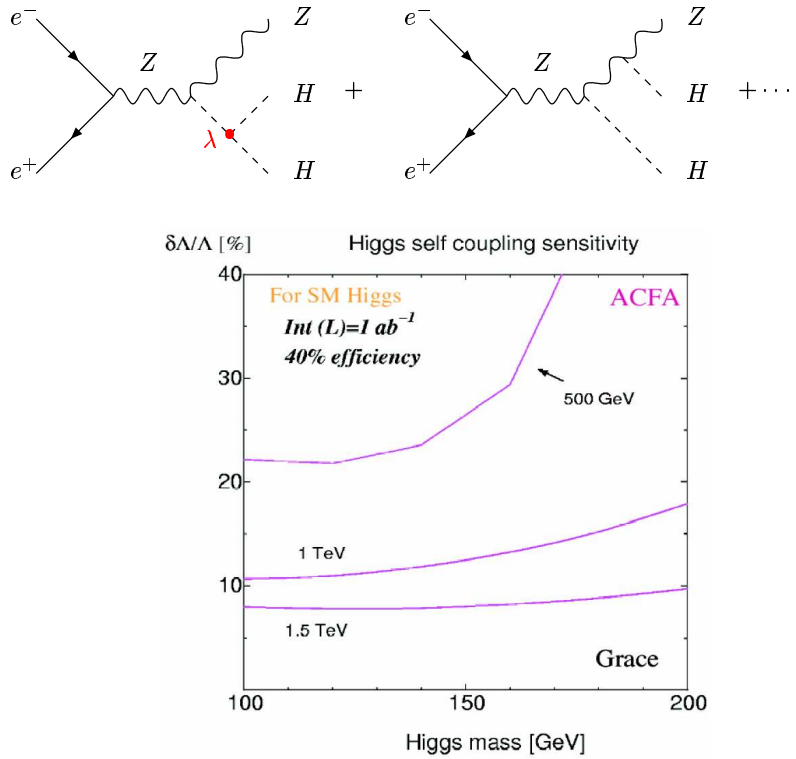

Figure 5: Upper: Generic diagrams of the double Higgs-strahlung process. Lower: The sensitivity of the double Higgs-strahlung and the WW fusion processes to the trilinear Higgs coupling Λ in the intermediate Higgs mass range for an integrated luminosity $\int \mathcal{L} = 1\ ab^{-1}$ at $\sqrt{s} =$ 500 GeV, 1 TeV and 1.5 TeV. Ref. [13].

3 Higgs Physics at the PLC

A photon collider can be constructed on top of the ILC by Compton backscattering of laser light off the e^- beams with a c.m. energy peaking at about 80% of the original e^+e^- energy [14]. This collider mode can be used to search for single s-channel Higgs boson production, since the Higgs particles couple to photon pairs by means of W boson and top/bottom triangle loops. The final state Higgs decay into $b\bar{b}$ pairs can be extracted from the background by appropriate cuts on the bottom scattering angles and by requiring two-jet configurations. In this way the cross section and thus the SM Higgs coupling to photon pairs can be measured with an accuracy at the per-cent level [15], see Fig. 6, for the SM Higgs boson in the intermediate mass range. Since the Higgs coupling to photons develops imaginary parts due to threshold effects inside the loop contributions, it turns out to be complex. The complex phase of the amplitude can be determined from the interference with the ZZ, W^+W^- and $t\bar{t}$ backgrounds at the level of a couple of per-cent at a photon collider [16, 17]. Moreover, the $\mathcal{CP}$ properties of Higgs bosons can

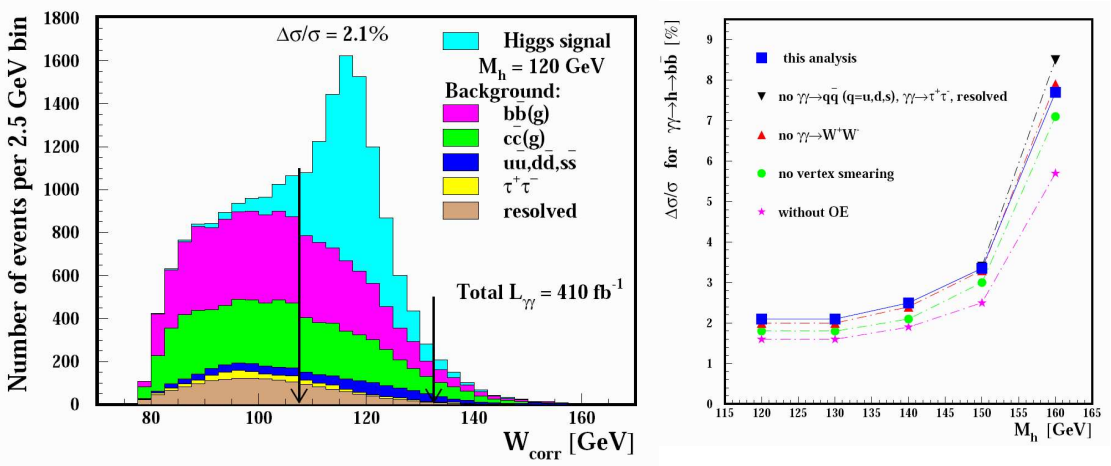

Figure 6: Experimental simulation of the production of SM Higgs bosons with subsequent decay into $b\bar{b}$ at a photon collider. Left: Reconstructed signal peak above backgrounds. Right: Expected accuracy of the cross section measurement. Ref. [15].

be studied at a PLC. The relative $\mathcal{CP}$-phase between the scalar and pseudoscalar components can be measured with an accuracy at the level of a few per-cent in Higgs decays to Z boson pairs [18] and into $t\bar{t}, \tau^+\tau^-$ pairs [17, 19].

The photon collider mode offers the opportunity to produce and search for supersymmetric MSSM Higgs boson in the wedge region in which the LHC can only find the light scalar Higgs boson. Its reach in the $b\bar{b}$ decay channel turns out to be up to about 600 GeV [20], i.e. far beyond the Higgs mass reach of a 500 GeV ILC. Experimental simulations have demonstrated that the production cross section can be measured in this wedge region with a precision at the 10%-level, see Fig. 7. This measurement provides a quantitative test of the photonic MSSM Higgs couplings of the heavy scalar and pseudoscalar Higgs particles, which are sensitive to the heavy charged particle spectrum of the MSSM.

The PLC will allow for a measurement of the trilinear Higgs couplings in Higgs boson pair production processes $\gamma\gamma \to HH$. Generic diagrams contributing to this process are shown in Fig. 8. By tuning the $\gamma\gamma$ c.m. energy according to the Higgs masses an accuracy in the 10% range can be reached at the PLC which is comparable to the accuracies reachable in the e^+e^- mode [21, 22].

Finally, the PLC will provide an additional opportunity to measure the MSSM parameter $\tan\beta$ in the τ-fusion processes $\gamma\gamma \to \tau^+\tau^- + h/H/A \to \tau^+\tau^- b\bar{b}$. By applying proper cuts, the signal processes can be extracted from the background processes which are dominated by $\tau^+\tau^-$ annihilation into bottom quarks and diffractive $\gamma\gamma \to (\tau^+\tau^-)(b\bar{b})$ events. The statistical accuracy, with which large $\tan\beta$ values can be measured, is exemplified for three $\tan\beta$ values in Tab. 2. The scalar and pseudoscalar processes have been combined, whenever the Higgs states are nearly mass degenerate. The absolute errors for the measurement of $\tan\beta$ are of $\mathcal{O}(1)$ which translates into accuracies in the per-cent to 10%-range depending on the size of $\tan\beta$ [23].

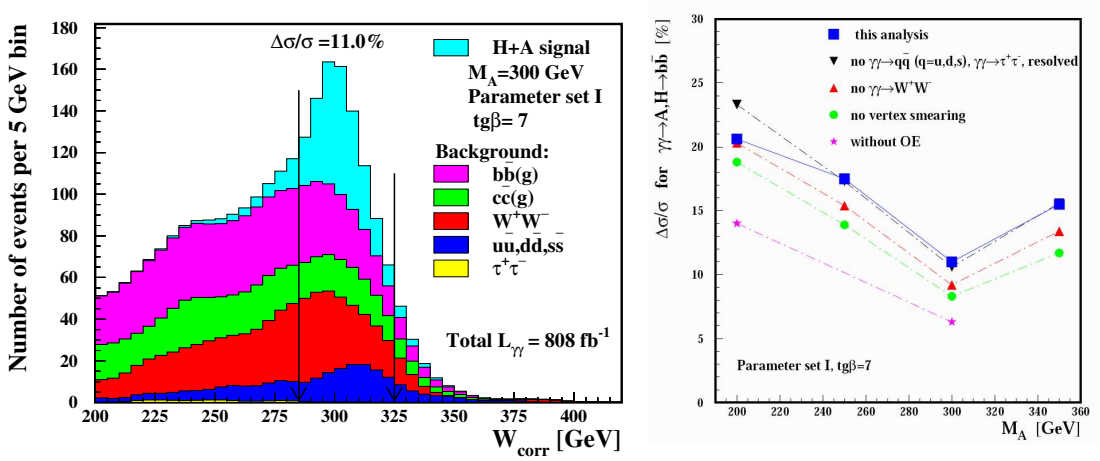

Figure 7: Experimental simulation of the production of heavy MSSM Higgs bosons with subsequent decay into $b\bar{b}$ at a photon collider. Left: Reconstructed signal peak above backgrounds. Right: Expected accuracy of the cross section measurement. Ref. [20].

	$E_{\gamma\gamma}=400$ GeV, $\mathcal{L}=100$ fb^{-1}				$E_{\gamma\gamma}=600$ GeV, $\mathcal{L}=200$ fb^{-1}				
$\tan\beta$	M_h [GeV]	$A\oplus H: M_A$ [GeV]			$A\oplus H: M_A$ [GeV]				
	100	100	200	300	100	200	300	400	500
10	12.9%	12.8%	10.7%	13.9%	12.3%	9.0%	11.2%	13.2%	16.5%
30	3.7%	3.7%	3.5%	4.6%	3.5%	3.0%	3.7%	4.4%	5.3%
50	2.2%	2.2%	2.1%	2.7%	2.1%	1.8%	2.2%	2.6%	3.2%

Table 2: *Relative errors* $\Delta\tan\beta/\tan\beta$ *on* $\tan\beta$ *measurements for* $\tan\beta = 10$, *30 and 50 based on: h [first column] and combined* $A\oplus H$ *[next three columns] assuming* $E_{\gamma\gamma}=400$ *GeV,* $\mathcal{L}=100$ *fb*$^{-1}$, *and* $A\oplus H$ *production [last four columns] with* $E_{\gamma\gamma}=600$ *GeV,* $\mathcal{L}=200$ *fb*$^{-1}$. *Ref. [23].*

References

[1] P. W. Higgs, Phys. Lett. **12**, 132 (1964), Phys. Rev. Lett. **13**, 508 (1964) and Phys. Rev. **145**, 1156 (1966); F. Englert and R. Brout, Phys. Rev. Lett. **13**, 321 (1964); G. S. Guralnik, C. R. Hagen and T. W. Kibble, Phys. Rev. Lett. **13**, 585 (1964).

[2] N. Cabibbo, L. Maiani, G. Parisi and R. Petronzio, Nucl. Phys. **B158** (1979) 295; M. Chanowitz, M. Furman and I. Hinchliffe, Phys. Lett. **B78** (1978) 285; R.A. Flores and M. Sher, Phys. Rev. **D27** (1983) 1679; M. Lindner, Z. Phys. **C31** (1986) 295; M. Sher, Phys. Rep. **179** (1989) 273; Phys. Lett. **B317** (1993) 159 and addendum **B331** (1994) 448; G. Altarelli and G. Isidori, Phys. Lett. **B337** (1994) 141; J. Casas, J. Espinosa and M. Quiros, Phys. Lett. **B342** (1995) 171; J. Espinosa and M. Quiros, Phys. Lett. **B353** (1995) 257; A. Hasenfratz, K. Jansen, C. Lang, T. Neuhaus and H. Yoneyama, Phys. Lett. **B199** (1987) 531; J. Kuti, L. Liu and Y. Shen, Phys. Rev. Lett. **61** (1988) 678; M. Lüscher and P. Weisz, Nucl. Phys. **B318** (1989) 705.

[3] G. Abbiendi et al., Phys. Lett. **B565** (2003) 61, [arXiv:hep-ex/0306033].

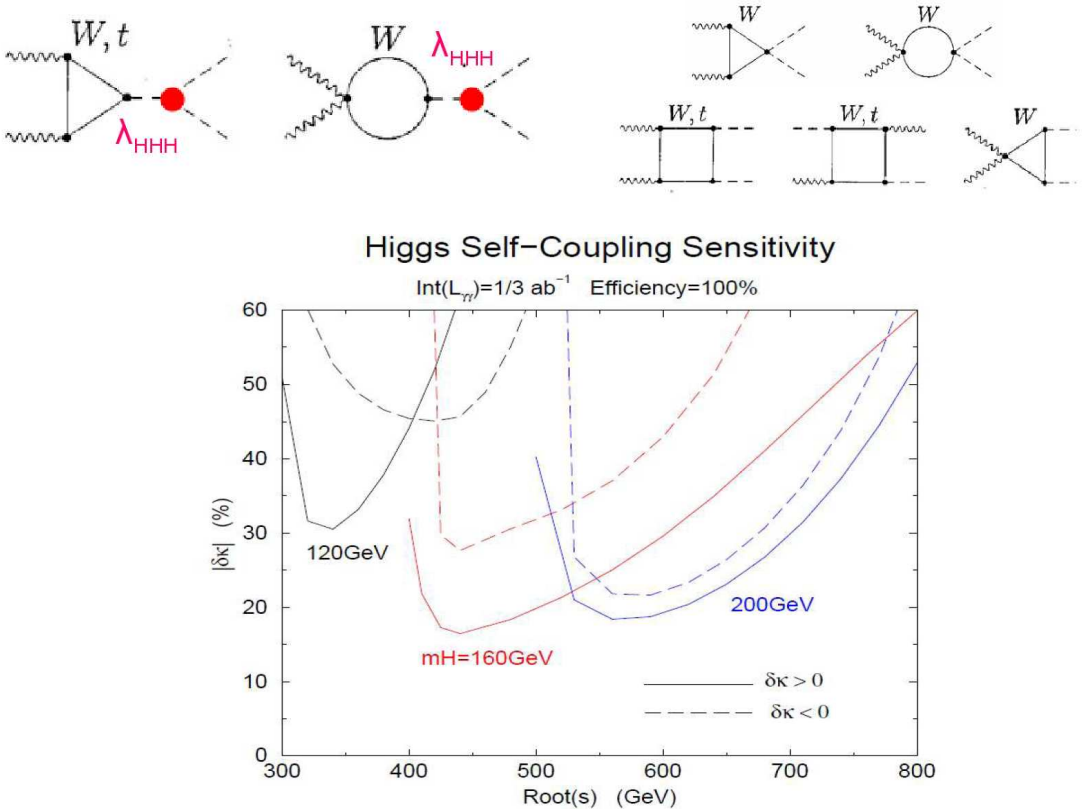

Figure 8: Upper: Generic diagrams contributing to Higgs pair production $\gamma\gamma \to HH$ in the SM. Lower: Experimental sensitivity of SM Higgs boson pair production to the trilinear Higgs coupling κ at a photon collider for different Higgs masses [22].

[4] ALEPH, CDF, D0, DELPHI, L3, OPAL and SLD Collaborations, LEP, SLD and Tevatron Electroweak Working Groups and Heavy Flavour Group, CERN-PH-EP/2008-020, arXiv:0811.4682 [hep-ex].

[5] see e.g. G. Degrassi, S. Heinemeyer, W. Hollik, P. Slavich and G. Weiglein, Eur. Phys. J. **C28** (2003) 133.

[6] S. P. Martin, Phys. Rev. **D75** (2007) 055005; R. V. Harlander, P. Kant, L. Mihaila and M. Steinhauser, Phys. Rev. Lett. **100** (2008) 191602, Erratum *ibid.* **101** (2008) 039901.

[7] M. Dührssen, S. Heinemeyer, H. Logan, D. Rainwater, G. Weiglein and D. Zeppenfeld, Phys. Rev. D **70** (2004) 113009.

[8] ATLAS: Detector and physics performance technical design report, CERN-LHCC-99-014 and CERN–LHCC–99–15; G. L. Bayatian *et al.* [CMS Collaboration], J. Phys. G **34** (2007) 995.

[9] E. Accomando et al., Phys. Rep. **299** (1998) 1; J.A. Aguilar-Saavedra et al., TESLA TDR, hep-ph/0106315; A. Djouadi et al., ILC RDR, arXiv:0709.1893 [hep-ph].

[10] V. Barger, K. Cheung, A. Djouadi, B.A. Kniehl and P. Zerwas, Phys. Rev. **D49** (1994) 79.

[11] D.J. Miller, S.Y. Choi, B. Eberle, M.M. Mühlleitner and P.M. Zerwas, Phys. Lett. **B505** (2001) 149; M.T. Dova, P. Garcia-Abia and W. Lohmann, LC-PHSM-2001-054 [arXiv:hep-ph/0302113].

[12] A. Djouadi, W. Kilian, M. Mühlleitner and P.M. Zerwas, Eur. Phys. J **C10** (1999) 27; M. Mühlleitner, arXiv:hep-ph/0008127; C. Castanier et al., arXiv:hep-ex/0101028, and references in Ref. [9].

[13] GLC project: Linear Collider for TeV physics, KEK-REPORT-2003-7.

[14] I.F. Ginzburg, G.L. Kotkin, V.G. Serbo and V.I. Telnov, Pizma ZhETF **34** (1981) 514, JETP Lett. **34** (1982) 491 and Nucl. Instrum. Meth. **205** (1983) 47; I.F. Ginzburg, G.L. Kotkin, S.L. Panfil, V.G. Serbo and V.I. Telnov, Nucl. Instrum. Meth. **A2** (1984) 5.

[15] G. Jikia, S. Söldner-Rembold, Nucl. Instrum. Meth. A 472 (2001) 133; P. Nieżurawski, A.F. Żarnecki and M. Krawczyk, arXiv:hep-ph/0307183; K. Mönig and A. Rosca, Eur. Phys. J. C **57** (2008) 535.

[16] P. Nieżurawski, A.F. Żarnecki and M. Krawczyk, JHEP **0211** (2002) 034;

[17] E. Asakawa and K. Hagiwara, Eur. Phys. J. C **31** (2003) 351.

[18] S. Y. Choi, D. J. . Miller, M. M. Mühlleitner and P. M. Zerwas, Phys. Lett. B **553** (2003) 61; P. Nieżurawski, A. F. Żarnecki and M. Krawczyk, Acta Phys. Polon. B **36** (2005) 833.

[19] E. Asakawa, S. Y. Choi, K. Hagiwara and J. S. Lee, Phys. Rev. D **62** (2000) 115005; R.M. Godbole, S. Kraml, S.D. Rindani and R.K. Singh, Phys. Rev. D **74** (2006) 095006 [Erratum-ibid. D **74** (2006) 119901].

[20] M. Mühlleitner, M. Krämer, M. Spira, P. Zerwas, Phys. Lett. B 508 (2001) 311; M.M. Mühlleitner, PhD thesis, DESY-THESIS-2000-033, hep-ph/0008127; D. M. Asner, J. B. Gronberg and J. F. Gunion, Phys. Rev. D **67** (2003) 035009; P. Nieżurawski, A.F. Żarnecki and M. Krawczyk, Acta Phys. Polon. B **37** (2006) 1187; M. Spira, P. Nieżurawski, M. Krawczyk and A.F. Żarnecki, Pramana **69** (2007) 931.

[21] R. Belusevic and G. Jikia, Phys. Rev. D **70** (2004) 073017.

[22] E. Asakawa, D. Harada, S. Kanemura, Y. Okada and K. Tsumura, arXiv:0902.2458 [hep-ph].

[23] S. Y. Choi, J. Kalinowski, J. S. Lee, M. M. Mühlleitner, M. Spira and P. M. Zerwas, Phys. Lett. B **606** (2005) 164 and arXiv:hep-ph/0407048.

Double Higgs Production at a Photon Collider

Abdesslam Arhrib[1,2], *Rachid Benbrik*[2,3,4], *Chuan-Hung Chen*[3,4] *and Rui Santos*[5]

[1] Faculté des Sciences et Techniques, Université Abdelmalek Essaâdi, B.P. 416, Tangier, Morocco
[2]LPHEA, Faculté des Sciences-Semlalia, B.P. 2390 Marrakesh, Morocco
[3] Department of Physics, National Cheng Kung University, Taiwan 701, Taiwan
[4] National Center for Theoretical Physics, Taiwan 701, Taiwan
[5] NExT Institute and School of Physics and Astronomy, University of Southampton Highfield, Southampton SO17 1BJ, UK

DOI: http://dx.doi.org/10.3204/DESY-PROC-2009-03/Santos

We study double Higgs production in photon-photon collisions in the framework of two Higgs Doublet Models. We show that the fusion processes $\gamma\gamma \to S_i S_j$, $S_i = h^0, H^0, A^0$, can be enhanced by threshold effects in the region $E_{\gamma\gamma} \approx 2m_{H^\pm}$. We have scanned the allowed parameter space of the two Higgs Doublet Model and found a vast region where the cross section is two orders of magnitude above the Standard Model cross section. We further show that the Standard Model experimental analysis can be used to discover or to constraint the two Higgs doublet model parameter space.

1 Introduction

With the eminent start of CERN's Large Hadron Collider (LHC), enthusiasm is growing in the particle physics community with the prospect of finding the scalar responsible for electroweak symmetry breaking. If the Higgs is found, the next task will be to identify the underlying model and in many cases, a complete identification can only be completed with the help of a $\gamma\gamma$ collider [1, 2]. Since photons couple directly to all fundamental fields carrying electromagnetic charge, $\gamma\gamma$ collisions provide a comprehensive means of exploring virtual aspects of the Standard Model (SM) and its extensions [3]. The production mechanism in hadron and e^+e^- machines are often more complex and model-dependent.

Neutral Higgs bosons are primarily produced in $\gamma\gamma$ collisions via $\gamma\gamma \to (h^0, H^0, A^0)$ [4, 5, 6, 7] However, triple and quartic Higgs couplings can only be explored through Higgs boson pair production processes. 2HDM triple Higgs couplings could be measured at e^+e^- colliders [8]. At photon-photon colliders, the cross section for neutral Higgs boson pair production has been calculated in [9, 10] in the SM and found to be rather small. In the 2HDM, the authors of [11, 12] found that the cross section for $\gamma\gamma \to h^0h^0$ can be substantially enhanced relative to the SM one in the decoupling limit.

In this work, we present a complete calculation of pair production of all neutral Higgs bosons at the one loop level in the 2HDM. We study the Higgs self couplings effects on the $\gamma\gamma \to h^0h^0$ and $\gamma\gamma \to A^0A^0$ cross sections and briefly comment on the $\gamma\gamma \to h^0A^0$, $\gamma\gamma \to h^0H^0$, $\gamma\gamma \to H^0A^0$ and $\gamma\gamma \to H^0H^0$ production modes. This exhausts all possible neutral scalar

production processes in the 2HDM. A measurement of these processes could shed some light on the 2HDM triple Higgs couplings. However, even if the situation regarding a measurement of the vertex is not clear because no peak is detected, a vast region of the 2HDM parameter space will be excluded. For a more detailed version of this study see [13].

2 The CP-conserving 2HDM

The 2HDM potential used in this work is an eight parameter potential invariant under the Z_2 discrete symmetry $\Phi_1 \to \Phi_1$, $\Phi_2 \to -\Phi_2$ except for the soft breaking term $[m_{12}^2 \Phi_1^\dagger \Phi_2 + \text{h.c.}]$. The vacuum structure is chosen such that the potential does not break CP spontaneously and the potential is written as

$$\begin{aligned} V(\Phi_1,\Phi_2) &= m_1^2 \Phi_1^\dagger \Phi_1 + m_2^2 \Phi_2^\dagger \Phi_2 + (m_{12}^2 \Phi_1^\dagger \Phi_2 + \text{h.c}) + \frac{1}{2}\lambda_1 (\Phi_1^\dagger \Phi_1)^2 + \frac{1}{2}\lambda_2 (\Phi_2^\dagger \Phi_2)^2 \\ &+ \lambda_3 (\Phi_1^\dagger \Phi_1)(\Phi_2^\dagger \Phi_2) + \lambda_4 (\Phi_1^\dagger \Phi_2)(\Phi_2^\dagger \Phi_1) + \frac{1}{2}\lambda_5 [(\Phi_1^\dagger \Phi_2)^2 + \text{h.c.}] \ , \end{aligned} \tag{1}$$

where Φ_i, $i = 1, 2$ are complex $SU(2)$ doublets and all parameters are real. After symmetry breaking, we end up with two CP-even Higgs states usually denoted by h^0 and H^0, one CP-odd state, A^0, two charged Higgs boson, $H^\pm$ and three Goldstone bosons. Because $v^2 = v_1^2 + v_2^2$ is fixed by $v^2 = (2\sqrt{2}G_F)^{-1}$, there are 7 independent parameters we can choose. We adopt as independent parameters, m_{h^0}, m_{H^0}, m_{A^0}, $m_{H^\pm}$, $\tan\beta = v_2/v_1$, α and m_{12}^2. The angle β is the rotation angle from the group eigenstates to the mass eigenstates in the CP-odd and charged sector. The angle α is the corresponding rotation angle for the CP-even sector. The Yukawa Lagrangian is a straightforward generalization of the SM one. The need to avoid tree-level flavor changing neutral currents (FCNCs) lead us to extend the Z_2 symmetry to fermions. It suffices that fermions of a given electric charge couple to no more than one Higgs doublet [14]. This can be accomplished naturally by imposing on all fields appropriate discrete symmetries that forbid the unwanted FCNC couplings. There are essentially four ways of doing this [15]: type I is the model where only the doublet ϕ_2 couples to all fermions; type II is the model where ϕ_2 couples to up-type quarks and ϕ_1 couples to down-type quarks and leptons; in a Type III model ϕ_2 couples to all quarks and ϕ_1 couples to all leptons; a Type IV model is instead built such that ϕ_2 couples to up-type quarks and to leptons and ϕ_1 couples to down-type quarks.

In our analysis we took into account all available experimental and constraints on the 2HDM parameter space. LEP direct searches give us a lower bound for particle masses (see [16] for details) except in some particular scenarios. In a general 2HDM all bounds on the Higgs masses, with the exception of the charged Higgs, can be avoided with a suitable choice of the angles and m_{12}. The extra contributions to the $\delta\rho$ parameter from the Higgs scalars [17] should not exceed the current limit from precision measurements [16]: $|\delta\rho| \lesssim 10^{-3}$. As this extra contribution to $\delta\rho$ vanishes when $m_{H^\pm} = m_{A^0}$, we demand either a small splitting between $m_{H^\pm}$ and m_{A^0} or a combination of parameters that produces the same effect. The constraint from the $B \to X_s\gamma$ branching ratio [18] gives a lower bound on the charged Higgs mass, $m_{H^\pm} \gtrsim 295\ GeV$, in 2HDM type II and III. These bounds do not apply to models type I and IV. Values of $\tan\beta$ smaller than ≈ 1 are disallowed both by the constraints coming from $Z \to b\bar{b}$ and from $B_q \bar{B}_q$ mixing [18]. Finally, we take into account the following theoretical constraints: perturbative unitarity as defined in [19, 20], vacuum stability conditions [21] that assure that the potential is bounded from below and perturbativity on the couplings, that is, $|\lambda_i| \leq 8\pi$ for all i. Finally we note that all 2HDM are protected against charge and CP-breaking [22].

3 Results and discussion

The processes $\gamma\gamma \to S_i S_j$, $S_{i,j} = h^0, H^0, A^0$ occur only at one-loop level. This makes them sensitive to virtual gauge bosons, fermions and especially charged Higgs particles. We have calculated all production modes but have paid particular attention to the $\gamma\gamma \to h^0 h^0$ mode. The one-loop amplitudes were generated and calculated with the packages FeynArts [23] and FormCalc [24]. The scalar integrals were evaluated with LoopTools and the CUBA library [25]. A cut of approximately 6^o relative to the beam axis was set on the scattering angle in the forward and backward directions. In our numerical analysis, we used $m_t = 171$ GeV, $m_b = 4.7$ GeV, $m_Z = 91.187$ GeV, $m_W = 80.45$ GeV, the Weinberg angle s_W is defined in the on-shell scheme as $s_W^2 = 1 - m_W^2/m_Z^2$ and $\alpha_{ew} = 1/137.035$.

3.1 The general 2HDM

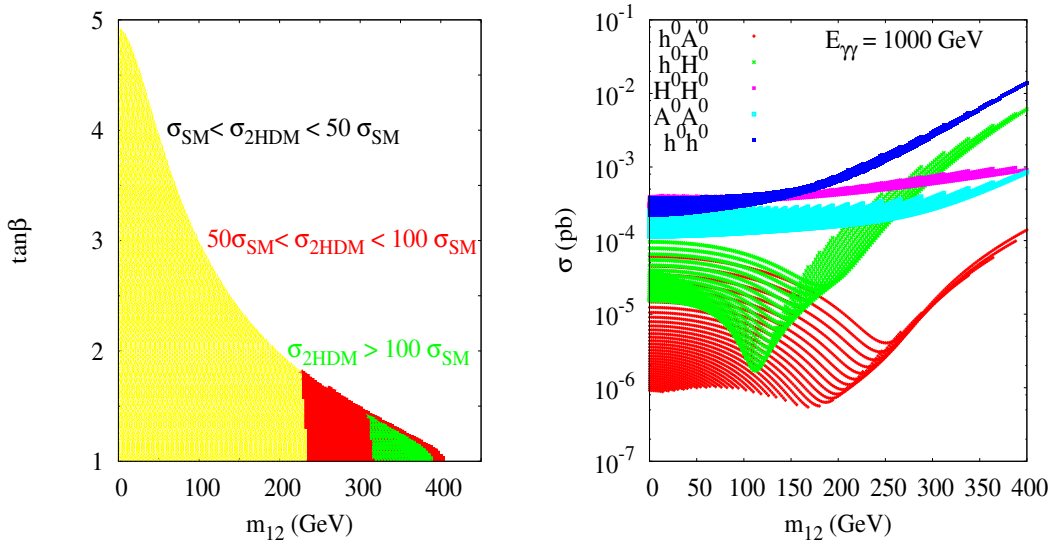

Figure 1: On the left panel we show the allowed region in the $(\tan\beta, m_{12})$ plane and the values of $\sigma(\gamma\gamma \to h^0 h^0)$ when compared to the SM ones, with $m_{h^0} = 115$ GeV, $m_{A^0} = 270$ GeV, $m_{H^\pm} = 350$ GeV, $m_{H^0} = 2m_{h^0}$, $E_{\gamma\gamma} = 500$ GeV, $-1 \leq \sin\alpha \leq 1$ and $1 \lesssim \tan\beta \lesssim 10$. On the right panel, we present $\sigma(\gamma\gamma \to S_i S_j)$, with $S_{i,j} = h^0, H^0, A^0$ as a function of m_{12}. We have taken $m_{h^0} = 115$ GeV, $m_{A^0} = m_{H^0} = 160$ GeV, $m_{H^\pm} = 250$ GeV, $\sin\alpha = -0.4$, $1 \lesssim \tan\beta \lesssim 10$ and $E_{\gamma\gamma} = 500$ GeV.

The very detailed parton-level study [10] concluded that for a 350 GeV center of mass energy photon collider and a Higgs mass of 120 GeV, an integrated $\gamma\gamma$ luminosity of 450 fb^{-1} would be needed to exclude a zero trilinear Higgs boson self-coupling at the 5σ level, considering only the statistical uncertainty. If one assumes the luminosity based on the TESLA design report [26] we conclude that this is an attainable luminosity in less than two years. A more recent study, although not as optimist, reaches similar conclusions [27]. Therefore, we have decided to perform a comprehensive scan of the parameter space of the 2HDM looking for regions where the 2HDM

dominate over the SM, that is, $\sigma_{2HDM}(\gamma\gamma \to h^0h^0) > \sigma_{SM}(\gamma\gamma \to h^0h^0)$, together with all theoretical and experimental constraints.

The results of this scan are shown in Fig. 1. From the left scan we conclude that to have m_{12} large, unitarity constraints require $\tan\beta$ to be rather small. It is clear that in order to have a 2HDM cross section for $\gamma\gamma \to h^0h^0$ much larger than the corresponding SM one, a large m_{12} is needed together with a small value for $\tan\beta$. In the right panel of Fig. 1 we present the cross section $\sigma(\gamma\gamma \to S_iS_j)$, $S_{i,j} = h^0, H^0, A^0$ as a function of m_{12}. All processes stand a chance of being observed at a gamma-gamma collider - for large values of m_{12} all processes can be above the SM cross section of double Higgs production. The main enhancement factor for all cross section is the virtual charged Higgs bosons exchange, particularly relevant near the threshold region $E_{\gamma\gamma} = 2m_{H\pm}$. The only difference between the mixed final states and the h^0h^0 and the A^0A^0 ones, is the absence of the H^0 resonant effect, since it can not decay neither to h^0H^0 nor to H^0H^0. The situation is the same as in the SM. If $m_{h^0} \approx m_{H^0}$ all processes h^0h^0, h^0H^0 and H^0H^0 can be of the same order of magnitude and may reach 0.1 pb. If the CP-even Higgs is heavy, phase space suppression occurs and the cross sections for h^0H^0 and H^0H^0 production are smaller.

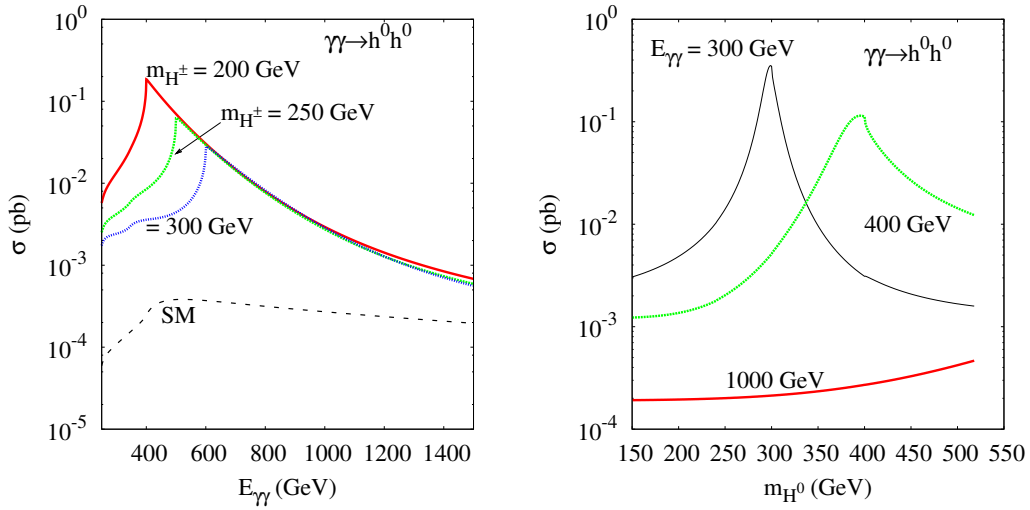

Figure 2: $\sigma(\gamma\gamma \to h^0h^0)$ as a function of the center of mass energy (left) and as a function of the heavy Higgs mass m_{H^0} (right) in the 2HDM. In the left panel the parameters are $m_{h^0}, m_{H^0}, m_{A^0}, m_{12} = 120, 200, 120, 300$ GeV, $\sin\alpha = -0.86$ and $\tan\beta = 1$. In the right panel the values are $m_{h^0}, m_{H^\pm}, m_{A^0}, m_{12} =$ 120, 250, 150, 200 GeV, $\sin\alpha = 0.9$ and $\tan\beta = 1.5$.

In Fig. 2 we present the total cross section for $\gamma\gamma \to h^0h^0$ as a function of the center of mass energy for several values of the charged Higgs mass and as a function of the heavy CP-even Higgs boson for different center of mass energies. These show the two most distinctive features of double h^0 production. First, there is an enhancement when $E_{\gamma\gamma} \approx 2m_{H\pm}$ - the cross section is largest when $\gamma\gamma \to H^+H^-$ is closed and subsequently suppressed when this threshold is crossed. This behavior is shown in the left panel of Fig. 2 where the cross section can reach 0.2 pbarn. In the left panel of Fig. 2 we show the total cross section for $\gamma\gamma \to h^0h^0$ as a function the heavy Higgs mass for several values of the center of mass energy. Once the

center of mass energy is close to m_{H^0}, one can see in both plots the effect of the resonance of the heavy CP-even Higgs. In both cases, the cross sections can reach 0.1 pb near the resonance $E_{\gamma\gamma} \approx m_{H^0}$.

3.2 Decoupling limit

The decoupling regime of the 2HDM is a scenario where the light Higgs couples to the SM particles, fermions and gauge bosons, with exactly the same strength as the SM Higgs. The triple self Higgs coupling is also the SM one and the triple Higgs coupling $\lambda^{(0)}_{h^0h^0H^0}$ vanishes at tree-level, so that the heavy Higgs cannot contribute to the process $\gamma\gamma \to h^0h^0$ and the result is independent of the mass m_{H^0}. All other Higgs are taken to be heavy. In the 2HDM, the decoupling limit can be achieved by taking the limit $\alpha \to \beta - \pi/2$.

There are mainly two non-decoupling effects that have a measurable impact on the cross section. One comes from the $\lambda^{2HDM}_{h^0H^+H^-}$ coupling and is present already at tree level. This is the case discussed in [11], where was shown that, at the 1-loop level, m^2_{12} and the charged Higgs mass are the parameters that regulate the non-decoupling effects. There is an very important contribution from the m_{12} parameter in the vertex that acts constructively for $m^2_{12} > 0$ and destructively for $m^2_{12} < 0$. The second comes from the one-loop corrections to the triple Higgs self-coupling $\lambda_{h^0h^0h^0}$ as described in Ref. [28] and was discussed in [12]. To account for this effect, in the calculation of the $\gamma\gamma \to h^0h^0$ cross section, one should replace the $\lambda^{(0)}_{h^0h^0h^0}$ coupling by its effective coupling which corresponds, in this limit, to an effective 2-loop 2HDM contribution. In this scenario non-decoupling effects have their origin in the large values of the remaining Higgs masses. In this section we will combine the effects of ref. [11] and ref. [12] to show that even in the limit when the cross sections is reduced, there are still regions where the 2HDM Higgs h^0 could be disentangled from the SM h_{SM}.

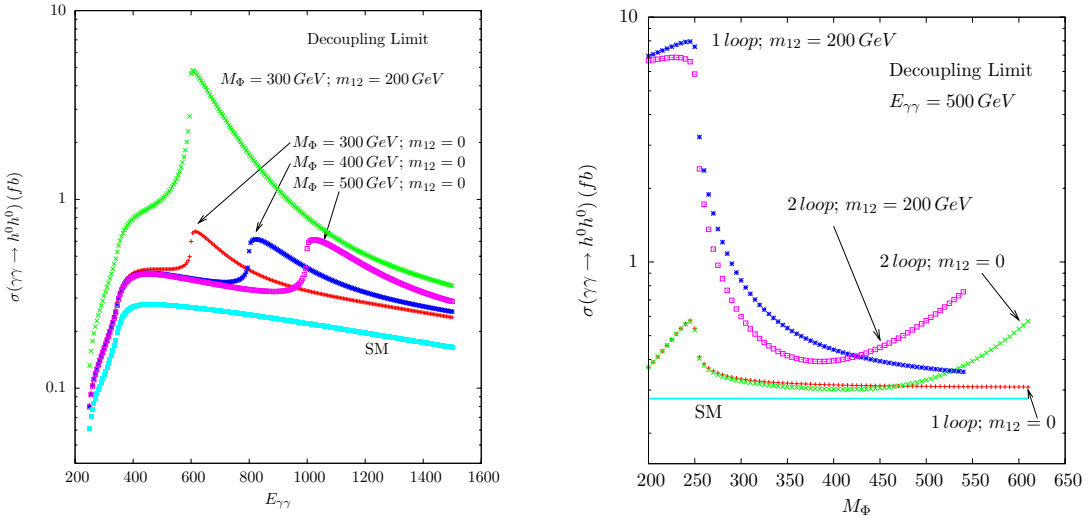

Figure 3: Cross sections for h^0h^0 production in the decoupling limit with unpolarized photons. On the right we show the loop contributions to the total cross section as a function of m_Φ and for two values of m_{12}, 0 and 200 GeV. On the left panel the cross section as a function $E_{\gamma\gamma}$ is shown for different values of m_Φ and m_{12}. The light Higgs mass is $m_{h^0} = 120\ GeV$.

In the left panel of Fig. 3 we show the cross section for $\gamma\gamma \to h^0h^0$ as a function of $E_{\gamma\gamma}$ for $m_\Phi = 300$, 400 and 500 GeV with $m_{12} = 0$ together with the case where $m_{12} = 200$ GeV and $m_\Phi = 300$ GeV. The coupling $h^0h^0h^0$ is taken at the tree-level and therefore the non-decoupling effects are only due to the charged Higgs mass threshold, $E_{\gamma\gamma} = 2\ m_\Phi$. This effect is enhanced for higher values of m_{12}. As shown in the plot, for a charged Higgs mass of 300 GeV and $m_{12} = 200\,GeV$ the cross section can reach 5 fbarn and this value grows with m_{12}. In the right panel of Fig. 3 we display the cross section of $\gamma\gamma \to h^0h^0$ as a function m_Φ. Here, besides the SM value we plot four different scenarios. The one-loop case with $m_{12} = 0$ and $m_{12} = 200\,GeV$ and the two-loop case with the higher order corrections for the same two values of m_{12}. One can see that the cross section enhancement due to the large corrections in $\lambda^{eff}_{h^0h^0h^0}$ take place only for large m_Φ if $m_{12} = 0$. As m_{12} grows the cross section grows as described in the left panel, but on top of that we get an extra enhancement due to the higher order corrections. Largest values of the cross section, that can reach 10 fbarn, are attained for the low mass region in m_Φ. We note that the cut on m_Φ at 610 GeV for $m_{12} = 0$ and on m_Φ at 550 GeV for $m_{12} = 200$ GeV is due to unitarity constraints.

4 Conclusions

In this section we sum up the main points of this work (see [13]):

- We have shown that the cross section for $\gamma\gamma \to h^0h^0$ can be more than 100 times larger than the corresponding SM one in vast regions of the parameters space. The parameter space will easily be probed for the largest allowed values of $\tan\beta$, m_{12}^2 and $|\sin\alpha|$. A light charged Higgs, that is, below the collider center of mass energy, is preferred. A variable energy collider would be a good option to detect the heavy Higgs resonance. We have shown that even with a charged Higgs mass of the order of 300 GeV, in agreement with $b \to s\gamma$, the cross section can have a substantial enhancement. In case of 2HDM type I, where a light charged Higgs is allowed the cross section could be 3 order of magnitude above the SM results;

- The analysis in [10] shows that the SM Higgs triple coupling could be probed at a photon collider. As described before, their analysis is mainly based on an invariant mass cut, on the identification of at least 3 jets as originating from b-quarks and on a the polar angle cut $|\cos\theta_b| < 0.9$. We have shown that the inclusion of the new 2HDM diagrams do not change the angular distribution so that the same cut could be applied. Moreover, for most Yukawa versions of the model and for most of the allowed parameter space, $BR(h \to b\bar{b})$ is at least the SM one if not larger. Because the invariant mass cut is the same, the analysis can be applied directly to the 2HDM case. Therefore, when a complete experimental analysis is completed for the SM, it is ready to be used to constraint the 2HDM parameter space. For heavier h^0 and for final states other then $b\bar{b}$ the analysis has to be redone. Finally we have shown that all the different final states stand a chance of being probed at a gamma gamma collider especially for large values of m_{12}.

- Although other regions give rise to higher cross sections, the very interesting case of the 2HDM decoupling limit can also be probed at the photon collider. The importance of the sign of m_{12}^2 was studied in a more general context. Clearly, positive m_{12}^2 (in our notation) can lead to large non-decoupling effects.

5 Acknowledgments

A.A is supported by the National Science of Theoretical Studies-Taipei under contract 980528731. R.B. is supported by National Cheng Kung University Grant No. HUA 97-03-02-063. C.C.H is supported by the National Science Council of R.O.C under Grant NSC-97-2112-M-006-001-MY3. R.S. is supported by the FP7 via a Marie Curie IEF, PIEF-GA-2008-221707.

References

[1] J. Brau *et al.* [ILC Collaboration], arXiv:0712.1950 [physics.acc-ph]; A. Djouadi, J. Lykken, K. Monig, Y. Okada, M. J. Oreglia and S. Yamashita, arXiv:0709.1893 [hep-ph]; N. Phinney, N. Toge and N. Walker, arXiv:0712.2361 [physics.acc-ph]; T. Behnke *et al.* [ILC Collaboration], arXiv:0712.2356 [physics.ins-det].

[2] V. I. Telnov, Acta Phys. Polon. **B37** 633 (2006).

[3] E. Boos *et al.*, Nucl. Instrum. Meth. **A472** 100 (2001).

[4] J. F. Gunion and H. E. Haber, Phys. Rev. **D48** 5109 (1993).

[5] D. L. Borden, D. A. Bauer and D. O. Caldwell, Phys. Rev. **D48**, 4018 (1993); D. L. Borden, V. A. Khoze, W. J. Stirling and J. Ohnemus, Phys. Rev. **D50**, 4499 (1994).

[6] M. M. Muhlleitner, M. Kramer, M. Spira and P. M. Zerwas, Phys. Lett. **B508** 311 (2001); M. M. Muhlleitner, arXiv:hep-ph/0008127.

[7] D. M. Asner, J. B. Gronberg and J. F. Gunion, Phys. Rev. **D67**, 035009 (2003).

[8] R. N. Hodgkinson, D. Lopez-Val and J. Sola, arXiv:0901.2257 [hep-ph]; A. Arhrib, R. Benbrik and C. W. Chiang, Phys. Rev. **D77**, 115013 (2008); G. Ferrera, J. Guasch, D. Lopez-Val and J. Sola, Phys. Lett. **B659** 297 (2008); M. N. Dubinin and A. V. Semenov, Eur. Phys. J. **C28** 223 (2003).

[9] G. V. Jikia and Yu. F. Pirogov, Phys. Lett. **B283** 135 (1992); G. V. Jikia, Nucl. Phys. **B412** 57 (1994).

[10] R. Belusevic and G. Jikia, Phys. Rev. **D70** 073017 (2004).

[11] F. Cornet and W. Hollik, Phys. Lett. **B669** 58 (2008).

[12] E. Asakawa, D. Harada, S. Kanemura, Y. Okada and K. Tsumura, Phys. Lett. **B672** 354 (2009) 354.

[13] A. Arhrib, R. Benbrik, C. H. Chen and R. Santos, arXiv:0901.3380 [hep-ph].

[14] S. L. Glashow and S. Weinberg, Phys. Rev. **D15** 1958 (1977).

[15] V. D. Barger, J. L. Hewett and R. J. N. Phillips, Phys. Rev. **D41** 3421 (1990).

[16] C. Amsler *et al.* [Particle Data Group], Phys. Lett. **B667** 1 (2008).

[17] A. Denner, R. J. Guth, W. Hollik and J. H. Kuhn, Z. Phys. **C51** 695 (1991).

[18] A. Wahab El Kaffas, P. Osland and O. Magne Ogreid, Phys. Rev. **D76**, 095001 (2007).

[19] S. Kanemura, T. Kubota and E. Takasugi, Phys. Lett. **B313**, 155 (1993).

[20] A. G. Akeroyd, A. Arhrib and E. M. Naimi, Phys. Lett. **B490**, 119 (2000); A. Arhrib, arXiv:hep-ph/0012353; J. Horejsi and M. Kladiva, Eur. Phys. J. **C46**, 81 (2006)

[21] N. G. Deshpande and E. Ma, Phys. Rev. **D18** 2574 (1978).

[22] P. M. Ferreira, R. Santos and A. Barroso, Phys. Lett. **B603** 219 (2004), [Erratum-ibid. **B629** 114 (2005)].

[23] T. Hahn, Comput. Phys. Commun. **140** 418 (2001); T. Hahn, C. Schappacher, Comput. Phys. Commun. **143** 54 (2002); J. Küblbeck, M. Böhm, A. Denner, Comput. Phys. Commun. **60** 165 (1990).

[24] T. Hahn and J. I. Illana, arXiv:0708.3652 [hep-ph]; T. Hahn and J. I. Illana, Nucl. Phys. Proc. Suppl. **160** 101 (2006); T. Hahn, M. Perez-Victoria, Comput. Phys. Commun. **118**, 153 (1999); T. Hahn and J. I. Illana, arXiv:0708.3652 [hep-ph]. T. Hahn, Nucl. Phys. Proc. Suppl. **89**, 231 (2000).

[25] G. J. van Oldenborgh, Comput. Phys. Commun. **66**, 1 (1991); T. Hahn, Acta Phys. Polon. **B30**, 3469 (1999); T. Hahn, Comput. Phys. Commun. **168** 78 (2005); T. Hahn, Nucl. Instrum. Meth. **A559** 273 (2006).

[26] B. Badelek *et al.* [ECFA/DESY Photon Collider Working Group], Int. J. Mod. Phys. A **A19** 5097 (2004).

[27] N. Maeda *et al.*, Presented at TILC09, Tsukuba, Japan.

[28] S. Kanemura, S. Kiyoura, Y. Okada, E. Senaha and C. P. Yuan, Phys. Lett. **B558** 157 (2003) S. Kanemura, Y. Okada, E. Senaha and C. P. Yuan, Phys. Rev. **D70** 115002 (2004).

Chapter 2

Photon Collider Technology

Convenor:

J. Gronberg (Lawrence Livermore)

Photon Collider Technology Overview

V. I. Telnov

Institute of Nuclear Physics, Novosibirsk 630090, Russia

DOI: http://dx.doi.org/10.3204/DESY-PROC-2009-03/Telnov

In this conference paper, I review the present status and technical problems of the Photon collider, as well as various additional applications of Compton scattering.

1 Intoduction

In this report, I provide an overview of the technical (and some political) aspects of the Photon Linear Collider (PLC). The physics program at the PLC is discussed in K. Mönig's talk at this conference [1].

The photon collider based on the conversion of electrons at a linear collider to high-energy photons through Compton scattering of laser photons has been discussed and developed since early 1980s [2, 3]. A photon collider would be a very natural and relatively cheap supplement to a high-energy e^+e^- linear collider. It would allow the study of New Physics in two additional types of collisions, $\gamma\gamma$ and γe with energies and luminosities close to those in e^+e^- collisions. A comprehensive description of the PLC is given in the TESLA TDR [4]; practically everything regarding the photon collider at TESLA is valid for the PLC at the ILC. Further progress on the PLC after 2001 has been summarized in my talks at PHOTON2005 [5, 6] and PHOTON2007 [7].

What's new since 2007? Unfortunately, the future of the ILC is still highly uncertain. A lot depends on the physics results from the LHC, but even the discovery of a new physics at the LHC would not guarantee the approval of the ILC (or CLIC?) construction due to its high cost ("high" as perceived by politicians). A possible way to overcome this barrier could be to build the linear collider in several stages. Recently, in October 2008, Prof. Hirotaka Sugawara suggested to the ILC Steering Committee the construction of a "Photon collider Higgs factory as a precursor to ILC," as the required energy for producing a 120 GeV Higgs is lower in $\gamma\gamma$ collisions than in e^+e^-, positrons are not needed, and therefore such a collider would be much cheaper. While laudable as an attempt to find a way out of the ILC stalemate, this suggestion has caused concern to many in the ILC community because it would have meant an additional delay of 5-6 years in the start of e^+e^- operations at the ILC. After consultations with PLC experts and additional study of the technical aspects and physics program for a low-energy startup scenario, the ILCSC rightfully concluded that it would more preferable to start with e^+e^- at $2E = 230$ GeV and investigate the Higgs in the $e^+e^- \to ZH$ process. This option's cost is not much higher than that of a 120 GeV PLC, but the physics case is stronger.

The other interesting activities in the last few years related to the photon collider and based on ideas originally proposed in the context of photon colliders are the developments of laser systems for various applications based on Compton scattering.

The outline of this paper is as follows. Basic properties of the PLC are considered in Sect. 2.

Technical aspects are overviewed in Sect. 3. The proposal of the PLC as the first stage of the ILC is discussed in Sect. 4. Various applications of Compton scattering are considered in Sect. 5.

2 Basics of the photon collider

Let us consider briefly the main characteristics of backward Compton scattering important for the photon collider.

Kinematics. In the conversion region, a laser photon of energy ω_0 collides with a high-energy electron of energy E_0 at a small collision angle α_0 (almost head-on). The energy of the scattered photon ω depends on the photon scattering angle ϑ with respect to the initial direction of the electron as follows [3]:

$$\omega = \frac{\omega_m}{1+(\vartheta/\vartheta_0)^2},\ \ \omega_m = \frac{x}{x+1}E_0;\quad \vartheta_0 = \frac{mc^2}{E_0}\sqrt{x+1};\ \ x = \frac{4E\omega_0}{m^2c^4}\cos^2\frac{\alpha_0}{2} \simeq 19\left[\frac{E_0}{\mathrm{TeV}}\right]\left[\frac{\mu\mathrm{m}}{\lambda}\right], \tag{1}$$

where ω_m is the maximum energy of scattered photons. For example: $E_0 = 250$ GeV, $\omega_0 = 1.17$ eV ($\lambda = 1.06$ μm) (for the most powerful solid-state lasers) $\Rightarrow$ $x = 4.5$ and $\omega_m/E_0 = 0.82$. Spectra of scattered photons are broad with enhancement at maximum energies. Formulae for the Compton cross section and graphs can be found elsewhere [3, 4].

Monochromatization. By collimating the photon beam, one can obtain monochromatic gamma (or X-ray) beams, which is important for various potential applications. At the photon collider, there are no collimators, but there is some monochromatization of collisions due to the fact that the higher-energy photons collide at smaller spot sizes and contribute more to the luminosity. In γe collisions, the resulting luminosity spectrum can, in principle, be very narrow (the electron beam collides with the most high-energy photons), while in $\gamma\gamma$ collisions the resulting luminosity spectra have the width at half-maximum of about 10-15% [8, 9].

Maximum energy of scattered photons. With increasing x, the energy of the backscattered photons increases and the energy spectrum becomes narrower. However, at large values of x photons may be lost due to creation of e^+e^- pairs in collisions with laser photons, which leads to a reduction of the $\gamma\gamma$ luminosity [3, 8, 9]. The threshold of this reaction is $x = 2(1+\sqrt{2}) \approx 4.83$. The corresponding wavelength of laser photons is $\lambda = 4.2E_0$ [TeV] μm. Hence, the maximum energy of photons at the PLC is about $0.8E_0$.

Polarization If laser photons are 100% circularly polarized, the backscattered photons at the highest photon energy also have 100% circular polarization (even for unpolarized electrons and for any value of x). The energy spectrum of scattered photons depends on the average electron helicity λ_e and that of the laser photons P_c. The relative number of hard photons increases when one uses beams with a negative value of the product $\lambda_e P_c$. For large x, the polarization of electrons increases the number of photons in the high-energy peak almost by a factor of 2 (or 4 in the $\gamma\gamma$ luminosity). The energy spectrum of the scattered photons for various helicities of the electron and laser beams can be found elsewhere [3, 4]. A high degree of photon's circular polarization is essential for the study of many physics processes, for example, for suppression of QED background in the study of the Higgs boson [4]. The ratio L_0/L_2 (0,2 is the total helicity of colliding photons) is larger when electron beams have a higher degree of longitudinal polarization [4]. Modern electron guns give polarization up to $\sim 85\%$, which is OK. A high electron polarization is practically mandatory for the photon collider. With unpolarized electron beams, it would be practically impossible to study the Higgs(120) (or even to observe it).

Nonlinear effects in the conversion. In order to convert nearly all electrons to high-energy photons, the density of laser photons at the conversion point should be so high that the electron can interact with several laser photons simultaneously. This nonlinear effect is characterized by the parameter $\xi^2 = 2n_\gamma r_e^2 \lambda/\alpha$, where n_γ is the density of laser photons, $r_e = e^2/mc^2$ and $\alpha = e^2/\hbar c$ ([4] and references therein). The transverse motion of the electron in the electromagnetic wave leads to an effective increase of the electron mass: $m^2 \to m^2(1+\xi^2)$, which decreases the maximum energy of the scattered photons: $\omega_m/E_0 = x/(1+x+\xi^2)$. The Compton spectrum is shifted towards lower energies, higher harmonics appear, and the $\gamma\gamma$ luminosity spectra become broader. At $x = 4.8$, the value of ω_m/E_0 decreases by about 5% for $\xi^2 = 0.3$, which can be considered the limit.

Laser flash energy. For small conversion coefficients $k = N_\gamma/N_e \sim 1 - \exp(-A/A_0)$, where the flash energy A_0 is determined by the diffractive divergence of the laser beam and geometric size of the electron beam. For head-on collisions and very narrow electron beams $A_0 \sim 2\hbar c\sigma_z/\sigma_c$ [9], where σ_z is the r.m.s. length of the electron beam and σ_c is the Compton cross section. For $x = 4.8$ $A_0 \sim 3\sigma_z$ [mm] J, while for $x \ll 1$ the Compton cross section approaches the Thomson one and the coefficients $3 \Rightarrow 1$. For the ILC ($\sigma_z = 0.3$) mm this estimate gives $A_0 \sim 1$ J. However, when $k \sim 1$ the nonlinear effects become important. In order to keep ξ^2 small one should make the conversion length longer, which increases the required flash energy. In calculating the flash energy, one should also take into account the collision angle between the laser and electron beams (when the laser optics is outside of the electron beam), the effective transverse size of the electron beam due to the tilt in the crab-crossing scheme of collisions and the angular size of the first quad (if optical mirrors are situated outside the detector). A realistic calculation for ILC(500) gives $A_0 \sim 9J$ [12, 11, 6].

3 Technical problems of photon colliders

3.1 $\gamma\gamma$, γe luminosities

In e^+e^- collisions, the maximum achievable luminosity is determined by beamstrahlung and beam instabilities. At photon colliders, the only effect that restricts the $\gamma\gamma$ luminosity is the conversion of the high-energy photons into e^+e^- pairs in the field of the opposing beam – that is, the coherent pair creation [13, 8]. For γe collisions, the luminosity is determined by beamstahlung, coherent pair creation, and the beam displacement during the collision [9, 4]. It is interesting to note that at the center-of-mass energies below 0.5–1 TeV and for electron beams that are not too short (the case of ILC), coherent pair creation is suppressed due to the broadening and displacement of the electron beams during the collision. For e^+e^-, the minimum horizontal beam size restricted by beamstrahlung is about 500 nm at the ILC, while the photon collider can work even with $\sigma_x \sim 10$ nm at $2E_0 = 500$ GeV, delivering a luminosity much higher than that in e^+e^- collisions [14, 15, 4]. In fact, the $\gamma\gamma$ luminosity is simply proportional to the *geometric* e^-e^- luminosity L_{geom}.

Unfortunately, the beam emittances in the damping-ring designs currently under consideration cannot achieve beam sizes that are smaller than $\sigma_x \sim 250$ nm and $\sigma_y \sim 5$ nm [6], though a reduction of σ_x by a factor of two seems possible. In principle, one can use electron beams directly from low-emittance photo-guns, avoiding the need for damping rings altogether, but at present they offer a product of the transverse emittances that is noticeably larger than can be obtained with damping rings: with polarized electron beams directly from photo-guns, the luminosity would be 100 times smaller!

Here is an approximate rule: the luminosity in the high-energy peak $L_{\gamma\gamma} \sim 0.1 L_{\rm geom}$ [4]. With "nominal" ILC beam parameters, the expected $\gamma\gamma$ luminosity in the high-energy peak of the luminosity spectrum $L_{\gamma\gamma}(z > 0.8 z_m) \sim 3.5 \times 10^{33}$ cm^{-2}s^{-1} $\sim 0.17\, L_{e^+e^-}$ [11, 6].

Taking into account the fact that cross sections for many interesting processes are larger in $\gamma\gamma$ collisions than those in e^+e^- by an order of magnitude [4], the event rate in $\gamma\gamma$ collisions with the nominal ILC beams would be similar, or perhaps somewhat larger, than in e^+e^- collisions. However, it is a highly unsatisfying situation to have the $\gamma\gamma$ luminosity limited by the beam emittances, an order of magnitude below its physics limit determined by collision effects. It is an extremely interesting and important task to search for a realistic technical solution for obtaining beams with smaller emittances, and the first order of business should be trying to optimize the damping rings for the specific requirements of achieving the highest possible luminosity at the photon collider, as it was emphasized in [11, 6, 16]. Up to now the ILC damping-ring design has been guided only by the baseline e^+e^- collisions.

The typical $\gamma\gamma$, γe luminosity spectra for the TESLA-ILC(500) parameters are shown in Fig. 1 [4]. One can see that $\gamma\gamma$ and γe luminosities are comparable and these processes can be studied simultaneously. However, it is much better to study γe collisions when only one of the electron beams is converted to photons. In this case, one can measure the γe luminosity much more precisely [19]. The problem of measuring the γe luminosity spectra when both beams are converted to photons is due to the uncertainty which direction the photon came from. For most

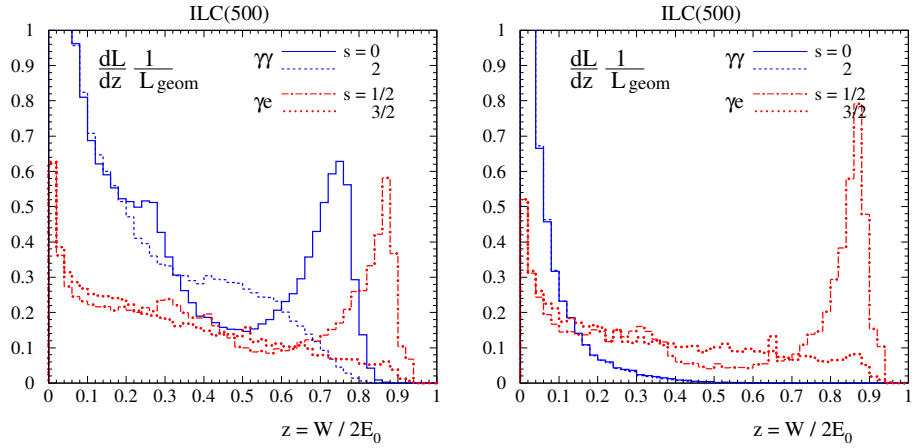

Figure 1: $\gamma\gamma$, γe luminosity spectra, left: both beams are converted to photons; right: only one beam is converted to photons.

measurements, the luminosity as high as possible is desired. However, sometimes very clean $\gamma\gamma$ collisions with good monochromaticity and a reduced luminosity (in order to avoid overlapping events) are needed. At large CP–IP distances and a non-zero crossing angle, the detector field serves as a deflecting magnet and allows more-or-less clean and quite monochromatic $\gamma\gamma$, γe collisions to be obtained with a reduced luminosity, which will be useful to QCD studies, [20, 21].

Luminosity stabilization. Beam collisions (luminosity) at linear colliders can be adjusted by a feedback system that measures the beam-beam deflection using beam position monitors and corrects beam positions by fast kickers. This method is considered for e^+e^- collisions and is assumed for $\gamma\gamma$ as well [4, 6], though there are some differences between the e^+e^- and $\gamma\gamma$ cases. This problem and a stabilization algorithm were considered in detail in Ref. [6].

Luminosity measurement. The measurement of the luminosity at the photon collider is not an easy task. The spectra are broad, and one should measure the luminosity and polarization as a function of energies E_1, E_2 of the colliding particles [19]. The luminosity spectrum and polarization can be measured using various QED processes. These are $\gamma\gamma \to l^+l^-$ $(l = e, \mu)$ [4, 19], $\gamma\gamma \to l^+l^-\gamma$ [19, 22] for $\gamma\gamma$ collisions and $\gamma e \to \gamma e$ and $\gamma e \to e^-e^+e^-$ for γe collisions [19]. Some other SM processes could be useful as well.

Absolute beam energy measurement. At the photon collider, the edge energy of the photon spectra and the electron beam energy E_0 are not strictly connected due to nonlinear effects in Compton scattering. The absolute energy calibration of the detector can be done using the process $\gamma e \ \to eZ$ (during normal runs in γe mode or mixed $\gamma\gamma$ and γe mode) [23].

3.2 Removal of used beams

The general scheme of the photon collider is shown in Fig. 2. The optimum $b \sim \gamma\sigma_y$, which is ~ 1.5 mm for $\sigma_y = 3$ nm and $2E_0 = 500$ GeV. This space is too small to fit any kind of a magnet for deflection of used electron beams. In this case, there is a mixture of $\gamma\gamma$, γe and e^-e^- collisions. After crossing the conversion region, the electrons have a very broad energy spectrum, $E = (0.02\text{–}1)\,E_0$ and large disruption angles due to deflection of low-energy electrons in the field of the opposing beam. The removal of such a beam from the detector is therefore far from trivial.

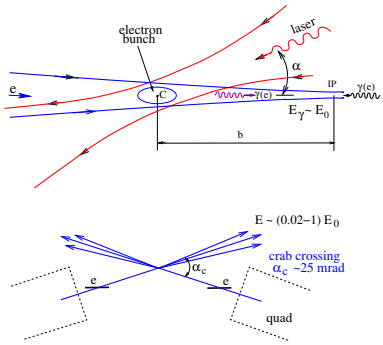

Figure 2: Scheme of $\gamma\gamma$, γe collider.

The "crab crossing" scheme of beam collisions solves the problem of beam removal at photon colliders [8, 9], Fig. 2 (bottom). In the crab-crossing scheme [25], the beams are collided at a crossing angle α_c. In order to preserve the luminosity, the beams are tilted by a special RF cavity by the angle $\alpha_c/2$. If the crossing angle is larger than the disruption angles, the beams just travel straight outside the quadrupoles.

The disrupted beams after the IP have an angular spread of about $\pm$ 12 mrad [4, 11, 6]. The disruption angle for low-energy particles is proportional to $\sqrt{N/\sigma_z E}$ [8, 9] and depends very weakly on the transverse beam sizes. The required crossing angle is determined by the disruption angle, the outer radius of the final quadrupole (about 5 cm [11, 6]), and the distance between the first quad and the IP (about 4 m), which gives $\alpha_c = 12 + 5/400 \approx 25$ mrad.

In the present ILC design [10] only one IP is planned, with a crossing angle of 14 mrad and two detectors in the pull-push configuration. On the other hand, at the photon collider the crossing angle should be at least 25 mrad. At first sight, it would therefore seem quite reasonable to design the ILC with 25 mrad crossing angle both for the e^+e^- and the photon collider. However, it was decided to make different collision angles due to very different requirements to the extraction lines and beam dumps. In the e^+e^- case, after collision the beams remain quite monochromatic, and so there is a possibility to measure their properties (the energy spectrum and polarization). At the photon collider, the situation is different: 1) the disrupted beams at a photon collider consist of an equal mixture of electrons and photons; 2) beams have a large angular spread and need exit pipes of a large diameter; 3) the photon beam after the Compton scattering is very narrow, it cannot be dumped directly at any solid or liquid material. There

exist an idea and simulations of a beam dump for the photon collider [24, 11, 6]. Conceptually, it is a long tube, the first 100 m of which is vacuum, followed by a 150 m long gas converter ending in a water-filled beam dump. In addition, there are fast sweeping magnet for electrons. Due to a large beam width, no detailed diagnostics are possible except, perhaps, for beam profile measurements.

So, it makes sense to have different crossing angles, separate extraction lines and beam dumps for e^+e^- and $\gamma\gamma$. For the transition from e^+e^- to $\gamma\gamma$, one has to move the detector and about 700 m of the up-stream beamline [26].

3.3 The laser and optics

The photon collider at ILC(500) requires a laser system with the following parameters [11, 6]: flash energy $A \sim 10$ J, $\sigma_t \sim 1.5$ ps, $\lambda \sim 1$ μm($\leq 5E_0$ [TeV] μm in a general case), and the ILC pulse structure: 3000 bunches within a 1 ms train and 5 Hz repetition rate for the trains, the total collision rate being 15 kHz.

In addition to the average repetition rate, the time structure is of great importance. The average power required of each of the two lasers for the photon collider at the ILC is 10 J $\times$ 15000 Hz $\sim$ 150 kW; however, the power within the 1 msec train is 10 J $\times$3000/0.001 $\sim$ 30 MW! The cost of diodes is about $\mathcal{O}$(1\$)/W, the pumping efficiency about 25%, so the cost of just the pumping diodes would be $\mathcal{O}$(\$100M).

Fortunately, at the PLC and other Compton scattering applications the same laser bunch can be used multiple times. The most attractive approach is a stacking optical cavity that is pumped by a laser via a semi-transparent mirror [14, 17, 15, 18, 4, 12]. The ILC pulse structure (3000 bunches in the train with inter-pulse distance 100 m) is sufficient to create a ring cavity around the detector. One can create inside such a cavity a light pulse with an intensity that is by a factor of Q (the quality factor of the cavity) greater than the incoming laser power. The value of Q achievable at such powers is several hundreds and (even $Q > 1000$ is not excluded). This means reduction of the required laser power by the large factor Q.

The external optical cavity (pulse stacking cavity) idea has proven to be a highly useful technique for HEP and other application (see the last Section). Recently at LAL, F. Zomer's group has received in a Fabry-Perot cavity an enhancement factor of 10000! [27] They found that a simple concentric Fabry-Perot cavity is very unstable and sensitive to displacements. Much more stable is the 2D (planar) concave 4-mirror system, but it also has a problem: astigmatic and only linearly (or elliptically) polarized eigenmodes due to different reflection for the s and p waves. A possible solation: 3D 4-mirror cavity that has reduced astigmatism and stable circularly polarized eigenmodes. The LAL group working in collaboration with Japanese colleagues (see T. Takahashi's talk in these proceedings) is in the process of developing such a 3D 4-mirror cavity, plans to install it at the KEK ATF2 facility and obtain 1 MW average power in the cavity. For the photon collider, very stable both circular and linear polarizations are needed. We see that this is not a simple task.

Recently, J. Gronberg and B. Stuart from LLNL have proposed a plan on possible stages in the development and construction of the laser system for the PLC [28]. They demonstrate that all the necessary technologies already exist. Pulse injection and intermediate amplification devices are off-the-shelf technologies; the main amplifier is not commercially available but at LLNL all required technologies exist (the Mercury laser is an existence proof). Gronberg and Stuart specified six stages, where the first one is the pre-conceptual design and the last one is the construction of a full-scale cavity and demonstration of its operation. The rough estimate

of the cost of the laser system is \$20 M ("once it is known technology"). These are very nice plans! (dreams?) Unfortunately, at present there are no resources for such a program, partially due to the very uncertain plans on the ILC.

In summary: at present, practically all laser technologies and components required for a photon collider are in existence; nevertheless, the construction of such a state-of-the-art laser system will not be an easy task. The next step will be the development (on paper) of a detailed laser scheme, its optimization, analyses of tolerances, methods of stabilization, figuring out what already exists and is known and what should be experimentally verified. Current development of passive stacking cavities for various applications based on Compton scattering is very helpful for the PLC.

4 Photon collider Higgs factory as a precursor to ILC

We have routinely assumed that a linear collider would start with e^+e^-, while $\gamma\gamma$,γe collisions would arrive several years later. However, on many occasions many people have suggested to build the photon collider before e^+e^- (or even without e^+e^-) because it is simpler (no e^+, may be no damping rings) and a somewhat lower beam energy is needed to produce an intermediate-mass Higgs boson. Several such suggestions (not all) are 1) V. Balakin et al. (1993)[29], based on the VLEPP and D. Asner et al. (2001) [30], based on CLIC-1 with $E_0 = 70$ GeV.

Recently, in October 2008, H. Sugawara gave a talk at the ILCSC meeting entitled "Photon-photon collider Higgs factory as a precursor to ILC". His main motivation was the following: the ILC(500) is too expensive, so let us build first a collider for the smallest reasonable energy. If the physics goal is H(120), then it could be produced in $\gamma\gamma \rightarrow H$ at $2E_0 \sim 160$ GeV, while $e^+e^- \rightarrow ZH$ needs higher energy. Besides, $\gamma\gamma$ does not need positrons. Before Sugawara's presentation at the ILCSC meeting, one of the ILCSC members sent me the slides of the proposal and asked for an opinion on this subject. My reply to the ILCSC and to Sugawara-san was the following (shortly):

- the cost of such a PLC will be not much cheaper because it needs damping rings with small emittance and polarized electrons. Polarization is absolutely necessary for the Higgs study. A polarized electron gun with small emittance does not exist, therefore damping rings are unavoidable;
- the laser system for the PLC is not simple, its developments have not started yet;
- the H(120) can be be studied much better in $e^+e^- \rightarrow ZH$ at $2E_0 = 230$ GeV;
- the ILC community will never agree with a proposal that shifts the start of e^+e^- experiments by about 5 years;
- the PLC gives a unique possibility to study new physics at the LC in two additional modes at a small additional cost, gives access to higher masses, but it would be better to plan the PLC as the second stage of the ILC (as it was usually assumed).

After the meeting, the ILCSC requested the LOI Physics pannel to look in more detail into the physics case, and the GDE to look at machine designs for this kind of a staged approach to ILC construction and operation. In January 2009, T. Barklow, J. Gronberg, M. Peskin and A. Seryi (BGPS) prepared a draft of the report, which was discussed at the expanded Physics panel with invited PLC experts and was not supported.

In February 2009, the BGPS report was reviewed at an ILCSC meeting and the conclusion was the following: "A 180 GeV gamma-gamma precursor would cost about half that of the

500 GeV ILC, but would produce much less physics. A better alternative for early Higgs studies would be a $\sim$ 230 GeV e^+e^- collider for studying the Higgs through ZH production; this would be about 30% more costly than the $\gamma\gamma$ collider. ILCSC decided not to pursue the gamma-gamma collider (as the ILC precursor) further at this time."

The PLC as the first stage of ILC was also discussed at TILC09 in April 2009: T. Barklow's plenary talk [31] and the discussion at Joint Physics session with my introductory talk [32]. All people have agreed that PLC is certainly necessary, but it would be better to start with $e^+e^-(230)$. Since $e^+e^-(230)$ is needed in any case, a PLC precursor results in no cost reduction at all. See also J. Gronberg's talk at PHOTON-2009 [33]. This is all about the PLC as a precursor to the ILC.

Nevertheless, proposals to build some type of a "cheap" low-energy PLC continue to resurface. It could have made sense if the production rates for some particles were higher than those at e^+e^- factories. However, simple estimates show that e^+e^- B-factories (and especially a future Super B factory) have much higher productivity for any particles of interest. So, the PLC should wait for its logical turn at the ILC (or CLIC, or other LC).

5 Applications based on Compton scattering

In 1981, when the PLC was proposed, the maximum $e \to \gamma$ conversion efficiency in Compton scattering of a laser light was at the level $k = N_\gamma/N_e \sim 10^{-7}$. For the PLC, $k \sim 1$ was needed. Our first journal paper was published only from the third attempt because the editors and reviewers considered the idea to be unrealistic. After invention of the chirped-pulse technique in 1985 [34], the required flash energy of several joules and ps duration became a reality. The remaining problem was the repetition rate. An optical pulse stacking cavity provides a nice solution to this problem. This technique was known for a long time (the Fabry–Perot resonator) but its wide application in HEP and other Inverse Compton Scattering (ICS) applications was triggered by PLC developments.

Collision of a relativistic electron bunch with an intense laser pulse generates photon beams with the following characteristics: source is bright (directional, ultra-fast); scattered light is monochromatic (after collimation); tunable wavelength, like FEL; much less expensive than XFEL; broad energy reach: keV, MeV, GeV TeV; polarization (useful for e^+ generation).

Let us enumerate some of the applications:

- Medical applications:
  - Dichromatic imaging: illuminate above and below contrast K-edge, digital image subtraction. Established at synchrotrons (access limited, expensive $100s);
  - Computer tomography with monochromatic X-rays. In mammography conventional X-ray imaging is difficult, soft-tissue contrast is poor. Monochromatic X-rays enable new techniques: phase contrast imaging 3D with low dose;
- Fast X-ray materials characterization: composition of materials, inspection of trucks and containers;
- Nuclear materials detection (in trucks and containers) by monochronatic γ beam;
- Defect profiling with e^+s. MeV photons produce positrons which gather at defects, detection of two 510 keV annihilation photons shows the source position (PET-tomography). Directly probe material defects.
- Nuclear waste assay. Resonance scattering of 1-5 MeV γ-quanta is a unique fingerprint of nuclides, radioactive and stable nuclides can be detected;

- Beam diagnostics and polarimetry at electron accelerators;
- Obtaining polarized e^+ for e^+e^- linear colliders [35]. Similar to the undulator source of polarized γ based on ~ 150 GeV main linac beams but needs much lower electron energies and is independent of the main collider. There is a very active collaboration named POSIPOL, which has already conducted four workshops on this topic;
- Laser cooling of electrons [36] can considerably reduce emittances of beams and increase the luminosity of photon colliders, provide a fast beam cooling in damping rings [37] for X-ray production and for e^+ production [35];
- The Photon Collider.

Already many ICS facilities are under construction in the world [38]. These activities (all enumerated above and some others) are called by people as the "Compton World Wide Web of Laser Compton." Let us hope that the Photon Collider will be eventually constructed somewhere in the world as well!

References

[1] K. Mönig, talk at Photon09, these proceedings.
[2] I.F. Ginzburg, G.L. Kotkin, V.G. Serbo, and V.I. Telnov, Pizma ZhETF, **34** 514 (1981); [JETP Lett. **34**, 491 (1982)].
[3] I.F. Ginzburg et.al., Nucl. Instrum. Meth. **205**, 47 (1983); ibid **A219**, 5 (1984).
[4] B. Badelek et. al., Intern. Journ. Mod. Phys. **A30**, 5097 (2004), hep-ex/0108012.
[5] V.I. Telnov, Acta Physica Polonica, **B37**, 633 (2006), physics/0602172.
[6] V.I. Telnov, Acta Physica Polonica, **B37**, 1049 (2006); physics/0604108.
[7] V.I.Telnov, Nuclear Physics B (Proc. Suppl.) **184** 271 (2008).
[8] V.I. Telnov, Nucl. Instrum. Meth.,**A294**, 72 (1990).
[9] V.I. Telnov, Nucl. Instrum. Meth. **A355**, 3 (1995).
[10] ILC Reference Design Report,ILC-Report-2007-001, arXiv:0712.2361 [physics.acc-ph].
[11] V.I. Telnov, Proc. of 2005 Intern. Linear Collider Physics and Detector Workshop and 2nd ILC Acceler. Workshop, Snowmass, Colorado, 14-27 Aug 2005, ECONF C0508141: PLEN0020,2005, physics/0512048.
[12] G. Klemz, K. Monig and I. Will, Nucl. Instrum. Meth. **A564**, 212 (2006), physics/0507078.
[13] P. Chen and V. I. Telnov, Phys. Rev. Lett., **63**, 1796 (1989).
[14] V.I. Telnov, Nucl. Phys. Proc. Suppl. **82**, 359 (2000), hep-ex/9908005.
[15] V.I. Telnov, Nucl. Instrum. Meth., **A472**, 43 (2001), hep-ex/0010033.
[16] V.I. Telnov, Pramana Journal of Physics, **69**, 957 (2007), physics/0610285.
[17] V.I. Telnov, Int. J. of Mod. Phys. **A15**, 2577 (2000), hep-ex/0003024.
[18] I. Will, T. Quast, H. Redlin and W. Sandner, *Nucl. Instrum. Meth.* **A472**, 79 (2001).
[19] A.V. Pak, D.V. Pavluchenko, S.S. Petrosyan, V.G. Serbo and V.I. Telnov, Nucl. Phys. Proc. Suppl., **126**, 379 (2004), hep-ex/0301037.
[20] V.I. Telnov, talk at the ECFA workshop on linear colliders, Montpellier, France, 12-16 November 2003; slides: `http://www-h1.desy.de/~maxfield/ggcol/montpellier_talks /Valery_lumispec_MONT1.PDF`
[21] V. I. Telnov, Nucl. Phys. Proc. Suppl.**179-180** (2008) 81.
[22] V. Makarenko, K. Monig and T. Shishkina, Eur. Phys. J. **C 32**, (2003) SUPPL1143.
[23] V.I.Telnov, Calibration of energies at the photon collider, talk at TILC09, April 17-21, 2009, Tsukuba, Japan. `http://tilc09.kek.jp`
[24] L.I. Shekhtman and V.I. Telnov, Proc. of Intern. Conf. on Linear Colliders (LCWS 04), Paris, France, 19-24 Apr 2004, *Paris 2004, Linear colliders*, v1, p.507; physics/0411253.
[25] R. B. Palmer, In *DPF Summer Study Snowmass '88: High Energy Physics in the 1990's, Snowmass, Colo., Jun 27 - Jul 15, 1988*, SLAC-PUB 4707.
[26] V.I. Telnov, Proc. LCWS06, India, March 2006. Pramana Journal of Physics, **69**, 1177 (2007), physics/0610287.
[27] F. Zomer, A. Jeremie, EUROTeV-Report-2008-096-1.
[28] J.Gronberg and B.Stuart, Photon Collider Laser Work at LLNL, talk at TILC09, April 17-21, 2009, Tsukuba, Japan. `http://tilc09.kek.jp`
[29] V. E. Balakin and I. F. Ginzburg, Proc. 2nd Intern. Workshop on Physics and Experiments with Linear e^+e^- Colliders, Waikoloa, Hawaii, 26-30 Apr, 1993, v2, p. 605.

[30] D. Asner *et al.*, Eur. Phys. J. C **28** (2003) 27, hep-ex/0111056.
[31] T. Barklow, Gamma-gamma collider physics report, talk at TILC09, April 17-21, 2009, Tsukuba, Japan, `http://tilc09.kek.jp`
[32] V.I.Telnov, Introduction to the discussion on Physics case of the PLC as the first stage of ILC, talk at TILC09, April 17-21, 2009, Tsukuba, Japan, `http://tilc09.kek.jp`
[33] J. Gronberg, Costs versus benefit of an early photon collider project, these proceedings.
[34] D. Strickland and G. Mourou, *Opt. Commun.*, **56**, 219 (1985).
[35] S. Araki *et al.*, Conceptual design of a polarised positron source based on laser Compton scattering, arXiv:physics/0509016. F. Zimmermann *et al.*, CLIC polarized positron source based on laser Compton scattering, CERN-CLIC-NOTE-674; M. Kuriki *et al.*, ILC positron source based on laser Compton, AIP Conf. Proc. **980** (2008) 92.
[36] V.I. Telnov, Phys. Rev. Lett.,**78**, 4757 (1997), Erratum: Phys. Rev. Lett. **80**, 2747 (1998); V.I. Telnov, Nucl. Instrum. Meth., **A455**, 63 (2000), hep-ex/0001029.
[37] Z. Huang and R. D. Ruth, Phys. Rev. Lett. **80**, 976 (1998).
[38] Workshop on Compton sources for X/gamma rays: Physics and Applications, 7-12 Sept, 2008, Alghero, Italy, `http://agenda.infn.it/conferenceTimeTable.py?confId=367`

Selected Problems for Photon Colliders

*I. F. Ginzburg**

Sobolev Institute of Mathematics and Novosibirsk State University, Novosibirsk, Russia

DOI: http://dx.doi.org/10.3204/DESY-PROC-2009-03/Ginzburg

The increase of energy of Photon Colliders up to 1-2 TeV in c.m.s. offers opportunity to study new series of fundamental physical problems. Among them – multiple production of gauge bosons, hunt for strong interaction in Higgs sector, search of exotic interactions in the process $\gamma\gamma \to \gamma\gamma$ with final photons having transverse momentum $\sim (0.5 \div 0.7)E_e$.

1 Introduction

Photon Colliders (PLC) of next generation have c.m.s. energy 1-2 TeV (ILC2, CLIC,...). There are two ways of building such collider.

• The first way is to use classical conversion scheme [1] with infrared laser or FEL to reach the highest luminosity. The laser photon energy will be 0.5-0.2 eV with $x = 4.8$ which prevents pair production in collision of high energy and laser photons. In this case maximum photon energy $\omega_m \approx 0.8E$, where E is the initial electron beam energy. To get high conversion coefficient, the conversion process has to take place with large non-linear QED effects, making final photon distributions less monochromatic and less polarized. Here one must work with infrared optics which causes additional difficulties (see discussion e.g. in [2]).

• The second way is to use the same laser (and the same optics) as for the electron beam energy 250 GeV (ILC1) but limit ourselves by a small conversion coefficient $k \leq 0.14$ [3]. This value assures that the losses of high energy photons due to e^+e^- pair production in collision of high energy photon with laser photon are small. At this value of conversion coefficient the non-linear QED effects are insignificant. Here the maximum photon energy is higher than in the first way, $\omega_m \approx (0.9-0.95)E$, energy distribution of high energy photons is more sharp, etc. These advantages allow to consider this option despite the reduction of $\gamma\gamma$ luminosity by about one order in comparison with the first way. Below I will have in mind these both ways. The second way seems more attractive to me. In the numerical estimates we have in mind $e\gamma$ and $\gamma\gamma$ luminosity integrals of about 100 fb^{-1} per year.

The standard list of problems for PLC at ILC1 is widely discussed (see e.g. [4]). The study of some of them (with increase of thresholds for search of new particles) will be a natural task for PLC with higher beam energy. We discuss here some new opportunities provided to us by enhancement of beam energy.

*This research has been supported by Russian grants RFBR 08-02-00334-a and NSh-1027.2008.2.

2 Multiple production of SM gauge bosons

The observation of pure interactions of SM gauge bosons (W and Z) or their interaction with leptons will allow to check SM with higher accuracy and observe signals of New Physics. The most ambitious goal is to find deviations from predictions of SM caused by New Physics interactions (and described by anomalies in effective Lagrangian). There are many anomalies relevant to the gauge boson interactions. Each process is sensitive to some group of anomalies. Large variety of processes obtainable at PLC's allows to separate anomalies from each other. The high energy PLC is the only collider among different future accelerators where one can measure large number of different processes of such type with high enough accuracy.

2-nd order processes. The cross sections of basic processes $\gamma\gamma \to W^+W^-$ and $e\gamma \to \nu W$ are so high (Fig. 1) that one can expect to obtain about 10^7 events per year providing accuracy better than 0.1%. The cross sections are almost independent of energy and photon polarization [5]. However, final distributions depend on polarization strongly [7].

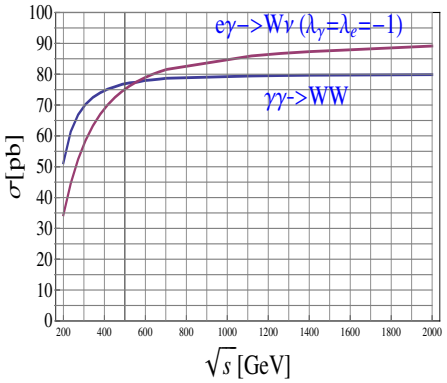

Figure 1: *Cross sections of 2-nd order processes*

The accuracy of measurement of these cross sections is sufficient to study in detail 2-loop radiative corrections. Together with standard problems of precise calculations one can note here two non-trivial problems, demanding detailed theoretical study:
(i) construction of S–matrix for system with unstable particles;
(ii) gluon corrections like Pomeron exchange between quark components of W's.

The mentioned high values of cross sections of the 2-nd order processes make it possible to measure their multiple "radiative derivatives" — processes of the 3-rd and 4-th order, depending in different ways on various anomalous contributions to the effective Lagrangian.

3-rd order processes. We consider here 3 processes. Total cross section $\sigma_{e\gamma\to eWW} \simeq$

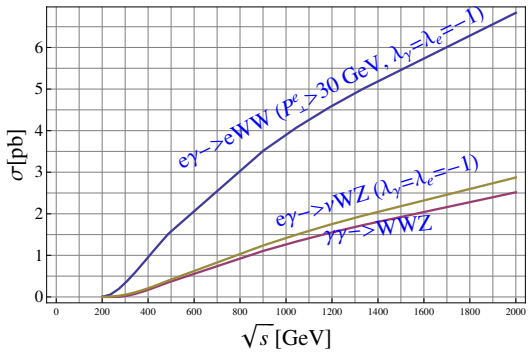

Figure 2: *Cross sections of 3-rd order processes*

$dn_\gamma \otimes \sigma_{\gamma\gamma\to WW}$. It is very high and easily estimated by equivalent photon method. This large contribution is not very interesting, being only a cross section of $\gamma\gamma \to W^+W^-$ averaged with some weight. However, at large enough transverse momentum of scattered electron this factorization is violated. Because of it we present $\sigma_{e\gamma\to eWW}$ only for $p_{\perp e} > 30$ GeV. Even this small fraction of total cross section appears so large that it allows *to separate contribution of* $\gamma Z \to WW$ *subprocess.*

4-th order processes. The cross sections of these processes (Fig. 3) are high enough to measure them with 1% precision. For the same reason as for process $e\gamma \to eWW$ we present cross section for process $e\gamma \to eZWW$ only for $p_{\perp e} > 30$ GeV. Even this small fraction of total cross section appears so large that it allows *to separate contribution of* $\gamma Z \to WWZ$ *subprocess.*

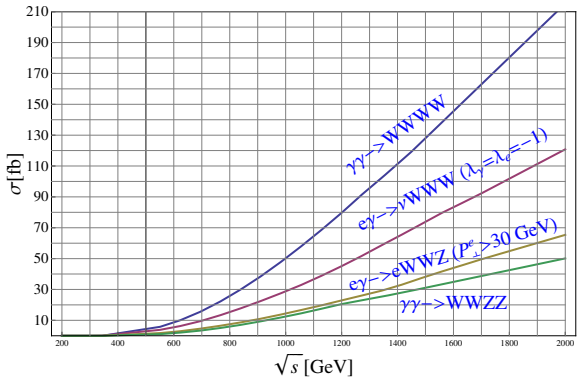

Figure 3: *Cross sections of 4-th order processes*

The study of the 2-nd order processes will allow to extract some anomalous parameters or their combinations. The study of the 3-rd order processes will allow to enlarge the number of extracted anomalous parameters and separate some of combinations extracted from the 2-nd order processes. The study of the 4-th order processes will again enlarge the number of separated anomalous parameters.

3 Study of strong interaction in Higgs sector

It is well known that at high values of Higgs boson self-coupling constant, the Higgs mechanism of Electroweak Symmetry Breaking in Standard Model (SM) can be realized without actual Higgs boson but with strong interaction in Higgs sector (SIHS) which will manifest itself as a strong interaction of longitudinal components of W and Z bosons. It is expected that this interaction will be similar to the interaction of π-mesons at $\sqrt{s} \lesssim 1.5$ GeV and will be seen in the form of W_LW_l, W_LZ_L and Z_LZ_L resonances. Main efforts to discover this opportunity are directed towards the observation of such resonant states. It is a difficult task for the LHC due to high background and it cannot be realized at the energies reachable at the ILC in its initial stages.

The problem of discovery of this strong interaction can be solved in the study of the charge asymmetry of produced $W^\pm$ in the process $e^-\gamma \to e^-W^+W^-$ similar to that which was dis-

cussed in low energy pion physics [8], [9]. To explain the set up of the problem we will discuss this process in SM.

We subdivide the diagrams of the process into three groups, where subprocesses of main interest are shown in boxes, sign $\otimes$ represents next stage of process and sign $\oplus$ represents adding of photon line to each charged line for subprocess in box:

$$\begin{array}{ll} a) & e^- \to e^-\gamma^*(Z^*) \otimes \boxed{\gamma\gamma^*(Z^*) \to W^+W^-}\,; \\ b) & \gamma e^- \to e^{-*} \to e^-\gamma^*(Z^*) \otimes \boxed{\gamma^*(Z^*) \to W^+W^-}\,; \\ c) & \gamma \oplus \boxed{e^- \to W^-W^+e^-}\,. \end{array} \qquad (1)$$

Diagrams of type a) contain subprocesses $\gamma\gamma^* \to W^+W^-$ and $\gamma Z^* \to W^+W^-$, modified by the strong interaction in the Higgs sector (*two–gauge contribution*).

Diagrams of type b) contain subprocesses $\gamma^* \to W^+W^-$ and $Z^* \to W^+W^-$, modified by the strong interaction in the Higgs sector (*one–gauge contribution*).

Diagrams of type c) are made by connecting the photon line to each charged particle line to the diagram shown inside the box. Strong interaction does not modify this contribution. These contributions are switched off at suitable electron polarization.

The subprocess $\gamma\gamma^* \to W^+W^-$ (from contribution a)) produces C-even system W^+W^-, the subprocess $\gamma^* \to W^+W^-$ (from contribution b)) produces C-odd system W^+W^-. The interference of similar contributions for the production of pions is responsible for large enough charge asymmetry, very sensitive to the phase difference of S (D) and P waves in $\pi\pi$ scattering, [8]. This very phenomenon also takes place in the discussed case of W's. However, for the production of $W^\pm$ subprocesses with the replacement of $\gamma^* \to Z^*$ are also essential. Therefore, the final states of each type have no definite C-parity. Hence, charge asymmetry appears both due to interference between contributions of types a) and b) and due to interference of γ^* and Z^* contributions each within their own types, like charge asymmetry in e^+e^- collision near Z– peak.

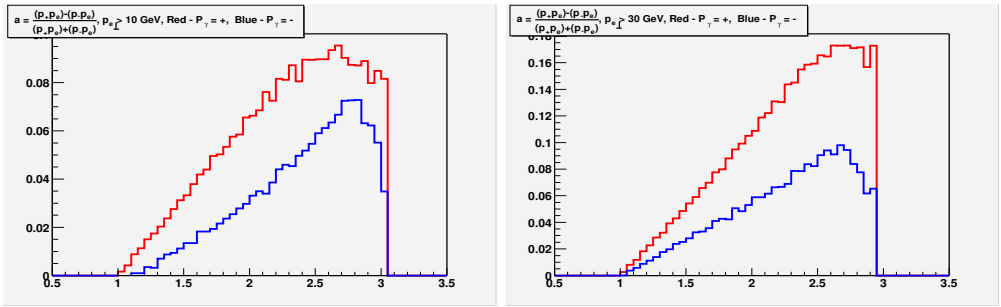

Figure 4: Dependence on polarization and cuts. Variable v_1.

Asymmetries in SM. To observe the main features of the effect of charge asymmetry and its potential for the study of strong interaction in the Higgs sector, we calculated some quantities describing charge asymmetry (charge asymmetric variables – CAV) for $e^-\gamma$ collision at $\sqrt{s} = 500$ GeV with polarized photons. We used CompHEP and CalcHEP packages [10] for simulation.

Denoting by $p^{\pm}$ momenta of $W^{\pm}$, by p_e – momentum of the scattered electron and by $W = \sqrt{(p_e^+ + p_e^-)^2}$, we studied W-dependence of the following averaged quantities

$$v_1 = \frac{\langle (p^+ - p^-)p_e \rangle}{\langle (p^+ + p^-)p_e \rangle}, \qquad v_2 = \frac{\langle (p_\parallel^+)^2 - (p_\parallel^-)^2 \rangle}{\langle (p_\parallel^+)^2 + (p_\parallel^-)^2 \rangle}, \qquad v_3 = \frac{\langle (p_\perp^+)^2 - (p_\perp^-)^2 \rangle}{\langle (p_\perp^+)^2 + (p_\perp^-)^2 \rangle}. \tag{2}$$

We applied the cut in transverse momentum of the scattered electron,

$$p_\perp^e \geq p_{\perp 0} \quad \text{with} \quad \begin{cases} a)\ p_{\perp 0} = 10\ GeV, \\ b)\ p_{\perp 0} = 30\ GeV. \end{cases} \tag{3}$$

Observation of the scattered electron allows to check kinematics completely.

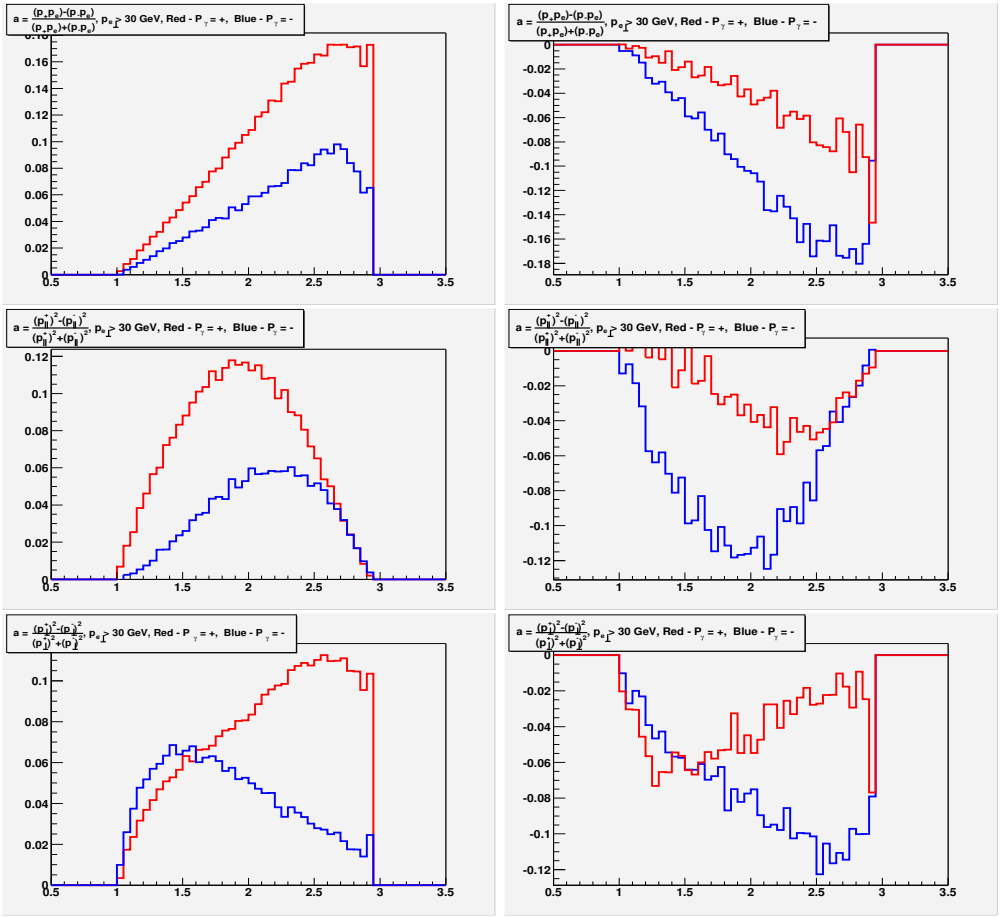

Figure 5: *Asymmetries in variables v_1, v_2 and v_3 (from top to bottom). Right – total, left – without one-gauge contributions. Upper curves for the right–handed polarized photons, lower curves for the left–handed polarized photons.*

• *Influence of polarization* for the charge asymmetry. Fig. 4 represents distribution in CAV v_1 for the right-hand (upper curves) and the left-hand (lower curves) polarized photons at

cuts $p_{\perp 0} = 10$ GeV (left) and $p_{\perp 0} = 30$ GeV (right). We did not study the dependence on electron polarization. This dependence is expected to be weak in SM where main contribution to cross section is given by diagrams of type a) with virtual photons having the lowest possible energy. These photons "forget" the polarization of the incident electron. The strong interaction contribution becomes essential at highest effective masses of WW system with high energy of virtual photon or Z, the helicity of which reproduces almost completely the helicity of incident electron [11]. Therefore, study of this dependence will be a necessary part of studies beyond SM.

• *Significance of different contributions.* To understand the extent of the effect of interest, we compared the entire asymmetry to that without one-gauge contribution (Fig. 5). Strong interaction in the Higgs sector modifies both one–gauge and two–gauge contributions. The study of charge asymmetry caused by their interference will be a source of information on this strong interaction. One can see that one–gauge contribution is so essential that neglecting on it even changes the sign of charge asymmetry (compared to that for the entire process).

Therefore, the influence of this potentially informative contribution to asymmetry is very high. The curves of Fig. 5 show that the value of this interference effect grows with the increase of the cut in $p_{e\perp}$. Photon polarization influences strongly the value of charge asymmetry. The role of electron polarization remains to be studied.

One can conclude that the charge asymmetry is very sensitive to the interference of two–gauge and one–gauge contributions which is modified under the strong interaction in the Higgs sector. The measurement of this asymmetry will be a source of data on the phase difference of different partial waves of $W_L W_L$ scattering.

4 Large angle high energy photons for exotics

The PLC allows to observe signals from the whole group of exotic models of New Physics in one common experiment. These are models with *large extra dimensions* [12], *point-like monopole* [13], *unparticles* [14]. All these models have common signature – the cross section for $\gamma\gamma \to \gamma\gamma$ production grows with energy as ω^6 ($\omega = \sqrt{s}/2$) and the photons are produced almost isotropically. Future observations either will give limits for scales of these exotics or will allow to see these effects by recording large $p_\perp \sim (0.5 \div 0.7)E_e$ photons[1]. The study of dependence on initial photon polarization will be useful to separate the mechanisms.

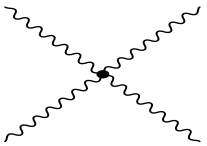

Figure 6: *Effective Lagrangian*

All these exotics at modern day energies can be described by effective point-like interaction of Fig. 6:

$$L \propto \frac{F^{\mu\nu}F^{\alpha\beta}F_{\rho\sigma}F_{\phi\tau}}{\Lambda^4}, \quad (\Lambda^2 \gg s/4). \tag{4}$$

In different models different orders of field indices are realized, Λ is characteristic mass scale, expressed via parameters of model. (In all cases s, t and u – channels are essential.)

Let us describe main features of matrix element (in the photon c.m.s.):
• gauge invariance provides factor ω for each photon leg;
• to make this factor dimensionless it should be written as ω/Λ. Therefore, the amplitude $\mathcal{M} \propto (\omega/\Lambda)^4 = s^2/(2\Lambda)^4$.

[1] *In my personal opinion it is hardly probable that these models describe reality.*

The characteristic scale Λ is large enough not to contradict modern day data. It accumulates other coefficients. The cross section

$$\sigma_{tot} = \frac{1}{32\pi s}\left(\frac{s}{4\Lambda^2}\right)^4, \quad d\sigma = \sigma_{tot}\Phi\left(\frac{p_\perp^2}{s}\right)\frac{2dp_\perp^2}{\sqrt{s(s-4p_\perp^2)}}. \tag{5}$$

with smooth function $\Phi(p_\perp^2/s)$, describing some composition of S and P-waves, dependent on details of model, and $\int \Phi(z)\,\frac{2dz}{\sqrt{1-4z}} = 1$. For large extra dimensions and monopoles entire s dependence is given by the factor $s^4/(2\Lambda)^8$ from (5), for unparticles additional factor $(s/4\Lambda^2)^{d_u-2}$ is added.

For the **large extra dimensions** case the point in Fig. 6 describes an elementary interaction, given by product of stress-energy tensors T_{ab} for the incident and the final photons, that are exchanging the tower of Kaluza-Klein excitations (with permutations),

	Λ	reference
Tevatron D0	175 GeV	[15]
LHC	2 TeV	[13]
$\gamma\gamma$ (100 fb^{-1})	$3E_e$	[13]
e^+e^- LC (1000 fb^{-1})	$2E_e$	[13]

Table 1: *The obtainable discovery limits.*

$$\mathcal{M}_{\gamma\gamma\to\gamma\gamma} \propto \left\langle \frac{T_{ab}T^{ab}}{\Lambda^4} \right\rangle \approx \frac{F^{\mu\nu}F_{\nu\alpha}F^{\alpha\beta}F_{\beta\mu}}{\Lambda^4} + \textit{permutations},$$

After averaging over polarizations for tensorial KK excitations

$$\Phi \propto 2\left(1-\frac{p_\perp^2}{\hat{s}}\right)^2 = \frac{(3+\cos^2\theta)^2}{8} = \frac{\hat{s}^4+\hat{t}^4+\hat{u}^4}{2\hat{s}^4}. \tag{6}$$

Unlike to ILC1, at high energy PLC the other channels (like $\gamma\gamma \to WW$) are less sensitive to the extra dimension effect.

The point–like Dirac monopole existence would explain mysterious quantization of an electric charge since in this case $ge = 2\pi n$ with $n = 1, 2, ...$ *There is no place for this monoplle in modern theories of our world but there are no precise reasons against its existence.* In this case the point in Fig. 6 corresponds to exchange of loop of heavy monopoles (like electron loop in QED – Heisenberg–Euler type lagrangian).

Let M be monopole mass. At $s \ll M^2$ the electrodynamics of monopoles is expected to be similar to the standard QED with effective perturbation parameter $g\sqrt{s}/(4\pi M)$ [13]. The $\gamma\gamma \to \gamma\gamma$ scattering is described by monopole loop, and it is calculated within QED,

$$\mathcal{L}_{4\gamma} = \frac{1}{36}\left(\frac{g}{\sqrt{4\pi}M}\right)^4\left[\frac{\beta_+ + \beta_-}{2}\left(F^{\mu\nu}F_{\mu\nu}\right)^2 + \frac{\beta_+ - \beta_-}{2}\left(F^{\mu\nu}\tilde{F}_{\mu\nu}\right)^2\right].$$

The coefficients $\beta_\pm$ and details of angular and polarization dependence depend strongly on the spin of the monopole.

After averaging over polarizations, the $p_\perp$ dependence and total cross section are described by the same equations as for the extra dimensions case. The parameter Λ is expressed via monopole mass and coefficient a_J, dependent on monopole spin J ($n = 1, 2, ...$):

$$\Lambda = (M/n)a_J, \quad \textit{where} \quad a_0 = 0.177, \;\; a_{1/2} = 0.125, \;\; a_1 = 0.069. \tag{7}$$

Unparticle $\mathcal{U}$ is an object, describing particle scattering via propagator which has no poles at real axis. It was introduced in 2007 [14]. This propagator behaves (in the scalar case) as

$(-p^2)^{d_U-2}$ where scalar dimension d_u is not integer or half-integer. The interaction carried by unparticle is described as $\frac{F^{\mu\nu}F_{\mu\nu}\mathcal{U}}{\Lambda^{2d_U}}$ with some phase factor. For matrix element it gives

$$\mathcal{M} = \frac{F^{\mu\nu}F_{\mu\nu}F^{\rho\tau}F_{\rho\tau}}{\Lambda^{4d_U}}(-P^2)^{d_U-2} \; + \; permutations\,.$$

$$|\mathcal{M}|^2 = C\frac{s^{2d_U}+|t|^{2d_U}+|u|^{2d_U}+\cos(d_u\pi)[(s|t|)^{d_U}+(s|u)^{d_U}]+(tu)^{d_U}}{\Lambda^{4d_U}}$$

The expected discovery limits for all these models are shown in the Table 1. The results of D0 experiment [15], recalculated to used notations, are also included here. For the unparticle model presented numbers are modified by corrections $\propto (d_U - 2)$.

References

[1] I.F. Ginzburg, G.L. Kotkin, V.G. Serbo, V.I. Telnov. *Nucl. Instr. Meth.* **205** (1983) 47–68; I.F. Ginzburg, G.L. Kotkin, S.L. Panfil, V.G. Serbo, V.I. Telnov. *Nucl. Instr. Meth.* **219** (1983) 5.

[2] V. Telnov. hep-ex/0012047

[3] I.F. Ginzburg, G.L. Kotkin, V.G. Serbo, in preparation

[4] B. Badelek et al. *TESLA TDR* hep-ex/0108012

[5] I.F. Ginzburg, G.L. Kotkin, S.L. Panfil, V.G. Serbo. *Nucl. Phys.* **B228** (1983) 285

[6] I.F. Ginzburg, V.A.Ilyin, A.E.Pukhov, V.G.Serbo, S.A.Shichanin. *Phys. At. Nucl.– Russian Yad Fiz.* **56** (1993) 57–63.

[7] D. A. Anipko, I. F. Ginzburg, K.A. Kanishev, A. V. Pak, M. Cannoni, O. Panella. *Phys. Rev.* **D 78** (2008) 093009; ArXive: hep-ph/0806.1760

[8] V.L. Chernyak, V.G. Serbo, *Nucl. Phys.* **B 67** (1973) 464;
I.F.Ginzburg, A.Schiller, V.G. Serbo, *Eur. Phys. J.* **C18** (2001) 731

[9] I.F.Ginzburg, *Proc. 9th Int. Workshop on Photon-Photon Collisions*, San Diego (1992) 474

[10] E. Boos et al. *Nucl. Instr. Meth.* **A534** (2004) 250; A. Pukhov. hep-ph/0412191

[11] I.F. Ginzburg, V.G. Serbo. *Phys. Lett.* **B 96** (1980) 68-70.

[12] K.R. Dienes, E. Dudas, T. Gherghetta. hep-ph/9803466, *Phys. Lett.* **B 436** (1998); M. Shifman. hep-ph/09073074

[13] I.F. Ginzburg, S.L. Panfil. Sov. Yad. Fiz. **36** (1982) 850; I.F. Ginzburg, A. Schiller. *Phys. Rev.* **D 60** (1999) 075016

[14] H. Georgy, *Phys. Rev. Let.* **98** (2007) 221601;hep-ph/0703.260; I.Sahin, S.C. Inan hep-ph/09073290

[15] B. Abbot et al. *Phys. Rev. Lett.* **81** (1998) 524, hep-ex/9803023

Supersymmetry and New Physics at $\gamma\gamma$ Collider

Rohini M. Godbole

Centre for High Energy Physics, Indian Institute of Science, Bangalore, 560012, India

DOI: http://dx.doi.org/10.3204/DESY-PROC-2009-03/Godbole

In this contribution we present a discussion of some aspects of the capabilities of a photon collider to probe physics beyond the standard model. I will take a few examples from Higgs physics, supersymmetry , extra dimensional theories as well as unparticles, pointing out the special rôle that a photon collider can play in each case.

1 Introduction

I have been asked to discuss new physics at the $\gamma\gamma$ collider [1]. In general, new physics can be discussed in two different ways:

a) In the framework of specific models proposed with a view to cure one or more of the ills of the SM, some well motivated and some speculative. Supersymmetry (SUSY), extra dimensional models (ED), Little Higgs models, noncommutative theories, unparticles etc. are some examples.

b) The second is to look at the effect on different aspects of phenomenology at a $\gamma\gamma$ collider such as jet production, $t\bar{t}$ production or Higgs physics studies etc., in a model independent manner.

In this contribution I will pick some combination of the two above mentioned strategies as well as that of the topics. I will mainly concentrate on physics of the sparticles and (BSM) Higgs at the $\gamma\gamma$ colliders, trying to identify where the $\gamma\gamma$ collider has a distinct advantage in terms of adding clarity to a particular study, and/or increasing the coverage in (SUSY) model parameter space as well as the reach in masses, compared to the e^+e^- option. I will also include some discussion of new physics such as extra dimensional theories or more speculative case of unparticles in the context of $\gamma\gamma$ colliders.

The two special features of the PLC of great help in this are: the very accurate measurements ($\sim 2\%$) of the $\Gamma_{\gamma\gamma}$ decay width for the Higgs boson into two photons and good control on the polarisation of the initial photon beams.

2 SUSY: LHC Wedge, LEP hole and LHC/ILC

It is necessary to summarise the LHC and LHC/ILC possibilities for SUSY studies and searches [2], before turning to a discussion of the possibilities at the PLC. Recall that the sparticle mass spectrum depends on the mechanism responsible for SUSY breaking and can vary widely, *but* the sparticle spins and couplings are predicted unambiguously. To establish SUSY with the help

of the two colliders LHC and ILC, we need to find the sparticles, measure their masses, spins and couplings. Another thing is to note that for $\tilde{\chi}^{\pm}, \tilde{\chi}^0_l$ as well as the supersymmetric partners of the third generation of the quarks/leptons, the masses as well as the couplings, can depend on the SUSY breaking mechanism and parameters. The LHC will be able to 'see' the strongly interacting sparticles if the SUSY scale is TeV. If the sparticle mass is within the kinematic reach of the ILC, we will be able to make accurate mass measurements and also can make a clean spin determination. In this situation the ILC can even help us determine the SUSY model parameters and hence the SUSY breaking mechanism as has been summarised in the SPA program [3]. In spite of this very impressive and exhaustive coverage of SUSY by the LHC and the ILC in e^+e^- mode, there are a few 'holes' in the SUSY parameter space. In the so called LHC wedge [4], $\tan\beta \simeq 4-10$, $M_A, M_H > 200$–250 GeV, only the light Higgs h of SUSY will be observable at the LHC and the H/A will not be visible at the first generation ILC. In case of CP violating MSSM also, there exists a 'hole' in the $\tan\beta$-$m_{H^\pm}$ plane, for low $\tan\beta \lesssim 3-5$. This corresponds to three neutral Higgses $\phi_i, i = 1-3$, which may not be CP eigenstates, in the mass range $m_{\phi_1} < 50$ GeV, $100 < m_{\phi_2} < 110$ GeV and $130 < m_{\phi_3} < 180$ GeV. This region cannot be ruled out by LEP searches, and the LHC also may not have enough reach [5]. The $\gamma\gamma$ collider (PLC) can indeed offer unique possibilities in this case. Further, discovery of any charged scalar would uniquely signal physics beyond the SM (BSM). In the following we will present examples of the special role that the PLC can play in this context.

3 Increased reach for new particle searches at the PLC

As already mentioned charged Higgs, for that matter, any charged scalar will be a signal of BSM physics beyond any doubt. The production cross-sections of such scalars are enhanced in $\gamma\gamma$ collisions, compared to that in e^+e^- collisions, by a factor of Q_S^2, where Q_S is the electromagnetic charge of the scalar S. This is relevant, for example, in the Little Higgs models, which have doubly charged scalars. Even for the singly charged scalars, the dependence of the pair production cross-section on the original $e^\pm$ beam energy depends on the polarisation combination of the two beams and can be used to increase the mass reach. The left panel in Figure 1, taken from Ref. [6], showing this polarisation dependence as function of $m_{H^{++}}$ illustrates this. In fact the right hand side panel of the same figure, taken from Ref. [7], showing the cross-section for scalar quark production, both in e^+e^- collisions and at the $\gamma\gamma$ collider, as a function of the scalar quark mass, directly illustrates how one can increase the reach in the charged scalar sector over the LC mode, at a 1 TeV LC.

The above discussion clearly highlights the advantage offered by a PLC in case of charged scalars with a clear increase in the range of scalar masses that can be probed with a given e^+/e^- beam energy. An increase in the range (by about a factor of 1.6) in the reach in the mass of the heavy Higgs of SUSY (H/A), due to the single Higgs production that is possible at the PLC, compared to that in pair production in e^+e^- colliders, had also been noted in the context of MSSM Higgs boson searches. This in fact can fill the LHC wedge region of the MSSM parameter space [8]. In addition to this, the PLC, in the e–γ option can increase the range of $m_{\tilde{e}_R}$ mass if the mass difference between the $\tilde{e}_R$ and $\tilde{\chi}^0_1$ is large. At an e-γ collider, the $e\gamma \to \tilde{e}_R\tilde{\chi}^\pm_1$ process has reach up to $m_{\tilde{e_R}} + m_{\tilde{\chi}^0_1} < 0.9\sqrt{s_{ee}}$, whereas at an e^+e^- collider the reach is $0.5\sqrt{s_{ee}}$. This has already been discussed in other talks at this conference [9]. Further, this is possible without the need of a polarised initial beam.

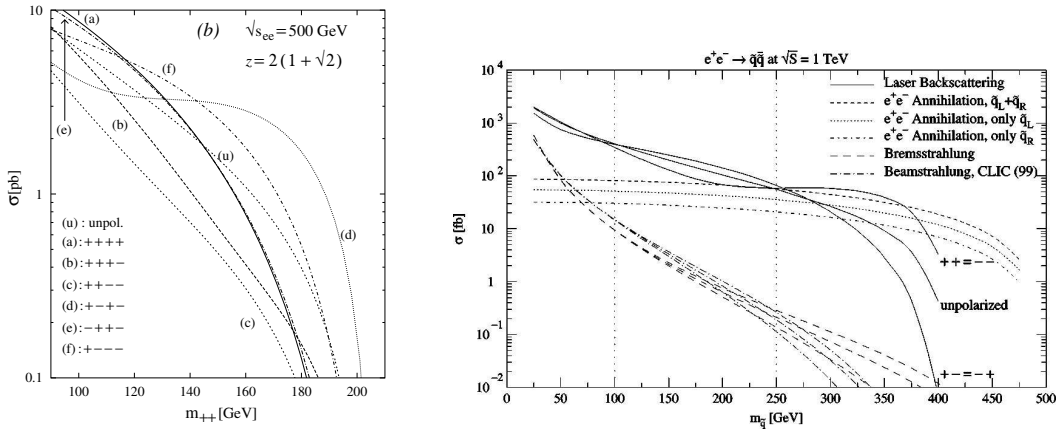

Figure 1: Beam polarisation dependence of the production cross-section for doubly charged scalars (left panel) [6] and for squarks (right panel) [7] as a function of the mass.

4 Better measurement of SUSY parameters

Not just for the charged scalars but also for the new charged fermions, like $\tilde{\chi}_1^{\pm}$, pair production in $\gamma\gamma$ collisions, can afford a good measurement of the B.R. ($\tilde{\chi}_1^{\pm} \to W\tilde{\chi}_1^0$) and can increase the accuracy of $\tan\beta$ determination in the SPA fit by over a factor 2–3 [9, 10], for a MSSM point with parameter choice very similar to that for SPS 1a.

In fact the determination of $\tan\beta$ at an e^+e^- collider is particularly notorious for the lack of accuracy at large $\tan\beta$ in the process $\tilde{\chi}^+\tilde{\chi}^-, \tilde{\chi}_j^0\tilde{\chi}_i^0$ mainly due to the fact that the observable involves $\cos 2\beta$ [11]. $\gamma\gamma \to \tau^+\tau^-\phi \to \tau^+\tau^- b\bar{b}$, on the other hand offers a very good measurement of $\tan\beta$. Results of a phenomenological calculation [12], show that at $\tan\beta = 30$ it may be possible to have $\Delta\tan\beta = 0.9$–1.3, to be contrasted with an accuracy of about 10–12 [11] at the e^+e^- option. It is clear that this process has the potential to help enormously in SUSY parameter determination. However, this needs to be backed up by detailed simulations.

5 Higgs physics and the PLC

An accurate measurement of $\Gamma(\phi \to \gamma\gamma)$, determination of the CP property of the Higgs, as well as measurement of CP mixing in case of CP violation, are the three important ways in which a PLC can make value addition compared to an e^+e^- collider. Many of these features, apart from the CP violation in the Higgs sector, both in the context of a particular model (SUSY) and in a model independent approach were already described in different talks [9, 13] at this conference. Almost any new physics, may it be SUSY, with and without CP violation [14, 15, 16, 17] or Two Higgs Doublet model [18] will in fact affect the $\gamma\gamma$-Higgs couplings and hence the width. In the CPV MSSM or the MSSM with non universal gaugino masses, these effects can be significant, yet being consistent with the current limits on all the sparticle masses.

A unique feature of a PLC is that the two photons can form a $J_z = 0$ state with both even and odd CP. As a result, unlike the gauge boson fusion mode which contributes mainly in the $e^+e\cdot-$ mode to the production, the PLC has a similar level of sensitivity for both the CP-odd

and CP-even components of a CP-mixed state:

$$\mathrm{CP-even}: \epsilon_1 \cdot \epsilon_2 = -(1+\lambda_1\lambda_2)/2, \quad \mathrm{CP-odd}: [\epsilon_1 \times \epsilon_2] \cdot k_\gamma = \omega_\gamma i\lambda_1(1+\lambda_1\lambda_2)/2, \qquad (1)$$

ω_i and λ_i denoting the energies and helicities of the two photons respectively; the helicity of the system is equal to $\lambda_1 - \lambda_2$. This contrasts the e^+e^- case, where it is possible to discriminate between CP-even and CP-odd particles but may be difficult to detect small CP-violation effects for a dominantly CP-even Higgs boson [5, 19].

In this talk I should like to concentrate on the CP violation and anomalous hVV couplings in the Higgs sector, pointing out the role that the PLC can play in their study, after briefly mentioning the prominent issues in the first two topics.

5.1 LHC-wedge

In the large $\tan\beta$ region, the dominant decay mode of the H/A is into the $b\bar{b}$ channel, where the $b\bar{b}$ background can be controlled by a judicious choice of photon polarisation. H/A separation can be achieved by choosing the polarisation vectors of the two photons to be perpendicular and parallel; but this has implications for the QED $q\bar{q}$ background as well. Results of a detailed simulation [20], which were already discussed at this conference, show that for a light Higgs it would be possible to measure the $\gamma\gamma$ rates accurate to $\simeq 2\%$ whereas for H/A measurement precision would be somewhat worse : $\sim 11\%$–21% . In fact in these region the supersymmetric decay of the H/A into $\tilde{\chi}^{\pm}, \tilde{\chi}^0_l$ pairs can also be used [8].

5.2 CP properties and CP violation in the Higgs sector

In the MSSM the properties of the Higgs sector, at the tree level, are determined in terms of two parameters $\tan\beta$ and μ. If some of the SUSY parameters have nonzero phases, then the Higgs sector can have loop generated CP violation, even with a CP conserving tree level scalar potential [21]. Recall the existence of the 'LEP-hole' mentioned earlier. The effect of this CP violation on the masses and the coupling of the Higgses in this parameter range can also affect the LHC reach and part of the 'hole' remains [5], even after the recovery of some part of the parameter space through the decay chain $t \to bH^+ \to bWh \to bWb\bar{b}$ [22].

A PLC will be able to produce such a neutral Higgs in all cases; independent of whether it is a state with even/odd or indeterminate CP parity. For the PLC, one can form three polarization asymmetries in terms of helicity amplitudes which give a clear measure of CP mixing [23]. Note however that these require linearly polarised photons in addition to the circular polarisation. With circular beam polarization almost mass degenerate (CP-odd) A and (CP-even) H of the MSSM may be separated [8, 20]. In addition, one can use information on the decay products of WW, ZZ [24]. Further, Higgs contribution to $\gamma\gamma \to f\bar{f}$ can give nontrivial information on the CP mixing [25, 26, 27, 28, 29, 30, 5].

• **$f\bar{f}$ final state.**

The process receives contributions from the s–channel Higgs exchange and the t-channel QED diagram. It is possible to determine the CP mixing, if present, by using the polarisation of the initial state γ or that of the fermions into which the ϕ_i decays. In the MSSM the CP-even H and the CP-odd A are degenerate. In the situation that the mass difference between the two is less than the sum of their widths, a coupled channel analysis technique [31] has to be used. The authors of Refs. [28] and [29] explore the use of beam polarisation and final state

fermion polarisation to analyse this situation, whereas the use of decay fermion polarisation for determination of the Higgs CP property for a generic choice of the MSSM parameters is explored in Ref. [30].

The most general couplings of a Higgs to $f\bar{f}$ and $\gamma\gamma$ can be written in a model independent way, accounting for possible CP violation, as [26, 27]:

$$\begin{aligned}\mathcal{V}_{f\bar{f}\phi} &= -ie\frac{m_f}{M_W}\left(S_f + i\gamma_5 P_f\right), \\ \mathcal{V}_{\gamma\gamma\phi} &= \frac{-i\sqrt{s}\alpha}{4\pi}\left[S_\gamma(s)\left(\epsilon_1.\epsilon_2 - \frac{2}{s}(\epsilon_1.k_2)(\epsilon_2.k_1)\right) - P_\gamma(s)\frac{2}{s}\epsilon_{\mu\nu\alpha\beta}\epsilon_1^\mu\epsilon_2^\nu k_1^\alpha k_2^\beta\right].\end{aligned}$$

When we consider this in the context of a particular model then the form-factors, $\{S_f, P_f, S_\gamma, P_\gamma\}$ depend upon model parameters. For example, for the CP violating MSSM these depend on $m_{H^+},\ \tan\beta,\ \mu,\ A_{t,b,\tau},\ \Phi_{t,b,\tau},\ M_{\tilde{q}},\ M_{\tilde{l}}$ etc. The model independent case and the specific case of

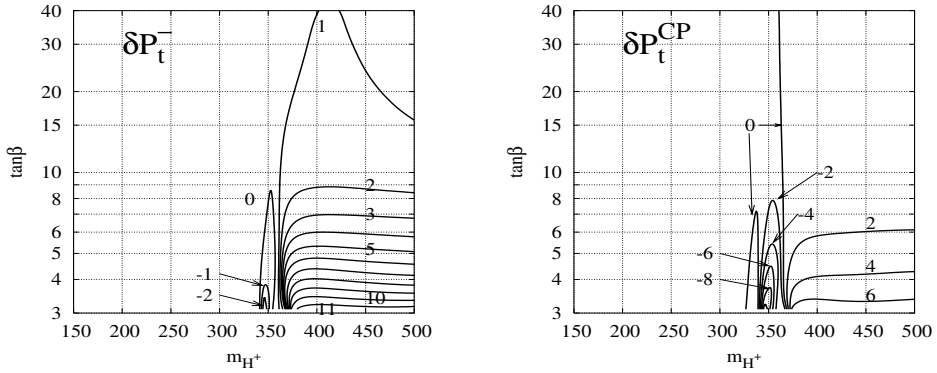

Figure 2: Expected values (in %) of δP_t^- and δP_t^{CP} for the top quarks produced in the process, $\gamma\gamma \to t\bar{t}$, including the s-channel Higgs exchange contribution, in the CPV MSSM, in the CPX scenario, in the m_H^+–$\tan\beta$ plane [30]

.

CP violating SUSY are analysed in Refs. [26, 27] and [30] respectively. The helicity amplitude for the production will in general involve CP even combinations such as $S_f\Re(S_\gamma)$(viz.x_i) as well as CP odd-combinations such as $S_f\Im(P_\gamma)$(viz.y_i). Note that the QED background is P, CP and chirality conserving. The Higgs exchange diagram violates these symmetries. This means that in the presence of the Higgs, the existence of chirality flipping interactions implies nonzero values of the various $\{x_i, y_j\}$ which in turn means that the fermion-polarisation carries a foot-print of the Higgs contribution as well as any CP violation in the $\phi\gamma\gamma$ and $\phi f\bar{f}$ couplings. It is also very gratifying that the heavier fermions t, τ which have the largest $\phi f\bar{f}$ coupling are also the fermions whose polarisation is amenable to experimental measurements. The polarisation of the initial state γ can be controlled by adjusting the initial laser and the e polarisation. The ϕ contribution is enhanced using the combination $\lambda_e \times \lambda_l = -1$. One can construct observables, with unpolarised and polarised laser and e beams in terms of expected fermion polarisation: P_f^U being the expected one for unpolarised initial states and P_f^{++}, P_f^{--} being the observables with polarised beams. Here $+/-$ in the (double) superscripts refer to the polarisation of the e, λ_e. P_f^{++}, P_f^{--} are nonzero even for the QED diagrams alone, but the P invariance of QED implies

$P_f^{++} = -P_f^{--}$ Hence a nonzero value for $P_f^{++} + P_f^{--}$ will clearly indicate parity violation. In case of C invariance this then is also CP violating. Thus P_f^U and $\delta P_f^{CP} = P_f^{++} + P_f^{--}$ are both probes of the CP violating contribution. Further, P_f^{++} is modified by the Higgs contribution such that $P_f^{++} - (P_f^{++})^{QED} \neq 0$ even if ϕ is CP eigenstate. Hence, $\delta P_f^+ = P_f^{++} - (P_f^{++})^{QED}$ and $\delta P_f^- = P_f^{--} - (P_f^{--})^{QED}$ are both probes of chirality flipping interactions. Figure 2, taken from Ref. [30], shows the values for δP_t^- and δP_t^{CP}, expected in the CP-violating MSSM, in the m_H^+–tan β plane, for the CPX scenario [21], in the left and the right panel respectively. A similar calculation of the expected τ polarisation indicates that the two fermion polarisations

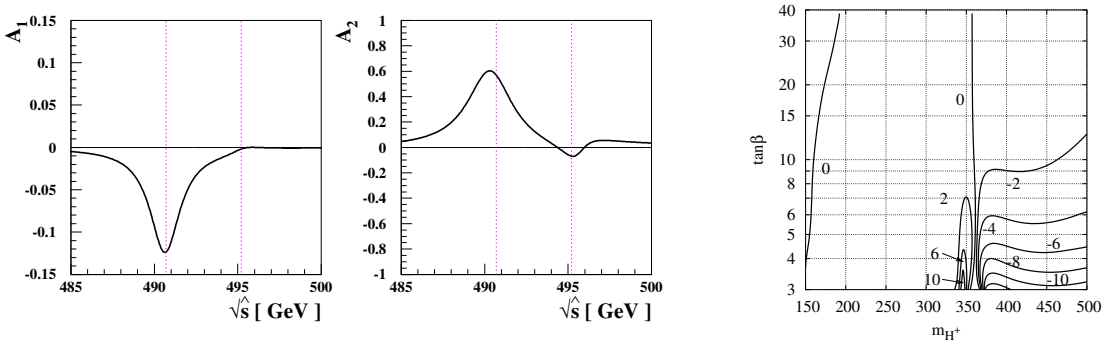

Figure 3: CP violating asymmetries constructed out of different combination of cross-sections with final state t helicity and initial state photon helicity for top quarks produced in the process, $\gamma\gamma \to t\bar{t}$, including the s-channel Higgs exchange contribution, in the degenerate ϕ_2/ϕ_3 case in CPV MSSM as a function of the $\gamma\gamma$ centre of mass energy (two left panels) [28] and the mixed lepton charge-photon helicity asymmetry (in %) for the generic case in the CPX scenario, in the m_H^+–tan β plane with a choice of e^+e^- beam energy to maximise the asymmetries (right panel) [30].

offer coverage in complementary regions of this parameter space, and part of the 'LEP'-hole, which cannot be covered at the LHC, can in fact be covered by these measurements. Note that the ILC can provide partial coverage of the region through production of other Higgs bosons, but $\gamma\gamma$ collisions and/or production in the decay of the charged Higgs [22], remain the only two modes for the light neutral Higgs, in this left over region of the 'LEP-hole'.

The expected values of the various observables presented in Figure 2 and the rightmost panel of 3, are for a value of the common CP violating phase $\Phi = 90°$ and the beam energy is adjusted for each point in the scan such that the peak of the photon spectrum matches with scaled mass $m_\phi/\sqrt{s_{\gamma\gamma}}$, m_ϕ being the average mass of the two states which may be close in mass. Nowhere in this range of the parameters are the two states extremely degenerate, and hence a coupled channel analysis is not required. We see that even in this case, the size of the expected asymmetries is not too small. Thus in a generic case of CPV MSSM, the PLC can probe this CP-mixing in the Higgs sector. In case of extreme degeneracy of the two states, the expected polarisation asymmetries for both the fermion final states containing τ and t, are enhanced resonantly and the observability is increased even more. The left two panels of Figure 3 taken from Ref. [28] show two such CP violating asymmetries constructed out of a combination of

cross-sections with different helicities for the initial state photons and final state quarks, as a function of $\sqrt{s_{\gamma\gamma}}$, with model parameter values chosen to maximise the effect.

Since the top quark decays before it hadronises, the decay products retain the top quark spin information. In fact, the decay lepton angular distribution is a particularly good probe of this polarisation due to the independence of the correlation between the polarisation and the angular distribution and any anomalous tbW vertex [32]. The above mentioned polarisation asymmetries translate into 'mixed beam polarisation-lepton charge asymmetry' constructed out of cross-sections with different photon helicity combinations as in Ref. [26], but for values of the form factors $S_f, P_f, S_\gamma, P_\gamma$, calculated in the CPX scenario as a function of the MSSM parameters $\tan\beta$–m_{H^+} plane. These, taken from Ref. [30] are shown in the rightmost panel of the Figure 3.

• **2HDM and WW/ZZ final states at a PLC**

As mentioned earlier, CP violation in the Higgs sector has also been studied in the context of a Two Higgs Doublet model, and the possibility of determining the CP violating phase through the kinematic distribution of the decay products of the W and the Z [24], with realistic photon spectra has been investigated. The phase Φ_{CP} and the relative strength of the ϕVV coupling relative to that in the SM can be measured to about $\lesssim$0.02–0.05 depending on the mass of the Higgs.. The errors are computed, assuming the SM value of 0 and 1 respectively for the two. The interesting part of this study is the fact that the two photon width, its phase and the relative normalisation of both samples, are all allowed to vary in the fit. The former, which is available only at a PLC, is seen to impact the results significantly.

In fact in the $e\gamma$ option the photon collider offers also a unique possibility of determining accurately the hWW anomalous coupling. The accuracy of determination of this coupling in the e^+e^- option is limited due to the big background from the ZZh contribution to the same final state. This does not require polarised beams either [33].

5.3 Higgs self coupling and the $\gamma\gamma$ collider

The ILC in the e^+e^- mode offers only a very limited information on the trilinear hhh coupling [2, 34]. This information can be obtained through a study of Higgs pair production at a $\gamma\gamma$ collider and is shown to be a good probe of hhh couplings and comparable perhaps to other probes at the LHC and the ILC. Recently, the modification of the hhh coupling in the framework of general Two Higgs Doublet models was addressed in a couple of analyses [35, 36, 37]. If the modification of the hhh coupling is due to new particles in the spectrum, then it will also modify $h\gamma\gamma$ as well as the $\gamma\gamma hh$ coupling. So in the framework of a Two Higgs Doublet model they calculate the net change in the cross-section $\gamma\gamma \to hh$ and show that the sensitivities possible at the PLC can indeed test these models.

6 Extra-dimensional models and the PLC

In the context of models with TeV scale gravity, i.e. models with extra dimensions, the $\gamma\gamma$ production of all the matter and gauge boson fields is altered substantially. The extra dimensions can be probed in the dijet final state [38], through the gauge boson couplings to a pair of photons [39], in the production of a $t\bar{t}$ pair [40] as well as in the $e\gamma$ mode [41], up to a scale comparable and/or somewhat higher level compared to the LC option. However, all these

calculations have been done at the theorist's level and an evaluation of the net gain due to PLC, when a realistic photon spectrum is used, is not available.

7 Unparticles and the PLC

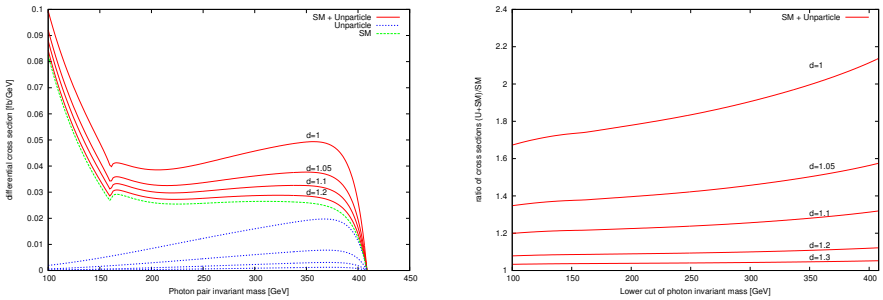

Figure 4: The $\gamma\gamma$ invariant mass distribution for a 500 GeV machine showing the effect of the scaling dimension of the unparticles (left panel) and the values of $\sigma_{\mathcal{U}} + \sigma_{SM}/\sigma_{SM}$ as a function of $\gamma\gamma$ centre of mass energy (right panel) [42].

Along with the very well motivated physics beyond the SM like supersymmetry and extra dimensions, the PLC can also probe speculative physics like unparticles. Among the different discussions that exist, I am going to give only one example taken from [42], where they consider the effect of unparticles on the process $\gamma\gamma \to \gamma\gamma$, which can be studied at a photon collider. In these theories a hidden conformal sector provides "unparticle" which couples to the Standard Model sector through higher dimensional operators in the low energy effective theory. If one focuses on operators which involve unparticle, the Higgs doublet and the gauge bosons, after electroweak symmetry breaking, a mixing between unparticle and Higgs boson ensues. In turn this can cause sizable shifts for the couplings between the Higgs boson and a pair of photons [43]. Since the process proceeds in the SM only at loop level, it has a great potential to probe new physics. The authors of Ref. [42] show that $\gamma\gamma$ collider in this case can be sensitive to a scale of 5 TeV for $\sqrt{s} = 500$ GeV. The plot in the left panel of Figure 4, taken from this reference, shows the cross-section as a function of the $\gamma\gamma$ invariant mass. The structure in this distribution reflects the scaling dimension of unparticle. The second plot (right panel) in Figure 4 shows ratio of $\sigma_{\mathcal{U}} + \sigma_{SM}/\sigma_{SM}$.

8 Conclusions

Thus a PLC can play an important and unique role in many ways in probing BSM physics. Loop effects on $\gamma\gamma$ processes and couplings can probe it indirectly. Further, it can affect search prospects of new charged scalars, a sure harbinger of New Physics, by providing comparable reach, if not more, as the e^+e^- option for a TeV energy LC. Polarisation dependence of the photon spectrum and cross-section can play an important role. $\Delta\beta \simeq 1$ at large $\tan\beta$ can be achieved using $\tau\tau$ fusion. There are major gains for the SUSY Higgs sector as it provides reach for H/A in regions where LHC does not have any. The s channel production increases reach in the mass of neutral Higgses by a factor ~ 1.6 due to single production that is possible.

Advantages of a $\gamma\gamma$ collider are even more if CP violation is present in the Higgs sector. The polarisation asymmetries constructed using initial state photon polarisation and final state fermion polarisations, can be a very good probe of the CP violation in the Higgs sector. The H/A contribution can be probed therefore through mixed polarisation-charge asymmetries, i.e. asymmetries in initial state polarisation and final state lepton charge. If CP violation makes the lightest Higgs dominantly pseduoscalar and hence 'invisible' at LEP/ILC/LHC, then a $\gamma\gamma$ collider is the only place where it can be produced directly. The PLC is capable of probing new physics such as extra dimensions through production of dijets, top pairs, gauge bosons etc. in $\gamma\gamma$ collisions.

9 Acknowledgments

I wish to complement the organisers for the excellent organisation of this meeting. This work was partially supported by the Department of Science and Technology, India under the grant of the J.C. Bose Fellowship, under project number Grant No. SR/S2/JCB-64/2007.

References

[1] B. Badelek et al. TESLA Technical Design Report, Part VI, Chapter 1: Photon collider at TESLA. *Int. J. Mod. Phys.*, A19:5097–5186, 2004.

[2] G. Weiglein et al. Physics interplay of the LHC and the ILC. *Phys. Rept.*, 426:47–358, 2006.

[3] Juan Antonio Aguilar-Saavedra et al. Supersymmetry parameter analysis: SPA convention and project. *Eur. Phys. J.*, C46:43–60, 2006.

[4] J. A. Aguilar-Saavedra et al. TESLA Technical Design Report Part III: Physics at an e+e- Linear Collider. hep-ph/0106315, 2001.

[5] E. Accomando et al. Workshop on CP Studies and Non-Standard Higgs Physics. hep-ph/0608079, 2006.

[6] Surajit Chakrabarti, Debajyoti Choudhury, Rohini M. Godbole, and Biswarup Mukhopadhyaya. Observing doubly charged Higgs bosons in photon photon collisions. *Phys. Lett.*, B434:347–353, 1998.

[7] S. Berge, M. Klasen, and Y. Umeda. Sfermion pair production in polarized and unpolarized gamma gamma collisions. *Phys. Rev.*, D63:035003, 2001.

[8] M. M. Muhlleitner, M. Kramer, M. Spira, and P. M. Zerwas. Production of MSSM Higgs bosons in photon photon collisions. *Phys. Lett.*, B508:311–316, 2001.

[9] K. Moenig. Physics at a gamma gamma collider. In these proceedings, 2009.

[10] G. Klamke and K. Moenig. Studies on chargino production and decay at a photon collider. *Eur. Phys. J.*, C42:261, 2005.

[11] S. Y. Choi et al. Reconstructing the chargino system at e+ e- linear colliders. *Eur. Phys. J.*, C14:535–546, 2000.

[12] S. Y. Choi et al. Determining tan(beta) in tau tau fusion to SUSY Higgs bosons at a photon collider. *Phys. Lett.*, B606:164–172, 2005.

[13] Spira M. Higgs Physics at ee and photon collider. These Proceedings, 2009.

[14] Abdelhak Djouadi. Squark effects on Higgs boson production and decay at the LHC. *Phys. Lett.*, B435:101–108, 1998.

[15] G. Belanger, F. Boudjema, F. Donato, R. Godbole, and S. Rosier-Lees. SUSY Higgs at the LHC: Effects of light charginos and neutralinos. *Nucl. Phys.*, B581:3–33, 2000.

[16] S. Moretti, S. Munir, and P. Poulose. Explicit CP violation in the MSSM through Higgs to gamma gamma. *Phys. Lett.*, B649:206–211, 2007.

[17] S. Hesselbach, S. Moretti, S. Munir, and P. Poulose. Exploring the Di-Photon Decay of a Light Higgs Boson in the MSSM With Explicit CP Violation. *Eur. Phys. J.*, C54:129–147, 2008.

[18] Ilya F. Ginzburg, Maria Krawczyk, and Per Osland. Potential of photon collider in resolving SM-like scenarios. *Nucl. Instrum. Meth.*, A472:149–154, 2001.

[19] R. M. Godbole et al. CP studies of the Higgs sector. hep-ph/0404024, 2004.

[20] M. Spira, P. Niezurawski, M. Krawczyk, and A. F. Zarnecki. Heavy neutral MSSM Higgs Bosons at the PLC - a comparison of two analyses. *Pramana*, 69:931–936, 2007.

[21] Apostolos Pilaftsis and Carlos E. M. Wagner. Higgs bosons in the minimal supersymmetric standard model with explicit CP violation. *Nucl. Phys.*, B553:3–42, 1999.

[22] Dilip Kumar Ghosh, R. M. Godbole, and D. P. Roy. Probing the CP-violating light neutral Higgs in the charged Higgs decay at the LHC. *Phys. Lett.*, B628:131–140, 2005.

[23] B. Grzadkowski and J. F. Gunion. Using back scattered laser beams to detect CP violation in the neutral Higgs sector. *Phys. Lett.*, B294:361–368, 1992.

[24] P. Niezurawski, A. F. Zarnecki, and M. Krawczyk. Model-independent determination of CP violation from angular distributions in Higgs boson decays to W W and Z Z at the Photon Collider. *Acta Phys. Polon.*, B36:833–844, 2005.

[25] Eri Asakawa, Jun-ichi Kamoshita, Akio Sugamoto, and Isamu Watanabe. Production of scalar Higgs and pseudoscalar Higgs in multi-Higgs doublet models at gamma gamma colliders. *Eur. Phys. J.*, C14:335–345, 2000.

[26] Rohini M. Godbole, Saurabh D. Rindani, and Ritesh K. Singh. Study of CP property of the Higgs at a photon collider using $\gamma\gamma \to t\bar{t} \to lX$. *Phys. Rev.*, D67:095009, 2003.

[27] Eri Asakawa and Kaoru Hagiwara. Probing the CP nature of the Higgs bosons by t anti-t production at photon linear colliders. *Eur. Phys. J.*, C31:351–364, 2003.

[28] John R. Ellis, Jae Sik Lee, and Apostolos Pilaftsis. Resonant CP violation in MSSM Higgs production and decay at gamma gamma colliders. *Nucl. Phys.*, B718:247–275, 2005.

[29] S. Y. Choi, J. Kalinowski, Y. Liao, and P. M. Zerwas. H / A Higgs mixing in CP-noninvariant supersymmetric theories. *Eur. Phys. J.*, C40:555–564, 2005.

[30] Rohini M. Godbole, Sabine Kraml, Saurabh D. Rindani, and Ritesh K. Singh. Probing CP-violating Higgs contributions in $\gamma\gamma \to f\bar{f}$ through fermion polarization. *Phys. Rev.*, D74:095006, 2006.

[31] Apostolos Pilaftsis. Resonant CP violation induced by particle mixing in transition amplitudes. *Nucl. Phys.*, B504:61–107, 1997.

[32] Rohini M. Godbole, Saurabh D. Rindani, and Ritesh K. Singh. Lepton distribution as a probe of new physics in production and decay of the t quark and its polarization. *JHEP*, 12:021, 2006.

[33] Debajyoti Choudhury and Mamta. Probing anomalous Higgs couplings at an e gamma collider using unpolarised beams. *Pramana*, 69:795–800, 2007.

[34] Gerald Aarons et al. International Linear Collider Reference Design Report Volume 2: PHYSICS AT THE ILC. 0709.1893, 2007.

[35] Eri Asakawa, Daisuke Harada, Shinya Kanemura, Yasuhiro Okada, and Koji Tsumura. Higgs boson pair production at a photon-photon collision in the two Higgs doublet model. *Phys. Lett.*, B672:354–360, 2009.

[36] Abdesslam Arhrib, Rachid Benbrik, Chuan-Hung Chen, and Rui Santos. Neutral Higgs boson pair production in photon-photon annihilation in the Two Higgs Doublet Model. *Phys. Rev.*, D80:015010, 2009.

[37] Fernando Cornet and Wolfgang Hollik. Pair Production of Two-Higgs-Doublet-Model Light Higgs Bosons in $\gamma\gamma$ Collisions. *Phys. Lett.*, B669:58–61, 2008.

[38] Dilip Kumar Ghosh, Prakash Mathews, P. Poulose, and K. Sridhar. Large extra dimensions and dijet production in gamma gamma collisions. *JHEP*, 11:004, 1999.

[39] Thomas G. Rizzo. Tests of low scale gravity via gauge boson pair production in gamma gamma collisions. *Phys. Rev.*, D60:115010, 1999.

[40] Prakash Mathews, P. Poulose, and K. Sridhar. Probing large extra dimensions using top production in photon photon collisions. *Phys. Lett.*, B461:196–202, 1999.

[41] Dilip Kumar Ghosh, P. Poulose, and K. Sridhar. Seeking TeV-scale quantum gravity at an e gamma collider. *Mod. Phys. Lett.*, A15:475–482, 2000.

[42] Tatsuru Kikuchi, Nobuchika Okada, and Michihisa Takeuchi. Unparticle physics at the photon collider. *Phys. Rev.*, D77:094012, 2008.

[43] Tatsuru Kikuchi and Nobuchika Okada. Unparticle physics and Higgs phenomenology. *Phys. Lett.*, B661:360–364, 2008.

Chapter 3

Low-Energy Photon Experiments

Convenor:

A. Ringwald (DESY)

The Physics Case for Low Energy Photon Experiments: Axions, WIMPs, WISPs and Other Weird Stuff

Joerg Jaeckel

Institute for Particle Physics and Phenomenology, Durham University, Durham DH1 3LE, UK

DOI: http://dx.doi.org/10.3204/DESY-PROC-2009-03/Jaeckel

Due to their enormous precision low energy experiments with photons provide a unique window towards fundamental physics. More generally, low energy but high precision experiments may provide for a powerful probe of new physics beyond the Standard Model which is complementary to collider experiments. In these notes we argue that Axions, WIMPs and WISPs are phenomena that can be tested in low energy experiments. At the same time these particles are motivated by experimental and observational evidence as well as the desire to test theoretical model building. This provides an excellent 'physics-case'to search for new phenomena at the low energy frontier.

1 Introduction – Hints for new physics

Over the years both theoretical as well as experimental evidence has accumulated that strongly suggests the existence of physics beyond the current standard model of particle physics (SM). The Large Hadron Collider currently starting up at CERN will test many of the ideas for such physics beyond the standard model (BSM) and hopefully will provide us with a wealth of new information. In this note we argue that there is also a very good motivation to search for new physics in low energy experiments that can provide us with powerful complementary information on currently open questions and in particular on how the standard model is embedded into a more fundamental theory.

Let us begin by briefly repeating some of the main reasons why we believe that there must be physics beyond the standard model.

On the theoretical side there are a number of deficiencies in the SM. Some of them could be just aesthetic defects but some may go deeper. First of all the SM has a relatively large number $\mathcal{O}(30)$ free parameters that cannot be determined from theory alone but must be measured experimentally. Although this does not indicate an inconsistency of the theory it certainly is not in line with the hope that a fundamental theory of everything should have very few, possibly only 1 or even 0, free parameters. Moreover, some of the parameters seemingly need to require an enormous degree of finetuning or appear unnaturally small. Well known examples are the Higgs mass but also the θ parameter of QCD (which must be extremely small in order not to be in conflict with the observed smallness of strong CP violation). Another dissatisfying feature is that gravity is not incorporated into the SM but rather treated as a separate part. This is

not just an aesthetic defect but also an expression of the fact that the quantization of gravity is still not (fully) understood. Finally, strictly speaking the SM will most likely not be valid up to arbitrary high energy scales. On the one hand this is due to our current inability to properly quantize gravity. But even the non-gravity parts are probably encountering problems in the form of Landau poles (places where the coupling becomes infinite) in the QED sector (at a very high scale much beyond the Planck scale) but probably also in the Higgs sector (where the problem is much more immediate and will occur at scales much below the Planck scale - depending on the Higss mass possibly even not much above the electroweak scale).

Next there are quite a few phenomena which are experimentally well established but for which there is no good explanation within the standard model. The most shocking of which is probably the realization that most of the matter and energy in the universe actually is not made up of SM particles. Cosmological and astrophysical observations give strong evidence that about 70 % of the energy in the universe is dark energy and another 25 % is dark matter [1]. These are things that simply do not appear in the current SM (although they could be accommodated see, e.g., [2]). But even within the standard model there are things which are experimentally well established but for which a good explanation is lacking. These are, e.g., the existence of three generations of SM particles, the mass hierarchies for the SM particles and the small parameters such as, e.g., the already mentioned θ parameter [3]. The latter is, of course, a repetition of some of the problems already mentioned as 'theoretical' problems showing that they actually arise from experimental results.

Finally, there is the direct experimental evidence for BSM physics. At the moment most of this is still relatively circumstantial but it definitely demonstrates that low energy experiments can provide information on BSM physics as well as opening new directions which can be explored (or close others). Examples are the deviation [4] of the muon $(g-2)$ from the SM expectation, the excess in the event rate of the DAMA [5] experiment and the PVLAS anomaly [6] (which has been retracted [7] but, as we will see, has inspired a lot of fruitful experimental and theoretical activity). Most recently, a lot of interest has been generated by the observation of a positron excess by the PAMELA satellite [8]. This has led to great interest in the existence of new "Dark Forces" which are relatively long range with force carries of mass $\sim$ GeV (see, e.g., [9]).

2 Bottom-up/phenomenological arguments

In this section we will present several examples for physics at the low energy frontier that arise from more phenomenological arguments - a line of thought that could be called 'bottom-up' and that follows a hands-on approach on fixing problems step by step.

Axions are a good example for this approach [10]. The extreme smallness of the θ-angle is unexplained in the standard model. This can be solved by introducing a new symmetry - the Peccei Quinn symmetry. As a consequence one predicts a pseudo-Goldstone boson, the axion. This is already a good motivation to experimentally search for the axion, for example in light shining through a wall experiments [11–14] (see also next section), laser polarization experiments (as, e.g., PVLAS) [6, 7, 15] or axion helioscopes [16]. The case for this search is then strengthened by the finding that the axion is also a valid candidate for dark matter [17]. This prediction, however, not only strengthens the physics case for searching axions but it also opens new ways to do so. One can search for axion dark matter, for example using resonant cavity techniques [18] or looking in the sky for axions decaying into photons.

Another example are WIMPs (for a review see [19]). As a solution for the hierarchy problem

in the SM one can, again, introduce a symmetry: SUSY. Introducing SUSY leads to many new particles, notably the heavy supersymmetric partners of the SM particles, which are weakly interacting and massive, i.e. WIMPs. Some of them are good candidates for dark matter. Again good motivation to perform a WIMP search. Another incentive is that SUSY also allows to explain the deviation of the muon $(g-2)$ from its SM value that was already mentioned in the introduction. SUSY might be discovered at a collider such as LHC. Such an experiment may even find a dark matter candidate. But in order to know that such a candidate really makes up all or most of the dark matter, i.e. if it was produced in sufficient quantities, one needs the low energy WIMP searches [5, 20] which therefore give us crucial information.

The PVLAS anomaly which was in contradiction to the SM expectation led to the introduction of several types of WISPs (weakly interacting slight (or sub-eV) particles). To check their result and to search for these WISPs the PVLAS group then improved their apparatus finding that the original result was probably an artifact of the apparatus [7]. However, this is not the end of the story. The introduction of WISPs also led people to realize that there is a large amount of unexplored parameter space for new physics that (e.g., due to the extremely weak interactions involved) cannot be tested in conventional colliders [21][1]. Yet, new ideas how to access this parameters space in low energy experiments and observations have been put forward [23]. Moreover, it was (re-)discovered that the extremely weak interactions of WISPs are often connected to very high energy scales $\gtrsim 10^5$ GeV, in some cases even as high as the string or the even Planck scale $\sim 10^{18}$ GeV. Showing that the new and improved low energy experiments can give us complementary information on very high energy physics. Let us see in the next section how the precision of low energy photon experiments turns them into a probe for very high energy scales.

3 Low energy photon probes

Let us look a little bit more closely how we can use low energy photon experiments to search for Axions and more general WISPs.

One of the most intriguing idea is a so-called light shining through a wall experiments [11–14]. The schematic setup is shown in Fig. 1. The power of this type of experiment lies in its enormous precision. Laser powers of the order of $\sim$ 100W corresponding to 10^{21} photons per second are easily achievable. Moreover, it is certainly possible to detect as little as 1 photon per second. This allows us to search for particles with a transition probability as low as 10^{-21}!

Let us further illustrate this with an example. Axions and axion like particles (a) couple to two photons with an interaction

$$\mathcal{L}_{\rm int} \sim \frac{1}{M} a F^{\mu\nu} \tilde{F}_{\mu\nu} \sim \frac{1}{M} a \mathbf{E} \cdot \mathbf{B}. \tag{1}$$

Here M roughly gives the energy scale where the new physics connected to the axion (like particle) happens. (In some cases there is an additional (small) coupling constant involved, e.g. the electromagnetic coupling, then we probe a scale $\sim \alpha M$.)

Experimentally the electric field is provided by the laser photons and a strong magnet (typically a recycled accelerator magnet) provides the magnetic field. In this situation the

[1] Astrophysical arguments are, however, a different matter. For an overview over pre-PVLAS work in this direction see, e.g., [22].

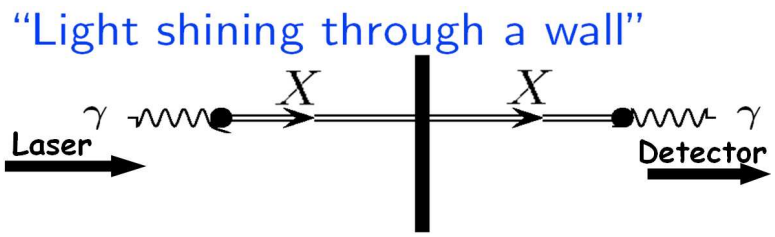

Figure 1: Schematic setup of a "light shining through a wall experiment". A laser is shone on an opaque wall. After the wall a detector is placed to search for photons that somehow make it through the wall. The idea is that some of the photons are converted into very weakly interacting particles X which can simply traverse the wall. After the wall the X particles reconvert into ordinary photons and can be detected. In some cases (e.g. Axions) the conversion can be stimulated by the presence of a magnetic field. In other cases (e.g. extra hidden, massive U(1) gauge bosons the conversion results from an oscillation between the photon and the new particle which is very similar to neutrino oscillations. Then it can happen even in vacuum.

probability for a photon to traverse the wall is given by

$$P_{\gamma\to a\to\gamma} \sim N_{\rm pass}\left(\frac{|\mathbf{B}|L}{M}\right)^4, \tag{2}$$

where L is the length of the magnetic field region. Moreover, we have included a factor $N_{\rm pass}$ accounting for the fact that we can use mirrors to reflect the light back and forth inside the interaction region to enhance the transition probability (see [11, 14] for experiments that have implemented this feature). $N_{\rm pass} \sim 100$, $B \sim 5\,\mathrm{T} \sim 1000\,\mathrm{eV}^2$ and $L \sim$ few $\times$ m $\sim (10^7 - 10^8)\,\mathrm{eV}^{-1}$ are realistic values. Inserting this into Eq. (2) and remembering that we can detect probabilities $\lesssim 10^{-21}$ we find that the experiments are sensitive to

$$M \sim (10^6 - 10^7)\mathrm{GeV}. \tag{3}$$

In other words we are probing for new physics connected to energy scales $(10^4 - 10^7)$GeV, much higher than the scale of current accelerator experiments.

The enormous precision is what makes photon experiments such a powerful tool to search for new physics. Here, we demonstrated this precision using light shining through a wall experiments searching for axion like particles as an example. This precision can also be exploited in a wide variety of other experiments [6, 7, 15, 23], including laser polarization experiments, experiments with microwave cavities, but also traditional tests of the Coulomb's law. These experiments can search for a huge variety of different WISPs such as hidden sector photons, minicharged particles and chameleon particles, as well as many other interesting things.

4 Top-down/theory arguments

Instead of taking small steps and fixing the problems, in the process often creating a more and more baroque model, one can also go back to the drawing board and rethink the very principles on which the original model was based. One such attempt (among others) is string theory. One of the main motivations for string theory is to unify the SM with gravity. To achieve this point

particles are replaced by extended strings. Currently string theory is not yet in a state where it provides a first principle derivation of the SM and corrections to the same. Nevertheless, it has a variety of general features that suggest avenues for model building and also specific phenomena.

One such general feature is that for consistency string theory likes SUSY. Following the arguments from the previous section SUSY provides a good physics case for WIMP searches. Accordingly string theory strengthens the physics case for such searches.

Another property of string theory is that in order to be consistent it needs the existence of extra (space) dimensions. In order to be in agreement with observation all except the well known three have to be compactified. However, compactification leaves its traces[2]. Shape and size deformations of the compactified dimensions correspond to scalar fields, so-called moduli. These could be very light (it is actually often difficult to give them any mass at all) and provide excellent WISP candidates (and may also be searched for in fifth force experiments [24]). In a similar manner also various types of axions appear in string theory (see, e.g., [25]). The physics of these particles (e.g. the small size of their interactions) is inherently linked to the string scale. Hence, suitable low energy experiments searching for such WISPs may give us the opportunity to probe the fundamental theory and its associated fundamental energy scale.

String theory also tends to have whole sectors of extra matter in addition to the ordinary SM matter. This matter often lives in so-called hidden sectors which have only extremely weak interactions with the SM particles. Accordingly particles in these sectors may avoid detection in collider experiments even if they are light, i.e. these hidden sector provide good candidates for WISPs[3]. Typical WISP candidates arising from such hidden sectors are extra 'hidden' U(1) gauge bosons and 'hidden' matter charged under those U(1)s [28, 29][4]. In many models these hidden sectors are located at a different place in the extra dimension than the SM sector[5]. Accordingly searching and testing these hidden sectors can give us crucial global information on the compactification that can hardly be obtained from collider experiments which probe the local structure that has relatively strong interactions.

Finally, string theory also motivates some surprising things. In particular, some models predict non-commutativity and other Lorentz symmetry violating effects [34]. This then can also be tested in low energy experiments and observations such as, e.g., comparing the spectrum of hydrogen and anti hydrogen atoms [35] or by observing if light from gamma-ray bursts arrives at (slightly) different times depending on its polarization [36]. These experiments and observations (see [37] for an overview) again provide an ultra high precision that can then give us insights into the fundamental theory at very high energy scales.

Let us again illustrate the power of precision by an example. In some models of non-

[2] If the size of the extra dimension is large enough there could actually be a very direct consequence: the inverse square law of the gravitational force would be modified. This, too, can be tested in low energy experiments [24].

[3] If the hidden sector particles are somewhat heavier they can also be WIMP candidates [26] (which in some cases can also be searched for at colliders [26, 27]). However, this also depends on how strict one takes the 'Weak' in the name WIMP. Often it is constraint to be the weak of electroweak. Then hidden sector particles cannot really be WIMPs.

[4] The hidden U(1)'s can interact with the SM via a kinetic [30], magnetic [31] or mass mixing [32] with the ordinary photon. The kinetic or magnetic mixing can then also lead to a small electric charge for the hidden matter [30, 31].

[5] An alternative to truly hidden sectors are sectors with hyperweak interactions [33]. Although in these models the new particles can have tree-level interactions with the standard model particles these are extremely weak. Effectively they are diluted because the hyperweak sector extends more into the extra dimensions. Accordingly these, too, contain more information about the global structure.

commutativity the two polarizations of light move at slightly different speed,

$$\frac{\Delta c}{c} \sim 10^{-34} \left(\frac{M_P}{M_{\rm NC}} \right)^2 . \tag{4}$$

Now assume that we observe light from a very distant source. For example, a gamma ray burst at a distance of $\sim 10^9$ lightyears. If the two polarization directions move with slightly different speeds one will arrive earlier than the other. If we can measure time differences of the order of 1 second we already have an enormous precision of 1 part in 10^{16} in the speed of light. In our example this means that we are probing energy scales of the order of 10^9 GeV. However, we can actually do much better. Using polarimetric measurements one can search for time differences corresponding to one wavelength or less. This gives us another amazing factor of $\gtrsim 10^{15}$ in the precision. Overall we can test for differences in the speed of light of the order of 1 part in $\gtrsim 10^{32}$. Comparing with Eq. (4) we see that this really tests Planck scale physics!

5 Conclusions

Both the phenomenological bottom-up and the more theory oriented top-down approach provide an excellent physics case motivating further experiments at the low-energy frontier such as searches for axions, WIMPs and WISPs and other interesting effects such as Lorentz violation. These phenomena are often connected to energy scales much higher than those reachable in near future accelerators. They provide experimental access to hidden sectors that may contain crucial information on the underlying global structure of a more fundamental theory. Moreover, they give us reasons to challenge and experimentally check basic assumptions as, e.g., Lorentz symmetry. In conclusion, low energy but high precision experiments provide crucial complementary information to uncover the nature of a more fundamental theory beyond the standard model.

Acknowledgements

The author wishes to thank the organizers of the *Photon 2009* for a very enjoyable meeting.

References

[1] E. Komatsu *et al.* [WMAP Collaboration], arXiv:0803.0547 [astro-ph].

[2] H. Davoudiasl, R. Kitano, T. Li and H. Murayama, Phys. Lett. B **609** (2005) 117.

[3] N. F. Ramsay, Phys. Rept. **43** (1977) 409; C. A. Baker *et al.*, Phys. Rev. Lett. **97** (2006) 131801.

[4] G. W. Bennett *et al.* [Muon g-2 Collaboration], Phys. Rev. Lett. **92** (2004) 161802.

[5] R. Bernabei *et al.* [DAMA Collaboration], Eur. Phys. J. C **56** (2008) 333 [arXiv:0804.2741 [astro-ph]].

[6] E. Zavattini *et al.* [PVLAS Collaboration], Phys. Rev. Lett. **96** (2006) 110406 [Erratum-ibid. **99** (2007) 129901].

[7] E. Zavattini *et al.* [PVLAS Collaboration], Phys. Rev. D **77** (2008) 032006.

[8] O. Adriani *et al.* [PAMELA Collaboration], Nature **458** (2009) 607.

[9] N. Arkani-Hamed, D. P. Finkbeiner, T. R. Slatyer and N. Weiner, Phys. Rev. D **79** (2009) 015014.

[10] R. D. Peccei and H. R. Quinn, Phys. Rev. Lett. **38**, 1440 (1977); Phys. Rev. D **16**, 1791 (1977); S. Weinberg, Phys. Rev. Lett. **40**, 223 (1978); F. Wilczek, Phys. Rev. Lett. **40**, 279 (1978); J. E. Kim, Phys. Rept. **150** (1987) 1.

[11] R. Cameron *et al.* [BFRT Collaboration], Phys. Rev. D **47** (1993) 3707;

[12] P. Sikivie, Phys. Rev. Lett. **51**, 1415 (1983) [Erratum-ibid. **52**, 695 (1984)]; A. A. Anselm, Yad. Fiz. **42**, 1480 (1985); M. Gasperini, Phys. Rev. Lett. **59**, 396 (1987); K. Van Bibber, N. R. Dagdeviren, S. E. Koonin, A. Kerman and H. N. Nelson, Phys. Rev. Lett. **59**, 759 (1987).

[13] K. Ehret *et al.*, arXiv:hep-ex/0702023; C. Robilliard,*et al* [BMV Collaboration], Phys. Rev. Lett. **99** (2007) 190403; A. S. Chou *et al.* [GammeV (T-969) Collaboration], Phys. Rev. Lett. **100** (2008) 080402; P. Pugnat *et al.* [OSQAR Collaboration], arXiv:0712.3362 [hep-ex]. M. Fouche *et al.* [BMV Collaboration], Phys. Rev. D **78** (2008) 032013; A. Afanasev *et al.* [LIPSS Collaboration], arXiv:0806.2631 [hep-ex]; arXiv:0810.4189 [hep-ex].

[14] K. Ehret *et al.* [ALPS collaboration], arXiv:0905.4159 [physics.ins-det].

[15] S. J. Chen, H. H. Mei and W. T. Ni [Q& A Collaboration], Mod. Phys. Lett. A **22** (2007) 2815; P. Pugnat *et al.* [OSQAR Collaboration], Czech. J. Phys. **55**, A389 (2005); Czech. J. Phys. **56**, C193 (2006); R. Battesti *et al.* [BMV Collaboration], Eur. Phys. J. D **46**, 323333 (2008); R. Battesti *et* al. [BMV Collaboration], Eur. Phys. J. D **46** (2008) 323.

[16] K. Zioutas *et al.* [CAST Collaboration], Phys. Rev. Lett. **94** (2005) 121301; S. Andriamonje *et al.* [CAST Collaboration], JCAP **0704** (2007) 010; M. Minowa, Y. Inoue, Y. Akimoto, R. Ohta, T. Mizumoto and A. Yamamoto, arXiv:0809.0596 [astro-ph].

[17] L. F. Abbott and P. Sikivie, Phys. Lett. B **120** (1983) 133; J. Preskill, M. B. Wise and F. Wilczek, Phys. Lett. B **120** (1983) 127; M. Dine and W. Fischler, Phys. Lett. B **120** (1983) 137.

[18] P. Sikivie, Phys. Rev. Lett. **51** (1983) 1415 [Erratum-ibid. **52** (1984) 695]; S. Asztalos *et al.*, Phys. Rev. D **64** (2001) 092003; L. D. Duffy *et al.*, Phys. Rev. D **74** (2006) 012006.

[19] G. Jungman, M. Kamionkowski and K. Griest, Phys. Rept. **267** (1996) 195.

[20] F. Probst *et al.*, Nucl. Phys. Proc. Suppl. **110** (2002) 67; D. S. Akerib *et al.* [CDMS Collaboration], Phys. Rev. Lett. **93** (2004) 211301; G. Angloher *et al.* [CRESST Collaboration], Astropart. Phys. **23** (2005) 325; V. Sanglard *et al.* [The EDELWEISS Collaboration], Phys. Rev. D **71** (2005) 122002; J. Angle *et al.* [XENON Collaboration], Phys. Rev. Lett. **100** (2008) 021303; Z. Ahmed *et al.* [CDMS Collaboration], arXiv:0802.3530 [astro-ph].

[21] E. Masso and J. Redondo, JCAP **0509** (2005) 015; P. Jain and S. Mandal, Int. J. Mod. Phys. D **15** (2006) 2095; J. Jaeckel, E. Masso, J. Redondo, A. Ringwald and F. Takahashi, hep-ph/0605313; Phys. Rev. D **75** (2007) 013004; E. Masso and J. Redondo, Phys. Rev. Lett. **97** (2006) 151802; H. Gies, J. Jaeckel and A. Ringwald, Phys. Rev. Lett. **97** (2006) 140402; R. N. Mohapatra and S. Nasri, Phys. Rev. Lett. **98** (2007) 050402; P. Brax, C. van de Bruck and A. C. Davis, Phys. Rev. Lett. **99** (2007) 121103; P. Brax, C. van de Bruck, A. C. Davis, D. F. Mota and D. J. Shaw, Phys. Rev. D **76** (2007) 085010; I. Antoniadis, A. Boyarsky and O. Ruchayskiy, Nucl. Phys. B **793** (2008) 246; M. Ahlers, H. Gies, J. Jaeckel, J. Redondo and A. Ringwald, Phys. Rev. D **76** (2007) 115005; Phys. Rev. D **77** (2008) 095001.

[22] G. G. Raffelt, Stars As Laboratories For Fundamental Physics: The Astrophysics of Neutrinos, Axions, and other Weakly Interacting Particles, University of Chicago Press, Chicago, 1996; S. Davidson, S. Hannestad and G. Raffelt, JHEP **0005** (2000) 003.

[23] A. Dupays, C. Rizzo, M. Roncadelli and G. F. Bignami, Phys. Rev. Lett. **95** (2005) 211302; H. Gies, J. Jaeckel and A. Ringwald, Europhys. Lett. **76** (2006) 794; A. Badertscher *et al.*, Phys. Rev. D **75** (2007) 032004; A. Dupays, E. Masso, J. Redondo and C. Rizzo, Phys. Rev. Lett. **98** (2007) 131802; M. Fairbairn, T. Rashba and S. V. Troitsky, Phys. Rev. Lett. **98** (2007) 201801; E. G. Adelberger, B. R. Heckel, S. A. Hoedl, C. D. Hoyle, D. J. Kapner and A. Upadhye, Phys. Rev. Lett. **98** (2007) 131104; M. Ahlers, H. Gies, J. Jaeckel and A. Ringwald, Phys. Rev. D **75** (2007) 035011; S. N. Gninenko, N. V. Krasnikov and A. Rubbia, Phys. Rev. D **75** (2007) 075014; A. Mirizzi, G. G. Raffelt and P. D. Serpico, Phys. Rev. D **76** (2007) 023001; A. Melchiorri, A. Polosa and A. Strumia, Phys. Lett. B **650** (2007) 416; J. Jaeckel and A. Ringwald, Phys. Lett. B **653** (2007) 167; D. Hooper and P. D. Serpico, Phys. Rev. Lett. **99** (2007) 231102; J. Jaeckel and A. Ringwald, Phys. Lett. B **659** (2008) 509; A. De Angelis, O. Mansutti and M. Roncadelli, Phys. Lett. B **659** (2008) 847; K. A. Hochmuth and G. Sigl, Phys. Rev. D **76** (2007) 123011; M. Ahlers, A. Lindner, A. Ringwald, L. Schrempp and C. Weniger, Phys. Rev. D **77** (2008) 015018; H. Gies, D. F. Mota and D. J. Shaw, Phys. Rev. D **77** (2008) 025016; S. N. Gninenko, arXiv:0802.1315 [hep-ph]. S. N. Gninenko

and J. Redondo, Phys. Lett. B **664** (2008) 180; J. Jaeckel, J. Redondo and A. Ringwald, arXiv:0804.4157 [astro-ph]; A. S. Chou *et al.*, arXiv:0806.2438 [hep-ex]; J. Jaeckel and J. Redondo, 0806.1115 [hep-ph]; P. L. Slocum, talk at the *4th Patras Workshop on Axions, WIMPs and WISPs* 2008, Hamburg, http://axion-wimp.desy.de/e30; M. Ahlers, J. Jaeckel, J. Redondo and A. Ringwald, arXiv:0807.4143 [hep-ph]; J. Jaeckel, arXiv:0807.5097 [hep-ph]. P. Williams, talk at the 5th Patras Workshop on Axions, WIMPs and WISPs, Durham 2009, http://axion-wimp.desy.de; M. Tobar, talk at the 5th Patras Workshop on Axions, WIMPs and WISPs, Durham 2009, http://axion-wimp.desy.de; J. Jaeckel, Phys. Rev. Lett. **103** (2009) 080402; F. Caspers, J. Jaeckel and A. Ringwald, arXiv:0908.0759 [hep-ex].

[24] C. D. Hoyle, U. Schmidt, B. R. Heckel, E. G. Adelberger, J. H. Gundlach, D. J. Kapner and H. E. Swanson, Phys. Rev. Lett. **86** (2001) 1418; J. Chiaverini, S. J. Smullin, A. A. Geraci, D. M. Weld and A. Kapitulnik, Phys. Rev. Lett. **90** (2003) 151101; V. V. Nesvizhevsky *et al.*, Nature **415** (2002) 297; E. G. Adelberger, B. R. Heckel and A. E. Nelson, Ann. Rev. Nucl. Part. Sci. **53** (2003) 77; J. C. Long, H. W. Chan, A. B. Churnside, E. A. Gulbis, M. C. M. Varney and J. C. Price, Nature **421** (2003) 922; V. V. Nesvizhevsky and K. V. Protasov, Class. Quant. Grav. **21** (2004) 4557; C. D. Hoyle, D. J. Kapner, B. R. Heckel, E. G. Adelberger, J. H. Gundlach, U. Schmidt and H. E. Swanson, Phys. Rev. D **70** (2004) 042004;

[25] P. Svrcek and E. Witten, JHEP **0606** (2006) 051.

[26] B. Kors and P. Nath, Phys. Lett. B **586** (2004) 366; B. Kors and P. Nath, JHEP **0507** (2005) 069; D. Feldman, B. Kors and P. Nath, Phys. Rev. D **75** (2007) 023503; D. Feldman, Z. Liu and P. Nath, AIP Conf. Proc. **939** (2007) 50; D. Feldman, Z. Liu and P. Nath, AIP Conf. Proc. **939** (2007) 50.

[27] C. Coriano, A. E. Faraggi and M. Guzzi, Phys. Rev. D **78** (2008) 015012.

[28] B. Batell and T. Gherghetta, Phys. Rev. D **73** (2006) 045016.

[29] K. R. Dienes, C. F. Kolda and J. March-Russell, Nucl. Phys. B **492** (1997) 104; D. Lüst and S. Stieberger, hep-th/0302221; S. A. Abel and B. W. Schofield, Nucl. Phys. B **685** (2004) 150; M. Berg, M. Haack and B. Kors, Phys. Rev. D **71** (2005) 026005; [arXiv:hep-th/0404087]; R. Blumenhagen, S. Moster and T. Weigand, Nucl. Phys. B **751** (2006) 186; S. A. Abel, J. Jaeckel, V. V. Khoze and A. Ringwald, Phys. Lett. B **666** (2008) 66; S. A. Abel, M. D. Goodsell, J. Jaeckel, V. V. Khoze and A. Ringwald, JHEP **0807** (2008) 124.

[30] B. Holdom, Phys. Lett. B **166** (1986) 196.

[31] F. Brummer, J. Jaeckel and V. V. Khoze, JHEP **0906** (2009) 037.

[32] L. B. Okun, Sov. Phys. JETP **56** (1982) 502 [Zh. Eksp. Teor. Fiz. **83** (1982) 892]; R. Foot and X. G. He, Phys. Lett. B **267** (1991) 509.

[33] C. P. Burgess, J. P. Conlon, L. Y. Hung, C. H. Kom, A. Maharana and F. Quevedo, JHEP **0807** (2008) 073.

[34] V. A. Kostelecky and S. Samuel, Phys. Rev. D **39** (1989) 683. N. Seiberg and E. Witten, JHEP **9909** (1999) 032; V. A. Kostelecky and R. Lehnert, Phys. Rev. D **63** (2001) 065008; M. S. Berger and V. A. Kostelecky, Phys. Rev. D **65** (2002) 091701; S. A. Abel, J. Jaeckel, V. V. Khoze and A. Ringwald, JHEP **0609** (2006) 074.

[35] R. Lehnert, hep-ph/0602097.

[36] V. A. Kostelecky and M. Mewes, Phys. Rev. Lett. **97** (2006) 140401.

[37] V. A. Kostelecky and M. Mewes, Phys. Rev. D **66** (2002) 056005; V. A. Kostelecky and N. Russell, arXiv:0801.0287 [hep-ph].

The Future of Low Energy Photon Experiments

Axel Lindner

DESY, Notkestraße 85, 22607 Hamburg, Germany

DOI: http://dx.doi.org/10.3204/DESY-PROC-2009-03/Lindner

"Light-shining-through-a-wall" experiments search for Weakly Interacting Sub-eV Particles (WISPs). The necessity and status of such enterprises as well as their future potential are sketched.

1 An Experimentalist's Motivation

Evidence is mounting that the known constituents of matter and forces beautifully summarized in the Standard Model do not fully describe the world around us. Such arguments arise from astrophysical and cosmological observations as well as from theoretical considerations. There are strong convictions among scientists that new experiments at the high energy frontier at LHC will provide insight into physics beyond the Standard Model. Although theoretically well motivated, focusing the search for new physics onto highest available energies neglects evidences pointing at the opposite energy scale. Extensions of the Standard Model may manifest themselves also at meV energy scales, nine orders of magnitude below the mass of the electron (see contribution of J. Jäckel to these proceedings).

Generally, new very light and very weakly interacting particles denoted as WISPs (Weakly Interacting sub-eV Particles) occur naturally in string-theory-motivated extensions of the Standard Model [1, 2, 3]. There could be bosons and fermions, charged and uncharged particles [2]. WISPs may interact with ordinary matter via the exchange of very heavy particles related to very high energy scales and thus give insight into physics at highest energy scales. The reader is referred to [4] and references therein for a more detailed view. One prime example for a WISP is the QCD axion [5, 6] invented to explain the CP conservation of the strong interaction. From astrophysical observations its mass should be below about 1 eV. For the QCD axion such a low mass implies very weak interactions with the other constituents of the Standard Model (see [7]). It is striking that a QCD axion with a mass around 1 μeV is a perfect candidate for cold dark matter in the Universe [8, 9]. A discovery of the axion could solve long lasting questions of particle physics and cosmology simultaneously. It is worthwhile to note that also dark energy might be attributed to new physics at the meV scale [10].

Interestingly, very different astrophysical observations suggest the existence of very light axion-like particles. The cooling of white dwarfs can be modeled significantly better if an additional energy loss due to axion-like particles is taken into account [11]. Luminosity relations of active galactic nuclei (AGN) show patterns which are best understood if axion-like particles do exist [12]. The surprisingly high transparency of the Universe to TeV photons from AGNs at cosmological distances may be explained by back and forth oscillations of photons into axion-like particles [13, 14]. Similarly, such oscillations might explain the candidate neutral ultra-high-

energy particles from distant BL Lac type objects [15]. The heating of the solar corona is not understood, but may be attributed to an energy flow mediated by axion-like particles [16].

2 WISP Searches

At present for most of the WISP species the most stringent limits on their existence originate from astrophysics considerations. In general, the existence of WISPs would for example open up new energy loss channels for hot environments in stars and thus shorten lifetimes or cooling cycles [7, 17]. They could also show up in analyses of the cosmic microwave background radiation [18, 19, 20, 21].

In addition direct searches for axion-like particles produced in the sun [16] or as constituents of galactic dark matter [22] have greatly progressed in recent years and reached impressive sensitivities.

However, interpretations of astrophysics data are always hampered by the uncontrolled production mechanism of WISPs. Effective theories have been presented, where the production of some WISP species is suppressed in hot environments [23, 24]. If such scenarios are true, astrophysics experiments might fail to detect WISPs while laboratory experiments could open up this new physics window. Literally, astrophysics deals with "astronomical" or "cosmological" distances on the one hand and microscopic distances in hot dense plasmas on the other hand for example. Intermediate distances are only probed in the laboratory.

The are numerous experimental efforts to probe for WISPs in the laboratory. Typically they are searched for by looking for new effects in gravitational or QED environments. The latter ones comprise atomic physics like Lamb shift, positronium decay, Casimir forces or photon-photon interaction.

3 Photon-photon Interactions and "Light-Shining-through-a-Wall"

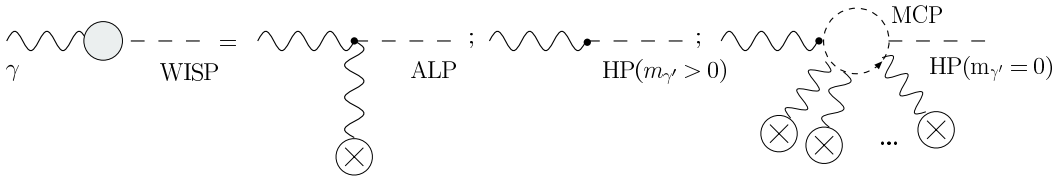

Figure 1: A collection of some Feynman diagrams responsible for the mixing term between photons and different hypothetical "weakly interacting sub-eV particles" (WISPs). Photon oscillations into Axion-like particles (ALPs) and massless hidden photons (HPs) via mini-charged particles (MCP) require the presence of a background electromagnetic field, denoted by crossed circles.

Since the discovery of the positron there is profound interest in light-light interaction, because two photons can couple via virtual electron-positron pairs. If an intense laser beam is shone into a strong magnetic field, the interaction of the laser light with the (virtual) photons of the magnetic field gives rise to the so-called magnetic vacuum birefringence [25]: light polarized

perpendicular to the magnetic field moves a little slower than photons polarized perpendicular. However, the effect is very tiny ($n_\perp - n_\parallel = 3.6 \cdot 10^{-22}$ for B = 9.5 T) and has escaped experimental verification since decades. Present day experiments have to be improved by about three orders of magnitude to verify this QED prediction. A similar phenomenon is the so-called photon splitting. Here the original photon vanishes with a probability depending on its polarization with respect to the magnetic field orientation. This reminds of a crystal's dichroism. Unfortunately, QED predicts only a very weak effect most likely beyond experimental reach for the foreseeable future (see also contribution of G. Cantatore to these proceedings).

The reason for the weakness of both effects is the high mass of the electron as compared to the eV photons. If WISPs with much smaller masses exist and couple to photons, they could give rise to the above mentioned two effects with amplitudes well above the QED expectations [26, 27]. Fig. 1 (see [4]) displays Feynman diagrams for the production of some WISP flavors due to the interaction of photons. WISPs could also be detected in a very convincing and spectacular manner by "light-shining-through-a-wall" (Fig. 2, see [4]). In the first part of such an experiment WISPs are produced from intense laser light, either by interaction with a strong magnetic field or by kinetic mixing. This first part is separated by a light-tight wall from the second part. Only WISPs can traverse the wall due to their very low cross-sections. Behind the wall they could convert back into photons with exactly the same properties as the light generating the WISPs. This gives the impression of "light-shining-through-a-wall" (LSW). This article will focus on the status and future of LSW experiments. Such installations offer the possibility to significantly increase sensitivities in the future.

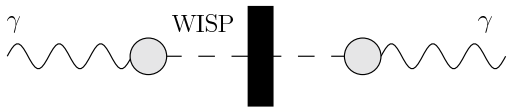

Figure 2: Sketch of a "light shining through a wall experiment". The grey blob indicates the mixing term between photons and the "weakly interacting sub-eV particles" (WISPs).

4 Present and Future LSW Experiments

In the following production and detection of axion-like particles (ALPs) will be considered in some detail. ALPs are of prime interest due to their similarity with the QCD axion, but please keep in mind that many other species (see above) may populate the WISP-zoo, which further enhances the discovery potential of LSW experiments.

4.1 Axion-Like Particles

Axion-like particles, ALPs, denote here neutral scalar or pseudoscalar particles coupling to electromagnetic fields similar to the QCD axion. If light is shone into a magnetic dipole field scalar (pseudoscalar) ALPs can be produced if the light is polarized perpendicular (parallel) to the direction of a magnetic dipole field. Assuming a symmetric set-up of an LSW experiment with the magnetic field length BL before and after the wall the photon-ALP-photon conversion probability reads

$$P(\gamma \to \phi \to \gamma) = \frac{1}{16\beta_\phi^2}(gBL)^4 \left(\frac{\sin\frac{1}{2}qL}{\frac{1}{2}qL}\right)^4, \qquad (1)$$

where β_ϕ denotes the velocity of the ALP and $q = p_\gamma - p_\phi$. The probability rises with $(BL)^4$ resulting from the coherent ALP-photon-ALP conversions. For a more detailed discussion of these effects the reader is referred to [4] and the references therein.

Note that for $qL \ll 1$ Eq.1 reduces to

$$P(\gamma \to \phi \to \gamma) = \frac{1}{16\beta_\phi^2}(gBL)^4. \tag{2}$$

If $qL \ll 1$ does not hold anymore the conversion probability drops and the limits on the coupling g worsens as visible in Fig. 3. This effect can be made lively by imaging an overlay of the wave functions of photons and ALPs. If the ALP's momentum decreases, its wavelength rises and hence runs out of phase compared to the photon wave function. The first LSW experiment was carried out by the BFRT collaboration [28]. Table 1 summarizes present-day experiments.

Experiment	Number of photons	Magnet $B \cdot L$	g [10^{-7}GeV^{-1}], 95% CL limit
ALPS @ DESY [4]	$5 \cdot 10^{24}$, 532 nm, cw	22+22 Tm	4.1
BMV @ Toulouse [29]	$6 \cdot 10^{23}$, 1060 nm, 82 pulses	4.4+4.4 Tm	10
GammeV @ FNAL [30]	$6 \cdot 10^{23}$, 532 nm, 5 Hz pulses	15+15 Tm	2.9
LIPSS @ JLAB [31]	$6 \cdot 10^{25}$, 935 nm, FEL	1.8+1.8 Tm	12
OSQAR @ CERN [32]	488+514 nm, cw	136+136 Tm	3.4

Table 1: Table of present-day LSW experiments. The second column lists the total number of photons used for the analyses, the last column shows typical sensitivities achieved. More details are given in the references shown.

For a typical experimental set-up similar to the ALPS experiment at DESY or GammeV at FNAL Eq. 2 reads

$$P(\gamma \to \phi \to \gamma) = 9.60 \cdot 10^{-25} \left(\frac{g}{10^{-7}\text{GeV}^{-1}} \frac{B}{5\text{T}} \frac{L}{4\text{m}} \right)^4. \tag{3}$$

It is evident that a very large flux of photons is required to probe for ALPs in an LSW experiment. Table 2 summarizes the main experimental parameters, the dependence of the sensitivity in g on these parameters and possible future improvements. As a benchmark the ALPS experiment at DESY in Hamburg is used.

In the near term future laboratory LSW experiments aim for reaching a sensitivity for the photon-ALP coupling of $g = 10^{-7}\text{GeV}^{-1}$. It's worth mentioning that this probes for new physics (if WISP exist) at the 100 TeV scale[1] already. However, at present astrophysics limits on the coupling of ALPs to photons are about 3 orders of magnitude more restrictive. On the long run laboratory experiments should strive for surpassing these limits.

[1]The axion-to-photon coupling g is given by $g = \alpha \cdot g_\gamma / \pi f_\alpha$, where f_α denotes the new energy scale and g_γ a factor derived from theory expected to vary by about an order of magnitude for the QCD axion.

Parameter	g dependence	ALPS aims	future exp.
Laser power (cw)	$g \propto P^{-\frac{1}{4}}$	P=1kW	P=100kW
Magnetic field	$g \propto (BL)^{-1}$	BL=22Tm	BL=600Tm
Detector sensitivity	$g \propto \epsilon^{\frac{1}{4}}$	ϵ = 4mHz	ϵ=0.02mHz
Measurement time	$g \propto t^{-\frac{1}{8}}$	t=25h	t=25h

Table 2: Table of the main parameters of a LSW experiment searching for ALPs. The second column gives the sensitivity of limits on the photon-ALP coupling on the experimental parameters. The third column lists the corresponding parameters aimed for at the ALPS experiment at DESY, while the forth column shows parameters of a possible future experiment.

4.1.1 Laser beam power

Usually LSW experiments shine laser light through long and tight magnet bores. At ALPS the open aperture amounts to only 16 mm [4] for a total length of about 17 m. Therefore the demands on the beam quality are rather high. Given these constraints optical or infrared lasers with cw powers of a few 10 W at maximum are available resulting in a photon number flux of roughly 10^{20} Hz. This can be improved significantly by recycling the photons with the help of an optical delay line (used by BFRT [28]) or by setting up a resonant optical cavity. This has been realized for the first time by the ALPS experiment [4]. Improvements of the ALPS resonator are under way aiming for an effective power of 1 kW from 4 W of primary laser power. Considering the laser R&D for gravitational wave antennas [33, 34] the next decade could result in primary lasers with powers of the order of 100 W. This power might be enhanced in an optical cavity by 3 orders of magnitude resulting in an effective power around 100 kW. Hence the mid term future might give effective photon fluxes close to 10^{24} Hz. Further significant improvements will demand focused R&D programs.

Some experiments use or have used different set-ups with pulsed lasers. This is a very reasonable approach as long as the photon detector sensitivity can be enhanced by triggering to suppress background noise (GammeV [30]) or if very strong pulsed magnets are used (BMV [29]). This is not discussed further in this article.

4.1.2 Magnets

ALPS is using a spare HERA dipole magnet. Half of the dipole is used for generating WISPs, the second half for converting them back into photons. This gives BL = 23 Tm for both processes. OSQAR at CERN is setting up an installation with one LHC dipole each for the generation and regeneration part resulting in 139 Tm. Four LHC dipoles or two DLHC dipole each would provide about 600 Tm. Such a set-up might be realized with limited costs in the mid-term future. Going beyond would require a considerable amount of resources for magnet developments and/or constructing very long dedicated cryogenic magnet stands for WISP experiments. Clearly such an enterprise would be worthwhile, because the sensitivity in g improves linearly with the magnetic field strength and length (see Table 2). For the time being BL = 600 Tm is assumed for the future, a factor of 26 compared to the present-day ALPS.

4.1.3 Detector sensitivity

Most of the present-day LSW experiments use commercial CCD cameras to search for reconverted photons from WISPs behind the wall. Because the light looked for has the same properties as the laser light shown into the experiment one can profit from the usually outstanding beam quality by focusing the beam spot onto very few pixels of the CCD. Signal areas smaller than 50x50 μm^2 are regularly achieved. An optical resonator in front of the wall does not harm, but improves this approach (while this strong focusing could hardly be realized with an optical delay line due to geometrical reasons). With a typical dark current of 10^{-3} electrons per pixel and second, a read-out noise of 3.8 electrons and a signal region of 3x3 pixels one expects for one hour exposures a RMS of only 12 electrons. Taking into account an overall photon detection efficiency of roughly 60% this translates into a RMS of 20 photons (assuming a gain factor of 1 electron/photon). Hence one expects a 95%CL photon flux limit around 4 mHz for about 10 one hour exposures (the typical order of magnitude for measurement times in LSW experiments). This corresponds to an energy flux of $2 \cdot 10^{-21}$ W for 532 nm photons.

In the future this sensitivity might be enhanced considerably by using transition edge sensors (TES) [35, 36]. Here a sensor is cooled down to about 100 mK and operated in the transition region between a superconducting and normal conducting state. Due to the very low heat capacity of such a state the energy deposit of a single photon results in a significant temperature rise and is well measurable. TES allow for essentially background-free counting of individual photons. Only radioactivity or cosmic ray interactions would provide some remaining background. From studies with many dark frames taken with the ALPS CCD the background rate is estimated as roughly 0.02 mHz in a 50x50 μm^2 signal. Hence it should be possible in future to set-up a detector system sensitive to an energy flux of at least two orders of magnitude below the above mentioned number, i.e. 10^{-23} W for 532 nm photons. This might be further improved by shielding and proper selection of materials. In addition TES detectors register the arrival time of individual photons and coarsely estimate their energies. This is a clear advantage compared to present-day long-exposure CCD frames.

The improvements listed above are judged as likely possibilities to be reached within the next few years. According to Table 2 $g = 10^{-7}\text{GeV}^{-1}$ as aimed for at ALPS is expected to be multiplied by a factor of $(100\text{kW}/1\text{kW})^{-\frac{1}{4}} \cdot (600\text{Tm}/23\text{Tm})^{-1} \cdot (0.02\text{mHz}/4\text{mHz})^{\frac{1}{4}} = 0.003$. Couplings significantly below 10^{-9}GeV^{-1} would be accessible in LSW experiments. However, a gap of about an order of magnitude would still have to be bridged to surpass present-day limits from astrophysics. A second optical resonator is a promising means to tackle this challenge.

4.1.4 Regeneration cavity

The idea of a resonantly enhanced axion photon regeneration was put forward first in 1993 by F. Hoogeveen and T. Ziegenhagen [37] and independently rediscovered in 2007 by P. Sikivie, D.B. Tanner and K. van Bibber [38]. The basic idea is to set-up an optical resonator also in the regeneration part of a LSW experiment very similar to the optical resonator in the first part. The second resonator effectively increases the conversion probability of a WISP into a photon. To understand this one has to consider that the freely propagating WISP-related wave behind the wall of the LSW experiment comprises a very tiny electromagnetic photon component. Due to this small component the WISP might convert into a real photon. An optical resonator enhances this small component in the same way as the wave amplitude for

real photons is increased. The transition probability of WISPs to photons rises with the power amplification factor of an optical resonator in the second part of the LSW experiment behind the wall. Consequently the sensitivity of such a set-up for the coupling constant g improves with the square root of this factor. The technical challenge is to lock the second cavity to exactly the same frequency and the same mode as the first cavity (used to enhance the effective laser photon flux). Obviously one can not use laser light of the same wavelength to produce WISPs and to lock the regeneration cavity without spoiling the sensitivity to detect photons from reconverted WISPs. One possibility rests on a two-colored laser. Such an installation is being used in the ALPS experiment at DESY, where part of the 1064 nm light from an infrared laser is frequency doubled to 532 nm [4]. In future the 532 nm light could be used to lock the generation and regeneration cavity while the (more powerful) 1064 nm radiation is used to produce WISPs and to search for regenerated photons behind the wall. A detector can be shielded from the 532 nm radiation leaving the regeneration cavity by properly suited bandpass filters (narrow bandwidth filters with 75% transmission at 1064 nm and optical densities larger than 5 at other wavelenths are easily available). Efforts to realize such a set-ups are starting in the US [39] and Europe. With a regeneration cavity it should be possible to improve the sensitivity of LSW experiments by another two orders of magnitude to reach $g = 10^{-11}\mathrm{GeV}^{-1}$ and lower values. Fig. 3 displays the reach of LSW experiments exploiting the power of a regeneration cavity. Present-day limits derived from astrophysics are likely to be surpassed in future. However, probing for the QCD-axion in the laboratory will probably remain a challenging target for quite some time.

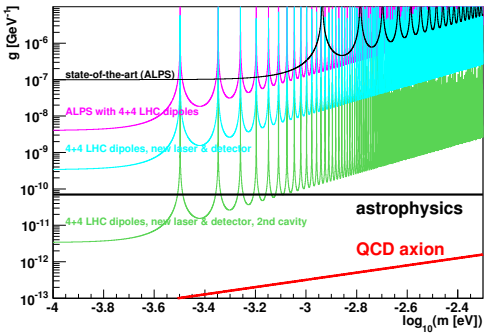

Figure 3: The sensitivity aimed for at present-day LSW experiments on the coupling of ALPs to photons vs. the ALPs mass as well as future experiments with stronger magnets, improved laser and detector system and an additional regeneration cavity (from top to bottom). The horizontal line indicates today's limits derived from astrophysics. Always the regions above the lines are excluded. The slanted line shows the order of magnitude expected for the coupling strength of the QCD-axion to photons.

5 Further Ideas

For illustration purpose the argumentation above has concentrated on axion-like particles. It should be stressed again that these are only one kind in a hypothetical zoo of WISPs. Another very interesting species are massive photons (dubbed "HP", because they might originate from the "hidden sectors" of string theory for example) with very weak couplings to Standard Model particles. If HPs exist they oscillate with photons back and forth in vacuum very similar to neutrino flavor mixing. Hence one can search for HPs also in LSW experiments, but without the necessity of an external electromagnetic field. The present experimental limits are shown in Fig. 5. It is interesting to note that the mass scale around 1 meV is hardly probed by astrophysics. Hence any improvement in laboratory-based HP searches probes unknown territory in the

parameter space. The improvements of lasers and detectors as well as the usage of a regeneration cavity could improve limits on the mixing parameter by more than two orders of magnitude.

The potential of LSW experiments at synchrotron sources [41] and with microwave cavities [42], the new possibilities at free electron lasers [43, 44] or "current-through-a-wall" experiments [45] could not be addressed here. The reader is referred to the references given.

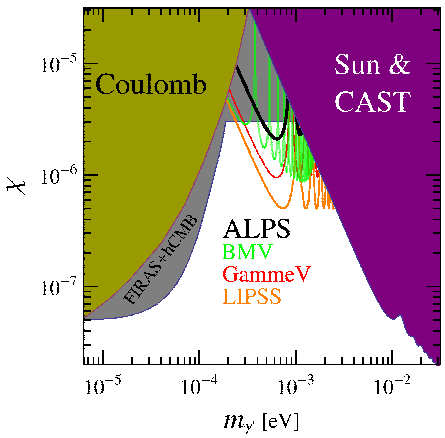

Figure 4: Present day limits for the mixing of photons with their massive counterparts from a "hidden sector". Laboratory experiments [4, 29, 30, 31, 40] surpass astrophysics limits in the mass region around 1 meV already now.

6 Summary

We witness a revival of experiments at the low energy frontier searching for new, very light and very weakly interacting particles. This complements enterprises at the high energy and intensity frontiers. In recent years various investigations have shown that the low energy frontier indeed may offer a window to physics beyond the Standard Model. This is strongly supported by theory, giving rise to a zoo of WISPs in addition to the QCD-axion, and interesting observations from astrophysics.

Laboratory experiments have the potential to surpass the reach of astrophysics in the search for WISPs. Some concentrated R&D efforts on laser technology, long optical resonators and single photon detectors are required to meet this aim. These can be achieved by new collaborations among the high energy physics and laser interferometer communities (operating gravitational wave antennas) for example. Firm bases exist and no major show-stoppers are envisaged today.

Present-day and future LSW experiments probe nature in a regime of very weak couplings and very low masses. In addition efforts should be strengthened to test the validity of the Standard Model in very strong fields (to test non-linear QED for example). The field of particle physics as a whole can only gain if such small-scale experiments complement the physics searched for in billion dollar installations at the high energy or intensity frontiers.

7 Acknowledgements

Many thanks to the organizers of PHOTON 2009 for giving me the opportunity to contribute to this interesting meeting with a broad physics scope! I thank my colleagues of the ALPS collaboration as well as G. Cantatore and J. Jäckel for stimulating and fruitful discussions.

References

[1] M. Goodsell, J. Jaeckel, J. Redondo and A. Ringwald, arXiv:0909.0515 [hep-ph].

[2] A. Ringwald, contrib. to the 4th Patras Workshop on Axions, WIMPs and WISPs, Hamburg, Germany (DESY-PROC-2008-02), arXiv:0810.3106 [hep-th].

[3] M. Ahlers, H. Gies, J. Jaeckel, J. Redondo and A. Ringwald, Phys. Rev. D **76**, 115005 (2007) [arXiv:0706.2836 [hep-ph]].

[4] K. Ehret *et al.* [ALPS collaboration], arXiv:0905.4159 [physics.ins-det].

[5] S. Weinberg, *Phys. Rev. Lett.* **40** (1978) 223–226.

[6] F. Wilczek, *Phys. Rev. Lett.* **40** (1978) 279–282.

[7] C. Amsler *et al.* [Particle Data Group], "Review of particle physics," Phys. Lett. B **667**, 1 (2008).

[8] L. F. Abbott and P. Sikivie,*Phys. Lett.* **B120** (1983) 133–136.

[9] P. Sikivie, arXiv:0909.0949 [hep-ph].

[10] E. Masso, J. Phys. Conf. Ser. **179**, 012001 (2009) [arXiv:0902.4851 [hep-th]].

[11] J. Isern, S. Catalan, E. Garcia-Berro and S. Torres, J. Phys. Conf. Ser. **172**, 012005 (2009) [arXiv:0812.3043 [astro-ph]].

[12] C. Burrage, A. C. Davis and D. J. Shaw, Phys. Rev. Lett. **102**, 201101 (2009) [arXiv:0902.2320 [astro-ph.CO]].

[13] M. Roncadelli, A. De Angelis and O. Mansutti, Nucl. Phys. Proc. Suppl. **188**, 49 (2009).

[14] M. A. Sanchez-Conde, D. Paneque, E. Bloom, F. Prada and A. Dominguez, Phys. Rev. D **79**, 123511 (2009) [arXiv:0905.3270 [astro-ph.CO]].

[15] M. Fairbairn, T. Rashba and S. Troitsky, arXiv:0901.4085 [astro-ph.HE].

[16] K. Zioutas, M. Tsagri, Y. Semertzidis, T. Papaevangelou, T. Dafni and V. Anastassopoulos, arXiv:0903.1807 [astro-ph.SR].

[17] S. N. Gninenko and J. Redondo, Phys. Lett. B **664**, 180 (2008) [arXiv:0804.3736 [hep-ex]].

[18] J. Jaeckel, J. Redondo and A. Ringwald, Phys. Rev. Lett. **101**, 131801 (2008) [arXiv:0804.4157 [astro-ph]].

[19] C. Burrage, J. Jaeckel, J. Redondo and A. Ringwald, arXiv:0909.0649 [astro-ph.CO].

[20] A. Mirizzi, J. Redondo and G. Sigl, JCAP **0903**, 026 (2009) [arXiv:0901.0014 [hep-ph]].

[21] A. Mirizzi, J. Redondo and G. Sigl, JCAP **0908**, 001 (2009) [arXiv:0905.4865 [hep-ph]].

[22] L. D. Duffy *et al.*, Phys. Rev. D **74**, 012006 (2006) [arXiv:astro-ph/0603108].

[23] J. Jaeckel, E. Masso, J. Redondo, A. Ringwald and F. Takahashi, Phys. Rev. D **75**, 013004 (2007) [arXiv:hep-ph/0610203].

[24] J. Redondo, contrib. to the 4th Patras Workshop on Axions, WIMPs and WISPs, Hamburg, Germany (DESY-PROC-2008-02), arXiv:0810.3200 [hep-ph].

[25] W. Heisenberg and H. Euler, Z. Phys. **98**, 714 (1936) [arXiv:physics/0605038].

[26] M. Ahlers, J. Jaeckel and A. Ringwald, Phys. Rev. D **79**, 075017 (2009) [arXiv:0812.3150 [hep-ph]].

[27] G. Cantatore, R. Cimino, M. Karuza, V. Lozza and G. Raiteri, arXiv:0809.4208 [hep-ex].

[28] **BFRT** Collaboration, R. Cameron *et al.*, *Phys. Rev.* **D47** (1993) 3707–3725.

[29] **BMV** Collaboration, M. Fouche *et al.*, *Phys. Rev.* **D78** (2008) 032013, `arXiv:0808.2800 [hep-ex]`.

[30] **GammeV** Collaboration, A. S. Chou *et al.*, *Phys. Rev. Lett.* **100** (2008) 080402, `arXiv:0710.3783 [hep-ex]`.

[31] **LIPSS** Collaboration, A. Afanasev *et al.*, *Phys. Rev. Lett.* **101** (2008) 120401, `arXiv:0806.2631 [hep-ex]`.

[32] **OSQAR** Collaboration, R. Ballou *et al.*, "Summary of OSQAR First Achievements and Main Requests for 2008." CERN-SPSC-2007-039S; PSC-M-762, December, 2007.

[33] H. Luck *et al.*, *Class. Quant. Grav.* **23** (2006) S71–S78.

[34] **LIGO** Collaboration, `arXiv:0711.3041v1 [gr-qc]`.

[35] D. Rosenberg *et al.*, *Phys. Rev. A.* **71** (2005) 061803, `arXiv:quant-ph/0506175v1`.

[36] R. W. Romani *et al.*, arXiv:astro-ph/0208070.

[37] F. Hoogeveen and T. Ziegenhagen, *Nucl. Phys.* **B358** (1991) 3–26.

[38] P. Sikivie, D. Tanner, and K. van Bibber, *Phys. Rev. Lett.* **172002** (2007).

[39] G. Mueller, P. Sikivie, D. B. Tanner and K. van Bibber, arXiv:0907.5387 [hep-ph].

[40] M. Ahlers, H. Gies, J. Jaeckel, J. Redondo, and A. Ringwald, *Phys. Rev.* **D77** (2008) 095001, arXiv:0711.4991 [hep-ph].

[41] A. G. Dias and G. Lugones, Phys. Lett. B **673**, 101 (2009) [arXiv:0902.0749 [hep-ph]].

[42] F. Caspers, J. Jaeckel and A. Ringwald, arXiv:0908.0759 [hep-ex].

[43] A. Ringwald, arXiv:hep-ph/0112254.

[44] R. Rabadan, A. Ringwald and K. Sigurdson, Phys. Rev. Lett. **96**, 110407 (2006) [arXiv:hep-ph/0511103].

[45] H. Gies, J. Jaeckel and A. Ringwald, Europhys. Lett. **76**, 794 (2006) [arXiv:hep-ph/0608238].

Chapter 4

Prompt Photons

Convenors:

S. Chekanov (Argonne) and M. Fontannaz (Orsay)

Probing QCD (Media) with Prompt Photons

François Arleo

LAPTH*, Université de Savoie, CNRS, BP 110, 74941 Annecy-le-Vieux cedex, France

DOI: http://dx.doi.org/10.3204/DESY-PROC-2009-03/Arleo

The QCD phenomenology of prompt photon production from e–p to p–p /p–$\overline{p}$ and A–A collisions is reviewed. The use of prompt photons as a probe of (i) parton distribution functions (in a proton or in nuclei) as well as (ii) fragmentation functions (into photons and hadrons) and their medium-modifications is highlighted.

1 Introduction

Prompt photons[1] are produced in hard QCD processes at large transverse momentum, i.e. $p_\perp \gg \Lambda_{\rm QCD}$, in e^+e^-, e–p and hadronic collisions. As we shall see throughout this short review article, final states involving prompt photons allow for probing various aspects of QCD. After recalling briefly the perturbative framework and comparing QCD predictions to recent measurements in Sect. 2, constraints given by prompt photons on parton distribution functions (PDF), either in a proton or in nuclei, are discussed (Sect. 3). The possibility to probe fragmentation functions (FF) and their modifications in heavy-ion collisions is mentioned in Sect. 4.

Apart from its own interest in QCD, the production of prompt photon pairs is one of the most important discovery channels for Higgs boson production in p–p collisions; also, they might probe physics beyond the Standard Model, such as models involving large extra dimensions (see e.g. [1]). Discussing these aspects however goes beyond the scope of these proceedings.

2 Probing perturbative QCD dynamics

2.1 Perturbative framework

The dynamics of prompt photon production in the final state is rather complex because of the very nature of the photon. Schematically, prompt photons can be produced either *directly* or by *fragmentation*. On the one hand, direct photons participate in the short-distance dynamics of the hard subprocess and behave like colorless hard partons. As a consequence, they are produced together with no (or little) hadronic activity in their vicinity. As discussed later, this process may be used to determine the kinematics of the hard QCD process, at least to some extent, thereby allowing one to get constraints on either parton densities or fragmentation functions. On the other hand, fragmentation photons are produced on long time-scales

*Laboratoire d'Annecy-le-Vieux de Physique Théorique, UMR5108

[1]Prompt photons are sometimes also referred to as *direct photons* since they do not originate from hadron electromagnetic decays, such as $\pi^0 \to \gamma\gamma$, which constitute the dominant background. We prefer not to adopt this terminology as it comes in conflict with the QCD *direct process* (see Sect. 2.1).

by the collinear fragmentation of hard partons, in a way similar to that of large-$p_\perp$ hadrons. Experimentally, fragmentation photons are likely produced inside a hadronic jet. Technically, the time-like cascade of a parton k eventually producing a photon yields collinear singularities which are absorbed into the fragmentation function of the parton k into photons, $D_{\gamma/k}(z, M_F)$. Fragmentation functions are defined in a given factorization scheme (often $\overline{\rm MS}$ in practice) and depend on the arbitrary scale, M_F, taken to be $\mathcal{O}(p_\perp)$ in order to minimize large logarithms. Note that unlike the FF into hadrons, $D_{\gamma/k}(z, M_F)$ obey *inhomogeneous* DGLAP equations because of the point-like coupling to quarks. From a phenomenological point of view, fragmentation functions are obtained from a fit to e^+e^- data [2]. Although useful, one should however keep in mind that the distinction between direct and fragmentation photons becomes meaningless beyond the Born level, since the fragmentation channel can be seen as a higher-order direct process (and vice-versa) depending on the value of the arbitrary fragmentation scale. Consequently, only the sum of these contributions is physical and depends much less on M_F than the individual unphysical dynamical components.

The hadronic nature of the photon also manifests itself in processes involving photons in the initial state, e.g. in electron–proton scattering. On top of the direct coupling of the photon to the (anti)quark at leading order, the hadronic structure of the photon can be resolved. In which case, the parton stemming from the photon will participate in the hard scattering dynamics. This *resolved* photon component thus leads to the concept of parton distribution functions in the photon, which can be extracted from experimental measurements just like in the proton case; see [4] for a review and [5] for a recent NLO analysis of e^+e^- data. Subsequently, resolved processes in e–p scattering prove very similar to hadronic collisions. The various dynamical components participating in prompt photon production in e–p scattering are nicely illustrated in Fig. 1 taken from [3]. The direct (respectively, fragmentation) diagrams in the final state are shown on the right (respectively, left). Regarding the photon dynamics in the initial state, direct and resolved processes are illustrated in the top and bottom diagrams, respectively. Within collinear factorization, the $\gamma\, p \to \gamma\, \mathrm{X}$ can be written quite generally as[2]

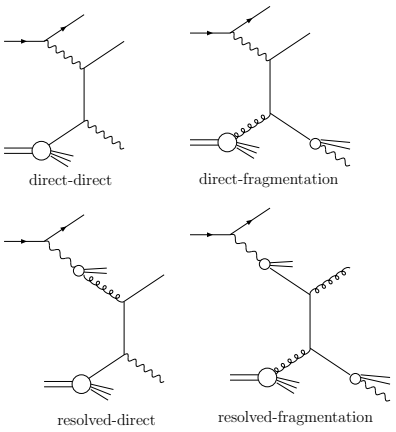

Figure 1: LO subprocesses in ep collisions. From [3].

$$\mathrm{d}\sigma^{\gamma p\to\gamma X} = \sum_{a,b,c} \int \mathrm{d}x_\gamma \int \mathrm{d}x_p \int \mathrm{d}z\, F_{a/\gamma}(x_\gamma, M) F_{b/p}(x_p, M) D_{\gamma/c}(z, M_F)\; \mathrm{d}\hat{\sigma}^{ab\to cX}(\mu, M, M_F) \tag{1}$$

where M, M_F are the factorization scales and μ the renormalization scale. When the photon couples directly in the initial (respectively in the final state), the photon PDF (resp. FF into the photon) reduces to a delta function, $F_{a/\gamma} = \delta_{a\gamma}\delta(1-x_\gamma)$ (resp. $D_{\gamma/c} = \delta_{\gamma c}\delta(1-z)$). From (1) the prompt photon hadroproduction cross section can easily be deduced.

Prompt photon has also been formulated within the $k_\perp$-factorization formalism – in which the parton distributions are *unintegrated* over the initial parton transverse momenta – in hadronic collisions [6] as well as in e–p scattering [7].

[2] We keep the compact notations of [3] and do not make explicit the dependence of $\hat{\sigma}$ on the external momenta.

2.2 Comparing data with theory

The inclusive prompt photon production has been measured at HERA in γ–p collisions (the so-called photoproduction process) by the H1 [8] and the ZEUS [9] collaborations. The NLO QCD predictions [10, 11] tend to underestimate both the transverse momentum and rapidity distributions, although the shape of the data is correctly captured by the calculations. Similarly, parton shower calculations such as HERWIG and PYTHIA are also unable to reproduce the magnitude of the measurements [8]. Disagreement between data and theory is also observed – yet not as pronounced – in the photon–jet channel [8, 12]. ZEUS results indicate in particular that NLO calculations fall below the data either at negative photon rapidity or at large jet rapidity, $\eta^{\rm jet} \simeq 2$. Interestingly, a good agreement is however recovered when applying a minimal cut of 7 GeV for the photon transverse energy. The LO $k_\perp$-factorization results [7] tend to better reproduce the photon–jet measurements as compared to the NLO calculations, although such LO calculations are expected to exhibit a stronger scale-dependence and therefore larger theoretical uncertainties. Apart from non-perturbative effects, the underlying event – which is not modeled in the QCD calculations – may be responsible for the disagreement between photon–jet data and theory. In particular, the hadronic activity coming from the resolved photon components could increase the number of "jets" measured experimentally [3]. Hopefully, the higher-precision preliminary results by H1 [13] will shed new light on the origin of the discrepancy.

In DIS $\gamma^\star$–p reactions, H1 [14] and earlier ZEUS [16] inclusive photon measurements have been compared to the LO calculation by [15]. As illustrated in Fig. 2, a rather good description of the data is obtained[3] at large $Q^2 \gtrsim 40$ GeV^2 while a discrepancy is seen at low Q^2, which may be cured by higher-order corrections. In the photon–jet channel, the NLO calculation achieved in [17] reproduces the shape of the data but not its normalization [14].

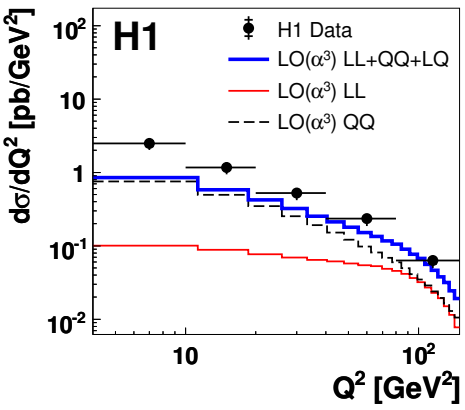

Figure 2: Single-photon H1 differential cross sections $d\sigma/dQ^2$ in DIS [14] compared to PYTHIA (lower curve) and LO QCD calculations [15] (upper curve).

The phenomenology of single prompt photon production in hadronic collisions has been reviewed and discussed in [21] including the recent PHENIX [22] and D0 [23] measurements. Remarkably, the world data from fixed-target (FNAL and SPS) to collider (ISR, RHIC, Tevatron) experiments are well reproduced by the NLO calculations, say within 20–30% which is the typical size of NLO uncertainties. It is all the more impressive that these measurements cover a wide range in $x_\perp \equiv 2p_\perp/\sqrt{s}$, $10^{-2} \leq x_\perp \leq 1$, and almost 10 orders of magnitude in the invariant production cross section[4]. The NLO expectations differ significantly only with the E706 data; the origin of this longstanding discrepancy is as yet not clarified. At Tevatron, data and theory agree

[3] In Fig. 2 the lowest two curves indicate the individual components in which the photon is emitted either by the lepton (LL) or the struck quark (QQ).

[4] Note also that the energy dependence of single photon $x_\perp$-spectra from $\sqrt{s} = 630$ GeV to $\sqrt{s} = 1800$ GeV is very well reproduced by NLO calculations, at variance with the single hadron production channel [24].

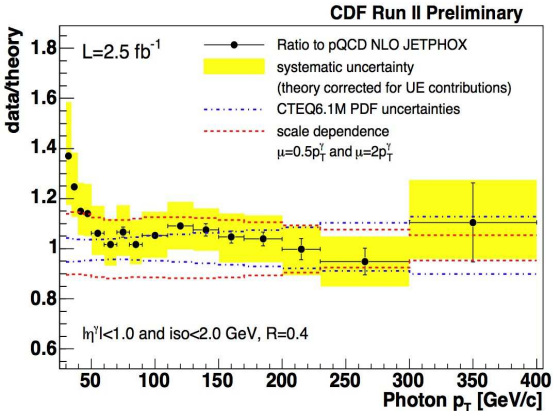

Figure 3: Ratio of CDF preliminary single-photon $p_\perp$-spectra to NLO calculations. Taken from [18].

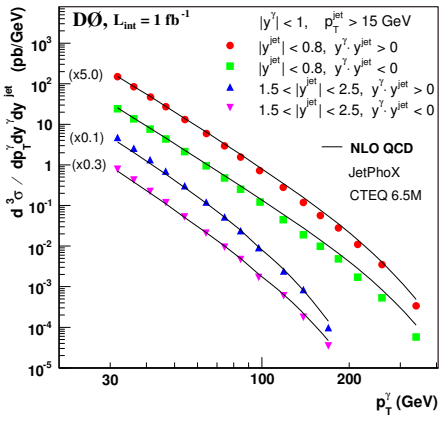

Figure 4: Photon $p_\perp$-spectra measured in photon–jet events by D0 [19] and compared to NLO calculations [20].

from $p_\perp = 50$ GeV up to $p_\perp = 400$ GeV, as shown by the $\sqrt{s} = 1.96$ TeV CDF preliminary results [18] over NLO calculations plotted in Fig. 3. At low $p_\perp \lesssim 40$ GeV nevertheless, CDF data tend to lie significantly above NLO calculations; an observation also reported by D0 [23]. In this respect, it would be interesting to perform measurements of inclusive jets at such low transverse momenta to investigate whether a similar discrepancy is observed in this channel as well. Finally, the production of prompt photons in association with a jet has been recently measured by D0 at $\sqrt{s} = 1.96$ TeV [19]. As can be seen in Fig. 4, the NLO calculations using the JETPHOX package [20] are able to reproduce correctly the D0 measurements, although the data-over-theory ratio indicates that the NLO photon $p_\perp$-spectra prove slightly harder than seen experimentally.

3 Probing parton distributions

We discuss in this Section some observables involving prompt photons which could be useful in order to constrain the parton densities either in a proton or in large nuclei.

3.1 Proton PDF

Constraining parton densities in the proton – especially in the gluon sector – is of course one of the most important requirements for high-precision QCD phenomenology at the LHC. In this respect, the versatility of prompt photon production in e–p photoproduction processes discussed in Sect. 2 offers interesting possibilities, as emphasized in [25]. Take for instance the case of photon–jet production in e–p collisions, and consider the observables

$$x_p^{\rm obs} = \frac{p_\perp^\gamma \exp\eta^\gamma + E_\perp^{\rm jet} \exp\eta^{\rm jet}}{2E^p} \quad ; \quad x_\gamma^{\rm obs} = \frac{p_\perp^\gamma \exp\left(-\eta^\gamma\right) + E_\perp^{\rm jet} \exp\left(-\eta^{\rm jet}\right)}{2E^\gamma}$$

which reduce at leading-order accuracy to the parton longitudinal momentum fraction in the proton and in the photon. Despite higher order corrections, the differential cross sections

$\mathrm{d}\sigma/\mathrm{d}x_{p,\gamma}^{\mathrm{obs}}$ should reflect to some extent the x-dependence of the proton and the photon PDF and eventually help discriminating between various sets. In the detailed NLO study [25], various kinematical cuts are discussed in order to maximize the sensitivity on the the gluon distribution in the proton. Despite rather small cross sections, constraints on G^p around $x \sim 10^{-2}$ could be achieved (similar results for G^γ are reported). The photon–jet channel has also been considered recently in hadronic collisions at Tevatron and LHC [26]. As can be seen in Fig. 5, the jet rapidity distribution (at fixed $y^\gamma = 0$) depends somehow on the PDF set used in the calculation.

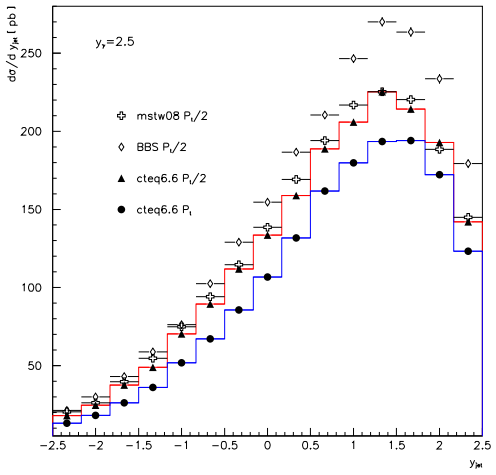

Figure 5: Jet rapidity distribution in photon–jet events at the LHC computed at NLO with JETPHOX [26].

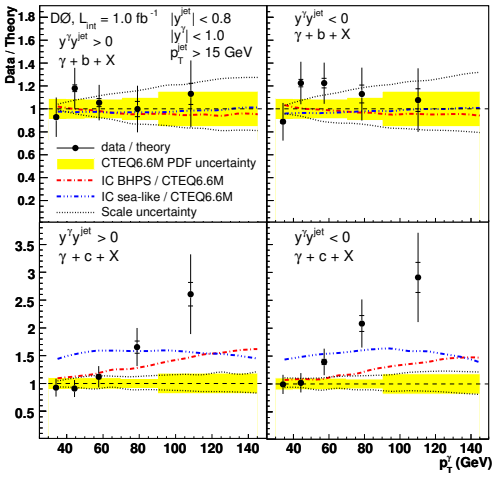

Figure 6: Ratio of γ–c jet and γ–b jet distributions measured by [27] to NLO calculations [28].

Prompt photon production in association with a c or b-tagged jet also proves a promising tool in order to probe the proton PDF in the heavy quark sector, through the $g\ Q \to \gamma\ Q$ Compton scattering process. Interestingly, the comparison of recent D0 measurements [27] with NLO calculations [28] reveals a disagreement in γ–c jet events at large $p_\perp^\gamma$, see Fig. 6. This observation might be interpreted as coming from an enhanced (intrinsic) heavy flavour component in the proton target [28]. However, the discrepancy could also come from the lack of the $g \to Q$ fragmentation component in the NLO calculations of [28].

3.2 Nuclear PDF

It is certainly desirable to increase the precision of the PDF in the proton; in the case of nuclear PDF (nPDF) this turns into an absolutely crucial requirement given the presently huge uncertainties, especially in the gluon sector at small values of x (see e.g. Fig. 12 of [29]). As a consequence, the current precision level for perturbative QCD cross sections in nuclear collisions (p–A or A–A) is rather poor and way below the current state-of-the-art achieved in p–p collisions. This is problematic since important signatures for quark-gluon plasma (QGP)

formation, such as jet quenching, require a precise knowledge of "baseline" NLO predictions in A–A collisions, independently of any medium effects.

Although single photon production does not entirely fix the kinematics of the underlying partonic process even at leading order, it was shown in the NLO analysis [30] that the nuclear production ratio,

$$R_{_{p\mathrm{A}}}(x_{_\perp}, y) = \frac{1}{A} \ \frac{\mathrm{d}^3\sigma}{\mathrm{d}y\ \mathrm{d}^2p_{_\perp}}(p + \mathrm{A} \to \gamma + \mathrm{X}\,) \Big/ \frac{\mathrm{d}^3\sigma}{\mathrm{d}y\ \mathrm{d}^2p_{_\perp}}(p + p \to \gamma + \mathrm{X}\,),$$

of isolated photons in p–A collisions at forward rapidity can be used as good approximation of $R_{_G}^{\mathrm{A}} = G^{\mathrm{A}}/G^p$ used in the calculation[5]. Provided that the systematic errors are under control, the future measurements of forward photons in d–Au collisions at RHIC should bring important constraints on nPDF prior to the start of heavy-ion collisions at the LHC, thus clarifying the effects of the medium on hard processes.

Let us mention that probing accurately the gluon nuclear density is also interesting in itself in order to shed light on non-linear evolution expected in QCD at small x [32]. Prompt photon production within a saturation picture has first been considered in [33]; it is demonstrated in particular that saturation effects dramatically show up in the γ–jet channel, when the photon and jet total transverse momentum is of the order of the saturation scale. More recently, it was shown in [34] that the nuclear production ratio of forward inclusive photons may be able to distinguish among various models including saturation physics. Finally, the importance of measuring prompt photons at large rapidity also in p–p collisions is highlighted in [35].

4 Probing (medium-modified) fragmentation functions

4.1 DIS and hadronic collisions

As compared to parton distributions, fragmentation functions into hadrons still suffer from rather large uncertainties despite important progress made from the inclusion of recent hadron collider data in global fit analyses (see e.g. [36, 37] for recent reviews). The situation is worse in the case of fragmentation functions into photons, where only e^+e^- data have been used so far, as discussed in Sect. 2.1. Attempts to probe photon FF also in e–p or in hadronic collisions have been discussed. In [38], the production of γ–$(0+1)$ jet events[6] in DIS has been investigated at leading-order accuracy. Using the democratic clustering procedure [39] in which the photon is clustered into a jet like any ordinary hadron, this study indicates that the photon spectrum inside the jet is very sensitive to the quark-to-photon FF, making this observable competitive with the standard e^+e^- measurements. In hadronic collisions, momentum correlations between a non-isolated photon and a jet has been considered [26]. In particular, the distribution in the momentum imbalance variable,

$$z_{\gamma\ \mathrm{jet}} = -\frac{\mathbf{p}_{_\perp}{}^{\gamma} \cdot \mathbf{p}_{_\perp}{}^{\mathrm{jet}}}{\|\mathbf{p}_{_\perp}{}^{\mathrm{jet}}\|^2}, \tag{2}$$

which reduces to the variable z of the photon fragmentation function in a leading-order kinematics, allows for the various FF sets proposed in [2] to be discriminated. Interesting constraints on FF into hadrons can similarly be obtained from the study of hadron–jet production.

[5] See also [31] regarding the sensitivity of prompt photon production with respect to various nPDF sets.

[6] "$(0+1)$ jet" meaning here that no jets are produced besides the one which contains the photon and the un-observed jet from the beam remnant.

Instead of using jets to gauge the energy of the "opposite" parton which fragments into a photon (or into a hadron), direct photons themselves could be used as an estimator of the energy of the fragmenting parton into hadrons in photon–hadron production. This observable is complementary to the hadron–jet channel: on the one hand it is spoiled by the fragmentation photon components, but on the other hand it does not require the experimentally challenging reconstruction of jets.

4.2 Heavy-ion collisions

The idea of "measuring" fragmentation functions into hadrons through photon–hadron correlations has been discussed in the context of heavy-ion collisions [40], where it could be used to investigate parton energy loss processes in the dense medium produced. Being colour neutral photons are not modified by the medium, at least as long as they are produced directly in the hard QCD process or, equivalently, on short time-scales. This makes photon–hadron observables in A–A collisions *a priori* much more attractive than hadron–jet measurements, despite the fragmentation photon component[7] which spoils the correlation between the prompt photon and the hadron.

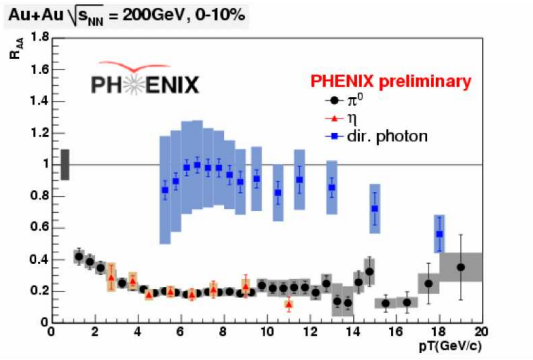

Figure 7: Quenching factor of prompt photons (squares), pions and etas (circles and triangles) in central Au–Au collisions at $\sqrt{s_{\rm NN}}$ = 200 GeV measured by PHENIX [41].

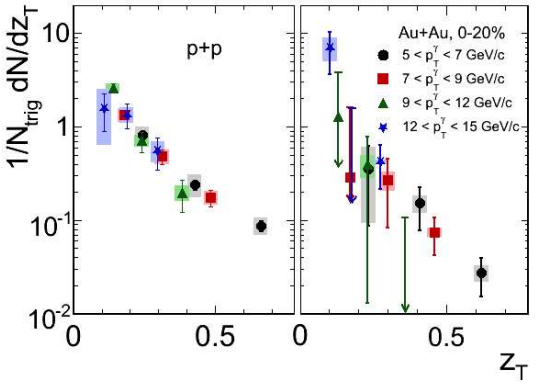

Figure 8: z_T-distribution of photon–hadron production in p–p (left) and Au–Au (right) collisions at $\sqrt{s_{\rm NN}}$ = 200 GeV and for various kinematic cuts. PHENIX data from [42].

The detailed dynamics of photon–hadron correlations from p–p to A–A collisions has been investigated at NLO at RHIC [43] and at the LHC [44]. It is shown in particular that, using appropriate kinematic cuts, the γ–h momentum imbalance distributions (see Eq. (2) above) offers strong similarities with the vacuum and medium-modified fragmentation functions, in p–p and A–A collisions respectively [45]. The possibility to constrain the probability distribution in the energy loss through photon–hadron production has been discussed in the leading-order analysis of [46]. On the experimental side, the PHENIX collaboration at RHIC recently reported on the first measurements of photon–hadron correlations in p–p and Au–Au collisions at $\sqrt{s_{\rm NN}}$ = 200 GeV, see Fig. 8. Despite the rather large error bars, these data are a promising first

[7] In A–A collisions, the huge hadronic background coming from the underlying event makes isolation criteria highly delicate.

step to constrain (medium-modified) fragmentation functions through this channel and thus, eventually, to lead towards a better understanding of parton energy loss in QCD media. At the LHC, preliminary studies by ALICE and CMS on photon–hadron correlation measurements also appear very encouraging [47].

The measurement of *single* photon production is also crucial as it allows for calibrating other hard QCD processes in heavy-ion collisions. In particular, the absence of single photon suppression reported by PHENIX in central Au–Au collisions at RHIC, $R^{\gamma}_{\rm AA} = \mathcal{O}(1)$ (see Fig. 7) is a clear hint that the significant suppression of large-$p_{\perp}$ pions arises from rescattering processes in the final state. The current interpretation of the preliminary single-photon data is not completely clear yet (see [48] for a detailed discussion). On the one hand, the preliminary data are compatible – yet slightly below – with trivial "isospin" corrections[8] together with nuclear PDF effects [43]. On the other hand, the trend both at low $p_{\perp} \simeq 6$–8 GeV and at high $p_{\perp} \simeq 18$–20 GeV is consistent with a slight suppression due to energy loss effects in the photon fragmentation channel [43]. Other processes such as jet-photon conversion [49] or photon emission induced by the parton multiple scattering in the medium [50] – which both enhance the emission of prompt photons in A–A as compared to p–p collisions – seem disfavoured, although not excluded [48].

5 Summary

Prompt photons are an ideal playground to probe QCD through a detailed comparison of perturbative calculations with the wealth of photoproduction, electroproduction and hadroproduction measurements. Furthermore it may serve as a sensitive probe to non-perturbative objects such as parton densities (either in photon, proton or in nuclei) as well as fragmentation functions (into photons and hadrons). In heavy ion collisions, prompt photons are crucial to understand the dynamics of parton energy loss processes in dense media at the origin of the significant suppression of large-$p_{\perp}$ hadrons in Au–Au collisions at RHIC.

Acknowledgments

It is a pleasure to thank warmly P. Aurenche, D. d'Enterria, J.-P. Guillet, G. Heinrich, and É. Pilon for stimulating discussions and useful remarks on this manuscript. I am also indebted to the organizers of the Photon 2009 conference and in particular the convenors of the prompt session, S. Chekanov and M. Fontannaz, and to the CERN PH-TH division for its hospitality.

References

[1] J. L. Hewett, Phys. Rev. Lett. **82** (1999) 4765.

[2] L. Bourhis, M. Fontannaz and J.-P. Guillet, Eur. Phys. J. **C2** (1998) 529.

[3] R. E. Blair, S. Chekanov, G. Heinrich, A. Lipatov and N. Zotov, 0809.0846.

[4] M. Krawczyk, A. Zembrzuski and M. Staszel, Phys. Rept. **345** (2001) 265.

[5] P. Aurenche, M. Fontannaz and J. P. Guillet, Eur. Phys. J. **C44** (2005) 395.

[6] M. A. Kimber, A. D. Martin and M. G. Ryskin, Eur. Phys. J. **C12** (2000) 655.

[8] The per-nucleon density of up quarks (to which photons mostly couple) in nuclei is smaller than that in a proton, leading to a trivial suppression in the nuclear production ratio of prompt photons [43].

[7] A. V. Lipatov and N. P. Zotov, Phys. Rev. **D72** (2005) 054002.
[8] **H1**, A. Aktas *et al.*, Eur. Phys. J. **C38** (2005) 437.
[9] **ZEUS**, J. Breitweg *et al.*, Phys. Lett. **B472** (2000) 175.
[10] M. Fontannaz, J. P. Guillet and G. Heinrich, Eur. Phys. J. **C21** (2001) 303.
[11] M. Krawczyk and A. Zembrzuski, Phys. Rev. **D64** (2001) 114017.
[12] **ZEUS**, S. Chekanov *et al.*, Eur. Phys. J. **C49** (2007) 511.
[13] K. Nowak, Talk given at DIS 2009, Madrid.
[14] **H1**, F. D. Aaron *et al.*, Eur. Phys. J. **C54** (2008) 371.
[15] A. Gehrmann-De Ridder, T. Gehrmann and E. Poulsen, Phys. Rev. Lett. **96** (2006) 132002.
[16] **ZEUS**, S. Chekanov *et al.*, Phys. Lett. **B595** (2004) 86.
[17] A. Gehrmann-De Ridder, G. Kramer and H. Spiesberger, Nucl. Phys. **B578** (2000) 326.
[18] **CDF**, C. Deluca, 0905.2201.
[19] **D0**, V. M. Abazov *et al.*, Phys. Lett. **B666** (2008) 435.
[20] S. Catani, M. Fontannaz, J. P. Guillet and E. Pilon, JHEP **05** (2002) 028.
[21] P. Aurenche, M. Fontannaz, J.-P. Guillet, E. Pilon and M. Werlen, Phys. Rev. **D73** (2006) 094007.
[22] **PHENIX**, S. S. Adler *et al.*, Phys. Rev. **D71** (2005) 071102.
[23] **D0**, V. M. Abazov *et al.*, Phys. Lett. **B639** (2006) 151.
[24] F. Arleo, S. J. Brodsky, D. S. Hwang and A. Sickles, in preparation.
[25] M. Fontannaz and G. Heinrich, Eur. Phys. J. **C34** (2004) 191.
[26] Z. Belghobsi *et al.*, Phys. Rev. **D79** (2009) 114024.
[27] **D0**, V. M. Abazov *et al.*, Phys. Rev. Lett. **102** (2009) 192002.
[28] T. P. Stavreva and J. F. Owens, 0901.3791.
[29] K. J. Eskola, H. Paukkunen and C. A. Salgado, JHEP **04** (2009) 065.
[30] F. Arleo and T. Gousset, Phys. Lett. **B660** (2008) 181.
[31] C. Brenner Mariotto and V. P. Goncalves, Phys. Rev. **C78** (2008) 037901.
[32] F. Gelis, T. Lappi and R. Venugopalan, Int. J. Mod. Phys. **E16** (2007) 2595.
[33] F. Gelis and J. Jalilian-Marian, Phys. Rev. **D66** (2002) 014021.
[34] M. A. Betemps and V. P. Gonçalves, JHEP **09** (2008) 019.
[35] B. Z. Kopeliovich, E. Levin, A. H. Rezaeian and I. Schmidt, Phys. Lett. **B675** (2009) 190.
[36] F. Arleo, Eur. Phys. J. **C61** (2009) 603–627.
[37] S. Albino, 0810.4255.
[38] A. Gehrmann-De Ridder, T. Gehrmann and E. Poulsen, Eur. Phys. J. **C47** (2006) 395.
[39] E. W. N. Glover and A. G. Morgan, Phys. Lett. **B334** (1994) 208.
[40] X.-N. Wang, Z. Huang and I. Sarcevic, Phys. Rev. Lett. **77** (1996) 231.
[41] **PHENIX**, T. Isobe, J. Phys. **G34** (2007) S1015–1018.
[42] **PHENIX**, A. Adare *et al.*, 0903.3399.
[43] F. Arleo, JHEP **09** (2006) 015.
[44] F. Arleo, P. Aurenche, Z. Belghobsi and J.-P. Guillet, JHEP **11** (2004) 009.
[45] F. Arleo, J. Phys. **G34** (2007) S1037.
[46] T. Renk, Phys. Rev. **C74** (2006) 034906.
[47] Y. Mao, G. Conesa Balbastre, M. Sano, Y. Schutz and D. Zhou, Eur. Phys. J. **C57** (2008) 613.
[48] C. Gale, 0904.2184.
[49] R. J. Fries, B. Müller and D. K. Srivastava, Phys. Rev. Lett. **90** (2003) 132301.
[50] B. G. Zakharov, JETP Lett. **80** (2004) 1.

Prompt Photons in Deep Inelastic Scattering at HERA

Peter Bussey

Department of Physics and Astronomy, Faculty of Physical Sciences,
University of Glasgow, Glasgow G12 8QQ, U.K.

for the ZEUS Collaboration

DOI: http://dx.doi.org/10.3204/DESY-PROC-2009-03/Bussey

Recent ZEUS results on the production of isolated high energy photons in deep inelastic scattering are presented.

1 Introduction

In the study of high energy collisions involving hadrons, events in which an isolated high-energy photon is observed can provide a direct probe of the underlying parton process, since the emission of these photons is largely unaffected by parton hadronisation. The study of such "prompt" photons gives new perspectives on QCD processes, allowing theoretical models to be tested from new viewpoints.

In this talk [1], I present new results from the ZEUS experiment on prompt photons produced in deep inelastic scattering (DIS) at HERA. The process studied is $ep \to e\gamma X$, where e denotes an electron or positron. (Both electrons and positrons will here be referred to as electrons.) The data were taken between 2003 and 2007 with the ZEUS detector and correspond to a total integrated luminosity of 320 ± 8 pb^{-1}. The results are compared to two theoretical calculations, from Gehrmann-De Ridder et al. [2] and Martin et al. [3].

2 Experiment and analysis

Outgoing photons and electrons were detected in the ZEUS electromagnetic calorimeter. This was used to identify electrons scattered in the angular range 140° - 172° as measured relative to the forward (proton) direction Z. The outgoing electron was required to have an energy of at least 10 GeV, and was distinguished from other particles by means of a standard ZEUS neural network tool. A standard definition was taken of the virtuality of the exchanged photon, namely $Q^2 = (k - k')^2)$, where k, k' are the four-momenta of the incoming and outgoing electrons. The quantity $x = Q^2/2P.(k - k')$ is also employed where P is the four-momentum of the incoming proton. DIS electrons with $10 < Q^2 < 350$ GeV^2 were used here. Well-measured DIS events were selected by requiring the sum of $E - p_Z$ for the final state particles to be in the range 35 - 65 GeV.

The central region of the ZEUS calorimeter was used to identify photons emerging in the rapidity (η) range -0.7 - 0.9. Photon candidates were initially identified as signals in clusters of cells in the fine-grained electromagnetic part of the calorimeter, with little energy in the hadronic part. Their transverse energy E_T was required to be in the range 4 - 15 GeV. To remove diffractive Compton events, and elastic Bethe-Heitler events, at least one charged track other than that of the scattered electron was demanded. To separate the photons of interest from those closely associated with electrons or jets, two isolation criteria were imposed. For the first, the photon was required not to lie close to a reconstructed track. For the second, a k_T-clustering jet reconstruction algorithm was applied. The photon candidate was rejected if it comprised part of a jet-like object such that its energy was less than 0.9 of the total jet energy,

Photons are distinguished from the background arising from decay products of mesons by the fact that the latter give rise to broader clusters of calorimeter cells than single photons, usually with less energy in a single cell. The quantity $\langle \delta Z \rangle$ is defined as the energy-weighted mean width in Z of the cluster relative to its centroid. The quantity f_{max} is the fraction of the total electromagnetic energy in the cell with highest energy. To separate the photon signal from the background, the latter was represented by a Monte Carlo calculation of neutral current DIS events, passed through a simulation of the ZEUS detector.

Two types of photon signal are simulated: events where the photon is radiated from an incoming or outgoing lepton (LL) and the true "prompt photons" that are emitted from a quark as part of a QCD process (QQ). The event distributions were fitted as the sum of a fixed theoretical LL contribution together with variable amounts of QQ signal and of hadronic background. These components to the fit were evaluated from Monte Carlo event samples, passed through a simulation of the apparatus. Figure 1 shows the fitted $\langle \delta Z \rangle$ and f_{max} distributions for the full data sample. The good fits to these shape parameters confirm that the calorimeter showers are well modelled, and in the case of $\langle \delta Z \rangle$ show a strong peak around 0.5 due to π^0 decays into two photons that are recorded strongly in two neighbouring cells. The photon signal shows itself at low $\langle \delta Z \rangle$ and at high f_{max}. For each of the kinematic variables studied in the analysis, namely photon transverse energy E_T, Q^2, photon pseudorapidity η and x, fits of this kind were performed in each bin of the measured variable to evaluate the acceptance and hence the differential cross sections.

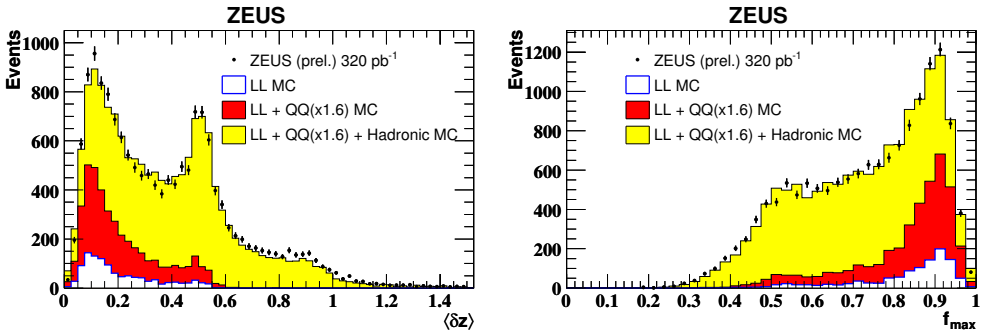

Figure 1: Distributions of $\langle \delta Z \rangle$ and f_{max}, with statistical error bars. In ascending order, the cumulative histograms include the predicted number of LL photons and the fitted numbers of QQ photons and the fitted background. The f_{max} distribution includes the requirement of $\langle \delta Z \rangle < 0.8$.

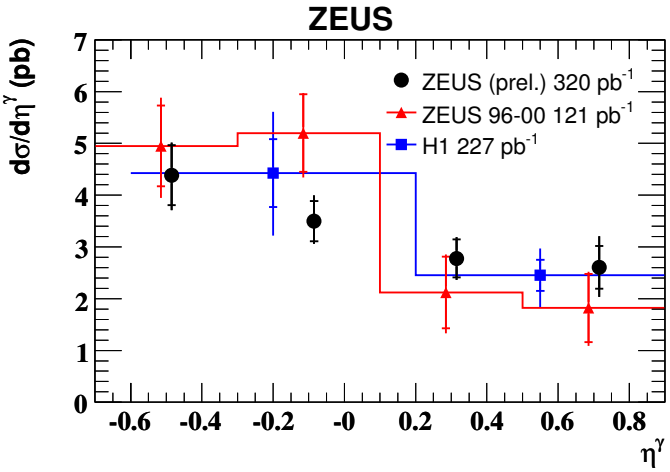

Figure 2: Present results compared to previous ZEUS analysis [4] and results of H1 [5]. Additional kinematic constraints $Q^2 > 35$ GeV^2 and $5 < E_T < 10$ GeV are applied.

3 Results and conclusions

Results of the fit to the signal and background are presented as differential cross sections. Figure 2 shows the present results compared to earlier ZEUS results and results from H1, using a common range of $Q^2 > 35$ GeV^2 and $5 < E_T < 10$ GeV for all three analyses. All three sets of results are in agreement. In Fig. 3, cross sections are presented as functions of Q^2, E_T, η and x within the selected kinematic range. The removal of diffractive Compton and elastic Bethe-Heitler events was incorporated by applying to the truth-level Monte Carlo a requirement that the mass W_X of the final state should be less than 5 GeV after subtracting out the photon and scattered electron. The agreement with the Monte Carlo is good for the photon variables, but the Monte Carlo is too high at low values of the electron variables Q^2 and x. The largest contribution to the systematic uncertainties arises from the uncertainty in the precise shape of the hadronic background to the photon signal.

In Fig. 4 the results are compared to the theories of Gehrmann-De Ridder et al. (GGP) and of Martin et al. (MRST). The approach of GGP is to evaluate prompt photons radiated from the quark line (QQ) and photons radiated from the lepton (LL) at leading order in the electromagnetic coupling. There is an interference term, but it is small. The MRST calculation neglects the QQ component but provides a fuller, resummed version of the LL component by assigning an effective photon density to the proton. It is seen from the figure that the GGP calculation describes the shape of most of the distributions but is too low, while MRST comes close to the data at regions where the LL contribution is predicted to be largest. A combination of the two approaches would seem recommended; unfortunately, there is an overlap in the calculations which means that the MRST cross sections cannot be simply added to the QQ part of GGP. However, in any case, at low Q^2 and low x the theory calculations appear to be too low.

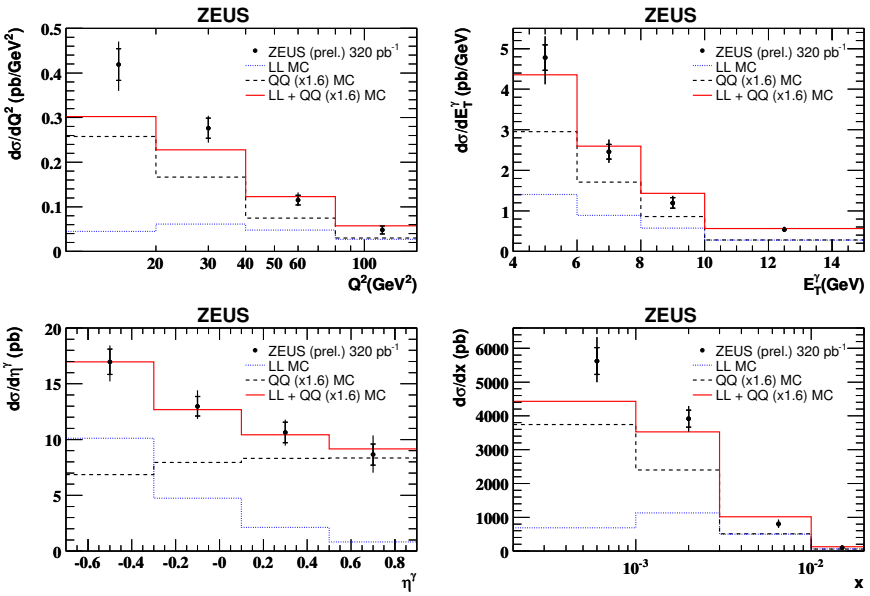

Figure 3: Measured cross sections for high energy isolated photons in DIS as functions of different kinematic variables, compared to the fitted Monte Carlo distributions. Statistical and (statistical + systematic) uncertainties are shown.

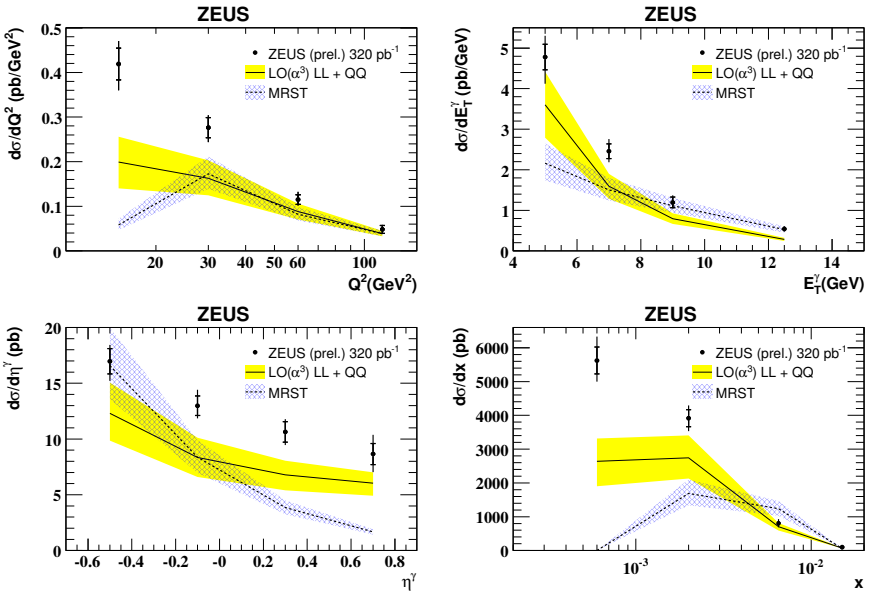

Figure 4: Measured cross sections for high energy isolated photons in DIS as functions of different kinematic variables, compared to the predictions of GGP and MRST (see text).

References

[1] https://indico.desy.de/materialDisplay.py?contribId=20&sessionId=5&materialId=slides&confId=1407

[2] A. Gehrmann-De Ridder et al., Phys. Rev. Lett. bf 96, 132002 (2006).

[3] A. D. Martin et al., Eur. Phys. J. **C 39**, 155 (2005).

[4] ZEUS Coll., S. Chekanov et al., Phys. Lett. **B 595**, 86 (2004).

[5] H1 Coll., F. D. Aaron et al., Eur. Phys. J. **C 54**, 371 (2008).

Direct Photons at RHIC

Klaus Reygers for the PHENIX Collaboration

Physikalisches Institut, Universität Heidelberg, Philosophenweg 12, 69120 Heidelberg, Germany

DOI: http://dx.doi.org/10.3204/DESY-PROC-2009-03/Reygers

A brief overview of direct-photon measurements in p+p and Au+Au collisions at $\sqrt{s_{NN}} = 200\,\mathrm{GeV}$ with the PHENIX experiment at the Relativistic Heavy Ion Collider (RHIC) is given. Direct-photon yields for $p_\mathrm{T} \gtrsim 4\,\mathrm{GeV}/c$ and photon-hadron azimuthal correlations were determined with the aid of an electromagnetic calorimeter. By detecting e^+e^- pairs from the internal conversion of virtual photons direct-photon yields were measured between $1 \lesssim p_\mathrm{T} \lesssim 4\,\mathrm{GeV}/c$. In Au+Au collisions thermal photons from a quark-gluon plasma (QGP) are expected to contribute significantly to the total direct-photon yield in this range.

1 Introduction

In heavy-ion physics direct photons are typically defined as the difference between all measured photons and background photons from hadronic decays [1]. Thus, isolated prompt photons with small hadronic activity around them accompanied by a jet on the away-side as well as photons produced in the fragmentation of jets (fragmentation photons) contribute to the direct-photon signal. The primary reason for the interest in direct photons is their large mean free path with respect to the dimensions of the created fireball. Thus, once produced photons leave the fireball unscathed and carry away information about the early stage of the collisions.

The measured direct-photon signal is an integral over the entire evolution of the fireball where different processes are dominant at different times. This is often regarded as a virtue, however, it also means that disentangling the different sources typically relies on comparisons with model calculations. The production of direct photons in ultra-relativistic A+A collision can be divided into the following stages [2]. At first, direct photons are produced in initial hard parton scatterings analogous to the production mechanism in p+p collisions. The yield of these photons can be calculated in perturbative QCD and they are the dominant direct-photon source at high p_T ($p_\mathrm{T} \gtrsim 6\,\mathrm{GeV}/c$ for Au+Au at $\sqrt{s_{NN}} = 200\,\mathrm{GeV}$). After a time on the order of $\tau_0 \approx 1\,\mathrm{fm}/c$ [3] it is expected that a medium of deconfined quarks and gluons (the quark-gluon plasma) forms for which a local temperature is a meaningful concept. In such a thermalized medium thermal direct photons will be produced whose momentum distribution reflects the temperature of the system. At a temperature of $T_c \approx 140 - 200\,\mathrm{MeV}$ [4, 5] a transition to a hot hadron gas takes place and thermal direct photons are also produced in this phase.

It was discovered at RHIC that quark and gluon jets in central A+A collisions are affected by the created medium. Jets apparently lose energy which results, *e.g.*, in a reduced yield of pions at high p_T [6]. This is referred to as jet quenching. The jet-medium interaction gives rise to further sources of direct photons. First, a direct photon can be produced in so-called

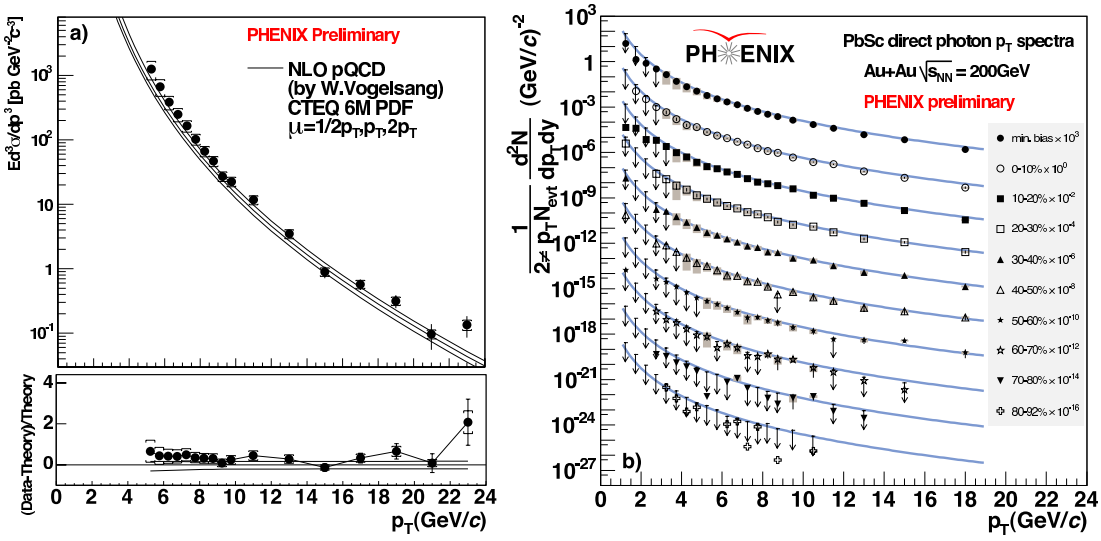

Figure 1: a) Direct-photon invariant cross section in p+p collisions at $\sqrt{s} = 200\,\mathrm{GeV}$ from the 2005 run. The data agree with a next-to-leading-order (NLO) QCD calculation. Final data from 2003 run were published in [9]. b) Direct-photons yields in Au+Au collisions at $\sqrt{s_{NN}} = 200\,\mathrm{GeV}$ from the 2004 run for various centralities. The data are compared a p+p NLO QCD calculation scaled by $\langle T_{\mathrm{AB}} \rangle = \langle N_{\mathrm{coll}} \rangle / \sigma^{\mathrm{NN}}_{\mathrm{inel}}$. Final results from the 2002 run were published in [10].

jet-photon conversions, *e.g.*, in gluon Compton scattering $q_{\mathrm{jet}} + g_{\mathrm{QGP}} \rightarrow q + \gamma$ [7]. In these processes the photon typically carries a large fraction of the initial jet energy. Second, the presence of the medium induces the emission of bremsstrahlung photons [8]. This is analogous to the induced gluon emission which is believed to be the dominant mechanism for the jet energy loss.

2 Direct Photons at High p_{T}

In the PHENIX experiment direct photons at midrapidity ($|y| < 0.35$) above $p_{\mathrm{T}} \approx 4\,\mathrm{GeV}/c$ are measured with an electromagnetic calorimeter (EMCal) [11]. This detector subtends $\Delta\phi \approx \pi$ in azimuth and consists of highly segmented lead-scintillator sampling (PbSc, 6 sectors) and lead-glass Cherenkov calorimeters (PbGl, 2 sectors). The two detector technologies have different systematics and provide the possibility of internal cross-checks. In the Au+Au analysis the ratio $(\gamma_{\mathrm{inclusive}}/\pi^0)_{\mathrm{meas}}$ of the inclusive photon spectrum, *i.e.*, the spectrum of photons from all sources including decay photons, and the π^0 spectrum is calculated. A direct-photon excess can then be found be dividing this ratio by $(\gamma_{\mathrm{decay}}/\pi^0)_{\mathrm{calc}}$, *i.e.*, by the calculated number of hadronic decay photons per π^0. The dominant contribution to these background photons comes from $\pi^0 \rightarrow \gamma\gamma$ and $\eta \rightarrow \gamma\gamma$. Extracting the direct-photon excess from the ratio $(\gamma_{\mathrm{inclusive}}/\pi^0)_{\mathrm{meas}}$ has the advantage that uncertainties of the energy scale of the calorimeter partially cancel. The

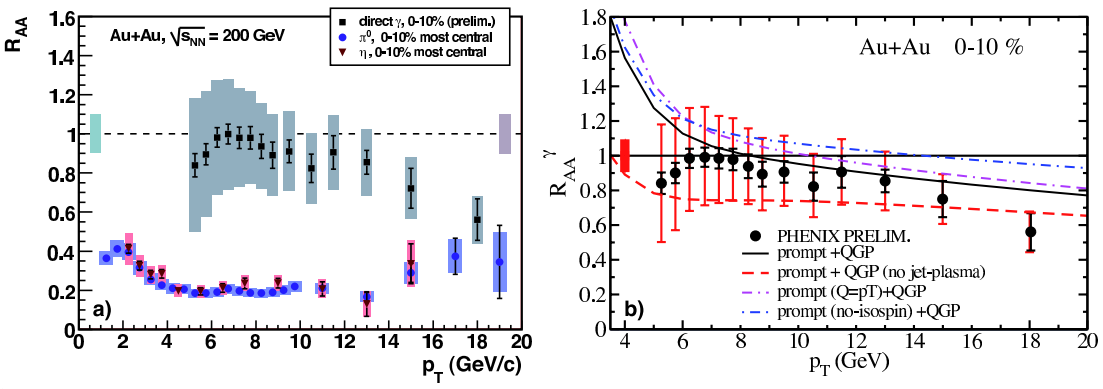

Figure 2: a) $R_{\rm AA}$ in central Au+Au collisions at $\sqrt{s_{\rm NN}} = 200\,\text{GeV}$ for direct photons, π^0's and η's. b) Direct-photon data from a) compared to a calculation which as a net result of different nuclear effects discussed in the main text predicts $R_{\rm AA} \approx 0.8$ at $p_{\rm T} \approx 20\,\text{GeV}/c$.

direct-photon yield is then calculated as

$$\gamma_{\rm direct} = \gamma_{\rm inclusive} - \gamma_{\rm decay} = \left(1 - R^{-1}\right) \times \gamma_{\rm inclusive} \quad \text{with} \quad R = \frac{\left(\gamma_{\rm inclusive}/\pi^0\right)_{\rm meas}}{\left(\gamma_{\rm decay}/\pi^0\right)_{\rm calc}} \,. \qquad (1)$$

In p+p collisions also a slightly different statistical subtraction method is employed [9].

Figure 1a shows that the measured invariant direct-photon cross section in p+p collisions at $\sqrt{s} = 200\,\text{GeV}$ agrees with a next-to-leading-order (NLO) QCD calculation. In the absence of nuclear effects yields of hard scattering processes are expected to scale as $\langle T_{\rm AB}\rangle \times E\,{\rm d}^3\sigma/{\rm d}^3p|_{p+p}$. The nuclear overlap function $\langle T_{\rm AB}\rangle$ reflects the nuclear geometry and is related to the number of inelastic nucleon-nucleon collisions $N_{\rm coll}$ according to $\langle T_{\rm AB}\rangle = \langle N_{\rm coll}\rangle/\sigma_{\rm inel}^{\rm NN}$ where $\sigma_{\rm inel}^{\rm NN}$ is the inelastic nucleon-nucleon cross section [12]. The scaled p+p NLO QCD cross section agrees well with the measured direct-photon yields as can be seen in Figure 1b.

The nuclear modification factor

$$R_{\rm AB}(p_{\rm T}) = \frac{{\rm d}N/{\rm d}p_{\rm T}|_{A+B}}{\langle T_{\rm AB}\rangle \times {\rm d}\sigma/{\rm d}p_{\rm T}|_{p+p}} \qquad (2)$$

is used to quantify nuclear effects on the single particle yields. The suppression of the π^0 and η yields by a factor of ~ 5 in central Au+Au collisions at $\sqrt{s_{NN}} = 200\,\text{GeV}$ [6] as shown in Figure 2a is interpreted as the result of energy loss of quark and gluon jets in a medium of high color-charge density. The yield of direct photons from initial hard parton scatterings in A+A collisions is expected to scale with $\langle T_{\rm AB}\rangle$ which is indeed observed in the region $6 \lesssim p_{\rm T} \lesssim 12\,\text{GeV}/c$. Thus, the direct-photon results at high $p_{\rm T}$ support the parton-energy loss interpretation.

At first sight the decrease of the direct photon $R_{\rm AA}$ below unity for $p_{\rm T} \gtrsim 14\,\text{GeV}/c$ spoils the simple picture of the last paragraph. However, $\langle T_{\rm AB}\rangle$ scaling of direct-photon yields is clearly an oversimplification. First, a Au+Au collision can be regarded as a superposition of p+p, p+n, and n+n collisions whereas only p+p collisions are used as reference in the calculation of $R_{\rm AA}$. This so-called isospin effect reduces $R_{\rm AA}$ at high $p_{\rm T}$. Moreover, the energy loss of jets will lead

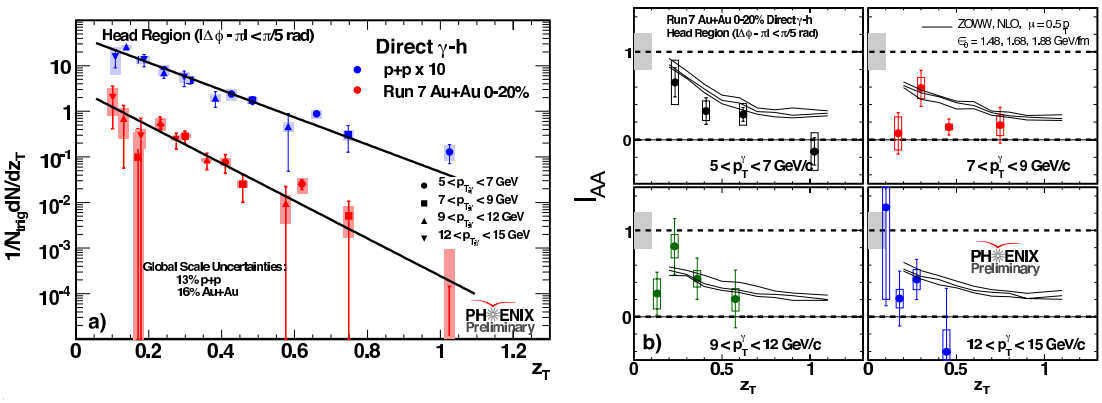

Figure 3: a) Charged-hadron yields opposite to a direct photon as a function of $z_{\rm T} = p_{\rm T}^{\rm hadron}/p_{\rm T}^{\gamma}$ in p+p (run 2005 + 2006) and Au+Au (run 2007) at $\sqrt{s_{NN}} = 200\,{\rm GeV}$. b) The ratio $I_{\rm AA} = D_{\rm A+A}(z_{\rm T})/D_{\rm p+p}(z_{\rm T})$ for four ranges of the trigger photon $p_{\rm T}$. Results from 2004 Au+Au run are published in [13].

to a reduced production of fragmentation photons. On the other hand, anti-shadowing of the parton distribution in the Au nucleus and bremsstrahlung photons from jet-plasma interactions will increase $R_{\rm AA}$. In the calculation in Figure 2 the combination of these effects results in an $R_{\rm AA} \approx 0.8$ at $p_{\rm T} = 20\,{\rm GeV}/c$. The experimental issue here is the correction for the merging of the two showers from $\pi^0 \rightarrow \gamma\gamma$. A detailed study of this effect will be carried out for the final publication.

3 Photon-Triggered Away-side Correlations

The pion yield at high $p_{\rm T}$ in a given bin at $p_{\rm T}^{\pi}$ results from jets with a large spread in transverse momentum $p_{\rm T}^{\rm jet} \gtrsim p_{\rm T}^{\pi}$. Thus, the measured pion $R_{\rm AA}$ contains only indirect information about the energy loss of a jet with a given energy. To better constrain the initial jet energy one can study jets opposite ($\Delta\phi \approx \pi$) to a direct photon as for leading order processes $p_{\rm T}^{\rm jet} = p_{\rm T}^{\gamma}$. Full jet reconstruction is difficult in heavy-ion reactions so that photon-triggered away-side correlations are a useful tool to study jet energy loss. One defines $z_{\rm T} = p_{\rm T}^{\rm hadron}/p_{\rm T}^{\gamma}$ and the distribution $D(z_{\rm T}) = 1/N_{\gamma}^{\rm trig}\,{\rm d}N^{\rm hadron}/{\rm d}z_{\rm T}$ approximates the light quark fragmentation function [13].

The $z_{\rm T}$ distributions of charged hadrons associated with a direct photon are shown in Figure 3. If the $z_{\rm T}$ distribution in p+p collisions is a good approximation of the fragmentation function the distribution should scale in $z_{\rm T}$, *i.e.*, it should only depend on $z_{\rm T}$ independent of the $p_{\rm T}$ of the trigger photons. This is approximately satisfied in p+p, but interestingly apparently also in Au+Au. The distributions in p+p and Au+Au are fit with an exponential $\exp(-bz_{\rm T})$. The difference between p+p ($b = 6.89 \pm 0.64$) and Au+Au ($b = 9.49 \pm 1.37$) reflects the energy loss in the medium.

The ratios $I_{\rm AA} = D_{\rm A+A}(z_{\rm T})/D_{\rm p+p}(z_{\rm T})$ for different $p_{\rm T}$ ranges of the trigger photon are shown in Figure 3. They are compared with a jet quenching calculation [14] in which an energy loss parameter was tuned to describe the single particle $R_{\rm AA}$. Overall a good agreement with the data is observed. However, the uncertainties of the data points are currently too large to

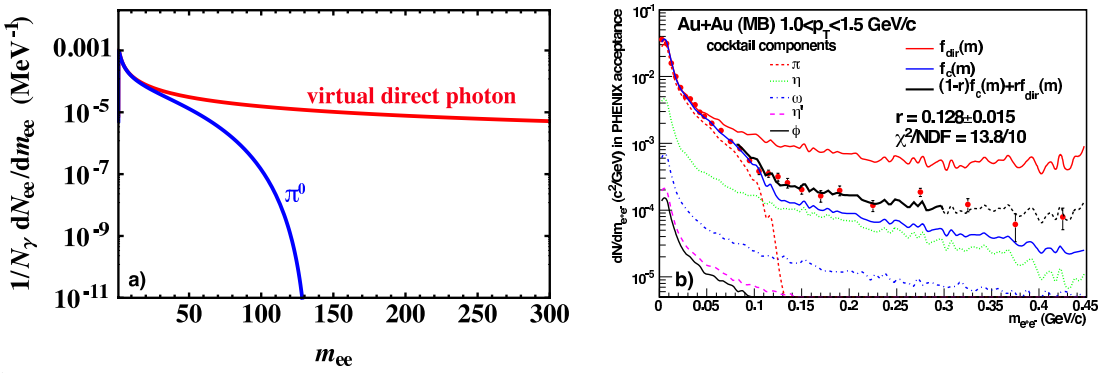

Figure 4: a) Mass distribution of e^+e^- pairs from internal conversion as given by Equation 3. b) Measured e^+e^- mass distribution in Au+Au collisions at $\sqrt{s_{NN}} = 200\,\mathrm{GeV}$. The data are well described by adding contributions from hadronic decays and virtual direct photons.

confirm the change of I_{AA} with the p_{T} of the photon trigger as predicted by the calculation.

4 Direct Photons at Low p_{T}

Systematic uncertainties related to the energy scale, the correction of detector effects and the extraction of the π^0 yields prevent the measurement of direct photons with the PHENIX EMCal below $p_{\mathrm{T}} \lesssim 4\,\mathrm{GeV}/c$. This is the range in which the contribution from thermal direct photons is expected to be largest. A solution to this quandary is the measurement of virtual photons with small mass via their internal conversion in e^+e^- pairs [15]. Electrons and positrons are identified within PHENIX with an Ring Imaging Cherenkov detector and by matching the measured track momentum with the energy signal in the EMCal. e^+e^- pairs from external conversions in the detector material are removed by a cut on the orientation of the pair in the magnetic field. The combinatorial background is subtracted using a mixed-event technique. The remaining correlated background is subtracted with the aid of constructing like-sign pairs.

The internal conversion method exploits the fact that any source of real photons also is a source of virtual photons and that the rate of internal conversions and the mass distribution of the e^+e^- pairs is calculable within QED. The number of e^+e^- pairs per real photon is given by [16]

$$\frac{1}{N_\gamma}\frac{\mathrm{d}N_{ee}}{\mathrm{d}m_{ee}} = \frac{2\alpha}{3\pi}\frac{1}{m_{ee}}\sqrt{1-\frac{4m_e^2}{m_{ee}^2}}\left(1+\frac{2m_e^2}{m_{ee}^2}\right)S\,. \tag{3}$$

For hadron decays, *e.g.*, the π^0 Dalitz decay, $S = |F(m_{ee}^2)|^2\left(1-m_{ee}^2/M_{\mathrm{h}}^2\right)^3$ where $F(m_{ee}^2)$ is the form factor and M_{h} the hadron mass. For a point-like process such as gluon Compton scattering ($q + g \to q + \gamma^* \to q + e^+ + e^-$) $S \approx 1$ for $p_{\mathrm{T}}^{ee} \gg m_{ee}$. The two cases are shown in Figure 4a.

At small masses $m_{ee} < 30\,\mathrm{MeV}$ the mass distribution is to very good approximation independent of the source, and the fraction of real direct photons can be expressed in terms of virtual photons, *i.e.*, $r \equiv \gamma_{\mathrm{direct}}/\gamma_{\mathrm{inclusive}} = (\gamma^*_{\mathrm{direct}}/\gamma^*_{\mathrm{inclusive}})_{m_{ee}<30\,\mathrm{MeV}}$. At larger masses e^+e^- pairs from hadronic decays are suppressed by the S factor and $m_{ee} < M_{\mathrm{h}}$ holds. Thus,

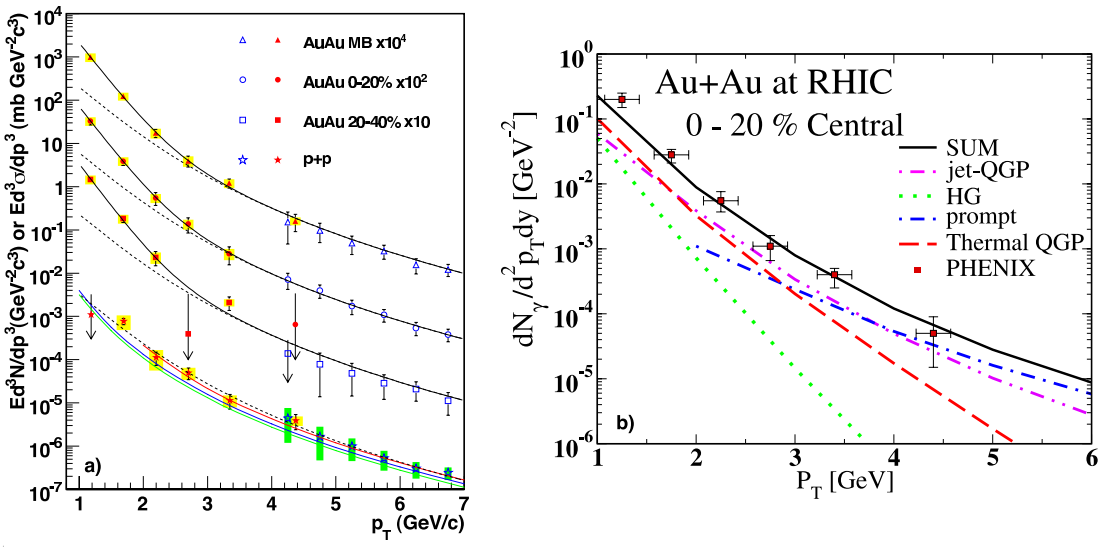

Figure 5: a) Invariant direct-photon cross sections (p+p) and yields (Au+Au) at $\sqrt{s_{NN}}$ = 200 GeV [15]. The closed symbols are from the internal conversion method, the open symbols from EMCal measurements. b) Comparison of the direct-photon spectrum in the 20% most central Au+Au collisions with a calculation from [2].

the background from π^0 Dalitz decays could be completely avoided by measuring virtual direct photons in the range $m_{ee} > M_{\pi^0}$. However, this comes at the expense of a loss in statistics as for every real direct photon there are only ~ 0.001 virtual direct photons with $m_{ee} > M_{\pi^0}$.

For a given $p_{\rm T}$ bin the direct-photon fraction r is determined as follows. First the mass distribution of e^+e^- pairs from hadronic decays $f_{\rm cocktail}$ with contributions from $\pi^0, \eta, \omega, \eta'$, and ϕ and the mass distribution for virtual direct photons $f_{\rm direct}$ are separately normalized to the data at $m_{ee} < 30\,{\rm MeV}$. Then r is extracted by fitting $f(m_{ee}) = (1-r) f_{\rm cocktail}(m_{ee}) + r f_{\rm direct}(m_{ee})$ in the range $80 < m_{ee} < 300\,{\rm MeV}$ (see Figure 4b).

The direct-photon spectra in p+p and Au+Au collisions at $\sqrt{s_{NN}} = 200\,{\rm GeV}$ from the internal conversion method are shown in Figure 5 along with the EMCal measurements. The p+p spectrum agrees with the NLO QCD calculation over the entire range $1 < p_{\rm T} < 7\,{\rm GeV}/c$. The p+p data can be parameterized with $f_{p+p}(p_{\rm T}) = A(1+p_{\rm T}^2/b)^{-n}$ (dashed line). For Au+Au the shape of the spectra differs significantly from the p+p spectrum and yields show a striking enhancement for $p_{\rm T} \lesssim 2\,{\rm GeV}/c$ with respect to $\langle T_{AB} \rangle \times f_{p+p}(p_{\rm T})$. A good fit of the Au+Au data can be obtained with $f_{Au+Au}(p_{\rm T}) = \langle T_{AB} \rangle \times f_{p+p}(p_{\rm T}) + B \exp(-p_{\rm T}/T)$. The exponential shape of the enhancement in Au+Au is consistent with the assumption that the excess photons come from a thermal source. For the 20% most central Au+Au collisions the extracted slope parameter is $T = (221 \pm 23 \pm 18)\,{\rm MeV}$. In hydrodynamical models the initial temperature of the thermalized quark-gluon plasma is typically 1.5 to 3 times T. Thus, if the excess photons are of thermal origin the measured slope parameter T would indicate an initial temperate well above the critical temperature for the QGP phase transition.

Figure 5b shows a comparison of the Au+Au direct-photon data at low $p_{\rm T}$ with a calculation which includes all the direct-photon sources discussed in section 1 [2]. The space-time evolution

of the fireball is modeled with ideal hydrodynamics and an equation of state with a transition from a non-interacting quark-gluon plasma to an chemically equilibrated hadron resonance gas at a critical temperature of $T_c = 164\,\mathrm{MeV}$. The contribution from the pre-equilibrium phase is accounted for by starting the hydro-evolution early at $\tau_0 = 0.2\,\mathrm{fm}/c$. Assuming full equilibrium at $\tau_0 = 0.6\,\mathrm{fm}/c$ corresponds to an initial temperature of $T_{\mathrm{initial}} = 340\,\mathrm{MeV}$ in this model. Another piece of evidence for the creation of a quark-gluon plasma is the fact that without photons from jet-plasma interactions the data cannot be described.

5 Conclusions

Direct photons at high p_{T} measured with the PHENIX EMCal played a crucial role in the discovery of jet quenching at RHIC. Neutral pions and other hadrons in central Au+Au collisions are suppressed whereas direct photons up to $p_{\mathrm{T}} \approx 14\,\mathrm{GeV}/c$ scale with T_{AB}, *i.e.*, with the increase of the parton luminosity per collision as expected from nuclear geometry. This strongly supports the interpretation of the high-p_{T} hadron suppression as being caused by the energy loss of quark and gluon jets in the created medium. Direct-photon hadron azimuthal correlations allow to better constrain the initial jet energy. The correlation data were compared to one particular jet quenching model which was only tuned to describe the single particle R_{AA} and agreement was found. A breakthrough is the measurement of low-p_{T} direct photons with the internal conversion method in p+p as well as in Au+Au collisions. The direct-photon spectrum in central Au+Au collisions spectra exhibits an enhancement above the scaled p+p spectrum for $p_{\mathrm{T}} \lesssim 2\,\mathrm{GeV}/c$. The exponential shape of this enhancement and the slope parameter $T > T_c$ are consistent with the assumption that thermal photons from a QGP phase contribute significantly to this enhancement.

References

[1] P. Stankus. Ann. Rev. Nucl. Part. Sci. 55 517 (2005).

[2] C. Gale (2009). arXiv:0904.2184[hep-ph].

[3] P. F. Kolb and U. W. Heinz (2003). nucl-th/0305084.

[4] Y. Aoki et al. (2009). arXiv:0903.4155[hep-lat].

[5] M. Cheng et al. Phys. Rev. D74 054507 (2006). hep-lat/0608013.

[6] K. Adcox et al. Nucl. Phys. A757 184 (2005). nucl-ex/0410003.

[7] R. J. Fries, B. Muller, and D. K. Srivastava. Phys. Rev. Lett. 90 132301 (2003). nucl-th/0208001.

[8] B. G. Zakharov. JETP Lett. 80 1 (2004). hep-ph/0405101.

[9] S. S. Adler et al. Phys. Rev. Lett. 98 012002 (2007). hep-ex/0609031.

[10] S. S. Adler et al. Phys. Rev. Lett. 94 232301 (2005). nucl-ex/0503003.

[11] L. Aphecetche et al. Nucl. Instrum. Meth. A499 521 (2003).

[12] M. L. Miller, K. Reygers, S. J. Sanders, and P. Steinberg. Ann. Rev. Nucl. Part. Sci. 57 205 (2007). nucl-ex/0701025.

[13] A. Adare et al. (2009). arXiv:0903.3399[nucl-ex].

[14] H. Zhang, J. F. Owens, E. Wang, and X.-N. Wang (2009). 0902.4000.

[15] A. Adare et al. (2008). arXiv:0804.4168[nucl-ex].

[16] N. M. Kroll and W. Wada. Phys. Rev. 98 1355 (1955).

Prompt Photon Production at the Tevatron

Ashish Kumar (for the DØ and CDF collaborations)
Department of Physics, The State University of New York at Buffalo, NY 14260, USA.

DOI: http://dx.doi.org/10.3204/DESY-PROC-2009-03/Kumar

Prompt photon production has been studied by the CDF and DØ experiments at the Fermilab Tevatron collider in $p\bar{p}$ collisions at the centre of mass energy of $\sqrt{s}$ =1.96 TeV. Measurements of the inclusive photon, inclusive photon plus jet, photon plus heavy flavor jet, and diphoton production cross sections are discussed. The analyses use data sample corresponding to integrated luminosity between 0.2 fb^{-1} and 1.02 fb^{-1}. The results are compared to the next to leading order (NLO) perturbative QCD (pQCD) calculations.

1 Introduction

Prompt photon production [1] have been extensively studied both theoretically and by various fixed-target and collider experiments during the last three decades. Prompt photons, sometimes referred to as direct photons, emerge unaltered from the hard interaction between two partons and thus provide a direct probe of the underlying hard-scattering process. Since they emerge without the hadronization phase, they also provide a clean probe without additional complication caused by the parton fragmentation and experimental systematic uncertainties related to jet identification and energy measurement. At the lowest order (LO) in perturbative QCD (pQCD), prompt photons are produced by quark-gluon Compton scattering $gq \rightarrow q\gamma$ and the annihilation subprocess $q\bar{q} \rightarrow g\gamma$. However, the Compton Scattering provides the dominant contribution for photons with moderate transverse momentum (p_T) and the annihilation contribution gains importance at high p_T region. Study of prompt photons, therefore, provide precision tests of our theoretical understanding based on pQCD as well as possible constraint on the relatively poorely measured gluon density of the proton since gluon is involved at tree level in contrast to deep inelastic scattering (DIS) and Drell-Yan (DY) processes where gluon is involved only at a higher order.

Photons in final state may be an important sign of new particles and /or physics beyond the Standard Model. Understanding the QCD production mechanisms of photons is, therefore, a prerequisite to searches for new physics. Prompt photon production cross section measurement is extremely challenging due to enormous background from jets fragmenting into a leading π^0 or η, particularly at low p_T. Photons arising from the decays of π^0 and η are largely suppressed by the photon selection requirements applied to data, and especially by the photon isolation, since these mesons are produced mainly within jets during fragmentation and are surrounded by other particles. Even after very tight selection criteria, highly electromagnetic jets provide a formidable background due to their large cross section. The two showers from the energetic

π^0 or η decaying to two photons coalesce in the calorimeter and mimic single photon shower. Consequently, they can not be rejected on an event-by-event basis and we must perform a statistical background subtraction in order to measure the cross section.

2 Inclusive photon cross section measurement by DØ

DØ has measured the inclusive isolated photon cross section based on an integrated luminosity of 380 pb^{-1} [2]. Central photons ($|\eta|$ <0.9) with p_T > 23 GeV are selected. Photon candidates are formed from clusters of electromagnetic (EM) calorimeter cells within a cone of radius $\mathcal{R} = \sqrt{(\Delta\eta)^2 + (\Delta\phi)^2} = 0.2$ in the space of pseudorapidity (η) and azimuthal angle (ϕ). Candidates are selected if there is significant energy in the EM layers (>95%), and the probability to have a spatially-matched track is less than 0.1%, and they satisfied an isolation requirement. As an isolation criterion, the transverse energy not associated to the photon in a cone of radius $\mathcal{R}$=0.4 around the photon direction has to be less than 0.10 times the energy of the photon. Potential backgrounds from cosmic rays and electrons from W boson decays are suppressed by requiring the missing transverse energy (E_T^{miss}) to be less than 0.7 p_T. To better select photons and estimate the residual background, an artificial neural network ($\gamma - ANN$) is constructed using the powerful discriminating variables exploiting information from the calorimeter and the tracker. The $\gamma - ANN$ was trained to discriminate between direct photons and background events. The photon purity ($\mathcal{P}$) is determined statistically for each photon p_T bin by fitting the $\gamma - ANN$ distribution in data to predicted $\gamma - ANN$ distributions for signal and background Monte Carlo (MC) samples.

The measured cross section, together with statistical and systematic uncertainties, is presented in Fig.1 and compared with the results from a next-to-leading order (NLO) pQCD calculation obtained from JETPHOX program [3] . These results were derived using the CTEQ6.1M parton distributions functions (PDFs) and the BFG fragmentation functions (FFs). The renormalization, factorization, and fragmentation scales were chosen to be equal to photon p_T. The ratio of the measured to predicted cross sections is also shown in Fig.1. The scale dependence, estimated by varying scales by factors of two, are displayed as dashed lines. As can be seen, the results are consistent with theory within uncertainties. The difference in shape between data and theory at low p_T is difficult to interpret due to the large theoretical and experimental uncertainties. Higher order calculations are expected to reduce the scale sensitivity and calculations that account for soft-gluon contributions are expected to provide better descriptions of the data at low p_T.

3 Inclusive photon cross section measurement by CDF

CDF has recently presented a preliminary result on the measurement of the inclusive isolated photon cross section using a data set corresponding to an integrated luminosity of 2.5 fb^{-1} [4]. Measurements are performed as a function of the photon p_T for photons with p_T >30 GeV and $|\eta|$ <1.0. Photon candidates are required to be isolated in the calorimeter with E_T^{iso} >2.0 GeV, where E_T^{iso} is defined as the transverse energy deposited in a cone of radius $\mathcal{R}$=0.4 around the photon candidate minus that of the photon. To reject electrons from W decays and non-collision backgrounds, candidates with $E_T^{miss} > 0.8 p_T$ are vetoed. The calorimeter isolation distribution

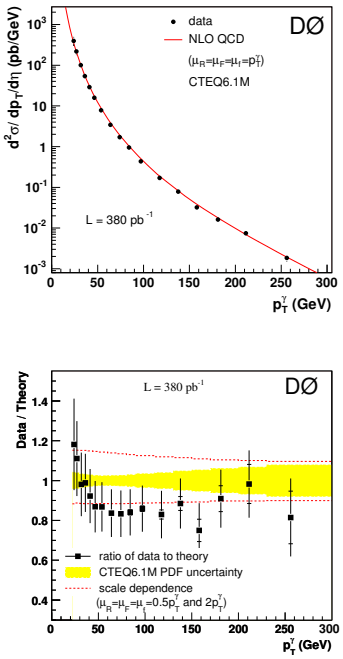

Figure 1: The measured differential cross section for isolated photon production by DØ (Top) and the ratio of measured to predicted cross section by JETPHOX (Bottom).

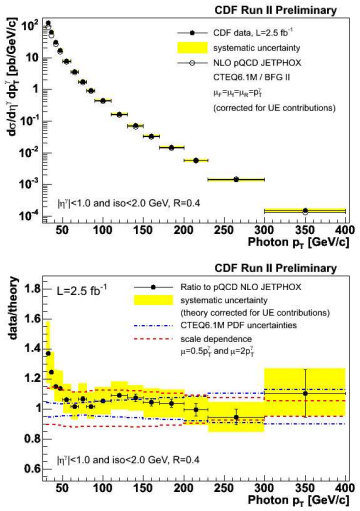

Figure 2: The inclusive isolated photon cross section as a function of the photon transverse momentum measured by the CDF experiment (Top). The p_T spectrum of the ratio of measured to NLO calculations is shown (Bottom).

is employed to discriminate photon signal from QCD background (dominated by π^0 decays). Templates for signal and background are constructed using Monte Carlo simulations and fitted to the data in each bin of p_T to estimate the photon purity in the selected sample. The obtained photon signal fraction varies from 70% to 100% as the photon p_T increases.

The p_T distribution of the measured cross section is unfolded back to the parton level for comparison with the theory. The unfolding factors, which takes into account both the efficiencies, detector resolution effects and acceptance effects, vary between 64% to 69% in the p_T range considered. The systematic uncertainties in the cross section range from 10% to 15%, dominated by the photon purity determination at low p_T and by the uncertainty in the photon energy scale at high p_T. The cross section is measured as a function of the photon p_T up to 400 GeV and compared to the NLO pQCD predictions as given by the JETPHOX program [3], with CTEQ6.1M PDFs and BFGII fragmentation functions. Figure 2 shows these results that test the pQCD over 6 orders of magnitude. The renormalization, factorization and fragmentation scales are all set to the photon p_T. The theory is corrected for the non-perturbative effects from the underlying event and this correction decreases the theoretical cross section by approximately 9%, and is independent of p_T. The ratio of the measured and predicted cross sections as a function of the photon p_T is also presented in Fig. 2. Theory and data agree well over the whole measured range except for $p_T < 40$ GeV. For p$p_T < 40$ GeV the data exhibits an excess and a different shape, consistent with similar observation in previous measurements.

4 Inclusive photon + jet cross section by DØ

The production of a photon with associated jets in the final state is more sensitive to the underlying dynamics of hard QCD interactions than the inclusive photon measurements. DØ has measured the inclusive differential cross section of photon plus jet production based on an integrated luminosity of 1.0 fb^{-1} [5]. The study considers different angular configurations between the photon and the jets to probe different regions of parton momentum fraction x and hard-scattering scales Q^2. Photons with $p_T > 30$ GeV and central rapidity $|\eta|$ <1.0 are considered in the analysis. Photon candidates are required to deposit at least 96% of the detected energy in the EM calorimeter layers and should not be spatially matched to a reconstructed track. The isolation criteria requires the transverse energy not associated to the photon in a cone of radius $\mathcal{R}$=0.4 around the photon direction to be less than 0.07 times the energy of the photon. Backgrounds from cosmics and electrons from W boson decays are vetoed by a missing transverse energy requirement of $E_T^{miss} < (12.5 + 0.36p_T)$ GeV. Electromagnetic cluster and track information is fed into a neural network to further increase the photon purity. Jets are reconstructed with a midpoint cone algorithm with $\mathcal{R}$=0.7. Events containing at least one jet are selected which must have p_T >15 GeV and can be either central (y^{jet} <0.8) or forward (1.5< y^{jet} <2.5). Finally, the photon candidate and the leading hadronic jet are required to be separated in η-ϕ phase space by > 0.7. The photon purity of the sample in different p_T bins is determined by fitting the MC templates of $\gamma - ANN$ in data.

The measured triple differential cross sections measured are shown in Fig. 3 as a function of photon p_T with the full experimental (systematic $\oplus$ statistical) errors for different kinematic regions (distinguished by central and forward jets and same-side and opposite-side photon and

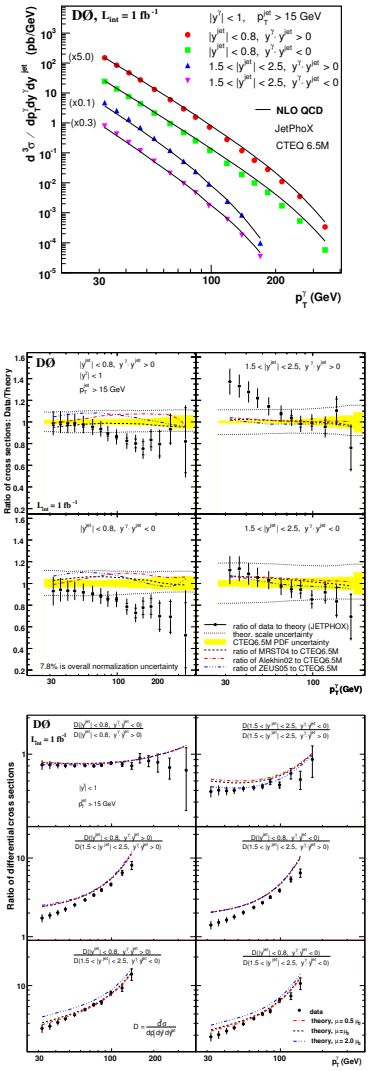

Figure 3: The differential photon + jet cross section as a function of the photon p_T in four different kinematic regions (Top), the corresponding data/theory ratio (Middle) and the ratios between the differential cross sections in each y^{jet} region.

jet rapidities). These four kinematic regions probe different momentum phase space of the two initial interacting partons. The largest uncertainties are caused by the purity estimation, photon and jet selections and luminosity. Statistical errors vary from 0.1% in the first p_T bin to $13-20\%$ in the last bin, while systematic errors are within $10-15\%$ depending on the region. The superimposed theoretical curve corresponds to the NLO QCD predictions based on the JETPHOX program [3] with the CTEQ6.5M set of PDFs and BFG set of fragmentation functions. The choice of renormalization (μ_R), factorization (μ_F) and fragmentation (μ_f) scales used is $\mu_R = \mu_F = \mu_f = p_T^\gamma f(y^\star)$ with $f(y^\star) = ([1+exp(-2|y^\star|)]/2)^{1/2}$ and $y^\star = 0.5(\eta^\gamma - \eta^{jet})$. Non-pQCD effects were considered to be negligible. The ratio of the measured cross sections to the NLO predictions are presented in Fig.3 for the different regions. As shown in Fig. 3, the predictions do not describe the shape of the data for the whole measured range, especially for jet y^{jet} <0.8 and p_T > 100 GeV and for 1.5< y^{jet} <2.5, $y^\gamma.y^{jet}$ >0 and p_T <50 GeV, where the difference in shapes is similar to those observed in previous inclusive photon measurements. Figure 3 also shows the ratio of measured cross sections in the different regions where the experimental systematic uncertainties are reduced further. In general, the shapes of the measured cross section ratios in data are qualitatively reproduced by the theory but a quantitative disagreement is observed for some kinematic regions even after taking into account the overall (experimental and theoretical) uncertainty.

5 Inclusive photon + heavy flavor jet cross section by DØ

DØ has performed the first measurements of the differential cross section of the inclusive photon production in association with heavy flavor (b and c) jets at a $p\bar{p}$ collider using 1.02 fb^{-1} of data [6]. The analysis considers one isolated photon with $p_T > 30$ GeV in the central rapidity region of $|\eta|$ <1.0. Photons are essentially subjected to the same selection as in Section 4. Background from dijet events containing π^0 and η mesons is suppressed using an artificial neural network ($\gamma - ANN$). Backgrounds from cosmics and electrons from W boson decays are vetoed by a missing transverse energy requirement of $E_T^{miss} < 0.7p_T$. Jets are reconstructed with a midpoint cone algorithm with radius of $\mathcal{R} = 0.5$. and are required to have $p_T > 15$ GeV and y^{jet} <0.8. Same side and opposite side photon and jet rapidity events are treated separately. The leading jet must have at least two tracks associated with hits in the silicon microstrip tracker for the heavy flavor tagging. A dedicated neural network ($b - ANN$) which exploits the longer lifetimes of heavy flavored hadrons is applied to enrich the heavy flavor jet content of the considered events. The $b - ANN$ selection has an efficiency of 55-62% for b jets and of 11-12% for c jets. Only 0.2-1% of light jets are misidentified as heavy-flavor jets. Photon purity is estimated in each p_T bin using the $\gamma - ANN$ distribution. The fractional contributions of b and c jets are determined by fitting templates of $P_{\text{HF-jet}} = -\ln\prod_i \text{Prob}^i_{\text{track}}$ (Fig. 4) to the data, where $\text{Prob}^i_{\text{track}}$ is the probability that a track originates from the primary vertex. The templates for b and c jets are obtained from MC, and the light jet templates come from a data sample enriched with light jets. Jets from heavy quarks have typically large values of $P_{\text{HF-jet}}$. The estimated fractions of b and c jets in the p_T bins vary between 25-34% and 40-48% respectively.

The measured differential cross sections are shown in Fig. 4 for $\gamma + b + X$ and $\gamma + c + X$ production as a function of photon p_T for two different kinematical regions defined by $y^\gamma y^{jet}$ >0 and $y^\gamma y^{jet}$ <0. The cross section falls by more than three orders of magnitude in the range

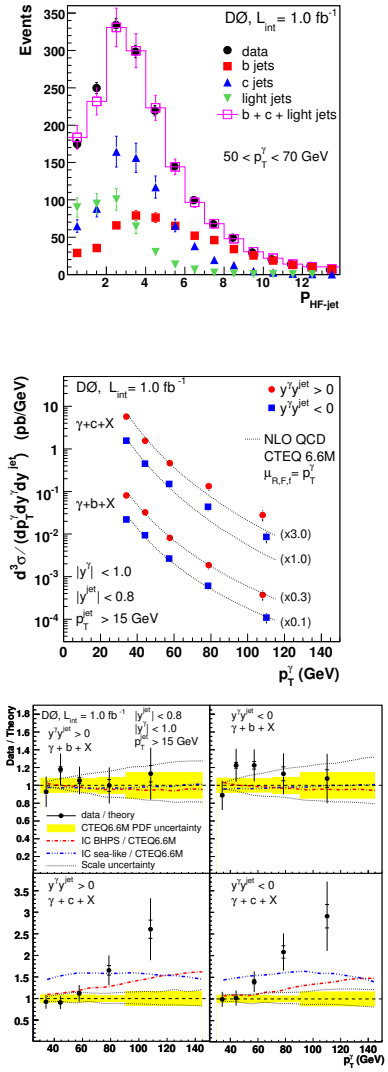

Figure 4: Distributions of observed events for P_{HF-jet} for photon p_T 50< p_T <70 GeV. The distributions for the b,c and light jet templates are also shown (Top). The $\gamma + b + X$ and $\gamma + c + X$ differential cross sections as a function of photon p_T in the two regions $y^{\gamma}y^{jet}$ >0 and $y^{\gamma}y^{jet}$ <0 (Middle). the data-to-theory ratio of cross sections for $\gamma + b + X$ and $\gamma + c + X$ in the corresponding regions (Bottom).

$30 < p_T < 150$ GeV. The statistical uncertainty on the results ranges from 2% in the first p_T bin to 9% in the last bin, while the total systematic uncertainty varies between 15% and 28%. The uncertainty at low p_T is mainly due to the photon purity, while at higher p_T, it is dominated by the heavy flavor fraction. The result is compared to the NLO pQCD predictions [7] with CTEQ6.6M PDFs and all the theory scales set to photon p_T ($\mu_R = \mu_F = \mu_f = p_T$). The predictions have been corrected for parton-to-hadron fragmentation effects by 7.5% (3%) in the b (c) jet cross section for low p_T and by 1% at high p_T. The ratio of the measured to predicted cross sections are also shown in Fig. 4. While the prediction agrees with the measured cross section for $\gamma + b + X$ production over the entire p_T range, the prediction underestimates the measured cross section for $\gamma+c+X$ production for p_T above 70 GeV. The measurements are also compared to predictions including two models with intrinsic charm parameterizations in the CTEQ6.6M PDF. Both non-perturbative models predict a higher $\gamma+c+X$, but, do not describe the measured cross section. The observed difference in the shape could be due to an underestimation of the $g \to Q\bar{Q}$ splitting in the annihilation process which becomes dominant at high p_T.

6 Inclusive diphoton cross section measurement by CDF

The measurements of prompt diphoton production provide a great test of QCD production mechanisms and they are also possible signatures of "new" physics. The diphoton anaysis allows a direct measurement of the transverse momentum of the $\gamma\gamma$ system (q_T) which is sensitive to initial-state soft gluon radiation. It is also one of the important backgrounds for Higgs $\to \gamma\gamma$ searches at the LHC. CDF has measured the inclusive diphoton cross section using a data sample of 207 pb^{-1} [8]. The leading contributions to the diphoton production arise from quark-antiquark annihilation and from gluon-gluon scattering. In addition to the prompt production, the diphoton cross section also receives contribution where one or both photons are produced in fragmentation processes which are largely suppressed by photon isolation. Central photon candidates ($|\eta|$ <0.9) with transverse energy (E_T) greater than 14 GeV (13 GeV) for the leading (softer) photons are selected based on lateral shower profile, preshower hit and no associated track requirements. The isolation requirement requires the transverse energy in a cone of radius R=0.4 around the photon direction, not associated with the photon, to be below 1 GeV. In total 427±59 (stat) diphoton events in 889 diphoton candidates are selected in the analysis.

Figure 5 shows the differential diphoton cross section as a function of invariant diphoton mass ($M_{\gamma\gamma}$), q_T , and the difference in azimuthal angle between two photons ($\Delta\phi_{\gamma\gamma}$). The results are compared to the theoretical predictions of DIPHOX [9], ResBos [10] and Pythia [11]. DIPHOX includes NLO matrix elements for both the direct contribution and the fragmentation contribution and the NNLO contribution from $gg \to \gamma\gamma$. ResBos includes the fragmentation contributions only at LO but it implements the resummation of soft initial-state gluon radiation which is relevant at low q_T. Also shown are the results for PYTHIA (LO matrix elements for both the direct and fragmentation contribution) which has been scaled by a factor of 2 to match the data. The contributions from fragmentation processes are especially large in regions of small $M_{\gamma\gamma}$, large q_T and small $\Delta\phi_{\gamma\gamma}$ and these regions are only described by DIPHOX which includes the NLO corrections for the fragmentation process. The kinematic regions at low q_T and large $\Delta\phi_{\gamma\gamma}$ are especially sensitive to soft initial-state gluon emissions and ResBos describes

this phase space, thanks to the resummation effects it incorporates. Describing the diphoton production in all regions of phase space simultaneously requires a full NLO calculation taking higher order $gg \rightarrow \gamma\gamma$ corrections and resummed soft-gluon radiation into account.

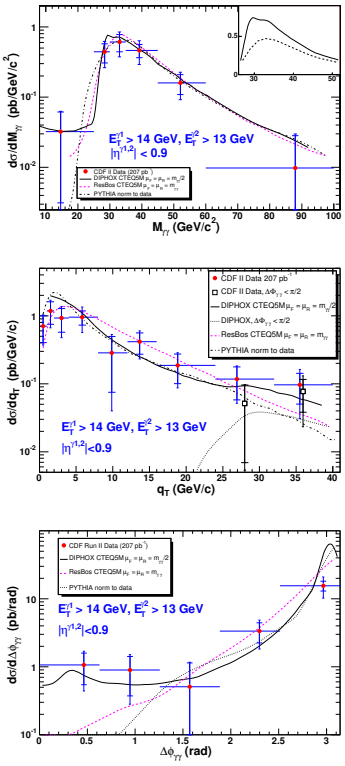

Figure 5: The differential diphoton cross section as a function of invariant diphoton mass ($M_{\gamma\gamma}$), transverse momentum of the diphoton system q_T , and the difference in azimuthal angle between two photons ($\Delta\phi_{\gamma\gamma}$) along with the predictions from DIPHOX, ResBos and Pythia.

7 Conclusions

Incluisve isolated photon, photon plus jet, diphoton and photon plus heavy flavor jet cross sections have been measured by the CDF and DØ experiments in $p\bar{p}$ collisions at the Fermilab Tevatron. Inclusive isolated photon cross section measurements show a different shape at low photon p_T consistent with observation in previous measurements by UA2, CDF and DØ . The differential photon plus jet cross section has been measured in four distinct kinematic regions resulting in similar shapes as in the inclusive photon measurement. The theory can not describe the measurement in the whole measured range, especially for y^{jet} <0.8 and $p_T > 100$ GeV and for 1.5< y^{jet} <2.5, $y^{\gamma}.y^{jet}$ >0 and p_T < 50 GeV. First measurements on $\gamma + b + X$ and $\gamma + c + X$ cross sections have been presented. Good agreement with theory is observed in case of b jets, while theory underestimates the measured $\gamma + c + X$ cross section for p_T >70

GeV. The differential diphoton production cross section has been measured as a function of diphoton invariant mass, transverse momentum and azimuthal opening angle and compared to the theoretical calculations. These quantities can not be described simultaneously by a single theoretical model.

References

[1] J.F. Owens, Rev. Mod. Phys. **59** 465 (1987).

[2] V. Abazov *et al.* (DØ collaboration), Phys. Lett. B**639** 151 (2006).

[3] S. Catani, F. Fontannaz,J.P. Guillet and E. Pilon, JHEP **05** 028 (2002).

[4] C. Deluca (CDF collaboration), arXiv:hep-ex/09052201 (2009).

[5] V. Abazov *et al.* (DØ collaboration), Phys. Lett. B**666** 435 (2008).

[6] V. Abazov *et al.* (DØ collaboration), accepted for publication in Phys. Rev. Lett., FERMILAB-PUB-**08-582-E**.

[7] T. Stavrera and J. Owens, Phys. Rev. D**79** 054017 (2009).

[8] D. Acosta *et al.* (CDF collaboration), Phys. Rev. Lett. **95** 022003 (2005).

[9] T. Binoth, J.P. Guillet, E. Pilon and M. Werlen, Eur. Phys. J. **C16** 311 (2000).

[10] C. Balazs, E.L. Berger, S. Mrenna and C.P. Yuan, Phys. Rev. D**57** 6934 (1998)

[11] T. Sjostrand *et al.*, Comp. Phys. Comm. **135** 238 (2001).

Future Pprospects for the Measurement of Direct Photons at the LHC

David Joffe on behalf of the ATLAS and CMS Collaborations
Southern Methodist University Department of Physics, 75275 Dallas, Texas, USA

DOI: http://dx.doi.org/10.3204/DESY-PROC-2009-03/Joffe

The energy scale of the LHC, as well as the large size of the ATLAS and CMS experiments, present new challenges for the detection of direct photons as well as new opportunities for physics observations. This talk will examine the direct photon energy and momentum measurement capabilities of the two general purpose experiments for both converted and unconverted photons, and the resulting prospects for diphoton physics channels such as H$\rightarrow \gamma\gamma$.

The Large Hadron Collider at CERN will provide an exciting new window into the physics of high-energy direct photons. For the LHC running at design energy, direct photon production (for photons with $p_{\mathrm{T}} \geq 20$ GeV) is expected to have a cross-section of 100 nb, and for photon pairs (both with $p_{\mathrm{T}} \geq 20$ GeV) the expected cross-section is 15 nb. The diphoton channel is also considered to be key for the discovery of a low-mass (120-140 GeV) Standard Model Higgs boson, but the relatively low diphoton branching ratio ($\sim 10^{-3}$) means that the effective cross-section for H$\rightarrow \gamma\gamma$ at the LHC is of the order of 20 fb, 6 orders of magnitude below the non-resonant direct diphoton cross-section. The ability to observe such a rare decay requires a very good understanding of the detectors. The relatively narrow (MeV-scale) decay width of the Standard Model Higgs boson in the low-mass range means that the measured width of any Higgs boson signal will be dominated by the detector resolution; such a signal should be visible as a small enhancement of the diphoton mass spectrum, requiring a detector resolution of order $\sigma(\mathrm{m})/\mathrm{m} \sim 1\%$, as well as a high level of rejection of jets and neutral pions. This note will attempt to summarize the energy and momentum measurement capabilities of the two general purpose experiments, and their ability to observe H$\rightarrow \gamma\gamma$ and other rare TeV-scale diphoton decays such as those predicted in universal extra-dimension theories [1].

1 The ATLAS and CMS detectors at the LHC

The ATLAS and CMS detectors are located at the Large Hadron Collider (LHC) at CERN. For proton-proton collisions, the LHC is designed to run with $\sqrt{s}$=14 TeV, with a bunch crossing frequency of 25 ns. The design luminosity for the LHC is 10^{33} cm^{-2} s^{-1} for low-luminosity initial operation, and 10^{34} cm^{-2} s^{-1} for high-luminosity operation. These energies and luminosities require a very large size and fine granularity for the detectors. Because of the unprecedented amount of material in the tracking detectors, particular attention has to be paid to material effects, particularly to photon conversions in the context of this paper. Further information

about the construction and expected performance of the general-purpose experiments can be found in refs. [2] and [3] for ATLAS, and refs. [4], [5] and [6] for CMS.

The dimensions of the ATLAS detector are 25 m in height and 44 m in length, with a 2 Tesla solenoidal magnetic field in the inner volume, and an overall mass of the detector of approximately 7000 tonnes. The CMS detector is more compact, but also more massive; it measures 15 m in height and 21 m in length, with a 4 Tesla solenoidal magnetic field and an overall mass of ∼12500 tonnes. The most crucial components of the detectors for direct photon measurements are the electromagnetic (EM) calorimeters; ATLAS and CMS use very different techniques in their calorimetry. The ATLAS EM calorimeter is a Liquid Argon (LAr) sampling calorimeter with three sampling layers with the middle sampling layer consisting of 86,400 channels. The CMS EM calorimeter is composed of ∼80,000 lead tungstate ($PbWO_4$) scintillating crystals. These two very different calorimeters each have their own strengths; the ATLAS LAr calorimeter, with its multiple sampling layers, is able to reconstruct shower shapes in all three dimensions, thereby providing excellent electron and photon identification, while the CMS EM calorimeter has extremely accurate energy reconstruction.

Both the ATLAS and the CMS EM calorimeters are highly segmented. The front layer of the ATLAS calorimeter is comprised of narrow strips with widths of 0.003 in η, and middle and back layers with widths of 0.025 in ϕ. The CMS EM calorimeter has a granularity of $\Delta\eta \times \Delta\phi = 0.0175 \times 0.0175$ in the barrel region. This fine segmentation is crucial for accurate reconstruction of narrow diphoton resonances.

Both the ATLAS and CMS detectors contain multi-layered inner trackers which direct photons must cross before reaching the calorimeters. The material in these inner trackers is substantial; in the case of ATLAS, there is approximately 0.5 radiation lengths of inner-detector material in the central region, and as much as 2 radiation lengths in the region around $|\eta| = 1.7$, and for CMS the numbers range from 0.4 radiation lengths in the central region to as much as 1.5 radiation lengths around $|\eta| = 1.7$. As the probability for photons to convert to e^+e^- pairs is proportional to the number of radiation lengths traversed, this large amount of material means that direct photons have a probability of $\sim 20\%$ of converting in the central region, and up to a maximum probability of $\sim 60\%$ of converting at larger $|\eta|$. Figure 1 shows probabilities of conversion for photons in the ATLAS detector as well as the positions of photons converted in the ATLAS inner detector as simulated in GEANT4 [3]; the tracking layers are clearly visible.

Efficiently reconstructing and identifying photon conversions while preserving the best possible EM calorimeter resolution is a challenging task. Figure 2 shows the efficiency of reconstruction of photon conversions in the ATLAS detector as a function of conversion radius and η, for photons from H$\rightarrow \gamma\gamma$ decay. In this figure, the points with error bars show the total reconstruction efficiency, the solid histograms show the conversion vertex reconstruction efficiency, and the dashed histograms show the single-track conversion reconstruction efficiency. Using both tracks with silicon hits, as well as tracks from the Transition Radiation Tracker (TRT), the total reconstruction efficiency ranges from $\sim 90\%$ for photons converting within 15 cm of the beam axis, to $\sim 60\%$ for conversions occuring more than 70 cm from the beam axis; these efficiencies are mostly independent of $|\eta|$ over the geometrical acceptance of the TRT which extends only to $|\eta| \sim 2$.

Both ATLAS and CMS have extremely good energy resolution in their EM calorimeters. For direct photons with energies of 100 GeV, the ATLAS LAr calorimeter has a resolution of better than 1.4% at $|\eta| = 1.075$ [3], while the CMS EM calorimeter has a resolution of better than 0.7% for 120 GeV electrons, after corrections [4]. Figure 3 shows the energy resolution for photons in the ATLAS detector as a function of energy and η; Figure 4 shows the energy resolution

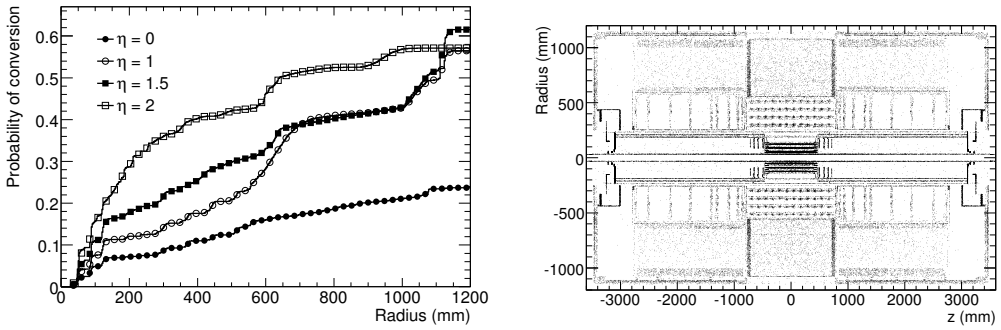

Figure 1: Probability of a high-energy photon to convert as a function of radius for different values of η in the ATLAS inner detector (left) and graphical representation of the ATLAS inner detector material in the (z-R) plane as obtained from the true positions of simulated photon conversions in minimum-bias events (right) [3].

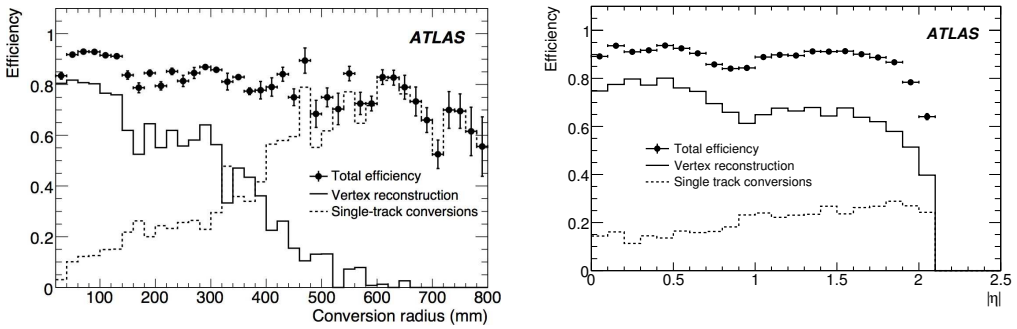

Figure 2: Reconstruction efficiencies for converted photons from H→ $\gamma\gamma$ decays in the ATLAS detector as a function of conversion radius (left) and pseudorapidity (right) [3].

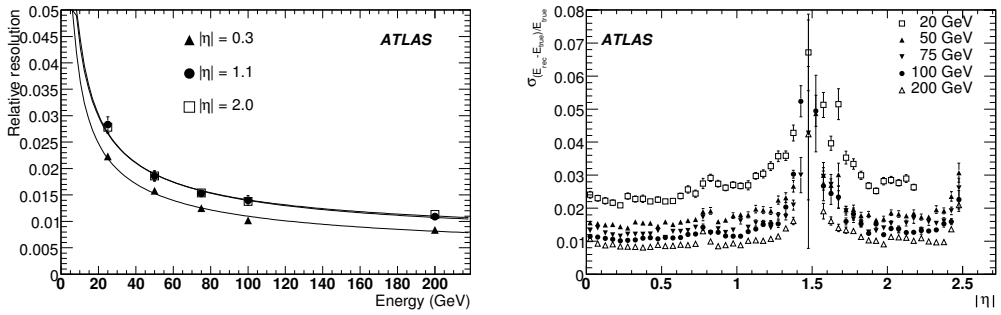

Figure 3: Energy resolution for all photons in ATLAS (left) and energy resolutions for photons in ATLAS (5×5 clusters) (right). [3]

of the ATLAS detector for 100 GeV photons (normalised to the true energy) and the energy resolution for unconverted barrel photon showers in CMS with $R9 \geq 0.943$, reconstructed in a 5×5 crystal array, as a function of energy, together with the fitted parametrization. The equation for the energy resolution in the barrel of the ATLAS LAr calorimeter can be expressed as $\sigma_E/E \approx 10\%/\sqrt{E} + 0.7\%$ [3], while for CMS the relation is given as $(\sigma/E)^2 = (3.6\%/\sqrt{E})^2 + (185(\text{MeV})/E)^2 + (0.66\%)^2$ [4]. The different equations for the relative resolutions reflect the very different properties of the two calorimeters.

To first order, the angular resolution for direct photons is determined by the granularity of the calorimeters; Figure 5 shows the angular resolution for photons in the ATLAS detector; the polar angle resolution from calorimeter layers 1 and 2 for 100 GeV photons is $\sigma_\theta \sim 50$ mrad$/\sqrt{E}$. The angular resolution in ATLAS is improved for the case of converted photons due to the high segmentation of the tracker, particularly in polar angle. For converted photons, the polar angle can be determined to a resolution of 0.3 mrad for photons originating from H$\rightarrow \gamma\gamma$ decays with $m_H = 120$ GeV [3].

Due to the large hadronic backgrounds present at the LHC, rejections of the order of 10^3 or better are required to separate direct photons from jets and neutral pions; this rejection is done primarily through the shower shapes. If isolation cuts are included, rejection rates of up to 10^4 may be achieved [3].

Photons may be reconstructed with quite high efficiencies in the LHC detectors; for photons from H$\rightarrow \gamma\gamma$ with $p_{\mathrm{T}} \geq 50$ GeV simulated in the ATLAS detector, the efficiency ranges from 80-90% depending on the selection cuts. This efficiency is largely independent of $|\eta|$, with the exception of the region between the barrel and end-cap of the LAr calorimeter around $|\eta| = 1.5$, where it is somewhat reduced [3]. These high efficiencies can be extended up to the TeV energy range; Figure 6 shows the photon reconstruction efficiency for high-p_{T} photons from the decay of gravitons with a mass of 500 GeV in the ATLAS detector [3].

2 Physics with diphoton resonances

The decay of the Standard Model Higgs boson into two photons is considered a key discovery channel and has been extensively studied in simulation by both ATLAS and CMS. Given the narrow Higgs boson width expected in the low-mass range (115-150 GeV), the shape of the signal is dominated by the energy and angular resolution of the detectors; the observed width of a Higgs boson with a mass of 120 GeV in the ATLAS detector is $\sim$1.4 GeV, with half of the signal events having at least one converted photon.

Due to the large number of diphoton events coming from QCD direct photon production, as well as the misidentification of jets and neutral pions as photons, the Standard Model Higgs boson signal will be observable only on top of a large background; this background is on the order of $\sim$100 times larger than the signal for the inclusive analyses. Thus, sizable statistics will be required to observe any Higgs boson signal with significances of 3σ or more. For the ATLAS standard cut-based combined analysis [3], 10 fb^{-1} of integrated luminosity allows for an observed signal significance of between 3σ and 4σ, depending on the Higgs boson mass. For the CMS optimized analysis [5], a 5σ signal may be observed with between 7 fb^{-1} and 15 fb^{-1} of data, depending on the Higgs boson mass.

The significance vs. luminosity plot for the H$\rightarrow \gamma\gamma$ signal in ATLAS, as well as an invariant mass plot of the signal, are shown in Fig. 7. In the significance plot the solid circles correspond to the sensitivity of the inclusive analysis using event counting. The solid triangles linked

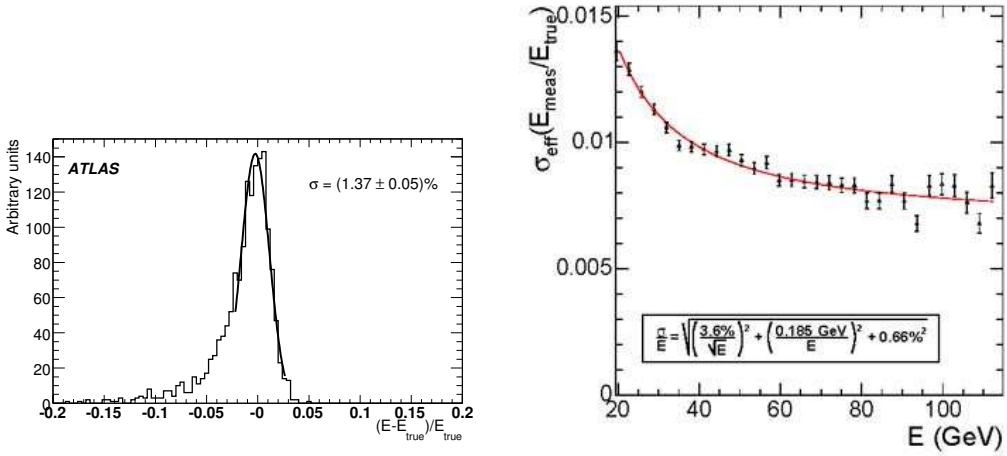

Figure 4: Difference between measured and true energy at E = 100 GeV for ATLAS photons with $|\eta| = 1.075$ (left) [3] and CMS barrel photon energy resolution (right) [4].

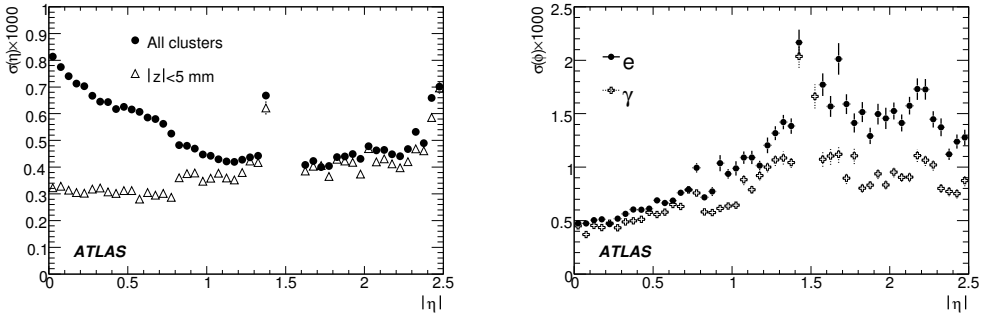

Figure 5: Resolution of η position measurement in ATLAS from calorimeter layers 1 and 2 combined for 100 GeV photons (left) and expected ϕ position resolution in ATLAS as a function of $|\eta|$ for electrons and photons with an energy of 100 GeV. [3]

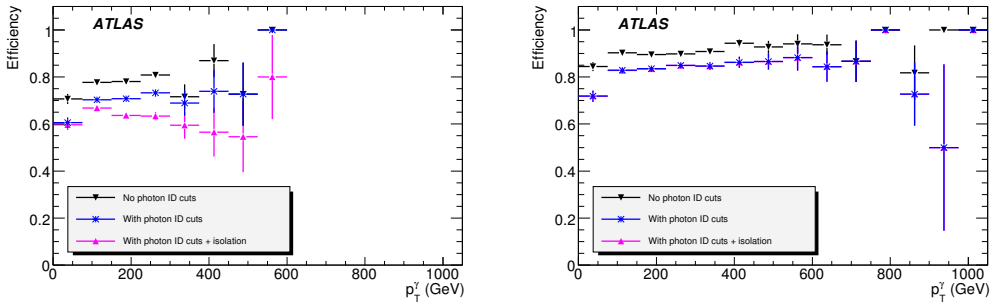

Figure 6: ATLAS photon reconstruction efficiency in the 500 GeV graviton sample as a function of p_T for end-cap (left) and barrel (right) calorimeters. [3]

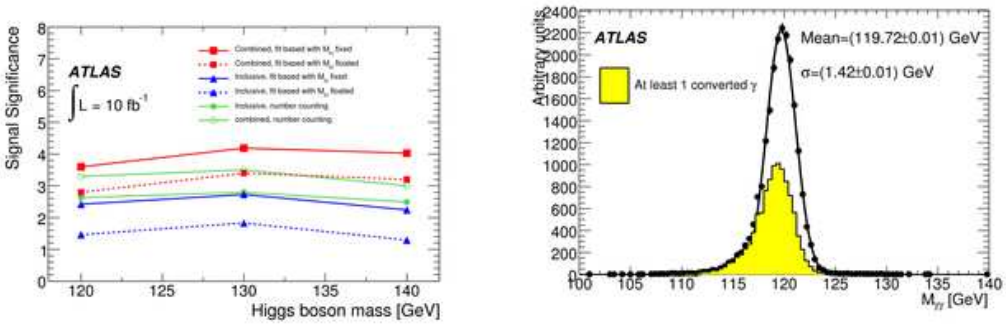

Figure 7: Expected signal significance for a Higgs boson in ATLAS using the H→ $\gamma\gamma$ decay for 10 fb^{-1} of integrated luminosity as a function of the mass (left) and ATLAS diphoton invariant mass distribution after trigger and identification cuts (right); the shaded histogram corresponds to events with at least one converted photon [3].

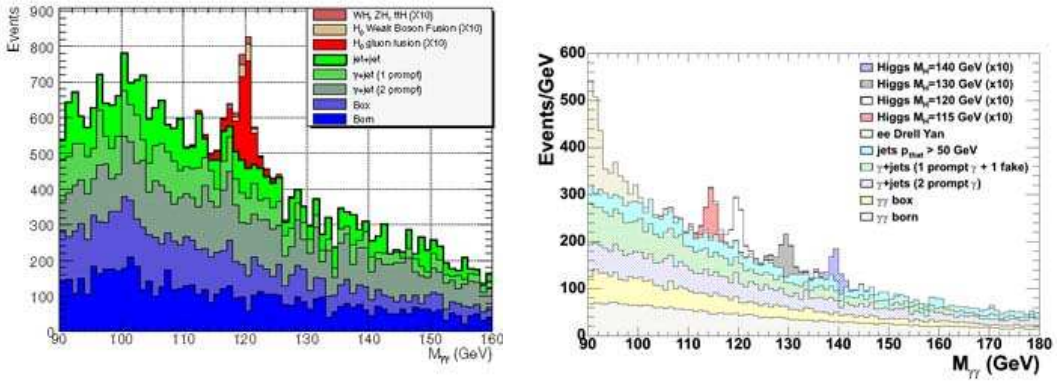

Figure 8: CMS diphoton mass distribution for H→ $\gamma\gamma$ signal and background after the application of a kinematic neural-net analysis (left), and a cut-based analysis (right) [5].

with solid and dashed lines correspond to the sensitivity of the inclusive analysis by means of one dimensional fits, with a fixed and floating Higgs boson mass, respectively. The solid squares linked with solid and dashed lines correspond to the maximum sensitivity that can be attained with a combined analysis. The CMS invariant mass plots for various diphoton channels, including the H→ $\gamma\gamma$ channel, can be seen in Fig. 8, showing the results of a categorized kinematic neural net analysis on the left for all barrel events with a neural net output greater than 0.85, and the cut-based analysis on the right. The neural net analysis is normalised to an integrated luminosity of 7.7 fb^{-1}, and the cut-based analysis to 1 fb^{-1}; the Higgs boson signal in all CMS plots is scaled upwards by a factor 10 for visibility.

As an example of the decay of a high-mass exotic resonance into two photons, both ATLAS and CMS have studied the possibility of observing the diphoton decay of the TeV-scale graviton [1]. Plots showing the significance of discovery for various integrated luminosities in both the H→ $\gamma\gamma$ channel and the G→ $\gamma\gamma$ channel for CMS can be seen in Fig. 9; the left part of the

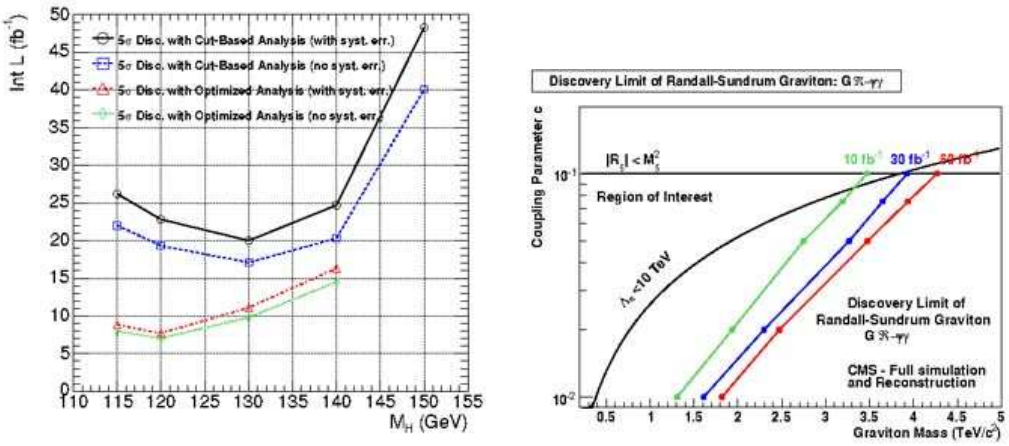

Figure 9: Integrated luminosity needed for a 5σ discovery in CMS for the H$\rightarrow \gamma\gamma$ channel (left) and the reach of the CMS experiment in the search for a heavy graviton decaying into the diphoton channel (right) [5].

G$\rightarrow \gamma\gamma$ discovery limit curve is the region where the significance exceeds 5σ. The limit is shown as a function of the coupling parameter c and the graviton mass for integrated luminosities of 10, 30 and 60 fb^{-1}; the signal is generally observable for graviton masses up to 2 TeV, and may be observable for masses as high as 4 TeV depending on the strength of the coupling parameter.

References

[1] L. Randall and R. Sundrum, Phys. Rev. Lett. **83**, 3370 (1999).

[2] ATLAS Collaboration (G. Aad *et al.*), JINST **3**:S08003 (2008).

[3] ATLAS Collaboration, Expected Performance of the ATLAS Experiment, Detector, Trigger and Physics, CERN-OPEN-2008-020, Geneva (2008).

[4] CMS Collaboration, CMS Physics TDR: Volume I, Detector Performance and Software, CERN-LHCC-2006-001, Geneva (2006).

[5] CMS Collaboration, CMS Physics TDR: Volume II, Physics Performance, CERN-LHCC-2006-021, Geneva (2006).

[6] CMS Collaboration (S Chatrchyan *et al.*), JINST **3**:S08004 (2008).

Chapter 5

Photon Structure

Convenors:

M. Klasen (Grenoble) and I. Vorobiev (Carnegie-Mellon)

Experimental Review of Photon Structure Function Data

Richard Nisius

Max-Planck-Institut für Physik (Werner-Heisenberg-Institut), Föhringer Ring 6, D-80805 München, Germany, E-mail: Richard.Nisius@mpp.mpg.de

DOI: http://dx.doi.org/10.3204/DESY-PROC-2009-03/Nisius

The present knowledge of the structure of the photon is presented based on results obtained by measurements of photon structure functions at e^+e^- collider. Results are presented both for the QED structure of the photon as well as for the hadronic structure, where the data are also compared to recent parametrisations of the hadronic structure function $F_2^\gamma(x, Q^2)$. Prospects of future photon structure function measurements, especially at an International Linear Collider are outlined.

1 Introduction

The measurements of photon structure functions have a long tradition since the first of such measurements was performed by the PLUTO Collaboration in 1981. The investigations concern the QED structure of the photon as well as the hadronic structure. For the hadronic structure function $F_2^\gamma(x, Q^2)$ the main areas of interest are the behavior at low values of x and the evolution with the momentum scale Q^2, which is predicted by QCD to be logarithmic. The experimental information is dominated by the results from the four LEP experiments.

This review is based on earlier work [1, 2] and as an extension provides a number of updated figures, together with a comparison of the experimental data with new parametrisations of $F_2^\gamma(x, Q^2)$ that became available since then. Only results on the structure of quasi-real photons are discussed here. The structure of virtual photons and the corresponding measurements of effective structure functions are detailed in [3].

2 Structure function measurements

The photon can fluctuate into a fermion–anti-fermion state consistent with the quantum numbers of the photon and within the limitations set by the Heisenberg uncertainty principle. These fluctuations are favored, i.e. have the longest lifetimes, for high energetic photons of low virtuality. If such a fluctuation of the photon is probed, the photon reveals its structure. Using this feature, measurements of photon structure functions are obtained from the differential cross-section of the deep-inelastic electron-photon scattering[1] process sketched in Figure 1. In this process the structure of the quasi-real photon, γ, radiated off an electron from one beam is

[1] In this paper, the term electron encompasses positrons throughout.

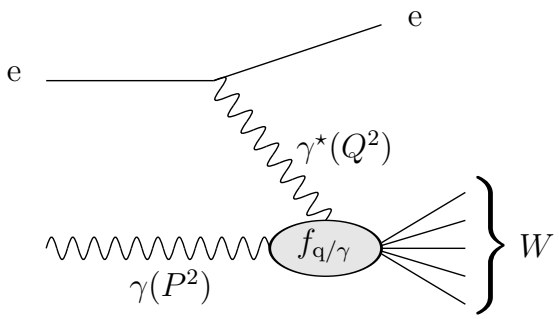

Figure 1: A sketch of the deep-inelastic electron-photon scattering process.

probed by the virtual photon, $\gamma^\star$. The $\gamma^\star$ is radiated off an electron from the other beam such that this electron is deflected into the detector.

The detailed formalism for the scattering of photons of arbitrary virtualities can be found in [1]. For deep-inelastic electron-photon scattering on quasi-real photons the equation reduces to the well known formula:

$$\frac{d^2\sigma_{\mathrm{e}\gamma\to\mathrm{e}X}}{dxdQ^2} = \frac{2\pi\alpha^2}{x\,Q^4}\left[\left(1+(1-y)^2\right)F_2^\gamma(x,Q^2) - y^2F_{\mathrm{L}}^\gamma(x,Q^2)\right] \text{ with: } x = \frac{Q^2}{P^2+Q^2+W^2}$$

The absolute values of the four momentum squared of the virtual and quasi-real photons are denoted Q^2 and P^2, with $P^2 \ll Q^2$. The symbols x and y denote the usual dimensionless variables of deep-inelastic scattering, W denotes the invariant mass of the final state excluding the electrons, and α is the fine structure constant. The flux of the incoming photons, $f_\gamma(z,P^2)$, where z is the fraction of the electron energy carried by the photon, is usually taken from the equivalent photon approximation, EPA. At leading order, the structure function $F_2^\gamma(x,Q^2)$ is proportional to the parton content, $f_{q/\gamma}$, of the photon, and therefore reveals the structure of the photon. In the region of small y studied, $y \ll 1$, the contribution of the term containing $F_{\mathrm{L}}^\gamma(x,Q^2)$ is small, and is usually neglected.

2.1 QED structure

The QED structure function $F_{2,\mathrm{QED}}^\gamma$ of the photon is measured from deep-inelastic electron-photon scattering events in which a pair of muons is produced by the $\gamma\gamma^\star$ system. Figure 2 shows the present world data on this measurement. An update is expected when the ongoing L3 analysis [4] is finalized. The data span a range of about two orders of magnitude in Q^2 and have a precision down to about 5%. With this precision, the treatment of the small but non-zero virtuality of the quasi-real photon is important, as are electroweak radiative corrections to the deep inelastically scattered electron. Unfortunately, the treatment of these corrections is different for the various experiments, see [1] for details.

In addition to the measurements of $F_{2,\mathrm{QED}}^\gamma$ further structure functions [5] have been obtained by analyzing the azimuthal correlation between the scattering plane of the deep inelastically scattered electron and the plane spanned by the muon pair. Good agreement between data and predictions has been found. Also the scattering of two highly virtual photons has been analyzed, and an indirect evidence for the presence of interference terms has been found [6]. Both these measurements are discussed in detail in [1].

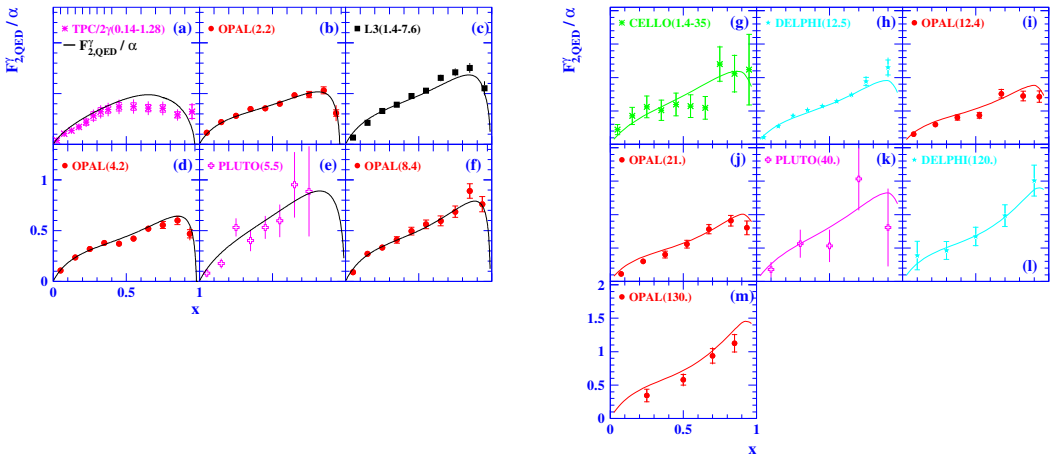

Figure 2: The world date on the QED structure function $F^{\gamma}_{2,\mathrm{QED}}$ of the photon.

Apart from shining light on the QED structure of the photon the determination of the QED structure functions of the photon serves two experimental purposes. It is a test bed for preparing the tools for the measurements of $F_2^{\gamma}(x, Q^2)$, and it sets the limit of precision that could possibly be obtained in the more complex case of hadronic final states.

2.2 Hadronic structure

The measurement of the hadronic structure of the photon is hampered by the fact that for measuring x, the invariant mass W of the hadronic final state has to be reconstructed. This is because the energy of the incoming quasi-real photon is not known, and consequently, reconstruction of x from the deep-inelastically scattered electron alone is impossible. Since the hadronic state is not perfectly described by the available Monte Carlo models, and part of the final state hadrons are scattered into the forward regions of the detectors which are only equipped with electromagnetic calorimeters, or even outside of the detector acceptance, the precision with which x can be obtained is limited, especially at large values of W and correspondingly low values of x. At large values of Q^2 the value of x is determined much more precisely, and also the data are much better described by the Monte Carlo models. The problems at low values of x are partly overcome by sophisticated unfolding techniques, and by constraining the Monte Carlo Models by utilizing combined LEP data on the hadronic final state [7]. Still the Monte Carlo description at low values of x is one of the dominant uncertainties in this measurement, such that some LEP experiments even refrained from assigning an error due to this model dependence, but published results for individual models instead.

There is one important difference between the structure function F_2^p of the proton and $F_2^{\gamma}(x, Q^2)$ of the photon, which originates in the different evolution equations the two have to obey. Whereas F_2^p results from a solution of a homogeneous evolution equation, the photon structure function $F_2^{\gamma}(x, Q^2)$ follows an inhomogeneous evolution equation, and therefore

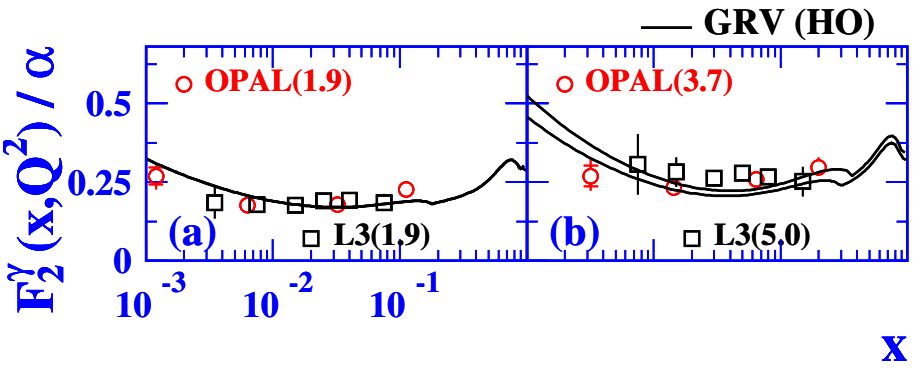

Figure 3: The world data on $F_2^\gamma(x,Q^2)$ unfolded on a logarithmic x scale.

receives two contributions. These are frequently called the hadron-like component, stemming from the general solution of the homogeneous evolution equation as for F_2^p, and the point-like component, resulting from a specific solution of the inhomogeneous evolution equation. This results in different scaling violations of F_2^p and $F_2^\gamma(x,Q^2)$.

The present status of the measurements of $F_2^\gamma(x,Q^2)$ is shown in Figures 3 and 4. Starting from the data used in [1] the TPC/2γ results are dropped. This is due to their unusual shape as a function of x for low values of Q^2, and consequently very bad χ^2/dof values wrt. several parametrisations of $F_2^\gamma(x,Q^2)$, see Tables 4 and 5 in [1]. In addition, all preliminary and not yet published LEP data have been excluded, and the newly published data from ALEPH [8] and L3 [9, 10] have been added. The data span a region in Q^2 from 1.9–780 GeV^2 and in x from 0.0025–0.98. The experimental precision is clearly dominated by the results from the LEP experiments. There is a nice consistency between the results obtained at LEP1 energies (open symbols) with the ones from LEP2 energy data (filled symbols), which at the same Q^2 illuminate different detector parts. The higher order parametrisation from the GRV group [11], which has been obtained before many of the shown datasets became available, still gives a fair description of the data.

Since the end of LEP there has been quite some effort made in obtaining new parametrisations of $F_2^\gamma(x,Q^2)$ by several groups of authors, namely CJK [12], AFG [13] and SAL [14]. Some important ingredients of the various theoretical analyses are given below, for further details the reader is referred to the original publications.

The CJK parametrisation is based on all available $F_2^\gamma(x,Q^2)$ data for $Q^2 > 1$ GeV^2 including the TPC/2γ data and the preliminary DELPHI data taken at LEP1 energies. Various ways of treating the heavy quark, i.e. c, b, contributions are explored by the CJK group, leading to various parametrisations. The parametrisation used in this review is the CJK NLO model, which is based on the ACOT(χ) variable-flavor number scheme. For brevity, it is denoted by CJK(HO). The parametrisation is evaluated in the DIS$_\gamma$ factorization scheme, the starting scale of the evolution as obtained from the fits is $Q_0^2 = 0.765$ GeV^2, and the strong coupling constant, α_s, uses $\Lambda_4^{\overline{\rm MS}} = 280$ MeV.

The AFG(HO) parametrisation is based on a subset of data, namely LEP1 data at medium Q^2, including the preliminary DELPHI data. The heavy quarks are taken to be massless, however, m_q^2/Q^2 corrections to the direct component of $F_2^\gamma(x,Q^2)$ are included in the calculation.

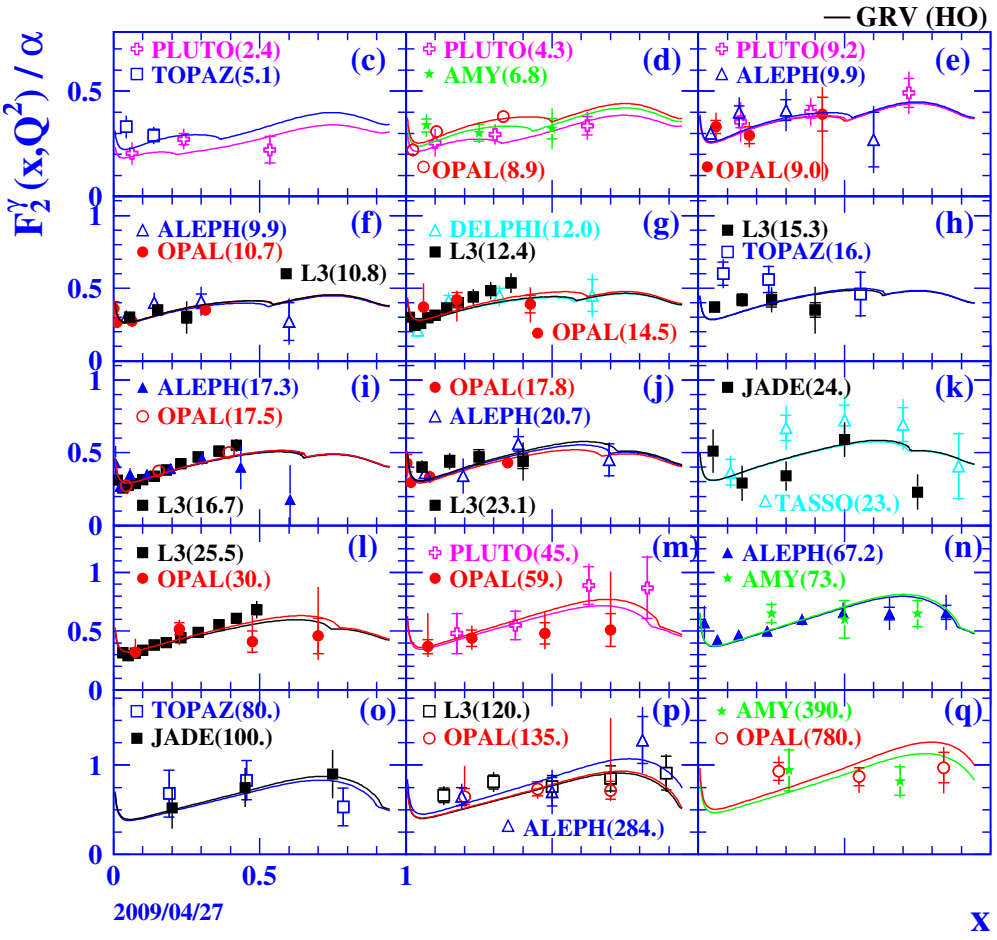

Figure 4: The world data on $F_2^\gamma(x,Q^2)$ unfolded on a linear x scale.

The AFG(HO) parametrisation is evaluated in the $\overline{\rm MS}$ factorization scheme, the starting scale for the evolution is $Q_0^2 = 0.7$ GeV^2, again as obtained from the fit, and $\Lambda_4^{\overline{\rm MS}} = 300$ MeV is used.

Finally, the SAL(HO) parametrisation is based on a completely different theoretical concept, namely the assumption of the Gribov factorization, which relates the total $\gamma\gamma$ cross-section to the total γp and pp cross-sections. At small values of x the following relation between the proton and photon structure functions is obtained: $F_2^\gamma = \frac{\sigma_{\gamma p}(W)}{\sigma_{pp}(W)} \cdot F_2^p \approx 0.43 \cdot F_2^p$, where the numerical value stems from the Donnachie-Landshoff parametrisation of the total cross-sections at large values of W. Consequently, the input data of $F_2^\gamma(x,Q^2)$ used, i.e. all published $F_2^\gamma(x,Q^2)$ data except the TPC/2γ data, are augmented by the ZEUS F_2^p results at $x < 0.01$ and $Q^2 < 100$ GeV^2. In the few overlapping regions the F_2^p data are much more precise than the corresponding $F_2^\gamma(x,Q^2)$ data. In addition the F_2^p results extend to much lower values

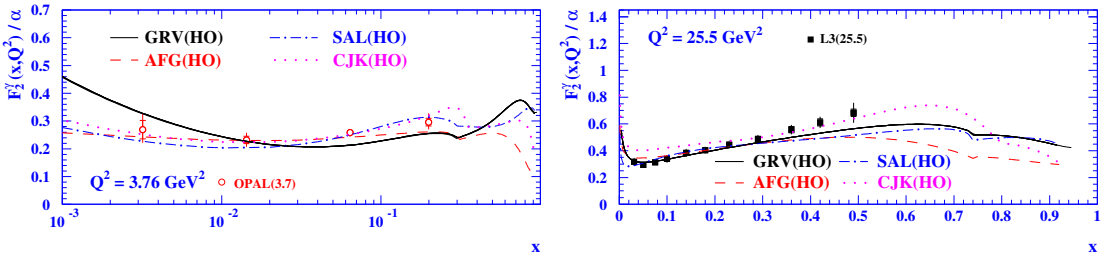

Figure 5: Parametrisations of $F_2^\gamma(x, Q^2)$ compared to LEP data at $Q^2 = 3.7$ and 25.5 GeV^2.

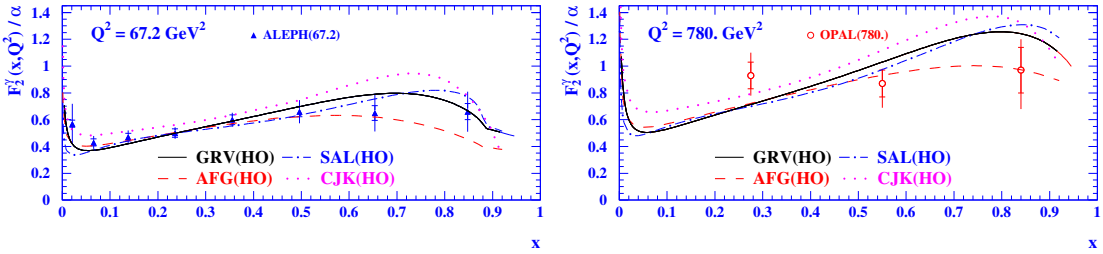

Figure 6: Parametrisations of $F_2^\gamma(x, Q^2)$ compared to LEP data at $Q^2 = 67.2$ and 780 GeV^2.

of x. Consequently, the F_2^p data determine the low-x behavior of $F_2^\gamma(x, Q^2)$. In addition, in an attempt to better constrain the gluon distribution of the photon, also ZEUS di-jet data measured in photo-production events are used. However, it turns out that in the present kinematical region of the data the sensitivity to the gluon from the photon is rather limited. The data are strongly dominated by contributions of quarks from the photon, while the fraction of events originating from gluons from the photon is very small. The relative division of data used for the fit for $F_2^\gamma(x, Q^2)/F_2^p$/di-jet is about 7/5/1. For the treatment of heavy quarks the SAL group derives an interpolation between the fixed flavor number scheme at low values of Q^2 and the zero-mass variable flavor number scheme at high values of Q^2. The SAL(HO) parametrisation is evaluated in the DIS$_\gamma$ factorization scheme, the starting scale of the evolution is chosen to be $Q_0^2 = 2.0$ GeV^2, and α_s uses $\Lambda_4^{\overline{\rm MS}} = 330$ MeV.

Despite their rather different theoretical framework all groups face a common difficulty, they have problems fitting the preliminary DELPHI data taken at LEP1 and/or LEP2 energies. Finally, this results in an inflation of the experimental error, or even in exclusion of this data.

The fact that all parametrisations are based on different theoretical prejudice and use different experimental input to their fits makes it even more interesting to compare their behavior to the experimental data. This comparison can be seen in Figures 5 and 6 for a number of Q^2 values spanning almost the entire experimental range of the LEP data. The data shown at $Q^2 = 3.7/25.5/67.2/780$ GeV^2 were partly used, (+), in the respective fit, and partly not, (-), where the corresponding patterns are for CJK(HO): (+/-/+/+), for AFG(HO): (+/-/-/-) and finally for SAL(HO): (+/-/+/+). Amongst the three new parametrisations CJK(HO) exhibits the steepest slope at low values of x, with increasing differences to the other parametrisations for increasing Q^2 values. At medium values of x the parametrisations are closer to each other,

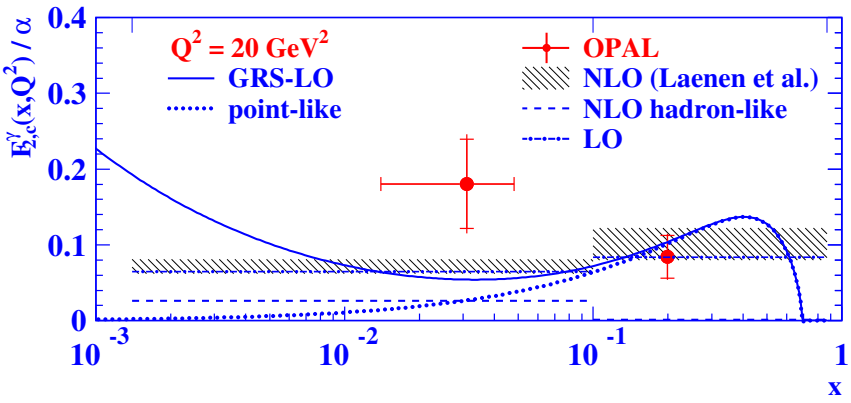

Figure 7: The measurement of $F_{2,c}^{\gamma}$ from OPAL.

and at high values the differences increase again, with the AFG(HO) $\overline{\text{MS}}$ parametrisation always yielding the lowest prediction. For comparison, the old GRV prediction generally lies in the middle of the new predictions, but for the lowest x values at $Q^2 = 3.7$ GeV^2. Overall there is good agreement of the new parametrisations with the data at $Q^2 = 3.7/67.2/780$ GeV^2 given the experimental uncertainties. The largest differences are seen for the data at $Q^2 = 25.5$ GeV^2, which have not been used by any of the fits and which have rather small uncertainties assigned. Here the most notable difference to the data is at low values of x when compared to the CJK(HO) prediction, which is significantly higher than the data.

Not only the inclusive structure function $F_2^{\gamma}(x, Q^2)$ has been obtained experimentally, but also its charm component, $F_{2,c}^{\gamma}$, has been measured [15]. The charm part has been identified from the inclusive data by selecting charmed D mesons. The analysis makes use of the small phase space of the pion in the decay $D^{\star} \rightarrow D^{\circ}\pi$, which leads to a peaking structure in the distribution of the mass difference of the $D^{\star}$ and D° mesons. The result for $F_{2,c}^{\gamma}$ in two bins of x and unfolded to $Q^2 = 20$ GeV^2 is shown in Figure 7 in comparison to several theoretical predictions. Shown are the purely perturbative calculations from [16, 17] at leading and next-to-leading order, NLO, and for the two data bins of x. This clearly shows that NLO corrections to $F_{2,c}^{\gamma}$ are small. In addition shown is the functional form of the leading order GRS [18] parametrisation for both the full $F_{2,c}^{\gamma}$ and the point-like part alone. The separation in x of the data has been such as to experimentally separate the point-like part, concentrated at large values of x, from the hadron-like part, dominating at low values of x, as can be seen e.g. by comparing to the GRS curves. Figure 7 demonstrates that the high x region is adequately described by the point-like NLO prediction with only α_s and the mass of the charm-quark, m_c, as free parameters. The behavior at low values of x is experimentally less well constrained. However, it can not be accommodated by the point-like part alone, e.g. as given by the GRS parametrisation, thereby suggesting a non-vanishing hadron-like part at low values of x also for $F_{2,c}^{\gamma}$. The uncertainty on the measurement at low values of x is relatively big, but largely dominated by statistical uncertainties (inner error bars), so a measurement of $F_{2,c}^{\gamma}$ by the other LEP experiments is highly desirable.

One key feature of $F_2^{\gamma}(x, Q^2)$ is the logarithmic behavior with Q^2 as predicted by perturbative QCD. It is the point-like contribution discussed above that results in positive scaling

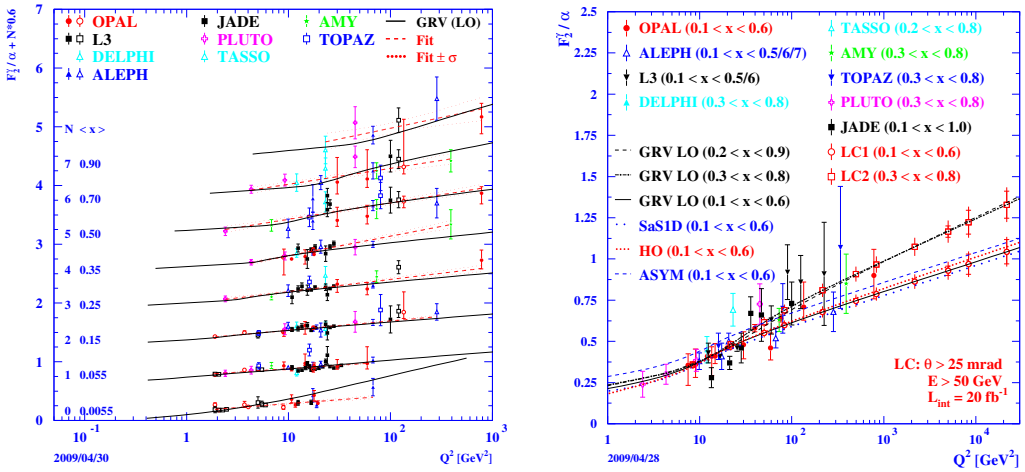

Figure 8: Positive scaling violations of $F_2^\gamma(x, Q^2)$ for various regions in x (left), and prospects for a measurement of the Q^2 evolution of $F_2^\gamma(x, Q^2)$ at an ILC (right).

violations of $F_2^\gamma(x, Q^2)$ for all values of x, in contrast to the proton, which exhibits negative scaling violations at high values of x, due to gluon radiation, and positive scaling violations at low values of x, due to pair creation of quark–anti-quark pairs. See [1] for a detailed assessment of this issue.

The positive scaling violations of $F_2^\gamma(x, Q^2)$ for all values of x is born out by the data as can be seen from Figure 8(left). The data are displayed as a function of Q^2 in bins of x, where each data point is shown at its nearest average x value chosen from the list on the left. In addition, for better visibility, the data points for the various bins in x are separated by constant offsets, N. Linear fits to the data of the form $F_2^\gamma(Q^2) = a + b \ln Q^2$ have been performed. The fitted values of b are significantly above zero for all bins of x, and a clear trend for increasing slope with increasing values of x is observed.

What about the future of $F_2^\gamma(x, Q^2)$ after LEP. There are two obvious candidates for future measurements, a short term opportunity is the measurement at the B-factories, where the Babar and Belle experiments are operating. The longer term option is the measurement of $F_2^\gamma(x, Q^2)$ at an International Linear Collider, ILC. The general prospects for Two-Photon physics at an ILC can be found in [19]. The higher beam energy and luminosity available at the ILC compared to LEP will allow to extend the available phase in Q^2 by about two orders in magnitude. For a detailed investigation of neutral current interactions see [20]. As an example, the measurement of the Q^2 evolution of F_2^γ at medium values of x at an e^+e^- collider is shown in Figure 8(right). At the ILC also novel features can be investigated like the measurement of the flavor decomposition of F_2^γ by exploring the exchange of W and Z bosons [21].

2.3 Summary

The measurement of photon structure functions is an interesting field of research. Unfortunately, experimentally it has come to a halt after the shut-down of LEP, since so far it has not been pursued at the B-factories and the prospects for an ILC are still uncertain.

Up to now, a wealth of data has been analyzed both in terms of the QED structure, and for the hadronic structure of the photon. In this short review only a part of the investigations could be discussed in detail. Concerning the QED structure, $F_{2,\mathrm{QED}}^{\gamma}$ was investigated, as well as additional structure functions from azimuthal correlations and the interactions of two virtual photons. For the hadronic structure the emphasis is on $F_2^{\gamma}(x, Q^2)$ and especially its behavior at low values of x and the logarithmic scaling violations with Q^2. In addition, the charm contribution $F_{2,\mathrm{c}}^{\gamma}$ has been measured, and the interaction of two virtual photons were investigated.

I strongly hope that the future will bring us additional information from the B-factories and an ILC.

Acknowledgments

I like to thank the organizers for this interesting conference, and for giving me the opportunity to refresh my memory on this interesting field of research.

References

[1] R. Nisius, Phys. Rep. **332** 165–317, (2000), updated figures available at: *http://www.mppmu.mpg.de/˜nisius/welcomeaux/struc.html*.

[2] R. Nisius, Nucl. Phys. B Proc. Suppl. **117** 258–261 (2003).

[3] K. Sasaki, this conference.

[4] K. Dehmelt, L3 Collaboration, this conference.

[5] R. Nisius and M.H. Seymour, Phys. Lett. **B452** 409–413 (1999).

[6] G. Abbiendi *et al.*, OPAL Collaboration, Eur. Phys. J. **C11** 409–425 (1999).

[7] The LEP Working Group for Two–Photon Physics, ALEPH, L3 and OPAL, Eur. Phys. J. **C23** 201–223 (2002).

[8] A. Heister *et al.*, ALEPH Collaboration, Eur. Phys. J. **C30** 145–158 (2003).

[9] M. Acciarri *et al.*, L3 Collaboration, Phys. Lett. **B483** 373–386 (2000).

[10] P. Achard *et al.* L3 Collaboration, Phys. Lett. **B622** 249–264 (2005).

[11] M. Glück, E. Reya and A. Vogt, Phys. Rev. **D46** 1973–1979 (1992).

[12] F. Cornet, P. Jankowski and M. Krawczyk, Phys. Rev. **D70** 093004 (2004).

[13] P. Aurenche, M. Fontannaz and J.Ph. Guillet, Eur. Phys. J. **C44** 395–409 (2005).

[14] W. Slomiński, H. Abramowicz and A. Levy, Eur. Phys. J. **C45** 633–641 (2006).

[15] G. Abbiendi *et al.*, OPAL Collaboration, Phys. Lett. **B539** 13–24 (2002).

[16] E. Laenen, S. Riemersma, J. Smith and W.L. van Neerven, Phys. Rev. **D49** 5753–5768 (1994).

[17] E. Laenen and S. Riemersma, Phys. Lett. **B376** 169–176 (1996).

[18] M. Glück, E. Reya and M. Stratmann, Phys. Rev. **D51** 3220–3229 (1995).

[19] R. Nisius, hep-ex/9811024 (1998).

[20] A. Vogt, Nucl. Phys. B Proc. Suppl. **82** 394–399 (2000).

[21] A. Gehrmann-De Ridder, H. Spiesberger, and P.M. Zerwas, Phys. Lett. **B469** 259–262 (1999).

Heavy Quark and Target Mass Effects on the Virtual Photon in QCD

Yoshio Kitadono[1], *Takahiro Ueda*[2], *Tsuneo Uematsu*[3], *Ken Sasaki*[4*]

[1]Hiroshima University, Higashi Hiroshima 739-8526, Japan
[2]University of Tsukuba, Tsukuba 305-8571, Japan
[3]Kyoto University, Kyoto 606-8501, Japan
[4]Yokohama National University, Yokohama 240-8501, Japan

DOI: http://dx.doi.org/10.3204/DESY-PROC-2009-03/Sasaki

We analyze the heavy quark mass effects on the virtual photon structure functions up to the NLO in the framework based on the operator product expansion supplemented by the mass-independent renormalization group method. We also investigate the target mass corrections for the virtual photon structure functions up to the NNLO.

1 Introduction

In e^+e^- collision experiments, the cross section for the two-photon processes $e^+e^- \to e^+e^- +$ hadrons, shown in Fig.1, dominates over other processes such as the annihilation process $e^+e^- \to \gamma^* \to$ hadrons at high energies. In particular, the two-photon processes in the double-tag events, where one of the virtual photon is very far off shell (large $Q^2 \equiv -q^2$) while the other is close to the mass shell (small $P^2 \equiv -p^2$), can be viewed as deep-inelastic electron-photon scattering and provide us the information on the structure of the photon.

In fact, the study of the photon structure has been an active field of research [1]. Recently we analyzed the photon structure function F_2^γ up to the next-to-next-to-leading order (NNLO) and F_L^γ up to the next-to-leading order (NLO) in perturbative QCD (pQCD) in the kinematical region $\Lambda^2 \ll P^2 \ll Q^2$, where Λ is the QCD scale parameter [2]. The interest of studying the photon structure in this kinematical region is that a definite prediction of the whole structure function, its shape and magnitude, may become possible. However, the above investigation of F_2^γ and F_L^γ has two flaws that need to be fixed. One is that we have treated all the quarks as massless. The other is that we have considered the logarithmic corrections arising from QCD higher-order effects, but ignored all the power corrections of the form $(P^2/Q^2)^k$ $(k = 1, 2, \cdots)$ coming from target mass effects.

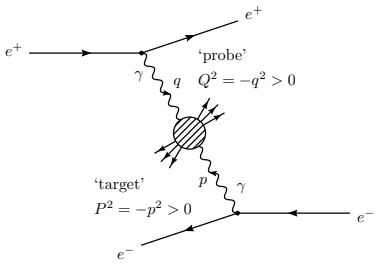

Figure 1: Deep-inelastic scattering on a virtual photon in the e^+e^- collider experiments

*Presented by Ken Sasaki

In this paper we discuss two topics which we have investigated recently, namely, heavy quark mass effects [4] and target mass effects [3] on the virtual photon structure functions. Heavy quark mass effects for the real photon were studied in the literature [5, 6].

2 Master formula for the moments with heavy quark

For the first topic, heavy quark mass effects, we consider the system which consists of n_f-1 massless quarks and one heavy quark $q^{n_f}=q_H$ together with gluons and photons. The extension to the case with more heavy quarks is straightforward. Applying the operator product expansion (OPE) for the product of two electromagnetic currents at short distance we get

$$\begin{aligned} i\int d^4x e^{iqx}T(J_\mu(x)J_\nu(0)) &= \left(g_{\mu\nu}-\frac{q_\mu q_\nu}{q^2}\right)\sum_{\substack{n=0\\ n=\text{even}}}\left(\frac{2}{Q^2}\right)^n q_{\mu_1}\cdots q_{\mu_n}\sum_i C^i_{L,n}O_i^{\mu_1\cdots\mu_n} \\ &+ \left(-g_{\mu\lambda}g_{\nu\sigma}q^2+g_{\mu\lambda}q_\nu q_\sigma+g_{\nu\sigma}q_\mu q_\lambda-g_{\mu\nu}q_\lambda q_\sigma\right) \\ &\times \sum_{\substack{n=2\\ n=\text{even}}}\left(\frac{2}{Q^2}\right)^n q_{\mu_1}\cdots q_{\mu_{n-2}}\sum_i C^i_{2,n}O_i^{\lambda\sigma\mu_1\cdots\mu_{n-2}}+\cdots\ , \end{aligned} \tag{1}$$

where $C^i_{L,n}$ and $C^i_{2,n}$ are the coefficient functions which contribute to the structure functions F_L^γ and F_2^γ, respectively, and $O_i^{\mu_1\cdots\mu_n}$ and $O_i^{\lambda\sigma\mu_1\cdots\mu_{n-2}}$ are spin-n twist-2 operators (hereafter we often refer to $O_i^{\mu_1\cdots\mu_n}$ as O_i^n). The sum on i runs over the possible twist-2 operators and $\cdots$ represents other terms with irrelevant coefficient functions and operators.

Let us denote n_f-1 massless quarks as a column vector $\psi=(q^1,q^2,\cdots,q^{n_f-1})^{\rm T}$. Then the relevant operators in quark sector are light-flavour-singlet quark (L), heavy quark (H) and light-flavour-nonsinglet quark (NS) operators as follows:

$$O_L^{\mu_1\cdots\mu_n} = i^{n-1}\overline{\psi}\gamma^{\{\mu_1}D^{\mu_2}\cdots D^{\mu_n\}}\mathbf{1}\psi-\text{trace terms}\ , \tag{2a}$$

$$O_H^{\mu_1\cdots\mu_n} = i^{n-1}\overline{q}_H\gamma^{\{\mu_1}D^{\mu_2}\cdots D^{\mu_n\}}q_H-\text{trace terms}\ , \tag{2b}$$

$$O_{NS}^{\mu_1\cdots\mu_n} = i^{n-1}\overline{\psi}\gamma^{\{\mu_1}D^{\mu_2}\cdots D^{\mu_n\}}(Q^2_{ch}-\langle e^2\rangle_{(n_f-1)}\mathbf{1})\psi-\text{trace terms}\ , \tag{2c}$$

where $\{\ \ \}$ means complete symmetrization over the Lorentz indices $\mu_1\cdots\mu_n$ and D^μ denotes covariant derivative. In quark operators O_L^n and O_{NS}^n given in Eqs.(2a) and (2c), $\mathbf{1}$ is an $(n_f-1)\times(n_f-1)$ unit matrix, Q^2_{ch} is the square of the $(n_f-1)\times(n_f-1)$ quark-charge matrix, and $\langle e^2\rangle_{(n_f-1)}=(\sum_i^{n_f-1}e_i^2)/(n_f-1)$ is the average charge squared of massless quarks. Note that we have a relation $\mathrm{Tr}(Q^2_{ch}-\langle e^2\rangle_{(n_f-1)}\mathbf{1})=0$. Due to this relation, the operator O_{NS}^n does not mix with operators O_L^n and O_H^n. In addition to the above quark operators, the gluon (O_G^n) and photon (O_γ^n) operators are also relevant and appear in the r.h.s. of Eq.(1). Here the importance of inclusion of the heavy quark operator should be stressed. We treat the heavy quark in the same way as the light quarks and assume that both heavy and light quarks are radiatively generated from the photon target. In contrast, in the case of the nucleon target, heavy quarks are treated as radiatively generated from the gluon and light quarks.

The coefficient function $C^i_{k,n}(k=2,L)$ corresponding to the operators $O_i^n(i=L,H,G,NS,\gamma)$ satisfies the following mass-independent renormalization group (RG) equation:

$$\left[\mu\frac{\partial}{\partial\mu}+\beta(g)\frac{\partial}{\partial g}+\gamma_m(g)m\frac{\partial}{\partial m}-\gamma_n(g,\alpha)\right]_{ij}C^j_{k,n}\left(\frac{Q^2}{\mu^2},\frac{m^2}{\mu^2},\bar{g}(\mu^2),\alpha\right)=0\ , \tag{3}$$

with $i,j = L,H,G,NS,\gamma$. Here $\beta(g)$ and $\gamma_m(g)$ are the beta function and the anomalous dimension for the mass operator, respectively, and $\gamma_n(g,\alpha)$ is a 5×5 anomalous dimension matrix. To the lowest order in the QED coupling constant α, this matrix has the following form:

$$\gamma_n(g,\alpha) \equiv \begin{pmatrix} \hat{\gamma}_n(g) & 0 \\ \boldsymbol{K}_n(g,\alpha) & 0 \end{pmatrix}, \quad \hat{\gamma}_n \equiv \begin{pmatrix} \gamma_{LL}^n & \gamma_{HL}^n & \gamma_{GL}^n & 0 \\ \gamma_{LH}^n & \gamma_{HH}^n & \gamma_{GH}^n & 0 \\ \gamma_{LG}^n & \gamma_{HG}^n & \gamma_{GG}^n & 0 \\ 0 & 0 & 0 & \gamma_{NS}^n \end{pmatrix}, \tag{4}$$

and $\boldsymbol{K}_n(g,\alpha)$ is the four-component row vector

$$\boldsymbol{K}_n = (K_L^n, K_H^n, K_G^n, K_{NS}^n) , \tag{5}$$

which describes the mixing between the photon operator and the remaining hadronic operators. The solution to the RG equation (3) is given by

$$C_{k,n}^i\left(\frac{Q^2}{\mu^2}, \frac{m^2}{\mu^2}, \bar{g}(\mu^2), \alpha\right) = \left\{ T\exp\left[\int_{\bar{g}(Q^2)}^{\bar{g}(\mu^2)} dg \frac{\gamma_n(g,\alpha)}{\beta(g)}\right]\right\}_{ij} C_{k,n}^j\left(1, \frac{\bar{m}^2(Q^2)}{Q^2}, \bar{g}(Q^2), \alpha\right) , \tag{6}$$

with $\bar{g}(\mu^2)$ being effective running QCD coupling constant and $\bar{m}(Q^2)$ is the running heavy quark mass evaluated at Q^2.

The matrix elements of the relevant operators O_i^n sandwiched by the photon states with momentum p are expressed as

$$\begin{aligned} \langle\gamma(p)|O_i^{\mu_1\cdots\mu_n}|\gamma(p)\rangle &= A_n^i\Big(\frac{P^2}{\mu^2}, \frac{\bar{m}^2(\mu^2)}{\mu^2}, \bar{g}(\mu^2)\Big) \{p^{\mu_1}\cdots p^{\mu_n} - \text{trace terms}\} \\ &\equiv A_n^i\Big(\frac{P^2}{\mu^2}, \frac{\bar{m}^2(\mu^2)}{\mu^2}, \bar{g}(\mu^2)\Big) \{p^{\mu_1}\cdots p^{\mu_n}\}_n , \end{aligned} \tag{7}$$

with $i = L,H,G,NS,\gamma$, and A_n^i is the reduced photon matrix element with μ being the renormalization point. Then the moment sum rules for the virtual photon structure functions F_2^γ and F_L^γ are given by $(k = 2, L)$

$$\begin{aligned} M_k^\gamma(n,Q^2,P^2) &= \int_0^1 dx x^{n-2} F_k^\gamma(x,Q^2,P^2) \\ &= \sum_{i=L,H,G,NS,\gamma} A_n^i\Big(\frac{P^2}{\mu^2}, \frac{\bar{m}^2(\mu^2)}{\mu^2}, \bar{g}(\mu^2)\Big) C_{k,n}^i\left(\frac{Q^2}{\mu^2}, \frac{m^2}{\mu^2}, \bar{g}(\mu^2), \alpha\right) . \end{aligned} \tag{8}$$

Now using Eq.(6) and choosing $\mu^2 = P^2$, we obtain the master formula for the moments for the case when a heavy quark exists,

$$\begin{aligned} M_k^\gamma(n,Q^2,P^2) &= \sum_{i,j=L,H,G,NS,\gamma} A_n^i\left(1, \frac{\bar{m}^2(P^2)}{P^2}, \bar{g}(P^2)\right) \left\{ T\exp\left[\int_{\bar{g}(Q^2)}^{\bar{g}(P^2)} dg \frac{\gamma_n(g,\alpha)}{\beta(g)}\right]\right\}_{ij} \\ &\quad \times C_{k,n}^j\left(1, \frac{\bar{m}^2(Q^2)}{Q^2}, \bar{g}(Q^2), \alpha\right) . \end{aligned} \tag{9}$$

The heavy quark mass effects appear in the reduced photon matrix element A_n^i and the coefficient function $C_{k,n}^j$ as the running quark mass $\bar{m}$.

3 Heavy quark mass effects in QCD

We focus on the moments $M_2^\gamma(n,Q^2,P^2)$ and consider the heavy quark mass effects up to the NLO. We take the difference between $M_2^\gamma(n,Q^2,P^2)$ and the one for the case when all n_f quarks are massless,

$$\Delta M_2^\gamma(n,Q^2,P^2,\bar{m}^2) = M_2^\gamma(n,Q^2,P^2) - M_2^\gamma(n,Q^2,P^2)\Big|_{\rm massless} . \tag{10}$$

We already know $M_2^\gamma(n,Q^2,P^2)\Big|_{\rm massless}$ (actually, up to the NNLO). The 1-loop (4×4) anomalous dimension matrix $\hat{\gamma}_n^{(0)}$ in hadronic sector in Eq.(4) has four eigenvalues λ_L^n, $\lambda_\pm^n$ and λ_{NS}^n and we find $\lambda_L^n = \lambda_{NS}^n (= \gamma_{\psi\psi}^{(0),n} = \gamma_{NS}^{(0),n})$. Diagonalizing the matrix $\hat{\gamma}_n^{(0)}$, we evaluate $M_2^\gamma(n,Q^2,P^2)$ in Eq.(9) up to the NLO and obtain

$$\begin{aligned}\Delta M_2^\gamma(n,Q^2,P^2,\bar{m}^2) &= \frac{\alpha}{4\pi}\frac{1}{2\beta_0}\Bigg[\sum_{i=\pm,NS}\Delta\mathcal{A}_i^n\left[1-\left(\frac{\alpha_s(Q^2)}{\alpha_s(P^2)}\right)^{d_i^n}\right] \\ &\quad + \sum_{i=\pm,NS}\Delta\mathcal{B}_i^n\left[1-\left(\frac{\alpha_s(Q^2)}{\alpha_s(P^2)}\right)^{d_i^n+1}\right] + \Delta\mathcal{C}^n\Bigg] + \mathcal{O}(\alpha_s) \ ,\end{aligned} \tag{11}$$

where $d_i^n = \lambda_i^n/2\beta_0$ $(i=\pm,NS)$ with $\beta_0 = 11-(2/3)n_f$. In the massive quark limit, $\Lambda^2 \ll P^2 \ll m^2 \ll Q^2$, the explicit expressions of $\Delta\mathcal{A}_i^n, \Delta\mathcal{B}_i^n, \Delta\mathcal{C}^n$ are

$$\Delta\mathcal{A}_{NS}^n = -12\beta_0 e_H^2(e_H^2 - \langle e^2\rangle_{n_f})(\Delta\tilde{A}_{nG}^\psi/n_f), \tag{12a}$$

$$\Delta\mathcal{A}_\pm^n = -12\beta_0 e_H^2\langle e^2\rangle_{n_f}(\Delta\tilde{A}_{nG}^\psi/n_f)\frac{\gamma_{\psi\psi}^{(0),n}-\lambda_\mp^n}{\lambda_\pm^n-\lambda_\mp^n}, \tag{12b}$$

$$\Delta\mathcal{B}_{NS}^n = 0, \qquad \Delta\mathcal{B}_\pm^n = 0, \qquad \Delta\mathcal{C}^n = 12\beta_0 e_H^4(\Delta\tilde{A}_{nG}^\psi/n_f) \ , \tag{12c}$$

where e_H is the heavy quark charge, $\langle e^2\rangle_{n_f} = \sum_{i=1}^{n_f} e_i^2/n_f$ is the average squared charge and

$$\begin{aligned}\Delta\tilde{A}_{nG}^\psi/n_f &= 2\Bigg[-\frac{n^2+n+2}{n(n+1)(n+2)}\ln\frac{\bar{m}^2}{P^2} + \frac{1}{n} - \frac{1}{n^2} \\ &\quad + \frac{4}{(n+1)^2} - \frac{4}{(n+2)^2} - \frac{n^2+n+2}{n(n+1)(n+2)}\sum_{j=1}^{n}\frac{1}{j}\Bigg] .\end{aligned} \tag{13}$$

We see from Eq. (11) that in our approach, using the OPE and the RG equation, the heavy quark mass effects start to appear at the NLO, but not at the LO. Also for the longitudinal structure function $F_L^\gamma(x,Q^2,P^2)$, heavy quark mass effects do not appear in the LO ($\mathcal{O}(\alpha)$).

4 Numerical analysis

The structure functions of the virtual photon are derived from the double-tag measurements of the reaction $e^+e^- \to e^+e^-+$ hadrons. So far there exist only two experimental results

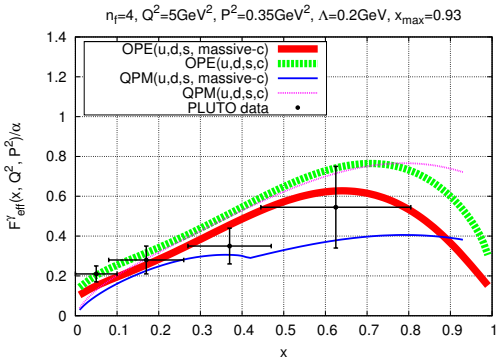

Figure 2: QCD and QPM predictions for $F_{\rm eff}^{\gamma}$ vs. PLUTO data

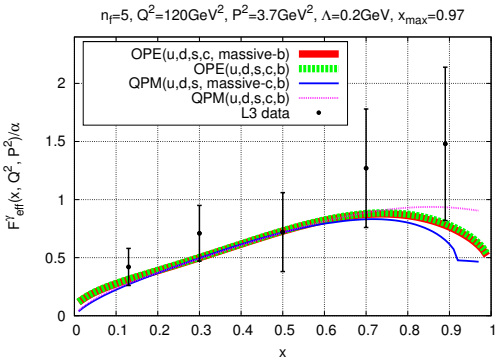

Figure 3: QCD and QPM predictions for $F_{\rm eff}^{\gamma}$ vs. L3 data

reported: one from the PLUTO Collaboration [7] and the other from the L3 Collaboration [8]. Both collaborations measured an effective photon structure function

$$F_{\rm eff}^{\gamma}(x,Q^2,P^2) = F_2^{\gamma}(x,Q^2,P^2) + \frac{3}{2}F_L^{\gamma}(x,Q^2,P^2)\ . \tag{14}$$

We evaluate $F_{\rm eff}^{\gamma}$ up to the NLO and compare our theoretical predictions with these data. The PLUTO (L3) data are at $Q^2 = 5$ (120) GeV^2 and $P^2 = 0.35$ (3.7) GeV^2. Therefore, we assume that the active flavours are u, d, s (massless) plus c (heavy) for the case of PLUTO and u, d, s, c (massless) plus b (heavy) for L3. We take the following values of the quark masses as inputs:

$$m_c = 1.3 \text{ GeV} \quad \text{(for PLUTO)}, \qquad m_b = 4.2 \text{ GeV} \quad \text{(for L3)}. \tag{15}$$

We plot $F_{\rm eff}^{\gamma}(x,Q^2,P^2)$ for $Q^2 = 5$ GeV^2 and $P^2 = 0.35$ GeV^2 together with the PLUTO data in Fig. 2. The thick red solid (green dashed) line represents the NLO QCD result with (without) charm quark mass effects. We have put $\Lambda = 0.2$ GeV. Although the condition $Q^2 \gg m_c^2$ is not satisfied, the predicted curve with mass effects shows a trend of reducing the "over-estimated" massless QCD calculation.

Also shown in Fig. 2 are the results by Quark Parton Model (QPM). In QPM $F_{\rm eff}^{\gamma}(x,Q^2,P^2)$ is expressed by the following four structure functions as

$$F_{\rm eff}^{\gamma}(x,Q^2,P^2) = \Big(\frac{5}{\widetilde{\beta}^2} - 3\Big)x\left[W_{TT} - \frac{1}{2}W_{TS}\right] + \frac{5}{\widetilde{\beta}^2}x\left[W_{ST} - \frac{1}{2}W_{SS}\right]\ , \tag{16}$$

where W_{TT}, W_{ST}, W_{TS}, and W_{SS} [9, 10] are functions of x and

$$\widetilde{\beta} = \sqrt{1 - \frac{P^2Q^2}{(p\cdot q)^2}}\ , \qquad \beta = \sqrt{1 - \frac{4m^2}{(p+q)^2}}\ , \qquad L = \ln\frac{1+\beta\widetilde{\beta}}{1-\beta\widetilde{\beta}}\ , \tag{17}$$

and charge factors $\delta_\gamma^i (= 3 \times e_i^4)$. The quark mass dependence resides in the parameter β. For the massless case we have $\beta = 1$. The thin blue solid (purple dashed) line represents the QPM result with (without) charm quark mass effects.

Figure 3 shows the results of $F_{\rm eff}^{\gamma}(x,Q^2,P^2)$ for $Q^2 = 120\ {\rm GeV}^2$ and $P^2 = 3.7\ {\rm GeV}^2$ together with the L3 data. In this case the condition $\Lambda^2 \ll P^2 \ll m_b^2 \ll Q^2$ is satisfied. The thick red solid line represents the NLO QCD prediction with bottom quark mass effects while the thick green dashed line shows the massless QCD result. Due to its charge factor, we see that the bottom quark mass effects are almost negligible. Also shown are the QPM results: the case for massive c and b (the thin blue solid line) and the case for massless u, d, s, c and b (the thin purple dashed line).

The heavy quark mass has an effect of reducing the photon structure functions in magnitude. This feature is explained by the suppression of the heavy quark production rate due to the existence of its mass. The kinematical constraint for the heavy quark production $(p+q)^2 \geq 4m^2$ gives $x_{\rm max} = \frac{1}{1+\frac{4m^2}{Q^2}+\frac{P^2}{Q^2}}$ below which the contribution of heavy quark to the structure functions exists and, therefore, the difference between the cases of massive and massless quark emerges above $x_{\rm max}$. This kinematical "threshold" effect is not clearly seen in our analysis since we adopted the framework based on the OPE and took into account only the leading twist-2 operators. But still we see in Fig. 2 that the difference between the two becomes bigger at larger x. It is also noted that the heavy quark mass effects are sensitive to the electric charge of the relevant quark. The photon structure functions depend on the quark-charge factors $\langle e^2 \rangle$ and $\langle e^4 \rangle$. Thus, as we see from Figs. 2 and 3, the up-type heavy quark has larger effects than the down-type heavy quark.

5 Target mass effects

For the case of massless quarks, we have studied in Ref.[2] the virtual photon structure functions $F_2^{\gamma}(x,Q^2,P^2)$ and $F_L^{\gamma}(x,Q^2,P^2)$ in pQCD for the kinematical region $\Lambda^2 \ll P^2 \ll Q^2$. There we have considered the logarithmic corrections arising from QCD higher-order effects, but ignored all the power corrections of the form $(P^2/Q^2)^k \quad (k = 1, 2, \cdots)$ coming either from target mass effects or from higher-twist effects. In fact, if the target is real photon ($P^2 = 0$), there is no need to consider target mass corrections. But when the target becomes off-shell ($P^2 \neq 0$) and for relatively low values of Q^2, contributions suppressed by powers of P^2/Q^2 may become important. Then we need to take into account these target mass contributions. The consideration of target mass effects (TME) is important by another reason. In the case of massless quarks, the maximal value of the Bjorken variable x for the virtual photon target is not 1 but $x_{\rm max} = \frac{1}{1+\frac{P^2}{Q^2}}$, due to the constraint $(p+q)^2 \geq 0$, which is in contrast to the nucleon case where $x_{\rm max} = 1$. The structure functions should vanish at $x = x_{\rm max}$. However, the NNLO QCD results [2] for $F_2^{\gamma}(x,Q^2,P^2)$ as well as $F_L^{\gamma}(x,Q^2,P^2)$ show that the predicted graphs do not vanish but remains finite at $x = x_{\rm max}$. This flaw is coming from the fact that TME have not been taken into account in the analysis.

As the second topic, we show TME for the virtual photon structure functions $F_2^{\gamma}(x,Q^2,P^2)$ up to the NNLO and $F_L^{\gamma}(x,Q^2,P^2)$ up to the NLO in QCD in the framework of the OPE. The photon matrix elements of the relevant traceless operators in the OPE are expressed by traceless tensors. These tensors contain many trace terms so that they satisfy the tracelessness conditions. The basic idea for computing the target mass corrections is to take account of these trace terms in the traceless tensors properly.

The operators which appear in the OPE in Eq.(1) are traceless and have totally symmetric Lorentz indices $\mu_1 \cdots \mu_n$ $(\lambda\sigma\mu_1 \cdots \mu_{n-2})$. Hence $\{p^{\mu_1} \cdots p^{\mu_n}\}_n$, which emerges in the photon

matrix elements of these operators in Eq.(7), is the totally symmetric rank-n tensor formed with the momentum p alone and satisfies the traceless condition $g_{\mu_i\mu_j}\{p^{\mu_1}\cdots p^{\mu_n}\}_n=0$. When we take the spin-averaged photon matrix element of the both sides of Eq.(1), we need to evaluate the contraction between $q_{\mu_1}\cdots q_{\mu_n}$ and the traceless tensors without neglecting any of the trace terms. The results are expressed in terms of Gegenbauer polynomials [11]:

$$q_{\mu_1}\cdots q_{\mu_n}\{p^{\mu_1}\cdots p^{\mu_n}\}_n = a^n C_n^{(1)}(\eta)\ , \tag{18a}$$

$$q_{\mu_1}\cdots q_{\mu_{n-2}}\{p^\lambda p^\sigma p^{\mu_1}\cdots p^{\mu_{n-2}}\}_n = \frac{1}{n(n-1)}\left[\frac{g^{\lambda\sigma}}{Q^2}a^n 2C_{n-2}^{(2)}(\eta)+\frac{q^\lambda q^\sigma}{Q^4}a^n 8C_{n-4}^{(3)}(\eta)\right.$$
$$\left.+p^\lambda p^\sigma a^{n-2}2C_{n-2}^{(3)}(\eta)+\frac{p^\lambda q^\sigma+q^\lambda p^\sigma}{Q^2}a^{n-1}4C_{n-3}^{(3)}(\eta)\right], \tag{18b}$$

where

$$a=-\frac{1}{2}PQ,\quad \eta=-\frac{p\cdot q}{PQ}\ , \tag{19}$$

and $C_n^{(\nu)}(\eta)$'s are Gegenbauer polynomials. Then we obtain the Nachtmann moments [11], the weighted integrals of the structure functions F_2^γ and F_L^γ for the definite spin-n contributions, in stead of the familiar moments of F_2^γ and F_L^γ (see Eq.(8)),

$$M_2^\gamma(n,Q^2,P^2) = \int_0^{x_{\max}} dx\frac{1}{x^3}\xi^{n+1}\left[\frac{3+3(n+1)r+n(n+2)r^2}{(n+2)(n+3)}\right]F_2^\gamma(x,Q^2,P^2), \tag{20}$$

$$M_L^\gamma(n,Q^2,P^2) = \int_0^{x_{\max}} dx\frac{1}{x^3}\xi^{n+1}\left[F_L^\gamma(x,Q^2,P^2)\right.$$
$$\left.+\frac{4P^2x^2}{Q^2}\frac{(n+3)-(n+1)\xi^2P^2/Q^2}{(n+2)(n+3)}F_2^\gamma(x,Q^2,P^2)\right]\ , \tag{21}$$

where r and ξ are defined as

$$r\equiv\sqrt{1-\frac{4P^2x^2}{Q^2}}\ ,\qquad \xi\equiv\frac{2x}{1+\sqrt{1-\frac{4P^2x^2}{Q^2}}}=\frac{2x}{1+r}. \tag{22}$$

The left hand sides of Eqs.(20) and (21) are expressed as

$$M_2^\gamma(n,Q^2,P^2) = \sum_i A_n^i(P^2,g)\ C_{2,n}^i(Q^2,P^2,g), \tag{23}$$

$$M_L^\gamma(n,Q^2,P^2) = \sum_i A_n^i(P^2,g)\ C_{L,n}^i(Q^2,P^2,g)\ , \tag{24}$$

respectively, and are calculable by pQCD. Since the maximal value of x is not 1 but $\frac{1}{1+\frac{P^2}{Q^2}}$, the allowed ranges of r and ξ turn out to be $r_{\min}\le r\le 1$ and $0\le\xi\le 1$, respectively, where $r_{\min}=r(x_{\max})=(1-P^2/Q^2)/(1+P^2/Q^2)$ and $\xi(x_{\max})=1$.

The inversion of the Nachtmann moments can be made to express the structure functions

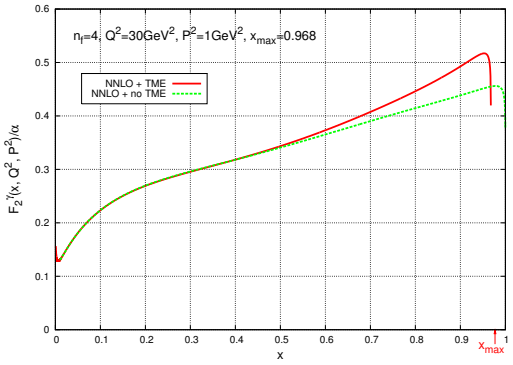

Figure 4: $F_2^\gamma(x, Q^2, P^2)$ with TME.

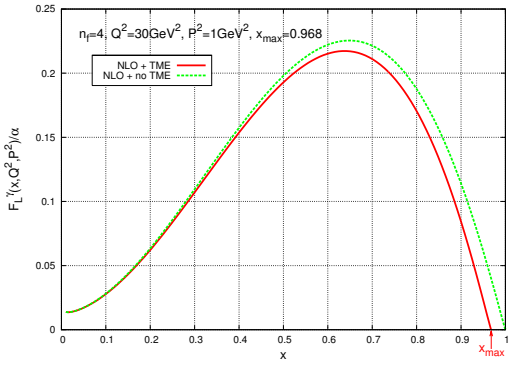

Figure 5: $F_L^\gamma(x, Q^2, P^2)$ with TME.

F_2^γ and F_L^γ explicitly as functions of x, Q^2 and P^2. Introducing the following functions,

$$G(\xi) \equiv \frac{1}{2\pi i}\int_{c-i\infty}^{c+i\infty} dn\, \xi^{-n+1}\frac{M_2^\gamma(n,Q^2,P^2)}{n(n-1)} , \tag{25a}$$

$$H(\xi) \equiv -\frac{dG(\xi)}{d\xi} = \frac{1}{2\pi i}\int_{c-i\infty}^{c+i\infty} dn\, \xi^{-n}\frac{M_2^\gamma(n,Q^2,P^2)}{n} , \tag{25b}$$

$$F(\xi) \equiv -\frac{dH(\xi)}{d\xi} = \frac{1}{2\pi i}\int_{c-i\infty}^{c+i\infty} dn\, \xi^{-n-1}M_2^\gamma(n,Q^2,P^2) , \tag{25c}$$

$$F_L(\xi) \equiv \frac{1}{2\pi i}\int_{c-i\infty}^{c+i\infty} dn\, \xi^{-n-1}M_L^\gamma(n,Q^2,P^2) , \tag{25d}$$

we find

$$F_2^\gamma(x,Q^2,P^2) = \frac{x^2}{r^3}F(\xi) - 6\kappa\frac{x^3}{r^4}H(\xi) + 12\kappa^2\frac{x^4}{r^5}G(\xi) , \tag{26}$$

$$F_L^\gamma(x,Q^2,P^2) = \frac{x^2}{r}F_L(\xi) - 4\kappa\frac{x^3}{r^2}H(\xi) + 8\kappa^2\frac{x^4}{r^3}G(\xi) . \tag{27}$$

Equations (26) and (27) are the final formulas for the photon structure functions F_2^γ and F_L^γ when target mass effects are taken into account.

We plot the graphs of $F_2^\gamma(x, Q^2, P^2)$ and $F_L^\gamma(x, Q^2, P^2)$ as functions of x in Fig.4 and Fig.5, respectively, for the case of $Q^2 = 30\text{GeV}^2$ and $P^2 = 1\text{GeV}^2$ with $x_{\max} = 0.968$. We take $\Lambda = 0.2$ GeV and $n_f = 4$ for the number of active quark flavours. The Bjorken variable x ranges from 0 to $x_{\max}$. We observe that TME become sizable at larger x region. While TME enhances F_2^γ at larger x, it reduces F_L^γ. The target mass correction is of order 10 % when compared at the maximal values for F_2^γ. In the case of F_L^γ, the maximal value is attained in the middle x, where the TME reduces the F_L^γ about 5 %.

6 Summary

Using the framework based on the OPE supplemented by the RG method, we investigated the heavy quark mass effects and also the target mass effects on the virtual photon structure

functions. As for the heavy quark effects, we assumed that heavy quark is generated radiatively from the target photon as well as light quarks. In terms of the OPE terminology, we included the heavy quark operator. Then, the heavy quark mass effects appear in the reduced photon matrix element of this operator and also in the coefficient functions. We evaluated $F_{\rm eff}^{\gamma}(x, Q^2, P^2)$ with quark mass effects up to the NLO and compared our results with the PLUTO and L3 data.. The predicted curve with charm quark mass effects in Fig. 2 shows a right trend of reducing the "over-estimated" massless QCD calculation. As we see in Fig. 3, the bottom quark mass effects are almost negligible due to its charge factor.

When we study the virtual photon structure functions in the framework based on the OPE we also need to consider target mass corrections. We derived the Nachtmann moments for the structure functions and then, by inverting the moments, we obtained the expressions in closed form for $F_2^{\gamma}(x, Q^2, P^2)$ and $F_L^{\gamma}(x, Q^2, P^2)$, both of which include the target mass corrections. We observe that the target mass effects appear at larger x and become sizable near $x_{\rm max}$.

References

[1] M. Krawczyk, A. Zembrzuski and M. Staszel, Phys. Rep. **345** 265 (2001); R. Nisius, Phys. Rep. **332** 165 (2001); M. Klasen, Rev. Mod. Phys. **74** 1221 (2002).

[2] T. Ueda, K. Sasaki and T. Uematsu, Phys. Rev. **D75** 114009 (2007).

[3] Y. Kitadono, K. Sasaki, T. Ueda and T. Uematsu, Prog. Theor. Phys. **121** 495 (2009).

[4] Y. Kitadono, K. Sasaki, T. Ueda and T. Uematsu, Phys. Rev. **D77** 054019 (2008).

[5] M. Glück and E. Reya, Phys. Rev. **D28** 2749 (1983); M. Glück, E. Reya and A. Vogt, Phys. Rev. **D46** 1973 (1992); M. Glück, E. Reya and C. Sieg, Phys. Lett. **B503** 285 (2001); Eur. Phys J. C **20** 271 (2001); M .Glück, E. Reya and I. Schienbein, Phys. Rev. **D60** 054019 (1999); Phys. Rev. **D63** 074008 (2001); I. Schienbein, Annals of Physics, **301** 128 (2002).

[6] F. Cornet, P. Jankowski, M. Krawczyk and A. Lorca, Phys. Rev. **D68** 014010 (2003); F. Cornet, P. Jankowski and M. Krawczyk, Phys. Rev. **D70** 093004 (2004).

[7] Ch. Berger *et al.*, Phys. Lett. **B142** 119 (1984).

[8] M. Acciarri *et al.*, Phys. Lett. **B483** 373 (2000).

[9] V.M. Budnev, I.F. Ginzburg, G.V. Meledin and V.G. Serbo, Phys. Rep. **15** 181 (1974).

[10] K. Sasaki, J. Soffer and T. Uematsu, Phys. Rev. **D66** 034014 (2002).

[11] O. Nachtmann, Nucl. Phys. **B63** 237 (1973); **B78** 455 (1974).

Photoproduction and Photon Structure at HERA

Katharina Müller

Physics Institute, University of Zurich, 8057 Zurich, Switzerland

DOI: http://dx.doi.org/10.3204/DESY-PROC-2009-03/Mueller

Many important QCD tests been performed with the experiments H1 and ZEUS at the HERA ep collider in the photoproduction regime. Differential cross sections of di-jets in photoproduction are shown in direct and resolved enhanced regions and different jet topologies and the sensitivity to different photon PDFs are studied. New results on prompt photons in photoproduction are presented. Further topics address the first measurement of diffractive scattering of quasi-real photons with large momentum transfer which is discussed in the BFKL framework and scaled momentum distributions of charged particles within jets.

1 Introduction

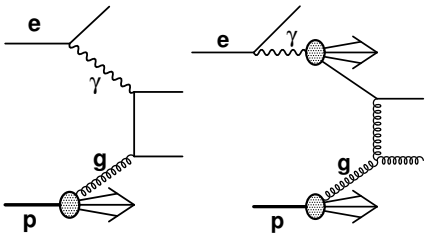

Figure 1: Examples of direct (left) and resolved (right) di-jet photoproduction diagrams in LO QCD.

High energy electron-proton scattering, as it has been carried out at the *ep* collider HERA, is dominated by so-called photoproduction processes, in which a beam lepton emits a quasi real photon which interacts with a parton from the proton. At leading order (LO) quantum chromodynamics (QCD) the scattering process may be classified into two basic types. In direct processes the entire photon interacts with a parton from the proton and there is no remnant in the photon direction, a typical LO diagram is shown in Fig. 1 (left).

In resolved processes, the incoming photon fluctuates into a partonic state out of which a parton with a momentum fraction x_γ participates in the hard scattering process as illustrated in Fig. 1 (right). There is a photon remnant carrying the fraction $1 - x_\gamma$ of the photon energy. Resolved processes are sensitive to the partonic structure of both the photon and the proton. At higher order in perturbative QCD (pQCD) the separation into two classes does not hold anymore.

The large statistics of the HERA data allows detailed tests of pQCD using hadronic jets and prompt (emerging from the hard interactions) photons. The hard scale is provided by the transverse energy E_T of the jet or the photon.

In this contribution recent results of di-jet and prompt photon production in photoproduction at HERA are discussed. In addition, some results with specific final states are presented: the diffractive production of photons with large momentum transfer and the multiplicity distribution of charged particles within jets.

2 Jets in Photoproduction

Experimentally, x_γ is estimated by x_γ^{obs}, which is reconstructed from the measurement of the transverse momenta E_T and pseudorapidities η[1] of the two jets, as

$$x_\gamma^{obs} = (E_T^{jet1} e^{-\eta(jet1)} + E_T^{jet2} e^{-\eta(jet2)})/(2yE_e).$$

Here, y is the inelasticity of the event and E_e the energy of the lepton beam. A pure LO direct process has $x_\gamma^{obs} = 1$ but initial and final state radiation as well as hadronisation may reduce it. Typically the resolved regime is defined to contain x_γ values below 0.75 or 0.8. The x_γ^{obs} distribution as measured in di-jet events, with $E_T^{jet1(2)} > 20(15)$ GeV and $-1 < \eta^{jet1,2} < 3$, is shown in Fig. 2 together with NLO predictions using five different parton density functions (PDFs) for the photon [1]. At high $x_\gamma^{obs} > 0.8$ the predictions are very similar as expected, since there is little sensitivity to the photon PDFs in this region, where towards low x_γ^{obs} the different PDFs vary by up to 70%. The prediction from CJK [2] deviates most from the others and does not describe the data, all other predictions describe the data within the experimental uncertainties.

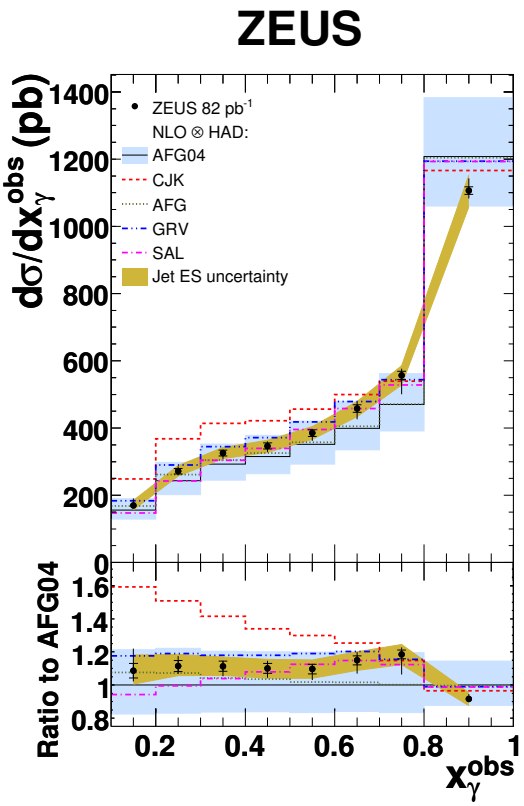

Figure 2: Measured cross section $d\sigma/dx_\gamma^{obs}$ compared with NLO QCD predictions with different PDFs for the photon. [1]

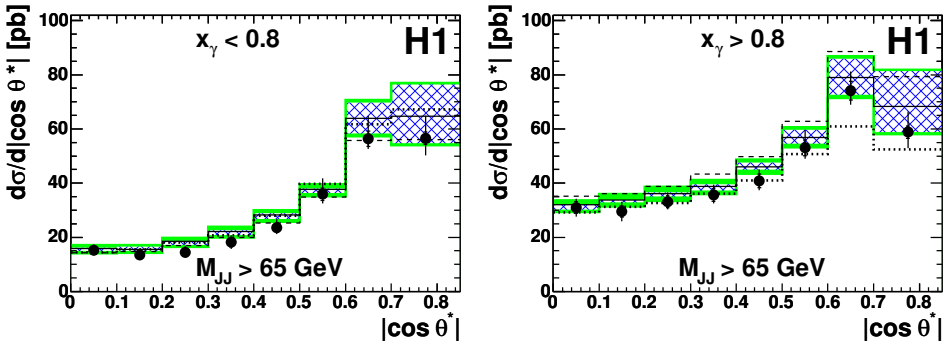

Figure 3: Di-jet cross section as a function of the cosine of the CMS scattering angle ($\cos\Theta^\star$) for a resolved (left) and direct (right) enriched sample [3].

[1]The pseudorapidity η is defined as $\eta = -\ln\tan(\theta/2)$, where θ is the polar angle with respect to the direction of the proton beam.

The concept of resolved and direct interactions of the photon can be tested by measuring the cross section as a function of $\cos\Theta^\star$, the cosine of the scattering angle in the centre of mass system (CMS). Statistically, direct interactions are dominated by quark propagators ($d\sigma/|d\cos\Theta^\star| \propto (1-|\cos\Theta^\star|)$), whereas the gluon propagator ($d\sigma/|d\cos\Theta^\star| \propto (1-|\cos\Theta^\star|)^{-2}$) dominates resolved interaction. Figure 3 shows the cross section as a function of $\cos\Theta^\star$ for di-jet events ($E_T^{jet1(2)} > 25(15)$ GeV and $-0.5 < \eta^{jet1,2} < 2.75$) with an invariant mass of the two jets larger than 65 GeV for a direct ($x_\gamma > 0.8$) and a resolved ($x_\gamma < 0.8$) enriched sample [3]. The cross section in the resolved enriched sample rises more rapidly with $\cos\Theta^\star$ than in the direct sample due to the dominating gluon propagator in the resolved sample.

Many more measurements of inclusive jet, di-jet and multijet production have been performed by the HERA experiments. In general data enriched with direct processes is well described by NLO QCD predictions, whereas resolved enhanced samples are less well described.

As an example, Fig. 4 [1] shows the transverse correlation of the two jets, $d\sigma/d|\Delta\Phi^{ij}|$, with $\Delta\Phi^{ij}$ being the azimuthal angle between the two jets, for x_γ^{obs} above and below 0.75. In the direct enhanced region, $x_\gamma^{obs} > 0.75$, the cross section falls steeply by three orders of magnitude, more steeply than for $x_\gamma^{obs} < 0.75$. The predictions from NLO QCD and the Monte Carlo (MC) generators HERWIG [4] and PYTHIA [5] are compared to the data. The MC predictions are normalised to the measured cross sections.

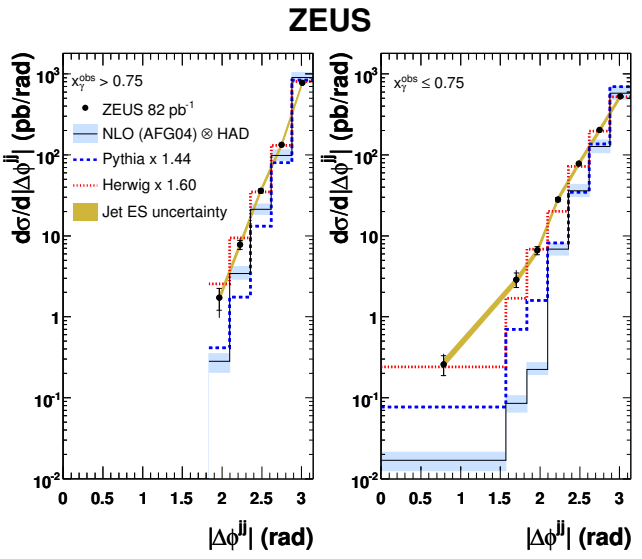

Figure 4: Measured cross section $d\sigma/d|\Delta\Phi^{ij}|$ for $x_\gamma^{obs} > 0.75$ (left) and $x_\gamma^{obs} \le 0.75$ (right). The measurement is compared to NLO predictions and to Monte Carlo predictions from HERWIG and PYTHIA [1].

At high x_γ^{obs}, NLO QCD agrees with data but it falls somewhat steeper, the PYTHIA prediction is very similar to NLO QCD, whereas HERWIG nicely describes the data. For low x_γ^{obs}, the NLO prediction is much too steep and significantly below the data except for the highest bin. Also the prediction from PYTHIA gives a poor description, HERWIG is in reasonable agreement with the data. This shows that the parton shower model as implemented in HERWIG gives a better description of higher order processes than PYTHIA.

As the pseudorapidities of the two jets are sensitive to the momentum distributions of the interacting partons, the cross sections as a function of x_p, the momentum fraction of the parton of the proton ($x_p = (E_T^{jet1} e^{\eta(jet1)} + E_T^{jet2} e^{\eta(jet2)})/(2E_p)$, with E_p the energy of the proton beam), are shown in Fig. 5 for $x_\gamma^{obs} > 0.8$ and two different jet topologies: in the left figure both jets are in the backward ($\eta^{jet1,2} < 1$), in the right figure, both jets are in the forward ($\eta^{jet1,2} > 1$) region [3]. The high x_p region can only be probed if both jets are pointing forward. The NLO QCD prediction describes the data well, except for the highest bin in x_p, where the

PDF uncertainty, indicated by the shaded area, is largest

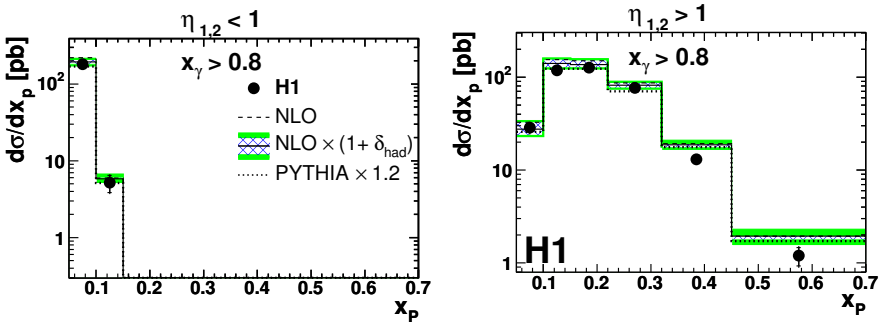

Figure 5: Cross section as a function of x_p for both jets pointing backwards (left) and forward (right). [3]

3 Prompt Photons in Photoproduction

Events with an isolated photon emerging from the hard subprocess $ep \to e\gamma X$ - so called prompt photons - offer an alternative access to study the hard interactions. The measurement with prompt photons require generally lower corrections for hadronisation than measurements relying on jets, since the photons emerge without the hadronisation process by which final state quarks or gluons form a jet. The analysis by H1 uses photoproduction data with an integrated luminosity of 340 pb^{-1}. Events are selected with an isolated photon with transverse energy $6 < E_T^\gamma < 15$ GeV and pseudorapidity $-1.0 < \eta^\gamma < 2.4$. For cross section measurements of prompt photons accompanied by a hadronic jet, the jet has to fulfil $4.5 < E_T^{jet}, -1.3 < \eta^{jet} < 2.3$. To ensure isolation of the photon, the photon has to carry more than 90% of the transverse energy of the jet in which it is contained, i.e. $z = E_T^\gamma / E_T^{photon-jet} > 0.9$. The isolation requirement rejects a large part from the background from decay photons of neutral hadrons. The photon signal is extracted from the sample which still contains background from the decay of neutral hadrons by a multivariate analysis which uses six different shower shape variables.

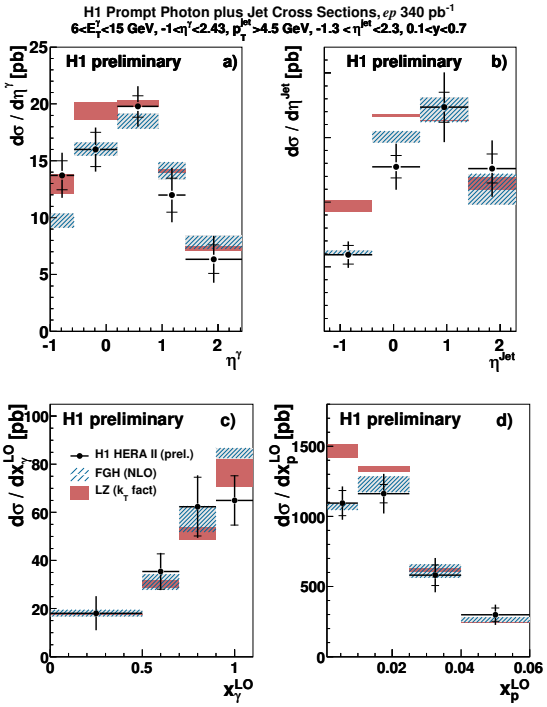

Figure 6: Differential cross sections for prompt photons with a hadronic jet $d\sigma/d\eta^\gamma$ (a), $d\sigma/d\eta^{jet}$ (b), $d\sigma/dx_\gamma^{LO}$(c) and $d\sigma/dx_p^{LO}$ (d).

Cross sections for the production of a prompt photon and a hadronic jet are presented in

Fig. 6 as a function of the variables η^γ, η^{jet}, x_γ^{LO} and x_p^{LO}, where

$$x_\gamma^{LO} = E_T^\gamma(e^{-\eta(\gamma)} + e^{-\eta(jet)})/(2yE_e) \text{ and } x_p^{LO} = E_T^\gamma(e^{\eta(\gamma)} + e^{\eta(jet)})/(2E_p).$$

At LO these definitions correspond to the longitudinal momentum fractions of the parton of the photon and the proton, respectively. The inner error bars correspond to the uncorrelated errors, including the statistical error, the outer error bars include the correlated errors added in quadrature. The results are compared to two sets of calculations, both corrected for hadronisation and multiple interaction effects: a next-to-leading order calculation by Fontannaz-Guillet-Heinrich (FGH) [6, 7] and a calculation based on the k_T-factorisation approach by Zotov-Lipatov (LZ) [8]. Both calculations give a reasonable description of the cross sections as a function of η^γ and x_γ^{LO} while only the NLO calculation well describes the cross sections as a function of η^{jet} of the associated hadronic jet and ${x_p}^{LO}$. Here, the LZ prediction is significantly too high for jets with $\eta^{jet} < 0.5$ which translates also in an overestimated cross section at low x_p. For the inclusive prompt photon measurements it is found that the NLO calculation is slightly below the data for backward photons ($\eta^\gamma < -0.06$). Both calculations have problems describing the transverse correlations between the photon and the jet which are sensitive to higher order effects. In general both calculations give a reasonable description of the different distributions but reveal problems in some kinematic regions.

4 Diffractive Scattering of high t Photons

Diffractive scattering of photons with large four-momentum transfer squared t,$\gamma p \to \gamma Y$, where Y is the proton dissociative system, was studied by H1 using an integrated luminosity of 46.2 pb^{-1} [9]. The analysis of high t photons complements the measurements of exclusive production of vector mesons, ρ, ϕ and J/Ψ [11], at HERA. For the production of photons the calculations are simplified by the absence of a vector meson wave function, it is an experimentally clean process and almost fully perturbatively calculable.

The study of exclusive diffractive processes in presence of a hard scale provides insight into the dynamics of the diffractive exchange. The four-momentum squared transferred at the proton vertex t, provides the relevant scale for the test of pQCD for $|t| >> \Lambda^2_{QCD}$. Diffractive photon scattering at high t can be modelled at sufficiently low values of Bjorken x in the leading log approximation (LLA) BFKL [10] model. Here, the gluon ladder couples to a single parton within the proton. The process is illustrated schematically in Figure 7.

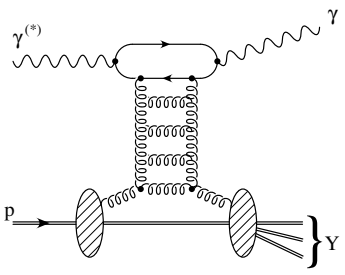

Figure 7: Schematic illustration of the process $\gamma p \to \gamma Y$ in a LLA BFKL approach

Due to the quasi-real nature of the incoming photon ($Q^2 < 0.01$ GeV^2), the transverse momentum of the final state photon, P_T^γ, is entirely transferred by the gluon ladder to the parton of the proton. The separation in rapidity between the parton scattered by the gluon ladder and the final state photon is given by $\Delta\eta \simeq log\hat{s}/(P_T^\gamma)^2)$, where $\hat{s}$ is the invariant mass of the incoming photon and the struck parton.

The data were recorded with the H1 detector during the running period 1999-2000 with an integrated luminosity of 46.2 pb^{-1}. Events are selected with a photon in the backward

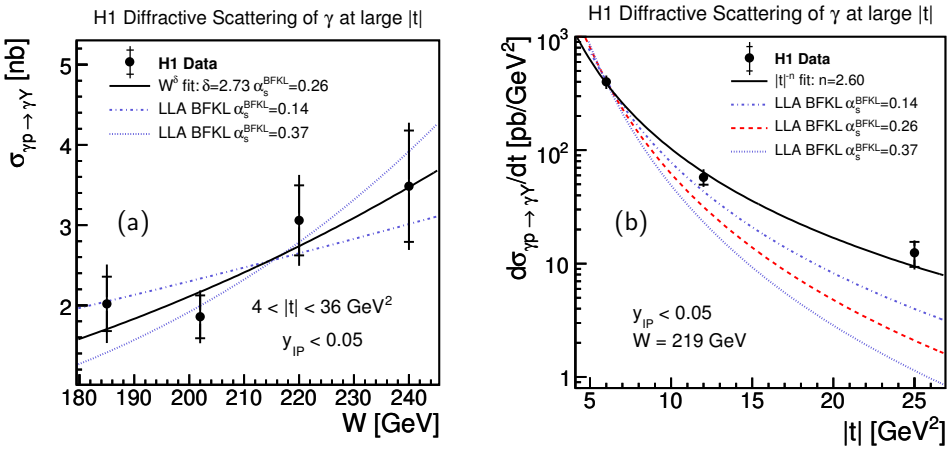

Figure 8: The γp cross section of diffractive scattering of photons as a function of W at $<|t|>= 6.1$ GeV^2 (a) and $|t|$ for $W = 219$ GeV^2 (b) [9].

calorimeter with $E_T^\gamma > 8$ GeV and a polar angle region $153° < \Theta < 177°$ and the scattered electron detected in the electron tagger, which restricts the virtuality of the incoming photon to $Q^2 < 0.01$ GeV^2. Diffractive events are selected by requiring that the event inelasticity $y_{I\!P} \simeq \Sigma_Y(E - P_z)/(2(E_e - E'_e)) < 0.05$ with E the energy and P_z the longitudinal momentum of a particle. The sum runs over all final state particles except the final state photon and the scattered electron. The cut on y_{IP} ensures a large rapidity gap between the photon and the proton dissociative system. The kinematic variable t reconstructs as $t = (P_T^\gamma)^2$ with a resolution of 11%. The γp centre of mass energy, W, is calculated from the energy of the scattered electron (E'_e) as $W \simeq \sqrt{1 - E'_e/E_e)s}$, where s is the ep centre of mass energy, with a relative resolution of 4%. These reconstructions are valid in the approximation of small scattering angles of the electron which is fulfilled for $Q^2 < 0.01$ GeV^2.

The $\gamma p \to \gamma Y$ cross section is shown in Figure 8 a) as a function of W for $4 < |t| < 36$ GeV^2. The cross section rises steeply with W which is usually interpreted as an indication of the presence of a hard sub-process in the diffractive interaction. A power-law dependence of the form $\sigma \propto W^\delta$ is fitted to the measured cross section. The δ value of $\delta = 2.73 \pm 1.02(\text{stat.})^{+0.56}_{-0.78}(\text{syst.})$ is compatible with the measurement for J/Ψ production. The data is also compared to predictions of the LLA BFKL model, using the HERWIG MC. The predictions are normalised to the measured cross section, as the normalisation is not predicted by the calculation. The W dependence can be used to measure α_s^{BFKL}, a free parameter in the theoretical prediction, which is the value of the strong coupling α_s used in the BFKL model. The W dependence is well described by the LLA BFKL prediction with $\alpha_s^{BFKL} = 0.26 \pm 0.10\ (\text{stat.})^{+0.05}_{-0.07}$ (syst.), as extracted from the fitted δ, using $\delta = 4(3\alpha_s/\pi)4ln2$. This value for α_s^{BFKL} is in agreement with the measurements using vector mesons.

The cross section as a function of $|t|$ is shown in Figure 8 b). It is compared to a fit of the form $d\sigma/dt \propto |t|^{-n}$. The fit yields $n = 2.60 \pm 0.19(\text{stat.})^{+0.03}_{-0.08}(\text{syst.})$. This $|t|$ dependence is significantly harder than measured for high $|t|$ diffractive photoproduction of J/Ψ mesons. The

BFKL model also predicts a too soft $|t|$ dependence and is unable to describe the data.

5 Scaled momentum distributions of charged particles

The measurement of soft charged particle distributions allows to study the formation of jets of hadrons which can be described as a convolution of parton showering and hadronisation. Parton showering can be calculated in pQCD as long as the energy scale is above Λ_{QCD} while hadronisation is a non perturbative process.

The study of charged particles with $P_T > 0.15$ GeV in jets was performed in di-jet events in photoproductionby the ZEUS collaboration using an integrated luminosity of 359 pb^{-1} [12].

The distributions are compared to predictions based on pQCD in the framework of the modified leading-logarithmic approximation (MLLA). Perturbative QCD based on the MLLA can be used to predict the multiplicity and momentum spectra of partons produced within cones centred on the initial parton direction. The MLLA may only be used to describe partons at scales above some minimum cutoff, $\Lambda_{\rm eff} > \Lambda_{\rm QCD}$. The value of $\Lambda_{\rm eff}$ is predicted to be independent of the process considered.

Figure 9 shows the number of charged particles as a function of $\xi = ln(1/x_{chp})$ where x_{chp} is the fraction of the jet momentum carried by the charged particle. The ξ distributions are shown for five bins in E_{jet} and three different cone opening angles Θ_c around the jet axis. The distributions are very similar and roughly Gaussian in shape with tails towards high ξ which corresponds to very low momentum particles.

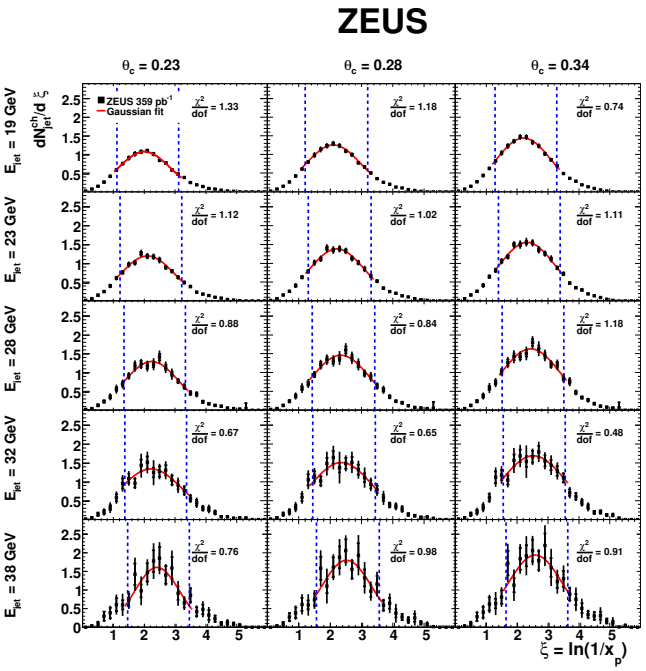

Figure 9: The ξ distribution for charged particles in jets for different bins in E_T of the jet and Θ_c the opening angle of the jet [12].

For each distribution, the peak position ξ_{peak} is extracted using a three-parameter Gaussian fit. The ξ_{peak} values for $\Theta_c = 0.23$ are shown in Fig. 10 as a function of $\mu \sin\Theta_c$, where the characteristic energy scale is $\mu = E_{jet}$. The peak value increases with the energy. The plot includes also results from ZEUS DIS [13], OPAL [14], TASSO [15], NOMAD [16] and CDF [17] at their characteristic energy scale. There is an approximately linear relationship between $\xi_{\rm peak}$ and $\ln(E_{\rm jet}\sin(\theta_c))$.

The MLLA predicts a small square-root correction to the linear dependence ($\xi^{\rm pl}_{\rm peak} = \frac{1}{2}Y + \sqrt{cY} + c$ with $c = 0.29$ and $Y = ln(\mu\sin(\Theta_c)/\Lambda_{eff})$. A single value of the intrinsic MLLA scale,

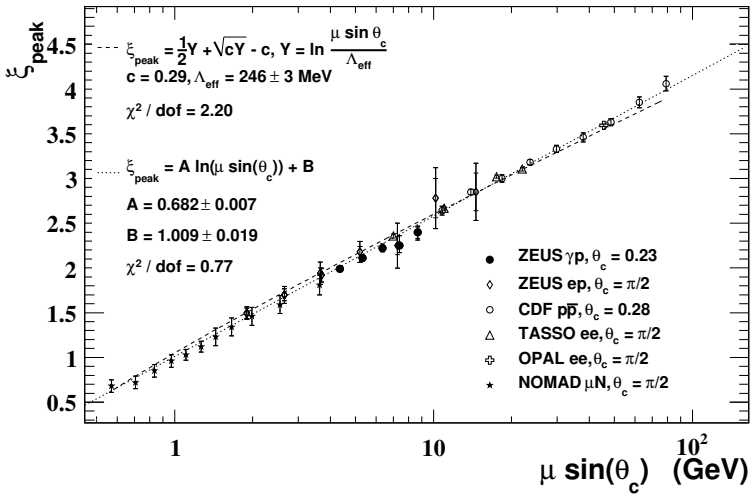

Figure 10: ξ_{peak} as a function of $\mu sin(\Theta_c)$, where μ is the characteristic energy scale for each specific process. The ZEUS γp data is shown together with ep, $p\bar{p}$ and e^+e^- data. The dashed line corresponds to the fit using the MLLA prediction [12].

$\Lambda_{\rm eff}$, is extracted by fitting the $\xi_{\rm peak}$ data according to the predicted relationship assuming $\Lambda_{\rm eff}$ is constant within the range of energies probed. The best fit value was found to be $\Lambda_{\rm eff} = 275 \pm 4({\rm stat.})^{+4}_{-8}({\rm syst.})$ MeV. The $\Lambda_{\rm eff}$ data are consistent with previously published data sets using different initial states, supporting the prediction that $\Lambda_{\rm eff}$ is universal.

6 Conclusions

Several measurements of jets and prompt photons in photoproduction have been presented. NLO calculations describe many aspects of jet samples which are dominated by direct interactions, whereas resolved enhanced samples are less well described. Prompt photon production in photoproduction is compared to a NLO calculation and to a calculation based on the k_T factorisation approach. Both calculation give a reasonable description of most of the distributions but reveal problems in some kinematic regions.

Diffractive scattering of photons at large momentum transfer was compared to predictions from a model based on the BFKL approach. While the W dependence of the cross section is well described, the data show a steeper t dependence than the model and and previous measurements with vector mesons.

The multiplicity distributions of charged particles within jets were measured and the intrinsic MLLA scale Λ_{eff} was extracted and found to be universal.

References

[1] S. Chekanov *et al.* [ZEUS Collaboration], Nucl. Phys. B **792** (2008) 1 [arXiv:0707.3749 [hep-ex]].

[2] F. Cornet, P. Jankowski and M. Krawczyk, Phys. Rev. D **70** (2004) 093004 [arXiv:hep-ph/0404063].

[3] A. Aktas *et al.* [H1 Collaboration], Phys. Lett. B **639** (2006) 21 [arXiv:hep-ex/0603014].

[4] G. Marchesini, B. R. Webber, G. Abbiendi, I. G. Knowles, M. H. Seymour and L. Stanco, Comput. Phys. Commun. **67** (1992) 465. G. Corcella *et al.*, JHEP **0101** (2001) 010 [arXiv:hep-ph/0011363].

[5] T. Sjostrand, P. Eden, C. Friberg, L. Lonnblad, G. Miu, S. Mrenna and E. Norrbin, Comput. Phys. Commun. **135** (2001) 238 [arXiv:hep-ph/0010017].
T. Sjostrand, Comput. Phys. Commun. **82** (1994) 74.

[6] M. Fontannaz, J. P. Guillet and G. Heinrich, Eur. Phys. J. C **21** 303 (2001) [arXiv:hep-ph/0105121].

[7] M. Fontannaz and G. Heinrich, Eur. Phys. J. C **34**, 191 (2004) [arXiv:hep-ph/0312009].

[8] A. V. Lipatov and N. P. Zotov, Phys. Rev. D **72** 054002 (2005) [arXiv:hep-ph/0506044].

[9] F. D. Aaron *et al.* [H1 Collaboration], Phys. Lett. B **672** (2009) 219 [arXiv:0810.3096 [hep-ex]].

[10] E. A. Kuraev, L. N. Lipatov and V. S. Fadin, Sov. Phys. JETP **45**, 199 (1977) [Zh. Eksp. Teor. Fiz. **72**, 377 (1977)].
I. I. Balitsky and L. N. Lipatov, Sov. J. Nucl. Phys. **28**, 822 (1978) [Yad. Fiz. **28**, 1597 (1978)].
L. N. Lipatov, Sov. Phys. JETP **63**, 904 (1986) [Zh. Eksp. Teor. Fiz. **90**, 1536 (1986)].

[11] S. Chekanov *et al.* [ZEUS Collaboration], Eur. Phys. J. C **26**, 389 (2003) [arXiv:hep-ex/0205081].
A. Aktas *et al.* [H1 Collaboration], Phys. Lett. B **638**, 422 (2006) [arXiv:hep-ex/0603038].
A. Aktas *et al.* [H1 Collaboration], Phys. Lett. B **568**, 205 (2003) [arXiv:hep-ex/0306013].
S. Chekanov *et al.* [ZEUS Collaboration], Eur. Phys. J. C **24**, 345 (2002) [arXiv:hep-ex/0201043].

[12] S. Chekanov *et al.* [ZEUS Collaboration], "Scaled momentum distributions of charged particles in dijet photoproduction at HERA", DESY-09-059, submitted to JHEP.

[13] M. Derrick *et al.* [ZEUS Collaboration], Z. Phys. C **67** (1995) 93 [arXiv:hep-ex/9501012].
J. Breitweg *et al.* [ZEUS Collaboration], Eur. Phys. J. C **11** (1999) 251 [arXiv:hep-ex/9903056].

[14] M. Z. Akrawy *et al.* [OPAL Collaboration], Phys. Lett. B **247** (1990) 617.

[15] W. Braunschweig *et al.* [TASSO Collaboration], Z. Phys. C **47** (1990) 187.

[16] J. Altegoer *et al.* [NOMAD Collaboration], Phys. Lett. B **445** (1999) 439.

[17] D. E. Acosta *et al.* [CDF Collaboration], Phys. Rev. D **68** (2003) 012003.

From Diphoton GDAs and Photon GPDs to the Chiral Odd Photon DA

Lech Szymanowski[1,2]

[1] Sołtan Institute for Nuclear Studies, Hoża 69, 00-681 Warsaw, Poland
[2] LPT, Université d'Orsay, CNRS, 91404 Orsay, France

DOI: http://dx.doi.org/10.3204/DESY-PROC-2009-03/Szymanowski

The photon is a very interesting object for QCD studies since it has both a pointlike coupling to quarks, which yields a perturbative part of photons wave function, and a non-perturbative coupling related to the magnetic susceptibility of the QCD vacuum and which builds its chiral-odd twist-2 distribution amplitude. The first feature allows us to compute the photon anomalous generalized parton distributions (GPD) and the diphoton generalized distribution amplitudes. The second feature allows us to use a transverse spin asymmetry to probe the chiral odd distribution amplitude of the photon.

1 Photon GPDs and diphoton GDAs

The factorization of the amplitude for the deeply virtual Compton scattering (DVCS) process $\gamma^*(Q)\gamma \to \gamma\gamma$ at high Q^2 is demonstrated in two distinct kinematical domains, allowing to define the photon generalized parton distributions and the diphoton generalized distribution amplitudes. Both these quantities exhibit an anomalous scaling behaviour and obey new inhomogeneous QCD evolution equations. The parton content of the photon has been the subject of many studies since the seminal paper by Witten [1] which allowed to define the anomalous quark and gluon distribution functions. Recent progress in exclusive hard reactions focuses on generalized parton distributions (GPDs), which are defined as Fourier transforms of matrix elements between different states, such as $\langle N'(p',s')|\bar{\psi}(-\lambda n)\gamma.n\psi(\lambda n)|N(p,s)\rangle$ and their crossed versions, the generalized distribution amplitudes (GDAs) which describe the exclusive hadronization of a $\bar{q}q$ or gg pair in a pair of hadrons, see Fig. 1. In the photon case, these quantities are perturbatively calculable [2, 3] at leading order in α_{em} and leading logarithmic order in Q^2. They constitute an interesting theoretical laboratory for the non-perturbative hadronic objects that hadronic GPDs and GDAs are.

1.1 The diphoton generalized distribution amplitudes

Defining the momenta as $q = p - \frac{Q^2 n}{s},\ q' = \frac{Q^2 n}{s},\ p_1 = \zeta p,\ p_2 = (1-\zeta)p$, where p and n are two light-cone Sudakov vectors and $2p \cdot n = s$, the amplitude of the process

$$\gamma^*(Q,\epsilon)\gamma(q',\epsilon') \to \gamma(p_1,\epsilon_1)\gamma(p_2,\epsilon_2) \tag{1}$$

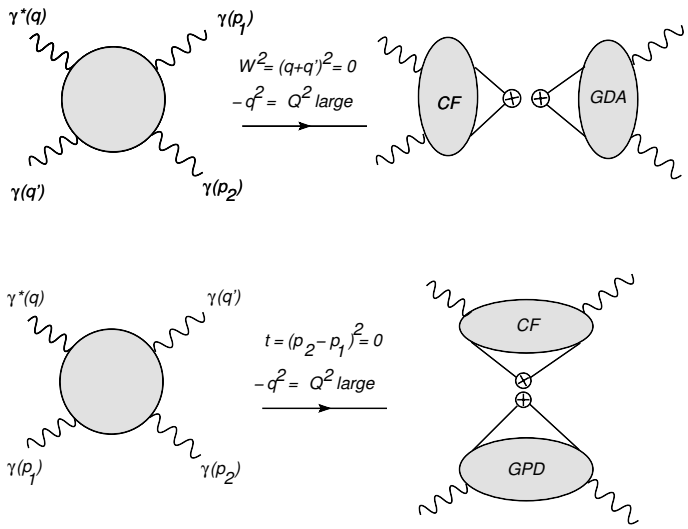

Figure 1: Factorizations of the DVCS process on the photon.

may be written as $A = \epsilon_\mu \epsilon'_\nu \epsilon_{1\alpha}^* \epsilon_{2\beta}^* T^{\mu\nu\alpha\beta}$. In forward kinematics where $(q+q')^2 = 0$, the tensorial decomposition of $T^{\mu\nu\alpha\beta}$ reads (see [3])

$$\frac{1}{4} g_T^{\mu\nu} g_T^{\alpha\beta} W_1^q + \frac{1}{8} \left(g_T^{\mu\alpha} g_T^{\nu\beta} + g_T^{\nu\alpha} g_T^{\mu\beta} - g_T^{\mu\nu} g_T^{\alpha\beta} \right) W_2^q + \frac{1}{4} \left(g_T^{\mu\alpha} g_T^{\nu\beta} - g_T^{\mu\beta} g_T^{\alpha\nu} \right) W_3^q \,. \quad (2)$$

At leading order, the three scalar functions W_i^q can be written in a factorized form which is particularly simple when the factorization scale M_F equals the photon virtuality Q. W_1^q is then the convolution $W_1^q = \int_0^1 dz\, C_V^q(z)\, \Phi_1^q(z,\zeta,0)$ of the coefficient function $C_V^q = e_q^2 \left(\frac{1}{z} - \frac{1}{1-z} \right)$ with the *anomalous* vector GDA ($\bar{z} = 1-z, \bar{\zeta} = 1-\zeta$) :

$$\Phi_1^q(z,\zeta,0) = \frac{N_C\, e_q^2}{2\pi^2} \log \frac{Q^2}{m^2} \left[\frac{\bar{z}(2z-\zeta)}{\bar{\zeta}} \theta(z-\zeta) + \frac{\bar{z}(2z-\bar{\zeta})}{\zeta} \theta(z-\bar{\zeta}) \right.$$
$$\left. + \frac{z(2z-1-\zeta)}{\zeta} \theta(\zeta - z) + \frac{z(2z-1-\bar{\zeta})}{\bar{\zeta}} \theta(\bar{\zeta} - z) \right] . \quad (3)$$

Conversely, W_3^q is the convolution of the function $C_A^q = e_q^2 \left(\frac{1}{z} + \frac{1}{\bar{z}} \right)$ with the axial GDA :

$$\Phi_3^q(z,\zeta,0) = \frac{N_C\, e_q^2}{2\pi^2} \log \frac{Q^2}{m^2} \left[\frac{\bar{z}\zeta}{\bar{\zeta}} \theta(z-\zeta) - \frac{\bar{z}\bar{\zeta}}{\zeta} \theta(z-\bar{\zeta}) - \frac{z\bar{\zeta}}{\zeta} \theta(\zeta - z) + \frac{z\zeta}{\bar{\zeta}} \theta(\bar{\zeta} - z) \right] \quad (4)$$

and $W_2^q = 0$. Note that these GDAs are not continuous at the points $z = \pm\zeta$. The anomalous nature of Φ_1^q and Φ_3^q comes from their proportionality to $\log \frac{Q^2}{m^2}$, which reminds us of the anomalous photon structure functions. A consequence is that $\frac{d}{d \ln Q^2} \Phi_i^q \neq 0$; consequently the QCD evolution equations of the diphoton GDAs obtained with the help of the ERBL kernel are non-homogeneous ones.

1.2 The photon generalized parton distributions

We now look at the same process in different kinematics, namely $q = -2\xi p + n,\ q' = (1+\xi)p,\ p_1 = n,\ p_2 = p_1 + \Delta = (1-\xi)p$, where $W^2 = \frac{1-\xi}{2\xi}Q^2$ and $t = 0$. The tensor $T^{\mu\nu\alpha\beta}$ is now decomposed on different tensors with the help of three functions $\mathcal{W}_i^q$ as (see [2]):

$$\frac{1}{4}g_T^{\mu\alpha}g_T^{\nu\beta}\mathcal{W}_1^q + \frac{1}{8}\left(g_T^{\mu\nu}g_T^{\alpha\beta} + g_T^{\alpha\nu}g_T^{\mu\beta} - g_T^{\mu\alpha}g_T^{\nu\beta}\right)\mathcal{W}_2^q + \frac{1}{4}\left(g_T^{\mu\nu}g_T^{\alpha\beta} - g_T^{\mu\beta}g_T^{\nu\alpha}\right)\mathcal{W}_3^q \tag{5}$$

These functions can also be written in factorized forms which have direct parton model interpretations when the factorization scale M_F is equal to Q: $\mathcal{W}_{1/3}^q = \int_{-1}^{1} dx C_{V/A}^q(x) H_{1/3}^q(x,\xi,0)$, $\mathcal{W}_2 = 0$. The coefficient functions are $C_{V/A}^q = -2e_q^2\left(\frac{1}{x-\xi+i\eta} \pm \frac{1}{x+\xi-i\eta}\right)$ and the unpolarized H_1^q and polarized H_3^q anomalous GPDs of quarks inside a real photon read :

$$H_1^q(x,\xi,0) = \frac{N_C\, e_q^2}{4\pi^2}\left[\theta(x-\xi)\frac{x^2+(1-x)^2-\xi^2}{1-\xi^2} + \theta(\xi-x)\theta(\xi+x)\frac{x(1-\xi)}{\xi(1+\xi)} - \theta(-x-\xi)\frac{x^2+(1+x)^2-\xi^2}{1-\xi^2}\right]\ln\frac{Q^2}{m^2}\ , \tag{6}$$

$$H_3^q(x,\xi,0) = \frac{N_C\, e_q^2}{4\pi^2}\left[\theta(x-\xi)\frac{x^2-(1-x)^2-\xi^2}{1-\xi^2} - \theta(\xi-x)\theta(\xi+x)\frac{1-\xi}{1+\xi} + \theta(-x-\xi)\frac{x^2-(1+x)^2-\xi^2}{1-\xi^2}\right]\ln\frac{Q^2}{m^2}\ . \tag{7}$$

Similarly as in the GDA case, the anomalous generalized parton distributions H_i^q are proportional to $\ln\frac{Q^2}{m^2}$, which violates the scaling. Consequently, the anomalous terms H_i^q supply to the usual homogeneous DGLAP-ERBL evolution equations of GPDs a non-homogeneous term which changes them into non-homogeneous evolution equations.

We do not anticipate a rich phenomenology of these photon GPDs, but in the case of a high luminosity electron - photon collider which is not realistic in the near future. However, the fact that one gets explicit expressions for these GPDs may help to understand the meaning of general theorems such as the polynomiality and positivity [4] constrains or the analyticity structure [5]. For instance, one sees that a D-term in needed when expressing the photon GPDs in terms of a double distribution. One also finds that, in the DGLAP region, $H_1(x,\xi)$ is smaller than its positivity bound by a sizeable and slowly varying factor, which is of the order of $0.7 - 0.8$ for $\xi \approx 0.3$.

2 Accessing the photon chiral-odd DA and the proton transversity

In Ref.[6], we describe a new way to access the photon distribution amplitude through the photoproduction of lepton pairs on a transversally polarized proton.

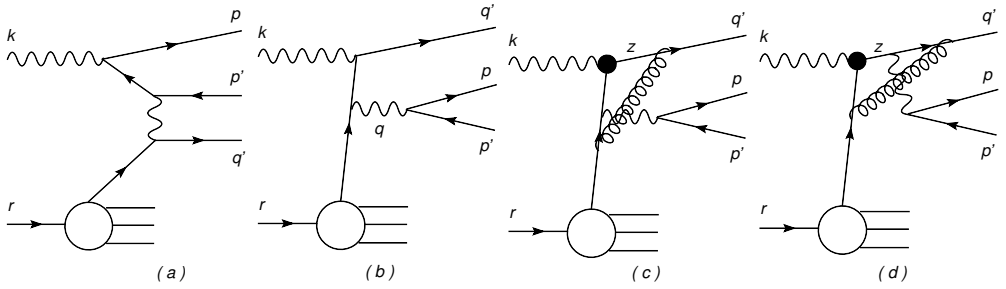

Figure 2: Some amplitudes contributing to lepton pair photoproduction. (a) : The Bethe-Heitler process. (b) : The Drell-Yan process with the photon pointlike coupling. (c) -(d) : The Drell-Yan process with the photon Distribution Amplitude.

The leading twist chiral-odd photon distribution amplitude $\phi_\gamma(u)$ reads [7]

$$\langle 0|\bar{q}(0)\sigma_{\alpha\beta}q(x)|\gamma^{(\lambda)}(k)\rangle = i\, e_q\, \chi\, \langle\bar{q}q\rangle \left(\epsilon_\alpha^{(\lambda)}k_\beta - \epsilon_\beta^{(\lambda)}k_\alpha\right) \int_0^1 dz\, e^{-iz(kx)}\, \phi_\gamma(z)\,, \tag{8}$$

where the normalization is chosen as $\int dz\, \phi_\gamma(z) = 1$, and z stands for the momentum fraction carried by the quark. The product of the quark condensate and of the magnetic susceptibility of the QCD vacuum $\chi\,\langle\bar{q}q\rangle$ has been estimated [8] with the help of the QCD sum rules techniques to be of the order of 50 MeV and a lattice estimate has recently been performed [9]. The distribution amplitude $\phi_\gamma(z)$ has a QCD evolution which drives it to an asymptotic form $\phi_\gamma^{as}(z) = 6z(1-z)$. Its $z-$dependence at non asymptotic scales is very model-dependent [10].

We consider the following process (s_T is the transverse polarization vector of the nucleon):

$$\gamma(k,\epsilon)N(r,s_T) \to l^-(p)l^+(p')X\,, \tag{9}$$

with $q = p + p'$ in the kinematical region where $Q^2 = q^2$ is large and the transverse component $|\vec{Q}_\perp|$ of q is of the same order as Q. Such a process occurs either through a Bethe-Heitler amplitude (Fig. 2a) where the initial photon couples to a final lepton, or through Drell-Yan type amplitudes (Fig. 2b) where the final leptons originate from a virtual photon. Among these Drell-Yan processes, one must distinguish the cases where the real photon couples directly (through the QED coupling) to quarks or through its quark content. We thus consider the contributions where the photon couples to the strong interacting particles through its lowest twist-2 chiral odd distribution amplitude (Fig. 2c and 2d). We will call this amplitude $\mathcal{A}_\phi$.

One can easily see by inspection that interfering the amplitude $\mathcal{A}_\phi$ with a pointlike amplitude is the only way to get at the level of twist 2 (and with vanishing quark masses) a contribution to nucleon transverse spin dependent observables. Reaction (9) thus opens a natural access to the photon distribution amplitude [11], provided the amplitude $\mathcal{A}_\phi$ interferes with the Bethe-Heitler or a usual Drell-Yan process. Moreover, since this amplitude has an absorptive part, *single spin* effects do not vanish. The amplitude where the photon interacts through its distribution amplitude at lowest order (Fig. 2c and 2d) and in Feynman gauge, reads

$$\begin{aligned}&\mathcal{A}_\phi(\gamma q \to l\bar{l}q) \\ &= 2i\frac{C_F}{4N_c}e_q^2 e 4\pi\alpha_s\chi\,\langle\bar{q}q\rangle\frac{1}{Q^2}\int dz\phi_\gamma(z)\bar{u}(q')[\frac{A_1}{x\bar{z}s(t_1+i\epsilon)} + \frac{A_2}{zu(t_2+i\epsilon)}]u(r)\bar{u}(p)\gamma^\mu v(p')\,,\end{aligned} \tag{10}$$

with $t_1 = (zk - q)^2$ and $t_2 = (\bar{z}k - q)^2$ and

$$A_1 = x\,\hat{r}\,\hat{\epsilon}\,\hat{k}\,\gamma^\mu + \gamma^\mu\,\hat{k}\,\hat{\epsilon}\,\hat{q}\,, \qquad A_2 = \hat{\epsilon}\,\hat{q}\,\gamma^\mu\,\hat{k} + \hat{k}\,\gamma^\mu\,\hat{q}\,\hat{\epsilon}\,, \tag{11}$$

which do not depend on the light-cone fraction z. Most interesting is the analytic structure of this amplitude since the quark propagators may be on shell so that the amplitude $\mathcal{A}_\phi$ develops an absorptive part proportional to

$$\int dz \phi_\gamma(z) \bar{u}(q')[\frac{A_1}{x\bar{z}s}\delta(t_1) + \frac{A_2}{zu}\delta(t_2)]u(r)\bar{u}(p)\gamma^\mu v(p')\,.$$

The $z-$integration, after using the $z - \bar{z}$ symmetry of the distribution amplitude, yields an absorptive part of the amplitude $\mathcal{A}_\phi$ proportional to $\phi_\gamma(\frac{\alpha Q^2}{Q^2+\vec{Q}_\perp^2})$. This absorptive part may be measured in single spin asymmetries and thus scans the photon chiral-odd distribution amplitude.

The cross section for reaction (9) can be decomposed as

$$\frac{d\sigma}{d^4Q\,d\Omega} = \frac{d\sigma_{BH}}{d^4Q\,d\Omega} + \frac{d\sigma_{DY}}{d^4Q\,d\Omega} + \frac{d\sigma_{\phi}}{d^4Q\,d\Omega} + \frac{\Sigma d\sigma_{int}}{d^4Q\,d\Omega}\,,$$

where $\Sigma d\sigma_{int}$ contains various interferences, while the transversity dependent differential cross section (we denote $\Delta_T\sigma = \sigma(s_T) - \sigma(-s_T)$) reads

$$\frac{d\Delta_T\sigma}{d^4Q\,d\Omega} = \frac{d\sigma_{\phi int}}{d^4Q\,d\Omega}\,, \tag{12}$$

where $d\sigma_{\phi int}$ contains only interferences between the amplitude $\mathcal{A}_\phi$ and the other amplitudes. Moreover, one may use the distinct charge conjugation property (with respect to the lepton part) of the Bethe Heitler amplitude to select the interference between $\mathcal{A}_\phi$ and the Bethe-Heitler amplitude :

$$\frac{d\Delta_T\sigma(l^-) - d\Delta_T\sigma(l^+)}{d^4Q\,d\Omega} = \frac{d\sigma_{\phi BH}}{d^4Q\,d\Omega}\,. \tag{13}$$

Conversely, one may use this charge asymmetry to cancel out the interference of $\mathcal{A}_\phi$ with the Bethe Heitler amplitude

$$\frac{d\Delta_T\sigma(l^-) + d\Delta_T\sigma(l^+)}{d^4Q\,d\Omega} \propto \frac{d\sigma_{\phi DY}}{d^4Q\,d\Omega}\,. \tag{14}$$

The simplest observable which contains all appealing features of our proposal is the interference of $\mathcal{A}_\phi$ and the Bethe-Heitler amplitudes, see Eq.13, in the unpolarized photon case. The polarization average of $d\sigma_{\phi BH}$ reads :

$$\begin{aligned} &\frac{1}{2}\sum_\lambda d\sigma_{\phi BH}(\gamma(\lambda)p \to l^-l^+X) \qquad (15)\\ &= \frac{(4\pi\alpha_{em})^3}{4s}\,\frac{C_F 4\pi\alpha_s}{2N_c}\,\frac{\chi\,\langle\bar{q}q\rangle}{\vec{Q}_\perp^2}\int dx \sum_q Q_l^3 Q_q^3 h_1^q(x) 2\mathcal{R}e(\mathcal{I}_{\phi BH})\,dLIPS\,, \end{aligned}$$

with the usual phase space factor dLips and

$$2\mathcal{R}e(\mathcal{I}_{\phi BH}) = \phi_\gamma[\frac{\alpha Q^2}{Q^2+\vec{Q}_\perp^2}]\,\frac{32\pi\alpha^2\bar{\alpha}}{xs(\bar{\alpha}Q^2+\vec{Q}_\perp^2)^2}(Q^2+\vec{Q}_\perp^2)[\epsilon^{rks_TQ_T}\mathcal{A}+\epsilon^{rks_Tl_T}\mathcal{B}]\,, \tag{16}$$

where $\mathcal{A}$ and $\mathcal{B}$ are algebraic functions [6]. Eqs. 15, 16 demonstate at the level of a highly differential cross section the existence of a non-vanishing observable proportional to the photon distribution amplitude $\Phi_\gamma(z=\frac{\alpha Q^2}{Q^2+\vec{Q}_\perp^2})$ and the nucleon transversity h_1.

Acknowledgements. This work is partly supported by the ECO-NET program, contract 18853PJ, the French-Polish scientific agreement Polonium and the Polish Grant N202 249235.

References

[1] E. Witten, Nucl. Phys. B **120** (1977) 189.

[2] S. Friot *et.al.*, Phys. Lett. B **645** (2007) 153 and Nucl. Phys. Proc. Suppl. **184**, 35 (2008).

[3] M. El Beiyad *et.al.*, Phys. Rev. D **78** (2008) 034009 and AIP Conf. Proc. **1038**, 305 (2008).

[4] B. Pire, J. Soffer and O. Teryaev, Eur. Phys. J. C **8** (1999) 103.

[5] I. V. Anikin *et.al.*, Phys. Rev. D **76**, 056007 (2007). M. Diehl *et.al.*, Eur. Phys. J. C **52** (2007) 919.

[6] B. Pire and L. Szymanowski, arXiv:0905.1258 [hep-ph].

[7] B. L. Ioffe and A. V. Smilga, Nucl. Phys. B **232**, 109 (1984); I. I. Balitsky, V. M. Braun and A. V. Kolesnichenko, Nucl. Phys. B **312**, 509 (1989); P. Ball, V. M. Braun and N. Kivel, Nucl. Phys. B **649**, 263 (2003).

[8] V. M. Belyaev and Y. I. Kogan, Yad. Fiz. **40**, 1035 (1984); I. I. Balitsky, A. V. Kolesnichenko and A. V. Yung, Sov. J. Nucl. Phys. **41**, 178 (1985).

[9] P. V. Buividovich *et al.* , arXiv:0906.0488 [hep-lat].

[10] V. Y. Petrov *et al.* , Phys. Rev. D **59**, 114018 (1999); A. E. Dorokhov, W. Broniowski and E. Ruiz Arriola, Phys. Rev. D **74**, 054023 (2006).

[11] For other proposals, see D. Y. Ivanov *et al.*, Phys. Lett. B **478**, 101 (2000) [Erratum-ibid. B **498**, 295 (2001)]; V. M. Braun *et al.*, Phys. Rev. Lett. **89**, 172001 (2002).

Leptonic Structure Functions measured with the L3 Detector

Klaus Dehmelt for the L3 collaboration

DESY, Notkestrasse 85, 22607 Hamburg, Germany, E-mail: klaus.dehmelt@desy.de

DOI: http://dx.doi.org/10.3204/DESY-PROC-2009-03/Dehmelt

The QED structure function F_2^γ can be rather easily extracted by means of the measurement of cross sections for electron tagged events in e^+e^- scattering. We report on a measurement of the QED structure functions of the photon with single tagged events, at Q^2 between 0.2 GeV^2 and 34 GeV^2. The data were collected with the L3 detector at LEP, for c.m.s. energies between 189 GeV and 206 GeV. The sub detectors for tagging the single beam electron were the Very Small Angle Tagger and the Luminosity detector of L3.

1 Introduction

Photons have structure and may interact with each other. This might be possible because photons can fluctuate into states of particles, which might be charged. Heisenberg's uncertainty relation $\Delta t \simeq \frac{2E_\gamma}{m^2_{pair}}$ *allows* photons to fluctuate into intermediate states, where m_{pair} represents the mass of such a state. If E_γ becomes large, Δt, i.e. the lifetime of the intermediate states can also become quite large. These intermediate states will then be responsible for the interaction of the photons and also for giving a structure to photons.
Since the fluctuation is a statistical process, the probability of the fluctuation into a particular state is described in terms of structure functions.

2 Two Photon Physics and QED

Two-photon physics nowadays is of interest, since it allows to test Quantum-Chromodynamics (QCD), the theory of strong interactions: the intermediate states might be strongly interacting particles.
Experimentally, it is very difficult to collide high energy photon beams. A very elegant way of avoiding this difficulty is the usage of virtual photons, e.g. the quantum fluctuation of an electron into an electron-photon state. Thus, high energy e^-e^+ storage rings like the Large-Electron-Positron collider (LEP) are an ideal tool for producing photons. Such accelerators can be considered as Photon-Photon colliders, since a portion of the incoming electrons (positrons) around collision points will be scattered into relatively large angles. Because of this scattering highly virtual photons will be radiated and can be interacting with photons which are emitted by the other beam particle. The increase of the photon emission probability with the increase

of the beam-particle's energy makes LEP a source of γ's with continuous energy. Its cross-section is much higher than in any previous e^-e^+-storage ring. Altogether, this fact allows to obtain photon fluxes of high intensity; however, the "beam-energies" of such photons can not be controlled.
The investigation of lepton pair production is a Quantum-Electrodynamics (QED) process (Fig. 1, left), of the order $\mathcal{O}(\alpha^4)$, where α is the Fine-Structure Constant. The study of

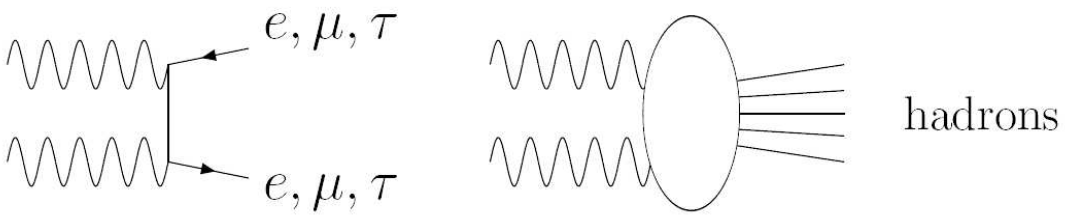

Figure 1: Inelastic processes for $\gamma\gamma$ scattering, left: QED, right: QCD.

$e^-e^+ \rightarrow e^-e^+\gamma\gamma \rightarrow e^-e^+l^-l^+ (l = e, \mu, \tau)$ allows to establish procedures to be adopted to studies in hadronic photon structure functions. However, although the production of final states with $e^\pm$, $\mu^\pm$, and $\tau^\pm$ have been measured, only the muonic case is feasible to extract the structure function from data [1].
The information of the kinematics of this process can be obtained by experimental observation, since the final state particles can be completely detected, in contrast to many QCD processes. Thus, the study of lepton pair production from $\gamma\gamma$-collisions will, besides supplying another test of QED, provide important tools for the application in QCD studies.

3 Two-photon scattering

The measurements of the structure functions of photons can be performed for three special cases due to experimental constraints [2]. The theoretical description as well as the measurements for these cases will be quite different. One distinguishes between

1. Single tagging
2. Anti-tagging
3. Double tagging

The differences for the cases are incumbent upon the measurement of the so called tagged electrons[1]. The measurements for the different cases define the *virtuality* of the radiated photons. The virtuality is a measure for the magnitude of the negative invariant masses squared of the photons and thus a measure how far the photon is off its mass-shell. This quantity is calculated from the squared four-momentum transfers of the electrons to the radiated photons, which are described by Q^2 respectively P^2, see Fig. 2. The configuration for the measure-

[1]Since the electron and positron behave identical in terms of two photon physics only the term *electron* will be used in the following.

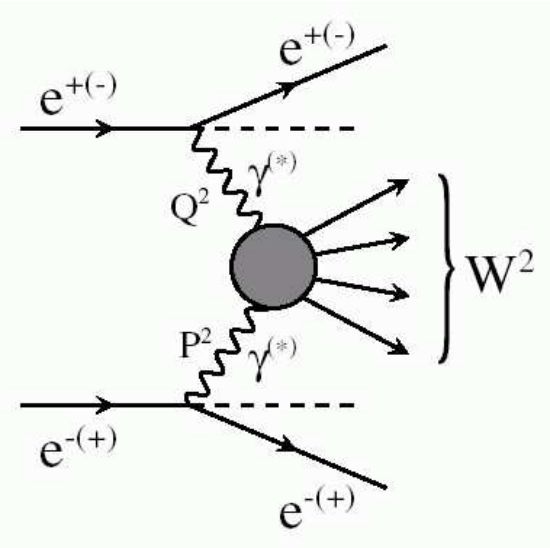

Figure 2: Two-photon production and scattering.

ment described herein is case 1: one of the scattered electrons is observed within an angular range $\theta_{low} < \theta_1 < \theta_{up}$, while the other electron is not observed over the angular range $\theta_{max} < \theta_2 < \pi - \theta_{max}$. This means, that the first electron is detected and precisely measured within a detector system with limited acceptance, whereas the second electron is considered being scattered into the cone with $\theta_2 < \theta_{max}$ or $\theta_2 > \pi - \theta_{max}$. If the angle θ_{max} is sufficiently small, the second electron will not be detected and is considered to be escaped close to the beam line, i.e. outside the detector acceptance. Hence, case 1 classifies a direct accessible $\gamma\gamma^*$ collision, since the four-momentum transfer to one photon will vanish, e.g. $P^2 \sim 0$ (quasi-real), whereas Q^2 is measured. The asterisk is used for virtual photons.
An additional feature of the QED treatment of $\gamma\gamma$-collisions is the access to further structure functions: $F_A^{\gamma,QED}$ and $F_B^{\gamma,QED}$, which correspond to transitions of photons with spin-flip (Fig. 3). The helicity is defined by the spin component in the direction of motion. Since real photons are massless, they cannot have a component parallel to their motion, i.e. they do not have a longitudinal, but only a transversal component. Virtual photons are off the mass-shell. This means, they can have a longitudinal polarization and therefore a non-zero helicity.
Since one photon is quasi-real, i.e. $m_\gamma \equiv 0$ in the case of single tagging, it does not have a longitudinal polarization. This photon is considered to be the target photon, whereas the other is the photon, which probes the structure of the target photon. Thus, the three amplitudes A_1, A_2, and A_3 are the only ones, which are independent from each other. In Fig. 3 one can schematically see the construction of the parameters A_i out of the total photon helicity states λ.
A_1 is described with the terms, (Fig. 3 from left to right) for $\lambda = 0, 2, 1$. A_2 and A_3 are made up by interference terms. These coefficients are related to $F_2^{\gamma,QED}$, $F_A^{\gamma,QED}$ and $F_B^{\gamma,QED}$ (see [3]).

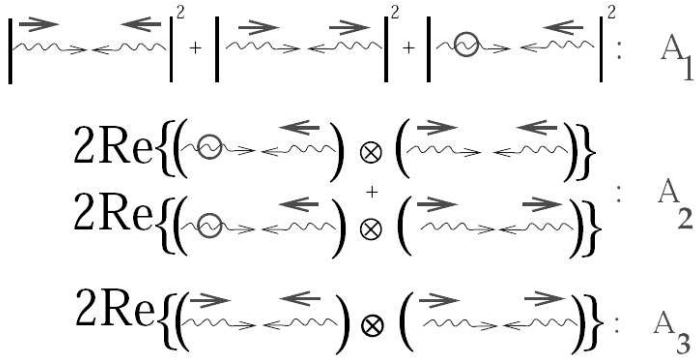

Figure 3: Helicity states for a single-tag configuration in two-photon collisions. The arrow depict the transverse helicity states, the circle the longitudinal helicity state of the probe photon.

4 Cross section and structure function

The differential cross-section can be then written in terms of cross-sections σ_{ab} and transition amplitudes τ_{ab} (see [4, 5]):

$$\begin{aligned} d\sigma &= K\Big(2|\rho_1^{+-}\rho_2^{+-}|\tau_{TT}\cos 2\tilde{\phi} \\ &\quad -8|\rho_1^{+0}\rho_2^{+0}|\tau_{TL}\cos\tilde{\phi} + 2\rho_1^{++}\rho_2^{00} \\ &\quad \times\big\{F_2(W,q_1^2,q_2^2)/D \\ &\quad -F_1(W,q_1^2,q_2^2)/C\big\} \\ &\quad +4\rho_1^{++}\rho_2^{++}F_1(W,q_1^2,q_2^2)/C\Big) \\ &\quad \times\frac{d^3p_1'd^3p_2'}{E_1E_2} \end{aligned} \tag{1}$$

where

$$\begin{aligned} F_1 &= \frac{\sqrt{\nu^2-q_1^2q_2^2}}{4\pi^2\alpha}(\sigma_{TT}-\frac{1}{2}\sigma_{TL}) \\ F_2 &= \frac{\nu|q_1^2|}{4\pi^2\alpha\sqrt{\nu^2-q_1^2q_2^2}} \\ &\quad \times\left(\sigma_{TT}+\sigma_{LT}-\frac{1}{2}(\sigma_{LL}+\sigma_{TL})\right) \\ &\quad \text{with } \nu = q_1\cdot q_2 \end{aligned} \tag{2}$$

The factors K and ρ_i depend on the four-momentum transfers, i.e. the measurable quantities p_i and q_i only, and the index T, L correspond to transversal and longitudinal polarization, respectively.
The structure-function F_2^γ can be accessed with a Monte-Carlo generator, which produces events according to (1). The basic idea of extracting F_2^γ is to set this parameter as a fixed value in the program and compare the measured differential cross-section with it. In other words,

one normalizes the structure-function to a fixed differential cross-section, say, $1\,nb$, and refers to the measured cross-section. The ratio of the differential cross-section and the normalized differential cross-section uncovers F_2^γ.
This can in principle be done with MC generators, like `VERMASEREN` [6], by means of modifying the program such, that it generates events according to $F_2 = 1\,nb$. However, there exists a Monte Carlo program, `GALUGA` [7], which can be used in a very convenient way.
It calculates the differential cross-section for $e^-e^+ \to e^-e^+X$ at given two-photon invariant mass W, or integrated over W. This cross-section is rewritten in terms of the photon virtualities q_i as the outermost integration variables (next to W), in order to simultaneously cope with anti-tagged and tagged electron modes.

5 Data analysis

The analyzed data sample was taken with the L3 detector at LEP/CERN in the years 1998-2000. The c.m.s. energy was between $189\,GeV$ and $208\,GeV$. The total integrated luminosity for the data sample used, was $\mathcal{L} = 600.2\,pb^{-1}$. The data sample was selected with single tag mode, i.e. only one electron had to be seen in the detector. Furthermore, the tagged electron had to be detected within the VSAT sub-detector ([8]) respectively the LUMInosity detector ([9]) of L3. The VSAT had a polar angular acceptance of $5mrad \leq \theta \leq 12mrad$, and accordingly for the other side of the vertex position. The range for the squared four-momentum transfer was $0.2\,GeV^2 \leq Q^2 \leq 0.85\,GeV^2$.
The LUMI had a polar angular acceptance of $32.6mrad \leq \theta \leq 63.6mrad$, and accordingly for the other side of the vertex position.

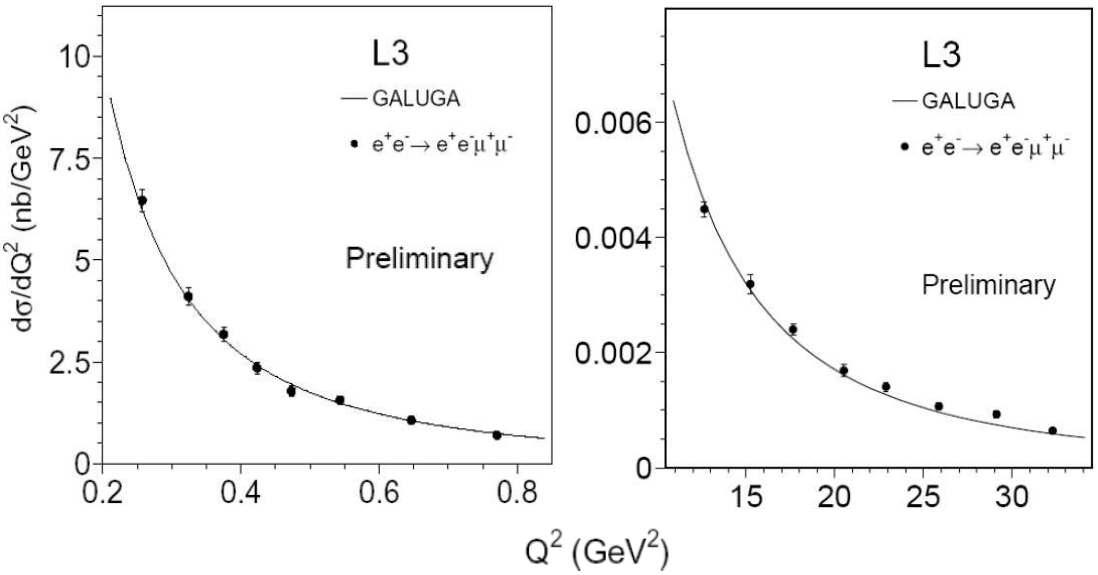

Figure 4: The differential cross-section as a function of Q^2 from the reaction $e^-e^+ \to e^-e^+\mu^-\mu^+$, left: with VSAT-tagged, right: with LUMI-tagged electrons. The QED curve has been obtained with the generator `GALUGA`. Only statistical errors are drawn.

The range for the squared four-momentum transfer was $11\,GeV^2 \leq Q^2 \leq 34\,GeV^2$.
The dimuon event was required to show exactly two well measured tracks where only one particle had to be identified as a muon in order to uniformly cover the angular range. The mean trigger efficiency for the years 1998 to 2000 was found to be $\varepsilon = 96.5 \pm 0.1\%$.

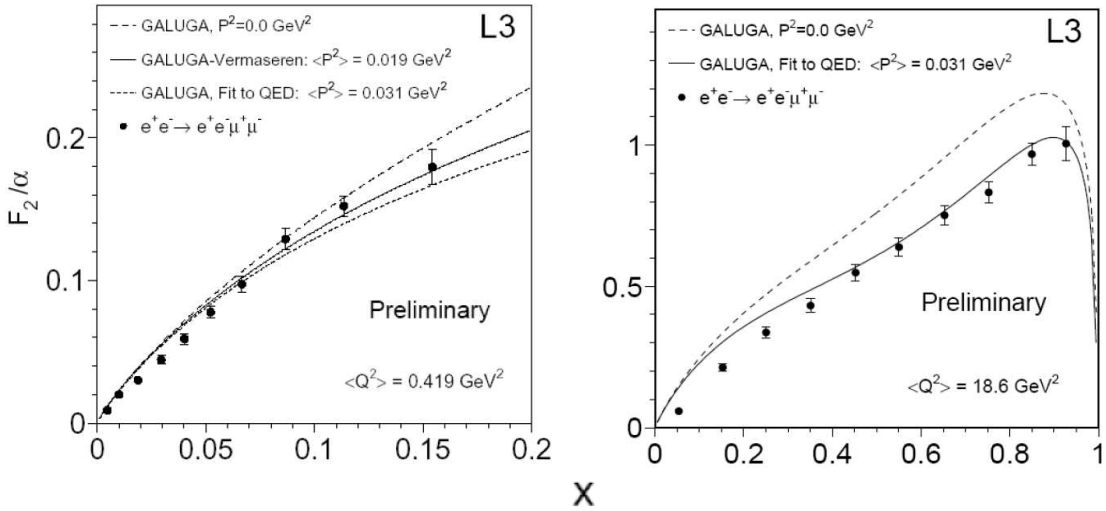

Figure 5: The structure function F_2 as a function of x from the reaction $e^-e^+ \to e^-e^+\mu^-\mu^+$, left: with VSAT-tagged, right: with LUMI-tagged electrons. The QED curves have been obtained with Eq.(2) and a mean virtuality of $P^2 = 0\,GeV^2$ (dashed line), $P^2 = 0.019\,GeV^2$ (solid line, MC), and $P^2 = 0.031\,GeV^2$ (dotted line, fit) for the target photon respectively. The data suggest that a non-zero virtuality should be used. Only statistical errors are drawn.

6 Results

The theoretical prediction of the differential cross-section was calculated with the MC generator `GALUGA`. Fig.4 shows a good agreement between data and the QED prediction. A series of differential cross-sections $d\sigma/dQ^2$ was calculated for a subdivision of Q^2-ranges within the range $0.2\,GeV^2 \leq Q^2 \leq 0.85\,GeV^2$ respectively for $11\,GeV^2 \leq Q^2 \leq 34\,GeV^2$. The crucial parameter used in `GALUGA` was the maximum polar angular range, in which the untagged electron can be scattered. The average Q^2 (center of gravity: c.o.g.) for each bin was calculated and the data points are depicted accordingly. The parameter x, which the structure function depends upon, is limited in its maximum to $x = 0.2$ for the VSAT-tagged sample. This is due to the fact that the range of Q^2 is rather small in connection with the minimum invariant mass of the two lepton event in its final state.
The measured structure function F_2 can be seen in Fig.5. There is a good agreement between data and prediction, based on Eq.(2). The structure function is suppressed as compared to non-vanishing virtualities of the probe photon. Although the effect of a non-zero virtuality of the target photon is not very significant at low x, the data suggest that $P^2 > 0\,GeV^2$. This becomes apparent for the case of higher four-momenta transfers (see Fig. 5 right). The average

value of $P^2 = 0.031 \pm 0.001\,GeV^2$ was obtained from a χ^2-fit procedure. A mean value of $P^2 = 0.019 \pm 0.001 GeV^2$ was obtained from the reconstructed MC sample for the VSAT-tagged sample.

References

[1] M. Krawczyk, M. Staszel, A. Zembrzuski. Phys. Rep. **345** (2001) 265.

[2] J.H. Field. "Lecture Notes in Physics: Photon Photon Collisions", v. **191** (1983) 270.

[3] G. Susinno Internal Report, L3 note 2193, 1997.

[4] V.M. Budnev, I.F. Ginzburg, G.V. Meledin and V.G. Serbo. Phys. Rep. **15**, (1975) 181.

[5] Ch. Berger and W. Wagner. Phys. Rep. **146**, (1987) 1.

[6] J.A.M. Vermaseren. Nucl. Phys. **B229** (1983) 347.

[7] G. A. Schuler Comp. Phys. Comm. **108** (1998) 279.

[8] F. Filthaut, F. Linde, T. van Rhee. Internal Report, L3 note 2117, 1997.

[9] I. C. Brock et al. Nucl. Inst. Meth. **A381** (1996) 236.

Chapter 6

Jets and Heavy Flavours

Convenors:

B. Kniehl (Hamburg) and K. Rabbertz (Karlsruhe)

Low & High & Multiple Energy Scales @ HERA

Günter Grindhammer (for the H1 and ZEUS collaborations)
Max-Planck-Institut für Physik , Föhringer Ring 6, 80805 Munich, Germany

DOI: http://dx.doi.org/10.3204/DESY-PROC-2009-03/Grindhammer

The latest QCD results from the H1 and ZEUS collaborations at HERA presented here cover a wide range in the energy scales relevant for the strong interactions. They comprise a study of the underlying event, measurements of jet production and of $\alpha_s(M_Z)$ as well as measurements of heavy flavor cross sections including the charm and beauty structure functions.

1 Introduction

Recent results from HERA on the hadronic final state in deep-inelastic scattering (DIS) and photoproduction (PHP) are presented, covering a wide range in the energy scales relevant for the strong interactions. The study of the underlying event probes low and high scales, while jet production is dominated by high scales. In heavy flavor production multiple scales play a role.

The HERA *ep*-collider operated with electrons or positrons of 27.6 GeV and protons of 820 or 920 GeV. Each of the two collider experiments H1 and ZEUS collected about 120 pb^{-1} from 1995 to 2000 (HERA-1) and after a luminosity upgrade about 370 pb^{-1} from 2003 to 2007 (HERA-2). Since the results presented here do not depend on whether the incident lepton was an electron or a positron, the term "electron" is used to mean either of them. During part of HERA-1 only H1 and since HERA-2 both experiments were equipped with micro-vertex detectors, which is of particular relevance for some of the heavy flavor results shown. The DIS kinematic region is defined by measuring the scattered electron in the main detector with photon virtualities $Q^2 > 1\ \text{GeV}^2$. The PHP region is defined by either not observing a scattered electron ($Q^2 < 1\,\text{GeV}^2$) or by requiring a signal in designated electron taggers ($Q^2 < 0.01\,\text{GeV}^2$). Requirements on the inelasticity y, measured via the scattered electron or the hadronic final state, complete the definition of the DIS or PHP phase space.

The slides of the talk which include more figures than possible in this written version can be found in [1].

2 Low & high scales: Underlying event in PHP

In *ep* collisions the quasi-real photon can directly interact with a parton from the proton or it can have fluctuated into partons of which one interacts with a parton from the proton as exemplified in Fig. 1. In the latter case additional interactions between the remnant partons of the photon and the proton may occur. They are usually referred to as underlying event and/or multi-parton interactions (MPI).

In leading order (LO) QCD one can distinguish between these *direct* and *resolved* interactions by measuring the transverse energies and pseudo-rapidities of the two hard jets and constructing the observable $x_\gamma = 1/(2yE_e)\,(E_{\mathrm{T,jet1}}\exp^{-\eta_{\mathrm{jet1}}} + E_{\mathrm{T,jet2}}\exp^{-\eta_{\mathrm{jet2}}})$, i.e. the fractional photon energy carried by the parton from the photon. For direct events $x_\gamma \to 1$ and for resolved events $0 < x_\gamma < 1$. Thus, at HERA MPI can be turned *on* by studying events with typically $x_\gamma < 0.7$ or *off* for $x_\gamma > 0.7$.

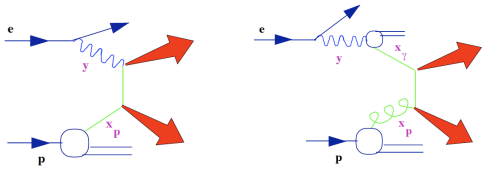

Figure 1: A direct (left) and a resolved (right) photon interaction diagram.

In case of a resolved photon event the additional interactions, besides the primary hard parton-parton interaction leading to a hard dijet, are of interest. The MPI may consist of additional *soft* interactions affecting the particle multiplicity, but also of *semi-hard* interactions leading to an increase in jet multiplicity. The interpretation of the measurements in terms of MPI is unfortunately not straightforward. Other effects, more or less well understood, due to additional parton radiation (higher order QCD effects), fragmentation and beam remnants, may lead to similar signatures as MPI. Since MPI provide an important background to precise QCD measurements and to searches for new physics, particularly at the TEVATRON and soon at the LHC, it is of great interest to improve the understanding and modeling of them.

H1 provided new preliminary measurements [2] of the mean charged particle multiplicity in different azimuthal regions. The method, illustrated in Fig. 2, follows closely an analysis [3] by the CDF collaboration. In PHP events, $Q^2 < 0.01\,\mathrm{GeV}^2$ and $0.3 < y < 0.65$, a leading and a sub-leading jet with $P_{\mathrm{T,jet}} > 5$ GeV and $|\eta_{\mathrm{jet}}| < 1.5$ were required. The jets were reconstructed in the laboratory frame using the longitudinally invariant $k_\perp$-cluster algorithm [4]. The leading jet at $\Phi^\star = 0°$ defines the *Toward region*, and the sub-leading jet is usually found in the *Away region*. The mean charged particle multiplicity, using tracks with $P_{\mathrm{T}} > 150$ MeV and $|\eta| < 1.5$, was measured in these and the transverse regions. The transverse regions are distinguished into *High* and *Low activity regions* depending on in which region the scalar sum over the transverse particle momenta is higher. The expectation is that the transverse regions, particularly the *Low activity region*, shows sensitivity to MPI.

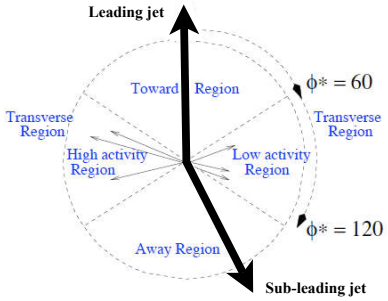

Figure 2: Definition of the four azimuthal regions.

For events satisfying the above mentioned requirements, the dependence of the mean charged particle multiplicity on the angle $\Delta\Phi$ between the leading jet and the charged particles is shown in [1, 2] together with comparisons to Pythia [5] simulations. It is observed that the resolved-enhanced events ($x_\gamma < 0.7$) are described by Pythia only when MPI are included.

The Pythia event generation includes direct and resolved processes in LO matched with DGLAP-type parton showers. MPI are simulated with additional *semi-hard* interactions down to $P_{\mathrm{T}} = 1.2$ GeV. The data are also compared to Cascade [6, 7] which contains direct processes using off-shell matrix elements in LO matched with CCFM-type parton showers, where the gluon emissions are not ordered in k_{T}. The gluon in the proton is described by k_{T} un-integrated gluon densities, i.e. the sets 2 and 3 [8], both of which describe the H1 data on the structure function

F_2. Note, Cascade simulates neither resolved photon processes nor MPI.

The mean charged particle multiplicities as a function of $P_{\mathrm{T,jet1}}$ in the *Toward* and *Away region* are shown in [1, 2] for direct and resolved enhanced events separately. The direct-dominated data are well described by both Pythia and Cascade. The resolved-dominated data are best described by Pythia with MPI. The contribution from MPI is largest at low $P_{\mathrm{T,jet1}}$. Cascade provides a reasonable description, except possibly at the lowest $P_{\mathrm{T,jet1}}$. The multiplicities as a function of $P_{\mathrm{T,jet1}}$ in the *High* and *Low activity regions* are shown in Fig.3. The direct-enhanced region ($x_\gamma > 0.7$) is again similarly well described by both Pythia with MPI and by Cascade. The resolved-enhanced region ($x_\gamma < 0.7$) is reasonably well described by Pythia with MPI. Cascade fails, but it is however closer to the data than Pythia without MPI.

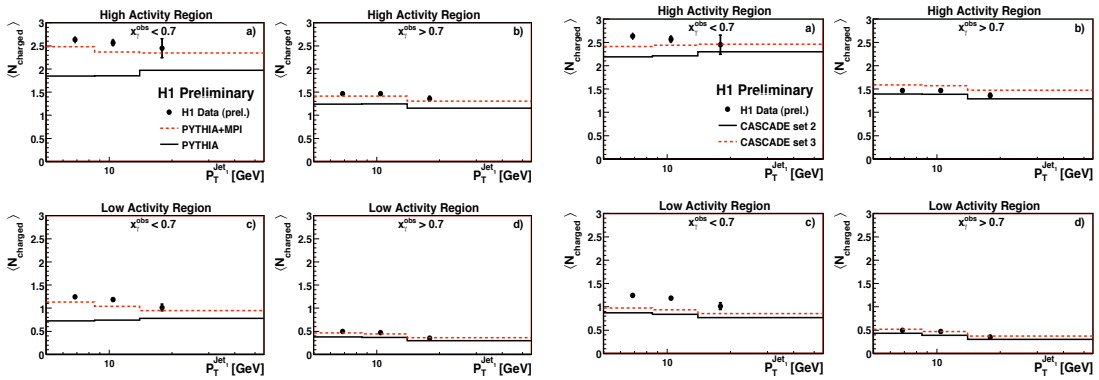

Figure 3: Mean charged particle multiplicity as a function of $P_{\mathrm{T,jet1}}$ in the *High* and *Low activity regions* for direct ($x_\gamma > 0.7$) and resolved ($x_\gamma < 0.7$) enhanced events. The data are compared to Pythia with and without MPI on the left and to Cascade for two different un-integrated gluon densities (sets 2 and 3) on the right.

It is interesting to note that Cascade is only somewhat worse in describing the resolved data, but is significantly better than Pythia without MPI. This is probably due to its different ansatz in calculating the primary hard interactions. If this picture could be confirmed, it would imply a smaller contribution from MPI. Clearly further studies at HERA and hadron-hadron colliders are needed.

3 High scales: Jet cross sections and $\alpha_s(M_Z)$ in DIS and PHP

In jet production in DIS there are two relevant high scales, i.e. Q and $P_{\mathrm{T,jet}}$, while in PHP there is only $P_{\mathrm{T,jet}}$. In order to have a smooth transition from DIS to PHP the scale $\sqrt{(Q^2 + P^2_{\mathrm{T,jet}})/2}$ is often used. In DIS we can have a more complicated interplay of the two scales. Depending on the kinematic regions in Q and $P_{\mathrm{T,jet}}$, either one of them can be larger than the other or they both can have rather similar magnitude. The precise measurements of jet cross sections in PHP and DIS by H1 and ZEUS are found to agree very well with NLO QCD calculations

such that precise values of the strong coupling $\alpha_s(M_Z)$ can be extracted.

A new preliminary extraction of $\alpha_s(M_Z)$ was obtained from a QCD re-analysis by ZEUS [10] of inclusive jet cross sections as a function of $E_{\mathrm{T,jet}}$ in PHP [9] from HERA-1. It is based on next-to-leading (NLO) pQCD calculations [12] and an estimation of the theoretical error from missing higher orders [11] not involving a refit of the data. This minimizes the theoretical error and leads to one of the most precise determinations of $\alpha_s(M_Z)$ at HERA. The method to extract α_s consisted of performing the NLO calculations with more recent PDFs [13], which had been extracted assuming different values of $\alpha_s(M_Z)$ when making the fits. The same value of $\alpha_s(M_Z)$ was used consistently in the calculation of the matrix elements and in the evolution of the PDFs. For the photon the GRV-HO [14] PDFs were used. The factorization and renormalization scales were set to $\mu_{\mathrm{R}} = \mu_{\mathrm{F}} = E_{\mathrm{T,jet}}$ of each jet.

The published data [9] and the new predictions are shown on the left of Fig. 4. The theoretical uncertainties indicated include those due to the conventional but arbitrary variation of the renormalization and factorization scales by a factor of 1/2 and 2, the PDF and the hadronization uncertainties. The dominant experimental error is due to the jet energy scale uncertainty of $\leq 1.5\,\%$. The extracted value for the strong coupling

$$\alpha_s(M_Z) = 0.1223 \pm 0.0001\,(\mathrm{stat})\,^{+0.0023}_{-0.0021}(\mathrm{exp})\,\pm 0.0030\,(\mathrm{theory})$$

is very similar to the older published one, but the theoretical uncertainty is reduced. The total uncertainty of $3.1\,\%$ is dominated by the theory uncertainty; the experimental contribution is $1.8\,\%$.

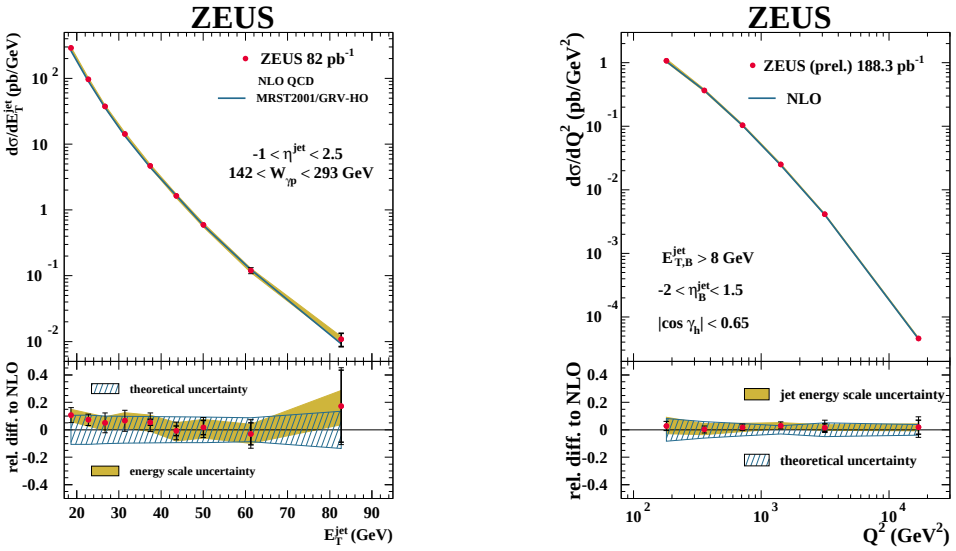

Figure 4: Inclusive jet cross section as a function of $E_{\mathrm{T,jet}}$ in PHP (left) and as a function of Q^2 in DIS (right) compared to NLO predictions.

New preliminary results from ZEUS [15] on single and double differential inclusive jet cross sections in neutral current DIS as a function of Q^2, $E_{\mathrm{T,jet}}$ and η_{jet} were presented this year. They made use of HERA-2 data corresponding to an integrated luminosity of 188 pb^{-1}. The

DIS phase space was defined by requiring $Q^2 > 125\,\mathrm{GeV}^2$ and the angle of the hadronic system $|\cos\gamma_h| < 0.65$. The jets were identified in the Breit frame [16] using the $k_\perp$ cluster algorithm [4]. In this frame they were required to have $E_{\mathrm{T,jet}} > 8$ GeV and $-2.0 < \eta_{\mathrm{jet}} < 1.5$. The dependence of the inclusive jet cross section on Q^2 is shown on the right of Fig. 4. The dominant experimental error is due to the jet energy scale uncertainty of $\leq 1.9\,\%$. The NLO predictions are shown to be in excellent agreement with the data. These calculations were performed using the program DISENT based on the dipole subtraction method [17]. The scales were chosen to be $\mu_{\mathrm{R}} = E_{\mathrm{T,jet}}$ and $\mu_{\mathrm{F}} = Q$, and for the proton PDFs the ZEUS-S parameterization [18] was taken. For the extraction of $\alpha_s(M_Z)$ the same method was used as described above for the jets in PHP. The theory uncertainty on $\alpha_s(M_Z)$ due to higher orders was estimated using the same method [11] as for the preliminary PHP result. The smallest error on $\alpha_s(M_Z)$ was obtained by fitting the Q^2 dependence for $Q^2 > 500\,\mathrm{GeV}^2$. In this region the experimental uncertainties are smaller than at lower Q^2, and also the theoretical uncertainties due to the PDFs and the missing higher orders are minimized, yielding:

$$\alpha_s(M_Z) = 0.1192 \pm 0.0009\,(\mathrm{stat})\,^{+0.0035}_{-0.0032}(\mathrm{exp})\,^{+0.0020}_{-0.0021}\,(\mathrm{theory})\,.$$

The total uncertainty is 3.5 %; in this case the experimental contribution of 2.9 % is somewhat larger than the theoretical one.

H1 has provided new single and double differential measurements of normalized NC jet cross sections [19], i.e. the ratio of inclusive jet, 2-jet and 3-jet cross sections to the inclusive DIS cross sections. By measuring normalized jet cross sections a number of experimental errors cancel partially, the luminosity error cancels completely, and the PDF uncertainty is also reduced. The dominant experimental error is due to the $\leq 1.5\,\%$ uncertainty on the jet energy scale. The data sample analyzed is from the years 1999 to 2007 and corresponds to an integrated luminosity of 395 pb^{-1}. The range covered in photon virtuality is $150 < Q^2 < 15000\,\mathrm{GeV}^2$ and in inelasticity $0.2 < y < 0.7$. The jet finding was performed in the Breit frame using the longitudinally invariant $k_\perp$ algorithm. Jets are accepted if in the laboratory frame they have $-0.8 < \eta_{\mathrm{jet}} < 2.0$. Furthermore, in the Breit frame the requirements are $P_{\mathrm{T,jet}} > 7$ GeV for inclusive jets and $P_{\mathrm{T,jet}} > 5$ GeV and additionally $M_{1,2} > 16$ GeV for 2-jet and 3-jet events. The normalized cross sections are measured as a function of Q^2, the jet transverse momentum and the proton momentum fraction [19].

Here, in Fig. 5, only the Q^2 dependence of the normalized inclusive jet and 2-jet cross section is shown. The NLO predictions for the jet cross sections were performed using the program NLOJET++ [20], and for the NC DIS cross sections the program DISENT [17] was used. The PDFs of the proton were taken from the CTEQ6.5M set [22]. For the jet calculations the factorization scale was taken to be $\mu_{\mathrm{F}} = Q$ and the renormalization scale to be $\mu_{\mathrm{R}} = \sqrt{(Q^2 + P_{\mathrm{T}}^2/2)/2}$, with P_{T} denoting the $P_{\mathrm{T,jet}}$ of the respective inclusive jet, or the arithmetic mean of the $P_{\mathrm{T,jet}}$ of the 2-jets or 3-jets. This choice is motivated by the presence of two hard scales in jet production in DIS. The theoretical errors on the normalized jet cross sections were determined in a similar way as described before for the ZEUS data.

For the extraction of the strong coupling, the jet cross sections were calculated as a function of $\alpha_s(\mu_{\mathrm{R}})$ using the FastNLO program [23], which allows to efficiently calculate cross sections based on the matrix elements from NLOJET++ and DISENT convoluted with the PDFS of the proton. From the measurements and predictions a $\chi^2(\alpha_s)$ was calculated using the Hessian method [24]. This method takes the correlations of experimental uncertainties into account. The dominant theory error is due to the uncertainty of the NLO prediction, which was estimated

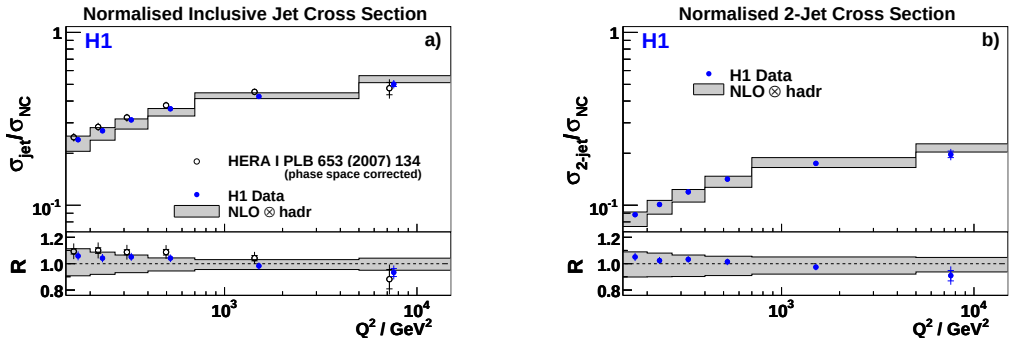

Figure 5: The normalized inclusive jet (left) and 2-jet (right) cross sections in NC DIS as functions of Q^2. They are compared to NLO predictions corrected for hadronization effects. The theory uncertainties associated with the renormalization and factorization scales, the PDFs and the hadronization are shown as grey bands.

by a variation of the renormalization and factorization scales by a factor of 1/2 and 2 of the nominal scale in fits of the data.

Fits of $\alpha_s(M_Z)$ to the individual normalized jet cross section data sets yielded consistent results. Therefore, all of them are used in a common fit taking correlations into account. This fit yields

$$\alpha_s(M_Z) = 0.1192 \pm 0.0007\,(\text{exp})\,^{+0.0046}_{-0.0030}\,(\text{theory})\;\pm 0.0016\,(\text{PDF})$$

with a fit quality $\chi^2/\text{ndf} = 65.0/53$. The total uncertainty of 3.6 % is dominated by the theory uncertainty; the experimental contribution is 0.6 % only.

On the left of Fig. 6 α_s is shown as a function of the scale Q extracted from the high Q^2 H1 data just discussed (6 rightmost points) and additionally as obtained from a preliminary low Q^2 H1 analysis [25]. The solid line shows the result of the evolution of the 2-loop solution of the renormalization group equation using the value of $\alpha_s(M_Z)$ extracted from the high Q^2 normalized jet cross sections. The inner (outer) band indicates the experimental (theoretical) uncertainties. As can be seen, the α_s values at low Q are nicely consistent with the prediction from high Q, and, interestingly, they lie within the theory uncertainty of the high Q^2 fit. When estimating the theory errors for the low Q values a much larger theoretical uncertainty is observed [25].

On the right of Fig. 6 the most recent values of $\alpha_s(M_Z)$ from jet measurements at HERA, from jet and event-shape measurements at LEP [27] and the 2009 world average by Bethke [27] are shown. The HERA $\alpha_s(M_Z)$ extractions have achieved an experimental precision compatible and competitive with the result from LEP and the world average. At this point in time the uncertainties at HERA are dominated by the NLO theory uncertainty. While advances in theory are most promising and most needed for being able to reduce the total uncertainty, one may also expect further experimental improvements by finalizing the analysis of all HERA data and by combining measurements from H1 and ZEUS.

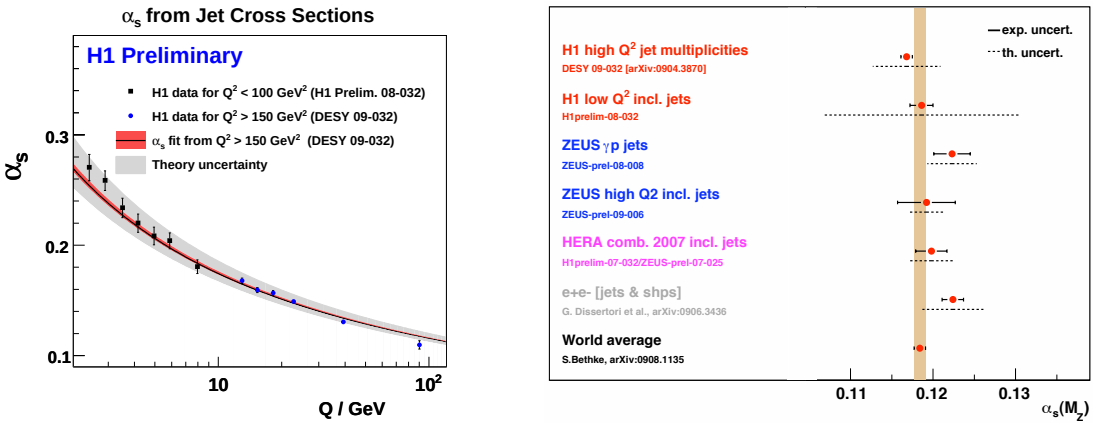

Figure 6: The running of the strong coupling as a function of the scale Q. The line shows the result of evolving the value of $\alpha_s(M_Z)$ extracted from the high Q^2 normalized jet cross sections down to the values of α_s obtained from the low Q^2 inclusive jet cross sections.

4 Multiple scales: Heavy flavor production

According to pQCD calculations, heavy quarks are mainly produced via the direct photon gluon fusion process $\gamma g \to Q\bar{Q}$. Therefore, measurements of $Q\bar{Q}$ production provide information on the gluon content of the proton. The heavy quark mass M is an additional hard scale in the calculations besides the momentum transfer of the exchanged photon Q and the transverse momentum P_{T} of the heavy quark. Due to this multi-scale problem, different approaches exist in the treatment of the pQCD series, depending on the relative magnitude of M, Q and P_{T}.

- At low scales when Q and $P_{\mathrm{T}} \approx M$, calculations in the *massive* fixed flavor number scheme (FFNS) appear appropriate. In this scheme the heavy quarks are produced only dynamically, they do not exist in the proton. The mass of the heavy quark is taken into account in the LO photon gluon fusion ($\gamma g \to Q\bar{Q}$) matrix element. NLO terms are of order α_s^2. Parton level calculations at NLO which take this approach are provided by the HVQDIS [29] program in DIS and by the FMNR [30] program in PHP. Also the PDF parameterizations CTEQ5F3 [31] and MRST2004FF3 [32] were obtained using this framework.

- At high scales when Q and $P_{\mathrm{T}} \gg M$, calculations in the zero mass variable flavor number scheme (ZM-VFNS) are applicable. In this scheme charm and beauty are treated as massless partons which exist already in the proton. At LO the quark parton model process ($\gamma Q \to Q$) provides the dominant contribution. At NLO photon gluon fusion and QCD Compton processes also contribute.

- Finally and more recently, calculations in the general mass variable flavor number scheme (GM-VFNS), which interpolate between the massless and the massive schemes, provide a description of heavy quark production over the whole range in Q^2. Such calculations are used in the latest global PDF fits, yielding the following PDF parameterizations: CTEQ6.6 NLO [33], MSTW08 NLO [34] and MSTW08 NNLO [34].

Measurements of the contributions of charm and beauty, $F_2^{c\bar{c}}$ and $F_2^{b\bar{b}}$, to the proton structure function F_2 allow to test these schemes. The gluon and heavy quark PDFs are important for the understanding of measurements of standard and beyond standard model physics processes at the TEVATRON and LHC. For this reason the focus here is on most recent measurements of charm and particularly beauty in DIS at HERA. Some of the results presented make use of the full HERA-2 data sample and thus offer a significant improvement in precision compared to previous HERA-1 results.

The fraction of charm production in total NC DIS is large, up to $\approx 30\%$ at HERA energies. Charm quarks are tagged predominantly by reconstructing the decays of charmed hadrons, $D^{\star\pm}$, $D^{\pm}$, $D_s^{\pm}$ and D^0 (see for example [35, 36]). The signal to background ratio of these measurements can be further improved by using information on the decay length provided by the decay vertex as reconstructed by the silicon vertex detectors of the H1 and ZEUS experiments.

Beauty quarks, in contrast to the large contribution of charm to deep-inelastic scattering, contribute at most a few % and an order of magnitude less at low Q^2. This makes the tagging of beauty in DIS events very challenging. To extract signals use is made of various properties of beauty hadrons: their semi-leptonic decays and their relatively large mass and long life-time. In semi-leptonic decays the large transverse momentum of the lepton w.r.t. the jet axis, $p_{\mathrm{T}}^{\mathrm{rel}}$, and the missing neutrino momentum projected onto the direction of the lepton, $p_{\mathrm{T}}^{\mathrm{miss}\|\mu}$, are used. In addition, information on the impact parameter δ of the lepton as obtained from the vertex detectors can be used. In analyses not requiring a lepton the impact parameter significance of all tracks with hits in the vertex detector and the distance significance of the secondary vertex are used by a neural network to discriminate between beauty, charm and light quarks. The c, b and light quark fractions in the data are extracted performing fits of simulated Monte Carlo (MC) templates to the measured distributions.

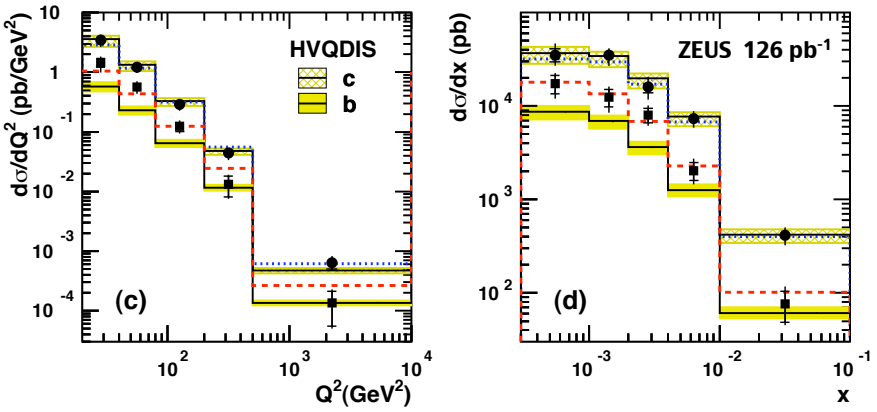

Figure 7: Differential muon cross sections for c and b production as a function of Q^2 and x. The bands show the NLO predictions by HVQDIS and the corresponding uncertainties.

Inclusive charm and beauty cross sections were measured by ZEUS [37] based on 126 pb^{-1} of HERA-2 data, using semi-leptonic decays of heavy hadrons into muons. The kinematic phase space covered is given by $Q^2 > 20\,\mathrm{GeV}^2$, the inelasticity $0.01 < y < 0.7$, $P_{\mathrm{T}}{}^{\mu} > 1.5$ GeV and $-1.6 < \eta^{\mu} < 2.3$. The charm and beauty contributions were extracted by simultaneous

fits of MC templates to the muon $p_{\mathrm{T}}^{\mathrm{rel}}$, $p_{\mathrm{T}}^{\mathrm{miss}\|\mu}$ and δ distributions (see [1, 37]). The relatively low cut on $P_{\mathrm{T}}{}^{\mu}$ allows both, the inclusive charm and beauty cross sections to be determined simultaneously as a function of $P_{\mathrm{T}}{}^{\mu}$, η^{μ}, Q^2 and x. They are shown as a function of Q^2 and x in Fig. 7 (see [1, 37] for the dependence on $P_{\mathrm{T}}{}^{\mu}$ and η^{μ}). The charm data are well described by HVQDIS, while for beauty the data lie above the predictions at low Q^2 and x. The measurements were extrapolated to the full phase space to provide charm and beauty structure functions (see Fig. 8 and Fig. 9 to be discussed below).

The H1 collaboration provided new data on the inclusive production of charm and beauty in DIS [38] in the kinematic region $5 < Q^2 < 650\,\mathrm{GeV}^2$ and $0.0002 < x < 0.032$ corresponding to an integrated luminosity of 189 pb^{-1}. This analysis used the impact parameter significance of tracks and the distance significance from the primary vertex to the decay vertex of the heavy hadrons as inputs to a neural network (see [1, 38]. As in the ZEUS analysis the charm and beauty contributions were obtained from fits of various distributions to MC templates. From these the visible cross sections were determined and extrapolated to the full phase space, providing measurements of the charm and beauty structure functions $F_2^{c\bar{c}}$ and $F_2^{b\bar{b}}$ respectively.

The results for $F_2^{b\bar{b}}$ together with the ones from ZEUS discussed above are shown in Fig. 8 as a function of Q^2 for different fixed values of x. They are in reasonable agreement, although the ZEUS results tend to be higher than the ones from H1 at low Q^2. The measurements of $F_2^{b\bar{b}}$ are well described by the latest GM-VFNS calculations (MSTW08) in NLO and NNLO. In the phase space region of the measurements the differences between NLO and NNLO are tiny, except for $Q^2 < M_b^2$.

A large number of measurements of the charm structure function $F_2^{c\bar{c}}$ using different methods are shown in Fig. 9 as a function of Q^2 for various fixed values of x. The data cover a large phase space in Q^2 and x due to the substantially higher statistics for charm. The acceptance of the different methods varies between 20% and 70%, but the results

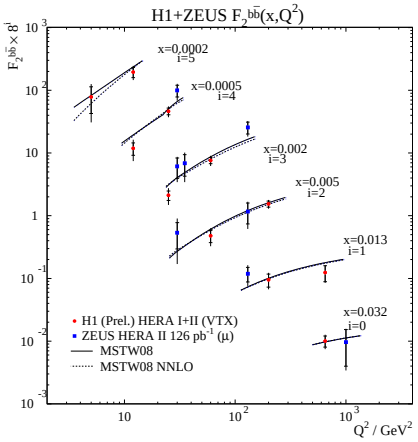

Figure 8: The structure function $F_2^{b\bar{b}}$ as a function of Q^2 for fixed values of x. Also shown are the GM-VFNS predictions MSTW08 in NLO and NNLO.

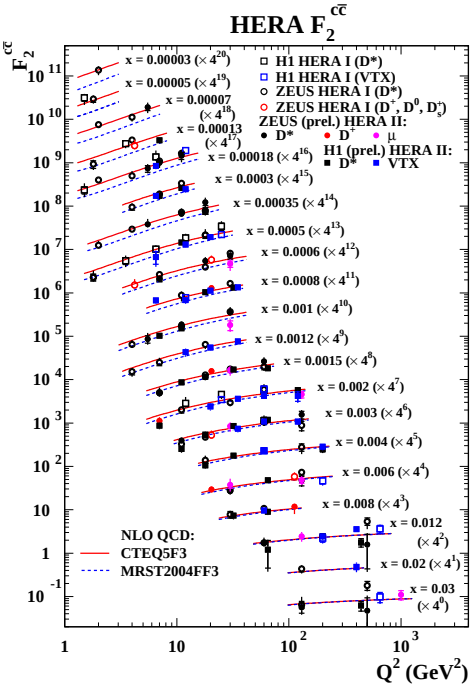

Figure 9: The structure function $F_2^{c\bar{c}}$ as a function of Q^2 for fixed values of x. Also shown are the massive FFNS predictions CTEQ5F3 and MRST2004FF3 in NLO.

agree well between them. The theory prediction based on the massive FFNS provides a reasonable description of the data. The largest differences between the CTEQ5F3 and MRST2004FF are in the region $Q^2 < 2M_c^2$ due to different inputs in this region when fitting the PDFs. The precision in $F_2^{c\bar{c}}$ and $F_2^{b\bar{b}}$ can be expected to be further improved by analyzing the full HERA statistics and by combining results using different methods within an experiment and within H1 and ZEUS.

5 Summary

Low & high scales – The study of the underlying event, which involves an understanding of the physics at high and at low scales, indicates that in resolved photon interactions the description of the mean charged particle multiplicity in different azimuthal regions requires multiple interactions when using Pythia to describe the data. The comparison of the data with CASCADE, which provides a different approach to hard interactions and also includes no MPI, suggests that within this model the importance of the underlying event is reduced. This requires further studies. If correct, this of course would have interesting and important consequences, particularly for understanding the data at the TEVATRON and LHC.

High scales – Jet production in DIS and PHP are found to be well described by NLO QCD. This allows for precise extractions of the strong coupling $\alpha_s(M_Z)$, competitive and compatible with results from e^+e^- annihilation at LEP and the world average. The experimental precision reached so far is among the best of the various measurements, however the theoretical precision at NLO is considerably worse. A significant increase in total precision can be expected from the calculation of higher orders beyond NLO.

Multiple high scales – The physics of charm and beauty production at HERA involves the interplay of the hard scales M, Q and P_{T}. Experimentally, many different techniques to tag charm or beauty have been employed for the measurement of differential cross sections and their extrapolation to the total inclusive cross sections or structure functions $F_2^{c\bar{c}}$ and $F_2^{b\bar{b}}$. They are all found to be overall well described by QCD calculations.

Work is continuing at HERA towards final results by analyzing the complete HERA data set with improved understanding of the detector and event reconstruction, and by combining H1 and ZEUS measurements.

6 Acknowledgments

I want to thank my colleagues in H1 and ZEUS who provided suggestions and help in preparing this talk. Thanks also to the organizers for this interesting conference.

References

[1] Slides: `http://indico.desy.de/contributionDisplay.py?contribId=27&sessionId=9&confId=1407`

[2] H1 Collaboration, *"Study of Multiple Interactions in Photoproduction at HERA"*, H1prelim-08-036.

[3] T. Affolder *et al.* [CDF Collaboration], Phys. Rev. D **65** (2002) 092002.

[4] S. Catani, Y.L. Dokshitzer, M.H. Seymour and B.R. Webber, Nucl. Phys. B **406** (1993) 187.

[5] T. Sjöstrand, S. Mrenna and P. Skands, JHEP **0605** (2006) 026 [arXiv:hep-ph/0603175].

[6] H. Jung and G.P. Salam, Eur. Phys. J. C **19** (2001) 351 [arXiv:hep-ph/0012143].

[7] H. Jung, Comput. Phys. Commun. **143** (2002) 100 [arXiv:hep-ph/0109102].

[8] M. Hansson and H. Jung, "Status of CCFM: Un-integrated gluon densities," arXiv:hep-ph/0309009.

[9] S. Chekanov *et al.* [ZEUS Collaboration], Phys. Lett. B **560** (2003) 7 [arXiv:hep-ex/0212064].

[10] ZEUS Collaboration, *"α_s from inclusive-jet cross sections in photoproduction at ZEUS"*, ZEUS-prel-08-008.

[11] R.W.L. Jones, M. Ford, G.P. Salam, H. Stenzel and D. Wicke, JHEP **0312** (2003) 007 [arXiv:hep-ph/0312016].

[12] M. Klasen, T. Kleinwort and G. Kramer, Eur. Phys. J. direct C **1** (1998) 1 [arXiv:hep-ph/9712256].

[13] A.D. Martin, R.G. Roberts, W.J. Stirling and R.S. Thorne, Eur. Phys. J. C **23** (2002) 73 [arXiv:hep-ph/0110215].

[14] M. Gluck, E. Reya and A. Vogt, Phys. Rev. D **45** (1992) 3986.

[15] ZEUS Collaboration, *"Inclusive-jet production in NC DIS with HERA II"*, ZEUS-prel-09-006.

[16] R.P. Feynman, "*Photon-Hadron Interactions.*" Benjamin, New York, (1972); K.H. Streng, T.F. Walsh and P.M. Zerwas, Z. Phys. C **2** (1979) 237.

[17] S. Catani and M.H. Seymour, Nucl. Phys. B **485** (1997) 291 [Erratum-ibid. B **510** (1998) 503] [arXiv:hep-ph/9605323].

[18] S. Chekanov *et al.* [ZEUS Collaboration], Phys. Rev. D **67** (2003) 012007 [arXiv:hep-ex/0208023].

[19] F.D. Aaron *et al.* [H1 Collaboration], arXiv:0904.3870 [hep-ex], to be published in Eur. Phys. J. C.

[20] Z. Nagy and Z. Trocsanyi, Phys. Rev. Lett. **87** (2001) 082001 [arXiv:hep-ph/0104315].

[21] J. Pumplin, D.R. Stump, J. Huston, H.L. Lai, P.M. Nadolsky and W.K. Tung, JHEP **0207** (2002) 012 [arXiv:hep-ph/0201195].

[22] W.K. Tung, H.L. Lai, A. Belyaev, J. Pumplin, D. Stump and C.P. Yuan, JHEP **0702** (2007) 053 [arXiv:hep-ph/0611254].

[23] T. Kluge, K. Rabbertz and M. Wobisch, published in procs. of "Deep-Inelastic Scattering DIS 2006", eds. M. Kuze *et al.*, 483, arXiv:hep-ph/0609285.

[24] M. Botje, Eur. Phys. J. C **14** (2000) 285 [arXiv:hep-ph/9912439].

[25] H1 Collaboration, *"Inclusive Jet Production at low Q^2 and determination of α_s"*, H1prelim-08-032.

[26] S. Kluth, J. Phys. Conf. Ser. **110** (2008) 022023 [arXiv:0709.0173 [hep-ex]].

[27] S. Bethke, "The 2009 Wolrd Average of $\alpha_s(M_Z)$," arXiv:0908.1135 [hep-ph].

[28] J. Smith and W.L. van Neerven, Nucl. Phys. B **374** (1992) 36.

[29] B.W. Harris and J. Smith, Phys. Rev. D **57** (1998) 2806 [arXiv:hep-ph/9706334].

[30] S. Frixione, M.L. Mangano, P. Nason and G. Ridolfi, Nucl. Phys. B **412** (1994) 225 [arXiv:hep-ph/9306337].

[31] H. L. Lai *et al.* [CTEQ Collaboration], Eur. Phys. J. C **12** (2000) 375 [arXiv:hep-ph/9903282].

[32] A. D. Martin, W. J. Stirling and R. S. Thorne, Phys. Lett. B **636** (2006) 259 [arXiv:hep-ph/0603143].

[33] P. M. Nadolsky *et al.*, Phys. Rev. D **78** (2008) 013004 [arXiv:0802.0007 [hep-ph]].

[34] A.D. Martin, W.J. Stirling, R.S. Thorne and G. Watt, arXiv:0901.0002 [hep-ph].

[35] H1 Collaboration, *"$D^\star$ production at low Q^2 with the H1 detector"*, H1prelim-08-072; *"$D^\star$ production at high Q^2 with the H1 detector"*, H1prelim-08-074.

[36] S. Chekanov *et al.* [ZEUS Collaboration], arXiv:0812.3775 [hep-ex].

[37] S. Chekanov *et al.* [ZEUS Collaboration], arXiv:0904.3487 [hep-ex].

[38] F.D. Aaron *et al.* [H1 Collaboration], arXiv:0907.2643 [hep-ex].

Review of Recent Tevatron Jet, W/Z+Jet and Heavy-flavor Production Results

Shin-Shan Yu

On behalf of the CDF and DØ Collaborations

Fermi National Accelerator Laboratory, P.O. Box 500, Batavia, IL 60510, USA

DOI: http://dx.doi.org/10.3204/DESY-PROC-2009-03/Yu

This paper reviews several recent measurements at the Fermilab Tevatron, including cross sections for inclusive jet, dijet production, cross sections for electroweak boson (W or Z) production in association with inclusive or heavy-flavor (b or c) jets, and b-jet shapes. In addition, searches for new physics using the dijet angular distributions are discussed. These analyses are based on integrated luminosities of 0.3–2.5 fb^{-1} of $p\overline{p}$ collisions at $\sqrt{s}$ = 1.96 TeV, collected with the CDF and DØ detectors. The results directly test the leading order and next-to leading order calculations of perturbative quantum chromodynamics and provide constraints on the parton distribution functions and physics beyond the standard model.

1 Introduction

Measurements using jet final states have been of great interest to both experimentalists and theorists for the following reasons. First, among high p_T physics processes at a hadron collider, jet production has the largest cross section. Therefore, jet production can test perturbative quantum chromodynamics (pQCD) with the highest reach in energy and rapidity (y). Second, measurements at the Tevatron, which are complementary to the measurements by HERA and fixed target experiments, may constrain parton distribution functions (PDFs) in the region of large Q^2 and medium-to-large x and reduce uncertainties on the gluon, b, and s quark PDFs. Measurements will have greater impacts on PDFs when the uncertainties on the cross sections due to variation of renormalization and factorization scales (pQCD uncertainties) are much smaller compared to the uncertainties from existing PDFs, *e.g.* measurements of inclusive jet cross section. Third, these measurements not only provide stringent tests of the standard model (SM) physics, but also probe physics beyond the SM. The production of W or Z in conjunction with inclusive or heavy-flavor jets is one of the major backgrounds to searches for SM Higgs, SUSY, and other models. Measurements of the cross sections of these processes decrease uncertainties on the estimation of backgrounds. The angular distributions of jet events, which are not very sensitive to PDFs, can also probe the presence of new physics.

Section 2 briefly describes the jet definition and reconstruction algorithms used at the Tevatron. Sections 3–10 discuss the results of these analyses. Section 11 gives the conclusion.

2 Jet Definition and Reconstruction

Jets are collimated sprays of particles originating from quarks or gluons. The most common jet reconstruction algorithms at the Tevatron are midpoint cone and k_T.[1] The midpoint cone and k_T algorithms cluster objects[2] based on their proximity in the geometry and momentum space, respectively. The midpoint cone algorithm starts from objects above an energy threshold (seeds) and sums the four-momentum vectors of all objects within a cone of radius $R_{\rm cone}$[3] around the seed. The total four-momentum vector of these objects defines a new jet axis. The process is iterated until the updated jet axis is within a tolerance from the previous jet axis; a stable cone is formed. Then, additional seeds are added at the midpoints between all pairs of stable cones whose separation is less than $2R_{\rm cone}$ and the clustering procedure is repeated using these additional seeds. Finally, geometrically overlapping cones are split or merged depending on the amount of shared momentum. The k_T algorithm starts by considering every object as a protojet and calculates $k^2_{T,i}$ for each protojet and $k^2_{T(i,j)}$ for each pair of protojets.[4] All $k^2_{T,i}$ and $k^2_{T(i,j)}$ are then collected into a single sorting list. If the smallest in this list is $k^2_{T,i}$, protojet i is promoted to a jet and removed from the list. If the smallest is $k^2_{T(i,j)}$, protojets i and j are combined into a single protojet. The procedure is iterated until the list is empty. The cone algorithm has simpler underlying event and multiple interaction corrections while the k_T algorithm is less sensitive to higher order perturbative QCD effects. More discussions of the strengths and weaknesses of these two algorithms are in Ref. [1].

Three levels of energies are defined, (i) parton level: the true energy of the parent parton (quark or gluon), (ii) particle level: the total true energy of all particles contained in a jet, including underlying event and products of fragmentation and hadronization, but excluding the energy from multiple $p\bar{p}$ interactions per crossing, (iii) detector level: energy measured in the calorimeters. The cross sections discussed here are presented as functions of particle-level energy.[5] Calorimeters may under- or over-measure the energies of particles due to finite resolution, non-uniformity, and inefficiency of detector. Programs that provide theoretical predictions of cross sections at the next-to leading order (NLO) typically do not include parton showering. Therefore, in order to have a valid comparison between data and theory, corrections have to be applied. For measurements in data, corrections of energy from the detector to the particle level follow the procedures described in Ref. [2, 3].[6] For theory predictions, corrections of energy from the parton to the particle level are obtained by comparing `PYTHIA` or `HERWIG` MC with parton shower and fragmentation switched on vs. switched off.[7]

[1] When comparing data and theory, the same algorithms are applied.

[2] In data, the "object" is a calorimeter cell with energy deposit. In theory, the "object" is a parton.

[3] $R^2_{\rm cone} \equiv \Delta y^2 + \Delta\phi^2$.

[4] Here, $k^2_{T,i} \equiv p^2_{T,i}$ and $k^2_{T(i,j)} \equiv min(p^2_{T,i}, p^2_{T,j})\Delta R^2_{i,j}/D^2$, where $R_{i,j}$ is the distance between the two protojets in the $y-\phi$ space and D is a parameter that controls the size of the jet.

[5] The energy at the particle level depends only on physics models, not detectors.

[6] The corrections are $\approx$ 20% (50%) of the jet energy at 50 GeV and $\approx$ 10 % (20%) at 400 GeV for CDF(DØ).

[7] The corrections are $\approx$ 10–20% at 50 GeV and drops quickly to below 5 % when energy is above 100 GeV.

3 Measurements of Inclusive Jet Cross Section

As mentioned in Section 1, inclusive jet production cross section provides constraints on the gluon PDF.[8] The inclusive jet cross section from Tevatron Run I [4] had excess in data with respect to NLO predictions at high p_T. Data had been included later in the global fits of CTEQ6 and MRST2001 and preferred larger contribution of gluons at high x. At Run II, CDF and DØ have measured inclusive jet cross section with midpoint cone [5, 6] and k_T algorithms [7]. The Run II measurements have extended the cross section reach significantly both in p_T and rapidity (y). The midpoint seeds are added[9] in the cone algorithm in order to reduce sensitivity to non-perturbative effects, such as radiation of soft gluons.

The cross section is measured as a function of corrected jet p_T (to the particle level), in 5–6 bins of jet rapidity. Dominant sources of systematic uncertainties are jet energy scale[10] and jet energy resolution. Measurements in data are compared to NLO predictions and CTEQ6.1M PDFs for CDF, CTEQ6.5M PDFs for DØ. The renormalization and factorization scales (μ_R and μ_F) are set to $0.5p_T^{\rm jet}$ for CDF and $p_T^{\rm jet}$ for DØ. Figure 1 and Figure 2 show the ratios of Run II data to theory using the cone algorithm and k_T algorithm, respectively. Although the PDFs and scales used are not exactly the same, all three measurements have a similar trend: at high p_T and large $|y|$ (equivalent to large x), the data prefer smaller values of cross section than the theory prediction. The CDF k_T and DØ cone measurements are already included in the global fit of MSTW2008 PDFs; not only the uncertainties of gluon component have decreased, but also the central values. There is an ongoing effort to include the CDF cone measurement and update CTEQ PDFs as well.

4 Measurements of Dijet Mass Spectra and Search for New Particles Decaying into Dijets

Measurements of dijet mass spectra provide an alternate method to constrain PDFs. In addition, new particles predicted by physics beyond SM may appear as resonances in the dijet mass spectra. These new particles and decays include: (i) $q^* \to qg$ (quark compositeness [8]), (ii) axigluon or coloron $\to q\bar{q}$ (chiral color model [9]), (iii) color-octet techni-ρ (ρ_{T8}) $\to q\bar{q}$ or gg (extended and topcolor-assisted technicolor [10]), (iv) Randall Sundrum graviton $\to q\bar{q}$ or gg (warped extra dimension [11]), (v) W' (Z') $\to q\bar{q}'(q\bar{q})$ (grand unified theories GUT [12]), (vi) diquark $\to qq$ or $\bar{q}\bar{q}$ (E_6 GUT [13]). The CDF measurement of dijet mass spectrum [14] requires both jets to be central ($|y^{\rm jet}| < 1.0$) while the DØ measurement [15] is performed in six bins of $|y|$ and extended to $|y|_{\rm max} = 2.4$, where $|y|_{\rm max}$ is the rapidity of the jet with the largest $|y|$ among the two leading jets (see Figure 3).[11] Both CDF and DØ have not seen significant discrepancy from the NLO predictions and the results are yet to be included in the global PDF fits. While the limits on W', Z', and RS graviton are not as stringent as those obtained by the lepton channels, CDF has set the world's best limits and excluded at 95% C.L. the mass of q^* at 260–870 GeV/c^2, of axigluon and coloron at 260–1250 GeV/c^2, of ρ_{T8} at 260–1100 GeV/c^2, and of E_6 diquark at 260–630 GeV/c^2. The DØ limits are work in progress.

[8] The inclusive jet cross section measured in the forward region will be most sensitive to gluon PDF since new physics is expected to appear mostly in the central region.

[9] There were no midpoint seeds at Run I.

[10] The uncertainty on the jet energy scale is 2–3(1.2–2)% for CDF(DØ).

[11] Ordered in jet p_T.

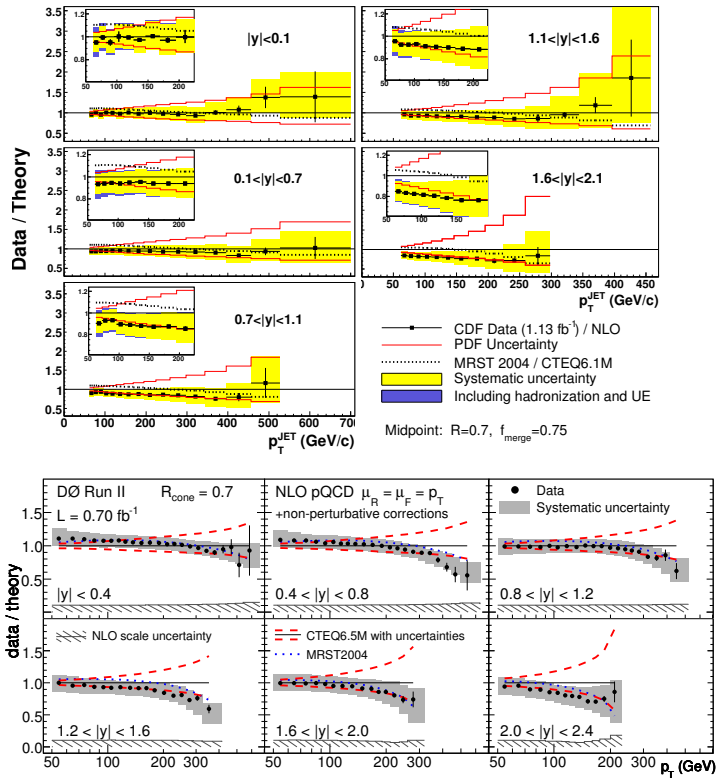

Figure 1: The Tevatron Run II results of inclusive jet cross section using midpoint cone algorithm. Ratios of CDF (top) and DØ (bottom) data to NLO theory are shown.

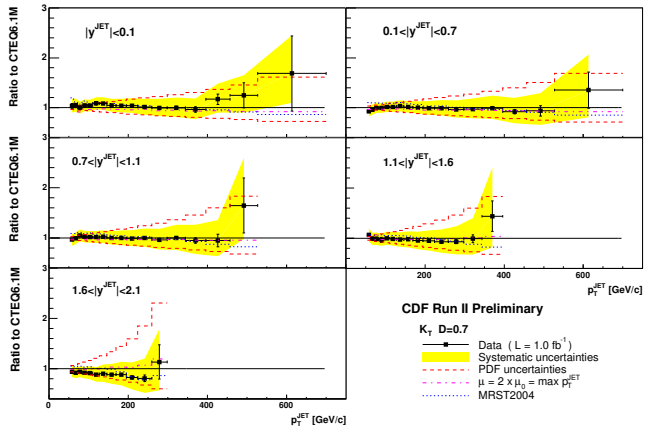

Figure 2: The Tevatron Run II results of inclusive jet cross section using k_T algorithm. Ratios of CDF data to NLO theory are shown.

5 Search for New Physics in the Dijet Angular Distributions

An excess in data may indicate presence of new physics, but may also imply that the PDFs have to be updated; matrix elements for hard scattering processes and PDFs are entangled in the calculation of absolute production cross sections. Instead, the shapes of angular distributions, which are disentangled from PDFs, are more sensitive to new physics. The shape of the dijet angular variable, $\chi_{\rm dijet}$[12], is flat for Rutherford scattering, and is more strongly peaked at small value of $\chi_{\rm dijet}$ in the presence of new physics;[13] the peak fraction increases as the dijet mass M_{jj} increases. CDF has focused on M_{jj} =0.55–0.95 TeV/c^2 and looked at the ratio of the number of events in two $\chi_{\rm dijet}$ regions: $N_{1<\chi_{\rm dijet}<10}/N_{15<\chi_{\rm dijet}<25}$, for four M_{jj} bins [16]. DØ has a wider mass range[14], 0.25–above 1.10 TeV/c^2, and has studied the normalized $\chi_{\rm dijet}$ distributions for ten M_{jj} bins (see Figure 3) [17]. Since no significant discrepancy is observed between the data and SM prediction, both experiments set limits on the compositeness scales [8], Λ_C, which characterizes the physical size of composite states. DØ has obtained the world's best limits: $\Lambda_C > 2.84$ (2.82) TeV for the interference term $\eta = +1(-1)$, assuming flat prior in the new physics cross section. DØ also set limits on ADD large extra dimension [18] and TeV^{-1} extra dimension [19].

6 Measurement of W + Inclusive Jet Cross Section

CDF has used early Run II data and measured the W + jet cross section [20]. While most jet cross section measurements have major uncertainties from the jet energy scale, this measurement also suffers from the uncertainty on the background estimate at large jet p_T and high jet multiplicity; this is the region where top pair production dominates. Measured results are compared with NLO predictions from MCFM and two different schemes of interfacing leading-order (LO) matrix element with parton shower generators and jet matching (MLM:`ALPGEN`+`HERWIG`+`MLM`, SMPR: `MADGRAPH`+`PYTHIA`+`CKKW`). Both LO and NLO predict well the cross section ratios of different jet multiplicity σ_n/σ_{n-1}. The NLO predictions also have good agreement with the measurement, both in shape and absolute cross section, as functions of jet multiplicity and jet E_T. As expected, the LO tends to under-predict the absolute cross section. Among the two LO schemes, SMPR has better agreement at low E_T due to a better underlying event model in `PYTHIA`.

7 Measurements of W + Heavy-flavor Jet Cross Section

The production of W boson in association with heavy-flavor jets is one of the major backgrounds to searches for new physics (*e.g.* Higgs). A sample of W boson with heavy-flavor jets may be obtained by requiring the jets to contain either secondary vertices (`SECVTX` tagging) or a soft electron or muon (soft lepton tagging).

[12]Here, $\chi_{\rm dijet} \equiv (1+\cos\theta^*)/(1-\cos\theta^*)$, where $\cos\theta^* = \tanh(y^*)$, $\pm y^*$ is the rapidity of each jet in the center-of-mass frame, and $y^* = \frac{1}{2}(y_1 - y_2)$.

[13]Here, the new physics models refer to quark compositeness, large extra dimension, and TeV^{-1} extra dimension.

[14]This is the same dataset that is used to measure the dijet mass spectrum, as described in Section 4.

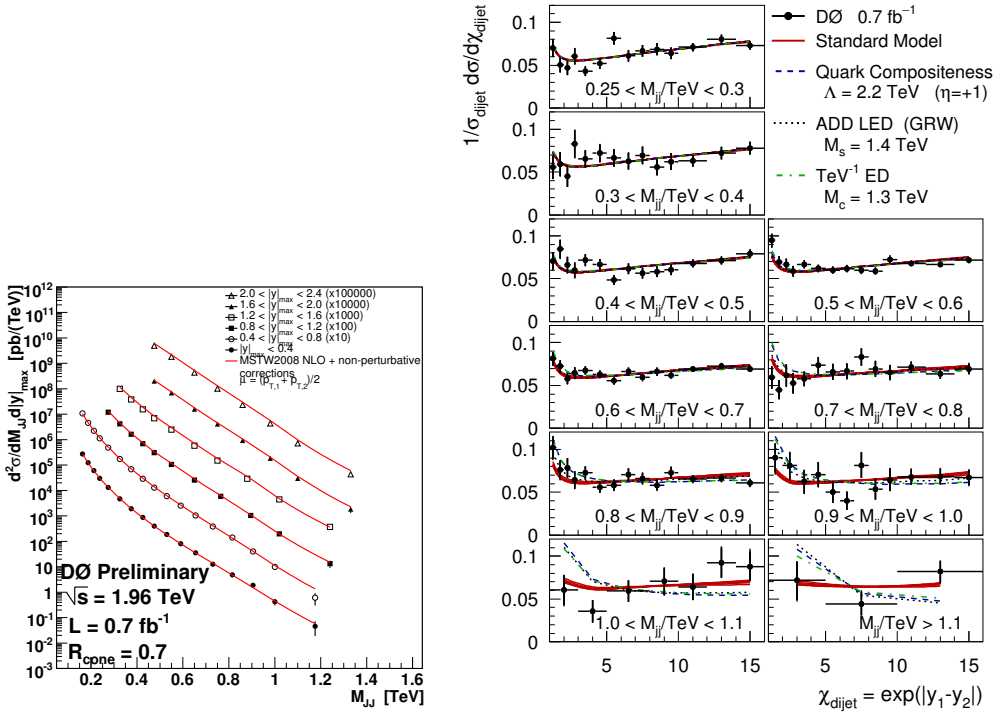

Figure 3: Measurements of dijet mass spectra by DØ (left) and normalized $\chi_{\rm dijet}$ distributions from the DØ data, SM, and new physics predictions (right).

CDF has measured the W + b jet production cross section, where the measurement is proportional to the number of b jets and restricted to the kinematic range: a charged lepton with $p_T > 20$ GeV/c and $|\eta| < 1.1$, a neutrino with $p_T > 25$ GeV/c, and one or two jets regardless of species with $E_T > 20$ GeV and $|\eta| < 2.0$ [21]. This definition of cross section has been chosen in order to minimize uncertainties on the acceptance. The jets are tagged by ultra-tight `SECVTX` [22].[15] The fraction of tagged jets originating from b quarks is extracted by fitting the mass reconstructed at the secondary vertices to templates of light, c, and b-flavor jets (see Figure 4). The cross section has been measured to be $2.74 \pm 0.27(stat) \pm 0.42(syst)$ pb, which is ≈ 3.5 times larger than the LO prediction of 0.78 pb from `ALPGEN`. The NLO calculations are available, but not yet implemented in an MC program that allows comparison of data and theory with user-defined kinematic requirements.

CDF and DØ have also studied samples of W boson with single charm candidate by tagging the charm quark with soft muon tagging [23, 24]. While `SECVTX` and soft lepton taggings could help separating heavy-flavor from light-flavor jets, a separation between b and c requires more advanced analysis techniques, such as neural network. Nevertheless, one could employ the fact that in W + single charm events, the muon from semileptonic decays of c hadrons and the

[15] The ultra-tight `SECVTX` is operated at a different point from the standard `SECVTX` [22] and further decreases the light (charm) backgrounds by a factor of 10 (4), at the expense 50% reduction in b-tagging efficiency.

charged lepton from W decays are oppositely charged, therefore, with a large asymmetry in the number of oppositely-charged vs. same-charged events, while background from $Wb\bar{b}$ or $Wc\bar{c}$ has zero asymmetry. CDF has measured the absolute cross section for $W \to \ell\bar{\nu}_\ell$, $p_T^c > 20$ GeV/c, and $|\eta^c| < 1.5$ to be 9.8 ± 3.2 pb. DØ has measured the cross-section ratio, $\sigma(W+c)/\sigma(W+jet)$ for jet $p_T > 20$ GeV/c and $|\eta| < 2.5$, to be $0.074 \pm 0.019(stat)\,^{+0.012}_{-0.014}(syst)$, and also measured the ratios as a function of jet p_T. Both experiments have found good agreement between data and LO or NLO predictions within uncertainties. Since the dominant process of Wc production is $gs \to Wc$, future Wc cross section measurements with reduced uncertainties may constrain the s quark PDF.

8 Measurements of Z + Inclusive Jet Cross Section

The measurements of Z boson production in association with inclusive jets contain only small amount of background from mis-identified leptons and are one of the cleanest channels to test pQCD. CDF has measured the Z + jet cross section as functions of jet multiplicity and jet E_T [25]. In addition, DØ has measured the cross section as a function of Z boson kinematics: $p_T(Z)$ and $y(Z)$, and the angular separation between Z and jets: $\Delta\phi(Z, \text{jet})$, $\Delta y(Z, \text{jet})$, and $y_{\text{boost}}(Z + \text{jet})$ [26, 27, 28]. Both CDF and DØ have seen good agreements between data and theory when NLO predictions are available. DØ has also compared their results with a number of LO matrix element generators and pure parton showering programs, such as `ALPGEN`, `SHERPA`, `PYTHIA`, `HERWIG`. Overall, the LO MC programs under-predict the cross sections, but the programs that interface matrix element generator with parton shower MC have better agreement with data in shapes. The results of these comparisons may provide inputs to the MC generation for LHC experiments.

9 Measurement of Z + Heavy-flavor Jet Cross Section

CDF has measured the ratio of Z+b jet cross section to inclusive Z cross section [29]. Measuring the ratio, instead of the absolute cross section, makes the systematic uncertainties from luminosity and lepton identification largely cancel. Analysis requires at least one jet tagged by the standard `SECVTX` algorithm and the b fraction is extracted by fitting the secondary vertex mass as described in Section 7. The per jet cross section ratio, $\sigma^{\text{jet}}(Z + b \text{ jet})/\sigma(Z)$, for $E_T^{b\ \text{jet}} > 20$ GeV, $|\eta^{b\ \text{jet}}| < 1.5$, $76 < M_{\ell\ell} < 106$ GeV/c^2, has been measured to be $(3.32 \pm 0.53(stat) \pm 0.42(syst)) \times 10^{-3}$. Although the measured results are consistent with predictions from MCFM, the predictions have a large dependence on scales, which is unexpected for NLO calculations. For example, the cross section ratio at $N_{\text{jet}} = 2$ for $Q^2 = \langle p_{T,\text{jet}}^2 \rangle$ is a factor of two of the prediction for $Q^2 = m_Z^2$. Several investigations show that MCFM does not provide full NLO predictions for one of the production diagrams: $q\bar{q} \to Zb\bar{b}$ when only one b jet is observed.[16] Similar to the case of W + b cross section, NLO calculations are available, but not yet implemented in an MC program that allows user-defined kinematic requirements. The other dominant production process is gluon initiated, $gb \to Zb$[17], therefore, future Z + b cross section measurements may constrain the b quark PDF.

[16] When the two b quarks are collinear, they may be reconstructed as single b jet. When the two b quarks are well separated, one of them may be outside of the detector acceptance.

[17] Equivalent to $gg \to Zb\bar{b}$.

10 Measurement of b-jet Shapes

The jet shape $\Phi(r)$ is defined as the fraction of momentum carried by particles within a cone of radius r, relative to the total momentum within the jet cone size R. By definition, $\Phi(R)$ is equal to one. The b-jet shapes provide an alternate method to probe the $b\bar{b}$ production mechanism, particularly the fraction of gluon splitting, which is complementary to the measurement of the $b\bar{b}$ angular correlation. A b-jet that originates from only one b quark has narrower[18] jet shape than a b-jet that originates from two b quarks; gluon splitting tends to produce more 2-b-quark jets. The CDF measurement has been compared to predictions by `PYTHIA` and `ALPGEN`, with the default 1-b-quark fraction f_{1b}, only one b quark, only two b quarks, and with $f_{1b} - 0.2$ [30]. Data have shown a preference over $f_{1b} - 0.2$ (see Figure 4).

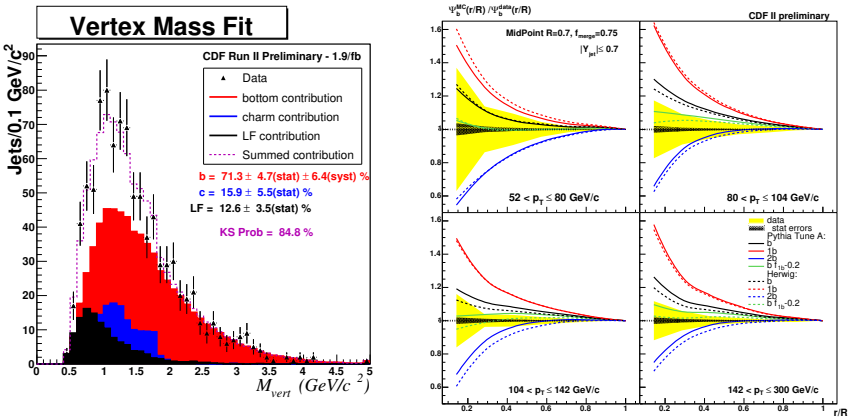

Figure 4: Fitting of secondary vertex mass measured in CDF data to templates of light, c, and b-flavor jets (left). The CDF measurement of b-jet shape in four p_T bins, and predictions from `PYTHIA` and `HERWIG` with various 1-b-quark fractions (right).

11 Conclusion

Measurements of inclusive jet, dijet mass, W/Z + inclusive jet cross sections provide stringent tests of pQCD and are in agreement with NLO predictions. The Run II inclusive jet cross section results have decreased the central value and uncertainty of gluon PDF at high x. The dijet mass spectrum and angular distributions have been used to set the world's best limits on parameters predicted by new physics, such as mass of excited quark, axigluon/coloron, and compositeness scale, *etc.* Measurement of b-jet shape suggests that the fraction of gluon-splitting for $b\bar{b}$ production has to be increased in `PYTHIA` and `HERWIG`. More data are being collected at the Tevatron and 8 fb^{-1} of $p\overline{p}$ collisions are expected by the end of 2010. Updates with more data will benefit the W/Z + heavy flavor measurements and also push the other analyses to a wider kinematic range. In addition, full NLO predictions for W/Z + heavy flavor in a user-friendly MC program will give more sensible data and theory comparisons. As the

[18] Narrower jet shape means more momentum at small r.

QCD productions of these processes are well measured and studied, our chance of discovery will be enhanced due to the better understanding of backgrounds.

12 Acknowledgments

I would like to thank the CDF and DØ QCD conveners and the authors of each individual analysis, for answering my endless questions.

References

[1] S. D. Ellis, J. Huston, K. Hatakeyama, P. Loch, and M. Tonnesmann, Prog. Part. Nucl. Phys. **60**, 484 (2008).

[2] A. Bhatti *et al.*, Nucl. Instrum. Meth. A **566**, 375 (2006).

[3] M. A. Voutilainen, Ph.D. thesis, University of Helsinki, 2008.

[4] F. Abe *et al.* (CDF Collaboration), Phys. Rev. Lett. **77**, 438 (1996); B. Abbott *et al.* (D0 Collaboration), Phys. Rev. Lett. **82**, 2451 (1999).

[5] A. Abulencia *et al.* (CDF Collaboration), Phys. Rev. D **74**, 071103 (2006); T. Aaltonen *et al.* (CDF Collaboration), Phys. Rev. D **78**, 052006 (2008) and Erratum-ibid. D **79**, 119902 (2009).

[6] V. M. Abazov *et al.* (D0 Collaboration), Phys. Rev. Lett. **101**, 062001 (2008).

[7] A. Abulencia *et al.* (CDF Collaboration), Phys. Rev. Lett. **96**, 122001 (2006); A. Abulencia *et al.* (CDF Collaboration), Phys. Rev. D **75**, 092006 (2007) and Erratum-ibid. D **75**, 119901 (2007).

[8] U. Baur, I. Hinchliffe, and D. Zeppenfeld, Int. J. Mod. Phys. A **2**, 1285 (1987); U. Baur, M. Spira, and P. M. Zerwas, Phys. Rev. D **42**, 815 (1990).

[9] P. H. Frampton and S. L. Glashow, Phys. Lett. B **190**, 157 (1987); J. Bagger, C. Schmidt, and S. King, Phys. Rev. D **37**, 1188 (1988); R. S. Chivukula, A. G. Cohen, and E. H. Simmons, Phys. Lett. B **380**, 92 (1996); E. H. Simmons, Phys. Rev. D **55**, 1678 (1997).

[10] K. D. Lane and M. V. Ramana, Phys. Rev. D **44**, 2678 (1991); K. Lane and S. Mrenna, Phys. Rev. D **67**, 115011 (2003).

[11] L. Randall and R. Sundrum, Phys. Rev. Lett. **83**, 3370 (1999).

[12] E. Eichten, I. Hinchliffe, K. D. Lane, and C. Quigg, Rev. Mod. Phys. **56**, 579 (1984) and Addendum-ibid. **58**, 1065 (1986).

[13] J. L. Hewett and T. G. Rizzo, Phys. Rept. **183**, 193 (1989).

[14] T. Aaltonen *et al.* (CDF Collaboration), Phys. Rev. D **79**, 112002 (2009).

[15] *http://www-d0.fnal.gov/Run2Physics/WWW/results/prelim/QCD/Q14/*

[16] *http://www-cdf.fnal.gov/physics/new/qcd/dijetchi_08/*

[17] V. M. Abazov *et al.* (D0 Collaboration), arXiv:0906.4819.

[18] N. Arkani-Hamed, S. Dimopoulos, and G. R. Dvali, Phys. Lett. B **429**, 263 (1998); D. Atwood, S. Bar-Shalom, and A. Soni, Phys. Rev. D **62**, 056008 (2000).

[19] K. R. Dienes, E. Dudas, and T. Gherghetta, Nucl. Phys. B **537**, 47 (1999); A. Pomarol and M. Quiros, Phys. Lett. B **438**, 255 (1998); K. m. Cheung and G. L. Landsberg, Phys. Rev. D **65**, 076003 (2002).

[20] T. Aaltonen *et al.* (CDF Collaboration), Phys. Rev. D **77**, 011108 (2008).

[21] *http://www-cdf.fnal.gov/physics/new/qcd/wbjets_1900_public/index.html*

[22] D. E. Acosta, *et al.* (CDF Collaboration), Phys. Rev. D **71**, 052003 (2005); C. Neu, FERMILAB-CONF-06-162-E.

[23] T. Aaltonen *et al.* (CDF Collaboration), Phys. Rev. Lett. **100**, 091803 (2008).

[24] V. M. Abazov *et al.* (D0 Collaboration), Phys. Lett. B **666**, 23 (2008).

[25] T. Aaltonen *et al.* (CDF Collaboration), Phys. Rev. Lett. **100**, 102001 (2008); *http://www-cdf.fnal.gov/physics/new/qcd/zjets_08/public.html*.

[26] V. M. Abazov *et al.* (D0 Collaboration), Phys. Lett. B **669**, 278 (2008).

[27] V. M. Abazov *et al.* (D0 Collaboration), Phys. Lett. B **678**, 45 (2009).

[28] *http://www-d0.fnal.gov/Run2Physics/WWW/results/prelim/QCD/Q12/*

[29] T. Aaltonen *et al.* (CDF Collaboration), Phys. Rev. D **79**, 052008 (2009).

[30] T. Aaltonen *et al.* (CDF Collaboration), Phys. Rev. D **78**, 072005 (2008).

High-Multiplicity Final States and Transverse-Momentum Dependent Parton Showering at Hadron Colliders

F. Hautmann

Theoretical Physics Department, University of Oxford, Oxford OX1 3NP

DOI: http://dx.doi.org/10.3204/DESY-PROC-2009-03/Hautmann

If large-angle multigluon radiation gives significant contributions to parton showers in the LHC high-energy region, appropriate generalizations of parton branching methods are required for Monte Carlo simulations of exclusive high-multiplicity final states. We discuss the use in this context of transverse-momentum dependent kernels which factorize in the region of high energies. We give examples based on ep and $p\bar{p}$ multi-jet data, and point to possible developments for distributions associated with massive final states at the LHC.

1 Introduction

Complex final states with high particle multiplicity are central to many aspects of the LHC physics program. Theoretical predictions for these processes require advanced QCD calculational tools, which rely both on perturbative results (at present, mostly next-to-leading-order) [1] and on parton shower event generators for realistic collider simulations [2].

This article discusses aspects of spacelike parton showers that depend on the structure of QCD multiparton matrix elements in the multiple-scale region of large center-of-mass energy $\sqrt{s}$ and fixed transferred momenta, and are likely to affect the form of the final states at high multiplicity.

Let us recall that the physical picture underlying the most commonly used branching Monte Carlo generators [2, 3] is based on collinear evolution of jets developing, both "forwards" and "backwards", from the hard event [4], supplemented (in the case of certain generators) by suitable constraints for angularly-ordered phase space [5]. The angular constraints are designed to take account of coherence effects from multiple soft-gluon emission [5, 6, 7].

The main new effect one observes when trying to push this picture to higher and higher energies is that soft-gluon insertion rules [6, 7] based on eikonal emission currents [8, 9] are modified in the high-energy, multi-scale region by terms that depend on the total transverse momentum transmitted down the initial-state parton decay chain [10, 11, 12]. As a result, the physically relevant distribution to describe initial-state showers becomes the analogue not so much of an ordinary parton density but rather of an "unintegrated" parton density, dependent on both longitudinal and transverse momenta.[1]

[1] Theoretical aspects of unintegrated pdfs from the point of view of QCD high-energy factorization are discussed in [13]. Associated phenomenological aspects are discussed in [14, 15], and references therein (see also [16, 17] for recent new work). See works in [18] for first discussions of a more general, nonlocal operator

The next observation concerns the structure of virtual corrections. Besides Sudakov form-factor effects included in standard shower algorithms [2, 3], one needs in general virtual-graph terms to be incorporated in transverse-momentum dependent (but universal) splitting functions [10, 18, 19, 20, 21] in order to take account of gluon coherence not only for collinear-ordered emissions but also in the non-ordered region that opens up at high $\sqrt{s}/p_\perp$.

These finite-$k_\perp$ corrections to parton branching have important implications for multiplicity distributions and the structure of angular correlations in final states with high multiplicity. In the next section we discuss examples of such effects in the case of multi-jet production in ep and $p\bar{p}$ collisions. In Sec. 3 we go on to possible developments involving the hadroproduction of massive states. In particular, we point to studies beginning to investigate the role of showering corrections versus multiparton interaction corrections in Monte Carlo event generators [22, 23, 24]. We give final remarks in Sec. 4.

2 Jet-jet correlations

In a multi-jet event the correlation in the azimuthal angle $\Delta\phi$ between the two hardest jets provides a useful measurement, sensitive to how well QCD multiple-radiation effects are described. In leading order one expects two back-to-back jets; higher-order radiative contributions cause the $\Delta\phi$ distribution to spread out. Near $\Delta\phi \sim \pi$ the measurement is mostly sensitive to infrared effects from soft-gluon emission; the behavior as $\Delta\phi$ decreases is driven by hard parton radiation. At the LHC such measurements may become accessible relatively early and be used to test the description of complex hadronic final states by Monte Carlo generators [25].

Experimental data on $\Delta\phi$ correlations are available from the Tevatron [26] and from Hera [27, 28]. These analyses indicate that the comparison of data with Monte Carlos and perturbative results are very different in the two cases. Observe in Fig. 1 that the Tevatron $\Delta\phi$ distribution drops by about two orders of magnitude over a fairly narrow range, essentially still close to the two-jet region. The measurement is dominated by leading-order processes, with small sub-leading corrections. Correspondingly, data are reasonably well described both by collinear showers (HERWIG and new PYTHIA tuning) and by fixed-order NLO calculations [25, 26].

The Hera $\Delta\phi$ measurements, on the other hand, are much more sensitive to higher orders, Fig. 2 [27]. NLO results for di-jet azimuthal distributions are affected by large corrections in the small-$\Delta\phi$ and small-x region, and begin to fall below the data for three-jet distributions in the smallest $\Delta\phi$ bins [27]. These measurements are likely relevant for extrapolation of initial-state showering effects to the LHC, given the large phase space available for jet production, and relatively small ratio of jet transverse energy to the center-of-mass energy.

Refs. [29, 30] analyze the effects of finite-$k_\perp$ corrections to initial-state showers, using data [27] on jet angular and momentum correlations, and factorization at fixed transverse momentum [11] valid for high energies. Fig. 3 shows results from the collinear HERWIG Monte Carlo [31] and from the $k_\perp$-shower CASCADE Monte Carlo [15] for the distributions in $\Delta\phi$ and Δp_t [27, 29], measuring the transverse momentum imbalance between the leading jets. The largest differences between the two Monte Carlos are at small $\Delta\phi$ and small Δp_t, where the two highest E_T jets are away from the back to back region and one has effectively three hard, well-separated jets. By examining the angular distribution of the third jet, Ref. [29] finds significant contributions from regions where the transverse momenta in the initial state shower

formulation of u-pdfs applied to parton showers beyond leading order.

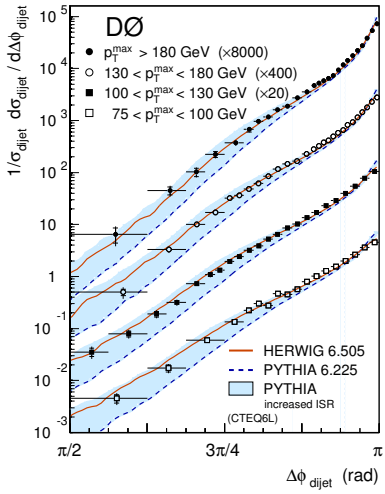

Figure 1: Dijet azimuthal correlations measured by D0 along with the HERWIG and PYTHIA results [26].

are not ordered. The description of the measurement by the $k_\perp$-shower is good, whereas the collinear-based HERWIG shower is not sufficient to describe the observed shape.

The physical picture underlying the $k_\perp$-shower method involves both transverse-momentum dependent pdfs and matrix elements. Fig. 4 [30] illustrates the relative contribution of these different components to the result, showing different approximations to the azimuthal dijet distribution normalized to the back-to-back cross section. The solid red curve is the full result [29]. The dashed blue curve is obtained from the same unintegrated pdf's but by taking the collinear approximation in the hard matrix element. The dashed curve drops much faster than the full result as $\Delta\phi$ decreases, indicating that the high-$k_\perp$ component in the ME [20] is necessary to describe jet correlations for small $\Delta\phi$. The dotted (violet) curve is the result obtained from the

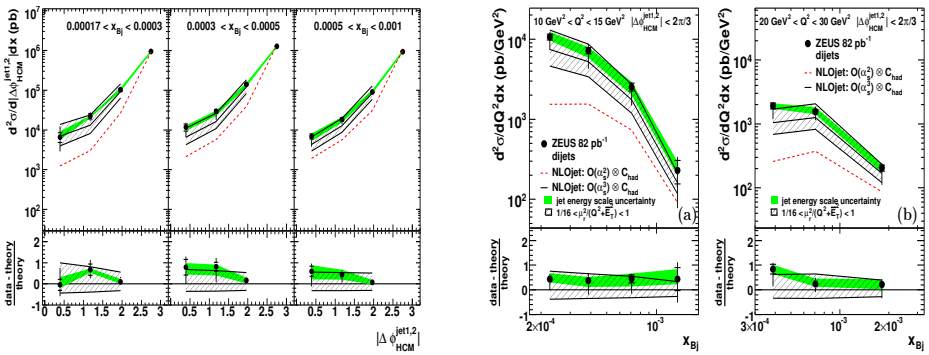

Figure 2: (left) Azimuth dependence and (right) Bjorken-x dependence of ep di-jet distributions [27], compared with NLO results.

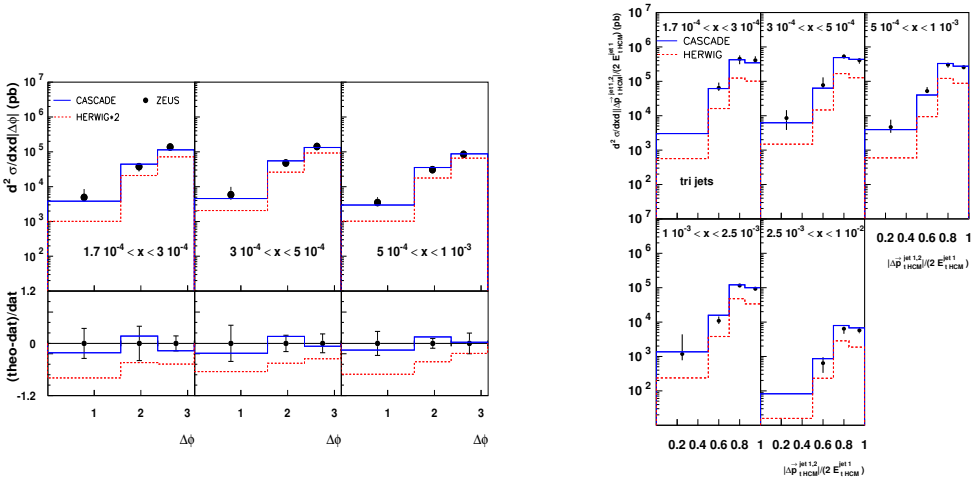

Figure 3: (left) Angular correlations and (right) momentum correlations [29] in three-jet final states measured by [27], compared with $k_\perp$-shower (CASCADE) and collinear-shower (HERWIG) Monte Carlo results.

unintegrated pdf without any resolved branching. This represents the contribution of the intrinsic distribution only, corresponding to nonperturbative, predominantly low-$k_\perp$ modes. That is, in the dotted (violet) curve one retains an intrinsic $k_\perp \neq 0$ but no effects of coherence. We see that the resulting jet correlations in this case are down by an order of magnitude. The inclusion of the perturbatively computed high-$k_\perp$ correction distinguishes the calculation [29] from other shower approaches (see e.g. [32]) that include transverse momentum dependence in the pdfs but not in the matrix elements.

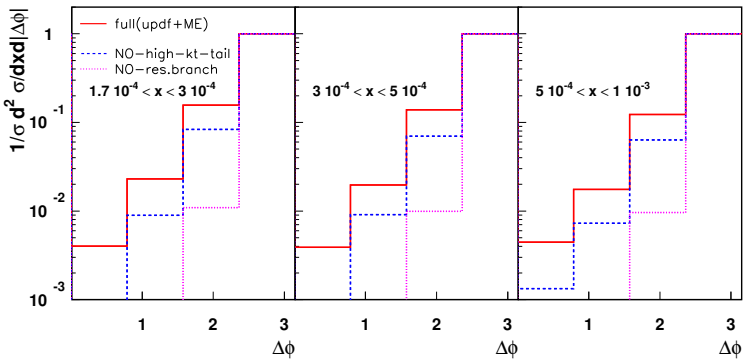

Figure 4: The dijet azimuthal distribution [30] normalized to the back-to-back cross section: (solid red) full result (u-pdf $\oplus$ ME); (dashed blue) no finite-$k_\perp$ correction in ME (u-pdf $\oplus$ $\mathrm{ME}_{collin.}$); (dotted violet) u-pdf with no resolved branching.

The above observations underline the role of accurate multi-jet measurements in events associated with proton scattering off virtual photons [16]. Further phenomenological analyses

of available jet correlation data (and multiplicity distributions [29]) will be helpful. In this respect note that the effects of coherence emphasized above dominate for sufficiently small $\Delta\phi$ and small x. But the unintegrated formulation of parton showers is potentially more general [18, 33, 34]. Such analyses can be of use in attempts to relate [35] shower effects in DIS event shapes [36] measuring the transverse momentum in the current region to vector-boson hadroproduction p_T spectra [22, 37].

3 Massive final states

Corrections to collinear-ordered showers affect heavy mass production, including the structure of the final states associated with heavy flavor and heavy boson production. We next point to examples that depend on the physics of unintegrated gluon distributions.

Measurements of angular correlations for bottom quark jets have recently been performed at the Tevatron [38, 39, 40]. See [16, 41, 42, 43] for reviews of related phenomenology. Results for b-jet distributions in invariant mass and azimuthal angle are shown in Fig. 5 [39] and Fig. 6 [40]. Monte Carlo simulations based on PYTHIA, HERWIG and MC@NLO do not appear to give satisfactory descriptions of the observations [2, 39] especially at small $\Delta\phi$. The measurement of b-jet correlations has considerable interest, given their potential sensitivity to soft underlying events [39, 44] and possibly models for multiple-parton interactions [22, 23].[2] In this context it is worth noting the possible role of showering corrections, at the level of single-parton interactions, due to transverse-momentum dependent parton branching.

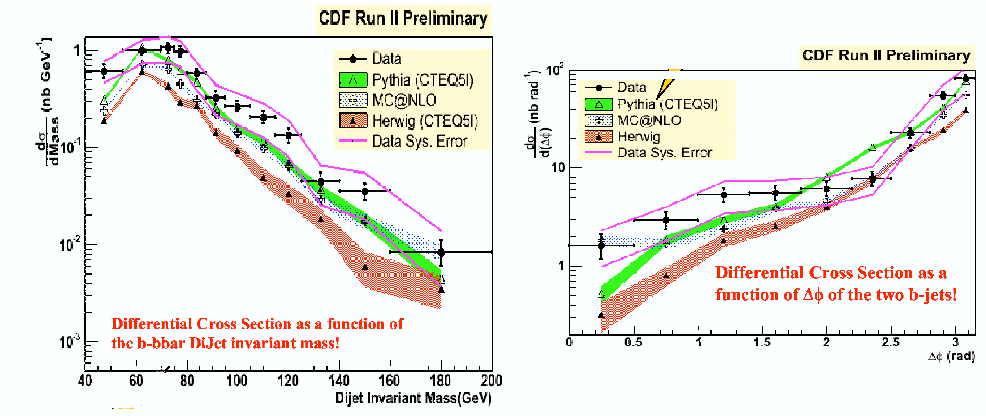

Figure 5: Invariant-mass distribution and azimuthal-angle distribution for production of b-jets at the Tevatron [39].

To this end let us recall that heavy flavor hadroproduction is dominated for sufficiently high energies by gluon splitting into heavy-quark pairs [13], $g \to Q\overline{Q}$ where g is produced from the spacelike jet. The high-energy asymptotic behavior is controlled by a triple-pole singularity [13] in the complex plane of the Mellin moment conjugate to the transferred $k_\perp$.

[2] This is unlike the DIS jet correlation data discussed in the previous section, where multiparton contributions are believed to be much suppressed [16].

The coefficient functions associated to this singularity enhance regions that are not ordered in transverse momentum in the initial state shower. In fact, such contributions are already found to be significant at the level of the NLO correction [42, 43].[3]

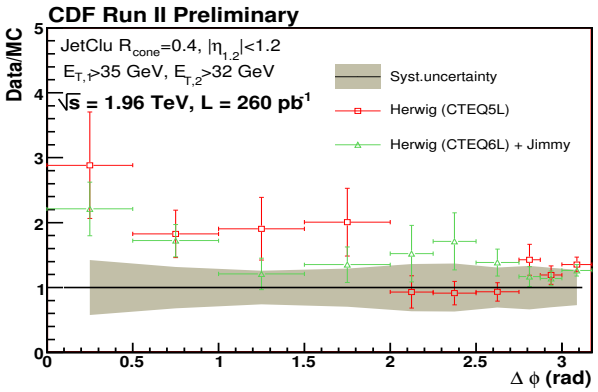

Figure 6: Comparison of data and Monte Carlos for b-jet azimuthal correlations at the Tevatron [40].

A typical contribution to $g \to Q\overline{Q}$ is pictured in Fig. 7a. Note that for small $\Delta\phi$ this graph gives effectively a contribution of leading order. Corrections of the next order from additional jet emission are shown in Fig. 7b. In the notation of Fig. 7, the triple-pole behavior is produced from regions in which $m_Q^2 \ll (k_T + k'_T)^2 \ll k_T^2 \simeq k_T'^2$, where m_Q is the heavy quark mass, and k_T, k'_T are transverse momentum vectors. Collinear shower calculations, even if supplemented by NLO matrix elements as in MC@NLO, are not designed to take account of this behavior. This is likely to reduce the numerical stability of predictions as one goes to higher and higher energies. It may cause a non-negligible contribution from showering to be missed in the b-jet $\Delta\phi$ distribution at small $\Delta\phi$. On the other hand, such corrections can be obtained by methods based on transverse-momentum dependent parton branching, as those discussed in the previous section. It is of interest to analyze these contributions in comparison with those, e.g. in Fig. 6, from multiple interactions.

Such an analysis would pay off as one goes from the Tevatron to the LHC. Parton showers at the LHC will be more influenced by the asymptotic high-energy pole. Let us observe that effects of a similar physical origin will affect the structure of final states associated to production processes predominantly coupled to gluons, e.g. central scalar boson production [45]. See studies of showering effects in this case [24]. These can affect the description of soft underlying events and minijets [44, 22] as well as the use of exclusive production channels [46].

4 Concluding remarks

Final states with high particle multiplicity acquire qualitatively new features at the LHC compared to previous collider experiments due to the large phase space opening up for events

[3] It is possible that terms of this kind at orders higher than NLO are responsible for the rather large theoretical uncertainties found [42, 43] in the NLO predictions when going from the Tevatron to the LHC.

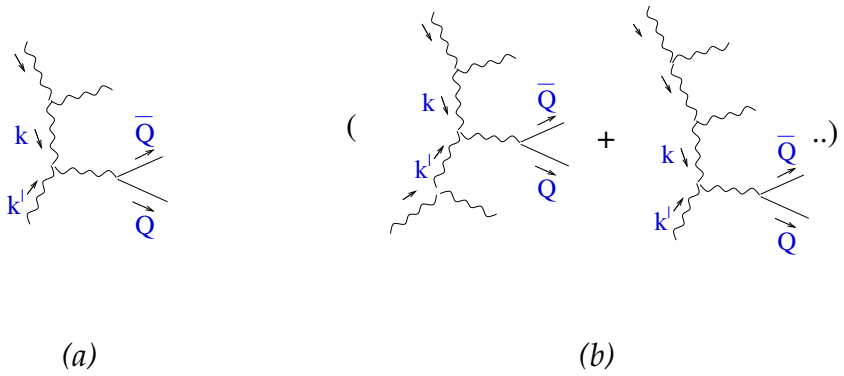

Figure 7: (a) Heavy quark hadroproduction from gluon showering at high energy; (b) next correction from extra jet emission.

characterized by multiple hard scales, possibly widely disparate from each other. This brings in potentially large perturbative corrections to the hard-scattering event and potentially new effects in the parton-shower components of the process.

If large-angle multigluon radiation gives significant contributions to parton showers at the LHC, appropriate generalizations of parton branching methods are required. We have discussed applications of transverse-momentum dependent kernels for parton showering that follow from factorization properties of QCD multiparton matrix elements in the high energy region, which are valid not only for collinear emission but also at finite angles.

While we have focused on observables that are sensitive primarily to the physics of initial-state gluonic showers, expressible in terms of "unintegrated" gluon densities, treatments of quark contributions to showers at unintegrated level are being worked on (see e.g. [16, 17]). In this respect, theoretical results [20] already applied for inclusive phenomenology could also be of use in calculations for exclusive final states.

Also, while we have considered production processes in the central rapidity region, techniques are being developed [47] to allow one to also address multi-particle hard processes in the forward rapidity region.

Acknowledgments. It is a pleasure to thank the organizers and convenors for the invitation to a very interesting conference.

References

[1] See e.g. C.F. Berger et al., arXiv:0905.2735 [hep-ph]; K. Melnikov et al., in Proc. XLIV Rencontres de Moriond, March 2009.

[2] B.R. Webber, CERN Academic Training Lectures (2008).

[3] R.K. Ellis, W.J. Stirling and B.R. Webber, *QCD and collider physics*, CUP 1996; Yu.L. Dokshitzer, V.A. Khoze, A.H. Mueller and S.I. Troian, *Perturbative QCD*, Ed. Frontieres, Gif-sur-Yvette (1991).

[4] J.C. Collins, D.E. Soper and G. Sterman, Adv. Ser. Direct. High Energy Phys. 5 (1988) 1.

[5] B.R. Webber, Ann. Rev. Nucl. Part. Sci. **36** (1986) 253.

[6] A. Bassetto, M. Ciafaloni and G. Marchesini, Phys. Rept. **100** (1983) 201.

[7] Yu.L. Dokshitzer, V.A. Khoze, A.H. Mueller and S.I. Troian, Rev. Mod. Phys. **60** (1988) 373.

[8] V.N Gribov, Sov. J. Nucl. Phys. **5** (1967) 399; F.E. Low, Phys. Rev. **110** (1958) 974.

[9] J. Frenkel and J.C. Taylor, Nucl. Phys. **B246** (1984) 231; R. Doria, J. Frenkel and J.C. Taylor, Nucl. Phys. **B168** (1980) 93.

[10] M. Ciafaloni, Nucl. Phys. **B296** (1988) 49.

[11] S. Catani, M. Ciafaloni and F. Hautmann, Phys. Lett. B**242** (1990) 97.

[12] G. Marchesini and B.R. Webber, Nucl. Phys. **B386** (1992) 215.

[13] S. Catani, M. Ciafaloni and F. Hautmann, Nucl. Phys. B**366** (1991) 135; Phys. Lett. **B307** (1993) 147.

[14] J.R. Andersen *et al.*, Eur. Phys. J. C **35** (2004) 67; B. Andersson *et al.*, Eur. Phys. J. C **25** (2002) 77.

[15] H. Jung, Mod. Phys. Lett. A **19** (2004) 1; Comput. Phys. Commun. **143** (2002) 100.

[16] H. Jung *et al.*, Proceedings of the Workshop "HERA and the LHC", arXiv:0903.3861 [hep-ph].

[17] S. Jadach and M. Skrzypek, arXiv:0905.1399 [hep-ph].

[18] J.C. Collins and X. Zu, JHEP **0503** (2005) 059; J.C. Collins, Phys. Rev. D **65** (2002) 094016; J.C. Collins and F. Hautmann, JHEP **0103** (2001) 016.

[19] J.C. Collins, Acta Phys. Polon. B **34** (2003) 3103.

[20] S. Catani and F. Hautmann, Nucl. Phys. B**427** (1994) 475; Phys. Lett. B**315** (1993) 157.

[21] F. Hautmann, Phys. Lett. B **655** (2007) 26.

[22] P.Z. Skands, arXiv:0905.3418 in Proc. Perugia Workshop (2008).

[23] M. Bähr, S. Gieseke and M. Seymour, JHEP **0807** (2008) 076.

[24] M. Deak, A. Grebenyuk, F. Hautmann, H. Jung and K. Kutak, in Proc. DIS09 Workshop (Madrid, 2009).

[25] M. Albrow *et al.* [TeV4LHC QCD Working Group], [arXiv:hep-ph/0610012].

[26] V.M. Abazov *et al.* [D0 Collaboration], Phys. Rev. Lett. **94** (2005) 221801 [arXiv:hep-ex/0409040].

[27] S. Chekanov *et al.* [ZEUS Collaboration], Nucl. Phys. B **786** (2007) 152 [arXiv:0705.1931 [hep-ex]].

[28] A. Aktas *et al.* [H1 Collaboration], Eur. Phys. J. C **33** (2004) 477 [arXiv:hep-ex/0310019].

[29] F. Hautmann and H. Jung, JHEP **0810** (2008) 113.

[30] F. Hautmann and H. Jung, arXiv:0804.1746 [hep-ph], in Proceedings of the 8th International Symposium on Radiative Corrections RADCOR2007; arXiv:0808.0873 [hep-ph]; arXiv:0712.0568 [hep-ph].

[31] G. Corcella *et al.*, JHEP **0101** (2001) 010 [arXiv:hep-ph/0011363]; G. Corcella *et al.*, arXiv:hep-ph/0210213.

[32] S. Höche, F. Krauss and T. Teubner, Eur. Phys. J. C**58** (2008) 17.

[33] F. Hautmann, Acta Phys. Polon. B **40** (2009) 2139.

[34] J.C. Collins and H. Jung, hep-ph/0508280.

[35] M. Dasgupta and Y. Delenda, JHEP **0608** (2006) 080.

[36] A. Banfi, arXiv:0906.4958 [hep-ph]; A. Banfi, M. Dasgupta and Y. Delenda, Phys. Lett. B **665** (2008) 86.

[37] S. Berge, P.M. Nadolski, F.I. Olness and C.P. Yuan, hep-ph/0508215; P.M. Nadolsky *et al.*, Phys. Rev. D **67** (2003) 074015; C. Balasz and C.P. Yuan, Phys. Rev. D **56** (1997) 5558.

[38] CDF Coll., Phys. Rev. D **71** (2005) 092001; Phys. Rev. D **78** (2008) 072005.

[39] R.D. Field, lectures at CTEQ School, Madison 2009; talk at the Tevatron Connection, Fermilab 2005.

[40] CDF Coll., FNAL 8939 (2007).

[41] J. Baines *et al.*, Report of the Heavy Quark Working Group, arXiv:hep-ph/0601164.

[42] P. Nason *et al.*, Report on bottom production, in "SM physics (and more) at the LHC", hep-ph/0003142.

[43] S. Frixione, P. Nason and B. R. Webber, JHEP **0308** (2003) 007 [arXiv:hep-ph/0305252].

[44] G. Gustafson, talk at Desy Workshop, Hamburg, March 2007; G. Gustafson, L. Lönnblad and G. Miu, JHEP **0209** (2002) 005.

[45] F. Hautmann, Phys. Lett. B **535** (2002) 159.

[46] L. Lönnblad and M. Sjödahl, JHEP **0402** (2004) 042.

[47] M. Deak *et al.*, arXiv:0908.0538 [hep-ph]; arXiv:0908.1870 [hep-ph].

Jets and Heavy Flavour at LHC with ATLAS and CMS

Anne-Marie Magnan on behalf of the ATLAS and CMS collaborations

Imperial College HEP Dept., Prince Consort Road, London SW7 2BW, UK

DOI: http://dx.doi.org/10.3204/DESY-PROC-2009-03/Magnan

The LHC experiments ATLAS and CMS plan to take advantage of large multi-jet samples with and without heavy flavour tagging and vector boson production to test QCD at the TeV scale. Initial multi-jet cross section measurements at LHC will demonstrate the understanding of the calibration of the detectors, the jet energy scale systematics and the trigger. Further in the LHC run, measurements of inclusive di-jet cross sections with heavy flavour tag, which provides the process hard scale, will probe QCD at scales never tested before. Jet production measurements with associated W and Z bosons provide a separate test of QCD in different and complementary channels. Measurements of these processes are essential to demonstrate the understanding of major backgrounds to Higgs and SUSY channels, such as those of top-quark production or W+jet/Z+jet.

1 Overview of ATLAS and CMS

A detailed description of the ATLAS (A Toroidal LHC ApparatuS) and CMS (Compact Muon Solenoid) experiments can be found respectively in [1] and [2]. ATLAS (CMS) has an overall length of 44 m (22 m), a diameter of 25 m (15 m), and weighs 7 000 tons (12 500 tons).

ATLAS is composed of a thin 2 T superconducting solenoid surrounding the inner-detector cavity, a high granularity liquid-argon (LAr) electromagnetic sampling calorimeter, followed by scintillator-tile/LAr hadronic calorimeters, three large superconducting toroids arranged with an eight-fold azimuthal symmetry around the calorimeters, and a muon spectrometer. The inner detector is made of semiconductor pixel and strip detectors, surrounded by straw-tube tracking detectors with the capability to generate and detect transition radiation. LAr forward calorimeters extend the pseudo-rapidity coverage from $|\eta| > 3$ to $|\eta| < 4.9$.

The central feature of the CMS apparatus is a superconducting solenoid of 6 m internal diameter. Within the field volume are the silicon pixel and strip tracker, the lead-tungstate crystal electromagnetic calorimeter (ECAL) and the brass-scintillator hadronic calorimeter (HCAL). Muons are measured in gas chambers embedded in the iron return yoke. CMS also has extensive forward calorimetry, extending the pseudo-rapidity coverage of the calorimeters from $|\eta| > 3$ to $|\eta| < 5$.

In ATLAS (CMS), the ECAL has an energy resolution of about 1 % (0.5 %) at 100 GeV, and represents 22 to 26 X_0 (24.7 to 25.8 X_0). The HCAL, when combined with the ECAL, measures jets with a resolution $\Delta E/E \approx 50\,\%/\sqrt{E} \oplus 3\,\%$ ($\approx 100\,\%/\sqrt{E} \oplus 5\,\%$). The calorimeter cells are grouped in projective towers, of granularity $\Delta\eta \times \Delta\phi = 0.1 \times 0.1$ (0.087×0.087) at central rapidity and 0.2×0.1 (0.175×0.175) at forward rapidity. The resolution in the ATLAS (CMS)

tracker is expected to be $\sigma/p_T \approx 5 \times 10^{-5} \times p_T \oplus 0.01$ ($\approx 1.5 \times 10^{-5} \times p_T \oplus 0.005$). Both apparatuses provide the vertex position with $\approx 100\,\mu$m accuracy for 1 GeV tracks, and below $20\,\mu$m accuracy for tracks above 20 GeV.

2 QCD and the LHC

QCD processes constitute the dominant source of interactions at the LHC due to their large cross sections relative to other processes, as detailed in Tab. 1 [3]. This makes QCD an attractive topic for early physics at LHC. By measuring jets, several objectives can be attained, both from theoretical and experimental points of view: commissioning of the detectors, confrontation of perturbative QCD (pQCD) at the TeV scale, tests of PDF evolution schemes, probes of α_S, understanding of multi-jet production (background to other searches), sensitivity to new physics.

Process	σ (nb)
Total	10^8
$W^{\pm} \to e\nu$	20
$Z \to e^+e^-$	2
$t\bar{t}$	0.8
$b\bar{b}$	5×10^5
$c\bar{c}$	10^7
central jets	
$p_T > 10$ GeV	2.5×10^6
$p_T > 100$ GeV	10^3
$p_T > 1000$ GeV	1.5×10^{-3}

Table 1: Cross-sections expected at the LHC for a few processes, at $\sqrt{s} = 10$ TeV.

The number of jets per bin in transverse momentum p_T, for a centre of mass energy of 10 TeV expected at start-up of the LHC, is shown in Fig. 1, for different ranges in rapidity y. With only 10 pb^{-1} of integrated luminosity, several tens of events are still expected with jets above 1 TeV, and so early measurements are possible for a large range in energy.

3 Jets at the LHC

3.1 Definition of a jet

From a theoretical point of view, a so-called *parton jet* originates from the proton-proton collision, and should contain the partons produced and the particles from initial- and final-state radiation (ISR/FSR). From an experimental point of view, a parton jet then undergoes hadronisation (decays, or interactions in the beam pipe/tracker material), after which point it can be reconstructed as a *particle jet* if individual particles are identified (so called *particle flow* algorithms). Electromagnetic and hadronic components will finally shower in the calorimeters, so that pure *calorimeter jets* can be reconstructed. Two types of algorithms exist: cone-based and sequential recombination. Cone-based can be seeded (at LHC, iterative, with sizes $\Delta R = 0.4$ (CMS 0.5) and 0.7), in which case they are not infrared- or collinear-safe, but are fast and reliable for triggering, or seedless (the Seedless Infrared Safe - SIScone - algorithm in CMS). The sequential recombination algorithm k_T is used in both ATLAS and CMS with sizes 0.4 and 0.6. To compare jets at each step, the same jet reconstruction algorithm should be employed. Inputs to the algorithms are hence either calorimetric energy depositions (towers or clusters), tracks, particle or energy flow reconstructed objects, simulated or generated particles.

The particle content of a jet is shown in Fig. 2 [4], and is independent of the jet transverse momentum, as expected since jet fragmentation functions are independent of the energy. Charged particles will carry 65% of the energy, hence use should be made of the good tracker resolution of both detectors. Photons will carry 25% of the energy, and the excellent EM

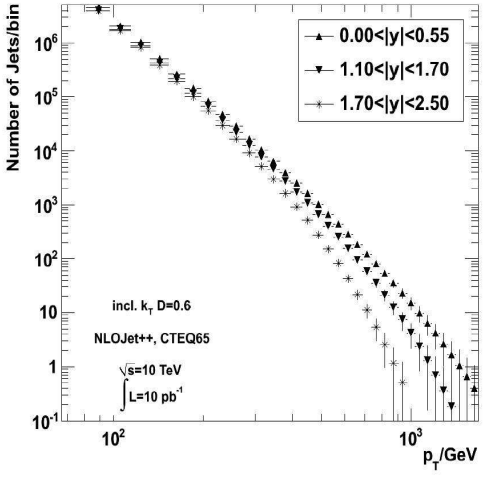

Figure 1: Expected number of jets per bin in p_T for $10\,\mathrm{pb}^{-1}$ of integrated luminosity at $\sqrt{s} = 10\,\mathrm{TeV}$.

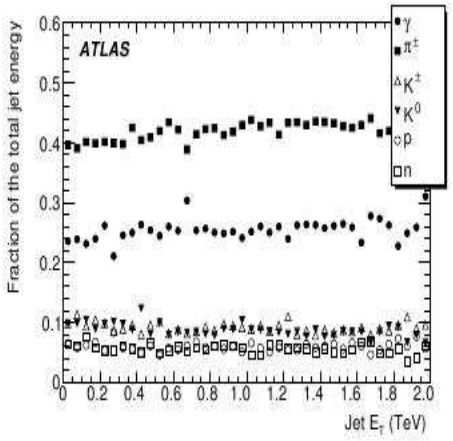

Figure 2: Particle content of a jet as a function of its transverse energy.

calorimeter resolution should help significantly in the overall jet energy resolution. Neutral particles will carry the remaining 10% of the energy, and represent the limiting factor to jet energy resolution.

3.2 Jet energy scale and jet energy resolution

In ATLAS, the jet energy scale is obtained by a calibration procedure described in detail in [4]. Several methods are used in order to improve the jet energy resolution. One of them involves using the track content of a jet. The method is illustrated in Fig. 3, left. The overall jet response is centred on the expected energy, but different bins in the fraction $f_{\mathrm{trk}} = \frac{p_T^{\mathrm{tracks}}}{p_T^{\mathrm{calo}}}$ show different central values for the response, leading to an artificially larger spread in the overall response. By correcting the energy as a function of f_{trk}, the jet energy resolution can be improved by $\approx 10\%$ at 40 GeV, as illustrated in Fig. 3, right, leaving the overall jet response unchanged.

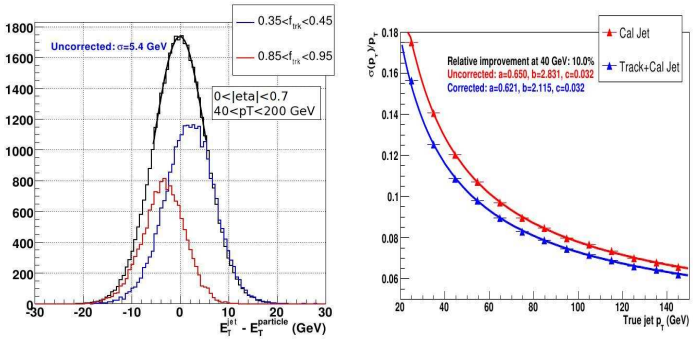

Figure 3: Track-based correction procedure in ATLAS: jet energy scale for different fractions of energy carried by the tracks associated to the jet (left) and jet energy resolution before and after corrections (right).

In CMS, the jet energy calibration uses a factorised approach, after which the jet response for calorimeter jets is flat in transverse momentum and pseudo-rapidity [5]. By using a more complete reconstruction of the events with a particle flow (PF) algorithm, making use of both iterative tracking and calorimeter clustering using calibrated clusters, it is possible to improve greatly the jet energy resolution [6]. The jet response before any correction is shown in Fig. 4, left, for both calorimeter and PF jets. The jet response is already nearly flat and close to the expected value for PF jets. The jet energy resolution after corrections of the calorimeter jets is shown in Fig. 4, right. PF reconstruction of the event leads to an improvement of $\approx 40\%$ on the jet energy resolution at 40 GeV, allowing to recover a value compatible with the one obtained in ATLAS.

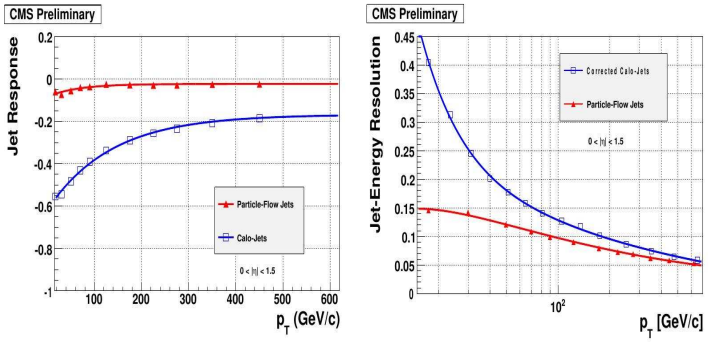

Figure 4: Jet response (left) and jet energy resolution (right) for calorimeter and particle flow jets in CMS.

3.3 First measurements with jets

In order to determine the jet energy scale with real data, different ranges in energy are treated differently. Jets with $10 < p_T < 200\,\text{GeV}$ ($200 < p_T < 500\,\text{GeV}$) are corrected using Z+jets (γ+jets) events. In ATLAS, the jet energy scale is expected to be measured with a statistical uncertainty of 1% (1-2%) with $300\,\text{pb}^{-1}$ ($100\,\text{pb}^{-1}$) of integrated luminosity [4] [7]. The systematic uncertainties, at the level of 5-10% at low p_T, reducing to 1-2% for $p_T > 100$ GeV, are due mainly to theoretical uncertainties on ISR/FSR and on the underlying event (UE). Above 500GeV, a multi-jet p_T-balance method is used: low-p_T jets with known jet energy scale (JES) are balanced against high-p_T jet with unknown JES. A statistical (systematic) uncertainty of 2% (7%) is expected for $1\,\text{fb}^{-1}$ of integrated luminosity.

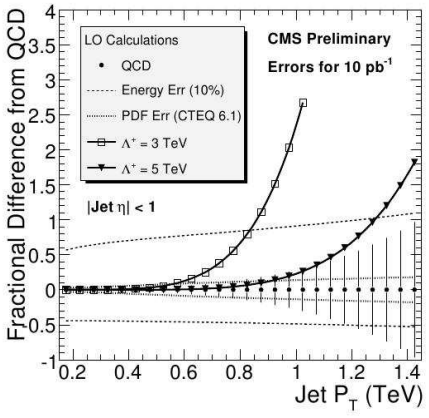

Figure 5: Uncertainties expected for $10\,\text{pb}^{-1}$ in di-jet events in CMS.

Another important step in the commissioning of the detector is the measurement of di-jet cross-sections. A small amount of data is shown to be enough to exceed the Tevatron p_T reach (700 GeV). With $10\,\text{pb}^{-1}$ at 14 TeV, the sensitivity to contact interactions goes beyond the Tevatron limit of 2.7 TeV [8]. With $100\,\text{pb}^{-1}$, the sensitivity to objects decaying into 2 jets (di-jet resonances: q*, Z', etc.) goes also beyond the Tevatron limit of 0.87 TeV. Uncertainties for such measurements are shown in Fig. 5 as a function of the jet p_T,

with the dominant one being due to the jet energy scale. Constraining the PDFs with such measurements will require a profound knowledge of the systematic uncertainties.

When the first data arrive, the first measurements involving jets will however be to characterise the underlying event, and to put constraints on the current Monte Carlo (MC) simulations. A method employed in CMS is described in detail in [9] and emphasises the search for variables allowing to discriminate between different MC models.

4 Heavy flavour at the LHC

4.1 B-tagging algorithms

Heavy-flavoured particles are characterised by a large lifetime: $c\tau$ =125-300 (500) μm for D (B) mesons. It is hence crucial for their identification to have a good reconstruction of tracks/vertices displaced from the primary vertex. In addition, semi-leptonic decays are important, with branching ratios BR(b→l+X) = 20% and BR(b→c→l+X) = 20%. Soft-lepton tagging methods will improve the identification. Furthermore, B hadrons take away about 70% of the b quark energy, so *high mass* states are looked for.

These criteria are used and combined differently in eleven algorithms in CMS, from the simple track-counting based algorithms to more evolved secondary-vertex finder algorithms. The current expected performance of a secondary-vertex tagging algorithm is of 1% mis-tagging rate for 50% (15%) b-tagging efficiency if no misalignment (start-up) scenario is applied.

4.2 Calibration on real data

In order to fully understand the detectors, the b-tagging efficiency and the mis-tagging rate must be extracted from real data. Two categories of methods are being developed, depending on the energy of the jets.

At low p_T, the efficiency is extracted from *muon-in-jet* QCD samples, using two methods in CMS. The p_T^{rel} method is based on estimating the muon content of jets, and the particularity of the projection of p_T^{μ} on the jet axis (p_T^{rel}), which is different for b- and u,d,s,g,c-jets. The System8 method [10] uses two di-jet samples of differing b-quark content, and two uncorrelated tagging algorithms (typically the soft muon one and the algorithm to be calibrated), to form a system of eight equations with eight unknown, from which the b-tag efficiency can be extracted. The result is shown in Fig. 6 for a track-counting based algorithm, for 10 pb^{-1} of integrated luminosity in CMS, and a 1% mis-tagging rate, as a function of the jet p_T. For 100 pb^{-1} of integrated luminosity in CMS, and a mis-tagging rate of 1%, an uncertainty of ≈8.6% is expected on the measurement of the b-tagging efficiency. Whereas the System8 method is expected to give reliable results at low p_T, it is however not suited for p_T larger than 80 GeV.

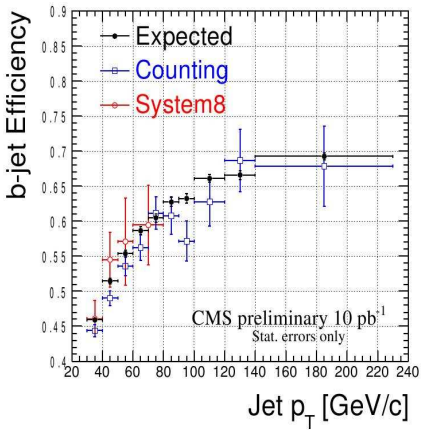

Figure 6: Expected b-tagging efficiency as a function of jet p_T, for 10 pb^{-1} of integrated luminosity in CMS.

At high p_T, a method developed in ATLAS relies on using jets from $t\bar{t}$ events to isolate a highly enriched b-jet sample [4]. Assuming that both top-quark decay into W+b, the events will indeed contain at least two b-jets. In addition, depending on the W decay mode, the topology studied will contain two leptons, or one lepton and two jets.

These events can be identified using a counting method: the number of events expected as a function of the number of tagged jets is shown in Fig. 7 for different MC samples, for $100\,\text{pb}^{-1}$ of integrated luminosity in ATLAS. When requiring more than one jet, $t\bar{t}$ events dominate by more than one order of magnitude compared to other samples. The b-tagging efficiency ϵ_b can be obtained with an uncertainty of $\Delta\epsilon_b/\epsilon_b \approx 2.7(4.2)(\text{stat.}) \oplus 3.4(3.5)(\text{syst.})\%$ for lepton+jets (di-lepton) final states with $100\,\text{pb}^{-1}$ of integrated luminosity.

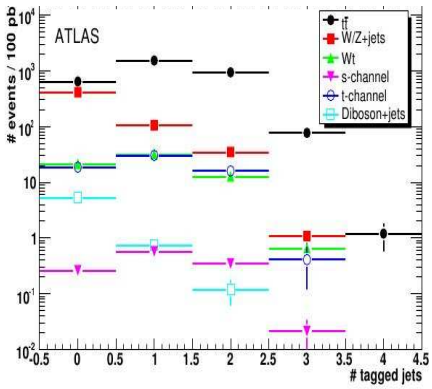

Figure 7: Number of b-tagged jets expected for different samples, with $100\,\text{pb}^{-1}$ of integrated luminosity in ATLAS.

$t\bar{t}$ events can also be identified using kinematic, topological or likelihood requirements. These methods require background subtraction, but allow to measure ϵ_b as a function of E_T and η of the jet. The resulting uncertainty is expected to be $\pm 10\%$ with 100 pb^{-1} in ATLAS (6-10% in CMS with $1\,\text{fb}^{-1}$).

4.3 Measurement of the bbZ cross-section

An example for a measurement involving b-tagging is the measurement of the b(b)Z cross-section. The gains of such an analysis are both theoretical and experimental: the same techniques are employed to calculate the b(b)H cross-section, and large theoretical uncertainties ($\approx 20\%$ uncertainty due to renormalisation and factorisation scales, and an additional 5-10% due to PDFs) exist, which could be constrained by a measurement [11].

A preliminary study has been done in CMS [12], using a selection of at least two leptons (e ($\eta < 2.5$) or μ ($\eta < 2$)) with $p_T > 20\,\text{GeV}$, with in addition at least two jets with $\eta < 2.4$ and $E_T > 30\,\text{GeV}$. A track-counting b-tagging discriminant is used, with a working point leading to a mis-tagging rate smaller than 1% (0.1%) for c (light-flavour) jets. The $t\bar{t}$ background is further reduced by a cut on the transverse missing energy $ME_T < 50\,\text{GeV}$. The main systematic uncertainties are due to: jet energy scale ($\pm 7.6\%$), ME_T ($\pm 7.4\%$), difference between NLO and LO for generator level cuts (-10%), luminosity

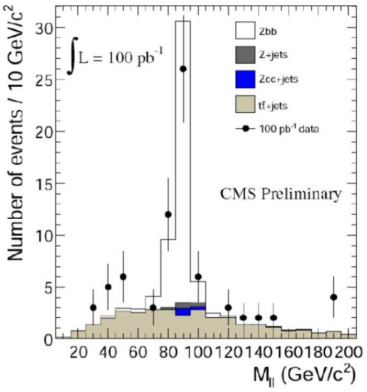

$$\delta\sigma = \pm^{21\%}_{25\%}\,(syst) \pm 15\%\,(stat.)$$

Figure 8: Invariant mass of the two leptons in a selection of bbZ events, with $100\,\text{pb}^{-1}$ of integrated luminosity in CMS.

(±10.%), b-tagging (±16%), mis-tagging (±1.%), $t\bar{t}$ background subtraction (±4.6%), with the numbers calculated for an integrated luminosity of $100\,\mathrm{pb}^{-1}$. With early data, it will hence already be possible to measure the bbZ cross-section with a total uncertainty of the order of the theoretical uncertainties.

5 Conclusion

LHC can probe (p)QCD, but the dominant experimental uncertainty, due to the jet energy scale, must be controlled. A large integrated luminosity will be needed to obtain a 1% error on the jet energy scale. Vice versa, QCD is essential to LHC discoveries: a better understanding of hard-scattering processes will lead to a better understanding of the backgrounds to new physics. Contact interactions and resonances decaying into di-jets can be discovered early on, even with 10% JES uncertainty at start-up. Theoretical uncertainties also need to be reduced to the size of the experimental uncertainties to increase the sensitivity to new physics. Feedback loops between measurements and theory are important in this respect.

References

[1] The ATLAS Collaboration, JINST 3 (2008) S08003.

[2] The CMS Collaboration, JINST 3 (2008) S08004.

[3] J.M. Campbell, J.W. Huston and W.J. Stirling, *Hard interactions of quarks and gluons: a primer for LHC physics*, Rep. Prog. Phys. **70** (2007).

[4] The ATLAS Collaboration, CERN-OPEN-2008-020 (2008) (arXiv:0901.0512).

[5] http://cms-physics.web.cern.ch/cms-physics/public/JME-07-002-pas.pdf.

[6] http://cms-physics.web.cern.ch/cms-physics/public/PFT-09-001-pas.pdf.

[7] C. Buttar, *Early QCD measurements with ATLAS*, XVII International Workshop on Deep-Inelastic Scattering and Related Subjects, Madrid, Spain (2009), http://indico.cern.ch/contributionDisplay.py?contribId=241&sessionId=3&confId=53294.

[8] http://cms-physics.web.cern.ch/cms-physics/public/SBM-07-001-pas.pdf.

[9] http://cms-physics.web.cern.ch/cms-physics/public/QCD-07-003-pas.pdf.

[10] http://cms-physics.web.cern.ch/cms-physics/public/BTV-07-001-pas.pdf.

[11] J. Campbell, R.K. Ellis, F. Maltoni and S. Willenbrock, arXiv:hep-ph/0510362 (2008).

[12] http://cms-physics.web.cern.ch/cms-physics/public/EWK-08-001-pas.pdf.

Quasi-Multi-Regge-Kinematics Approach, Quark Reggeization and Applications

Vladimir Saleev, Alexandera Shipilova

Samara State University, Academika Pavlova Street 1, 443011 Samara, Russia

DOI: http://dx.doi.org/10.3204/DESY-PROC-2009-03/Saleev

We study inclusive production of prompt photons and D mesons at HERA and the Tevatron within the framework of the quasi-multi-Regge-kinematics approach applying the quark Reggeization hypothesis. We use the Reggeon-Reggeon to particle and the particle-Reggeon to particle effective vertices in the leading order approximation of the quasi-multi-Regge-kinematics approach. We describe well and without free parameters the relevant data obtained at HERA and the Tevatron. At the stage of numerical calculations we use the Kimber-Martin-Ryskin prescription for unintegrated quark and gluon distribution functions, with the Martin-Roberts-Stirling-Thorne collinear parton densities for a proton as input.

1 Introduction

The study of the inclusive production of photons and D mesons with large transverse momenta originating from the hard interaction between photon and parton or between two partons in the high-energy collisions provide precision tests of perturbative quantum chromodynamics (QCD) as well as information on the parton densities within proton and photon. Also, these studies increase our potential for the observation of a new dynamical regime, namely the high-energy Regge limit, which is characterized by the following condition $\sqrt{S} >> \mu >> \Lambda_{QCD}$, where $\sqrt{S}$ is the total collision energy in the center of mass reference frame, Λ_{QCD} is the asymptotic scale parameter of QCD, μ is the typical energy scale of the hard interaction. At this high-energy limit, the contribution from the partonic subprocesses involving $t-$channel parton (quark or gluon) exchanges to the production cross section can become dominant. In the region under consideration, the transverse momenta of the incoming partons and their off-shell properties can no longer be neglected, and we deal with "Reggeized" $t-$channel partons.

The quasi-multi-Regge-kinematics (QMRK) approach [1] is particularly appropriate for this kind of high-energy phenomenology. It is based on an effective quantum field theory implemented with the non-Abelian gauge-invariant action including fields of Reggeized gluons [2] and Reggeized quarks [3]. Roughly speaking, the Reggeization of amplitudes is a trick that offers an opportunity to take into account efficiently large radiation corrections to the processes under Regge limit condition beyond the collinear approximation of the parton model. The particle Reggeization is known in high-energy quantum electrodynamics (QED) for electrons only [4] and for gluons and quarks in QCD [5, 6].

In the leading order (LO) approximation of the QMRK approach an inclusive production of particles is described by the Reggeon-Reggeon to particle and the particle-Reggeon to par-

ticle effective vertices. The relevant squared matrix elements of the $2 \to 1$ inclusive particle production processes can be presented as follows:

$$\overline{|M(Q\bar{Q} \to \gamma)|^2} = \frac{4}{3}\pi\alpha e_q^2(t_1 + t_2), \quad (1)$$

$$\overline{|M(RQ \to q)|^2} = \frac{2}{3}\pi\alpha_s(t_1 + t_2 + 2\sqrt{t_1 t_2}\cos\phi), \quad (2)$$

$$\overline{|M(\gamma Q \to q)|^2} = 4\pi\alpha e_q^2 t_2, \quad (3)$$

$$\overline{|M(RR \to g)|^2} = \frac{3}{2}\pi\alpha_s(t_1 + t_2 + 2\sqrt{t_1 t_2}\cos\phi), \quad (4)$$

where R is the Reggeized gluon, Q is the Reggeized quark, e_q is the quark electric charge, $t_i = \vec{q}_{iT}^{\,2}$ is the transverse momentum of the Reggeized particle, $i = 1, 2$, and ϕ is the azimuthal angle between $\vec{q}_{1T}$ and $\vec{q}_{2T}$.

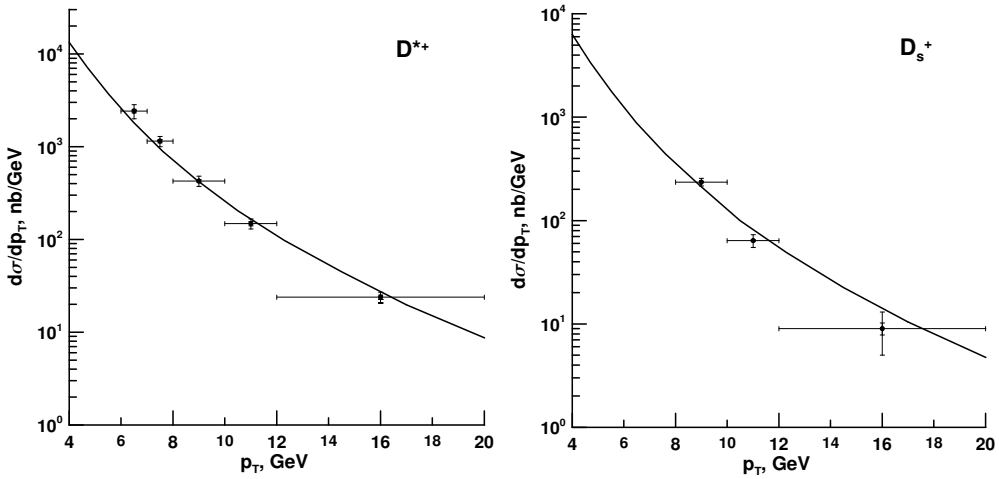

Figure 1: The p_T distributions of inclusive D^{*+} (left) and D_s^+ (right) hadroproduction for $\sqrt{S} = 1.96$ TeV and $|y| \leq 1$. The CDF data from Ref. [12] are compared with LO predictions from the QMRK approach with the quark Reggeization hypothesis.

2 Inclusive open charm production

In this section we study D-meson production via charm-quark fragmentation under HERA and Tevatron experimental conditions for the first time in the framework of the QMRK approach complemented with the quark Reggeization hypothesis [7]. In our numerical calculations below, we adopt the prescription proposed by Kimber, Martin, and Ryskin [8] to obtain unintegrated gluon and quark distribution functions for the proton from the conventional integrated ones, as implemented in Watt's code [9]. As input for this procedure, we use the Martin-Roberts-Stirling-Thorne [10] proton PDFs. As for the $c \to D$ fragmentation function $D_{c\to D}$, we adopt the non-perturbative D-meson sets determined in the zero-mass variable-flavor-number scheme with initial evolution scale $\mu_0 = m_c$ [11] from fits to OPAL data from CERN LEP1.

2.1 D-meson production at the Tevatron

CDF [12] measured the p_T distributions of D^0, D^+, D^{*+}, and D_s^+ mesons with rapidity $|y| \leq 1$ inclusively produced in hadroproduction in run II at the Tevatron, with $\sqrt{S} = 1.96$ TeV. To leading order (LO) in the QMRK approach there is only one partonic subprocess $C_{p(\overline{p})} R_{\overline{p}(p)} \to c$, where the subscript indicates the mother particle. This subprocess is described via the Reggeized-quark–Reggeized gluon effective vertex C^q_{RQ} from Ref. [3].

In Fig. 1, our results for D^{*+} and D_s^+ mesons are compared with the CDF data [12]. We find that the theoretical predictions generally agree rather well with the experimental data, except perhaps for the slope. In fact, the predictions exhibit a slight tendency to undershoot the data at small values of p_T and to overshoot them at large values of p_T. However, we have to bear in mind that these are just LO predictions, so that there is room for improvement by including higher orders.

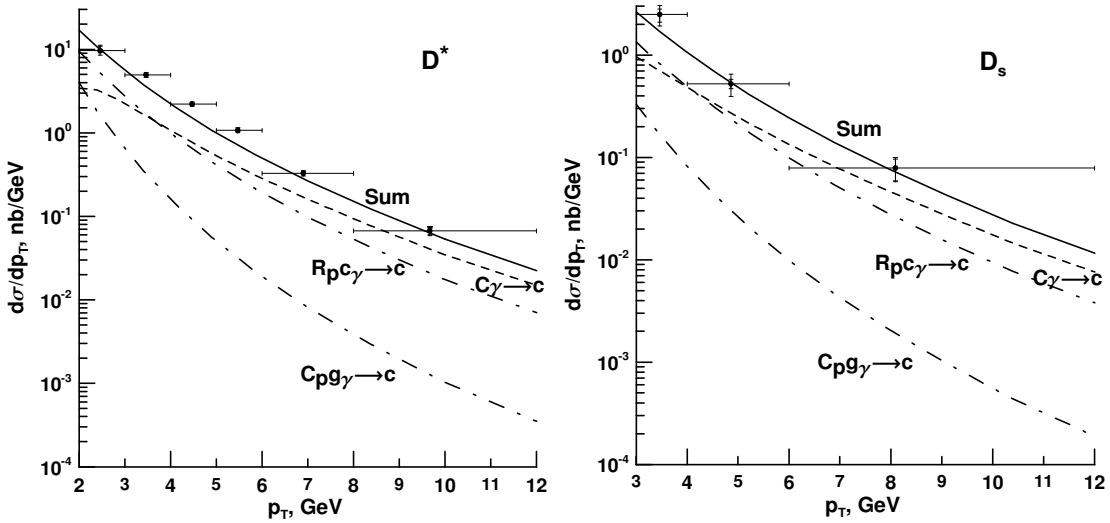

Figure 2: The p_T distributions of inclusive $D^{*\pm}$ (left) and $D_s^{\pm}$ (right) photoproduction for $\sqrt{S} = 300$ GeV and $|y| \leq 1.5$. The ZEUS data from Ref. [13] and Ref. [14] are compared with LO predictions from the QMRK approach with the quark Reggeization hypothesis.

2.2 D-meson photoproduction at HERA

On the experimental side, ZEUS measured the p_T distributions of $D^{*\pm}$ [13] and $D_s^{\pm}$ [14] mesons with rapidity $|y| \leq 1.5$ inclusively produced in photoproduction at HERA I, with proton energy $E_p = 820$ GeV and lepton energy $E_e = 27.5$ GeV in the laboratory frame, in the ranges $2 \leq p_T \leq 12$ GeV and $3 \leq p_T \leq 12$ GeV, respectively. Since we neglect finite quark and hadron mass effects, pseudorapidity and rapidity coincide. In this section, we compare this data with our QMRK predictions. At leading order (LO), we need to consider only three $2 \to 1$ partonic subprocesses, namely $C_p\gamma \to c$ for direct photoproduction and $C_p g_\gamma \to c$ and $R_p c_\gamma \to c$ for resolved photoproduction, using the effective vertices $C^q_{Q\gamma}$ from Ref.[3], C^q_{Qg} and C^q_{Rq}, respectively.

In Fig. 2 our results for $D^{*\pm}$ and $D_s^{\pm}$ mesons, respectively, are broken down to the $C_p\gamma \to c$, $C_p g_\gamma \to c$, and $R_p c_\gamma \to c$ contributions and are compared with the ZEUS data [13, 14]. We find that the theoretical predictions are dominated by direct photoproduction and agree rather well with the experimental data over the whole p_T range considered.

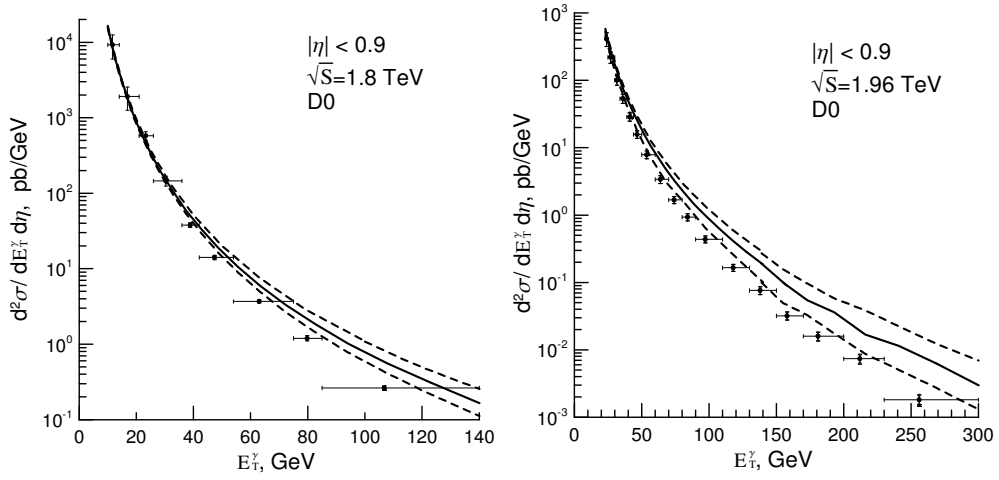

Figure 3: The E_T spectra of prompt photons at $\sqrt{S} = 1.8$ TeV (left) and $\sqrt{S} = 1.96$ TeV (right), and $|\eta| < 0.9$. The data are from D0 Collaboration [19].

3 Inclusive prompt photon production

In this part we consider an inclusive production of isolated photons at the Fermilab Tevatron and DESY HERA Colliders. In the QMRK approach the leading order (LO) contribution comes from the direct Reggeized quark-Reggeized antiquark annihilation into a photon ($Q\bar{Q} \to \gamma$) via the effective vertices $C^{\gamma}_{\bar{Q}Q}$ [3, 6]. In case of photoproduction at HERA it takes place in the resolved production, in which one quark (or anti-quark) comes from a photon. The additional small contributions originate from the fragmentation of produced quarks and gluons into the photon, which is described by the parton to photon fragmentation functions. We have obtained, the same as it was shown in Ref. [15], the contribution of the fragmentation mechanism is strongly suppressed by the isolation cone condition, which is applied to the experimental data [16, 17, 18, 19]. Such a way, we estimate the above mentioned contribution as a small one and do not take it into account in the presented analysis.

3.1 Prompt photon production at the Tevatron

The transverse momentum p_T spectra of isolated photons were studied by the CDF and D0 Collaborations [18, 19] at the energies $\sqrt{S} = 1.8$ TeV and $\sqrt{S} = 1.96$ TeV. The inclusive prompt photon production cross sections were measured in the range of $10 \le p_T \le 300$ GeV, both in the central region of pseudorapidity $|\eta| < 0.9$, and in the forward region, where one takes values in the range of $1.6 < |\eta| < 2.5$.

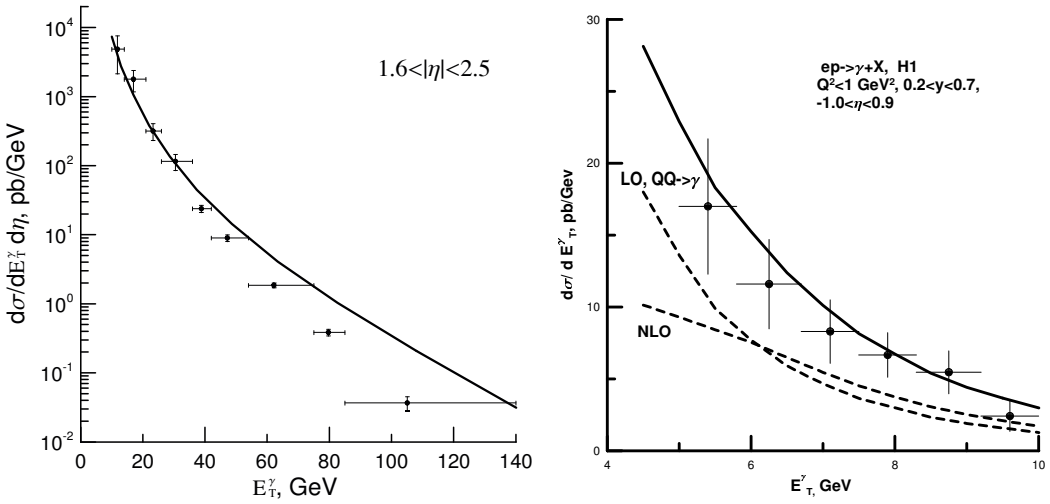

Figure 4: The E_T spectrum of prompt photons at $\sqrt{S} = 1.8$ TeV and $1.6 < |\eta| < 2.5$; the data are from D0 Collaboration [19](left). The E_T spectrum of prompt photons at $\sqrt{S} = 319$ GeV, $-1.0 < \eta < 0.9$, and $0.2 < y < 0.7$; the data are from H1 Collaboration [16] (right).

In the Figure 3 one can find the agreement between our calculations and the experimental data in the central pseudorapidity region of Run-I (Fig. 3, left) and Run-II (Fig. 3, right), up to $p_T \simeq 100$ GeV. That directly demonstrates valid behavior and correct normalization of the quark unintegrated structure functions $\Phi_q^p(x, t, \mu^2)$ obtained by using KMR prescription [8], in the wide range of parameters x, μ^2 and t. The solid and dashed lines correspond to the different choices of factorization scale μ^2, which is taken as $\mu^2 = p_T^2/4, p_T^2,$ and $4p_T^2$. The above choices have strong effects in the region of $p_T > 100$ GeV, where theoretical results overestimate the experimental data. Note that in this region of the photon transverse momentum the parton longitudinal momentum fractions become non-small and no longer satisfy the conditions of particle Reggeization. At very large p_T one has $x_{1,2} \geq 0.1$ and so far the collinear parton model should be applied, where the squared Reggeized amplitude $|M(Q\bar{Q} \to \gamma)|^2 \to 0$ and the $2 \to 2$ parton subprocesses ($qg \to q\gamma, q\bar{q} \to g\gamma$, etc.) are needed to take into account.

The similar situation takes place also considering the prompt photon production in the interval of large pseudorapidity $1.6 < |\eta| < 2.5$ (Figure 4, left). In this case we consider the parton Reggeization in the one channel, because the only one parton has the longitudinal momentum fraction $x \ll 1$ under the non-symmetric kinematical conditions at the $|\eta| > 1.6$. We have found that the number of events involving both interacting partons with non-small x is large even at $p_T > 50$ GeV. This fact provides an explanation of the discrepancy between our predictions and the experimental data at the large p_T.

3.2 Prompt photon production at HERA

The H1 Collaboration [16] has measured the inclusive prompt photon production at the HERA Collider in the region of a small exchange photon virtuality $Q^2 < 1$ GeV^2, i.e. in the photoproduction processes. Figure 4 (right) shows that LO contribution, coming from parton

subprocesses $Q_p\bar{q}_\gamma \to \gamma$ and $\bar{Q}_p q_\gamma \to \gamma$, does not describe data. The preliminary study of the next-to-leading order (NLO) corrections have been performed in the Ref. [20], where the contributions of the $2 \to 2$ subprocesses ($\gamma R_p \to \gamma g$, $\gamma Q_p \to \gamma q$, $R_\gamma Q_p \to gq$, $Q_\gamma R_p \to gq$ and $Q\bar{Q} \to \gamma g$) were analyzed. The Reggeon-particle to particle-particle effective vertices $C^{\gamma g}_{\gamma R}$ and $C^{\gamma q}_{\gamma Q}$ were written down in the same manner as in the Ref. [3] and the relevant contributions were calculated. Note, if we take into account isolation cone conditions the contribution of the $2 \to 2$ subprocesses to the inclusive photon spectra is free from singularities. The inclusion of such type of NLO corrections makes the agreement between theoretical predictions and experimental data more adequate. To perform this comparison more precise, for prompt photons we need to take into account the so-called hadronization effects too [16], which inclusion slightly decrease the resulting cross section.

Acknowledgments

V. S. thanks the Organizing Committee for the kind hospitality during the conference and for the financial support. A. S. thanks the Dinastiya Foundation for the partly financial supporting of this work. We thank L. N. Lipatov and V. S. Fadin for the discussion of the questions under consideration in this paper. We especially thank B. A. Kniehl with whom a part of the presented results has been obtained.

References

[1] V. S. Fadin and L. N. Lipatov, Nucl. Phys. **B477**, 767 (1996); Nucl. Phys. **B406**, 259 (1993).

[2] L. N. Lipatov, Nucl. Phys. **B452**, 369 (1995).

[3] L. N. Lipatov and M. I. Vyazovsky, Nucl. Phys. **B597**, 399 (2001).

[4] M. Gell-Mann, M. L. Goldberger, F. E. Low, E. Marx, and F. Zachariasen, Phys. Rev. **133**, 145B (1964).

[5] E. A. Kuraev, L. N. Lipatov, and V. S. Fadin, Sov. Phys. JETP **44**, 443 (1976) [Zh. Eksp. Teor. Fiz. **71**, 840 (1976)]; I. I. Balitsky and L. N. Lipatov, Sov. J. Nucl. Phys. **28**, 822 (1978) [Yad. Fiz. **28**, 1597 (1978)].

[6] V. S. Fadin and V. E. Sherman, JETP Lett. **23**, 548 (1976); JETP **45**, 861 (1977).

[7] B. A. Kniehl, A. V. Shipilova, and V. A. Saleev, Phys. Rev. **D79**, 034007 (2009).

[8] M. A. Kimber, A. D. Martin, and M. G. Ryskin, Phys. Rev. **D63**, 114027 (2001).

[9] G. Watt, URL: `http://www.hep.ucl.ac.uk/~watt/`; G. Watt, A. D. Martin, and M. G. Ryskin, Eur. Phys. J. **C31**, 73 (2003).

[10] A. D. Martin, R. G. Roberts, W. J. Stirling, and R. S. Thorne, Phys. Lett. **B531**, 216 (2002).

[11] J. Binnewies, B. A. Kniehl, and G. Kramer, Phys. Rev. **D58**, 014014 (1998); B. A. Kniehl and G. Kramer, *ibid.* **71**, 094013 (2005); **74**, 037502 (2006).

[12] CDF Collaboration, D. E. Acosta *et al.* , Phys. Rev. Lett. **91**, 241804 (2003).

[13] ZEUS Collaboration, J. Breitweg *et al.* , Eur. Phys. J. **C6**, 67 (1999).

[14] ZEUS Collaboration, J. Breitweg *et al.* , Phys. Lett. **B481**, 213 (2000).

[15] V. A. Saleev, Phys. Rev. **D78**, 034033 (2008); Phys. Rev. **D78**, 114031 (2008).

[16] H1 Collaboration, DESY 04-118; Eur. Phys. J. Phys. (2004).

[17] ZEUS Collaboration, J. Breitweg *et al.* Phys. Lett. **B472**, 175 (2000).

[18] CDF Collaboration, D. Acosta *et al.*, Phys. Rev. **D70**, 074008 (2004).

[19] D0 Collaboration, B. Abbott *et al.*, Phys. Rev. Lett. **84**, 2786 (2000); D0 Collaboration, V. M. Abazov *et al.*, Phys. Lett. **B639**, 151 (2006).

[20] V. A. Saleev, Talk presented at the Int. Workshop "DIS and related subjects", Madrid, Spain, 2009 (to be published in the Proceedings).

Measurement of the Gluon Polarization in the Nucleon via Spin Asymmetries of Charmed Mesons at COMPASS

Jörg Pretz

Physikalisches Institut, Universität Bonn, Nußallee 12, 53115 Bonn, Germany
on behalf of the COMPASS collaboration

DOI: http://dx.doi.org/10.3204/DESY-PROC-2009-03/Pretz

This article discusses a measurement of the gluon polarization in the nucleon, $\Delta g/g$. It concentrates on the most direct and cleanest way, the measurement of double spin asymmetries of charmed mesons produced in deep inelastic muon-nucleon scattering. The method, the experimental set-up and the analysis leading to the result

$$\frac{\Delta g}{g} = -0.39 \pm 0.24(\text{stat.}) \pm 0.11(\text{syst.})$$

at an average gluon momentum fraction $x_g \approx 0.11$ and a scale $\mu^2 \approx 13$ GeV^2 are presented.

1 Introduction: The Nucleon Spin Puzzle

One of the open questions in hadron physics is the decomposition of the nucleon spin of 1/2 among helicity and orbital angular momentum contributions of its constituents. The naive expectation, supported by the static quark model, is that the valence quarks are responsible for the spin of the nucleon. Results from deep inelastic scattering show that the helicity contribution of quarks to the nucleon spin, $\Delta\Sigma$, is only ≈ 30 % [1] by interpreting the matrix element of the singlet axial current, a_0, as $\Delta\Sigma$.

This interpretation is not free of ambiguities. It depends on the renormalization scheme used. In schemes where $\Delta\Sigma$ does not depend on the renormalization scale, a large helicity contribution of gluons, $\Delta G = 2 - 3$, would lead to a much higher value of $\Delta\Sigma$, consistent with quark models [2].

Here ΔG denotes the first moment of the gluon helicity distribution, $\Delta g(x_g)$, i.e. $\Delta G \equiv \int_0^1 \Delta g(x_g)\mathrm{d}x_g = \int_0^1 g^\uparrow(x_g) - g^\downarrow(x_g)\mathrm{d}x_g$. $g^\uparrow$ ($g^\downarrow$) is the number density of gluons with spin parallel (antiparallel) to the nucleon spin at a momentum fraction x_g. The unpolarized gluon distribution is thus given by $g(x_g) = g^\uparrow(x_g) + g^\downarrow(x_g)$.

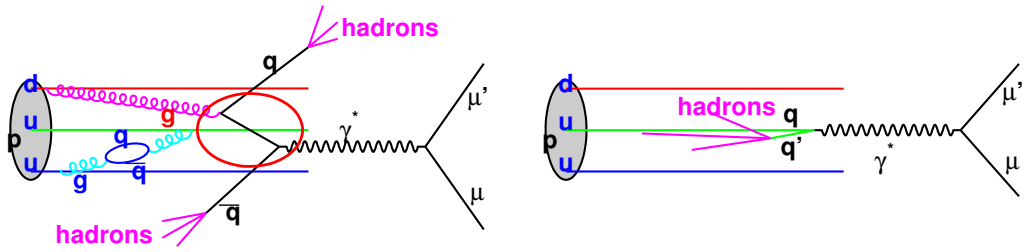

Figure 1: Deep inelastic μ-proton event with the photon-gluon-fusion process (left) and the absorption of the virtual photon by a quark (right) as the underlying partonic subprocess.

2 How to measure ΔG?

2.1 Tagging the gluon

The main tool to study the partonic structure of the nucleon is deep inelastic lepton nucleon scattering (DIS). In the quark parton model, deep inelastic scattering is interpreted as an incoherent sum of scattering processes off partons inside the nucleon. Of particular interest for the discussion here is the process shown in Figure 1, left. It shows a deep inelastic event in the proton-photon center of mass system where the participating parton is a gluon. The partonic subprocess $\gamma^* g \to q\bar{q}$ (indicated by the red ellipse) is called photon-gluon-fusion (PGF). Identifying this process among the much more abundant leading processes where the virtual photon is directly absorbed by one of the quarks inside the nucleon (Fig. 1, right) is the main difficulty. The cleanest way to tag the PGF process is to especially look for the production of charm quarks in the PGF process, i.e. $\gamma^* g \to c\bar{c}$. This process can be identified by the observation of charmed mesons produced in the fragmentation of the c and $\bar{c}$ quarks. At lepton energies considered here, intrinsic charm in the nucleon can be neglected and the production of charmed mesons in the fragmentation process is also strongly suppressed, i.e. the PGF process $\gamma^* g \to c\bar{c}$ is the dominating process for the production of charmed hadrons. They are identified experimentally via the invariant mass of their decay products.

The cross section is schematically given by

$$\sigma^{\mu N \to \mu' D X} \propto \int \sigma^{\mu g} \, D_c^D \, g(x_g) \, \mathrm{d}x_g \, ,$$

where $g(x_g)$ is the gluon distribution, $\sigma^{\mu g}$ the cross section for the partonic process $\mu g \to \mu' c\bar{c}$ and D_c^D a fragmentation function describing the probability for a c quark to fragment into a D meson. To simplify the formula the dependence of the quantities on various kinematic variables was omitted. The integral indicates that for a fixed event kinematics the gluon density is probed in a given range of the gluon momentum fraction x_g. This is in contrast to the leading process where the quark momentum fraction is identical to the Bjorken variable x_{Bj} accessible from the event kinematics.

2.2 Learning about the helicity contribution of gluons

To investigate the helicity contribution of the gluons to the nucleon spin, in addition to identifying processes where the gluon participated, a longitudinally polarized beam and target are

needed. The polarized lepton-nucleon cross section is related to the gluon distribution in the following way:

$$\sigma^{\mu(\uparrow)N(\downarrow)} \propto \int (\sigma^{\mu(\uparrow)g(\downarrow)} g^{\uparrow} + \sigma^{\mu(\uparrow)g(\uparrow)} g^{\downarrow})\, D_c^D \,\mathrm{d}x_g \,, \tag{1}$$

$$\sigma^{\mu(\uparrow)N(\uparrow)} \propto \int (\sigma^{\mu(\uparrow)g(\uparrow)} g^{\uparrow} + \sigma^{\mu(\uparrow)g(\downarrow)} g^{\downarrow})\, D_c^D \,\mathrm{d}x_g \,. \tag{2}$$

The arrows indicate the spin direction.

The muon-nucleon asymmetry, $A^{\mu N\to\mu' DX}$, gives access to the gluon helicity distribution $\Delta g = g^{\uparrow} - g^{\downarrow}$.

$$\begin{aligned} A^{\mu N\to\mu' DX} &= \frac{\sigma^{\mu(\uparrow)N(\downarrow)} - \sigma^{\mu(\uparrow)N(\uparrow)}}{\sigma^{\mu(\uparrow)N(\downarrow)} + \sigma^{\mu(\uparrow)N(\uparrow)}} \\ &= \frac{\int \left(\sigma^{\mu(\uparrow)g(\downarrow)} - \sigma^{\mu(\uparrow)g(\uparrow)}\right)\, (g^{\uparrow} - g^{\downarrow}) D_c^D \,\mathrm{d}x_g}{\int \left(\sigma^{\mu(\uparrow)g(\downarrow)} + \sigma^{\mu(\uparrow)g(\uparrow)}\right)\, (g^{\uparrow} + g^{\downarrow}) D_c^D \,\mathrm{d}x_g} \\ &= \frac{\int \frac{\Delta g}{g}\, a_{LL}\, \sigma^{\mu g}\, g\, D_c^D \mathrm{d}x_g}{\int \sigma^{\mu g}\, g\, D_c^D \,\mathrm{d}x_g} \end{aligned} \tag{3}$$

where the partonic asymmetry

$$a_{LL} = \frac{\sigma^{\mu(\uparrow)g(\downarrow)} - \sigma^{\mu(\uparrow)g(\uparrow)}}{\sigma^{\mu(\uparrow)g(\downarrow)} + \sigma^{\mu(\uparrow)g(\uparrow)}} \tag{4}$$

has been introduced. It depends on the photon-gluon kinematics. At leading order [1] (LO) QCD an expression can be found in [3]. Finally one arrives at

$$A^{\mu N\to\mu' DX}(X) = \langle a_{LL}\rangle(X)\, \langle \Delta g/g\rangle_x \tag{5}$$

where

$$\langle a_{LL}\rangle = \frac{\int a_{LL}\, \sigma^{\mu g}\, g\, D_c^D \,\mathrm{d}x_g}{\int \sigma^{\mu g}\, g\, D_c^D \,\mathrm{d}x_g} \,.$$

and

$$\langle \Delta g/g\rangle_x = \frac{\int \Delta g/g\, a_{LL} \sigma^{\mu g} \mathrm{d}x_g}{\int a_{LL} \sigma^{\mu g} \mathrm{d}x_g} \,.$$

The argument X for $\langle a_{LL}\rangle$ indicates the dependence on kinematic variables, like for example the photon virtuality Q^2, the energy of the virtual photon divided by the energy of the incoming lepton in the target rest system, y, the energy of the D-meson divided by the energy of the virtual photon, z_{D^0}, and the transverse momentum of the D meson with respect to the virtual photon axis, p_T. The measurement of the double spin asymmetry, $A^{\mu N\to\mu' DX}$, gives thus access to the gluon polarization in the nucleon, $\langle \Delta g/g\rangle_x$, averaged over a certain range in x_g.

[1] Note that the terminology is sometimes confusing. For the open charm analysis presented here the PGF process shown in Fig. 1, left is leading order (LO) since it is the process with the lowest order in α_s where charm quarks are produced. Whereas in an inclusive analysis the process shown in Fig. 1, right is LO and the left diagram is next-to-leading order (NLO).

3 The COMPASS experiment at CERN

From the discussion in the previous section one can read off the main requirements for the measurement of $\Delta g/g$. These are

- a high energetic polarized lepton beam
- a polarized target
- good particle identification to identify the decay products of D mesons.

The COMPASS experiments meets these requirements. COMPASS is a fixed target experiment at CERN using hadron and muon beams to study the structure of the nucleon and spectroscopy of hadrons. For the subject discussed here, a 160 GeV naturally polarized positively charged muon beam is used. Its polarization is -0.80 ± 0.04. ^{6}LiD serves as target material. The target material is placed in a superconducting solenoid and is polarized via dynamic nuclear polarization. ^{6}Li can be considered as a helium nucleus plus a deuteron. Thus 4 out of the 8 nucleons in ^{6}LiD are polarizable. This would lead to a so called dilution factor of $4/8 = 0.5$. Talking into account additional non polarizable material in the target leads to a dilution factor of approximately 0.4. The exact value depends on the kinematics and is calculated event by event. Its relative uncertainty is 5%. The target polarization reached is 50% with a relative error of 5%. For the years 2002-2004 two target cells oppositely polarized were in use. In 2006, 3 target cells were used, the outer two had opposite polarization compared to the central cell. The use of 2 (or 3) target cells oppositely polarized and simultaneously exposed to the muon beam is mandatory for the extraction of asymmetries. Combining data sets with two different polarizations with respect to the muon polarization, allows, to a large extend, a cancellation of possible acceptance variations during the data taking.

The scattered muon and the produced hadrons are detected and identified in a two stage magnetic spectrometer. Of special importance for this analysis is the Ring Imaging Cherenkov Detector for charged particle identification. It allows a pion-kaon separation from threshold (9 GeV) up to momenta of 40 GeV at a 2.5 σ level. For a more detailed description of the experimental setup see [4].

4 Analysis

4.1 Event selection

For the present analysis events with an incoming muon, a scattered muon and at least two additional reconstructed tracks of opposite charge are selected. Note that the event sample comprises events from quasi-real photon production $Q^2 \approx m_\mu^2 y^2/(1-y)$ to the maximum Q^2 of about 100 GeV^2 attainable at this beam energy. Even events at very low Q^2 can be interpreted in perturbative QCD since a hard scale, μ, is given by $\mu^2 \approx 4m_c^2$ and not simply by the virtuality of the photon Q^2. All events are in the deep inelastic region, i.e. the invariant mass of the hadronic final state, W, is larger than 4 GeV^2.

The D mesons are reconstructed via their decay in $K\pi$ pairs. The analysis is performed independently for the following decay channels (charge conjugate channels are always implied)

1. $D^0 \to K^-\pi^+$

2. $D^{*+} \to D^0 \pi^+$
   $\hookrightarrow D^0 \to K^- \pi^+$

3. $D^{*+} \to D^0 \pi^+$
   $\hookrightarrow D^0 \to K^- \pi^+ (\pi^0)$,
   π^0 is not reconstructed.

4. $D^{*+} \to K^- \pi^+ \pi^+$
   kaons below the threshold of RICH,
   kaons are identified by neither giving a signal corresponding to a pion or an electron in the RICH.

The corresponding invariant mass spectra are shown in Fig. 2. The channel $D^0 \to K^- \pi^+ (\pi^0)$, where the π^0 is not reconstructed shows up in Figure 2 (center) as a shoulder at $M(K\pi) - M(D^0) \approx 0.250$ GeV. The final event samples amount to 37400, 8700, 6200, 1800 for the four samples, respectively.

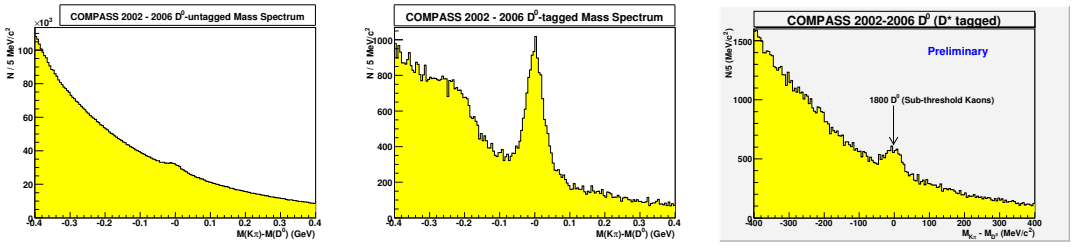

Figure 2: Invariant mass distributions of the $K\pi$ pairs for channel 1 (left), channel 2 and 3 (center) and channel 4 (right).

4.2 Determination of $\Delta g/g$

As derived in section 2.2, information on the gluon polarization is contained in the asymmetry

$$A^{\mu N \to \mu' D^0 X} = \frac{\sigma^{\mu(\uparrow) N(\downarrow)} - \sigma^{\mu(\uparrow) N(\uparrow)}}{\sigma^{\mu(\uparrow) N(\downarrow)} + \sigma^{\mu(\uparrow) N(\uparrow)}} \,.$$

This asymmetry is related to the number of observed events by

$$\frac{\mathrm{d}^k N}{\mathrm{d}m \, \mathrm{d}X} = a\phi n(s+b) \left[1 + P_\mathrm{t} P_\mu f \left(\frac{s}{s+b} A^{\mu N \to \mu' D^0 \mathrm{X}} + \frac{b}{s+b} A_\mathrm{B} \right) \right] \,. \tag{6}$$

Here a, Φ and n are the spectrometer acceptance, the time integrated muon flux and the number of target nucleons, respectively. P_t, P_μ denote the target and beam polarizations and f the dilution factor. The factor $s/(s+b)$ is the ratio of signal (s) to signal plus background (b) events. It can be obtained as a function of the invariant mass from Fig. 2. The term $b/(s+b)\, A_B$ takes into account a possible asymmetry of the combinatorial background.

In a LO QCD analysis $A^{\mu N \to \mu' D^0 \mathrm{X}}$ is replaced by $< a_{LL} > (X) \langle \Delta g/g \rangle_x$ according Eq. 5. To make best use of the data in terms of the statistical error, $\langle \Delta g/g \rangle_x$ is not simply determined from the counting rate asymmetry of the number of observed events but rather with a weighting

procedure where every event is weighted by its analyzing power which is essentially [2] the factor in front of $\langle \Delta g/g \rangle_x$, i.e. $w_S = P_\mu f \frac{s}{s+b} < a_{LL} >$. Introducing a similar weight for the background allows a simultaneous extraction of signal and background asymmetries. It can be shown that this methods provides the smallest possible statistical error [5].

To evaluate $\langle \Delta g/g \rangle_x$, apart from the number of (weighted) events, the various factors $P_\mathrm{t}, P_\mu, f, \frac{s}{s+b}$ and a_{LL} have to be known. Whereas this is straight forward for the two polarizations and the dilution factor, it is much more difficult for $\langle a_{LL} \rangle$ and $\frac{s}{s+b}$. $\langle a_{LL} \rangle$ depends on the partonic event kinematics and is thus not known event by event. With the help of a neural network it is parameterized in terms of the known event kinematics. The neural network is trained on an AROMA MC sample and uses a leading order QCD expression for a_{LL}. The a_{LL} parameterizations for the different decay channels are almost identical. Figure. 3 shows a correlation of 81% between the generated and the parameterized a_{LL}.

The dependence on the invariant mass of $s/(s+b)$ can be directly obtained from the plots in Fig. 2. However it turns out that there is a strong anticorrelation between $s/(s+b)$ and a_{LL}. This means that it is not sufficient to determine $s/(s+b)$ as a function of the invariant mass, it is also necessary to include the dependence on the other kinematic variables. Moreover this provides a smaller statistical error.

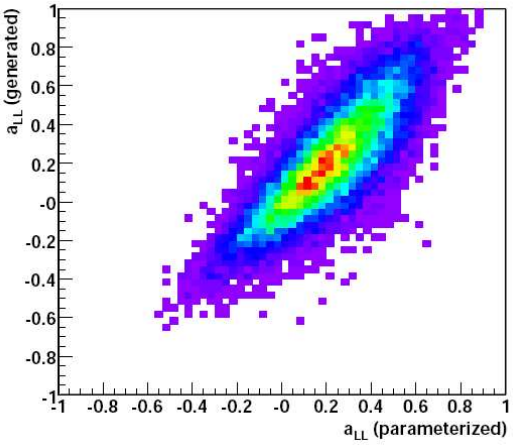

Figure 3: Correlation between the generated and reconstructed a_{LL}.

This is achieved with an iterative multivariate procedure, where $s/(s+b)$ is build as a function of kinematic variables and the response of the RICH detector [6, 7]. For the decay channels with less statistics (no. 3) and 4)) this method has difficulties and a new way to determine s/(s+b) was invented. Here a neural network (NN) is trained on kinematic variables and the information from the RICH. A training set is obtained from wrong charge combinations (wcc), $K^-\pi^+\pi^-$, for the background and good charge combinations (gcc), $K^-\pi^+\pi^+$, for the signal. Figure 4 shows one of the input variables of the NN, namely the polar angle of the kaon in the rest system of the D^0, $|\cos\theta^*|$, in the peak region and outside the peak region, once for the good and once for the wrong charge combination. One clearly observes the different shape for the events with the good charge combination in the peak region.

In both methods the parameterization is validated by verifying that the signal purity, $s/(s+b)$, obtained by the procedure in a given bin in $s/(s+b)$ agrees with the value obtained from a fit to the invariant mass spectrum in this bin. Combining data taken with two oppositely polarized target cells before and after a reversal of the target spin allows to extract $\langle \Delta g/g \rangle_x$ and A_B largely independent of acceptance and flux variations as explained in [7].

[2] The target polarization, P_T, is not included in the weight since it changes with time and may lead to a bias in the asymmetry extraction.

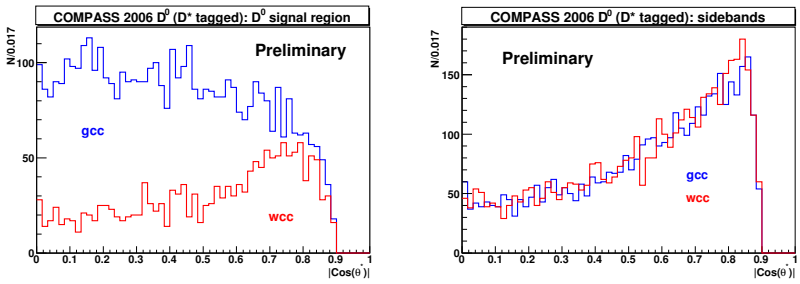

Figure 4: Distribution of $|\cos\theta^*|$ in the signal region (left) and in the sidebands (right) for the good charge combination (gcc) and the wrong charge combination (wcc).

5 Results

Figure 5 shows the results obtained for the four decay channels used in the analysis. The right most point is the weighted average. The gluon distribution is probed at an average momentum fraction $\langle x_g \rangle = 0.11^{+0.11}_{-0.05}$ and at a scale $\mu^2 \approx 4m_c^2 + p_T^2 = 13\,\mathrm{GeV}^2$. The background asymmetries come out to be consistent with 0.

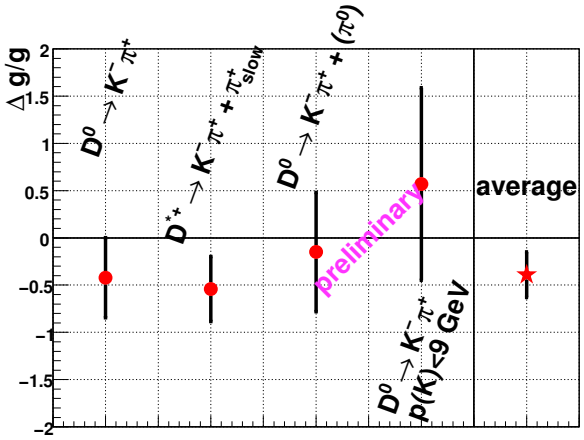

Figure 5: Results on $\langle \Delta g/g \rangle_x$ for the different decay channels used in the analysis. Only the statistical error is shown.

5.1 Systematic Error

Tab. 1 shows a detailed list of systematic errors for channel 1) and 2). The largest contribution to the systematic error comes from the parameterization of the signal purity in the case of the D^0 sample (channel 1) and possible experimental false asymmetries in the D^* sample (channel 2). The systematic error of the other two channels are of similar size. To be conservative a fully correlated systematic error of 0.11 is assigned to all four decay channels. Note that the

source	$\langle \Delta g/g \rangle_x$	source	$\langle \Delta g/g \rangle_x$
False asymmetry	0.05(0.05)	Beam polarization P_μ	0.02
$S/(S+B)$	0.07(0.01)	Target polarization P_t	0.02
a_LL	0.05(0.03)	Dilution factor f	0.02
Total error	0.11(0.07)		

Table 1: Systematic error contributions to $\langle \Delta g/g \rangle_x$ for $D^0(D^*)$ channels.

major contributions to the systematic error can be lowered with more statistics.

5.2 Final result

The final result is

$$\langle \Delta g/g \rangle_x = -0.39 \pm 0.24(\mathrm{stat.}) \pm 0.11(\mathrm{syst.})$$

at an average gluon momentum fraction $x_g \approx 0.11$ and a scale $\mu^2 \approx 13$ GeV^2.

This result is obtained in LO QCD analysis. In Ref. [7] also photon-nucleon asymmetries defined by $A^{\gamma N \to DX} = A^{\mu N \to \mu' DX}/D$, where D is the depolarization factor describing the polarization transfer from the muon to the virtual photon, are published. This asymmetry is independent of the interpretation in LO QCD.

5.3 Comparison to other results

Figure 6 shows the open charm result in comparison with other results obtained by using hadrons with large transverse momentum with respect to the virtual photon to tag the PGF process. In this method the signal purity has to be determined in a model dependent way from MC simulations in contrast to the open charm method where the signal purity is obtained from the invariant mass spectra.

The results clearly favor a small value of $\Delta g/g$ at $x \approx 0.1$ and exclude first moments of $\Delta G = 2-3$. This is also supported by results obtained from polarized proton-proton scattering at RHIC [11] and NLO fits to inclusive DIS data [1].

6 Summary & Outlook

The measurement presented here together with other measurements shows that the polarization of gluons around $x_g \approx 0.1$ is consistent with 0 and incompatible with large contribution of the first moment $\Delta G = \int g(x_g) \mathrm{d}x_g = 2-3$, though still consistent with $\Delta G = \int g(x_g) \mathrm{d}x_g = 0.5$, i.e. the gluons carrying 100% of the nucleon spin. The next steps are the inclusion of data taken in 2007 in the analysis and an analysis in next-to-leading order QCD.

At present COMPASS is the only experiment being able to use charmed meson for the determination of $\Delta g/g$. In the future, a polarized electron nucleon collider would offer much better opportunities for this method. One would not suffer from the absorption of hadrons in a solid state target. This will increase the number of reconstructed D mesons. Moreover it will offer the possibility to reconstruct both charmed particles produced in one event. This gives a better access to the gluon momentum fraction x_g.

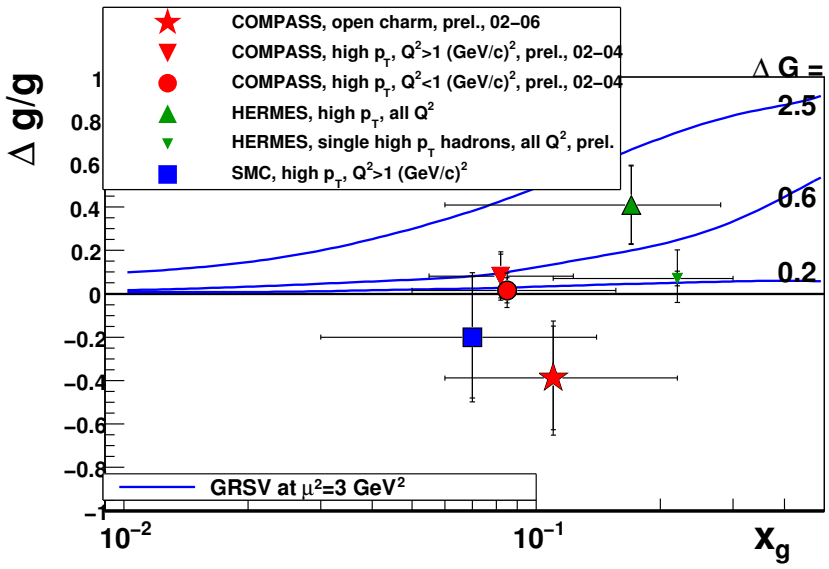

Figure 6: Comparison of the $\Delta g/g$ measurements from open charm and high p_T hadron production by COMPASS, SMC [8] and HERMES [9] as a function of x_g. Horizontal bars indicate the range in x_g for each measurement, vertical ones give the statistical and the total errors (if available). The open charm measurement is at a scale of about 13 GeV^2, other measurements and curves at 3 GeV^2. The solid (blue) curves are a parameterizations [10] with a first moment $\Delta G = \int_0^1 \Delta g(x_g) \mathrm{d}x_g = 0.2, 0.6, 2.5$.

References

[1] E. S. Ageev *et al.* [Compass Collaboration], Phys. Lett. B **647** (2007) 330 [arXiv:hep-ex/0701014].

[2] E. Leader, Spin in Particle Physics, Cambridge University Press, 2001

[3] A. Bravar, K. Kurek and R. Windmolders, Comput. Phys. Commun. **105** (1997) 42

[4] P. Abbon *et al.* [COMPASS Collaboration], Nucl. Instrum. Meth. A **577** (2007) 455 [arXiv:hep-ex/0703049].

[5] J. Pretz and J. M. Le Goff, Nucl. Instrum. Meth. A **602** (2009) 594 [arXiv:0811.1426 [physics.data-an]].

[6] F. Robinet, PhD thesis (Saclay), Univ. Paris Diderot (Paris 7), 2008

[7] M. Alekseev *et al.* [COMPASS Collaboration], arXiv:0904.3209 [hep-ex]. Phys. Lett. B **676** (2009) 31

[8] SMC, B. Adeva *et al.*, Phys. Rev. D **58** (1998) 112001.

[9] HERMES, A. Airapetian *et al.*, Phys. Rev. Lett. **84** (2000) 2584;
P. Liebig, AIP Conf. Proc. **915** (2007) 331

[10] M. Glück, E. Reya, M. Stratmann and W. Vogelsang, Phys. Rev. D **63**, 094005 (2001)

[11] F. Ellinghaus [PHENIX Collaboration and STAR Collaboration], arXiv:0810.3178 [hep-ex].

Chapter 7

Vacuum Polarisation and Light-by-Light Scattering

Convenor:

Z. Zhang (Orsay)

Leading Theoretical Uncertainties in the Muon $g-2$

G. López Castro

Departamento de Física, Cinvestav, A.P. 14-740, México D.F., México

DOI: http://dx.doi.org/10.3204/DESY-PROC-2009-03/LopezCastro

A brief overview of the standard model (SM) prediction for the muon magnetic anomaly is given with main emphasis in the leading order (LO) hadronic contribution which provides at present the main source of uncertainty. Combining data on the 2π spectral functions from τ decays at Belle with previous measurements and using new calculations of the isospin breaking (IB) corrections we give a new determination of the LO term, which is closer to the one based on e^+e^- data. Further progress in understanding IB effects combined with more precise data on hadron production at e^+e^- machines can produce an accurate determination of the LO terms as required by future measurements of the muon magnetic anomaly.

1 Introduction

For a particle of charge e and mass m, its intrinsic magnetic dipole moment and spin vectors are related by $\vec{\mu} = g(e/2m)\vec{s}$. In a quantum field theory description, an elementary fermion has a gyromagnetic ratio $g = 2$; the quantum corrections of the self-interacting fermion naturally generates a magnetic anomaly $a \equiv (g-2)/2 \neq 0$. In the following we will be concerned with the magnetic anomaly of the muon which will be denoted by a_μ (for some comprehensive recent articles, see for example [1]).

The most precise measurements of the muon magnetic anomaly have been achieved by the BNL-E821 Collaboration in recent years (an account of previous measurements can be found in [1]). The current world average from positive and negative muons is $a_\mu^{exp} = 116592080(63) \times 10^{-11}$ [2], an impressive accuracy of 0.54 ppm. This experimental accuracy has prompted improved theoretical calculations in recent years, which include the effects of the three standard model interactions beyond the one-loop level. It becomes also sensitive to the effects expected from New Physics contributions. In view of current proposals aiming to reduce the experimental uncertainty up to $\pm 15 \times 10^{-11}$ [3], improved theoretical calculations are required to make a meaningful test of the SM and, eventually, to establish the existence of physics beyond it [3].

In this contribution we give an overview of the present SM calculation in the determination of the muon magnetic anomaly, where current uncertainties stems mainly from hadronic contributions. We focus on some recent progress in the evaluation of the LO hadronic contribution based on tau lepton and electron-positron data.

2 Brief summary of the SM prediction

It is customary to separate the theoretical calculation according to the contributions of the three SM interactions: $a_\mu^{SM} = a_\mu^{QED} + a_\mu^{EW} + a_\mu^{had}$ [1]. The QED and electroweak EW contributions can be calculated from the first principles of perturbative field theory, whereas the hadronic contributions rely either on input data or tools to deal with strong interactions in the non-perturbative regime.

The calculation of the QED contribution involve only loops of leptons and photons. The result is known in analytic form up to the third order in α, in a numerical form at the fourth order and even the leading-logs of order α^5 have been evaluated (references to original works can be found in [1]). By using the most precise evaluation of the fine structure constant $\alpha^{-1} = 137.035999710(96)$ from the measured value of the electron anomalous magnetic moment [4] one obtains the following QED prediction (see for instance the most recent reviews in [1]):

$$a_\mu^{QED} = (116584718.09 \pm 0.14 \pm 0.04) \times 10^{-11} \tag{1}$$

where the first and second uncertainties stems from the error estimate of the order α^5 corrections and from the experimental uncertainty in the measured value of α, respectively.

The EW corrections involve loops with at least one weakly interacting boson. The one-loop corrections were calculated long ago and the two-loop corrections were completed until recently in Refs. [5]. Even some estimates of the leading-logs of third order have been reported in the literature [6]. The final numerical results reads:

$$a_\mu^{EW} = (154 \pm 2 \pm 1) \times 10^{-11} \ , \tag{2}$$

where the first error bar includes uncertainties in the Higgs boson and top quark masses and third order loop effects, while the second includes hadronic uncertainties associated to triangle graphs [5]. It is clear that the uncertainties from QED and EW corrections are very small and do not pose a problem for present and even future comparisons of theory and experiment.

The most uncertain contribution in the SM calculation does arise from corrections involving hadronic loops. There are three kinds of such hadronic corrections:

$$a_\mu^{had} = a_\mu^{had,LO} + a_\mu^{had,HO} + a_\mu^{had,LBL} \ , \tag{3}$$

where superscripts refers to leading order (LO, at $O(\alpha^2)$), higher order (HO, at $O(\alpha^3)$) and light by light (LBL, at $O(\alpha^3)$) effects.

The different contributions in Eq.(3) cannot be calculated with arbitrary high accuracy as they involve strong interactions in the non-perturbative regime. Inputs from experimental data or models of hadronic interactions at low energies are useful in this case to come to a reliable result. By far, the largest contribution in Eq. (3) is the leading order correction, which needs to be calculated with a precision below the 1 % level and will be discussed in further detail in the next section. The accuracy required in the higher order HO and LBL corrections to match the experimental precision is much lower. The second term in Eq. (3) can be calculated using the same input data as the one used to compute the LO contribution. We just reproduce here the value obtained using electron-positron data (the numerical value obtained using τ lepton data is approximately 3% larger) [7]:

$$a_\mu^{had,HO} = (-98 \pm 1) \times 10^{-11} \ , \tag{4}$$

where the uncertainty stems mainly from input experimental data.

The hadronic light-by-light contribution is by far the most difficult to compute and the least precise ingredient of a_μ. There is not a direct connection to measurable quantities as in the case of the other two terms in Eq. (3). For the purposes of comparison with experiment, we use the results of a recent calculation [8]:

$$a_\mu^{had,LBL} = (105 \pm 26) \times 10^{-11} \ . \tag{5}$$

More details about recent improvements leading to Eq. (5) and a comparison with results of previous calculations are described in the accompanying paper by J. Prades [9].

3 The hadronic contribution at leading order

The hadronic contribution at leading order is obtained by inserting one loop of quarks or hadrons in the photonic propagator as indicated in Figure 1. The LO hadronic contribution

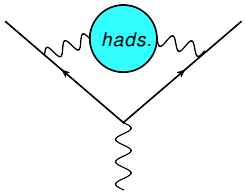

Figure 1: Hadronic contribution at leading order.

can be evaluated by means of the dispersion integral [10, 11]

$$a_\mu^{had,LO} = \frac{1}{3}\left(\frac{\alpha}{\pi}\right)^2 \int_{4m_\pi^2}^{\infty} ds \frac{K(s)}{s} \frac{\sigma^0(e^+e^- \to \text{hadrons})}{\sigma^{\text{point}}(e^+e^- \to \mu^+\mu^-)} \ , \tag{6}$$

where the superscript '0' denotes the cross section for hadron production with photonic corrections to the initial state and vacuum polarization effects removed but with final state photonic corrections included. The QED kernel $K(s)/s \sim s^{-2}$ [12] gives a large weight to low energy hadronic cross sections which makes the dominant contributions fall into the non-perturbative domain of strong interactions. Thus for instance, the 2π channel below 1.8 GeV contributes approximately 73% of the integral (6) and 82% of its total uncertainty, while the total contribution above 5.0 GeV is only 1.4%. The small contributions from large values of s, typically $\sqrt{s} \geq 5$ GeV, can be reliably obtained from perturbative QCD.

In this section we present an update of the 2π contribution to the muon magnetic anomaly taking into account recent data from the KLOE collaboration in the case of e^+e^- [13]. We also take advantage of a high-statistics study of the 2π hadronic spectrum from Belle [14] and recent calculations of the IB effects in the τ lepton case to re-evaluate the LO from τ data. For further details we refer the reader to our recent paper [15].

3.1 2π contribution using electron-positron data

The most relevant measurements of the 2π cross section in electron-positron collisions have been reported by the CMD2 [16, 17], SND [18] and, very recently, the KLOE [13] collaborations. The

accuracy of these data sets around the $\rho(770)$ resonance peak is below the 1% level, as required for theoretical predictions to match the experimental accuracy. The recent data published by KLOE [13] have reduced uncertainties and are slightly closer to CMD2 and SND results than before [19]. The Babar Collaboration [20] has reported preliminary measurements of this channel for center of mass energies between 0.5 and 3.0 GeV with an accuracy below the 0.6% level, which looks promissing for future improved analysis.

Previous evaluations of the 2π contribution to the muon magnetic anomaly using CMD2, SND and older KLOE measurements, can be found in [21, 22, 23, 24, 25]. In Ref. [15] we have presented an updated evaluation of the two-pion contribution by using the published data from CMD2, SND and KLOE. The evaluations of $a_\mu^{2\pi,LO}$ have been compared for the energy regions where data from different experiments overlap. As in previous analysis [23, 24], a good agreement is found between results based on CMD2 and SND data, while KLOE gives a lower result. Thus, we quote two results (either by including or excluding KLOE data) from combined data sets in the energy region where they overlap. As in previous analysis [21, 23], the evaluation of $a_\mu^{2\pi,LO}$ in the low energy region (chosen as $\sqrt{s} = 2m_\pi - 0.36$ GeV in Ref. [15]) is done by using a cubic expansion in s for the pion form factor as described in [21]. Our updated evaluation for the two-pion contribution gives [15]:

$$a_\mu^{2\pi,LO}(e^+e^-) = \begin{cases} (5027.7 \pm 30.1 \pm 11.1) \times 10^{-11}, & \text{including KLOE} \\ (5038.3 \pm 37.9 \pm 16.5) \times 10^{-11}, & \text{excluding KLOE} \end{cases} \tag{7}$$

where the first uncertainty stems from experimental input data and the second from the procedure used to extrapolate between data points in the dispersion integral [15]. As expected, using KLOE data [13] leads to a more precise but a slightly lower result.

3.2 2π contribution using tau decay data

The conserved vector current (CVC) hypothesis allows to replace data on the production of an even number of pions in e^+e^- collisions via the $I = 1$ current by the isospin analogous final state produced in τ lepton decays [26] ($\mathcal{B}_X$ denotes the branching fraction for final state X in τ decays):

$$\sigma(e^+e^- \to X_0^{I=1}) = \left(\frac{4\pi\alpha^2}{s}\right) \frac{m_\tau^2}{6|V_{ud}|^2} \frac{\mathcal{B}_{X_-}}{\mathcal{B}_e} \left(\frac{1}{N_X}\frac{dN_X}{ds}\right) \left(1 - \frac{s}{m_\tau^2}\right)^{-2} \left(1 + \frac{2s}{m_\tau^2}\right)^{-1} \frac{R_{IB}(s)}{S_{EW}} \,. \tag{8}$$

In our numerical evaluations we use [15]: $|V_{ud}| = 0.97418 \pm 0.00019$ [27], $\mathcal{B}_e = (17.818 \pm 0.032)\%$ [28], $S_{EW} = 1.0235 \pm 0.0003$ for the short-distance electroweak corrections [29]. We denote $(1/N_X)dN_X/ds$ as the normalized hadronic mass distribution in $\tau \to X^-\nu$ decays. In the case of the two-pion final state we use $\mathcal{B}_{2\pi} = (25.42 \pm 0.10)\%$, which corresponds to the weighted average of different measurements [15].

The s-dependent factor $R_{IB}(s)$ encodes the information about IB corrections that must be applied to the hadronic spectrum in τ decays in order to be used in the dispersion integral ($R_{IB}(s) = 1$ in the absence of IB effects or in the limit of exact CVC). It is defined as:

$$R_{IB}(s) = \frac{FSR}{G_{EM}(s)} \cdot \left(\frac{\beta_0(s)}{\beta_-(s)}\right)^3 \left|\frac{F_0(s)}{F_-(s)}\right|^2 \,. \tag{9}$$

The factor FSR [30] refers to the final state photonic corrections to the $e^+e^- \to \pi^+\pi^-$ cross section, $G_{EM}(s)$ denotes the long-distance radiative corrections to $\tau \to \pi\pi\nu$ decays [31],

$(\beta_0/\beta_-)^3$ is the ratio of pion velocities in their center of mass frame and $F_{0,-}(s)$ refers to the pion form factors (the subscripts $0,-$ refer to the electric charge of the 2π system). In Figure 2 we plot the s-dependent IB correction factors that enter the definition of $R_{IB}(s)$. Note that the first two factors in Eq. (9) have an important effect close to threshold $s = 4m_\pi^2$, while the IB effects in the ratio of pion form factors are more important around the ρ resonance region.

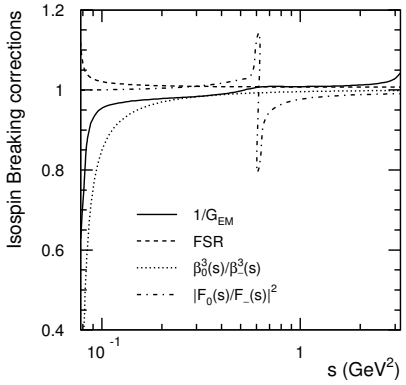

Figure 2: s dependence of IB correction factors defined in Eq. (9).

Some of the most recent evaluations of the 2π contribution using τ data from ALEPH [33], OPAL [34] and CLEO [35] Collaborations were reported in [21, 23]. Very recently, the Belle collaboration has reported a high-statistics study of the hadronic spectrum in $\tau \to \pi\pi\nu$ decay [14]. In addition, new calculations of the $G_{EM}(s)$ corrections to this decay [32] and of the width difference of $\rho^0 - \rho^\pm$ vector mesons [36] have become available. Particularly important is the role that plays the width difference $\Delta\Gamma_\rho$ given the wide resonance shape of the 2π cross section in the ρ meson region. The new calculation of $\Delta\Gamma_\rho$ takes into account the full radiative corrections to the dominant $\rho \to \pi\pi$ decay modes [36] including the effects of hard photons. All these new ingredients have prompted the analysis undertaken in Ref. [15].

In Table I we summarize the effects produced in $a_\mu^{\pi\pi,LO}(\tau)$ by the different sources of IB corrections that enter Eq. (9). Other numerical values of the IB parameters required in the

Source	$\Delta a_\mu^{\pi\pi,LO}(\tau)[10^{-11}]$
S_{EW}	-121.9 ± 1.5
G_{EM}	-18.6 ± 8.8
FSR	$+46.4 \pm 4.6$
$\rho - \omega$ interference	$+24.0 \pm 3.5$
$m_{\pi^\pm} - m_{\pi^0}$ in cross section	-77.1
$m_{\pi^\pm} - m_{\pi^0}$ in ρ widths	$+41.1 \pm 4.0$
$m_{\rho^\pm} - m_{\rho^0}$	-0.8 ± 3.5
$\pi\pi\gamma$ em decays	-59.4 ± 5.9
total	-165.5 ± 15.5

Table 1: Contributions to $\Delta a_\mu^{\pi\pi,LO}$ from isospin-breaking corrections.

form factors can be found in Ref. [15]. The most important changes with respect to previous

evaluations [21, 23] come from the width difference of ρ mesons. The largest uncertainty in Table 1 comes from the difference in the IB corrections from $G_{EM}(s)$ as calculated in [32] and that from Ref. [31]. We have attributed a 10% uncertainty to the IB effects that arise from FSR and $\Delta\Gamma_\rho$ due to neglected effects induced by the electromagnetic structure of pions in virtual corrections. Finally, the uncertainties quoted in the fourth, sixth and seventh rows of Table 1 arise from taking the difference between results obtained using the Gounaris-Sakurai (GS) and Kuhn-Santamaria parametrizations of the pion form factors (see [15]). Despite the conservative estimate of errors in Table 1, the total uncertainty becomes smaller than before [21].

Using the combined $\pi^-\pi^0$ mass spectrum of ALEPH, CLEO, OPAL and Belle collaborations, and applying the IB corrections discussed above, the dispersion integral Eq. (6) together with (8) and (9) yields [15]:

$$a_\mu^{\pi\pi,LO}(\tau) = (5143 \pm 12 \pm 22 \pm 16) \times 10^{-11} \ , \tag{10}$$

where the quoted errors arise, respectively, from uncertainties in the measured hadronic spectrum, in the $\pi^-\pi^0$ branching ratio and in the IB corrections.

A comparison of Eqs. (7) and (10), yields the following difference in the $\pi\pi$ channel,

$$\delta a_\mu^{\pi\pi,LO} = a_\mu^{\pi\pi,LO}(\tau) - a_\mu^{\pi\pi,LO}(e^+e^-) = \begin{cases} (115.3 \pm 43.8) \times 10^{-11}, & \text{incl. KLOE} \\ (114.7 \pm 50.1) \times 10^{-11}, & \text{excl. KLOE} \end{cases} , \tag{11}$$

which should be compared with previously obtained $\delta a_\mu^{\pi\pi,LO} = (154 \pm 49) \times 10^{-11}$ [23]. These results makes explicit the impact of new data and the new calculation of IB effects.

CVC can be used to predict other contributions to $a_\mu^{had,LO}$ that involve an even number of pions. Currently, data on the 4π mass spectrum in τ decays yields [23] (in units of 10^{-11}): $214 \pm 25 \pm 6_{IB}$ (for $\pi^+\pi^-2\pi^0$)) and $123 \pm 10 \pm 4_{IB}$ (for $2\pi^+2\pi^-$). Including other hadronic contributions from e^+e^- data (see Ref. [23]) we get the following results for the LO hadronic contribution [15]:

$$a_\mu^{had,LO} = \begin{cases} (6901 \pm 44 \pm 19_{rad} \pm 7_{QCD}) \times 10^{-11}, & e^+e^- \text{ excl. KLOE} \\ (6891 \pm 38 \pm 19_{rad} \pm 7_{QCD}) \times 10^{-11}, & e^+e^- \text{ incl. KLOE} \\ (7044 \pm 35 \pm 7_{rad} \pm 18_{IB}) \times 10^{-11}, & \tau \text{ decay data} \end{cases} \tag{12}$$

The discrepancy between the predictions of the LO terms based on τ and e^+e^- data is at the 2.2σ (2.5σ) level obtained by excluding (including) KLOE data.

4 Updated SM prediction for a_μ

The SM prediction is obtained by adding up results in Eqs. (1), (2), (4), (5) and (12):

$$a_\mu^{SM} = \begin{cases} (116591780.1 \pm 55.0) \times 10^{-11}, & \text{from } e^+e^- \text{ (excl. KLOE)} \\ (116591770.1 \pm 50.3) \times 10^{-11}, & \text{from } e^+e^- \text{ (incl. KLOE)} \\ (116591923.1 \pm 47.7) \times 10^{-11}, & \text{from } \tau \text{ data} \end{cases} \tag{13}$$

All error bars were added in quadrature. They are dominated by the hadronic uncertainties from LO and light-by-light contributions.

In Figure 3 we plot the deviations of the SM predictions from the experimental value of the muon magnetic anomaly. The predictions of other recent analysis [21, 23, 24, 25] that include recent CMD2 and SND results and the previous SM prediction based on τ decay data are also shown for comparison.

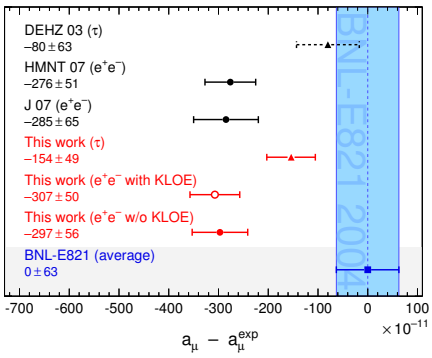

Figure 3: Deviations of SM predictions from experiment for the muon anomaly.

5 CVC prediction for the branching fraction

An independent consistency test of the 2π spectral functions is provided by comparing the measured branching fraction of τ decays with its prediction based on e^+e^- data using CVC. The formula relating these quantities is given by [15]:

$$B(\tau \to \pi\pi\nu) = \frac{3}{2}\frac{B_e|V_{ud}|^2}{\pi\alpha^2 m_\tau^2}\int_{s_{min}}^{m_\tau^2} ds\sigma^0_{\pi^+\pi^-}(s)\left(1-\frac{s}{m_\tau^2}\right)^2\left(1+\frac{2s}{m_\tau^2}\right)\frac{S_{EW}}{R_{IB}(s)}\ . \qquad (14)$$

In the limit of isospin symmetry, $S_{EW} = 1$ and $R_{IB}(s) = 1$. A previous evaluation of this branching ratio [21, 23] exhibited a discrepancy at the 4.5σ level when compared to the average of direct measurements. Including the new calculation of the isospin breaking effects increases the CVC-based prediction by the amount $(+0.73 \pm 0.19)\%$ [15]. This error bar is dominated by the uncertainties in the long-distance radiative corrections to $\tau \to \pi\pi\nu$ decays due to neglected pion form factor effects in virtual corrections [15].

In Figure 4 we compare the direct measurements of the branching ratio for τ decays, with the predictions based on e^+e^- data from CMD2, SND and KLOE corrected by IB effects according to Eq. (14). The difference between direct measurements of the branching fraction and predictions based on IB corrected e^+e^- data are now $(0.61 \pm 0.27)\%$ and $(0.47 \pm 30)\%$, respectively, by including and excluding KLOE data. This shows a smaller discrepancy than in previous results [21] and gives further support to the use of τ decay data to predict the muon magnetic anomaly.

6 Conclusions

Recent progress in calculations of the hadronic leading order and light-by-light contributions, allows to predict the muon magnetic anomaly a_μ with a better accuracy that its measured value. The prediction of a_μ based on e^+e^- data persistently shows a disagreement with the experimental value, currently at the 3.5σ level. Taking advantage of the high-statistics measurements of the 2π hadronic spectrum from Belle [14], and using new calculations of the IB effects, we have found [15] a SM prediction based on τ data which is closer to the one based on e^+e data; the discrepancy between both predictions still remains large given their smaller

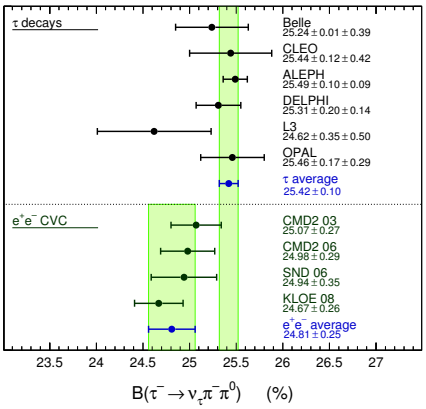

Figure 4: Branching fraction of τ decay compared to predictions based on CVC.

current uncertainties. On the other hand, this brings further support to the use of tau decay data in the search of an improved prediction of a_μ as required by future measurements.

An even better accuracy of the SM prediction can be achieved with more precise measurement of the $e^+e^- \to$ hadrons cross sections at CMD2, SND, KLOE and BaBar. Although some advances have been done [15] in understanding IB effects in the 2π spectral functions when comparing τ and e^+e- data, further work is required to solve completely the discrepancy between both sets of data. Solving this discrepancy will help to reach a precise prediction for a_μ as required by the E969 experiment.

7 Acknowledgments

It is a pleasure to thank the organizers of PHOTON09 for inviting me to present this talk. I am also thankful to M. Davier, A. Hoecker, B. Malaescu, X. Mo, G. Toledo, P. Wang, C. Yuan and Z. Zhang for very fruitful and stimulating discussions. Financial support from Conacyt (México) under projects 82291 and 60784 is gratefully acknowledged.

References

[1] M. Davier and W. J. Marciano, Ann. Rev. Nucl. Part. Sci. **54** 115 (2004);
J. P. Miller, E. de Rafael and B. L. Roberts, Rept. Prog. Phys. **70** 795 (2007);
B. L. Roberts, Prog. Theor. Phys. Suppl. **170** (2007);
F. Jegerlehner and A. Nyffeler, Phys. Rept. **477** 1 (2009);
M. Passera, Pramana **72**, 195 (2009);
S. I. Eidelman, Nucl. Phys. Proc. Suppl. **189** 208 (2009).

[2] G. W. Bennett *et al.* [Muon G-2 Collaboration], Phys. Rev. D **73** 072003 (2006).

[3] D. W. Hertzog, J. P. Miller, E. de Rafael, B. Lee Roberts and D. Stockinger, arXiv:0705.4617 [hep-ph];
C.J.G. Onderwater *these proceedings*

[4] D. Hanneke, S. Fogwell and G. Gabrielse, Phys. Rev. Lett. **100** 120801 (2008)

[5] A. Czarnecki, B. Krause and W. J. Marciano, Phys. Rev. Lett. **76** 3267 (1996);
A. Czarnecki, W. J. Marciano, and A. Vainshtein, Phys. Rev. **D67** 3006 (2003), Erratum-ibid **D73** 119901 (2006).

[6] G. Degrassi and G. F. Giudice, Phys. Rev. **D58**, 053007 (1998);
A. Czarnecki, W. J. Marciano and A. Vainshtein, Phys. Rev. **D67**, 073006 (2003).

[7] B. Krause, Phys. Lett. **B390** 392 (1997);
K. Hagiwara, A. D. Martin, D. Nomura and T. Teubner, Phys. Lett. **B557** 69 (2003).

[8] J. Prades, E. de Rafael and A. Vainshtein, arXiv:0901.0306 [hep-ph].

[9] J. Prades, arXiv:0907.2938 [hep-ph].

[10] C. Bouchiat and L. Michel, J. Phys. Radium **22** 121 (1961).

[11] M. Gourdin and E. de Rafael, Nucl. Phys. **B10** 667 (1969).

[12] S. Brodsky and E. de Rafael, Phys. Rev. **168** 1620 (1968).

[13] F. Ambrosino *et al.*[KLOE Collaboration], Phys. Lett. **B670** 285 (2009).

[14] M. Fujikawa *et al.*[Belle Collaboration], Phys. Rev. D **78** 072006 (2008).

[15] M. Davier *et al.*, arXiv:0906.5443 [hep-ph].

[16] R.R. Akhmetshin *et al.*[CMD-2 Collaboration], Phys. Lett. **B578** 285 (2004).

[17] V. M. Aulchenko *et al.*[CMD-2 Collaboration], JETP Lett. **82** 743 (2005);
R. R. Akhmetshin *et al.*[CMD-2 Collaboration], JETP Lett. **84** 413 (2006);
R. R. Akhmetshin *et al.*[CMD-2 Collaboration], Phys. Lett. **B648** 28 (2007).

[18] M. N. Achasov *et al.*[SND Collaboration], JETP Lett. **103** 380 (2006).

[19] A. Aloisio *et al.*[KLOE Collaboration], Phys. Lett. **B606** 12 (2005).

[20] M. Davier, Nucl. Phys. Proc. Suppl. **189** 222 (2009).

[21] M. Davier, S. Eidelman, A. Hoecker and Z. Zhang, Eur. Phys. J. **C27** 497 (2003).

[22] M. Davier, S. Eidelman, A. Hoecker and Z. Zhang, Eur. Phys. J. **C31** 503 (2003).

[23] M. Davier, Nucl. Phys. Proc. Suppl. **169** 288 (2007).

[24] K. Hagiwara, A. Martin, D. Nomura and T. Teubner, Phys. Lett. **B649** 173 (2007).

[25] F. Jegerlehner, Acta Phys. Polon. **B38** 3021 (2007); Nucl. Phys. Proc. Suppl. **181-182** 26 (2008).

[26] R. Alemany, M. Davier and A. Höcker, Eur. Phys. J. **C2** 123 (1998).

[27] J. Charles *et al.*[CKMfitter Group], Eur. Phys. J. **C41** 1 (2005).

[28] M. Davier, A. Hoecker and Z. Zhang, Rev. Mod. Phys. **78** 1043 (2006).

[29] A. Sirlin, Rev. Mod. Phys. **50** 573 (1978) [Erratum-ibid. **50** 905 (1978);
W. Marciano and A. Sirlin, Phys. Rev. Lett. **61** 1815 (1988);
E. Braaten and C. S. Li, Phys. Rev. **D42** 3888 (1990);
J. Erler, Rev. Mex. Phys. **50** 200 (2004).

[30] J. S. Schwinger, *Particles, Sources and Fields*, Vol. 3, Reading, Mass. (1989);
M. Drees and K. Hikasa, Phys. Lett. **B252** 127 (1990).

[31] V. Cirigliano, G. Ecker and H. Neufeld, Phys. Lett. B513, 361 (2001); J. High Energy Phys. **08** 002 (2002).

[32] F. Flores-Baéz, A. Flores-Tlalpa, G. López Castro, and G. Toledo Sánchez, Phys. Rev. **D74** 071301 (2006);
Nucl. Phys. Proc. Suppl. **169** 250 (2007).

[33] R. Barate *et al.*[ALEPH Collaboration], Z. Phys. **C76** 15 (1997);
S. Schael *et al.*[ALEPH Collaboration], Phys. Rep. **421** 191 (2005).

[34] K. Ackerstaff *et al.*[OPAL Collaboration], Eur. Phys. J. C7 571 (1999).

[35] S. Anderson *et al.*[CLEO Collaboration], Phys. Rev. **D61** 112002 (2000).

[36] F. Flores-Baéz, G. López Castro, and G. Toledo Sánchez, Phys. Rev. **D76** 096010 (2007);
G. López Castro, Nucl. Phys. Proc. Suppl. **189** 245 (2009).

The Hadronic Light-by-Light Contribution to Muon g-2: A Short Review

Joaquim Prades

CAFPE and Departamento de Física Teórica y del Cosmos,
Campus de Fuente Nueva, E-18002 Granada, Spain

DOI: http://dx.doi.org/10.3204/DESY-PROC-2009-03/Prades

I review the recent calculations and current status of the hadronic light-by-light scattering contribution to muon g-2. In particular, I discuss the main results obtained in a recent work together with Eduardo de Rafael and Arkady Vainshtein where we came to the estimate $a_\mu^{\rm HLbL} = (10.5 \pm 2.6) \times 10^{-10}$. How the two-photon physics program of low energy facilities can help to reduce the present model dependence is also emphasized.

1 Introduction

One momenta configuration out of the six possible ones contributing to the hadronic light-by-light to muon g-2 is depicted in Fig. 1 and described by the vertex function

$$\begin{aligned}\Gamma^\mu(p_2,p_1) &= -e^6 \int \frac{{\rm d}^4k_1}{(2\pi)^4} \int \frac{{\rm d}^4k_2}{(2\pi)^4} \frac{\Pi^{\mu\nu\rho\sigma}(q,k_1,k_2,k_3)}{k_1^2\,k_3^2\,k_3^2} \\ &\times \gamma_\nu(\not p_2 + \not k_2 - m)^{-1}\gamma_\rho(\not p_1 - \not k_1 - m)^{-1}\gamma_\sigma\end{aligned} \tag{1}$$

where $q \to 0$ is the momentum of the photon that couples to the external magnetic source, $q = p_2 - p_1 = -k_1 - k_2 - k_3$ and m is the muon mass.

The dominant contribution to the hadronic four-point function

$$\begin{aligned}&\Pi^{\rho\nu\alpha\beta}(q,k_1,k_3,k_2) \;=\; \\ &i^3 \int {\rm d}^4x \int {\rm d}^4y \int {\rm d}^4z\; {\rm e}^{i(-k_1\cdot x + k_3\cdot y + k_2\cdot z)} \,\langle 0|T\left[V^\mu(0)V^\nu(x)V^\rho(y)V^\sigma(z)\right]|0\rangle\end{aligned} \tag{2}$$

comes from the three light quark ($q = u,d,s$) components in the electromagnetic current $V^\mu(x) = \left[\overline{q}\,\widehat{Q}\,\gamma^\mu\,q\right](x)$ where $\widehat{Q} \equiv {\rm diag}(2,-1,-1)/3$ denotes the quark electric charge matrix. We are interested in the limit $q \to 0$ where current conservation implies

$$\Gamma^\mu(p_2,p_1) = -\frac{a^{\rm HLbL}}{4m}\,[\gamma^\mu,\gamma^\nu]\,q_\nu\,. \tag{3}$$

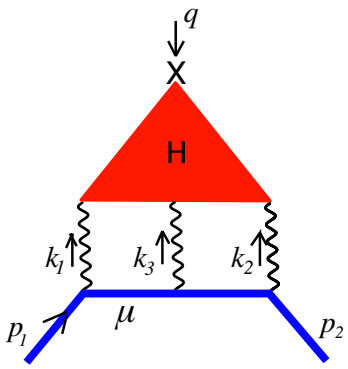

Figure 1: Hadronic light-by-light scattering contribution.

Therefore, the muon anomaly can then be extracted as

$$a^{\rm HLbL} = \frac{e^6}{48m}\int\frac{d^4k_1}{(2\pi)^4}\int\frac{d^4k_2}{(2\pi)^4}\frac{1}{k_1^2k_2^2k_3^2}\left[\frac{\partial}{\partial q^\mu}\Pi^{\lambda\nu\rho\sigma}(q,k_1,k_3,k_2)\right]_{q=0}$$
$$\times\,{\rm tr}\left\{(\not p+m)[\gamma_\mu,\gamma_\lambda](\not p+m)\gamma_\nu(\not p+\not k_2-m)^{-1}\gamma_\rho(\not p-\not k_1-m)^{-1}\gamma_\sigma\right\}\,. \qquad (4)$$

Here I discuss the results of [1] and [2]. Previous work can be found in [3, 4, 5, 6, 7, 8, 9, 10, 11, 12] and recent reviews are in [13, 14, 15, 16].

The hadronic four-point function $\Pi^{\mu\nu\rho\sigma}(q,k_1,k_3,k_2)$ is an extremely difficult object involving many scales and no full first principle calculation of it has been reported yet –even in the simpler large numbers of colors N_c limit of QCD. Notice that we need it with momenta k_1, k_2 and k_3 varying from 0 to ∞. Unfortunately, unlike the hadronic vacuum polarization, there is neither a direct connection of $a^{\rm HLbL}$ to a measurable quantity. Two lattice groups have started exploratory calculations [17, 18] but the final uncertainty that these calculations can reach is not clear yet.

Attending to a combined large number of colors of QCD and chiral perturbation theory (CHPT) counting, one can distinguish four types of contributions [19]. Notice that the CHPT counting is only for organization of the contributions and refers to the lowest order term contributing in each case. In fact, Ref. [1] shows that there are chiral enhancement factors that demand more than Nambu-Goldstone bosons in the CHPT expansion in the light-by-light contribution to the muon anomaly. See more comments on this afterwards.

The four different types of contributions are:

- Nambu-Goldstone boson exchanges contribution are $\mathcal{O}(N_c)$ and start at $\mathcal{O}(p^6)$ in CHPT.
- One-meson irreducible vertex contribution and non-Goldstone boson exchanges contribute also at $\mathcal{O}(N_c)$ but start contributing at $\mathcal{O}(p^8)$ in CHPT.
- One-loop of Goldstone bosons contribution are $\mathcal{O}(1/N_c)$ and start at $\mathcal{O}(p^4)$ in CHPT.
- One-loop of non-Goldstone boson contributions which are $\mathcal{O}(1/N_c)$ but start contributing at $\mathcal{O}(p^8)$ in CHPT.

Based on the counting above there are two full calculations [3, 4, 6] and [5, 7]. There is also a detailed study of the π^0 exchange contribution [8] putting emphasis in obtaining analytical expressions for this part.

Recently, two new calculations of the pion exchange using also the organization above have been made. In Ref. [10], the pion pole term exchange is evaluated within an effective chiral model. These authors also study the box diagram one-meson irreducible vertex contribution. The results are numerically very similar to the ones found in the literature as can be seen in Table 1. In Ref. [11], the author uses a large N_c model $\pi^0\gamma^*\gamma^*$ form factor with the pion also of-shell. This has to be considered as a first step and more work has to be done in order to have the full light-by-light within this approach. In particular, it would be very interesting to calculate the contribution of one-meson irreducible vertex contribution within this model.

Using operator product expansion (OPE) in QCD, the authors of [12] pointed out a new short-distance constraint of the reduced full four-point Green function

$$\langle 0|T\left[V^\nu(k_1)V^\rho(k_3)V^\sigma(-(k_1+k_2+q))\right]|\gamma(q)\rangle \tag{5}$$

when $q \to 0$ and in the special momenta configuration $-k_1^2 \simeq -k_3^2 >> -(k_1+k_3)^2$ Euclidean and large. In that kinematical region,

$$T\left[V^\nu(k_1)V^\rho(k_3)\right] \sim \frac{1}{\hat{k}^2}\,\varepsilon^{\nu\rho\alpha\beta}\hat{k}_\alpha\,\left[\overline{q}\,\hat{Q}^2\,\gamma_\beta\gamma_5\,q\right] \tag{6}$$

with $\hat{k} = (k_1-k_3)/2 \simeq k_1 \simeq -k_3$. See also [20]. This short distance constraint was not explicitly imposed in previous to [12] calculations.

2 Leading in $1/N_c$ Results

Using effective field theory techniques, the authors of [9] shown that leading large N_c contribution to $a^{\rm HLbL}$ contains an enhanced term at low energy by $\log^2(M_\rho/m_\pi)$ where the rho mass M_ρ acts as an ultraviolet scale and the pion mass m_π provides the infrared scale.

$$a^{\rm HLbL}(\pi^0) = \left(\frac{\alpha}{\pi}\right)^3 N_c \frac{m^2 N_c}{48\pi^2 f_\pi^2}\,\left[\ln^2\,\frac{M_\rho}{m_\pi} + \mathcal{O}\left(\ln\,\frac{M_\rho}{m_\pi}\right) + \mathcal{O}(1)\right] \tag{7}$$

This leading logarithm is generated by the Goldstone boson exchange contributions and is fixed by the Wess–Zumino–Witten (WZW) vertex $\pi^0\gamma\gamma$. In the chiral limit where quark masses are neglected and at large N_c, the coefficient of this double logarithm is model independent and has been calculated and shown to be positive in [9]. All the calculations we discuss here agree with these leading behaviour and its coefficient including the sign. A global sign mistake in the π^0 exchange in [3, 4, 5] was found by [8, 9] and confirmed by [6, 7] and by others [21, 22]. The subleading ultraviolet scale μ-dependent terms [9], namely, $\log(\mu/m_\pi)$ and a non-logarithmic term $\kappa(\mu)$, are model dependent and calculations of them are implicit in the results presented in [3, 4, 5, 7, 12]. In particular, $\kappa(\mu)$ contains the large N_c contributions from one-meson irreducible vertex and non-Goldstone boson exchanges. In the next section we review the recent model calculations of the full leading in the $1/N_c$ expansion contributions.

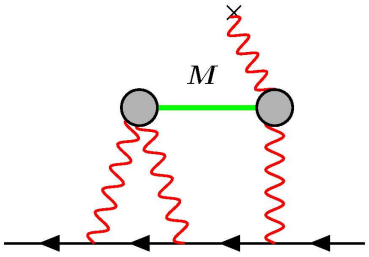

Figure 2: A generic meson exchange contribution to the hadronic light-by-light part of the muon $g-2$.

Table 1: Results for the π^0, η and η' exchange contributions.

Reference	$10^{10} \times a$	
	π^0 only	π^0, η and η'
[3, 4, 6]	5.7	8.3 ± 0.6
[5, 7]	5.6	8.5 ± 1.3
[8] with $h_2 = 0$	5.8	8.3 ± 1.2
[8] with $h_2 = -10$ GeV^2	6.3	
[10]	6.3 ∼ 6.7	
[11]	7.2	9.9 ± 1.6
[12]	7.65	11.4±1.0

2.1 Model Calculations

The pseudo-scalar exchange is the dominant numerical contribution and was saturated in [3, 4, 5, 6, 7, 8, 10, 11] by Nambu-Goldstone boson's exchange. This contribution is depicted in Fig. 2 with $M = \pi^0, \eta, \eta'$. The relevant four-point function was obtained in terms of the off-shell $\pi^0\gamma^*(k_1)\gamma^*(k_3)$ form factor $\mathcal{F}(k_1^2, k_3^2)$ and the off-shell $\pi^0\gamma^*(k_2)\gamma(q=0)$ form factor $\mathcal{F}(k_2^2, 0)$ modulating each one of the two WZW $\pi^0\gamma\gamma$ vertex.

In all cases several short-distance QCD constraints were imposed on these form-factors. In particular, they all have the correct QCD short-distance behaviour

$$\mathcal{F}(Q^2, Q^2) \to \frac{A}{Q^2} \quad \text{and} \quad \mathcal{F}(Q^2, 0) \to \frac{B}{Q^2} \tag{8}$$

when Q^2 is Euclidean and large and are in agreement with $\pi^0\gamma^*\gamma$ low-energy data [1]. They differ slightly in shape due to the different model assumptions (VMD, ENJL, Large N_c, NχQM) but they produce small numerical differences always compatible within quoted uncertainty $\sim 1.3 \times 10^{-10}$ –see Table 1.

Within the models used in [3, 4, 5, 6, 7, 8, 10, 11], to get the full contribution at leading in $1/N_c$ one needs to add the one-meson irreducible vertex contribution and the non-Goldstone

[1] See however the new measurement of the $\gamma\gamma^* \to \pi_0$ transition form factor by BaBar [23] at energies between 4 and 40 GeV^2

Table 2: Sum of the short- and long-distance quark loop contributions [5] as a function of the matching scale Λ.

Λ [GeV]	0.7	1.0	2.0	4.0
$10^{10} \times a^{\rm HLbL}$	2.2	2.0	1.9	2.0

Table 3: Results for the axial-vector exchange contributions from [3, 4, 6] and [5, 7].

References	$10^{10} \times a^{\rm HLbL}$
[3, 4, 6]	0.17 ± 0.10
[5, 7]	0.25 ± 0.10

boson exchanges. In particular, below some scale Λ, the one-meson irreducible vertex contribution was identified in [5, 7] with the ENJL quark box contribution with four dressed photon legs. While to mimic the contribution of short-distance QCD quarks above Λ, a loop of bare massive heavy quark with mass Λ and QCD vertices was used. The results are in Table 2 where one can see a very nice stability region when Λ is in the interval [0.7, 4.0] GeV. Similar results for the quark loop below Λ were obtained in [3, 4] though these authors didn't discuss the short-distance long-distance matching.

In [5, 7], non-Goldstone boson exchanges were saturated by the hadrons appearing in the model, i.e. the lowest scalar and pseudo-vector hadrons. Both states in nonet-symmetry –this symmetry is exact in the large N_c limit. Within the ENJL model, the one-meson irreducible vertex contribution is related trough Ward identities to the scalar exchange which we discuss below and *both* have to be included [5, 7]. The result of the scalar exchange obtained in [5] is

$$a^{\rm HLbL}({\rm Scalar}) = -(0.7 \pm 0.2) \times 10^{-10}\,. \tag{9}$$

The scalar exchange was not included in [3, 4, 6, 8]. The result of the axial-vector exchanges in [3, 4, 6] and [5, 7] can be found in Table 3.

Melnikov and Vainshtein used a model that saturates the hadronic four-point function in (2) at leading order in the $1/N_c$ expansion by the exchange of the Nambu-Goldstone π^0, η, η' and the lowest axial-vector f_1 states. In that model, the new OPE constraint of the reduced four-point function found in [12] mentioned above, forces the $\pi^0\gamma^*(q)\gamma(p_3 = 0)$ vertex to be point-like rather than including a $\mathcal{F}(q^2, 0)$ form factor.

There are also OPE constraints for other momenta regions [24] which are not satisfied by the model in [12] though they argued that this made only a small numerical difference of the order of 0.05×10^{-10}. In fact, within the large N_c framework, it has been shown [25] that in general for other than two-point functions, to satisfy fully the QCD short-distance properties requires the inclusion of an infinite number of narrow states.

3 Next-to-leading in $1/N_c$ Results

For the next-to-leading in $1/N_c$ contributions to the $a^{\rm HLbL}$ there is no model independent result at present and is possibly the most difficult component. Charged pion and kaon loops saturated this contribution in [3, 4, 5, 6, 7]. To dress the photon interacting with pions, a particular Hidden Gauge Symmetry (HGS) model was used in [3, 4, 6] while a full VMD was used in [5, 7]. The results obtained are $-(0.45 \pm 0.85) \times 10^{-10}$ in [3] and $-(1.9 \pm 0.5) \times 10^{-10}$

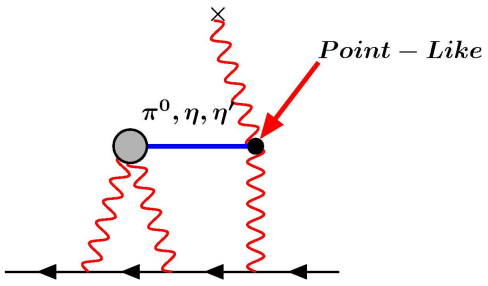

Figure 3: Goldstone boson exchange in the model in [12] contributing to the hadronic light-by-light.

Table 4: Results for the full hadronic light-by-light contribution to $a^{\rm HLbL}$.

Full Hadronic Light-by-Light	$10^{10} \times a_\mu$
[3, 4, 6]	8.9± 1.7
[5, 7]	8.9 ± 3.2
[12]	13.6 ± 2.5

in [5] while using a point-like vertex one gets -4.6×10^{-10}. Both models satisfy the known constraints though start differing at $\mathcal{O}(p^6)$ in CHPT. Some studies of the cut-off dependence of the pion loop using the full VMD model was done in [5] and showed that their final number comes from fairly low energies where the model dependence should be smaller. The authors of [12] analyzed the model used in [3, 4] and showed that there is a large cancellation between the first three terms of an expansion in powers of $(m_\pi/M_\rho)^2$ and with large higher order corrections when expanded in CHPT orders but the same applies to the π^0 exchange as can be seen from Table 6 in the first reference in [2] by comparing the WZW column with the others. The authors of [12] took $(0 \pm 1) \times 10^{-10}$ as a guess estimate of the total NLO in $1/N_c$ contribution. This seems too simple and certainly with underestimated uncertainty.

4 Comparing Different Calculations

The comparison of individual contributions in [3, 4, 5, 6, 7, 8, 10, 11, 12] has to be done with care because they come from different model assumptions to construct the full relevant four-point function. In fact, the authors of [10] have shown that their constituent quark loop provides the correct asymptotics and in particular the new OPE found in [12]. It has more sense to compare results for $a^{\rm HLbL}$ either at leading order or at next-to-leading order in the $1/N_c$ expansion.

The results for the final hadronic light-by-light contribution to $a^{\rm HLbL}$ quoted in [3, 4, 5, 6, 7, 12] are in Table 4. The apparent agreement between [3, 4, 6] and [5, 7] hides non-negligible differences which numerically almost compensate between the quark-loop and charged pion and [12] are in Table 4. Notice also that [3, 4, 6] didn't include the scalar exchange. Comparing the results of [5, 7] and [12], as discussed above, we have found several differences of order 1.5×10^{-10} which are not related to the new short-distance constraint used in [12]. The different

axial-vector mass mixing accounts for -1.5×10^{-10}, the absence of the scalar exchange in [12] accounts for -0.7×10^{-10} and the use of a vanishing NLO in $1/N_c$ contribution in [12] accounts for -1.9×10^{-10}. These model dependent differences add up to -4.1×10^{-10} out of the final -5.3×10^{-10} difference between [5, 7] and [12]. Clearly, the new OPE constraint used in [12] accounts only for a small part of the large numerical final difference.

5 Conclusions and Prospects

To give a result at present for the hadronic light–by–light contribution to the muon anomalous magnetic moment, the authors of [1], from the above considerations, concluded that it is fair to proceed as follows

Contribution to $a^{\rm HLbL}$ from π^0, η and η' exchanges

Because of the effect of the OPE constraint discussed above, we suggested to take as central value the result of Ref. [12] with, however, the largest error quoted in Refs. [5, 7]:

$$a^{\rm HLbL}(\pi\,,\eta\,,\eta') = (11.4 \pm 1.3) \times 10^{-10}\,. \tag{10}$$

Recall that this central value is quite close to the one in the ENJL model when the short–distance quark loop contribution is added there.

Contribution to $a^{\rm HLbL}$ from pseudo-vector exchanges

The analysis made in Ref. [12] suggests that the errors in the first and second entries of Table 2 are likely to be underestimates. Raising their ± 0.10 errors to ± 1 puts the three numbers in agreement within one sigma. We suggested then as the best estimate at present

$$a^{\rm HLbL}({\rm pseudo-vectors}) = (1.5 \pm 1) \times 10^{-10}\,. \tag{11}$$

Contribution to $a^{\rm HLbL}$ from scalar exchanges

The ENJL–model should give a good estimate for these contributions. We kept, therefore, the result of Ref. [5, 7] with, however, a larger error which covers the effect of other unaccounted meson exchanges,

$$a^{\rm HLbL}({\rm scalars}) = -(0.7 \pm 0.7) \times 10^{-10}\,. \tag{12}$$

Contribution to $a^{\rm HLbL}$ from a dressed pion loop

Because of the instability of the results for the charged pion loop and unaccounted loops of other mesons, we suggested using the central value of the ENJL result but wit a larger error:

$$a^{\rm HLbL}(\pi{\rm -dressed\ loop}) = -(1.9 \pm 1.9) \times 10^{-10}\,. \tag{13}$$

From these considerations, adding the errors in quadrature, as well as the small charm contribution 0.23×10^{-10}, we get

$$a^{\rm HLbL} = (10.5 \pm 2.6) \times 10^{-10}\,, \tag{14}$$

as our final estimate.

The proposed new $g_\mu - 2$ experiment accuracy goal of 1.6×10^{-10} calls for a considerable improvement in the present calculations. The use of further theoretical and experimental constraints could result in reaching such accuracy soon enough. In particular, imposing as many as

possible short-distance QCD constraints [3, 4, 5, 6, 7, 8, 11] has result in a better understanding of the numerically dominant π^0 exchange. At present, none of the light-by-light hadronic parametrization satisfy fully all short distance QCD constraints. In particular, this requires the inclusion of infinite number of narrow states for other than two-point functions and two-point functions with soft insertions [25]. A numerical dominance of certain momenta configuration can help to minimize the effects of short distance QCD constraints not satisfied, as in the model in [12].

More experimental information on the decays $\pi^0 \to \gamma\gamma^*$, $\pi^0 \to \gamma^*\gamma^*$ and $\pi^0 \to e^+e^-$ (with radiative corrections included [22, 26, 27]) can also help to confirm some of the neutral pion exchange results. A better understanding of other smaller contributions but with comparable uncertainties needs both more theoretical work and experimental information. This refers in particular to pseudo-vector exchanges. Experimental data on radiative decays and two-photon production of these and other C-even resonances can be useful in that respect.

New approaches to the pion dressed loop contribution, together with experimental information on the vertex $\pi^+\pi^-\gamma^*\gamma^*$ in the intermediate energy region $(0.5 - 1.5$ GeV) would also be very welcome. Measurements of two-photon processes like $e^+e^- \to e^+e^-\pi^+\pi^-$ can be useful to give information on that vertex and again could reduce the model dependence. The two-gamma physics program low energy facilities like the experiment KLOE-2 at DAΦNE will be very useful and well suited in the processes mentioned above which information can help to decrease the present model dependence of $a_\mu^{\rm HLbL}$.

6 Acknowledgments

It is a pleasure to thank Hans Bijnens, Elisabetta Pallante, Eduardo de Rafael and Arkady Vainshtein for enjoyable collaborations and discussions with Andreas Nyffeler on the different topics discussed here. This work has been supported in part by MICINN, Spain and FEDER, European Commission (EC) Grant No. FPA2006-05294, by the Spanish Consolider-Ingenio 2010 Programme CPAN Grant No. CSD2007-00042, by Junta de Andalucía Grants No. P05-FQM 347 and P07-FQM 03048 and by the EC RTN FLAVIAnet Contract No. MRTN-CT-2006-035482.

References

[1] J. Prades, E. de Rafael and A. Vainshtein in *Lepton Dipole Moments*, B.L. Roberts and W.J. Marciano, (eds) (World Scientific, Singapore, 2009) 309-324, arXiv:0901.0306.

[2] J. Bijnens and J. Prades, Mod. Phys. Lett. A **22** (2007) 767; Acta Phys. Polon. B **38** (2007) 2819.

[3] M. Hayakawa, T. Kinoshita and A.I. Sanda, Phys. Rev. Lett. **75** (1995) 790; Phys. Rev. D **54** (1996) 3137.

[4] M. Hayakawa and T. Kinoshita, Phys. Rev. D **57** (1998)465.

[5] J. Bijnens, E. Pallante and J. Prades, Nucl. Phys. B **474** (1996) 379; Phys. Rev. Lett. **75** (1995) 1447; Erratum-ibid. **75** (1995) 3781.

[6] M. Hayakawa and T. Kinoshita, Phys. Rev. D Erratum. **66** (2002) 073034.

[7] J. Bijnens, E. Pallante and J. Prades, Nucl. Phys. B **626** (2002) 410.

[8] M. Knecht and A. Nyffeler, Phys. Rev. D **65** (2002) 073034.

[9] M. Knecht, A. Nyffeler, M. Perrottet and E. de Rafael, Phys. Rev. Lett. **88** (2002) 071802.

[10] A.E. Dorokhov and W. Broniowski, Phys. Rev. D **78** (2008) 073011.

[11] A. Nyffeler, Phys. Rev. D **79** (2009) 073012.

[12] K. Melnikov and A. Vainshtein, Phys. Rev. D **70** (2004) 113006.

[13] J. Prades, Nucl. Phys. B (Proc. Suppl.) **181-182** (2008) 15; arXiv:0905.3164 (to be published in Eur. Phys. J C);

[14] E. de Rafael, Nucl. Phys. B (Proc. Suppl.) **186** (2009) 211; PoS **EFT09** (2009) 050; D.W. Hertzog *et al.*, arXiv:0705.4617; J.P. Miller, E. de Rafael and B.L. Roberts, Rept. Prog. Phys. **70** (2007) 795.

[15] F. Jegerlehner, Lect. Notes Phys. **745** (2008) 9; Acta Phys. Polon. B **38** (2007) 3021.

[16] F. Jegerlehner and A. Nyffeler, Phys. Rept. **477** (2009) 1;

[17] T. Blum and S. Chowdhury, Nucl. Phys. B (Proc. Suppl.) **189** (2009) 251; M. Hayakawa, T. Blum, T. Izubuchi and N.Yamada, PoS **LAT2005** (2006) 353.

[18] P. Rakow for QCDSF Collaboration, Talk at "Topical Workshop on the Muon g-2", 25-26 October 2007, Glasgow, UK.

[19] E. de Rafael, Phys. Lett. B **322** (1994) 239.

[20] M. Knecht, S. Peris, M. Perrottet and E. de Rafael, JHEP **03** (2004) 035.

[21] I.R. Blokland, A. Czarnecki and K. Melnikov, Phys. Rev. Lett. **88** (2002) 071803.

[22] M. Ramsey-Musolf and M.B. Wise, Phys. Rev. Lett. **89** (2002) 041601.

[23] B. Aubert, *et al*, [The BABAR Collaboration], arXiv:0905.4778 [hep-ex]

[24] V.A. Novikov, M.A. Shifman, A.I. Vainshtein, M.B. Voloshin and V.I. Zakharov, Nucl. Phys. B **237** (1984) 525.

[25] J. Bijnens, E. Gámiz, E Lipartia and J. Prades, JHEP **04** (2004) 055.

[26] K. Kampf, M. Knecht and J. Novotny, Eur. Phys. J. C **46** (2006) 191.

[27] K. Kampf and B. Moussallam, Phys. Rev. D **79** (2009) 076005; K. Kampf, arXiv:0905.0585.

Chapter 8

Small x, Diffraction and Total Cross Sections

Convenors:

J. Bartels (Hamburg) and S. Levonian (DESY)

HERA Inclusive Diffraction & Factorisation Tests

Paul Newman (for the H1 and ZEUS Collaborations)
School of Physics & Astronomy, University of Birmingham, B15 2TT, UK

DOI: http://dx.doi.org/10.3204/DESY-PROC-2009-03/Newman

HERA measurements of diffractive *ep* scattering - the quasi-elastic scattering of the photon in the proton colour field - are summarised. Emphasis is placed on the most recent data.

1 Introduction

Between 1992 and 2007, the HERA accelerator provided *ep* collisions at centre of mass energies beyond 300 GeV at the interaction points of the H1 and ZEUS experiments. Perhaps the most interesting results to emerge relate to the newly accessed field of perturbative strong interaction physics at low Bjorken-x, where parton densities become extremely large [1]. Questions arise as to how and where non-linear dynamics tame the parton density growth [2] and challenging features such as geometric scaling [3] are observed. Central to this low x physics landscape is a high rate of diffractive processes, in which a colourless exchange takes place and the proton remains intact. In particular, the study of semi-inclusive diffractive deep-inelastic scattering (DDIS), $\gamma^* p \to Xp$ [4] has led to a revolution in our microscopic, parton level, understanding of the structure of elastic and quasi-elastic high energy hadronic scattering [5]. Comparisons with hard diffraction in proton-(anti)proton scattering have also improved our knowledge of absorptive and underlying event effects in which the diffractive signature may be obscured by multiple interactions in the same event [6]. In addition to their fundamental interest in their own right, these issues are highly relevant to the modelling of chromodynamics at the LHC [7].

The kinematic variables describing DDIS are illustrated in figure 1a. The longitudinal momentum fractions of the colourless exchange with respect to the incoming proton and of the struck quark with respect to the colourless exchange are denoted $x_{I\!P}$ and β, respectively, such that $\beta\, x_{I\!P} = x$. The squared four-momentum transferred at the proton vertex is given by the Mandelstam t variable. The semi-inclusive DDIS cross section is usually presented in the form of a diffractive reduced cross section $\sigma_r^{D(3)}$, integrated over t and related to the experimentally measured differential cross section by [8]

$$\frac{\mathrm{d}^3\sigma^{ep\to eXp}}{\mathrm{d}x_{I\!P}\ \mathrm{d}x\ \mathrm{d}Q^2} = \frac{2\pi\alpha^2}{xQ^4}\cdot Y_+ \cdot \sigma_r^{D(3)}(x_{I\!P}, x, Q^2)\ , \tag{1}$$

where $Y_+ = 1+(1-y)^2$ and y is the usual Bjorken variable. The reduced cross section depends at moderate scales, Q^2, on two diffractive structure functions $F_2^{D(3)}$ and $F_L^{D(3)}$ according to

$$\sigma_r^{D(3)} = F_2^{D(3)} - \frac{y^2}{Y_+}F_L^{D(3)}. \tag{2}$$

For y not too close to unity, $\sigma_r^{D(3)} = F_2^{D(3)}$ holds to very good approximation.

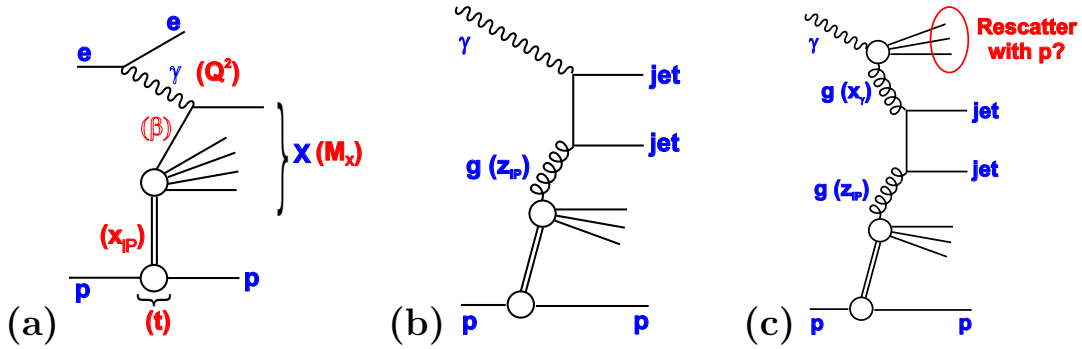

Figure 1: Sketches of diffractive ep processes. (a) Inclusive DDIS at the level of the quark parton model, illustrating the kinematic variables discussed in the text. (b) Dominant leading order diagram for hard scattering in DDIS or direct photoproduction, in which a parton of momentum fraction $z_{I\!P}$ from the DPDFs enters the hard scattering. (c) A leading order process in resolved photoproduction involving a parton of momentum fraction x_γ relative to the photon.

2 Measurement methods and comparisons

Experimentally, diffractive ep scattering is characterised by the presence of a leading proton in the final state, retaining most of the initial state proton energy, and by a lack of hadronic activity in the forward (outgoing proton) direction, such that the system X is cleanly separated and its mass M_X may be measured in the central detector components. These signatures have been widely exploited at HERA to select diffractive events by tagging the outgoing proton in the H1 Forward Proton Spectrometer or the ZEUS Leading Proton Spectrometer ('LPS method' [9, 10, 11]) or by requiring the presence of a large gap in the rapidity distribution of hadronic final state particles in the forward region ('LRG method' [8, 10, 12]). In a third approach, not considered in detail here, the inclusive DIS sample is decomposed into diffractive and non-diffractive contributions based on their characteristic dependences on M_X [12, 13]. Whilst the LRG and M_X-based techniques yield better statistics than the LPS method, they suffer from systematic uncertainties associated with an admixture of proton dissociation to low mass states, which is irreducible due to the limited forward detector acceptance.

The H1 collaboration recently released a preliminary proton-tagged measurement using its full available FPS sample at HERA-II [11]. The integrated luminosity is 156 pb^{-1}, a factor of 20 beyond previous H1 measurements. The new data tend to lie slightly above the recently published final ZEUS LPS data from HERA-I [10], but are within the combined normalisation uncertainty of around 10%. The most precise test of compatibility between H1 and ZEUS is obtained from the LRG data. The recently published ZEUS data [10] are based on an integrated luminosity of 62 pb^{-1} and thus have substantially improved statistical precision compared with the older H1 published results [8]. The normalisation differences between the two experiments are most obvious here, having been quantified at 13%, which is a little beyond one standard deviation in the combined normalisation uncertainty. After correcting for this factor, very good agreement is observed between the shapes of the H1 and ZEUS cross sections throughout most of the phase space studied, as shown in figure 2. A more detailed comparison between different diffractive cross section measurements by H1 and ZEUS and a first attempt to combine the results of the two experiments can be found in [14].

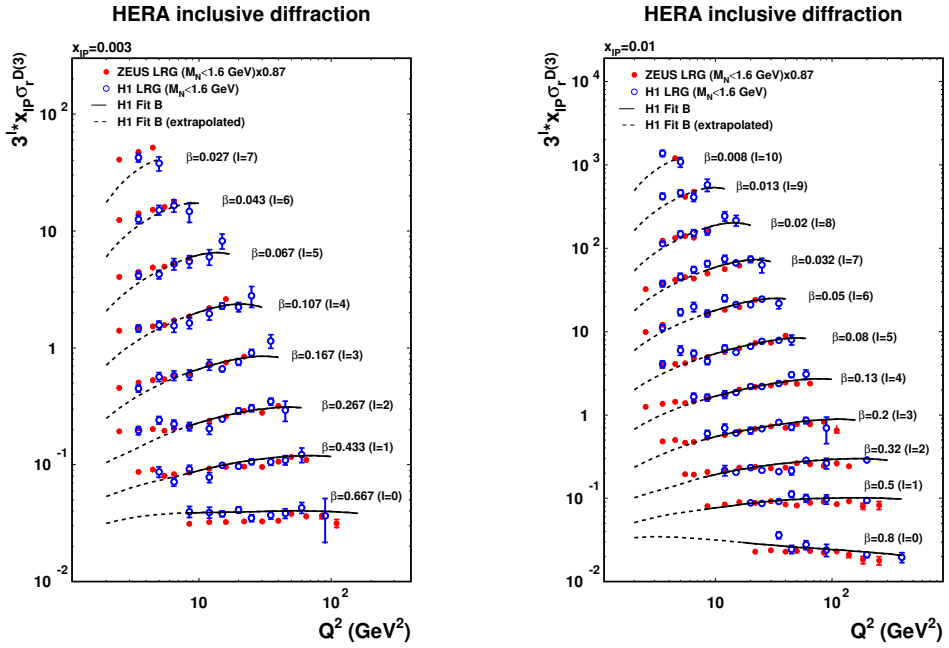

Figure 2: H1 and ZEUS measurements of the diffractive reduced cross section at two example $x_{I\!P}$ values [14]. The ZEUS data are scaled by a factor of 0.87 to match the H1 normalisation. The data are compared with the results of the H1 2006 Fit B DPDF based parameterisation [8] for $Q^2 \geq 8.5$ GeV^2 and with its DGLAP based extrapolation to lower Q^2.

3 Soft physics at the proton vertex

To good approximation, LRG and LPS data show [8, 9, 10] that DDIS data satisfy a 'proton vertex factorisation',[1] whereby the dependences on variables which describe the scattered proton ($x_{I\!P}$, t) factorise from those describing the hard partonic interaction (Q^2, β). For example, the slope parameter b, extracted in [10] by fitting the t distribution to the form $\mathrm{d}\sigma/\mathrm{d}t \propto e^{bt}$, is shown as a function of DDIS kinematic variables in figure 3a. There are no significant variations from the average value of $b \simeq 7$ GeV^{-2} anywhere in the studied range. The measured value of b is significantly larger than that from 'hard' exclusive vector meson production ($ep \to eVp$) [15]. It is characteristic of an interaction region of spatial extent considerably larger than the proton radius, indicating that the dominant feature of DDIS is the probing with the virtual photon of non-perturbative exchanges similar to the pomeron of soft hadronic physics [18].

Figure 3b shows the Q^2 dependence of the effective pomeron intercept $\alpha_{I\!P}(0)$, which is extracted from the $x_{I\!P}$ dependence of the data [10]. No significant dependence on Q^2 is observed, again compatible with proton vertex factorisation. These results are consistent with the H1

[1] This factorisation is not expected to hold to indefinite precision, due for example to the presence of a 'hard', fully perturbatively tractable diffractive exchange which governs exclusive vector meson production in the presence of hard scales [15]. This leads to a higher twist contribution to σ_r^D for $\beta \to 1$ [16, 17]. However, this contribution seems to be numerically small when compared with the the inclusive diffractive cross section.

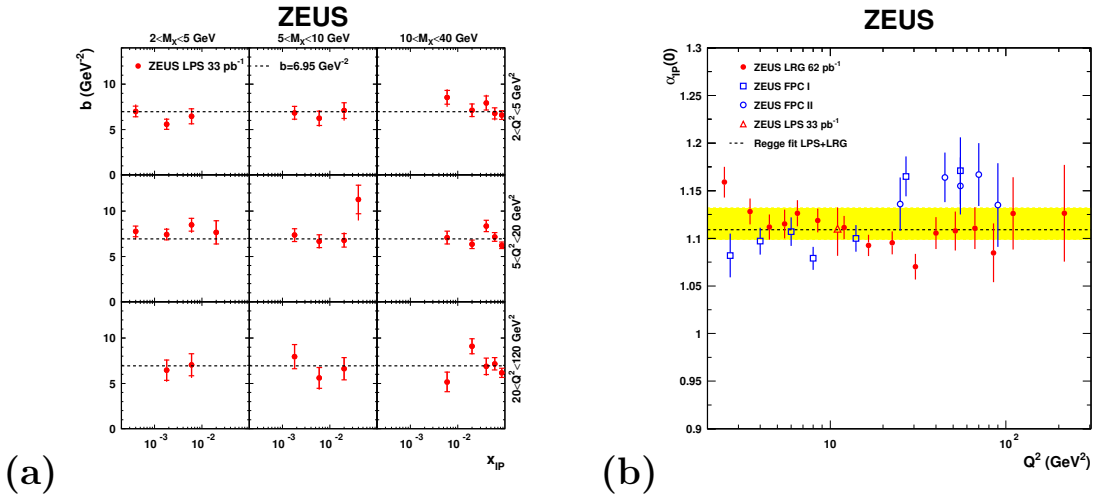

Figure 3: a) Measurements of the exponential t slope from ZEUS LPS data, shown as a function of Q^2, $x_{I\!P}$ and M_X. b) ZEUS extractions of the effective pomeron intercept describing the $x_{I\!P}$ dependence of DDIS data at different Q^2 values [10].

value of $\alpha_{I\!P}(0) = 1.118 \pm 0.008$ (exp.) $^{+0.029}_{-0.010}$ (model) [8]. Both collaborations have also extracted a value for the slope of the effective pomeron trajectory, the recently published ZEUS value being $\alpha'_{I\!P} = -0.01 \pm 0.06$ (stat.) ± 0.06 (syst.) GeV^{-2} [10].

The intercept of the effective pomeron trajectory is consistent within errors with the 'soft pomeron' results from fits to total cross sections and soft diffractive data [19]. Although larger effective intercepts have been measured in hard vector meson production [15], no deviations with either Q^2 or β have yet been observed in inclusive DDIS. The measured slope of the effective trajectory is smaller than the canonical soft diffractive value of 0.25 GeV^{-2} [20], though it is compatible with results from the soft exclusive photoproduction of ρ^0 mesons at HERA [21].

4 Diffractive Parton Density Functions

In the framework of the proof [22] of a hard scattering collinear QCD factorisation theorem for semi-inclusive DIS processes such as DDIS, the concept of 'diffractive parton distribution functions' (DPDFs) [23] may be introduced, representing conditional proton parton probability distributions under the constraint of a leading final state proton with a particular four-momentum. The differential DDIS cross section may then be written in terms of convolutions of partonic cross sections $\hat{\sigma}^{ei}(x, Q^2)$ with DPDFs f_i^D as

$$\mathrm{d}\sigma^{ep\to eXp}(x, Q^2, x_{I\!P}, t) = \sum_i f_i^D(x, Q^2, x_{I\!P}, t) \otimes \mathrm{d}\hat{\sigma}^{ei}(x, Q^2) \; . \tag{3}$$

The empirically motivated proton vertex factorisation property (section 3) suggests a further factorisation, whereby the DPDFs vary only in normalisation with the four-momentum of the final state proton as described by $x_{I\!P}$ and t:

$$f_i^D(x, Q^2, x_{I\!P}, t) = f_{I\!P/p}(x_{I\!P}, t) \cdot f_i(\beta = x/x_{I\!P}, Q^2) \; . \tag{4}$$

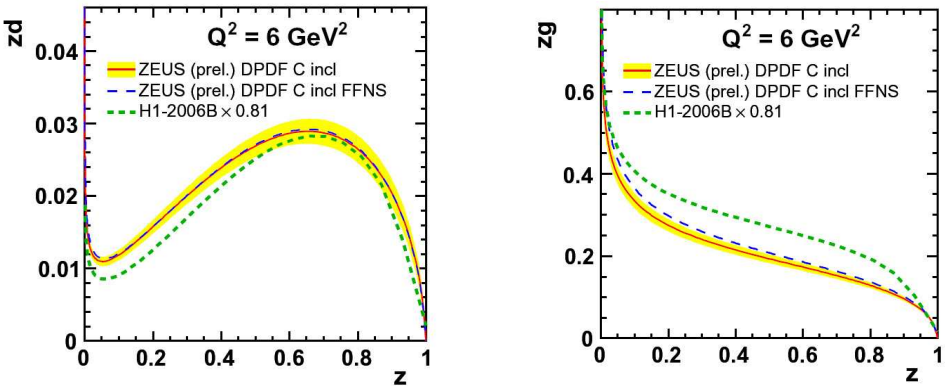

Figure 4: ZEUS down quark (one sixth of the total quark + antiquark) and gluon densities as a function of generalised momentum fraction z at $Q^2 = 6$ GeV^2 [25]. Two heavy flavour schemes are shown, as well as H1 results [8] corrected for proton dissociation with a factor of 0.81.

Parameterising $f_{I\!P/p}(x_{I\!P}, t)$ using Regge asymptotics, equation 4 amounts to a description of DDIS in terms of the exchange of a factorisable pomeron with universal parton densities [24]. The β and Q^2 dependences of σ_r^D may then be subjected to a perturbative QCD analysis based on the DGLAP equations in order to obtain DPDFs. Whilst F_2^D directly measures the quark density, the gluon density is only indirectly constrained, via the scaling violations $\partial F_2^D / \partial \ln Q^2$.

The high statistics ZEUS LRG and LPS data [10] have recently been fitted to extract DPDFs [25]. The method and DPDF parameterisation are similar to an earlier H1 analysis [8], the main step forward being in the heavy flavour treatment, which now follows the general mass variable flavour number scheme [26]. In figure 4, the resulting DPDFs are compared with results from both ZEUS and H1 using a fixed flavour number scheme. The agreement between the experiments is reasonable when the uncertainty on the H1 DPDFs is also taken into account and the conclusion that the dominant feature is a gluon density with a relatively hard z dependence is confirmed. The error bands shown in figure 4 represent experimental uncertainties only. Whilst the quark densities are rather well known throughout the phase space, the theoretical uncertainties on the gluon density are large. Indeed, in the large z region, where the dominant parton splitting is $q \to qg$, the sensitivity of $\partial F_2^D / \partial \ln Q^2$ to the gluon density becomes poor and different DPDF parameterisations lead to large variations [8, 25]. Improved large z constraints have been obtained by including dijet data in the QCD fits [27, 25].

In common with the inclusive proton PDFs at low x [1], the DPDFs exhibit a ratio of around 7:3 between gluons and quarks, consistent with a common QCD radiation pattern far from the valence region. Qualitatively, the diffractive quark density is similar in shape to that of the photon [28], which might be expected if the high z quarks are generated from initial basic $g \to q\bar{q}$ splittings, similar to the $\gamma \to q\bar{q}$ splitting in the photon case.

5 Factorisation Tests in Diffractive DIS

According to [22], the diffractive parton densities extracted from σ_r^D should be applicable to the prediction of a wide range of other observables in diffractive DIS. There have been many tests of

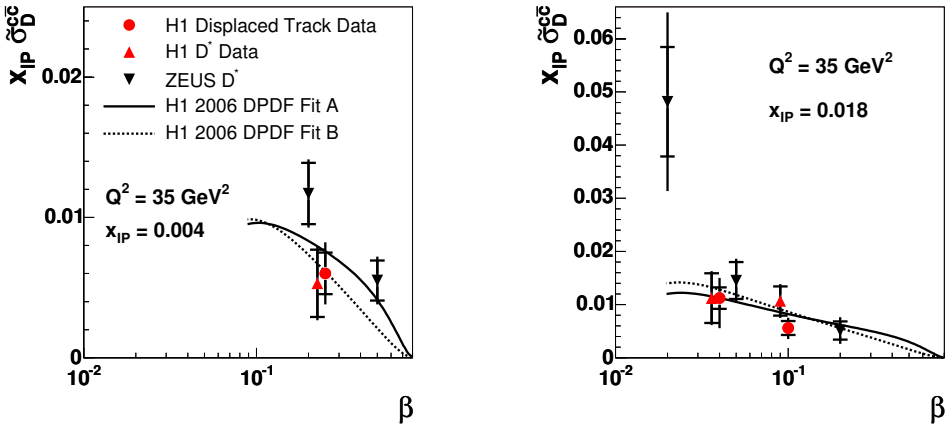

Figure 5: Comparisons [32] of measurements of diffractive open charm production with predictions based on DPDFs extracted from σ_r^D data [8].

this diffractive hard scattering factorisation over the years, the most precise and detailed arising from jet [29, 30, 27] and heavy flavour [31, 32] cross section measurements. Being dominated by the boson-gluon fusion parton level process $\gamma^* g \to q\bar{q}$ (figure 1b), these data are directly sensitive to the diffractive gluon density, in contrast to σ_r^D. Such tests have been successful at moderate values of z, as shown for the example of diffractive charm quark production in figure 5. As mentioned in section 4, the situation changes at large $z \gtrsim 0.4$, where the gluon density from σ_r^D has a large uncertainty and dijet data give the best constraints.

At low x and Q^2, the longitudinal diffractive structure function, F_L^D, is closely related to the diffractive gluon density [33] and thus gives a complementary test of diffractive factorisation and the role of gluons to those provided by jet and charm cross sections. Measurements of F_L^D became possible following the reduced proton beam energy runs at the end of HERA operation. According to equation 2, F_L^D and F_2^D may then be separated through the $y = Q^2/(s\,\beta\,x_{I\!P})$ dependence as s varies at fixed Q^2, β and $x_{I\!P}$.

The H1 collaboration recently released preliminary F_L^D data, as shown in figure 6. The results [34], when integrated over β show that F_L^D is non-zero at the 3σ level. It is also clearly incompatible with its maximum possible value of F_2^D. The measured ratio of longitudinal to transverse photon induced cross sections in diffraction is similar to that in inclusive DIS measurements [35], though the errors in the diffractive case are large. The measured F_L^D is in agreement with all reasonable predictions based on DPDFs extracted from σ_r^D. Dipole model predictions such as [2, 16] have thus far

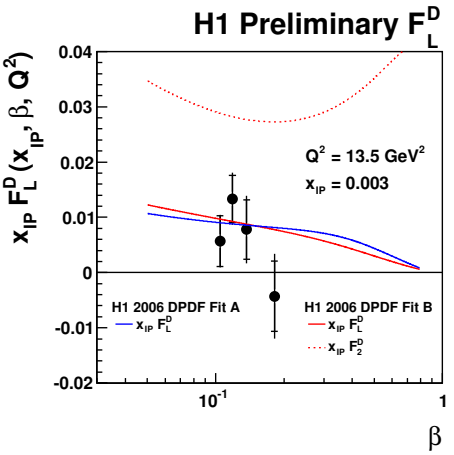

Figure 6: First measurement of the longitudinal diffractive structure function [34], compared with DPDF based predictions.

neglected any contribution from a leading twist F_L^D and formally give predictions very close to zero in the relatively low β range covered. A hybrid approach [36] which mixes a leading twist DPDF based F_L^D with a higher twist contribution at high β derived from [2], is in good agreement with the data.

6 Hard Diffractive Photoproduction and Rapidity Gap Survival Probabilities

As expected [22, 37], DPDF-based predictions for hard diffractive processes in $p\bar{p}$ scattering fail by around an order of magnitude [38]. This factorisation breaking is generally attributed to absorptive corrections, corresponding to the destruction of the outgoing proton coherence and the rapidity gap due to multiple interactions within a single event. These effects are associated with the presence of a proton remnant, in contrast to the point-like photon coupling in DDIS. The corresponding 'rapidity gap survival probability' can be treated semi-quantitatively [6] and its prediction at LHC energies is a major current issue [7].

The questions of DPDF applicability and rapidity gap survival can be addressed in hard diffractive photoproduction, where the virtuality of the exchange photon coupling to the electron is close to zero [39]. Under these circumstances, the photon can develop an effective partonic structure via $\gamma \to q\bar{q}$ fluctuations and further subsequent splittings. In a simple leading order picture, there are thus two classes of hard photoproduction: 'resolved' interactions (figure 1c), where the photon interacts via its partonic structure and only a fraction x_γ of its four-momentum participates in the hard subprocess and 'direct' interactions (figure 1b), where the photon behaves as a point-like particle and $x_\gamma = 1$. The gap survival probability has been estimated to be 0.34 for resolved processes [40] and is expected to be unity for direct photon interactions.

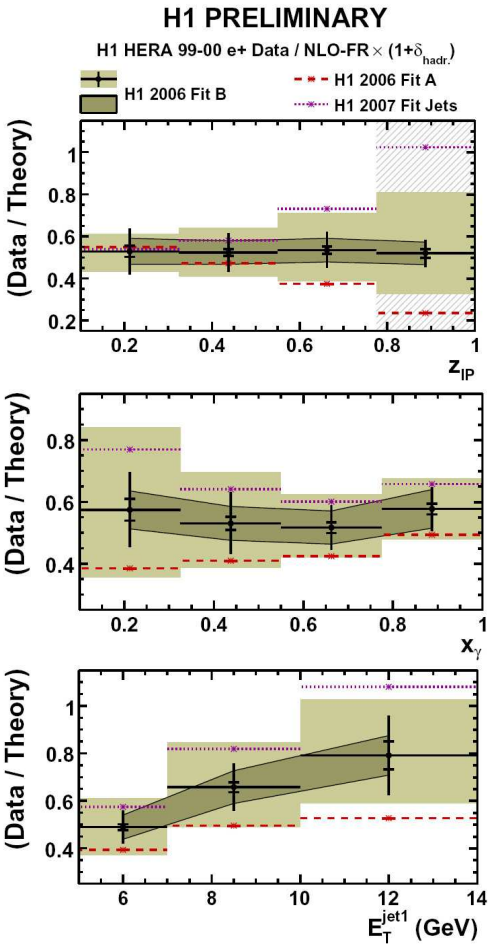

Figure 7: Ratios of diffractive dijet photoproduction cross sections measured by H1 to NLO QCD calculations [41].

Figure 7 [41] shows ratios of H1 measurements of diffractive dijet photoproduction cross sections to NLO QCD calculations which neglect absorptive effects [42]. Results are shown differentially in the leading jet transverse energy E_T^{jet1} and in hadron level estimators of $z_{I\!P}$ and x_γ, obtained as described in [30]. For most of the measured points, the ratios are significantly below unity. When taking the H1 Fit B DPDFs [8], which

describe a wide range of DDIS observables, there is little dependence of the ratio on $z_{I\!P}$.

Figure 8 shows a recent ZEUS measurement [43] as a function of x_γ compared with predictions based on H1 [27] and ZEUS [25] DPDFs extracted by fitting σ_r^D and diffractive dijet electroproduction data. In contrast to the H1 case, these data are compatible with NLO predictions. A possible explanation for the apparent discrepancy between the two collaborations is offered by indications of a dependence of the data-to-theory ratio on the jet transverse energy (figure 7c) [30, 43, 41]. The ZEUS measurement is made for $E_t^{\rm jet1} > 7.5$ GeV, whereas H1 measure for $E_t^{\rm jet1} > 5$ GeV. There is as yet no accepted theoretical explanation for this effect.

Intriguingly, the ratios of data to theory measured by both collaborations have at most a weak dependence on x_γ, in contrast to theoretical expectations [40, 44]. Since the correlations between the variables are complicated (e.g. E_T^{jet1} and x_γ are strongly positively correlated through the kinematic restrictions), more differential studies are required to fully unfold the dynamics.

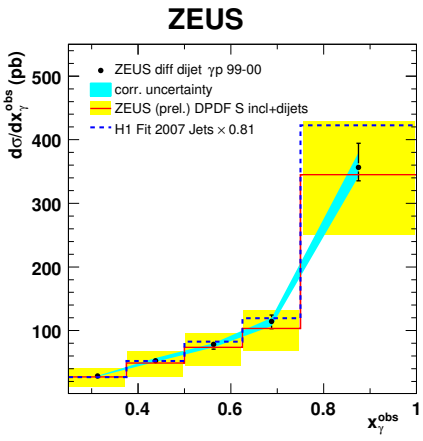

Figure 8: ZEUS diffractive dijet photoproduction data [43], compared with DPDF based predictions.

7 Summary

Recent H1 and ZEUS semi-inclusive diffractive DIS (DDIS) data are in fair agreement within their normalisation uncertainties. The data exhibit proton vertex factorisation to good approximation. Dependences on variables describing the coupling to the proton lead to a picture in which DDIS probes a diffractive exchange whose origins lie in the soft dynamics below typical factorisation scales, and which is similar to that exchanged in soft hadronic scattering. The parton densities (DPDFs) associated with this exchange have a structure dominated by a hard gluon density, which successfully describes all measured observables in diffractive DIS, including the longitudinal diffractive structure function, F_L^D. The rapidity gap survival probability derived from DPDF-based predictions of hard diffractive photoproduction data is surprisingly similar for direct and resolved photon interactions, a fact which remains under investigation.

References

[1] M. Klein, these proceedings.

[2] K. Golec-Biernat, M. Wüsthoff, Phys. Rev. D **59** (1999) 014017 [hep-ph/9807513].

[3] A. Stasto, K. Golec-Biernat, J. Kwiecinski, Phys. Rev. Lett. **86** (2001) 596 [hep-ph/0007192].

[4] ZEUS Collaboration, Phys. Lett. B **315** (1993) 481;
H1 Collaboration, Nucl. Phys. B **429** (1994) 477.

[5] A. Hebecker, Phys. Rept. **331** (2000) 1 [hep-ph/9905226].

[6] A. Kaidalov, V. Khoze, A. Martin, M. Ryskin, Eur. Phys. J. C **21** (2001) 521 [hep-ph/0105145].

[7] M. Arneodo, M. Diehl, V. Khoze, P. Newman, proc. of the 2006-8 HERA-LHC Workshop, DESY-PROC-2009-02, 397, and references therein.

[8] H1 Collaboration, Eur. Phys. J. C **48** (2006) 715 [hep-ex/0606004].

[9] H1 Collaboration, Eur. Phys. J. C **48** (2006) 749 [hep-ex/0606003].

[10] ZEUS Collaboration, Nucl. Phys. B **816** (2009) 1 [hep-ex/0812.2003].

[11] H1 Collaboration, *'Measurement of diffractive DIS with a leading proton at HERA-2'* [H1prelim-09-012].

[12] H1 Collaboration, *'Measurement of Inclusive Diffractive DIS at HERA (99-04 data)'* [H1prelim-06-014].

[13] ZEUS Collaboration, Nucl. Phys. B **800** (2008) 1 [hep-ex/0802.3017].

[14] P. Newman, M. Ruspa, proc. of the 2006-8 HERA-LHC Workshop, DESY-PROC-2009-02, 401 [hep-ex/0903.2957].

[15] S. Kananov, these proceedings.

[16] J. Bartels, J. Ellis, H. Kowalski, M. Wüsthoff, Eur. Phys. J. C **7** (1999) 443 [hep-ph/9803497].

[17] A. Hebecker, T. Teubner, Phys. Lett. B **498** (2001) 16 [hep-ph/0010273].

[18] E. Feinberg, I. Pomeranchuk, Suppl. Nuovo. Cimento. **3** (1956) 652;
V. Gribov, JETP Lett. **41** (1961) 667.

[19] A. Donnachie, P. Landshoff, Phys. Lett. B **296** (1992) 227 [hep-ph/9209205];
J. Cudell, K. Kang, S. Kim, Phys. Lett. B **395** (1997) 311 [hep-ph/9601336].

[20] G. Jaroszkiewicz, P. Landshoff, Phys. Rev. D **10** (1974) 170;
P. Landshoff, Nucl. Phys. Proc. Suppl. **12** (1990) 397.

[21] ZEUS Collaboration, Eur. Phys. J. C **14** (2000) 213 [hep-ex/9910038];
H1 Collaboration, *'Measurement of Pomeron Trajectory in Elastic ρ^0 Photoproduction'* [H1prelim-06-016]

[22] J. Collins, Phys. Rev. D **57** (1998) 3051 [Erratum-ibid. D **61** (2000) 019902] [hep-ph/9709499].

[23] L. Trentadue, G. Veneziano, Phys. Lett. B **323** (1994) 201;
A. Berera, D. Soper, Phys. Rev. D **53** (1996) 6162 [hep-ph/9509239].

[24] G. Ingelman, P. Schlein, Phys. Lett. B **152** (1985) 256;
A. Donnachie, P. Landshoff, Phys. Lett. B **191** (1987) 309 [Erratum-ibid. B **198** (1987) 590].

[25] ZEUS Collaboration, *'A QCD analysis of diffractive DIS data from ZEUS'* [ZEUS-pub-09-010].

[26] R. Thorne, R. Roberts, Phys. Rev. D **57** (1998) 6871 [hep-ph/9709442].

[27] H1 Collaboration, JHEP **0710** (2007) 042 [hep-ex/0708.3217].

[28] R. Nisius, these proceedings.

[29] H1 Collaboration, Eur. Phys. J. C **20** (2001) 29 [hep-ex/0012051];
ZEUS Collaboration, Eur. Phys. J. C **52** (2007) 813 [hep-ex/0708.1415].

[30] H1 Collaboration, Eur. Phys. J. C **51** (2007) 549 [hep-ex/0703022].

[31] H1 Collaboration, Phys. Lett. B **520** (2001) 191 [hep-ex/0108047];
ZEUS Collaboration, Nucl. Phys. B **672** (2003) 3 [hep-ex/0307068].

[32] H1 Collaboration, Eur. Phys. J. C **50** (2007) 1 [hep-ex/0610076].

[33] P. Newman, proc. of the 2004-5 HERA-LHC Workshop, CERN-2005-014, 514 [hep-ex/0511047].

[34] H1 Collaboration, *'Measurement of F_L^D at HERA II'* [H1prelim-09-011].

[35] H1 Collaboration, Phys. Lett. B **665** (2008) 139 [hep-ex/0805.2809];
ZEUS Collaboration, DESY 09-046 [hep-ex/0904.1092].

[36] K. Golec-Biernat, A. Luszczak, Phys. Rev. D **76** (2007) 114014 [hep-ph/0704.1608].

[37] J. Collins, L. Frankfurt, M. Strikman, Phys. Lett. B **307** (1993) 161 [hep-ph/9212212];
A. Berera, D. Soper, Phys. Rev. D **50** (1994) 4328 [hep-ph/9403276].

[38] CDF Collaboration, Phys. Rev. Lett. **84** (2000) 5043;
M. Klasen, G. Kramer, [hep-ph/0908.2531].

[39] J. Butterworth, M. Wing, Rept. Prog. Phys. **68** (2005) 2773 [hep-ex/0509018].

[40] A. Kaidalov, V. Khoze, A. Martin, M. Ryskin, Phys. Lett. B **567** (2003) 61 [hep-ph/0306134].

[41] H1 Collaboration, *'Diffractive photoproduction of jets with the H1 detector '* [H1prelim-08-012].

[42] S. Frixione, Z. Kunzst, A. Signer, Nucl. Phys. B **467** (1996) 399 [hep-ph/9512328];
S. Frixione, Nucl. Phys. B **507** (1997) 295 [hep-ph/9706545].

[43] ZEUS Collaboration, Eur. Phys. J. C **55** (2008) 177 [hep-ex/0710.1498].

[44] M. Klasen, G. Kramer, Mod. Phys. Lett. A **23** (2008) 1885 [hep-ph/0806.2269].

Photons and Exclusive Processes at Hadron Colliders

Joakim Nystrand

Department of Physics and Technology, University of Bergen, Bergen, Norway

DOI: http://dx.doi.org/10.3204/DESY-PROC-2009-03/Nystrand

The theoretical and experimental aspects of particle production from the strong equivalent photon fluxes present at high energy hadron colliders are reviewed. The goal is to show how photons at hadron colliders can improve what we have learnt from experiments with lepton beams. Experiments during the last 5-10 years have shown the feasibility of studying photoproduction in proton-proton and heavy-ion collisions. The experimental and theoretical development has revealed new opportunities as well as challenges.

1 Introduction

During the last decade the idea to study electromagnetic particle production at hadron and heavy-ion colliders has developed theoretically as well as experimentally. At the previous conference in this series (Photon 07, held at the Sorbonne in Paris), a session was devoted to this topic. I gave a summary of photoproduction at hadron colliders, in particular in heavy-ion collisions, at that meeting [1]. Since then, several new results have been published and an update of the latest developments will be given here. More comprehensive reviews of the field can be found e.g. in [2] and [3].

There are several reasons to study photon-induced reactions in collisions between hadrons. At the Large Hadron Collider (LHC) at CERN, the accessible two-photon center-of-mass energies will be much higher than at LEP and the photon-nucleon energies will be higher than at HERA. The LHC will thus explore a new and uncharted territory also in interactions mediated by photons. Heavy-ion interactions at the Relativistic Heavy-Ion Collider and at the LHC provide an opportunity to study photons from strong electromagnetic fields where the coupling is $Z\sqrt{\alpha}$ rather than $\sqrt{\alpha}$. At a hadron collider both projectiles can act as photon emitter and target, and this leads to some interesting interference phenomena, which will be discussed below. Furthermore, the electromagnetic contribution is important for understanding other types of exclusive particle production, e.g. through Pomeron+Pomeron interactions in pp or $p\overline{p}$ collisions. It has been been proposed to use two-photon production of $\mu^+\mu^-$–pairs as a luminosity monitor at the LHC.

To separate the electromagnetic interactions from the "background" of strong, hadronic processes, it is in practice necessary to restrict the study to so-called ultra-peripheral collisions, where the impact parameters are larger than the sum of the beam particle radii. This means impact parameters in the range $\approx$1.4(14) - 100 fm in proton-proton (heavy-ion) collisions. The upper range 100 fm is somewhat arbitrary but in practice the fields at current colliders are too weak to produce particles outside this range. The exception is production of

low-mass e^+e^-–pairs, where impact parameters above 1000 fm can give a significant contribution. Experimentally, interactions mediated by photons can be separated from purely hadronic interactions by their lower multiplicity and the presence of rapidity gaps. If the entire event is reconstructed, charge conservation and the low total transverse momentum also provide strong background rejection.

2 Results from RHIC

Ultra-peripheral collisions have been studied at the Relativistic Heavy-Ion Collider (RHIC) at Brookhaven National Laboratory by the two large experiments PHENIX and STAR. The first results on ρ^0 photoproduction were published by the STAR collaboration based on data from the first run at RHIC in the year 2000. STAR has so far mainly focussed on low-mass states, such as photoproduction of the ρ^0 meson and low-mass e^+e^- pairs. The study of ultra-peripheral collisions in PHENIX has been directed towards heavy vector meson production (J/Ψ) and high-mass e^+e^- pairs. The first preliminary results from PHENIX were presented at the Quark Matter 2005 conference [4], and earlier this year the final results were published [5]. The final results also include cross sections for two-photon production of e^+e^- pairs.

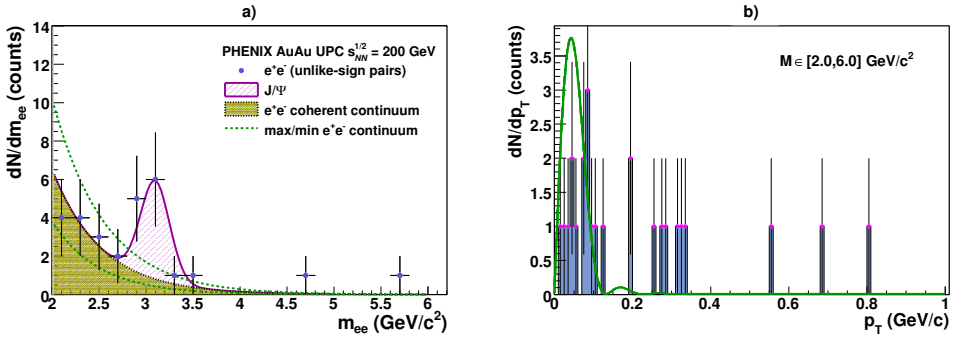

Figure 1: Invariant mass (a) and transverse momentum (b) distributions of e^+e^- pairs in ultra-peripheral Au+Au collisions as measured by PHENIX[5]. The event selection is described in the text.

PHENIX has implemented a trigger where an energy deposit of $E \gtrapprox 0.8$ GeV in the mid-rapidity electromagnetic calorimeters is combined with two rapidity gaps at intermediate rapidities. The rapidity gaps are defined by an absence of a signal in the Cherenkov Beam-Beam Counters (BBC) covering the pseudorapidity range $3.0 < |\eta| < 3.9$ on either side of midrapidity. It is furthermore required that there should be a signal ($E \gtrapprox 30$ GeV) in one or both of the Zero-Degree Calorimeters (ZDC) situated 18 m downstream from the interaction point. This requirement means that the central production occurs in coincidence with exchange of one or more additional photons which lead to the break up of one or both nuclei.

A data sample with an integrated luminosity of $141 \pm 12\mu$b from the 2004 high-luminosity run at RHIC has been analyzed. This luminosity corresponds to around $960 \cdot 10^6$ inelastic Au+Au events ($\sigma_{inel} = 6.8$ b). The UPC trigger as described above collected $8.5 \cdot 10^6$ events out of which $6.7 \cdot 10^6$ satisfied standard data quality assurance criteria. The electrons and positrons were tracked and identified in the PHENIX central tracking arms, covering $|\eta| <$

m_{inv} $[GeV]$	$d\sigma/dm_{inv}dy$ ($\|y\| < 0.35$)	$d\sigma/dm_{inv}dy$ ($\|y\| < 0.35, \|\eta_{1,2}\| < 0.35$)
$2.0 \leq m_{inv} \leq 2.8$	$86 \pm 23(stat) \pm 16(syst)$	$0.95 \pm 0.25(stat) \pm 0.18(syst)$
$2.0 \leq m_{inv} \leq 2.3$	$129 \pm 47(stat) \pm 28(syst)$	$1.43 \pm 0.52(stat) \pm 0.31(syst)$
$2.3 \leq m_{inv} \leq 2.8$	$60 \pm 24(stat) \pm 14(syst)$	$0.65 \pm 0.26(stat) \pm 0.15(syst)$

Table 1: Differential cross sections for two-photon production of e^+e^- pairs [5]. The variables y and m_{inv} refer, respectively, to the rapidity and invariant mass of the pair. The rightmost column shows the cross section when one requires both the e^+ and e^- to be within $|\eta| < 0.35$.

0.35 and $\Delta\phi = 90^o$ each. Tracking was performed by multi-layer drift chambers and multi-wire proportional chambers in each arm, and electrons were identified by their signals in the Ring-Imaging-Cherenkov (RICH) detectors and the electromagnetic calorimeters. In the offline analysis, it was required that the event should contain exactly 2 tracks of opposite charge satisfying the UPC electron/positron identification criteria and that the event vertex should be within $|Z| < 30$ cm from the center of the detector. It was required that each electron/positron should have $E > 1$ GeV to be well above the trigger threshold ($E \gtrapprox 0.8$ GeV). This gave a sample with 28 events, the invariant mass and p_T distributions of which are shown in Fig. 1. There was no like-sign background after the offline cuts had been applied. The results are consistent with production of e^+e^-–pairs through two-photon interactions, $\gamma + \gamma \rightarrow e^+e^-$, and photonuclear production (coherent and incoherent) of J/Ψ, $\gamma + Au \rightarrow J/\Psi + Au$, followed by the decay $J/\Psi \rightarrow e^+e^-$. The background from hadronically produced e^+e^- pairs in the ultra-peripheral sample was estimated from measurements of e^+e^- pairs in proton-proton collisions and was found to be negligible (< 1 event). The majority of the events are from coherent production, as can be seen from the transverse momentum distribution in Fig. 1 b). The curve shows for comparison the nuclear (Au) form factor.

The cross section for J/Ψ production, $d\sigma/dy = 76 \pm 31(stat) \pm 15(syst)\mu$b with nuclear break up, is consistent with theoretical predictions [6, 7, 8, 9], but the size of the experimental errors precludes a discrimination between the models. The cross sections for continuum e^+e^- production are shown in Table 1. The results are in good agreement with calculations using the method of equivalent photons as implemented in the Starlight Monte Carlo [11].

The mid-rapidity cross section for J/Ψ is a measure of the J/Ψ+ Nucleon cross section in nuclear matter [7] and is also affected by nuclear gluon shadowing [10]. Recent calculations by Baltz [12] for two-photon production of di-muons and di-electrons have found that higher-order terms reduce the cross section by 20-30% in heavy-ion collisions. A recent calculation has however not found such large reductions from higher order terms, particularly not for $\mu^+\mu^-$ pairs [13]. A measurement with smaller errors could settle this issue experimentally.

The STAR collaboration has studied coherent and incoherent photoproduction of ρ^0 mesons in Au+Au collisions at $\sqrt{s_{NN}} = 130$ and 200 GeV [14, 15]. The pions from the decay $\rho^0 \rightarrow \pi^+\pi^-$ were reconstructed in the STAR Time-Projection Chamber (TPC), which covers the pseudorapidity range $|\eta| < 1$ with full coverage in azimuth. Two trigger classes were defined. One class was based on having two roughly back-to-back hits in the Central Trigger Barrel (CTB), a set of 240 scintillators surrounding the TPC. This trigger ("topology trigger") selects photoproduced ρ^0 mesons with and without nuclear break up. The second trigger class ("minimum bias (MB)") required the events to have a signal in both ZDCs, and thus selected photoproduction

in coincidence with mutual Coulomb breakup of both Au nuclei. The cross sections, rapidity and p_T distributions have been published earlier and have been found to be in good agreement with calculations [14, 15].

Both nuclei can act as photon emitter and target in an ultra-peripheral collision. Since the two possibilities cannot be distinguished, they might interfer quantum mechanically. The separation of the two nuclei when a ρ^0 meson is produced at RHIC energies is typically 14–40 fm, with a different distribution depending on whether the ρ^0 is produced with or without nuclear breakup. The median impact parameters are $< b >= 46$ fm for the total production and $< b >= 18$ fm with mutual break up [6]. The ρ^0 meson is always produced near the surface of one of the nuclei because of the short range of the nuclear force. The system thus acts as a two-source interferometer and, depending on the separation of the nuclei and the wave length of the ρ^0, interference might occur. The interference will be destructive in collisions between particles and constructive in collisions between particles and anti-particles. For production at mid-rapidity, where the amplitudes for the two possibilities are equal, the cross section for a meson with tranverse momentum $\vec{p_T}$ in a collision with impact parameter $\vec{b}$ is

$$\sigma(\vec{p_T}, \vec{b}) = 2\sigma_1(\vec{p_T}, \vec{b}) \left(1 \pm cos(\vec{p_T} \cdot \vec{b})\right) \ , \tag{1}$$

where $\sigma_1(\vec{p_T}, \vec{b})$ is the cross section for emission from a single source. The total production cross section is obtained by integrating over all allowed impact parameters. For $p_T \ll 1/ < b >$, the cross section will be affected by the interference. This is illustrated in Fig. 2, where the solid curve shows the expected $t = p_T^2$ spectrum with interference and the dashed curve shows the expected spectrum without interference. The smaller mean impact parameters in collisions with nuclear breakup means that the interference extends to higher transverse momenta, as seen in Fig. 2b.

The presence of interference and its effect on the vector meson transverse momentum spectrum was predicted [16]. It has now been experimentally confirmed by the STAR collaboration [17]. The measured transverse momentum distributions for the two trigger classes are shown in Fig. 3. As one moves away from mid-rapidity, the amplitudes for the two target and photon-emitter configurations will be different and one expects the interference to decrease. This can be seen in the two plots to the right in Fig. 3.

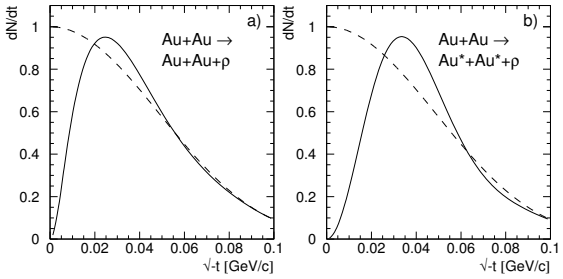

Figure 2: Predicted ρ^0 transverse momentum spectra with (solid curve) and without (dashed curve) interference [6, 16]. The left plot shows the spectrum for all events while the right plot shows the spectrum for events with mutual Coulomb break up.

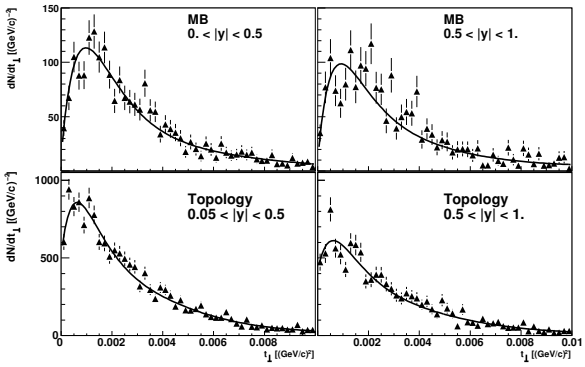

Figure 3: Transverse momentum ($p_T^2 = t_\perp$) spectrum for photoproduction of ρ^0 mesons in ultra-peripheral Au+Au collisions as measured by STAR [17]. The top plots are for minimum bias data and the bottom plots are for the topology trigger. The plots in the left column show production at mid-rapidity and those in the right column show production away from mid-rapidity. The curves are fits to a function with an interference term.

What makes this interference particularly interesting is the fact that the life-time of the ρ^0 is much smaller than the separation between the nuclei divided by the speed of light. The interference must therefore occur between the decay products of the ρ^0, which are in an entangled state. The interference is the result of the large separation between the nuclei in an ultra-peripheral collision and is expected to be different for other coherent production mechanisms, e.g. Odderon–Pomeron fusion.

3 Results from the Tevatron

Two-photon and photonuclear interactions have been studied by the CDF collaboration in proton-anti-proton collisions at the Tevatron. The latest results include exclusive di-muon production in the invariant mass range $3 \leq m_{\mu\mu} \leq 4$ GeV [18] and two-photon production of di-leptons with $m_{ll} > 40$ GeV [19]. The produced particles have been detected at central rapidities, $|\eta| < 0.6$ for intermediate mass di-muons and $|\eta| < 4$ for the high mass di-leptons. The centrally produced particles are observed in an otherwise empty event, which is defined by other detectors with a coverage out to $|\eta| < 7.4$. Further details on the experimental setup, trigger, and the exact phase space coverage can be found in Refs. [18, 19].

The exclusive di-muon events were identified as coming from exclusive photoproduction of J/Ψ and Ψ' followed by the decay to $\mu^+\mu^-$ and two-photon continuum production of $\mu^+\mu^-$ pairs. The background from the χ_c mesons produced in exclusive Pomeron-Pomeron interactions decaying to $\chi_c \to J/\Psi + \gamma$ was estimated. Measurements were made where a J/Ψ was produced in coincidence with a photon with energy $E_\gamma > 80$ MeV. From this, it could be estimated that the background from χ_c events where the photon is not detected contributed about 4% to the exclusive J/Ψ sample.

The exclusive events can be simulated with the Starlight Monte Carlo, which is based on the model in [25]. The photon-proton cross sections as measured by experiments at HERA and at fixed target experiments with lepton beams are used as input to the calculations. These are

combined with the equivalent photon spectrum to give the cross section for $p + \overline{p} \rightarrow p + \overline{p} + V$, where V is a vector meson. Starlight can also calculate the cross section for $\mu^+\mu^-$ pairs produced in two-photon interactions. The differential cross section, $d\sigma/dy$, for vector meson production is given by

$$\begin{array}{lcl} \frac{d\sigma(p+\overline{p}\rightarrow p+\overline{p}+V)}{dy} & = & \\ k_1 \frac{dn_\gamma}{dk_1}\sigma_{\gamma p}(k_1) & + & k_2 \frac{dn_\gamma}{dk_2}\sigma_{\gamma p}(k_2). \end{array} \quad (2)$$

Here, dn/dk is the photon spectrum and $\sigma_{\gamma p}$ the cross section for $\gamma + p \rightarrow V + p$. A J/Ψ produced at central rapidity within $|y| < 0.5$ corresponds to photoproduction with photon-proton center-of-mass energies between $60 \leq W_{\gamma p} \leq 100$ GeV. Exclusive J/Ψ and Ψ' production has been studied at HERA in this energy range by both the Zeus [20] and H1 [21] collaborations. The $\gamma + p \rightarrow J/\Psi + p$ cross sections are thus known experimentally, with errors typically in the range 6–9 %.

The photon spectrum associated with a relativistic proton can be calculated from that of a point charge modulated by a form factor [22]. A problem with this approach is that it does not properly exclude collisions where the protons interact hadronically. A different approach is therefore used here. The method is similar to that used for nuclear collisions, where one has to require that the impact parameter be larger than the sum of the nuclear radii to exclude strong interactions [23]. The proton has a more diffuse surface, however, so applying a sharp cut-off in impact parameter space is unphysical. A more realistic approach is to calculate the (hadronic) interaction probability as function of impact parameter by applying a Fourier transform to the pp elastic scattering amplitude [24]. To set a conservative upper limit on the photon spectrum, it is also calculated with a cut on the impact parameter $b > 0.7$ fm. This gives a photon spectrum very similar to that obtained when using the proton form factor.

The transverse momentum distributions for the three final states are shown in Fig. 4 together with Starlight predictions. The transverse momenta of the vector mesons reflect the proton form factor and extend out to around ≈ 1 GeV/c, whereas the transverse momenta of the two-photon final state are considerably lower. The agreement between data and Starlight is very good.

For the calculations of the cross sections, the latest results from HERA were used to make a new fit to the $\gamma + p \rightarrow V + p$ cross sections. These fits are slightly different from the ones used earlier [25]. The uncertainties in the calculated cross sections are determined from the uncertainty in the measured γp cross sections and the calculation of the photon spectrum with

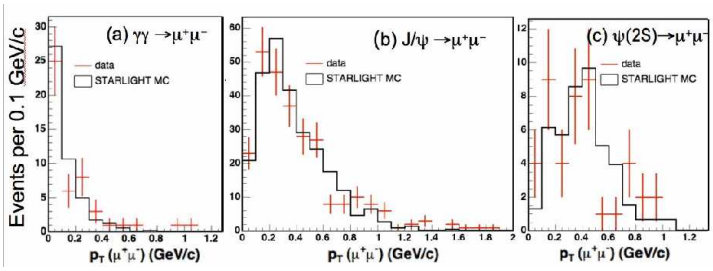

Figure 4: Transverse momentum distributions of exclusive $\mu^+\mu^-$ pairs in $p\overline{p}$ collisions, as measured by the CDF collaboration [18]. The crosses show the experimental results and the histograms are the Starlight predictions, normalized to the data. Fig. a) shows $\mu^+\mu^-$ pairs in the invariant mass ranges $3.2 \leq m_{inv} \leq 3.6$ and $3.8 \leq m_{inv} \leq 4.0$ GeV.

$b > 0.7$ fm. The results are

$$J/\Psi: \quad \left.\frac{d\sigma}{dy}\right|_{y=0} = 2.7^{+0.6}_{-0.2}\ nb \qquad , \qquad \Psi': \quad \left.\frac{d\sigma}{dy}\right|_{y=0} = 0.45^{+0.11}_{-0.04}\ nb\ . \tag{3}$$

These can be compared with the measured values, $3.92 \pm 0.25(stat) \pm 0.52(syst)$ nb and $0.53 \pm 0.09(stat) \pm 0.01(syst)$ nb, for the J/Ψ and Ψ', respectively [18]. The measured cross section for the J/Ψ is thus about two standard deviations above the calculated value and about one standard deviation above the calculated upper limit. The CDF collaboration has concluded that the upper limit for an Odderon contribution (Odderon+Pomeron$\rightarrow J/\Psi$) is less than $d\sigma(y=0)/dy < 2.3$ nb with 95% confidence level.

4 Outlook to the LHC

The results from RHIC and the Tevatron show the feasibility of studying two-photon and photon-nucleon interactions at hadron colliders. The results have been found to be in general agreement with predictions, but the statistics at least for heavy final states have so far been rather low.

The situation should be more advantageous at the LHC for at least two reasons: First, the cross section increases dramatically with the increased collision energy. This is illustrated in Fig. 5, which shows the excitation function for J/Ψ production at mid-rapidity in heavy-ion collisions. The increase in cross section is about a factor of 100 between RHIC and LHC energies. Secondly, the large and versatile experiments at the LHC should have the capability to trigger on and reconstruct particles produced in ultra-peripheral collisions over a wide range of phase space.

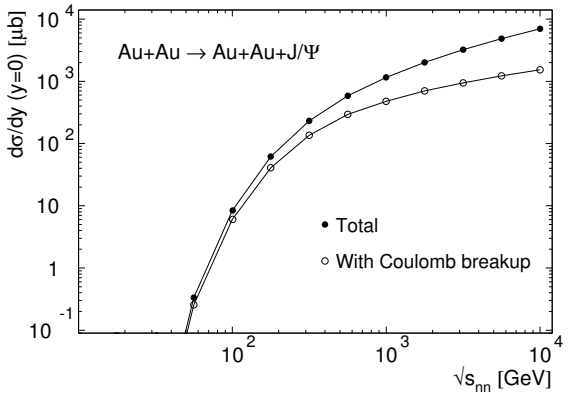

Figure 5: Calculated excitation function for mid-rapidity photoproduction of J/Ψ in Au+Au collisions, based on [6].

Several topics can be studied in ultra-peripheral collisions at the LHC. The CMS collaboration has for example investigated the possibilities for studying exclusive Υ production in Pb+Pb collisions [26] and two-photon production of supersymmetric pairs in pp collisions [27].

ALICE, which is primarily aimed for studying heavy-ion collisions, has performed simulations of J/Ψ and two-photon production in heavy-ion and proton-proton collisions [28].

Most studies so far, both at the existing colliders RHIC and the Tevatron as well as at the LHC, have focussed on exclusive production of a single particle or pair of particles. It should however be possible to extract as much information from inclusive processes, for example heavy quark production from photon-gluon fusion and photon-induced jet production.

To summarize, ultra-peripheral collisions are an interesting enhancement of the physics programs at hadron colliders. They can be studied at existing and planned experiments with no or only minor modifications. The results from RHIC and the Tevatron have followed the theoretical expectations. Further studies at the LHC and at existing accelerators with increased luminosities will hopefully lead to useful constraints on e.g. the parton density distributions and possibly even to the discovery of new phenomena.

References

[1] J. Nystrand, Nucl. Phys. Proc. Suppl. **184** (2008) 146.

[2] C. A. Bertulani, S. R. Klein and J. Nystrand, Ann. Rev. Nucl. Part. Sci. **55** (2005) 271.

[3] K. Hencken *et al.*, Phys. Rept. **458** (2008) 1.

[4] D. G. d'Enterria, arXiv:nucl-ex/0601001.

[5] S. Afanasiev *et al.* [PHENIX Collaboration], Phys. Lett. B **679** (2009) 321.

[6] S. Klein and J. Nystrand, Phys. Rev. C **60** (1999) 014903; A. J. Baltz, S. R. Klein and J. Nystrand, Phys. Rev. Lett. **89** (2002) 012301.

[7] M. Strikman, M. Tverskoy and M. Zhalov, Phys. Lett. B **626** (2005) 72

[8] Yu. P. Ivanov, B. Z. Kopeliovich and I. Schmidt, arXiv:0706.1532 [hep-ph].

[9] V. P. Goncalves and M. V. T. Machado, J. Phys. G **32** (2006) 295; V. P. Goncalves and M. V. T. Machado, arXiv:0706.2810 [hep-ph].

[10] A. L. Ayala Filho, V. P. Goncalves and M. T. Griep, Phys. Rev. C **78** (2008) 044904.

[11] A. J. Baltz, Y. Gorbunov, S. R. Klein and J. Nystrand, Phys. Rev. C **80** (2009) 044902.

[12] A. J. Baltz, Phys. Rev. Lett. **100** (2008) 062302; Phys. Rev. C **80** (2009) 034901.

[13] U. D. Jentschura and V. G. Serbo, arXiv:0908.3853 [hep-ph], to appear in Eur. Phys. J C.

[14] C. Adler *et al.* [STAR Collaboration], Phys. Rev. Lett. **89** (2002) 272302.

[15] B. I. Abelev *et al.* [STAR Collaboration], Phys. Rev. C **77** (2008) 034910.

[16] S. R. Klein and J. Nystrand, Phys. Rev. Lett. **84** (2000) 2330.

[17] B. I. Abelev *et al.* [STAR Collaboration], Phys. Rev. Lett. **102** (2009) 112301.

[18] T. Aaltonen *et al.* [CDF Collaboration], Phys. Rev. Lett. **102** (2009) 242001 [arXiv:0902.1271 [hep-ex]].

[19] T. Aaltonen *et al.* [CDF Collaboration], Phys. Rev. Lett. **102** (2009) 222002.

[20] S. Chekanov *et al.* [ZEUS Collaboration], Eur. Phys. J. C **24** (2002) 345.

[21] A. Aktas *et al.* [H1 Collaboration], Eur. Phys. J. C **46** (2006) 585.

[22] M. Drees and D. Zeppenfeld, Phys. Rev. D **39** (1989) 2536.

[23] R. N. Cahn and J. D. Jackson, Phys. Rev. D **42** (1990) 3690; G. Baur and L. G. Ferreira Filho, Nucl. Phys. A **518** (1990) 786.

[24] L. Frankfurt, C. E. Hyde, M. Strikman and C. Weiss, Phys. Rev. D **75** (2007) 054009.

[25] S. R. Klein and J. Nystrand, Phys. Rev. Lett. **92** (2004) 142003.

[26] D. G. . d'Enterria *et al.* [CMS Collaboration], J. Phys. G **34** (2007) 2307.

[27] N. Schul and K. Piotrzkowski, Nucl. Phys. Proc. Suppl. **179-180** (2008) 289.

[28] B. Alessandro *et al.* [ALICE Collaboration], J. Phys. G **32** (2006) 1295; J. Nystrand [ALICE Collaboration], Nucl. Phys. Proc. Suppl. **179-180** (2008) 156.

Exclusive Processes in Leptoproduction at COMPASS

Andrzej Sandacz
on behalf of the COMPASS Collaboration

Sołtan Institute for Nuclear Studies, ul. Hoża 69, 00681 Warsaw, Poland

DOI: http://dx.doi.org/10.3204/DESY-PROC-2009-03/Sandacz

Selected topics on exclusive ρ^0 production from the COMPASS experiment are discussed. They include the transverse target spin asymmetry, the longitudinal double-spin asymmetry and the spin density matrix elements. Future plans for the GPD studies at COMPASS and results from a DVCS test run are also presented.

1 Introduction

Exclusive processes in electro- and muoproduction have played an important role in studying strong interactions and gained a renewed interest, as they can give access to Generalized Parton Distributions (GPDs) and thus to a wealth of information on the nucleon structure. A study of Hard Exclusive Meson Production and Deeply Virtual Compton Scattering (DVCS) is a part of the COMPASS physics program. In addition, COMPASS provides also large statistics data for meson production in the non-perturbative region at low Q^2.

The recent results from COMPASS on the transverse target spin asymmetries for ρ^0 production off polarised protons and deuterons will be discussed in Sect. 3. Other advanced analyses are those of the longitudinal double spin asymmetry (Sect. 4), of the spin density matrix elements (Sect. 5), and of Q^2- and W-dependence of unpolarised cross sections, separated σ_L and σ_T cross sections and the $t-$ slopes of cross sections $\mathrm{d}\sigma/\mathrm{d}t$. Experimental tests of feasibility to isolate exclusive single photon events have just started at COMPASS and the results will be briefly discussed in Sect. 6.

2 COMPASS experimental set-up

A high intensity positive muon beam from the CERN SPS, of 160 GeV/c momentum and -76% average polarisation, impinges on a large solid-state polarised target. The polarisable material is either ^{6}LiD with 50% deuteron polarisation or NH_3 with 90% proton polarisation. Both protons and deuterons could be polarised either longitudinally or transversely with respect to the beam direction. The targets contain either two or three separate cells with polarisable material, placed one after another along the beam. The beam traverses 120 cm of the total length of polarised material. Polarisation directions in the alternate cell are opposite and are periodically reversed.

The COMPASS detector consists of two high resolution magnetic spectrometers equipped with tracking detectors, electromagnetic and hadronic calorimetry and muon identification. The first, large angle spectrometer is equipped with the RICH detector. A detailed description of the COMPASS apparatus can be found in [1].

3 Transverse target spin asymmetries for ρ^0 production

3.1 Theoretical motivation

It was pointed out that vector meson production on a transversely polarised target is sensitive to the nucleon helicity-flip GPD E [2, 3]. This GPD offers unique views on the orbital angular momentum carried by partons in the proton [4] and on the correlation between polarisation and spatial distribution of partons [5].

The reference [6] provides a detailed framework to our study. The cross section of the reaction $\mu + N \to \mu' + \rho^0 + N'$ on a transversely polarised nucleon is a function of the kinematic variables x_B, Q^2, t, ϕ and ϕ_S. Here ϕ is the azimuthal angle between the lepton plane and the hadron plane and ϕ_S is the azimuthal angle of the the target spin vector S_T w.r.t. the virtual photon direction. An observable which allows access to the GPD E is the transverse target spin asymmetry w.r.t. virtual photon direction defined as

$$A_{UT}(\phi, \phi_S) = \frac{1}{S_T} \cdot \frac{d\sigma(\phi, \phi_S) - d\sigma(\phi, \phi_S + \pi)}{d\sigma(\phi, \phi_S) + d\sigma(\phi, \phi_S + \pi)} \,. \tag{1}$$

The modulation of asymmetry as a function of $\sin(\phi - \phi_{\rm s})$ in deep inelastic kinematics region can be expressed as

$$A_{UT}^{\sin(\phi-\phi_{\rm s})}(\phi, \phi_S) \quad \propto \quad \frac{\mathrm{Im}(\sigma_{++}^{+-} + \epsilon\, \sigma_{00}^{+-})}{\frac{1}{2}(\sigma_{++}^{++} + \sigma_{++}^{--}) + \epsilon\, \sigma_{00}^{++}} \,. \tag{2}$$

The notation for the cross sections and interference terms is that of Ref. [6], with the lower indices referring to the helicities of the virtual photon and the upper ones to the helicities of the target proton, and ϵ is the virtual photon polarisation parameter. The only leading-twist observables are the longitudinal cross section σ_{00}^{++} and the interference term σ_{00}^{+-}. They can be written as:

$$\frac{1}{\Gamma'}\frac{d\sigma_{00}^{++}}{dt} = (1-\xi^2)|\mathcal{H}_M|^2 - (\xi^2 + \frac{t}{4M_p^2})|\mathcal{E}_M|^2 - 2\xi^2 \mathrm{Re}(\mathcal{E}_{\rm M}^* \mathcal{H}_{\rm M}), \tag{3}$$

$$\frac{1}{\Gamma'}\frac{d\sigma_{00}^{+-}}{dt} = -\sqrt{1-\xi^2}\frac{\sqrt{t_0 - t}}{M_p}\mathrm{Im}(\mathcal{E}_{\rm M}^* \mathcal{H}_{\rm M}) \,, \tag{4}$$

where $\Gamma' = \alpha_{em}/Q^6 \times x_B^2/(1-x_B)$, the skewedness variable is $\xi = x_B/(2-x_B)$ and the minimal four-momentum transfer is $t_0 = -4\xi^2 M_p^2/(1-\xi^2)$. The quantities $\mathcal{H}_M$ and $\mathcal{E}_M$ are weighted sums of integrals over the GPD $H^{q,g}$ and $E^{q,g}$ respectively. The weights depend on the contributions of quarks of various flavours and of gluons to the production of meson M (ρ^0 in present analysis).

3.2 Event sample

The results presented in Sect. 3 were obtained using the full sets of data with transversely polarised protons from the NH_3 target taken in 2007, and with transversely polarised deuterons from the ^{6}LiD target taken in 2002-2004. As an example, the selection of the sample of incoherent exclusive ρ^0 production will be described here for the 2007 data.

In order for an event to be accepted, it was required to originate inside the target, have reconstructed beam and scattered muon tracks and have only two additional tracks, which correspond to charged pions from the decay of ρ^0. A cut on the invariant mass of two pions, $0.47 < m_{\pi\pi} < 1.07\,\mathrm{GeV}/c^2$, selects the ρ^0. As the slow recoil target particles are not detected, in order to select exclusive events we use the cut on the missing energy, $-2.5 < E_{miss} < 2.5\,\mathrm{GeV}$, on the transverse momentum of ρ^0 with respect to the direction of virtual photon, $p_t^2 < 0.5\,(\mathrm{GeV/c})^2$, and on the ρ^0 energy, $E_\rho > 15\,\mathrm{GeV}$. Here $E_{miss} = (M_X^2 - M_p^2)/2M_p$, where M_X is the missing mass of an unobserved recoiling system and M_p is the proton mass. Coherent interactions on the nitrogen and other nuclei in the target are removed by a cut $p_t^2 > 0.05\,(\mathrm{GeV/c})^2$. To obtain a final data sample of events in the deep inelastic region, the negative four-momentum squared of the virtual photon is restricted to $Q^2 > 1.0\,(\mathrm{GeV}/c)^2$, while the region of hadron resonances is excluded by applying a cut on the total energy in the $\gamma^* N$ center of mass system, $W > 5.0$ GeV. Another cut is applied on the variable y, $0.1 < y < 0.9$, in order to remove events with large radiative corrections (large y) or poorly reconstructed kinematics (low y).

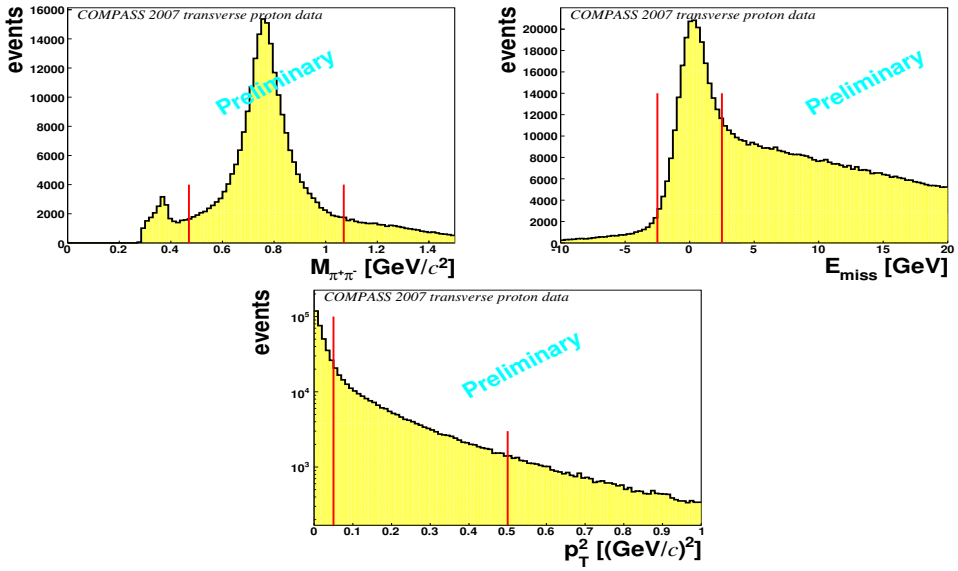

Figure 1: Distributions of $M_{\pi\pi}$ (top left), E_{miss} (top right) and p_t^2 (bottom) for the exclusive sample. The arrows show cuts imposed on each variable to define the final sample.

The distributions of $m_{\pi\pi}$, E_{miss} and p_t^2 are shown in Fig. 1. Each plot is obtained applying all cuts except those corresponding to the displayed variable. On the left top panel of Fig. 1 a clear peak of the ρ^0 resonance is visible on the top of the small contribution of background

of the non-resonant $\pi\pi$ pairs. A small bump below 0.4 GeV/c^2 is due to assignment of the charged pion mass to the kaons from decays of ϕ mesons.

On the right top panel of the figure the peak at $E_{miss} \approx 0$ is the signal of exclusive ρ^0 production. The width of the peak, $\sigma \approx 1.1$ GeV, is due to the spectrometer resolution. Non-exclusive events, where in addition to the recoil nucleon other undetected hadrons are produced, appear at $E_{miss} > 0$.

The p_t^2 distribution shown on the bottom panel of the figure indicates a contribution from coherent production on target nuclei at small p_t^2 values. A three exponential functions fit to this distribution was performed, which indicates also a contribution of non-exclusive background increasing with p_t^2. Therefore to select the sample of exclusive incoherent ρ^0 production, the aforementioned p_t^2 cuts, indicated by arrows, were applied.

After all selections the final sample for incoherent exclusive ρ^0 production consists of about 230 000 events.

3.3 Extraction of the transverse target spin asymmetry

The numbers of events as a function of the angle $\eta = \phi - \phi_S$ is given by

$$N(\eta) = Fn\sigma a(\eta)(1 + \epsilon sin(\eta)) \,, \tag{5}$$

where F is the muon flux, n the number of target particles, σ the spin averaged cross-section, $a(\eta)$ the product of angular acceptance and efficiency of the apparatus and ϵ is the raw asymmetry. It should be taken into account that $a(\eta)$ is not known precisely enough and it is different for the different target cells. To minimize acceptance effects, the double ratio method was chosen. The double ratio (DR) is calculated for 10 angular bins in η

$$F(\eta) = \frac{(N_u^{\uparrow}(\eta) + N_d^{\uparrow}(\eta)) \cdot N_c^{\uparrow}(\eta)}{(N_u^{\downarrow}(\eta) + N_d^{\downarrow}(\eta)) \cdot N_c^{\downarrow}(\eta)} = \frac{(1 + \epsilon \cdot sin(\eta))^2}{(1 - \epsilon \cdot sin(\eta))^2} \,, \tag{6}$$

where $\uparrow(\downarrow)$ indicate up/down target polarisation and $u/c/d$ refer to the upstream/central/downstream target cells. This relation is obtained with a plausible assumption that the ratio of combinations of acceptances for various cells is the same before and after the polarisation reversal

$$\frac{a_u^-(\eta) + a_d^-(\eta)}{a_c^+(\eta)} = \frac{a_u^+(\eta) + a_d^+(\eta)}{a_c^-(\eta)} \,. \tag{7}$$

The raw asymmetry ϵ is determined from a fit to the DR dependence on the angle $\eta = \phi - \phi_S$. The transverse target asymmetry is extracted using expression

$$A_{UT}^{\sin(\phi-\phi_s)} = \frac{\epsilon}{f \cdot \langle P_T \rangle} \,, \tag{8}$$

where $f \simeq 0.14$ is the mean value of the dilution factor for the polarised target and $\langle P_T \rangle \simeq 0.9$ is the mean value of the proton polarisation.

3.4 Results for $A_{UT}^{\sin(\phi-\phi_s)}$

The transverse target spin asymmetry $A_{UT}^{\sin(\phi-\phi_s)}$ for the proton is shown in Fig. 2 as a function of Q^2, x_B and p_t^2. The average values of kinematic variables for this sample are $\langle Q^2 \rangle =$

2.2 $(\mathrm{GeV}/c)^2$, $\langle x_{Bj} \rangle = 0.4$ and $\langle p_t^2 \rangle = 0.18\,(\mathrm{GeV}/c)^2$. The errors shown are statistical ones. Preliminary estimates of systematic errors indicate that they are smaller than the statistical ones. The asymmetry is consistent with zero within the statistical errors.

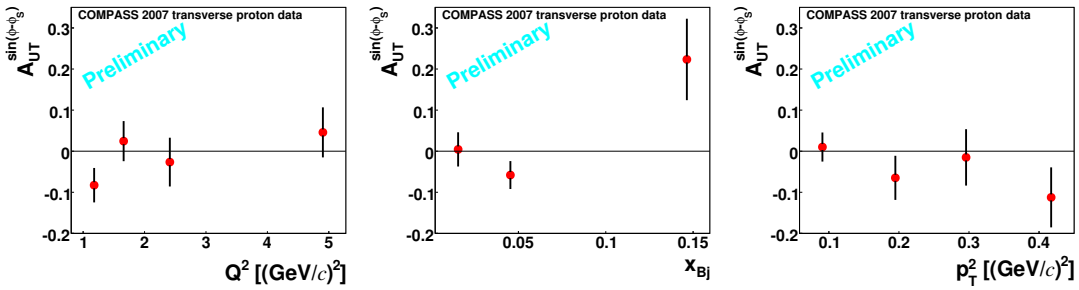

Figure 2: $A_{UT}^{\sin(\phi-\phi_s)}$ for the proton target as a function of Q^2, x_B and p_t^2.

A similar analysis of $A_{UT}^{\sin(\phi-\phi_s)}$ for the deuteron was done using the data taken in 2002-2004 with transversely polarised ^{6}LiD target. The selections for the exclusive ρ^0 sample were similar to these for the NH_3 data, except the coherent and incoherent contributions to the exclusive production on the deuteron were not separated. The applied cut on p_t^2 was $0.01 < p_t^2 < 0.5\,(\mathrm{GeV}/c)^2$.The number of events for this sample is about 270 000. The transverse target spin asymmetry for the deuteron is shown in Fig. 3 as a function of Q^2, x_B and p_t. (Note the difference in the transverse momentum scales in Figs 2 and 3.) The asymmetry for the deuteron is consistent with zero as well.

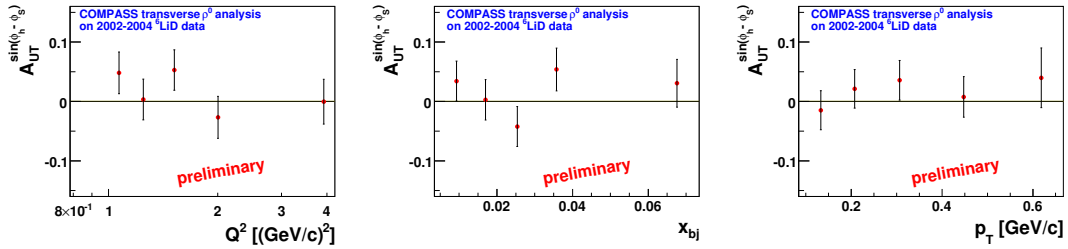

Figure 3: $A_{UT}^{\sin(\phi-\phi_s)}$ for the deuteron target as a function of Q^2, x_B and p_t.

A further analysis is in progress to separate the leading term σ_{00}^{+-} and the subleading term σ_{++}^{+-} (cf. Eq. 2), both for protons and deuterons, to separate coherent and incoherent contributions for the deuterons and to estimate effects of the non-exclusive background on the systematic errors.

The asymmetry $A_{UT}^{\sin(\phi-\phi_s)}$ for ρ^0 for the proton target was first obtained by the HERMES collaboration [7]. The HERMES results are consistent with zero within statistical errors, which are of a comparable magnitude as for COMPASS. The longitudinal and transverse separation has also been accomplished by HERMES.

Theoretical predictions for $A_{UT}^{\sin(\phi-\phi_s)}$ for ρ^0 have been done by Goloskokov and Kroll [8,

9]. The predicted values for asymmetry on the proton is about -0.02 for ρ^0 production, but significantly higher, about -0.10, for ω production.

4 Double spin asymmetry in exclusive ρ^0 production

Here we discuss the longitudinal double-spin asymmetry $A_1^\rho = (\sigma_{1/2} - \sigma_{3/2})/(\sigma_{1/2} + \sigma_{3/2})$ for incoherent ρ^0 production on polarized deuterons. The cross sections $\sigma_{1/2}$ and $\sigma_{3/2}$ refer to the cases when the absolute value of the total photon-nucleon angular momentum component along the virtual photon axis is 1/2 or 3/2, respectively. In the Regge approach the longitudinal double spin asymmetry A_1^ρ can arise due to the interference of amplitudes for exchange in the t-channel of Reggeons with natural parity (Pomeron, ρ, ω, f, A_2) with amplitudes for Reggeons with unnatural parity (π, A_1). For large Q^2 (> 3 GeV^2), a pQCD-inspired model involving GPDs has been proposed by Goloskokov and Kroll [8], in which the non-leading twist longitudinal double spin asymmetry results from the interference between the dominant GPD H_g and the helicity-dependent GPD $\tilde{H}_g$. The asymmetry is estimated to be of the order $k_T^2 \tilde{H}_g/(Q^2 H_g)$, where k_T is the transverse momentum of the quark and the antiquark.

The longitudinal double spin asymmetry A_1^ρ for the exclusive production of ρ^0 meson, $\mu + N \rightarrow \mu' + \rho^0 + N'$, has been measured by scattering longitudinally polarised muons off longitudinally polarised deuterons from the ^{6}LiD target and selecting incoherent exclusive ρ^0 production. The COMPASS results for 2002 and 2003 data [10] cover a wide kinematic range, $3 \cdot 10^{-3} \leq Q^2 \leq 7$ (GeV/c)^2 and $5 \cdot 10^{-5} \leq x \leq 0.05$. The measured asymmetry is shown as a function of Q^2 and x_{Bj} in Fig. 4. It is compatible with zero in the whole covered kinematic

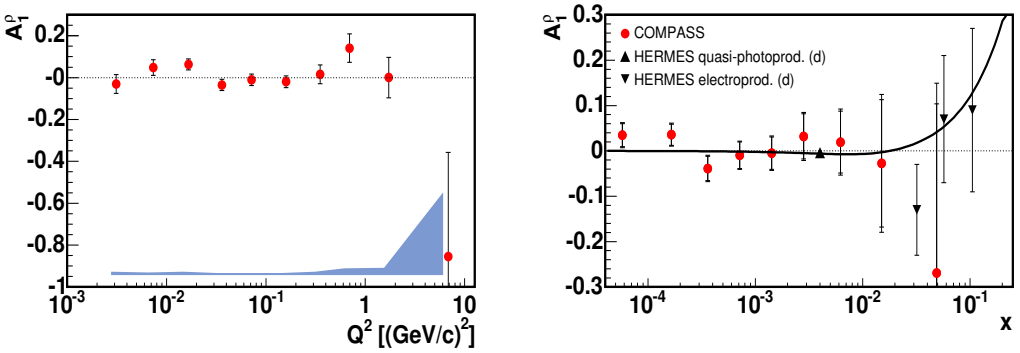

Figure 4: A_1^ρ as a function of Q^2 *(left)* and of x_{Bj} *(right)* from the present analysis compared to HERMES results on the deuteron target. The curve is described in the text.

range. This may indicate that the role of unnatural parity exchanges like π- or A_1-Reggeon exchange is small in that kinematic domain. The asymmetry is compared to HERMES results on the deuteron target [11]. The results from both experiments are consistent within errors. The kinematic range covered by the COMPASS measurements extends further towards small values of Q^2 and x_{Bj} by almost two orders of magnitude.

The x_{Bj} dependence of measured A_1^ρ is compared with the prediction $A_1^\rho = 2A_1/(1 + (A_1)^2)$ [12], which relates A_1^ρ with the A_1 asymmetry for inclusive inelastic lepton scattering at

the same x_{Bj}. The curve in Fig. 4 was obtained using the parameterisation of A_1 obtained from a fit [10] to the world data from polarised deuteron targets, including COMPASS measurements of A_1 at very low Q^2 and x_{Bj}. Within the present accuracy the results on A_1^ρ are consistent with this prediction.

5 Results for ρ^0 spin density matrix elements

Here we present preliminary results of the analysis of angular distributions for exclusive incoherent ρ^0 production $\mu + N \to \mu' + \rho^0 + N'$ and subsequent decay $\rho^0 \to \pi^+\pi^-$. The angular distributions allow one to determine ρ^0 spin density matrix elements (SDME) [13], which carry information on the spin structure of the production amplitudes. In particular, SDMEs allow one to test the s-channel helicity conservation (SCHC) and to determine $R = \sigma_L/\sigma_T$, the ratio of the longitudinal to transverse virtual photon cross section for $\gamma^* + N \to \rho^0 + N'$. The ρ^0 angular distribution $W(\cos\theta, \varphi, \phi)$ is studied in the s-channel helicity frame. The ρ^0 direction in the virtual photon-nucleon centre of mass system is taken as the quantization axis. The angle θ is the polar angle and φ the azimuthal angle of the positive decay meson in the ρ^0 centre of mass system. The angle φ is then that between the decay plane and the ρ^0 production plane (the γ^*-ρ^0 plane). The angle ϕ is that of the ρ^0 production plane with respect to the lepton scattering plane (cf. Sect. 3.1.).

The preliminary results presented here come from COMPASS 2002 data taken with the longitudinally polarised ^{6}LiD target. For the analysis of the spin density matrix elements the data with opposite target polarisations were merged resulting in the average target polarisation close to 0.

In this analysis we consider only single-dimensional projections of $W(\cos\theta, \varphi, \phi)$. For $\cos\theta$ and φ they are given by the following formulae

$$W(\cos\ \theta) = \frac{3}{4}[(1 - r^{04}_{00}) + (3\, r^{04}_{00} - 1)\cos^2\theta]\,, \tag{9}$$

$$W(\varphi) = \frac{1}{2\pi}[1 - 2r^{04}_{1-1}\cos 2\varphi + P_\mu\sqrt{1-\epsilon^2}\; 2\,\Im m\, r^3_{1-1}\sin 2\varphi]\,. \tag{10}$$

In above equations the r's are the spin density matrix elements for exclusive ρ^0 production, P_μ is the polarisation of muon beam and ϵ is the virtual photon polarisation parameter [13].

The element r^{04}_{00} is determined from $\cos\theta$ distribution, and can be interpreted as the fraction of longitudinal (helicity 0) ρ^0 in the sample. If SCHC holds, R can be obtained using

$$R = \frac{1}{(\epsilon + \delta)}\,\frac{r^{04}_{00}}{1 - r^{04}_{00}}\,, \tag{11}$$

where δ is the correction [13] to the ratio of the longitudinal and transverse virtual photon fluxes due to the finite lepton mass.

The COMPASS results on the Q^2 dependence of R are compared to other experiments in Fig. 5 (*left*). At small Q^2 the production by transverse photons (σ_T) dominates, while with increasing Q^2 the contribution of the production by longitudinal photons (σ_L) takes over at $Q^2 \simeq 2\,(\mathrm{GeV}/c)^2$.

From φ distribution one could determine two matrix elements r^{04}_{1-1} and $\Im m r^3_{1-1}$. COMPASS preliminary results are compared to other experiments in Fig. 5 (*right*). Note, that $\Im m\, r^3_{1-1}$ could be accessed only with polarised lepton beams. COMPASS measurements exhibit small

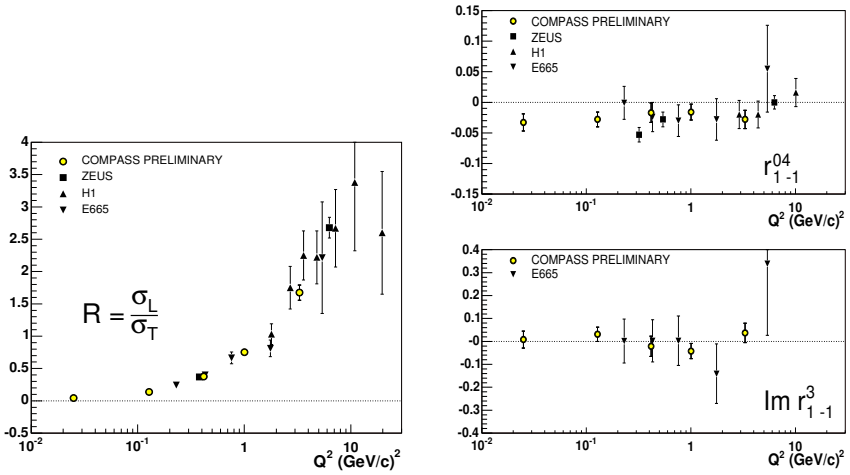

Figure 5: Q^2 dependence of $R = \sigma_L/\sigma_T$ (*left*) and of matrix elements r^{04}_{1-1} and $\Im m\, r^3_{1-1}$ (*right*)

negative values of r^{04}_{1-1} (≈ -0.03) approximately independent of Q^2, whereas $\Im m\, r^3_{1-1}$ is consistent with 0. The non-zero value of r^{04}_{1-1} indicates a small contribution of amplitudes with helicity flip.

In conclusion, the high precision COMPASS data on ρ^0 spin density matrix elements, which cover a wide range $0.01 < Q^2 < 10\,(\mathrm{GeV}/c)^2$, are consistent with a substantial increase of R with Q^2 and a weak violation of SCHC in agreement with other high energy experiments.

6 Future GPD program and 2008 DVCS test run

The study of GPDs using Deeply Virtual Compton Scattering and Hard Exclusive Meson Production is one of the topics proposed for the COMPASS future plans (COMPASS Phase II). The physics motivations are briefly described in a Letter of Intent [14] submitted to the CERN/SPSC in January 2009. A full proposal of the experiment will be submitted in 2009. The first stage of this program requires a 4 m long recoil detector (RPD) together with a 2.5 m long liquid hydrogen (LH) target. Upgrades of electromagnetic calorimeters to enlarge coverage at large x_{Bj} and reduce background are foreseen. The second stage requires a transversely polarised NH_3 target and a RPD.

The setup presently used for the meson spectroscopy measurements with hadron beams happens to be an excellent *prototype* to perform validation measurements for DVCS. A first measurements of exclusive γ production on a 40 cm long LH target, with detection of the slow recoiling proton in the RPD has been performed during a short (< 2 days) test run in 2008 using 160 GeV μ^+ and μ^- beams. The measurements were performed with the present hadron setup, all the standard COMPASS tracking detectors, the ECAL1 and ECAL2 electromagnetic calorimeters for photon detection and appropriate triggers. An efficient selection of single photon events, and suppression of the background is possible by using the combined information from the forward COMPASS detectors and the RPD.

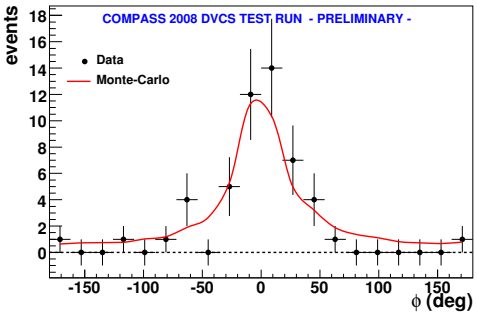

Figure 6: The distribution of the azimuthal angle ϕ for observed exclusive single photon production (points). The line is the Monte Carlo prediction normalised to the data.

A way to tag the observed process, $\mu + p \rightarrow \mu' + \gamma + p'$, to which both the DVCS and Bethe-Heitler process contribute, is to look at the angle ϕ between the leptonic and hadronic planes. The Bethe-Heitler contribution, which dominates the sample, show a peak at $\phi \simeq 0$. The observed distribution, after applying all cuts and selections and for $Q^2 > 1$ (GeV/c)^2, is displayed in Fig. 6 with the prediction from the Monte Carlo simulation. The shape of the observed distribution is compatible with the dominant Bethe-Heitler process. The overall detection efficiency can be deduced from the relative normalisation of the two distributions. The efficiency is equal to about 0.3.

7 Acknowledgments

This work was supported in part by Polish MSHE grant 41/N-CERN/2007/0.

References

[1] COMPASS Collab., P. Abbon *et al.*, Nucl. Instr. Meth. **A577** 455 (2007).
[2] K. Goeke, M.V. Polyakov, M. Vanderhaeghen, Prog. Part. in Nucl. Phys. **47** 401 (2001), hep-ph/0106012.
[3] F. Ellinghaus, W.-D. Nowak, A.V. Vinnikov, and Z. Ye, Eur. Phys. J. **C46** 729 (2006), hep-ph/0506264.
[4] X. Ji, Phys. Rev. Lett. **78** 610 (1997), hep-ph/9603249.
[5] M. Burkardt, Int. J. Mod. Phys. **A18** 173 (2003), hep-ph/0207047.
[6] M. Diehl and S. Sapeta, Eur. Phys. J. **C41** 515 (2005), hep-ph/0503023;
M. Diehl, JHEP 0709:064 (2007), hep-ph/0704.1565.
[7] HERMES Collab., A.Rostomyan *et al*, hep-ex/07072486 and DIF08, AIP Conf. Proc. 1105 (2009).
[8] S.V. Goloskokov, P. Kroll, Eur. Phys. J. **C42** 281 (2005), hep-ph/0501242;
S.V. Goloskokov, P. Kroll, Eur. Phys. J. **C53** 367 (2008), hep-ph/0708.3569;
[9] S.V. Goloskokov, P. Kroll, Eur. Phys. J. **C59** 809 (2009), hep-ph/0809.4126.
[10] COMPASS Collab., M. Alekseev *et al.*, Eur. Phys. J. **C 52** 255 (2007).
[11] HERMES Collab., A. Airapetian *et al.*, Eur. Phys. J. **C 29** 171 (2003).
[12] HERMES Collab., A. Airapetian *et al.*, Phys. Lett. **B 513** 301 (2001).
[13] K.Schilling and G.Wolf, Nucl.Phys. **B61** 381 (1973).
[14] COMPASS Collab., *COMPASS Medium and Long Term Plans*, CERN-SPSC-2009-003,SPSC-I-238.

Looking for the Odderon in Photon Collisions

B. Pire[1], *F. Schwennsen*[1,2], *L. Szymanowski*[3], *and S. Wallon*[2]

[1]CPhT, École Polytechnique, CNRS, 91128 Palaiseau, France
[2]LPT, Université Paris-Sud, CNRS, 91405 Orsay, France
[3]Soltan Institute for Nuclear Studies, Warsaw, Poland

DOI: http://dx.doi.org/10.3204/DESY-PROC-2009-03/Schwennsen

We discuss the production of two pion pairs in photon collisions at high energies. We calculate the according matrix elements in k_T-factorization and discuss the possibility to reveal the existence of the perturbative Odderon by charge asymmetries.

1 Introduction

At high energies amplitudes of reactions with rapidity gaps in hadronic interactions are dominated by the exchange of a color singlet, C-even state – called the Pomeron. In the language of perturbative QCD – at lowest order – the Pomeron can be described as the exchange of two gluons in the color singlet state. In contrast to the very well settled notion of the Pomeron, the status of its C-odd partner – the Odderon – is less safe. Although it is needed *e.g.* to describe properly the different behaviors of pp and $\bar{p}p$ elastic cross sections [1], it still evades confirmation in the perturbative regime, where – again at lowest order – it can be described by the exchange of three gluons in the color singlet state.

The main reason lies in its smaller exchange amplitude in comparison to the Pomeron exchange such that in the cross section, obtained after squaring the sum of both amplitudes, the Pomeron amplitude squared dominates. In this contribution we present results of our study [2] of a charge asymmetry in the production of two pion pairs in photon-photon collisions where that Pomeron squared part vanishes. This observable is thus linearly sensitive to the Odderon contribution.

In the present analysis we deal with the hard Pomeron and the hard Odderon exchanges, *i.e.* both treated within perturbative QCD. This approach can be confronted with a description of the Pomeron-Odderon interference based on soft, non-perturbative physics and developed in Refs. [3]. The experimental observation of the P-O interference effects will thus shed a light on the important question which of the above mechanisms is more appropriate for the description of data.

2 Kinematics, amplitudes and GDAs

Figure 1 shows a sample diagram of the process under consideration. We consider large $\gamma\gamma$ energies such that the amplitude can be expressed in terms of two impact factors convoluted over the transverse momenta of the exchanged gluons. The impact factors are universal and consist of a perturbative part – describing the transition of a photon into a quark-antiquark

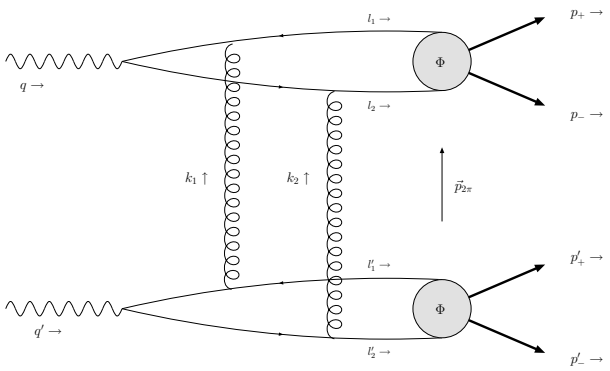

Figure 1: Kinematics of the reaction $\gamma\gamma \to \pi^+\pi^-\ \ \pi^+\pi^-$ in a sample Feynman diagram of the two gluon exchange process.

pair – and a non-perturbative part, the two pion generalized distribution amplitude (GDA) parametrizing the quark-antiquark hadronization into the the pion pair [4, 5]. This comes as a variant of the approach which has been previously proposed in the case of the electroproduction of a pion pair [6, 7, 8], and which is based on the fact that the $\pi^+\pi^-$-state does not have any definite charge parity. These GDAs which are functions of the longitudinal momentum fraction z of the quark, of the angle θ (in the rest frame of the pion pair) and of the invariant mass $m_{2\pi}$ of the pion pair are the only but nevertheless essential phenomenological inputs. In principle, they have to be extracted from experiments but this is a very challenging task and has not been done so far. However, after an expansion in Gegenbauer polynomials $C_n^m(2z-1)$ and in Legendre polynomials $P_l(\beta\cos\theta)$ (where $\beta = \sqrt{1-4m_\pi^2/m_{2\pi}^2}$) [4], it is believed that only the first terms give a significant contribution:

$$\begin{aligned}
\Phi^{I=1}(z,\theta,m_{2\pi}) &= 6z\bar{z}\beta f_1(m_{2\pi})\cos\theta, \\
\Phi^{I=0}(z,\theta,m_{2\pi}) &= 5z\bar{z}(z-\bar{z})\left[-\frac{3-\beta^2}{2}f_0(m_{2\pi}) + \beta^2 f_2(m_{2\pi})P_2(\cos\theta)\right],
\end{aligned}$$

where $f_1(m_{2\pi})$ can be identified with the electromagnetic pion form factor $F_\pi(m_{2\pi})$. For the $I=0$ component we use different models. The first model follows Ref. [6] and expresses the functions $f_{0/2}$ in terms of the Breit-Wigner amplitudes of the according resonances. A second model has been elaborated in Ref. [8] and interprets the functions $f_{0/2}$ as corresponding Omnès functions for $S-$ and $D-$waves constructed by dispersion relations from the phase shifts of the elastic pion scattering. It has been argued [8, 9] that the actual phases of the GDA might be closer to the phases $\delta_{T,l}$ of the corresponding T matrix elements $\frac{\eta_l e^{2i\delta_l}-1}{2i}$, where η_l is the inelasticity factor. The third model for the $I=0$ component of the GDA takes this into account by using the technique of model 2 with these phases $\delta_{T,l}$ of the T matrix elements. Indeed, measurements at HERMES [10] do not observe a resonance effect at the f_0-mass, but concerning the f_2 both phases (δ_2 and $\delta_{T,2}$) are compatible with data [8]. Having this in mind, we consider also a fourth model – a mixed description with the f_0 contribution from model 3 and the f_2 contribution from model 2.

Recently the BaBar experiment reported a new measurement of the reaction $\gamma^\star\gamma \to \pi^0$ up to photon virtualities squared of 40 GeV^2 [11]. In the latter study, the reaction $\gamma^\star\gamma \to \pi^0\pi^0$

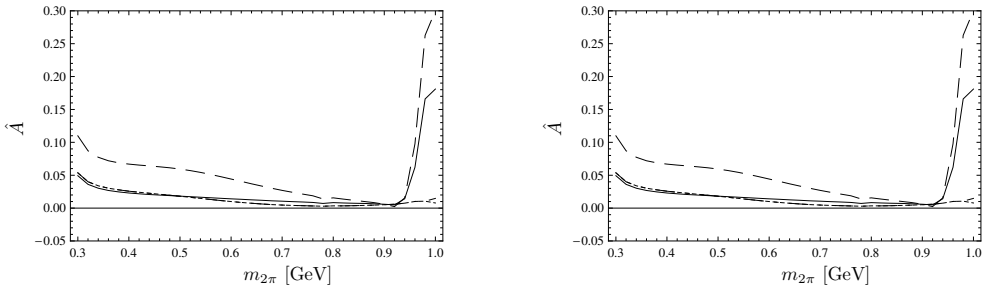

Figure 2: Asymmetry $\hat{A}$ at $t = -1\,\mathrm{GeV}^2$ for model 1 (solid), 2 (dashed), 3 (dotted), and 4 (dash-dotted) – model 3 and 4 are nearly on top of each other. Left column has $m_{\min} = .3\,\mathrm{GeV}$ and $m_{\max} = m_\rho$, while right column has $m_{\min} = m_\rho$ and $m_{\max} = 1\,\mathrm{GeV}$.

was investigated in the $f_0(980)$ and $f_2(1270)$resonance regions as a potential background for the study of the π^0 transition form factor. This low-W^2 kinematical region should soon be analysed in the framework of generalised two-meson distribution amplitudes [12]. This will settle the question of the adequate model to be used.

3 Charge asymmetries and rates

The key to obtain an observable which linearly depends on the Odderon amplitude is the orthogonality of the C-even GDA (entering the Odderon process) and the C-odd one (entering the Pomeron process) in the space of Legendre polynomials in $\cos\theta$. Due to an additional multiplication by $\cos\theta$ before the angular integration only the interference term survives. We have to do this for both the pion pairs. Moreover we integrate over the invariant mass of one of the pion pairs to reduce the complexity of our observable. Finally, we define the charge asymmetry in the following way:

$$\hat{A}(t, m_{2\pi}^2; m_{\min}^2, m_{\max}^2) = \frac{\int_{m_{\min}^2}^{m_{\max}^2} dm_{2\pi}'^2 \int \cos\theta\, \cos\theta'\, d\sigma(t, m_{2\pi}^2, m_{2\pi}'^2, \theta, \theta')}{\int_{m_{\min}^2}^{m_{\max}^2} dm_{2\pi}'^2 \int d\sigma(t, m_{2\pi}^2, m_{2\pi}'^2, \theta, \theta')}$$
$$= \frac{\int_{m_{\min}^2}^{m_{\max}^2} dm_{2\pi}'^2 \int_{-1}^{1} d\cos\theta \int_{-1}^{1} d\cos\theta'\, 2\cos\theta\, \cos\theta'\, \mathrm{Re}\,[\mathcal{M}_{\mathbb{P}}(\mathcal{M}_{\mathbb{O}} + \mathcal{M}_\gamma)^*]}{\int_{m_{\min}^2}^{m_{\max}^2} dm_{2\pi}'^2 \int_{-1}^{1} d\cos\theta \int_{-1}^{1} d\cos\theta' \left[|\mathcal{M}_{\mathbb{P}}|^2 + |\mathcal{M}_{\mathbb{O}} + \mathcal{M}_\gamma|^2\right]}.$$

An analytic calculation of the Odderon matrix element would demand the notion of analytic results for two-loop box diagrams, whose off-shellness for all external legs is different. With the techniques currently available such a calculation is not straightforward and we choose to rely on a numerical evaluation by Monte Carlo methods. In particular we make use of a modified version of VEGAS as it is provided by the CUBA library [13]. The result for $\hat{A}$ is shown in Fig. 2 where we took two different choices for the integrated region of the invariant mass of the two pions system. Since our framework is only justified for $m_{2\pi}^2 < -t$, (in fact strictly speaking, one even needs $m_{2\pi}^2 \ll -t$), we keep $m_{2\pi}$ below 1 GeV.

To answer the question whether it is possible to measure this asymmetry, we adress the two main issues here. First, one has to convolute the $\gamma\gamma$ cross section obtained by our calculations

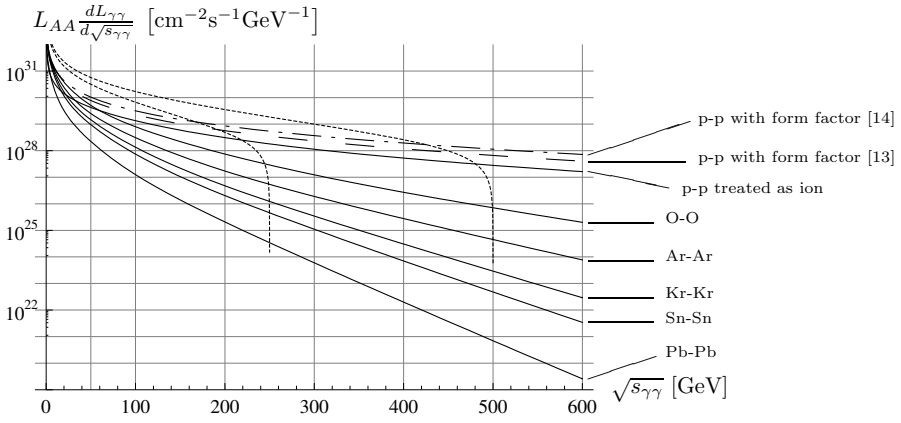

Figure 3: Effective $\gamma\gamma$ luminosities for the collision of p-p based on Ref. [15] (dash-dotted) and Ref. [16] (dashed). The results using the parametrization of Ref. [17] for ions are given by solid lines for p-p, O^{8}_{16}-O^{8}_{16}, Ar^{18}_{40}-Ar^{18}_{40}, Kr^{36}_{84}-Kr^{36}_{84}, Sn^{50}_{120}-Sn^{50}_{120}, Pb^{82}_{208}-Pb^{82}_{208} from top to bottom. For ions we used the average luminosities as given in Ref. [18], for proton we used $L_{pp} = 10^{34}\,\mathrm{cm}^{-2}\mathrm{s}^{-1}$. For comparison also effective $\gamma\gamma$ luminosities at the ILC are given for $\sqrt{s_{e^+e^-}} = 250\,\mathrm{GeV}$ and $\sqrt{s_{e^+e^-}} = 500\,\mathrm{GeV}$ (both as dotted lines).

with the effective photon flux at a certain collider. As we discuss in Ref. [2] in detail, the most recent review on this topic [14] presents an overview of photon fluxes for different colliding hadrons which is flawed by an inconsistency in the underlying hadron-hadron luminosities. Therefore, we show a consistent comparison for the design luminosities of different colliding particles in Fig. 3. For the proton case we display the different luminosities based on either the proton form factor [15, 16] or on the asymptotic formula for large nuclei.

Although photon fluxes are important in p-p collisions at the designed LHC luminosity ($10^{34}\,\mathrm{cm}^{-2}\mathrm{s}^{-1}$), data collected under these conditions will suffer from the pile up of events, which will prevent an analysis of the process considered here from being performed. At lower luminosity, rates may be marginally sufficient for values of $-t \approx 1\mathrm{GeV}^2$, but designing a trigger strategy to record interesting events seems very difficult: typical triggers on high p_t mesons demand a minimum p_T of a few GeV, which is incompatible with such low values of $-t$ and the corresponding limit of $m_{2\pi} < \sqrt{-t}$. Moreover, an important issue is the background in case of hadron colliders. In contrast to electromagnetic processes which have been proposed to be studied in ultraperipheral collisions, pions are produced by pure QCD processes as well. It is not easy to demonstrate quantitatively that one can separate these two processes by relying on the fact that ultraperipheral processes are strongly peaked at low t, contrarily to the flatter depence of the Pomeron induced ones [19].

In nucleus-nucleus collisions, the trigger problem is easily solved by detecting neutrons from giant dipole resonances in the Zero Degree Calorimeters, but the rates are much lower, especially for the heavier ions. The best compromise may be Oxygen-Oxygen collisions, which is by no means the priority of the heavy ion physics community.

In contrast, an electron-positron collider such as the projected ILC would be the ideal environment to study the process under consideration. Photon photon collisions are indeed the

dominant processes there and no pile up phenomenon can blur the picture of a scattering event. Studies of similar exclusive processes like diffractive double J/ψ [20] or double ρ production [21] show that high rates are expected. Maybe an alternative, which we did not study, is a large energy electron ion collider in its ultraperipheral mode.

In conclusion, our proposal to discover the perturbative Odderon through asymmetries in the production of two pion pairs in ultraperipheral collisions at the LHC seems to have a hard time to win over quite severe experimental constraints. Will the perturbative Odderon continue to escape detection for the next 10 years?

Acknowledgements

We acknowledge discussions with Mike Albrow, Gerhard Baur, Máté Csanád, David d'Enterria, Bruno Espagnon, Oldrich Kepka, Spencer Klein, Joakim Nystrand, Christophe Royon, and Rainer Schicker. This work is supported in part by the Polish Grant N202 249235, the French-Polish scientific agreement Polonium, by the grant ANR-06-JCJC-0084 and by the ECO-NET program, contract 12584QK.

References

[1] L. Łukaszuk and B. Nicolescu, Nuovo Cim. Lett. **8** 405 (1973).

[2] B. Pire, F. Schwennsen, L. Szymanowski, and S. Wallon, Phys. Rev. **D78** 094009 (2008), 0810.3817.

[3] I. F. Ginzburg, I. P. Ivanov, and N. N. Nikolaev, Eur. Phys. J. direct **C5** 02 (2003), hep-ph/0207345; I. F. Ginzburg, I. P. Ivanov, and N. N. Nikolaev, Eur. Phys. J. **C32S1** 23 (2003); I. F. Ginzburg and I. P. Ivanov, Eur. Phys. J. **C45** 193 (2006), hep-ph/0401180.

[4] M. V. Polyakov, Nucl. Phys. **B555** 231 (1999), hep-ph/9809483.

[5] M. Diehl, T. Gousset, and B. Pire, Phys. Rev. **D62** 073014 (2000), hep-ph/0003233.

[6] P. Hägler, B. Pire, L. Szymanowski, and O. V. Teryaev, Phys. Lett. **B535** 117 (2002), hep-ph/0202231.

[7] P. Hägler, B. Pire, L. Szymanowski, and O. V. Teryaev, Eur. Phys. J. **C26** 261 (2002), hep-ph/0207224.

[8] N. Warkentin, M. Diehl, D. Y. Ivanov, and A. Schafer, Eur. Phys. J. **A32** 273 (2007), hep-ph/0703148.

[9] B. Ananthanarayan *et al.*, Phys. Lett. **B602** 218 (2004), hep-ph/0409222.

[10] HERMES, A. Airapetian *et al.* Phys. Lett. **B599** 212 (2004), hep-ex/0406052.

[11] B. Aubert [The BABAR Collaboration], arXiv:0905.4778 [hep-ex].

[12] We thank Vladimir Druzhinin for useful correspondence on this point.

[13] T. Hahn, Comput. Phys. Commun. **168** 78 (2005), hep-ph/0404043.

[14] K. Hencken *et al.*, Phys. Rept. **458** 1 (2008), arXiv:0706.3356[nucl-ex], with regard to $\gamma\gamma$ luminosities in p-p collisions, Fig. 3 should be modified to account for a realistic p-p luminosity, as we discuss in section IV of Ref. [2].

[15] M. Drees and D. Zeppenfeld, Phys. Rev. **D39** 2536 (1989).

[16] J. Nystrand, Nucl. Phys. **A752** 470 (2005), hep-ph/0412096.

[17] R. N. Cahn and J. D. Jackson, Phys. Rev. **D42** 3690 (1990).

[18] D. Brandt, CERN-LHC-PROJECT-REPORT-450 (2000).

[19] K. Piotrzkowski, Phys. Rev. **D63** 071502 (2001), hep-ex/0009065; V. A. Khoze, A. D. Martin, and M. G. Ryskin, Eur. Phys. J. **C14** 525 (2000), hep-ph/0002072.

[20] J. Kwiecinski and L. Motyka, Phys. Lett. B **438**, 203 (1998).

[21] B. Pire *et al.*, Eur. Phys. J. C **44**, 545 (2005); M. Segond *et al.*, Eur. Phys. J. C **52** (2007) 93.

Total Cross Section and Elastic Scattering from TEVATRON to LHC

Hasko Stenzel

on behalf of the ATLAS Collaboration
Justus-Liebig Universität Giessen, II. Physikalisches Institut
Heinrich-Buff Ring 16, D-35392 Giessen, Germany

DOI: http://dx.doi.org/10.3204/DESY-PROC-2009-03/Stenzel

A review of measurements of the total cross section in $p\overline{p}$ collisions at the TEVATRON and an outlook on the expected performance for similar determinations at the LHC is given. The experimental method is based on the optical theorem to determine the total cross section independent of the machine luminosity. It consists of the extrapolation of the t-spectrum for elastic scattering to $t \to 0$ with a simultaneous measurement of the total inelastic rate.

1 Introduction

One of the most elementary observables at hadron colliders is the total cross section. Precise measurements at high energies have been pioneered at the SPS by the UA4 [1] collaboration. The method requires an instrumentation of the forward region far away from the interaction point but close enough to the beam to measure small-angle elastic scattering. At high energies the t-value for elastic $p\bar{p}$ and pp scattering can be obtained from a measurement of the scattering angle θ by $-t = (p \cdot \theta)^2$ with the beam momentum p. The scattering angle is reconstructed from the proton impacts in the forward tracking devices, usually located in movable beam pockets, the so-called Roman Pots. On the other side, simultaneously with the elastic measurement, the total inelastic rate must be determined, which requires an extended pseudorapidity η coverage. In this case the total cross section is given by

$$\sigma_{\rm tot} = \frac{16\pi}{1+\rho^2} \frac{{\rm d}R_{\rm el}/{\rm d}t|_{t\to 0}}{R_{\rm in+}R_{\rm el}} \ , \ \rho = \left.\frac{Re(F_{\rm el}(t))}{Im(F_{\rm el}(t))}\right|_{t\to 0} \ ,$$

independent of the machine luminosity. In this formula, $R_{\rm in(el)}$ is the inelastic (elastic) rate, and the F are the corresponding amplitudes. In the following we shall review the measurements performed by the TEVATRON experiments and summarise the potential for the LHC experiments.

2 Measurements at the TEVATRON

2.1 E710

At the FNAL TEVATRON $p\overline{p}$-accelerator the first total cross section measurement was done by the E710 experiment [2]-[4] at $\sqrt{s} = 1.8$ TeV. The E710 set-up was located around the E0 interaction point and was equipped with two Roman Pots at each side of E0 for the measurement of elastic protons. The Roman Pots were instrumented with wire chambers for the tracking and trigger scintillators. The locations of these detectors were in between 25 and 124 m from the interaction point. Under suitable beam conditions with high $\beta^\star$ optics and low emittance the detector could be moved close to the beam at a distance of a few millimetres. In this case the impact position $u = x, y$ is related to the scattering angle by $u \propto \sqrt{\beta^\star \beta_{\rm RP}}\,\theta$, where β is the betatron oscillation function resulting from the magnetic lattice. The measured t spectrum from E710 is shown in fig. 1. The t-spectrum exhibits an approximately exponential fall-off with

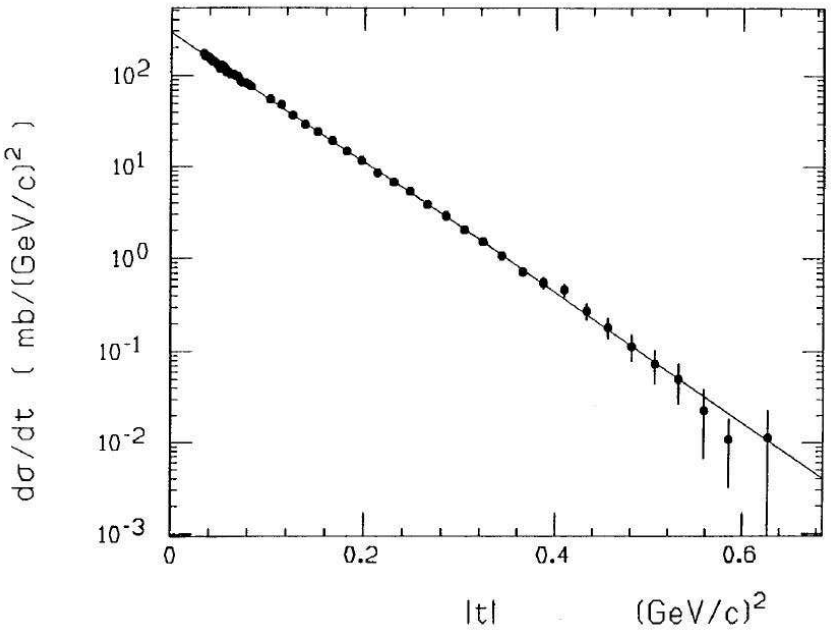

Figure 1: Elastic t spectrum at 1.8 TeV measured by E710 [2].

the nuclear slope B in the considered range. The elastic differential cross section is normally given by

$$\begin{aligned} \frac{\mathrm{d}\sigma}{\mathrm{d}t} &= \frac{1}{16\pi}\left|F_{\rm C}(t) + F_{\rm N}(t)\right|^2 \ ; \\ F_{\rm C}(t) &= -8\pi\alpha\hbar c\frac{G^2(t)}{t}\exp\left(i\alpha\Phi(t)\right) \ ; \\ F_{\rm N}(t) &= (\rho+i)\frac{\sigma_{\rm tot}}{\hbar c}\exp\left(\frac{-Bt}{2}\right) \ , \end{aligned} \tag{1}$$

with the Coulomb and nuclear amplitudes F_C resp. F_N, the electric form factor of the proton $G^2(t)$ and the Coulomb phase $\Phi(t)$. The Coulomb contribution is rather small in the t-range covered by E710, thus only the nuclear component was used to fit the spectrum (line in fig. 1) in order to determine the optical point, which is defined by the value of the fit at $t = 0$.

The total inelastic rate was measured in E710 by the set-up depicted in fig. 2. It consisted of

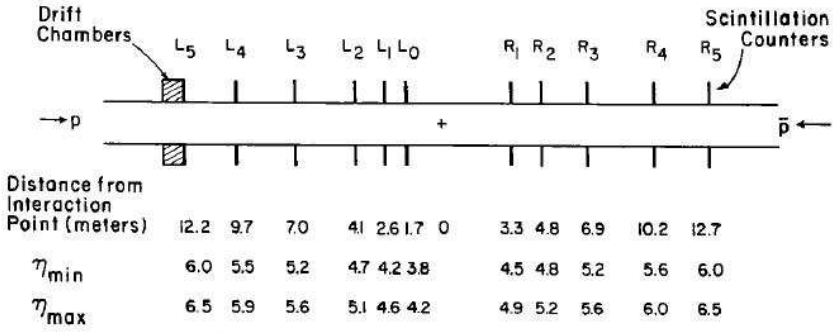

Figure 2: Inelastic detectors of E710.

various annular scintillator counters segmented in four quadrants along the beam line covering a pseudo-rapidity range from 3.8 to 6.5, supplemented by drift chambers for precision tracking. With a trigger coincidence between the left and right arm about 70% of the inelastic interactions are covered. Some events, in particular from single diffraction processes escaped the left-right detection and were recovered by a single-arm OR trigger condition. This trigger is dominated by background from beam-gas interactions or halo protons which was measured using non-colliding bunches in the machine and then subtracted. A small fraction of events could still not be detected because of the limited angular acceptance coverage. The acceptance corrections were also obtained from the data using the drift chamber extrapolation the rate as function of the cosine of the maximum detected angle to zero, following a method developed by UA4 [1]. The final results from E710 are summarised in Table 1.

Table 1: Results from TEVATRON experiments.

$\sigma_{\rm tot}$[mb]	$\sigma_{\rm el}$[mb]	$\sigma_{\rm tot}/\sigma_{\rm el}$	experiment
80.03 ± 2.24	19.70 ± 0.85	0.246 ± 0.004	CDF
71.42 ± 2.41	15.79 ± 0.87	0.220 ± 0.008	E811
72.8 ± 3.1	16.6 ± 1.6	0.230 ± 0.012	E710

2.2 CDF

The second experiment to perform measurements of elastic and total cross sections at the TEVATRON was CDF [5],[6]. The elastic spectrometer of CDF consisted of three Roman Pot stations on the $\bar{p}$-side and two on the p-side, each instrumented with wire chambers, silicon strip detectors and trigger scintillators. The acceptance for elastic scattering was obtained from a detailed beam transport simulation and is shown in fig. 3. The inelastic measurement

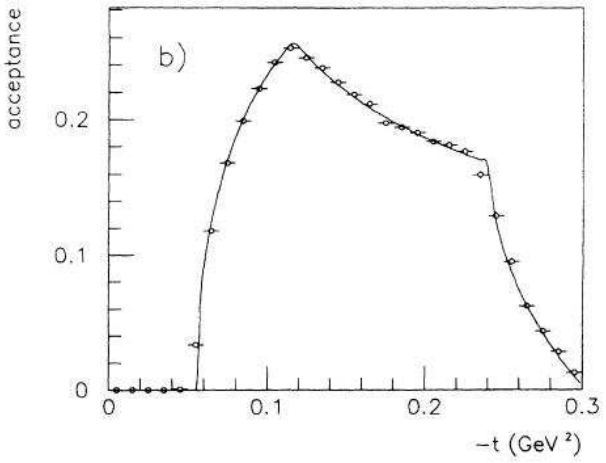

Figure 3: Acceptance of CDF for elastic scattering.

of CDF profited from the rich instrumentation around the interaction point; in particular the vertex TPC covering up to $|\eta| \leq 3.5$ allowed for a high-quality vertexing and enabled efficient background rejection. In the forward region a telescope of drift chambers from UA4 covering $3.8 \leq |\eta| \leq 5.5$ and a movable telescope enclosing completely the beam pipe when in beam position and covering then to $|\eta| \leq 7$ were installed. For the determination of the inelastic rate, in addition to the traditional left-right coincidence, a dedicated single-diffraction trigger consisting of a coincidence between the elastic spectrometer on one side detecting the diffractive proton and the opposite inelastic detectors tagging remnants of the diffractive dissociation was set up. Acceptance corrections for the limited angular coverage of the inelastic detectors and for losses of the diffractively scattered protons were obtained from detector and beam line simulations. The result from CDF, given in Table 1, is somewhat larger than the E710 result, both for the elastic and the total cross section. It should be noted that CDF has also provided a measurement [6] at 546 GeV, $\sigma_{\rm tot} = 61.26 \pm 0.93$ mb, compatible with the UA4 result [1].

2.3 E811

Given the discrepancy between E710 and CDF, another experiment E811 [7] was built upgrading the E710 location. E811 used the same inelastic detectors as E710 but replaced the elastic detectors by a scintillating fibre tracked coupled to a CCD read-out yielding a spatial resolution of 20 μm. The analysis technique was similar to the E710 method but E811 accumulated larger statistics, extended the t-range and improved the systematic uncertainties [8]. Their final result [9] confirms the first E710 measurement and differs from CDF by 2.6 σ on the total and by 2.9 σ on the elastic cross section. The total cross section measurements are shown in fig. 4 together with lower energy $p\bar{p}$ results.

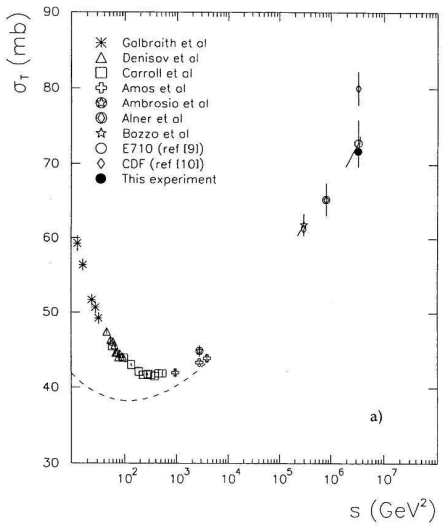

Figure 4: Summary of total cross section measurements at TEVATRON compared to lower energy data. *This experiment* is E811, taken from [8]

3 Prospect for measurements at LHC

3.1 TOTEM

At the LHC similar measurements are proposed by the TOTEM experiment [10],[11] and ATLAS [12] with its dedicated ALFA subsystem [13]. TOTEM shares the interaction point with CMS and has Roman Pot stations at 147 and 220 m distance, with both detection in the vertical and horizontal planes to cover elastic scattering and diffraction and to ease alignment. The elastic set-up is shown in fig. 5; each station houses silicon detectors for high-precision tracking and triggering. At each location two stations separated by a few meters allow for the determination of the local track slope. The detectors consist of 10 planes of silicon strips alternating in U- and V-Geometry, in a novel edgeless technology allowing to approach the beam as close as possible. The running scenario foresees a dedicated beam optics for the total cross section measurement with a $\beta^\star$ value of 1540 m, in which case a good t-acceptance between 0.002 and 1.5 GeV^2 is achieved. But also other configurations with smaller $\beta^\star$ are considered which opens up access to large t values up to 10 GeV^2 and to extended diffractive studies.

The inelastic detectors are shown in fig. 6. They consist of two tracking telescopes T1 and T2 in the pseudorapidity region $3.1 \leq |\eta| \leq 6.5$. T1 is of conical shape and inserted underneath the CMS flux return yoke at a distance between 7.5 and 10.5 m from the interaction point. Given the requirements on rate capabilities and radiation hardness, cathode strip chambers were selected as technology choice. The compact T2 telescope is installed in the forward shield of CMS in front of the CASTOR calorimeter at about 13.5 m from the interaction point. For T2 gaseous electron multiplier detectors were selected because of their excellent ageing performance. The telescopes will be used to trigger inelastic events with high efficiency and for the reconstruction of the primary vertex to discriminate against beam-gas and beam-halo background. In addition, integrated cross sections for hard and soft diffraction can be measured, also differentially in t

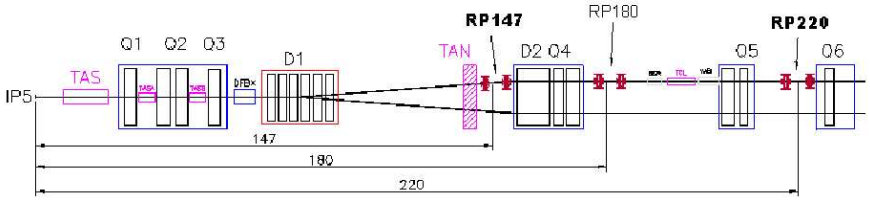

Figure 5: TOTEM elastic detectors.

and in the diffractive mass M_x.

The systematic uncertainties for the total cross section depend on the optics used. For the intermediate optics with $\beta^\star$=90 m an uncertainty of 4% is anticipated, dominated by the uncertainty of the optical functions needed for the t-reconstruction, but for the high $\beta^\star$ optics the uncertainty may decrease to 1%.

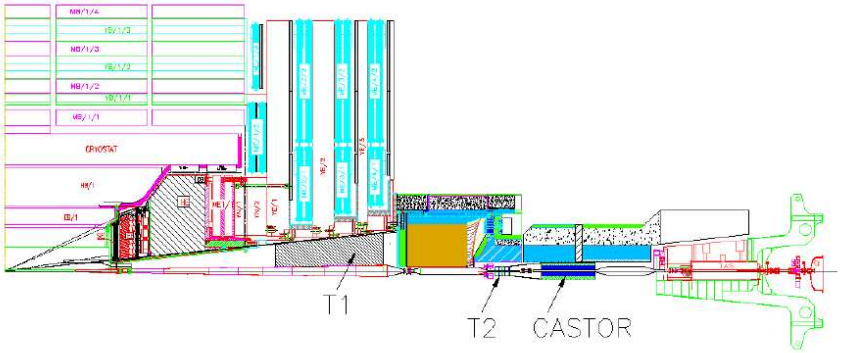

Figure 6: Inelastic detector T1 and T2 of TOTEM embedded in CMS components.

3.2 ATLAS ALFA

The primary focus of the ATLAS ALFA detector is on the absolute luminosity calibration for the different relative luminosity monitors of ATLAS and specifically the dedicated relative monitor LUCID. Therefore the detector is designed to run only for a short period and under special beam conditions at low luminosity, thereby relaxing the constraints on the radiation tolerance. The luminosity can be determined according to eq. 1 without using a measurement of the inelastic rate if the Coulomb-nuclear interference (CNI) region is covered. In this case the total cross section and the luminosity decouple because of the appearance of the Coulomb term. From a fit of the elastic t spectrum the luminosity, total cross section, B and ρ parameters can be determined simultaneously. An example of a fit to the t-spectrum reconstructed with ALFA is shown in fig. 7. This requires, however, that the CNI point where $|F_C| \approx |F_N|$, i.e. $t \approx 6.5 \cdot 10^{-4}$ GeV^2 is reached. It is therefore envisaged to use a very high $\beta^\star$ optics with 2600 m

at a low luminosity of about 10^{27} cm^{-2}s^{-1} with low emittance. In this case the detector can approach the beam as close as 1.5 mm (12 σ) and the CNI point is covered.

The ALFA detector is located at 240 m from the ATLAS interaction point; at each location two vertical Roman Pot stations will be installed at a distance of 4 m from each other. The Roman Pots are instrumented with 10 planes of scintillating fibres, each double-sided plane carrying 64 U- and 64 V- fibres. The fibres have a good sensitivity also at the edge oriented to the beam, which is essential for a high acceptance at small t. The scintillation light is recorded by multi-anode photomultipliers. Since the detector is operated only for short periods it is foreseen to be removed after each period in order to prevent radiation damages during normal LHC operations. The scintillating fibre tracker is supplemented by plain scintillator tiles for triggering. The selected optics provides a parallel-to-point focusing in the vertical plane, and the accuracy of the t-scale depends crucially on an accurate vertical alignment. This is obtained by dedicated overlap detectors, which are made of horizontally aligned scintillating fibres housed in extrusions of the Roman Pots. When the Roman pots are in beam position the upper and lower overlap detector will measure the same halo tracks and the distance between the two pots can be determined with $\pm$ 10 μm precision.

The elastic trigger will consist of a left-right coincidence requesting a signal from an upper detector on one side and from a lower one on the other side in agreement with the back-to-back topology of elastic events, while coincidences of the same detector type can be used to measure the beam related background. Further background rejection can be achieved by using the local slope information from the two stations at each location. This enables a reconstruction of the transverse interaction vertex position through the beam transfer matrices.

The systematic uncertainties are dominated by the knowledge of the optical functions, the detector alignment and the background determination. According to simulation a total uncertainty of 3% is achievable, for a running time of about 100 hours at a luminosity of 10^{27}cm^{-2}s^{-1}.

4 Conclusion

The long-standing tradition of total cross section measurements at hadron colliders from elastic scattering and the optical theorem has been successfully pursued at the TEVATRON with several measurements by CDF, E710 and E811 with an accuracy of about 3%. At the LHC the dedicated TOTEM experiment will continue along these lines and even more precise measurements of 1% accuracy are expected, which will also be measured by ATLAS experiment with their dedicated ALFA system.

5 Acknowledgments

This research was supported in part by the German Helmholtz Alliance “Physics at the Terascale”.

References

[1] M. Bozzo *et al.*, UA4 Collaboration, Phys. Lett. **B147** (1984) 392.

[2] N. Amos *et al.*, E710 Collaboration, Phys. Lett. **B247** (1990) 127.

[3] N. Amos *et al.*, E710 Collaboration, Phys. Lett. **B243** (1990) 158.

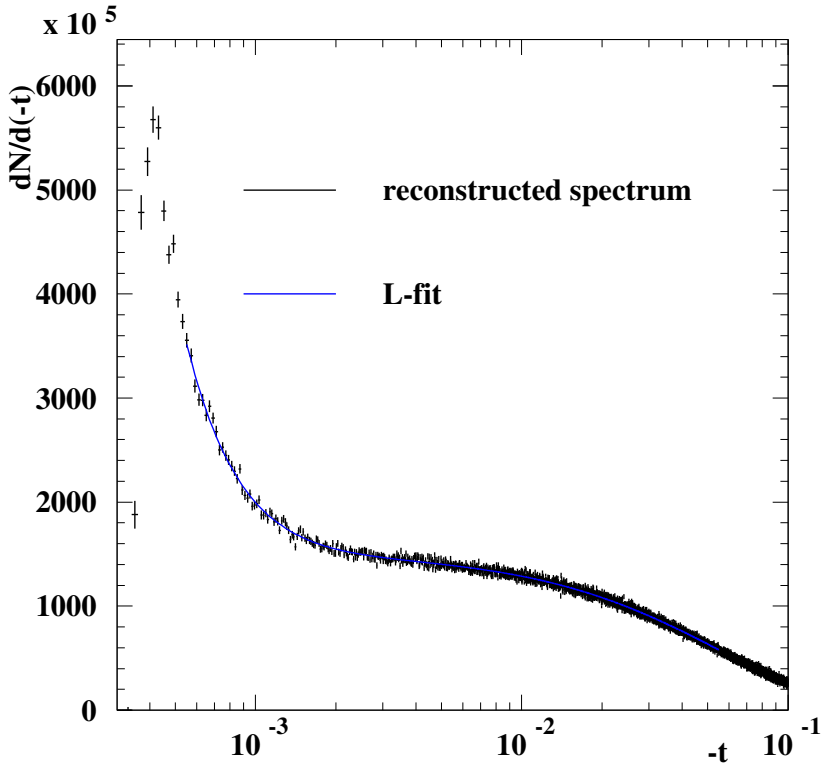

Figure 7: Simulated t-spectrum after reconstruction by the ATLAS ALFA detector compared to the fit yielding the absolute luminosity calibration.

[4] N. Amos *et al.*, E710 Collaboration, Phys. Rev. Lett. **B68** (1992) 192.
[5] F. Abe *et al.*, CDF Collaboration, Phys. Rev. **D50**, (1994) 5518.
[6] F. Abe *et al.*, CDF Collaboration, Phys. Rev. **D50**, (1994) 5550.
[7] C. Da Via *et al.*, Nucl. Instrum. Meth. **A323** (1992) 419.
[8] C. Avila *et al.*, E811 Collaboration, Phys. Lett. **B445** (1999) 419.
[9] C. Avila *et al.*, E811 Collaboration, Phys. Lett. **B537** (2002) 41.
[10] G. Anelli *et al.*, TOTEM technical design report, CERN/LHCC/2004-002.
[11] G. Anelli *et al.*, TOTEM Collaboration, JINST **3** S08007.
[12] G. Aad *et al.*, ATLAS Collaboration, JINST **3** S08003.
[13] ATLAS ALFA technical design report, ATLAS Collaboration, CERN/LHCC/2008-004

Small-x Evolution of Structure Functions in the Next-to-Leading Order

Giovanni A. Chirilli

Physics Dept, Old Dominion Univ., Norfolk, VA 23529, and
Theory Group, JLab, 12000 Jefferson Ave, Newport News, VA 23606
E-mail: chirilli@jlab.org

DOI: http://dx.doi.org/10.3204/DESY-PROC-2009-03/Chirilli

The high-energy behavior of amplitudes in gauge theories can be reformulated in terms of the evolution of Wilson-line operators. In the leading order this evolution is governed by the non-linear Balitsky-Kovchegov (BK) equation. In QCD the NLO kernel has both conformal and non-conformal parts. To separate the conformally invariant effects from the running-coupling effects, we calculate the NLO evolution of the color dipoles in the conformal $\mathcal{N} = 4$ SYM theory, then we define the "composite dipole operator", and the resulting Möbius invariant kernel for this operator agrees with the forward NLO BFKL calculation.

1 Small-x_B evolution of color dipoles

The high-energy scattering processes in a gauge theory can be described in terms of Wilson lines - infinite gauge factors ordered along the straight lines (see e.g. the review [2]). The fast particle moves along its straight-line classical trajectory and the only quantum effect is the eikonal phase factor acquired along this propagation path. In QCD, for high energy scattering of quark or gluon off some hadronic target, this eikonal phase factor is a Wilson line which is an infinite gauge link ordered along the straight line collinear to particle's velocity n^μ:

$$U^\eta(x_\perp) = \mathrm{Pexp}\Big\{ig\int_{-\infty}^{\infty} du\; n_\mu\; A^\mu(un + x_\perp)\Big\} \tag{1}$$

Here A_μ is the gluon field of the target, $x_\perp$ is the transverse position of the particle which remains unchanged throughout the collision, and the index η is the rapidity of the particle.

To obtain the high-energy behavior of QCD amplitudes we study the evolution of color dipoles. Let us consider the small-x behavior of structure functions of deep inelastic scattering (DIS). At high energies the virtual photon decomposes into quark and antiquark pair which propagate along the straight lines separated by transverse distance and form a color dipole - two-Wilson-line operator.

$$\hat{\mathcal{U}}^\eta(x_\perp, y_\perp) = 1 - \frac{1}{N_c}\mathrm{tr}\{\hat{U}^\eta(x_\perp)\hat{U}^{\dagger\eta}(y_\perp)\} \tag{2}$$

The energy dependence of the structure function is then translated into the dependence of the color dipole on the rapidity η. There are two ways to restrict the rapidity of Wilson lines: one can consider Wilson lines with the support line collinear to the velocity of the fast-moving particle or one can take the light-like Wilson line and cut the rapidity integrals "by hand". While the former method appears to be more natural, it is technically simpler to get the conformal results with the latter method of "rigid cutoff" in the longitudinal direction.

Thus, the small-x behavior of the structure functions is governed by the rapidity evolution of color dipoles [3, 4]. At relatively high energies and for sufficiently small dipoles we can use the leading logarithmic approximation (LLA) where $\alpha_s \ll 1,\ \alpha_s \ln x_B \sim 1$ and get the non-linear BK evolution equation for the color dipoles [5, 6]:

$$\frac{d}{d\eta}\,\hat{\mathcal{U}}^\eta(z_1,z_2) \;=\; \frac{\alpha_s N_c}{2\pi^2}\int d^2z_3\;\frac{z_{12}^2}{z_{13}^2 z_{23}^2}[\hat{\mathcal{U}}^\eta(z_1,z_3)+\hat{\mathcal{U}}^\eta(z_3,z_2)) \\ -\hat{\mathcal{U}}^\eta(z_1,z_3)-\hat{\mathcal{U}}^\eta(z_1,z_3)\hat{\mathcal{U}}^\eta(z_3,z_2)] \tag{3}$$

where $\eta = \ln\frac{1}{x_B}$ and $z_{12} \equiv z_1 - z_2$ etc. (As usual, we denote operators by "hat"). The first three terms correspond to the linear BFKL evolution [7] and describe the parton emission while the last term is responsible for the parton annihilation. For sufficiently low x_B the parton emission balances the parton annihilation so the partons reach the state of saturation [8] with the characteristic transverse momentum Q_s growing with energy $1/x_B$ (for a review, see [9])

It is easy to see that the BK equation (3) is conformally invariant in the two-dimensional space. This follows from the conformal invariance of the light-like Wilson lines. Indeed, the Wilson line

$$U(x_\perp) \;=\; \mathrm{Pexp}\left\{ig\int_{-\infty}^{\infty} dx^+\; A_+(x^+,x_\perp)\right\} \tag{4}$$

is invariant under the inversion $x^\mu \to x^\mu/x^2$ (with respect to the point with zero (-) component). Indeed, $(x^+,x_\perp)^2 = -x_\perp^2$ so after the inversion $x_\perp \to x_\perp/x_\perp^2$ and $x^+ \to x^+/x_\perp^2$ and therefore

$$U(x_\perp) \;\to\; \mathrm{Pexp}\left\{ig\int_{-\infty}^{\infty} d\frac{x^+}{x_\perp^2}\; A_+(\frac{x^+}{x_\perp^2},x_\perp)\right\} \;=\; U(x_\perp/x_\perp^2) \tag{5}$$

It is easy to check that the Wilson line operators lie in the standard representation of the conformal Möbius group SL(2,C) with conformal spin 0.

2 NLO evolution of color dipoles

The NLO evolution of color dipole in QCD [10] is not expected to be Möbius invariant due to the conformal anomaly leading to dimensional transmutation and running coupling constant. However, the NLO BK equation in QCD [10] has an additional term violating Möbius invariance and not related to the conformal anomaly. To understand the relation between the high-energy behavior of amplitudes and Möbius invariance of Wilson lines, it is instructive to consider the conformally invariant $\mathcal{N} = 4$ super Yang-Mils theory. This theory was intensively studied in recent years due to the fact that at large coupling constants it is dual to the IIB string theory in the AdS_5 background. In the light-cone limit, the contribution of scalar operators to Maldacena-Wilson line [11] vanishes so one has the usual Wilson line constructed from gauge fields and therefore the LLA evolution equation for color dipoles in the $\mathcal{N} = 4$ SYM has the

same form as (3). At the NLO level, the contributions from gluino and scalar loops enter the picture.

As we mentioned above, formally the light-like Wilson lines are Möbius invariant. Unfortunately, the light-like Wilson lines are divergent in the longitudinal direction and moreover, it is exactly the evolution equation with respect to this longitudinal cutoff which governs the high-energy behavior of amplitudes. At present, it is not known how to find the conformally invariant cutoff in the longitudinal direction. When we use the non-invariant cutoff we expect, as usual, the invariance to hold in the leading order but to be violated in higher orders in perturbation theory. In our calculation we restrict the longitudinal momentum of the gluons composing Wilson lines, and with this non-invariant cutoff the NLO evolution equation in QCD has extra non-conformal parts not related to the running of coupling constant. Similarly, there will be non-conformal parts coming from the longitudinal cutoff of Wilson lines in the $\mathcal{N}=4$ SYM equation. In [1] we demonstrate that it is possible to construct the "composite conformal dipole operator" (order by order in perturbation theory) which mimics the conformal cutoff in the longitudinal direction so the corresponding evolution equation has no extra non-conformal parts. This is similar to the construction of the composite renormalized local operator in the case when the UV cutoff does not respect the symmetries of the bare operator - in this case the symmetry of the UV-regularized operator is preserved order by order in perturbation theory by subtraction of the symmetry-restoring counterterms.

Let us present our result for the NLO evolution of the color dipole in the adjoint representation (hereafter we use notations $z_{ij}\equiv z_i-z_j$ and $(T^a)_{bc}=-if^{abc}$)

$$
\begin{aligned}
&\frac{d}{d\eta}\big[\mathrm{Tr}\{\hat U^\eta_{z_1}\hat U^{\dagger\eta}_{z_2}\}\big]^{\mathrm{conf}} \qquad (6)\\
&= \frac{\alpha_s}{\pi^2}\int d^2z_3\,\frac{z_{12}^2}{z_{13}^2z_{23}^2}\Big[1-\frac{\alpha_sN_c}{4\pi}\frac{\pi^2}{3}\Big]\big[\mathrm{Tr}\{T^a\hat U^\eta_{z_1}\hat U^{\dagger\eta}_{z_3}T^a\hat U_{z_3}\hat U^{\dagger\eta}_{z_2}\}-N_c\mathrm{Tr}\{\hat U^\eta_{z_1}\hat U^{\dagger\eta}_{z_2}\}\big]^{\mathrm{conf}}\\
&-\frac{\alpha_s^2}{4\pi^4}\int d^2z_3d^2z_4\frac{z_{12}^2}{z_{13}^2z_{24}^2z_{34}^2}\Big\{2\ln\frac{z_{12}^2z_{34}^2}{z_{14}^2z_{23}^2}+\Big[1+\frac{z_{12}^2z_{34}^2}{z_{13}^2z_{24}^2-z_{14}^2z_{23}^2}\Big]\ln\frac{z_{13}^2z_{24}^2}{z_{14}^2z_{23}^2}\Big\}\\
&\times\mathrm{Tr}\{[T^a,T^b]\hat U^\eta_{z_1}T^{a'}T^{b'}\hat U^{\dagger\eta}_{z_2}+T^bT^a\hat U^\eta_{z_1}[T^{b'},T^{a'}]\hat U^{\dagger\eta}_{z_2}\}[(\hat U^\eta_{z_3})^{aa'}(\hat U^\eta_{z_4})^{bb'}-(z_4\to z_3)]
\end{aligned}
$$

where

$$
\begin{aligned}
\big[\mathrm{Tr}\{\hat U^\eta_{z_1}\hat U^{\dagger\eta}_{z_2}\}\big]^{\mathrm{conf}} &= \mathrm{Tr}\{\hat U^\eta_{z_1}\hat U^{\dagger\eta}_{z_2}\}+\frac{\alpha_s}{2\pi^2}\int d^2z_3\,\frac{z_{12}^2}{z_{13}^2z_{23}^2}[\mathrm{Tr}\{T^n\hat U^\eta_{z_1}\hat U^{\dagger\eta}_{z_3}T^n\hat U^\eta_{z_3}\hat U^{\dagger\eta}_{z_2}\}\\
&\qquad -N_c\mathrm{Tr}\{\hat U^\eta_{z_1}\hat U^{\dagger\eta}_{z_2}\}]\ln\frac{az_{12}^2}{z_{13}^2z_{23}^2} \qquad (7)
\end{aligned}
$$

is the "composite dipole" with the conformal longitudinal cutoff in the next-to-leading order and a is an arbitrary dimensional constant. In fact, $a(\eta)=ae^\eta$ plays the same role for the rapidity evolution as μ^2 for the usual DGLAP evolution: the derivative $\frac{d}{da}$ gives the evolution equation (6). The kernel in the r.h.s. of Eq. (6) is obviously Möbius invariant since it depends on two four-point conformal ratios $\frac{z_{13}^2z_{24}^2}{z_{14}^2z_{23}^2}$ and $\frac{z_{12}^2z_{34}^2}{z_{13}^2z_{24}^2}$. In [1] we also demonstrate that Eq. (6) agrees with forward NLO BFKL calculation of Ref. [12].

3 Acknowledgments

This work was supported by DOE grant DE-FG02-97ER41028 and by the Jefferson Lab Graduate Fellowship. The author thanks the organizers for the warm hospitality received during this conference.

References

[1] I. Balitsky and G.A. Chirilli, arXiv:0903.5326 [hep-ph].

[2] I. Balitsky, *"High-Energy QCD and Wilson Lines"*, In *Shifman, M. (ed.): At the frontier of particle physics, vol. 2*, p. 1237-1342 (World Scientific, Singapore,2001) [hep-ph/0101042]

[3] A.H. Mueller, *Nucl. Phys.* **B415**, 373 (1994); A.H. Mueller and Bimal Patel, *Nucl. Phys.* **B425**, 471 (1994).

[4] N.N. Nikolaev and B.G. Zakharov, *Phys. Lett.* **B 332**, 184 (1994); *Z. Phys.* **C64**, 631 (1994); N.N. Nikolaev B.G. Zakharov, and V.R. Zoller, *JETP Letters* **59**, 6 (1994).

[5] I. Balitsky, *Nucl. Phys.* **B463**, 99 (1996); *"Operator expansion for diffractive high-energy scattering"*, [hep-ph/9706411];

[6] Yu.V. Kovchegov, *Phys. Rev.* **D60**, 034008 (1999); *Phys. Rev.* **D61**,074018 (2000).

[7] V.S. Fadin, E.A. Kuraev, and L.N. Lipatov, *Phys. Lett.* **B 60**, 50 (1975); I. Balitsky and L.N. Lipatov, *Sov. Journ. Nucl. Phys.* **28**, 822 (1978).

[8] L.V. Gribov, E.M. Levin, and M.G. Ryskin, *Phys. Rept.* **100**, 1 (1983), A.H. Mueller and J.W. Qiu, *Nucl. Phys.* **B268**, 427 (1986); A.H. Mueller, *Nucl. Phys.* **B335**, 115 (1990).

[9] E. Iancu and R. Venugopalan , In *Hwa, R.C. (ed.) et al.: Quark gluon plasma* 249-3363, [e-Print: hep-ph/0303204];
H. Weigert , *Prog.Part.Nucl.Phys.***55**, 461(2005);
J. Jalilian-Marian and Yu.V. Kovchegov, *Prog.Part.Nucl.Phys.***56**, 104(2006).

[10] I. Balitsky and G.A. Chirilli, *Phys.Rev.***D77**, 014019(2008)

[11] J.M. Maldacena, *Phys.Rev.Lett.* **80**, 4859 (1998).

[12] A.V. Kotikov and L.N. Lipatov, *Nucl. Phys.* **B582**, 19 (2000); *Nucl. Phys.* **B5661**, 19 (2003). Erratum-ibid., **B685**, 405 (2004).

Photon Interactions at Strong Coupling

Edmond Iancu

Institut de Physique Théorique de Saclay, F-91191 Gif-sur-Yvette, France

DOI: http://dx.doi.org/10.3204/DESY-PROC-2009-03/Iancu

After briefly recalling the experimental motivations for studying high energy scattering at strong coupling, as coming from the heavy–ion collisions at RHIC, I will focus on two related topics: (i) a lattice test for strong coupling behaviour in QCD at finite temperature, and (ii) the use of string theory, via the AdS/CFT correspondence, for describing photon interactions (deep inelastic scattering and electron–positron annihilation) at strong coupling. I will emphasize some striking predictions of the strong–coupling scenario, like the absence of pointlike constituents in a hadron wavefunction and the lack of jets in the final state of a hadronic collision.

1 Introduction: Jet quenching at RHIC

Some of the experimental discoveries at RHIC, notably the unexpectedly large medium effects known as elliptic flow and jet quenching, led to the suggestion that the deconfined hadronic matter produced in the intermediate stages of a heavy ion collision behaves like a strongly coupled plasma. The coupling constant $\alpha_s = g^2/4\pi$ in QCD can never become large, because of asymptotic freedom, but it can be of order one at scales of order $\Lambda_{\rm QCD}$, and this might lead to an effectively strong–coupling behavior. It is notoriously difficult to do reliable estimates in QCD when $\alpha_s \simeq 1$, so it has become common practice to look to the $\mathcal{N} = 4$ supersymmetric Yang–Mills (SYM) theory, whose strong coupling regime can be addressed within the AdS/CFT correspondence [1], for guidance as to general properties of strongly coupled plasmas (see the review papers [2, 3, 4]). Since conformal symmetry is an essential property of $\mathcal{N} = 4$ SYM, this theory is probably not a good model for the dynamics in QCD in the vicinity of the deconfinement phase transition ($T \simeq T_c \simeq 200$ MeV), where the conformal anomaly associated with the running of the coupling in QCD is known to be important. But lattice QCD studies [5] also show that the conformal anomaly decreases very fast with increasing T above T_c and becomes unimportant for temperatures $T \gtrsim 2T_c$. Hence, there is a hope that, within the intermediate range of temperatures at $2T_c \lesssim T \lesssim 5T_c$, which is the relevant range for the phenomenology of heavy ion collisions at RHIC and LHC, the dynamics in QCD may be at least qualitatively understood by analogy with $\mathcal{N} = 4$ SYM theory at strong coupling.

The most intriguing among the RHIC data are those referring to *jet quenching*, *i.e.*, the energy loss and the transverse momentum broadening for a relatively 'hard' probe — a heavy and/or energetic quark or lepton, with transverse momentum of a few GeV —, for which one would naively expect a weak–coupling behavior, because of the asymptotic freedom of QCD. Yet, perturbative QCD seems to be unable to explain the strong suppression of particle production in Au+Au collisions, as shown in Fig. 1 (the left figure). Namely, the ratio R_{AA} between the particle yield in Au+Au collisions and that in p+p collisions rescaled by the number

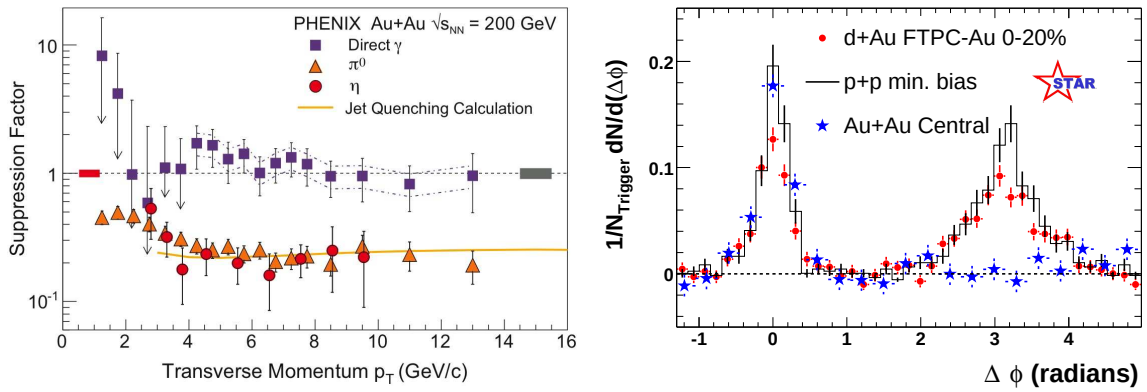

Figure 1: *Left: The ratio R_{AA} of measured versus expected yield of various particles (π^0, η, γ) in Au+Au collisions at $\sqrt{s_{\rm NN}} = 200$ GeV as function of the transverse momentum p_T (RHIC, PHENIX collaboration). Right: Azimuthal correlations for jet measurements at RHIC (STAR collaboration) in p+p, d+Au, and Au+Au collisions.*

of participants would be one if a nucleus–nucleus collision was the incoherent superposition of collisions between the constituents nucleons of the two incoming nuclei. But the RHIC measurements show that R_{AA} is close to one only for direct photon production, whereas for hadron production it is close to 0.2. This suggests that, after being produced through a hard scattering, the partonic jets are somehow absorbed by the surrounding medium.

Additional evidence in that sense comes from studies of jets, cf. Fig. 1 right. A high–energy proton–proton (or electron–positron) collision generally produces a pair of partons whose subsequent evolution (via fragmentation and hadronisation) leaves two jets of hadrons which propagate back–to–back in the center of mass frame. Hence, the distribution of the final state radiation w.r.t. the azimuthal angle $\Delta\Phi$ shows two pronounced peaks, at $\Delta\Phi = 0$ and π; this is the curve denoted as 'p+p min. bias' in Fig. 1 right. A similar distribution is seen in deuteron–gold collisions, but not in central Au+Au collisions, where the peak at $\Delta\Phi = \pi$ has disappeared, as shown by the respective RHIC data in Fig. 1 right. It is then natural to imagine that the hard scattering producing the jets has occurred near the edge of the interaction region, so that the near side jet has escaped to the detector, while the away side jet has been absorbed within the medium.

One should nevertheless keep in mind that this phenomenology is quite difficult and not devoid of ambiguities: strong assumptions are necessary in order to compute the energy loss of, say, a heavy quark in the medium, and also to extract its value from the RHIC data.

2 A lattice test of the coupling strength in QCD

In view of the experimental difficulties, it is natural to ask whether lattice gauge theory can illuminate this question. In what follows, we shall describe a recent proposal in that sense [6], which involves the lattice measurement of leading–twist operators. These are the operators with spin n, classical dimension $d = n + 2$, and twist $t = d - n = 2$, which in the weak coupling regime control the operator product expansion (OPE) of deep inelastic scattering (DIS) at

large photon virtuality Q^2 [7]. There are two infinite sequences of leading–twist operators — the fermionic ones and the gluonic ones — among which we only show here those with $n = 2$:

$$\mathcal{O}_f^{\mu\nu} \,\equiv\, \frac{1}{2}\,\bar{q}\big(\gamma^\mu iD^\nu + \gamma^\nu iD^\mu\big)q\,, \tag{1}$$

(the sum over quark flavors is implicit and we neglect the quark masses) and

$$\mathcal{O}_g^{\mu\nu} \,\equiv\, -F_a^{\mu\alpha}F_\alpha^{\nu,a} \,+\, \frac{1}{4}\,g^{\mu\nu}F_a^{\alpha\beta}F^a_{\alpha\beta}\,. \tag{2}$$

These two operators are recognized as the energy–momentum tensors for quarks and gluons, respectively. More generally, the hadron expectation values of the spin–n leading–twist operators measure the $(n-1)$–th moment of the longitudinal momentum fraction carried by the quark and gluon constituents of that hadron.

Being composite, these operators are well defined only with a renormalization prescription, and thus implicitly depend upon the renormalization scale Q^2. Physically, this dependence expresses the fact that quantum fields can radiate and their internal structure in terms of 'bare' quanta depends upon the resolution scale Q^2 at which one probes this structure.

For instance, the success of the valence parton model for high–energy scattering in QCD is deeply related to the asymptotic freedom property of QCD. This property guarantees that parton branching at $Q^2 \gg \Lambda^2_{\rm QCD}$ is controlled by weak coupling, via the bremsstrahlung process. This in turn favors the emission of 'soft' and 'collinear' quanta, *i.e.* quanta which carries only a small fraction x of the longitudinal momenta of their parent partons and relatively small transverse momenta. Hence, although there are many small–x gluons in the proton wavefunction at high energy, most of the proton longitudinal momentum is still carried by the point–like valence quarks.

By contrast, at strong coupling one expects parton branching to be 'quasi democratic' : the energy of the parent parton is quasi equally shared by the daughter partons, so that all partons will cascade down to low–momentum constituents [8, 9, 10]. At finite temperature, it is natural to assume that the branchings have taken place between the temperature scale T and the "hard" resolution scale Q, with $Q \gg T$, at which the operator is evaluated. Hence, although there is in principle no contradiction in having a quasiparticle picture for a strongly–coupled plasma on the thermal scale T (as shown by the similarity between the strong–coupling and, respectively, zero–coupling results for the entropy density of the $\mathcal{N} = 4$ SYM plasma [1]), one expects these 'quasiparticles' to be highly composite, without a pointlike core carrying a significant fraction of the quasiparticle energy.

These physical considerations find a precise mathematical expression in the renormalization group equations describing the evolution of the leading–twist operators with the resolution scale μ^2. Up to operator mixing issues to which we shall return in a moment, these equations read

$$\mu^2\frac{\mathrm{d}}{\mathrm{d}\mu^2}\,\mathcal{O}^{(n)} \,=\, \gamma^{(n)}\mathcal{O}^{(n)} \quad\Longrightarrow\quad \frac{\mathcal{O}^{(n)}(Q^2)}{\mathcal{O}^{(n)}(\mu_0^2)} \,=\, \exp\left\{\int_{\mu_0^2}^{Q^2}\frac{\mathrm{d}\mu^2}{\mu^2}\,\gamma^{(n)}(\mu^2)\right\}, \tag{3}$$

for a generic spin–n operator $\mathcal{O}^{(n)}$. Here $\gamma^{(n)}$ is the corresponding anomalous dimension and is strictly negative — meaning that the evolution increases the number of partons with small longitudinal momentum fraction x while decreasing that of the partons with larger x —, except

for the total energy–momentum operator

$$T^{\mu\nu} \,=\, \mathcal{O}_f^{\mu\nu} \,+\, \mathcal{O}_g^{\mu\nu}\,, \tag{4}$$

which has zero anomalous dimension since it is a conserved quantity (and hence it does not depend upon the resolution scale Q^2). Hence, in the continuum limit $Q^2 \to 0$, the expectation values of all the leading–twist operators except for T must vanish. But the rate of this evolution is very different at weak and respectively strong coupling.

`(i) Weak coupling :` To lowest order in the running coupling, one has

$$\gamma^{(n)}(\mu^2) \,=\, -a^{(n)}\,\frac{\alpha_s(\mu^2)}{4\pi} \quad\Longrightarrow\quad \frac{\mathcal{O}^{(n)}(Q^2)}{\mathcal{O}^{(n)}(\mu_0^2)} \,=\, \left[\frac{\ln(\mu_0^2/\Lambda^2_{\rm QCD})}{\ln(Q^2/\Lambda^2_{\rm QCD})}\right]^{a^{(n)}/b_0}\,, \tag{5}$$

with $\alpha_s(\mu^2) = 4\pi/[b_0 \ln(\mu^2/\Lambda^2_{\rm QCD})]$, $b_0 = (11N_c - 2N_f)/3$, and $a^{(n)} > 0$. Thus, the perturbative evolution is rather slow — merely logarithmic.

`(ii) Strong coupling & conformal field theory :` At strong coupling, direct calculations in QCD are not possible anymore, but we shall use the corresponding results for $\mathcal{N} = 4$ SYM as a hint towards what could be the behavior in QCD in such a strong–coupling scenario. In a conformal field theory, $\gamma^{(n)}$ is scale–independent and negative (with the exception of $T^{\mu\nu}$, of course), so the evolution is power–like:

$$\frac{\mathcal{O}^{(n)}(Q^2)}{\mathcal{O}^{(n)}(\mu_0^2)} \,=\, \left[\frac{\mu_0^2}{Q^2}\right]^{|\gamma^{(n)}|}\,. \tag{6}$$

Moreover, AdS/CFT predicts that, at strong coupling $\lambda \equiv g^2 N_c \gg 1$, all the non–zero anomalous dimensions are very large $|\gamma^{(n)}| \sim \lambda^{1/4}$ [11], hence the leading–twist operators rapidly die away with increasing Q^2 (meaning that all partons have fallen down to small values of x). In particular, the DIS structure functions at strong coupling are controlled by $T^{\mu\nu}$ together with protected higher–twist operators which have zero anomalous dimensions [8].

These results suggest that a natural way to measure the strength of the coupling in QCD at finite temperature is to compute thermal expectation values of leading–twist operators in lattice QCD [6]. These operators evolve from the natural physical scale T up to the resolution scale Q set by the lattice spacing: $Q = a^{-1}$. In practice, the ratio $Q/T = aT$ is not very large, $Q/T \lesssim 10$, so if the evolution is perturbative, cf. (5), the expectation value of an unprotected operator is only slightly reduced. On the other hand, if the plasma is effectively strongly coupled at the scale T, than at least the early stages of the evolution (say from the scale T up to an intermediate scale $\mu \approx$ a few times T) should involve a large negative anomalous dimension, leading to a strong suppression in the expectation value measured at the final scale Q.

The previous argument applies to the unprotected operators, which include all the higher–spin operators with $n \geq 4$. Unfortunately, however, it turns out that it is very difficult, if not impossible, to accurately measure on the lattice such high–spin operators. There is another possibility, though, which should be easier in practice: this is to measure the linear combination of the spin–2 operators in Eqs. (1)–(2) which is orthogonal to $T^{\mu\nu}$ within the renormalization flow and therefore has a non–zero, and negative, anomalous dimension. There is however a serious problem with this proposal too: finding the proper orthogonal contribution requires the knowledge of the relevant anomalous dimensions, which in full QCD are computable only in perturbation theory, and hence at weak coupling.

Fortunately, there is a simpler version of the theory where the identification of this operator becomes possible for any value of the coupling: this is *quenched* QCD. Loosely speaking, this is the theory obtained from QCD after removing all the quark loops. On the lattice, this is non–perturbatively defined by removing the fermionic determinant from the QCD action. Note that the quark fields are still present in this theory, but only as external probes. As argued in Ref. [6], $\mathcal{O}_f^{\mu\nu}$ is the operator orthogonal to $T^{\mu\nu}$ in quenched QCD. Indeed, in quenched QCD, a quark can emit gluons, but the emitted gluons, as well as those from the thermal bath, are not allowed to emit quark–antiquark pairs. Hence, when the system is probed on a sufficiently hard scale, most of the total energy appears in the gluon fields. In the continuum limit, the total energy–momentum tensor reduces to its gluonic component: $T^{\mu\nu} \to \mathcal{O}_g^{\mu\nu}(Q^2)$ as $Q^2 \to \infty$.

To summarize, the proposal made in Ref. [6] is to measure the thermal expectation value $\langle \mathcal{O}_f^{00}(Q^2)\rangle_T$ of the quark energy density in lattice quenched QCD, for a temperature $T = 2T_c \simeq 600$ MeV and for an inverse lattice spacing $Q = a^{-1} \simeq 8T$. If the deviation from the corresponding result for the ideal Fermi–Dirac gas turns out to be relatively small, $\lesssim 30\%$, then one can conclude that the QCD plasma is weakly coupled at the scale T. If on the other hand the lattice result turns out to be considerably smaller, then there must be a regime in μ around T where QCD is effectively strongly coupled. Simple estimates together with the RHIC phenomenology of jet quenching suggest that a suppression by a factor of 5 could be expected in the strong–coupling scenario [6].

3 DIS and parton saturation at strong coupling

The previous discussion has emphasized the importance of understanding parton evolution at strong coupling. The OPE provides a valuable tool in that sense [8], but this applies only for sufficiently large Q^2 — where it teaches us that, at strong coupling, the partons disappear through branching — and thus it cannot tell us what is the final fate of these partons, after cascading down to lower momenta. In particular, this is inappropriate to study the unitarity corrections to scattering at high energy. Fortunately, the gauge/string duality also allows us to directly compute the cross–sections for elementary processes, with results which shed further light on the parton evolution at strong coupling [3, 4, 8, 9, 10, 12].

The simplest version of the formalism, known as the 'supergravity approximation', is obtained by taking the large–N_c limit, or, equivalently, the large 't Hooft coupling limit: $\lambda = g^2 N_c \to \infty$ with g fixed and small ($g \ll 1$). This is generally not a good limit to study a scattering process, since the corresponding amplitude is suppressed as $1/N_c^2$ [8, 9], yet it is meaningful for processes taking place in a deconfined plasma, like those of interest for heavy ion physics: indeed, the plasma involves N_c^2 degrees of freedom per unit volume, thus yielding finite amplitudes when $N_c \to \infty$. In this limit, the $\mathcal{N} = 4$ SYM plasma at finite temperature is described as a black–hole (BH) embedded in AdS_5 and the dynamics reduces to classical gravity in this curved space–time [1, 2, 3, 4]. This BH is homogeneous in the physical 4 dimensions[1], so like the plasma that is it dual to, but it has an horizon in the radial, or 'fifth', dimension of AdS_5, at a position which is determined by the temperature of the plasma.

The AdS_5 BH geometry is illustrated in Fig. 2, which also shows the supergravity process dual to DIS off the $\mathcal{N} = 4$ SYM plasma: A space–like virtual photon, with 4–momentum $q^\mu = (\omega, 0, 0, q)$ and virtuality $Q^2 \equiv q^2 - \omega^2 \gg T^2$, acts as a perturbation on the Minkowski

[1] More recently, a finite–length plasma 'slice' has been considered too, as a model for a nucleus which admits a simple supergravity dual (a 'shockwave') [13].

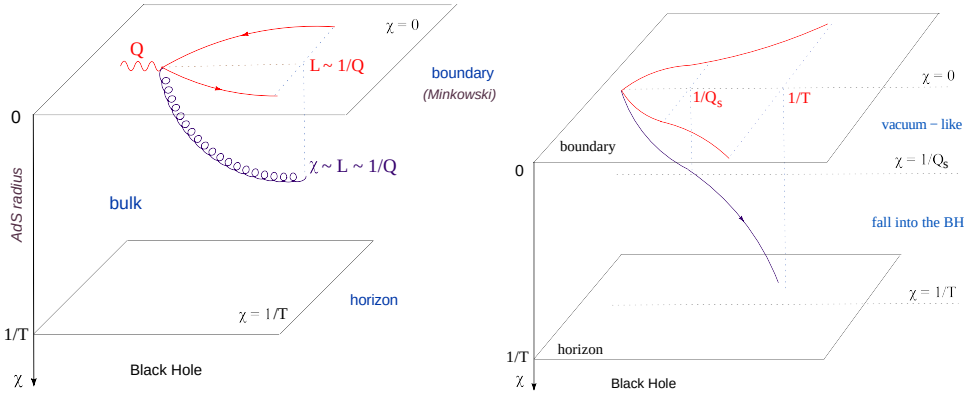

Figure 2: *Space–like current in the plasma: the trajectory of the wave packet in AdS_5 and its 'shadow' on the boundary. Left: the low energy case — the Maxwell wave gets stuck near the boundary up to tunnel effect. Right: the high energy case — the wave has an accelerated fall into the BH.*

boundary of AdS_5 ($\chi = 0$), thus inducing a massless, vector, supergravity field A_m (with $m = \mu$ or χ) which propagates within the bulk of AdS_5 ($\chi > 0$), according to the Maxwell equations in curved space–time:

$$\partial_m\big(\sqrt{-g}g^{mp}g^{nq}F_{pq}\big) \,=\, 0\,, \qquad \text{where} \quad F_{mn} = \partial_m A_n - \partial_n A_m\,. \tag{7}$$

Here, g^{mn} is the metric tensor in 5–dimensions which in particular contains the information about the BH horizon at $\chi = 1/T$ (we follow the conventions in [3]). Thus (7) describes the gravitational interaction between the Maxwell field A_m and the BH. The strength of this interaction is proportional to the product $\omega^2 T^4$ between the energy densities in the two interacting systems — the virtual photon and the plasma. Interestingly, there is a threshold value for this quantity, of order Q^6, below which there is essentially no interaction [10]: so long as $\omega T^2 \ll Q^3$, the Maxwell wave is stuck within a distance $\chi \lesssim 1/Q \ll 1/T$ from the Minkowski boundary and does not 'see' the BH (cf. Fig. 2 left). But for higher energies and/or temperatures, such that $\omega T^2 \gtrsim Q^3$, the wave gets attracted by the BH and eventually falls into it. Physically, this means that the energetic space–like photon is absorbed with probability one into the plasma — the 'black disk limit' for DIS (cf. Fig. 2 right).

This critical value $Q_s \sim (\omega T^2)^{1/3}$, together with the physical picture of the scattering, can be understood with the help of the 'UV/IR correspondance', which relates the 5th dimension of AdS_5 to the momenta (or typical sizes) of the quantum fluctuations which are implicitly integrated out in the boundary gauge theory. Namely, the radial penetration χ of the Maxwell wave packet in AdS_5 is proportional to the transverse size L of the quantum fluctuation of the virtual photon in the dual gauge theory. By the uncertainty principle, we expect an energetic space–like photon with $\omega \simeq q \gg Q$ to fluctuate into a partonic system with transverse size $L \sim 1/Q$ — which indeed matches the radial penetration of the dual Maxwell field, as illustrated in Fig. 2 left — and lifetime $\Delta t \sim \omega/Q^2$. The space–like fluctuation cannot decay into on–shell partons (at least, not in the vacuum), because of energy–momentum conservation. But the situation can change in the presence of the plasma: unlike the photon, which is color neutral, its partonic fluctuation has a dipolar color moment and thus can interact with the plasma. Via such interactions, the partons can acquire the energy and momentum necessary to get on–shell,

and then the fluctuation decays: the space–like photon disappears (cf. Fig. 2 right).

Let us now return to the threshold value $Q_s \sim (\omega T^2)^{1/3}$, to which we shall refer as the *saturation momentum*. The condition $Q \sim Q_s$ can be rewritten as

$$Q \sim \frac{\omega}{Q^2}\, T^2\,, \tag{8}$$

which admits the following interpretation [10] : the scattering becomes strong when the lifetime $\Delta t \sim \omega/Q^2$ of the partonic fluctuation is large enough for the mechanical work $W = \Delta t \times F_T$ done by the *plasma force* $F_T \sim T^2$ acting on these partons becomes sufficient to compensate for the energy deficit Q of the space–like system. This plasma force $F_T \sim T^2$ represents in an average way the effect of the strongly–coupled plasma on color dipole fluctuations and can be viewed as a prediction of the AdS/CFT calculation.

Introducing the Bjorken x variable $x \equiv Q^2/(2\omega T)$ for DIS off the plasma — as usual, this represents the longitudinal momentum fraction of the plasma constituent which absorbs the virtual photon —, one can rewrite the plasma *saturation line* as $Q_s(x) = T/x$ or, alternatively, $x_s(Q) = T/Q$. The AdS/CFT results then suggest a partonic picture for the strongly–coupled plasma [10]. For $Q \gg Q_s(x)$ (or, equivalently, $x \gg x_s(Q)$), the scattering is negligible and the DIS structure function F_2 is exponentially small: $F_2(x, Q^2) \sim \exp\{-Q/Q_s(x)\}$. This shows that there are no pointlike constituents in the strongly coupled plasma, in agreement with the OPE argument in Sect. 2. For $x \lesssim x_s(Q)$, on the other hand, the scattering is maximal and the structure function is found to be large: $F_2(x, Q^2) \sim x N_c^2 Q^2$. This is in agreement with our physical expectation that partons must somehow accumulate at small values of x, as a result of branching, and is moreover consistent with energy–momentum conservation, which requires the integral $\int_0^1 \mathrm{d}x\, F_2(x, Q^2)$ to have a finite limit as $Q^2 \to \infty$ [7]. The previous results imply

$$\int_0^1 \mathrm{d}x\, F_2(x, Q^2) \;\simeq\; x_s F_2(x_s, Q^2) \;\sim\; N_c^2 T^2\,, \tag{9}$$

where the integral is dominated by $x \simeq x_s(Q)$: the energy and momentum of the plasma as probed on a 'hard'resolution scale $Q^2 \gg T^2$ is fully carried by the partons 'along the saturation line', *i.e.*, those having $x \simeq T/Q$. A similar picture holds for other hadronic targets so like a 'glueball' [8, 9] or a 'nuclear' shockwave [13], but the respective saturation momentum rises slower with $1/x$ than for the infinite plasma: $Q_s^2(x) \propto 1/x$ for a finite–size 'hadron' as opposed to $Q_s^2(x) \propto 1/x^2$ for the plasma. The additional factor $1/x$ in the case of the plasma comes from the lifetime $\Delta t \sim \omega/Q^2 \sim 1/xT$ of the partonic fluctuation: since the medium is infinite, the effects of the scattering accumulate all the way along the parton lifetime.

4 High–energy scattering at strong coupling

The parton picture at strong coupling as just described has some striking physical consequences for the high–energy scattering problem which are vastly different from everything that we know about the corresponding problem in real–life QCD. For instance, the rapid energy growth $Q_s^2(x) \propto 1/x$ of the saturation momentum, which is automatic in this gravity context, is much faster than the respective growth observed in the HERA data, namely $Q_s^2 \sim 1/x^\omega$ with $\omega \simeq 0.2 \div 0.3$, and which is in fact well accounted for by perturbative QCD [14]. Also, the absence of large–x partons in a hadronic wavefunction at strong coupling means that, in a hypothetical

scattering between two such hadrons, there would be no hard particle production at either forward or backward rapidities: the two nuclei colliding with each other at strong coupling would fully stop each other [15]. This is in sharp contrast to the situation at RHIC, where the large–x partons from the incoming nuclei are seen to emerge from the collision, as hadronic jets, along their original trajectories ('leading baryons').

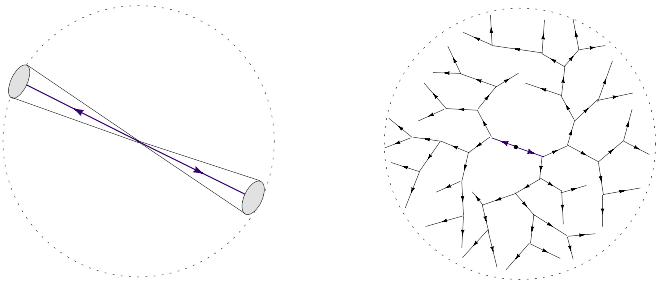

Figure 3: *Final state in e^+e^- annihilation. Left: weak coupling. Right: strong coupling.*

Another striking prediction of AdS/CFT is the absence of jets in electron–positron annihilation at strong coupling [10, 12]. Fig. 3 exhibits the typical, 2–jet, final state in e^+e^- annihilation at weak coupling (left) together with what should be the corresponding state at strong coupling (right). In both cases, the final state is produced via the decay of a time–like photon into a pair of partons and the subsequent evolution of this pair. At weak coupling this evolution is rather slow and consists mostly in the emission of soft and collinear gluons, with the result that the leading partons get dressed into a pair of well–collimated jets of hadrons (cf. Fig. 3 left). Multi–jet ($n \geq 3$) events are possible as well, but they have a lower probability, as they require hard parton emissions in the final state, which are suppressed by asymptotic freedom [7]. At strong coupling, on the other hand, parton branching is much more efficient, as previously explained: all splittings are hard and happen very fast, so they rapidly split the original energy over many quanta which carry energies and momenta of the order of the soft, confinement, scale, and which are almost isotropically distributed in space, because of their large number. Thus, the respective final state shown no sign of jets, but only an isotropic distribution of hadronic matter (cf. Fig. 3 right) [12].

Let us finally return to our original motivation for studying the dynamics at strong coupling, which was the propagation of a 'hard probe' through a strongly–coupled plasma. Consider the energy loss by a heavy quark towards the plasma: the respective AdS/CFT calculation has been given in [16], but the result can be also inferred via physical arguments, using the previously explained parton picture at strong coupling [17]. Among the virtual, space–like, quanta which are continuously emitted and reabsorbed by the heavy quark, only those can escape to the plasma which have a virtuality Q lower than the plasma saturation momentum $Q_s(x)$ for a value of x set by the lifetime of the fluctuation: $1/x \sim T\Delta t$ with $\Delta t \sim \omega/Q^2$. Since $\mathrm{d}E/\mathrm{d}t \propto \omega/\Delta t \sim Q^2$, the energy loss is controlled by the fluctuations having the maximal possible value for the virtuality, that is, those having $Q \sim Q_s(x)$ with x set by the rapidity γ of the heavy quark. Using $\gamma = \omega/Q$ and $Q_s \sim T/x \sim \gamma T^2/Q_s$, one finds $Q_s \sim \sqrt{\gamma}T$ and hence

$$-\frac{\mathrm{d}E}{\mathrm{d}t} \simeq \sqrt{\lambda}\,\frac{\omega}{(\omega/Q_s^2)} \simeq \sqrt{\lambda}\,Q_s^2 \sim \sqrt{\lambda}\,\gamma\,T^2\,, \tag{10}$$

where the factor $\sqrt{\lambda}$ enters via the normalization of the Nambu-Goto action and expresses the fact that, at strong coupling, the heavy quark does not radiate just a single quanta per time Δt, but rather a large number $\sim \sqrt{\lambda}$. Eq. (10) is parametrically consistent with the respective AdS/CFT result [16]. Note the strong enhancement of the medium effects at high energy, as expressed by the Lorentz γ factor in the r.h.s of (10): this is in qualitative agreement with the strong suppression of particle production seen in Au+Au collisions at RHIC, but one should be very careful before directly comparing such AdS/CFT results with the QCD phenomenology.

To summarize, the strong–coupling picture of high–energy scattering appears to be very different from everything we know, theoretically and experimentally, about real–life QCD. There are no valence partons, the saturation momentum (and hence the hadronic cross–sections) grow much too fast with increasing energy, and there are no jets in the final state of any kind of collision. This is not necessarily a surprise: within QCD, these high–energy phenomena are controlled by hard momentum exchanges and thus by weak coupling, by virtue of the asymptotic freedom. On the other hand, AdS/CFT might give us some qualitative insight in the semi–hard physics of particle production in heavy ion collisions, and also in some longstanding problems like thermalization and the emergence of hydrodynamics in the late stages of such a collision.

References

[1] O. Aharony, S. S. Gubser, J. M. Maldacena, H. Ooguri, and Y. Oz, "Large N field theories, string theory and gravity", *Phys. Rept.* **323** (2000) 183.

[2] D. T. Son and A. O. Starinets, "Viscosity, Black Holes, and Quantum Field Theory," *Ann. Rev. Nucl. Part. Sci.* **57** (2007) 95, `arXiv:0704.0240 [hep-th]`.

[3] E. Iancu, "Partons and jets in a strongly-coupled plasma from AdS/CFT," *Acta Phys. Polon.* **B39** (2008) 3213, `arXiv:0812.0500 [hep-ph]`.

[4] S. S. Gubser, S. S. Pufu, F. D. Rocha, and A. Yarom, "Energy loss in a strongly coupled thermal medium and the gauge-string duality," `arXiv:0902.4041`.

[5] M. Cheng *et al.*, *Phys. Rev.* **D77** (2008) 014511.

[6] E. Iancu and A. H. Mueller, "A lattice test of strong coupling behaviour in QCD at finite temperature," `arXiv:0906.3175 [hep-ph]`.

[7] M. E. Peskin and D. V. Schroeder, "An Introduction to quantum field theory,". Reading, USA: Addison-Wesley (1995) 842 p.

[8] J. Polchinski and M. J. Strassler, *JHEP* **05** (2003) 012.

[9] Y. Hatta, E. Iancu, A. H. Mueller, *JHEP* **01** (2008) 026.

[10] Y. Hatta, E. Iancu, A. H. Mueller, *JHEP* **01** (2008) 063; *JHEP* **05** (2008) 037.

[11] S. S. Gubser, I. R. Klebanov, A. M. Polyakov, *Nucl. Phys.* **B636** (2002) 99.

[12] D. M. Hofman and J. Maldacena, *JHEP* **05** (2008) 012.

[13] A. H. Mueller, A. I. Shoshi, B.-W. Xiao, *Nucl. Phys.* **A822** (2009) 20; E. Avsar, E. Iancu, L. McLerran, D. N. Triantafyllopoulos, `arXiv:0907.4604 [hep-th]`.

[14] E. Iancu, Nucl. Phys. Proc. Suppl. **191** (2009) 281, `arXiv:0901.0986 [hep-ph]`.

[15] J. L. Albacete, Y. V. Kovchegov, A. Taliotis, *JHEP* **0807** (2008) 100.

[16] C. P. Herzog, A. Karch, P. Kovtun, C. Kozcaz, L. G. Yaffe, *JHEP* **0607** (2006) 013; S. S. Gubser, *Phys. Rev.* **D 74** (2006) 126005.

[17] F. Dominguez, C. Marquet, A. H. Mueller, B. Wu, B. W. Xiao, *Nucl. Phys.***A811** (2008) 197; G. C. Giecold, E. Iancu, A. H. Mueller, *JHEP* **0907** (2009) 033.

Chapter 9

Exclusive Channels and Resonances

Convenors:

L. Szymanowski (Warsaw) and S. Uehara (KEK)

Hard Exclusive Processes: Theoretical Status

Samuel Wallon

LPT, Université Paris-Sud, CNRS, 91405, Orsay, France *&*
UPMC Univ. Paris 06, faculté de physique, 4 place Jussieu, 75252 Paris Cedex 05, France

DOI: http://dx.doi.org/10.3204/DESY-PROC-2009-03/Wallon

We review the descriptions of hard exclusive processes based on QCD factorization.

1 Introduction

Since a decade, there have been much developments in hard exclusive processes, based on collinear factorization. This was initiated by form factors studies more than 30 years ago, leading to the concept of Distribution Amplitudes (DA) [1], which describes the partonic content of a hadron facing an elastic scattering off a hard photonic probe. These DAs were then extended to Generalized Distribution Amplitudes (GDA) [2, 3, 4] in which two or more hadrons are produced. Independently, starting from inclusive DIS which relates Parton Distribution Functions (PDFs) to the discontinuity of the forward $\gamma^* p \to \gamma^* p$ amplitude, it was shown [5, 3] that the partonic interpretation remains valid for the Deep Virtual Compton Scattering (DVCS) amplitude $\gamma^* p \to \gamma\, p$ itself, leading to the concept of Generalized Parton Distributions (GPDs), and to more general exclusive processes studies. In a parallel way, tremendous progresses in experimental facilities (high luminosity beams, improvement of detectors...) opened the way to studies and measures with increasing precision of these non forward matrix elements [6, 7, 8, 9].

2 The illuminating example of $\rho-$electroproduction

DVCS and GPD [10]

The factorization of the DVCS amplitude in the large Q^2 limit follows two steps. First, one should factorize it in momentum space. This can be set up more easily when using the Sudakov decomposition (introducing two light-cone vectors $p_{1(2)}$ $(+(-)$ directions) with $2\, p_1 \cdot p_2 = s$)

$$\begin{array}{ccccccc} k & = & \alpha\, p_1 & + & \beta\, p_2 & + & k_\perp \\ & & + & & - & & \perp \end{array} \tag{1}$$

In the limit $Q^2 \to \infty$, the only component of the momentum k to be kept in the hard blob H is k_- . In particular, this means that the quark-antiquark pair entering H can be considered as being collinear, flying in the direction of the p_2 momentum. Therefore, the amplitude reads

$$\int d^4k\; S(k,\, k+\Delta)\, H(q,\, k,\, k+\Delta) \;=\; \int dk^-\; \int dk^+ d^2k_\perp\, S(k,\, k+\Delta)\; H(q,\, k^-,\, k^- + \Delta^-)\,,$$

as illustrated in Fig.1. The Fierz identity in spinor and color space then shows that the DVCS amplitude completely factorizes, and reads symbolically: $\mathcal{M} = \mathrm{GPD} \otimes \mathrm{Hard\ part}$.

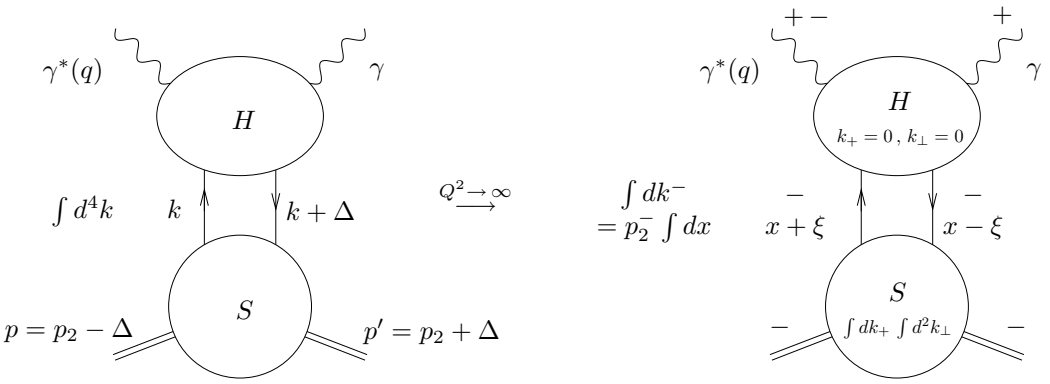

Figure 1: Factorization of the DVCS amplitude in the hard regime. The signs + and − indicate corresponding flows of large momentum components.

ρ−meson production: from the wave function to the DA

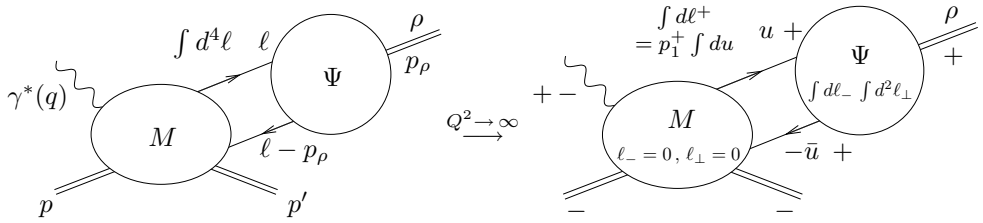

Figure 2: Factorization of the amplitude of hard ρ−electroproduction.

We now replace the produced photon by a ρ−meson, described in QCD by its wave function Ψ which reduces in hard processes to its Distribution Amplitude. As for DVCS, in the limit $Q^2 \to \infty$, the amplitude of diffractive electroproduction of a ρ−meson can be written as

$$\int d^4\ell\ M(q,\,\ell,\,\ell - p_\rho)\,\Psi(\ell,\,\ell - p_\rho)\ = \int d\ell^+ M(q,\,\ell^+,\,\ell^+ - p_\rho^+) \int d\ell^- \int^{|\ell_\perp^2| < \mu_F^2} d^2\ell_\perp\ \Psi(\ell,\,\ell - p_\rho) \quad (2)$$

(see Fig.2). This factorization involves the ρ−wave function integrated over $\ell_\perp$ (and ℓ^-), which is the DA already involved in the partonic description of the hard meson form factor [1].

ρ−meson production: factorization with a GPD and a DA [11]

Combining the previous factorizations, one can describe the hard electroproduction of a ρ−meson in a fully factorized form involving a GPD and a DA, as illustrated in Fig.3. It reads

$$\int d^4k\, d^4\ell\ S(k,\,k+\Delta)\, H(q,\,k,\,k+\Delta)\, \Psi(\ell,\,\ell - p_\rho) = \int dk^- d\ell^+ \quad (3)$$

$$\times \int dk^+ \int^{|k_\perp^2| < \mu_{F_2}^2} d^2k_\perp\, S(k, k+\Delta)\ \ H(q; k^-, k^- + \Delta^-; \ell^+, \ell^+ - p_\rho^+)\ \int d\ell^- \int^{|\ell_\perp^2| < \mu_{F_1}^2} d^2\ell_\perp \Psi(\ell,\,\ell - p_\rho)\,.$$

GPD $F(x,\,\xi,\,t,\,\mu_{F_2}^2)$ Hard part $T(x/\xi, u, \mu_{F_1}^2, \mu_{F_2}^2)$ DA $\Phi(u, \mu_{F_1}^2)$

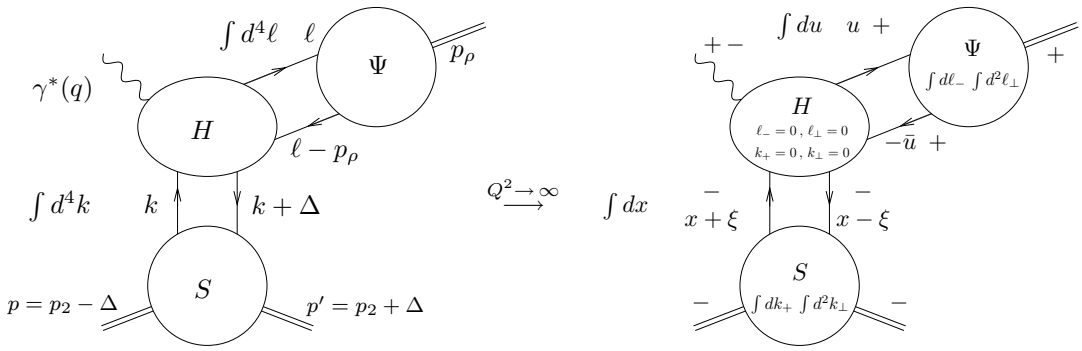

Figure 3: Full factorization of the amplitude of hard electroproduction of a $\rho-$meson.

Chiral-even DA

As discussed above, DAs are obtained from wave functions through $\int d\ell^- \int d^2\ell_\perp$ integration, and thus related to non-local correlators between fields separated by a light-like distance z (along p_2, conjugated to the + direction by Fourier transformation). The vector correlator reads

$$\langle 0|\bar{u}(z)\gamma_\mu d(-z)|\rho^-(P,\lambda)\rangle = f_\rho m_\rho \left[p_\mu \frac{e^{(\lambda)}\cdot z}{p\cdot z}\int_0^1 du\, e^{i(u-\bar{u})p\cdot z}\phi_\parallel(u,\mu_F^2) \right.$$
$$\left. + \quad e_{\perp\mu}^{(\lambda)}\int_0^1 du\, e^{i(u-\bar{u})p\cdot z} g_\perp^{(v)}(u,\mu_F^2) - \frac{1}{2}z_\mu \frac{e^{(\lambda)}\cdot z}{(p\cdot z)^2} m_\rho^2 \int_0^1 du\, e^{i(u-\bar{u})p\cdot z} g_3(u,\mu_F^2)\right]$$

where $\phi_\parallel$, $g_\perp^{(v)}$, g_3 are DAs respectively of twist 2, 3 and 4, with $p = p_1$, $P = p_\rho$. Correspondingly, the axial correlator calls for the introduction of a twist 3 DA, as

$$\langle 0|\bar{u}(z)\gamma_\mu\gamma_5 d(-z)|\rho^-(P,\lambda)\rangle = \frac{1}{2}\left[f_\rho - f_\rho^T \frac{m_u+m_d}{m_\rho}\right] m_\rho\, \epsilon_\mu{}^{\nu\alpha\beta} e_{\perp\nu}^{(\lambda)}\, p_\alpha\, z_\beta \int_0^1 du\, e^{i\xi p\cdot z} g_\perp^{(a)}(u,\mu_F^2)\,.$$

Selection rules and factorization status

Since for massless particle chirality = + (resp. -) helicity for a (anti)particule and based on the fact that QED and QCD vertices are chiral even (no chirality flip during the interaction), one deduces that the total helicity of a $q\bar{q}$ pair produced by a γ^* should be 0. Therefore, the helicity of the γ^* equals $L_z^{q\bar{q}}$ (z projection of the $q\bar{q}$ angular momentum). In the pure collinear limit (i.e. twist 2), $L_z^{q\bar{q}} = 0$, and thus the γ^* is longitudinally polarized. Additionaly, at $t = 0$ there is no source of orbital momentum from the proton coupling, which implies that the helicity of the meson and of the photon should be identical. In the collinear factorization approach, the extension to $t \neq 0$ changes nothing from the hard side, the only dependence with respect to t being encoded in the non-perturbative correlator which defines the GPDs. This implies that the above selection rule remains true. Thus, only 2 transitions are possible (this is called $s-$channel helicity conservation (SCHC)): $\gamma_L^* \to \rho_L$, for which QCD factorization holds at t=2 at any order (i.e. LL, NLL, etc...) [11] and $\gamma_T^* \to \rho_T$, corresponding to twist $t = 3$ at the amplitude level, for which QCD factorization is not proven, an explicit computation [12] at leading order showing in fact that the hard part has end-point singularities like $\int_0^1 du/u$.

Some solutions to factorization breaking?

In order to extend the factorization theorem at higher twist, several solutions have been discussed. First, one may add contributions of 3-parton DAs [13] for ρ_T [14, 15] (of dominant twist equal 3 for ρ_T). This in fact does not solve the problem, while reducing the level of divergency, but is needed for consistency. Next, it was suggested to keep a transverse $\ell_\perp$ dependency in the q, $\bar{q}$ momenta, used to regulate end-point singularities, leading to the Improved Collinear Approximation (ICA). Soft and collinear gluon exchange between the valence quarks are responsible for large double-logarithmic effects which exponentiate. This is made easier when using the impact parameter space $b_\perp$ conjugated to $\ell_\perp$, leading to Sudakov factor

$$\exp[-S(u,b,Q)]\,.$$

S diverges when $b_\perp \sim O(1/\Lambda_{QCD})$ (large transverse separation, i.e. small transverse momenta) or $u \sim O(\Lambda_{QCD}/Q)$ [16]. This regularizes end-point singularities for $\pi \to \pi\gamma^*$ and $\gamma\gamma^* \to \pi^0$ form factors [17]. This perturbative resummation tail effect combined with an ad-hoc non-perturbative gaussian ansatz for the DAs

$$\exp[-a^2\,|k_\perp^2|/(u\bar{u})]\,,$$

which gives back the usual asymptotic DA $6\,u\,\bar{u}$ when integrating over $k_\perp$, provides practical tools for the phenomenology of meson electroproduction [18].

Chiral-odd sector

The $\pm$ chiralities are defined by the decomposition

$$q_\pm(z) \equiv \frac{1}{2}(1 \pm \gamma^5)q(z) \quad \text{with} \qquad q(z) = q_+(z) + q_-(z)\,,$$

implying that $\bar{q}_\pm(z)\gamma^\mu q_\pm(-z)$ or $\bar{q}_\pm(z)\gamma^\mu\gamma^5 q_\pm(-z)$ conserve chirality (chiral-even) while $\bar{q}_\pm(z)\cdot 1\cdot q_\mp(-z)$, $\bar{q}_\pm(z)\cdot\gamma^5\cdot q_\mp(-z)$ or $\bar{q}_\pm(z)[\gamma^\mu,\gamma^\nu]q_\mp(-z)$ change chirality (chiral-odd). In the specific case of ρ, the chiral odd sector involves DAs of twists 2 and 4 for ρ_T and DAs of twist 3 for ρ_L . Correspondingly, chiral-odd 3-partons DAs are of dominant twist equal to 3 for ρ_L [13].

Since QED and QCD are chiral even, chiral-odd objects can only appear in pairs. While the amplitude of ρ_T electroproduction on linearly polarized N vanishes at leading twist 2 (a single gluon exchange between hard lines is not enough to prevent the vanishing of Dirac traces) [19], this vanishing can be avoided [20], for example in the electroproduction of a π^+ and ρ_T^0 pair on a nucleon N [21], the hard scale being provided by the p_T of the produced mesons.

3 Generic results for DAs

Gauge invariance

The non-local correlators $\langle 0|\bar{\Psi}(z)\gamma_\mu\Psi(-z)|\rho\rangle$ are gauge invariant since they should be understood as $\langle 0|\bar{\Psi}(z)\gamma_\mu[z,-z]\Psi(-z)|\rho\rangle$ where $[,]$ is a Wilson line along p_2 . This implies that even at twist 2, gluons are there, although hidden. The Taylor expansion with respect to z involves the covariant derivative $\overleftrightarrow{D_\mu}$. This can be used for studying hard electroproduction of exotic (non $q\bar{q}$ quantum numbers) hybrids mesons $|q\bar{q}g\rangle$ with $J^{PC} = 1^{-+}$ which cannot be described by the quark model. Thus, $\gamma^* p \to H^0 p$ is not suppressed: it is twist 2. The expected

order of magnitude of the cross-section is comparable with ρ-electroproduction [22], with possible tests at JLab and Compass. The same conclusion applies for the process $\gamma\gamma^* \to H^0$ with the advantage of avoiding the mixing with GPDs [23]. Tests should be possible at BaBar, BELLE, BEPC-II. A possible candidate for the neutral hybrid H^0 could be the $\pi_1(1400)$.

Equations of motion

The Dirac equation leads to $\langle i(\overrightarrow{\not{D}}(0)\psi(0))_\alpha\, \bar{\psi}_\beta(z)\rangle = 0$ which, after applying the Fierz decomposition to 2 and 3-parton correlators, implies Equations Of Motion (EOM) relating the various 2 and 3-body DAs.

Renormalization group equations

Back to the factorization (2) or (3) of the process in term of a DA, which symbolically reads

$$\mathcal{M}(Q^2) = \Phi^*(x,\mu_F^2) \otimes T_H(x,Q^2,\mu_F^2)\,, \tag{4}$$

the arbitrariness of the factorization scale μ_F^2 leads to the Efremov-Radyushkin, Brodsky-Lepage equation [24] for the DA $\Phi(u,\,\mu_F^2)$:

$$\mu_F^2 \frac{\partial}{\partial \mu_F^2}\Phi(x,\mu_F^2) = V(x,u,\mu_F^2) \otimes \Phi(u,\mu_F^2)\,.$$

Collinear conformal invariance [25]

The full conformal group $SO(4,2)$ is defined as transformations which only change the scale of the metric. In the limit $Q^2 \to \infty$, hadron states are replaced by a bunch of partons that are collinear to p_1, which thus lives along p_2, implying that z is the only remaining variable. The transformations which map the light-ray in the p_2 direction into itself is the collinear subgroup of the full conformal group $SO(4,2)$, that is $SL(2,\mathbb{R})$, made of translations $z \to z + c$, dilatations $z \to \lambda\, z$ and special conformal transformations $z \to z' = z/(1 + 2\,a\,z)$. The Lie algebra of $SL(2,\mathbb{R})$ is $O(2,1)$. One remaining additional generator commutes with the 3 previous ones: the collinear-twist operator. Interestingly, the light-cone operators which enter the definition of DAs can be expressed in terms of a basis of conformal operators. Since conformal transformations commute with exact EOM (they are not renormalized), EOM can be solved exactly (with an expansion in terms of the conformal spin $n+2$). For example the twist 2 DA for ρ_L can be expressed, for unpredicted $a_n^{\parallel}(\mu)$, as [26]

$$\phi_\parallel(u,\,\mu_0) = 6\,u\,\bar{u}\sum_{n=0}^{\infty} a_n^{\parallel}(\mu)\, C_n^{3/2}(u-\bar{u}) \qquad C_n^{3/2} = \text{Gegenbauer polynomial}\,.$$

Since the Leading Order renormalization of the conformal operators is diagonal in the conformal spin (counterterms are tree level at this accuracy and they thus respect the conformal symetry of the classical theory), this implies that

$$\phi_\parallel(u,\,\mu) = 6\,u\,\bar{u}\sum_{n=0}^{\infty} a_n^{\parallel}(\mu_0)\left(\frac{\alpha_s(\mu)}{\alpha_s(\mu_0)}\right)^{\gamma_n^{(0)}/\beta_0} C_n^{3/2}(u-\bar{u}) \overset{\mu\to\infty}{\longrightarrow} 6\,u\,\bar{u} \text{ asymptotic DA}$$

with the anomalous dimensions

$$\gamma_n^{(0)} = C_F\left(1 - \frac{2}{(n+1)(n+2)} + 4\sum_{m=2}^{n+1}\frac{1}{m}\right).$$

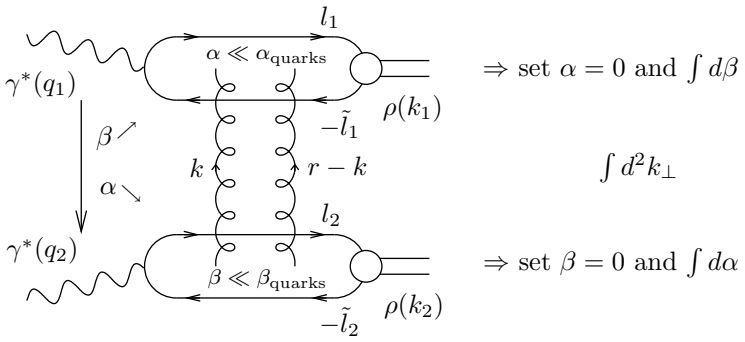

Figure 4: k_T-factorization in the case of $\gamma^*\,\gamma^* \to \rho\,\rho$.

At Next to Leading Order conformal symetry is broken; studying conformal anomalies provides the NLO anomalous dimensions and the corresponding ERBL kernels [27].

4 The specific case of QCD at large s

Theoretical motivations and k_T-factorization

The dynamics of QCD in the perturbative Regge limit is governed by gluons (dominance of spin 1 exchange in t channel). The BFKL Pomeron (and extensions: NLL, saturations effects, ...) is expected to dominate with respect to Born order at large relative rapidity in any diffractive or inclusive process. In this regime, the key tool is the k_T-factorization, shown in Fig.4 in the case of $\gamma^*\,\gamma^* \to \rho\,\rho$. Using the Sudakov decomposition (1) for which $d^4k = \frac{s}{2}\,d\alpha\,d\beta\,d^2k_\perp$ and noting that $t-$channel gluons with non-sense polarizations ($\epsilon_{NS}^{up/down} = \frac{2}{s}\,p_{2\,/1}$) dominate at large s, and then rearranging the k-integration (see Fig.4) leads to the impact representation

$$\mathcal{M} = is \int \frac{d^2\,\underline{k}}{(2\pi)^2 \underline{k}^2\,(\underline{r}-\underline{k})^2} \Phi^{\gamma^*(q_1)\to\rho(p_1^\rho)}(\underline{k}, \underline{r}-\underline{k})\; \Phi^{\gamma^*(q_2)\to\rho(p_2^\rho)}(-\underline{k}, -\underline{r}+\underline{k}) \qquad (5)$$

where $\Phi^{\gamma^*(q)\to\rho(p^\rho)}$ is the $\gamma^*_{L,T}(q)\,g(k_1) \to \rho_{L,T}(p^\rho)\,g(k_2)$ impact factor (with $k_\perp^2 = -\underline{k}^2$). QCD gauge invariance implies, for colorless probes, that the impact factor should vanish when $\underline{k} \to 0$ or $\underline{r}-\underline{k} \to 0$. In particular, at twist 3 level (for $\gamma^*_T \to \rho_T$ transition), gauge invariance is a non-trivial statement which requires 2- *and* 3-parton correlators. Recently, HERA provided data for vector mesons with detailled polarization studies, in particular for our example $\gamma^*_{L,T} + p \to \rho_{L,T} + p$ [9]. It exhibits a total cross-section which strongly decreases with Q^2, with a dramatic increase with $W^2 = s_{\gamma^* P}$. The transition from soft to hard regime is governed by Q^2. The transitions $\gamma^*_L \to \rho_L$, $\gamma^*_{T(-)} \to \rho_{T(-)}$ and $\gamma^*_{T(+)} \to \rho_{T(+)}$ dominate with respect to any other possible transition, as expected from SCHC discussed above. In particular at $t = t_{min}$ one can experimentally distinguish two transitions: $\gamma^*_L \to \rho_L$ which dominate (twist 2 dominance) and the $\gamma^*_{T(\pm)} \to \rho_T(\pm)$ which is sizable, although of twist 3. This calls for detailled studies beyond the applicability of the collinear factorization theorem.

Phenomenological applications: meson production at HERA

The production of mesons in diffraction-type experiments at HERA has been studied extensively in various situations [9, 8]. In the safe case, like J/Ψ photoproduction, collinear factor-

ization holds and combined with k_T-factorization a consistent description of H1 and ZEUS data was obtained [28, 29]. In the more intricate case of exclusive light vector meson (ρ, ϕ) photoproduction at large t, relying on k_T-factorization, one can describe H1 and ZEUS data, which seem to favor BFKL [29, 30]. One needs to regularize end-point singularities for ρ_T, using for example a quark mass $m = m_\rho/2$, and a rather poor understanding of the whole spin density matrix has been achieved. The exclusive vector meson electroproduction $\gamma^*_{L,T} + p \to \rho_{L,T} + p$ has been described [18] based on the ICA for DA coupling and collinear factorization with GPDs, as explained above, without any use of k_T factorization. However, it turns out that at moderate value of s, HERMES [8] measured the interference phase between $L \to L$ and $T \to T$ transitions which cannot be described within perturbative QCD at the moment.

A full twist 3 treatment of ρ-electroproduction in k_T-factorisation is possible [31]. It relies on the computation of the $\gamma^*_T \to \rho_T$ impact factor at twist 3 including consistently all twist 3 contributions, i.e. 2-parton and 3-parton correlators. This gives a gauge invariant impact factor, and an amplitude which is free of end-point singularities due to the presence of k_T.

Exclusive processes at Tevatron, RHIC, LHC, ILC

Exclusive $\gamma^{(*)}\gamma^{(*)}$ processes are golden places for testing QCD at large s, in particular at Tevatron, RHIC, LHC and ILC. Several proposals in order to test perturbative QCD in the large s limit (t-structure of the hard Pomeron, saturation, Odderon...) have been made, including $\gamma^{(*)}(q) + \gamma^{(*)}(q') \to J/\Psi\, J/\Psi$ [32], or $\gamma^*_{L,T}(q) + \gamma^*_{L,T}(q') \to \rho_L(p_1) + \rho_L(p_2)$ process in $e^+\, e^- \to e^+\, e^- \rho_L(p_1) + \rho_L(p_2)$ with double tagged lepton at ILC [33, 34]. This could be feasible at ILC (high energy and high luminosity), with an expected BFKL NLL enhancement with respect to Born and DGLAP. The elusive Odderon (C-parity of Odderon = -1) is hard to reveal directly when entering in the amplitude of a process. When considering processes where it enters linearly, through interference with the Pomeron, the signal becomes more favorable [35], as in $\gamma + \gamma \to \pi^+\pi^-\pi^+\pi^-$: a $\pi^+\pi^-$ pair has no fixed C-parity, allowing for both Odderon and Pomeron exchange, which can interfere in the charge asymmetry [36]. More generally exclusive ultraperipheral processes are very promising.

5 Light-Cone Collinear Factorization

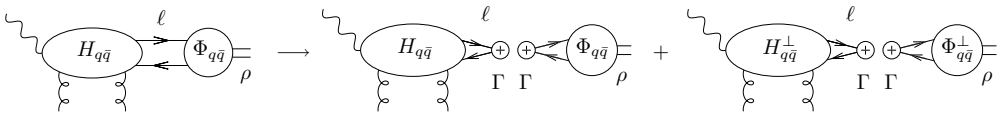

Figure 5: Factorization of 2-parton contributions in the example of the $\gamma^* \to \rho$ impact factor.

There are basically two ways of dealing with collinear factorization when including higher twist corrections. The Light-Cone Collinear Factorization developped first for polarized DIS [37], is self-consistent for exclusive processes [38, 39], while non-covariant, and very efficient for practical computations [31]. Using the Sudakov decomposition ($p = p_1$, $n = 2\,p_2/s$ thus $p \cdot n = 1$)

$$\begin{array}{lccccccc} \ell_\mu & = & u\,p_\mu & + & \ell^\perp_\mu & + & (\ell \cdot p)\,n_\mu, & \qquad u = \ell \cdot n \\ \text{scaling:} & & 1 & & 1/Q & & 1/Q^2 & \end{array} \tag{6}$$

one decomposes $H(k)$ around the p direction:

$$H(\ell) = H(u\,p) \quad + \quad \left.\frac{\partial H(\ell)}{\partial \ell_\alpha}\right|_{\ell=up} (\ell - u\,p)_\alpha + \dots \quad \text{with} \;\; (\ell - u\,p)_\alpha \approx \ell_\alpha^\perp$$

from which the twist 3 term $l_\alpha^\perp$ turns after Fourier transform into the derivative of the soft term $\int d^4z\; e^{-i\ell\cdot z}\langle\rho(p)|\psi(0)\, i\, \overleftrightarrow{\partial}_{\alpha^\perp}\bar{\psi}(z)|0\rangle$. Using the Fierz transformation, this gives finally a factorized expression up to twist 3, as illustrated in Fig.5 for 2-parton contributions in the example of the $\gamma^* g \to \rho\, g$ impact factor. This requires the parametrization of matrix elements of non-local correlators defined along the light-like prefered direction $z = \lambda\, n$ conjugated to p. In the case of the ρ-electroproduction, 7 DAs at twist 3 (2- and 3-parton DAs) are needed. Their number is reduced to a minimal set of 3 DAs when combining the 2 equations of motions and the $n-$independency condition [37, 38, 39, 14] of the full factorized amplitude (which provides 2 process-independent equations). A second approach, the Covariant Collinear Factorization [13], fully covariant but less convenient when practically computing coefficient functions, can equivalently be used. The dictionary and equivalence between the two approaches has recently been obtained, and explicitly checked for the $\gamma_T^* \to \rho_T$ impact factor at twist 3 [31].

6 Conclusion

Since a decade, there has been much progress in the understanding of hard exclusive processes: at moderate energies, combined with GPDs, there is now a framework starting from first principles to describe a huge number of processes; at high energy, the impact representation is a powerful tool for describing exclusive processes in diffractive experiments, which are and will be essential for studying QCD in the hard Regge limit (Pomeron, Odderon, saturation...). Still, some problems remain: proofs of factorization have been optained only for a very few processes (ex.: $\gamma^* p \to \gamma\, p$, $\gamma_L^* p \to \rho_L\, p$, $\gamma^* p \to J/\Psi\, p$). For some other processes factorization is highly plausible, but not fully demonstrated at any order (ex.: processes involving Transition Distribution Amplitudes [40]) while some processes explicitly show signs of breaking of factorization (ex.: $\gamma_T^* p \to \rho_T p$ which has end-point singularities at Leading Order). Models and results from the lattice for the non-perturbative correlators entering GPDs, DAs, GDAs, TDAs are needed, even at a qualitative level. The effect of QCD evolution and renormalization/factorization scale, as well as studies at the full NLL order, might be relevant with the increasing precision of data in the near future. Finally, let us insist on the fact that links between theoretical and experimental communities are very fruitful, in particular at HERA, Jlab, Compass. It is now time to use the potential of high luminosity e^+e^- machine like BaBar, BELLE, BEPC-II which are golden places for hard exclusive processes studies in $\gamma^*\gamma^{(*)}$ channels.

References

[1] V.L. Chernyak *et al.*, JETP Lett. **26** (1977) 594.

[2] K. Watanabe, Prog. Theor. Phys. **67** (1982) 1834.

[3] D. Müller *et al.*, Fortschr. Phys. **42** (1994) 101.

[4] M. Diehl *et al.*, Phys. Rev. Lett. **81** (1998) 1782; Phys. Rev. D **62** (2000) 073014.

[5] B. Geyer *et al.*, Z. Phys. **C26** (1985) 591; T. Braunschweig *et al.*, Z. Phys. **C33** (1986) 275; F. M. Dittes *et al.*, Phys. Lett. **B209** (1988) 325; X. D. Ji, Phys. Rev. Lett. **78** (1997) 610; A. V. Radyushkin, Phys.

Lett. B **380** (1996) 417; ibid. **385** (1996) 333; Phys. Rev. D **56** (1997) 5524; X. D. Ji *et al.*, Phys. Rev. D **58** (1998) 094018.

[6] A. Airapetian *et al.* [HERMES Coll.], Phys. Rev. Lett. **87** (2001) 182001; S. Stepanyan *et al.* [CLAS Coll.], ibid. **87** (2001) 182002.

[7] V. Y. Alexakhin *et al.* [COMPASS Coll.], Eur. Phys. J. C **52** (2007) 255; S. A. Morrow *et al.* [CLAS Coll.], ibid. A **39** (2009) 5.

[8] A. Airapetian *et al.* [HERMES Coll.], arXiv:0901.0701 [hep-ex].

[9] A. Bruni *et al.*, arXiv:0812.0539 [hep-ph]; S. Chekanov *et al.* [ZEUS Coll.], PMC Phys. A **1** (2007) 6.

[10] For reviews see M. Diehl, Phys. Rept. **388** (2003) 41; A. V. Belitsky *et al.*, Phys. Rept. **418** (2005) 1.

[11] J. C. Collins *et al.*, Phys. Rev. D **56** (1997) 2982.

[12] L. Mankiewicz and G. Piller, Phys. Rev. D **61** (2000) 074013.

[13] P. Ball *et al.*, Nucl. Phys. B **529** (1998) 323; Phys. Rev. D **54** (1996) 2182.

[14] I. V. Anikin and O. V. Teryaev, Phys. Lett. B **554** (2003) 51.

[15] I. V. Anikin and O. V. Teryaev, Nucl. Phys. A **711** (2002) 199.

[16] J. Botts and G. Sterman, Nucl. Phys. B **325** (1989) 62.

[17] H. n. Li and G. Sterman, Nucl. Phys. B **381** (1992) 129.

[18] S. V. Goloskokov and P. Kroll, Eur. Phys. J. C **42** (2005) 281; ibid. C **50** (2007) 829; ibid. **53** (2008) 367.

[19] M. Diehl *et al.*, Phys. Rev. D **59** (1999) 034023; J. C. Collins *et al.*, Phys. Rev. D **61** (2000) 114015.

[20] D. Y. Ivanov *et al.*, Phys. Lett. B **550** (2002) 65; R. Enberg *et al.*, Eur. Phys. J. C **47** (2006) 87.

[21] M. El Beiyad *et al.*, in preparation.

[22] I. V. Anikin *et al.*, Phys. Rev. D **70** (2004) 011501; ibid. **71** (2005) 034021; Eur. Phys. J. C **42** (2005) 163.

[23] I.V. Anikin *et al.*, Eur. Phys. J. C **47** (2006) 71.

[24] G. R. Farrar and D. R. Jackson, Phys. Rev. Lett. **43** (1979) 246; S. J. Brodsky and G. P. Lepage, Phys. Lett. B **87** (1979) 359; A. V. Efremov and A. V. Radyushkin, Phys. Lett. B **94** (1980) 245.

[25] For a review see V. M. Braun *et al.*, Prog. Part. Nucl. Phys. **51** (2003) 311.

[26] T. Ohrndorf, Nucl. Phys. B **198** (1982) 26.; V. M. Braun and I. E. Filyanov, Z. Phys. C **48** (1990) 239 [Sov. J. Nucl. Phys. **52** (1990 YAFIA,52,199-213.1990) 126].

[27] A. V. Belitsky *et al.*, Phys. Lett. B **461** (1999) 270; *ibid* **464** (1999) 249; Nucl. Phys. B **574** (2000) 347.

[28] M. G. Ryskin, Z. Phys. C **57** (1993) 89; J. R. Forshaw and M. G. Ryskin, Z. Phys. C **68** (1995) 137; L. Frankfurt *et al.*, Phys. Rev. D **57** (1998) 512.

[29] J. Bartels *et al.*, Phys. Lett. B **375** (1996) 301; J. R. Forshaw *et al.*, Eur. Phys. J. C **26** (2003) 411.

[30] D. Y. Ivanov *et al.*, Phys. Lett. B **478** (2000) 101 [Erratum-ibid. B **498** (2001) 295]; R. Enberg *et al.*, JHEP **0309** (2003) 008; JHEP **0312** (2003) 002.

[31] I. V. Anikin *et al.*, AIP Conf. Proc. **1105** (2009) 390 [arXiv:0811.2394 [hep-ph]]; arXiv:0903.4797 [hep-ph]; arXiv:0904.1482 [hep-ph]; arXiv:0909.4038 [hep-ph]; arXiv:0909.4042 [hep-ph]; arXiv:0909.4090 [hep-ph].

[32] J. Kwiecinski and L. Motyka, Phys. Lett. B **438** (1998) 203.

[33] D. Y. Ivanov *et al.*, Nucl. Phys. B **732** (2006) 183; Eur. Phys. J. C **49** (2007) 947.

[34] B. Pire *et al.*, Eur. Phys. J. C **44** (2005) 545; Phys. Lett. B **639** (2006) 642; R. Enberg *et al.*, Eur. Phys. J. C **45** (2006) 759 [Erratum-ibid. C **51** (2007) 1015]; M. Segond *et al.*, Eur. Phys. J. C **52** (2007) 93.

[35] S. J. Brodsky *et al.*, Phys. Lett. B **461** (1999) 114; I. F. Ginzburg *et al.*, Eur. Phys. J. direct C **5** (2003) 2 [Eur. Phys. J. direct C **30** (2003) 2]; Eur. Phys. J. C **32S1** (2003) 23; Ph. Hagler *et al.*, Phys. Lett. B **535** (2002) 117 [Erratum-ibid. B **540** (2002) 324]; Eur. Phys. J. C **26** (2002) 261.

[36] B. Pire *et al.*, Phys. Rev. D **78** (2008) 094009; AIP Conf. Proc. **1105** (2009) 377; arXiv:0906.5512 [hep-ph]; arXiv:0908.1475 [hep-ph]; arXiv:0909.3450 [hep-ph].

[37] A. V. Efremov and O. V. Teryaev, Sov. J. Nucl. Phys. **36** (1982) 140 [Yad. Fiz. **36** (1982) 242]; E. V. Shuryak and A. I. Vainshtein, Nucl. Phys. B **199** (1982) 451, Nucl. Phys. B **201** (1982) 141; R.K. Ellis *et al.*, Nucl. Phys. B **212** (1983) 29; A.V. Efremov and O.V. Teryaev, Sov. J. Nucl. Phys. **39** (1984) 962; O. V. Teryaev, arXiv:hep-ph/0102296; A. V. Radyushkin and C. Weiss, Phys. Rev. D **64** (2001) 097504.

[38] I. V. Anikin *et al.*, Phys. Rev. D **62** (2000) 071501.

[39] I. V. Anikin and O. V. Teryaev, Phys. Lett. B **509** (2001) 95.

[40] B. Pire and L. Szymanowski, Phys. Rev. D **71** (2005) 111501; Phys. Lett. B **622** (2005) 83.

Deeply Virtual Compton Scattering at Jefferson Lab

Franck Sabatié

SPhN/Irfu, CEA, Centre de Saclay, 91191 Gif sur Yvette, France

DOI: http://dx.doi.org/10.3204/DESY-PROC-2009-03/Sabatie

The Generalized Parton Distribution framework was introduced in the late 90's and describes the nucleon in a revolutionary way, correlating the information from both momentum and transverse position space into experimentally accessible functions. After a brief introduction, this article reviews the Jefferson Lab 6 GeV measurements of Deeply Virtual Compton Scattering in Halls A and B, which give a unique access to Generalized Parton Distributions (GPD). The second part of this article reviews the Jefferson Lab 12 GeV upgrade in general terms, and then focuses on the GPD program in Halls A and B.

1 Introduction

The nucleon electromagnetic structure is still a challenge to modern day physicists after more than 50 years of experimental scrutiny. The nucleon, which appeared to be an elementary particle at first, turned out to have a complicated structure, described in turns by Form Factors (FF) measured in elastic scattering, and Parton Distribution Functions (PDF) measured in Deep Inelastic Scattering (DIS). With the advent of higher energy and higher luminosity accelerators, coupled to high resolution and/or acceptance detectors, it is possible to extend the landscape of hard scattering from inclusive processes such as DIS to exclusive processes, which contain a wealth of new information about the nucleon structure. Similar to parton distributions for DIS, the Generalized Parton Distributions (GPD) which can be obtained through the study of Deep Exclusive Scattering (DES) processes contain information on the quark/antiquark and gluon correlations, and more specifically on both the transverse spatial and longitudinal momentum dependences.

Generalized Parton Distributions not only contain the usual Form Factors and Parton Distribution functions, but using the fully correlated transverse position - momentum information, they can be used to provide 2D tomographic images of the nucleons [1, 2], or even genuine 3D images using their full kinematical dependence [3]. Last but not least, GPD's will allow us to quantify the role of the quark angular orbital momentum in the nucleon spin sum rule [4], which is an open issue since polarized DIS was first investigated.

Jefferson Lab has been a key contributor in the field of GPD's since 2001, especially studying the Deeply Virtual Compton Scattering (DVCS) process. The rest of this article will review the DVCS Jefferson Lab measurements and the future prospects after the 12 GeV upgrade.

2 Deeply Virtual Compton Scattering to access GPD's

About 10 years ago, Mueller, Ji, Radyushkin and others [5, 6, 7, 8, 9] showed that the Deeply Virtual Compton Scattering reaction $\gamma^* p \to \gamma p$ can, in the Bjorken limit, be factorized into a hard scattering kernel and a non-perturbative part, containing information about the electromagnetic structure of the nucleon parametrized into Generalized Parton Distributions. This factorization of the DVCS reaction is represented in Fig.1, where the virtual photon scatters on a single quark, which almost instantly re-emits a real photon. The quark is then inserted back into the nucleon, which is kept intact. In kinematical terms, this factorization is valid when the virtuality of the incoming photon is large ($Q^2 = -q^2$, with q the virtual photon 4-vector) but the transfer to the nucleon small compared to this scale ($-t << Q^2$). The soft structure of the nucleon is parametrized at twist-2 level by four GPD's: E, H, $\widetilde{E}$ and $\widetilde{H}$.

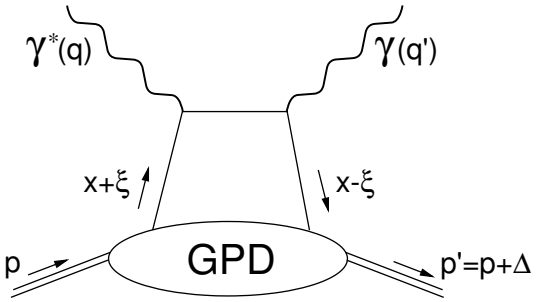

Figure 1: Handbag diagram to the DVCS process. See text for definition of variables.

DVCS is accessible through the electroproduction of real photons $ep \to ep\gamma$. This reaction has a very interesting feature: the real photon can either be emitted by the proton (DVCS) or from one of the electron lines (Bethe-Heitler or BH). Both processes are not distinguishable, therefore they interfere at the amplitude level. By measuring the difference of cross sections for opposite lepton helicities or opposite target polarization, one is sensitive to the interference term alone, which is basically the product of the DVCS amplitude imaginary part by the BH amplitude. This is especially useful at moderate energy at Jefferson Lab since Bethe-Heitler is strong in these kinematics and the cross section difference is therefore sizeable. The difficulties of such measurements lie in the need for exclusivity, which usually means the detection of the three-particle final state, as well as the low cross section which can be compensated by high luminosity and/or acceptance.

3 Jefferson Lab DVCS 6 GeV measurements

3.1 Hall A

The E00-110 experiment in Hall A took data in the fall 2004 with 5.75 GeV electron beam energy impinging on a 15 cm liquid hydrogen target. The experiment was the first ever dedicated DVCS experiment worldwide, its main goal was to check the factorization in the DVCS reaction, by means of a Q^2 scaling scan at fixed x_B. This experiment used the Hall A High Resolution Spectrometer (HRS) to detect the scattered electron, a 132-block lead-fluoride calorimeter to

detect the emitted photon and an array of out-of-plane scintillator blocks to detect the recoil proton. An important feature of this experiment was the high 10^{37} cm^{-2}s^{-1} luminosity which allowed very accurate measurements of the helicity dependent cross sections. The cross section difference and the total cross section are shown on Fig.2 (left) as a function of ϕ, the angle between the leptonic and hadronic planes [10]. The Q^2 dependence of the $\sin\phi$ coefficient is shown on Fig. 2 (right) and shows no visible dependence, which is a good indication the handbag diagram is indeed the dominant process in DVCS even at rather low Q^2. The analysis of the total cross section in terms of GPD's is made more complicated by the fact that one cannot disentangle the DVCS^2 terms from the interference contributions with a simple fit to the data. Only a Rosenbluth-type extraction, using the different energy dependences of these contributions would allow for a complete extraction.

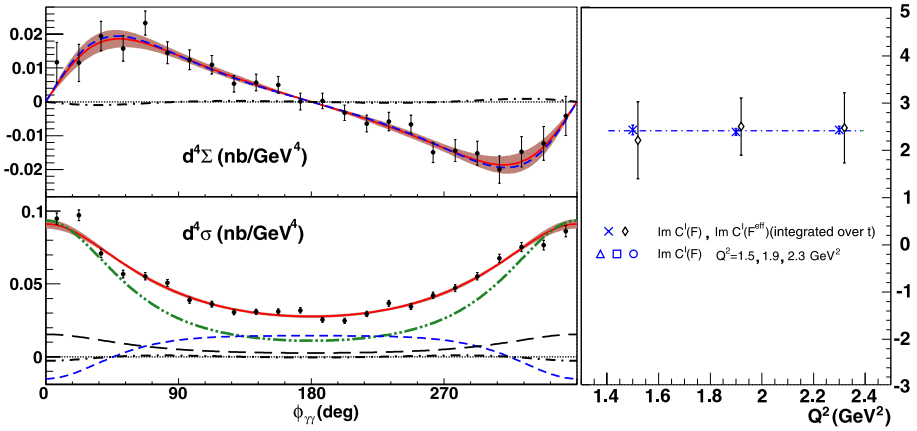

Figure 2: Left: Cross section difference (top) and total cross section (bottom) for $x_B = 0.36$, Q^2=2.3 GeV^2 and $-t$=-0.28 GeV^2. Right: Scaling of the $\sin\phi$ and $\sin 2\phi$ coefficients indicating a handbag dominance. Data and more information can be found in [10].

The E03-106 experiment in Hall A immediately followed E00-110 and took data on a liquid deuterium target in order to extract information on neutron GPD's. Indeed, by subtracting the proton contribution to the deuterium, up to nuclear effects included in systematics, one can extract the cross section difference on the neutron, from which the $\sin\phi$ coefficient is shown on Figure 3 (left, bottom). The collaboration compared their results with the VGG calculations [11] in order to constrain the total angular momentum carried by the u and d quarks through the parametrization of the GPD E [12], as shown on Figure 3 (right). Even though this extraction is highly model dependent, it is a step in the right direction and shows clear potential with more data and other more realistic models. The deuteron $\sin\phi$ coefficient is also shown on Figure 3 (left, top).

3.2 Hall B

The Hall B CLAS collaboration ran the E1-DVCS experiment in 2005 using a 5.77 GeV electron beam impinging on a 2.5 cm-long liquid hydrogen target. In contrast with the Hall A experiments, the operating luminosity was much lower at 2×10^{34} cm^{-2}s^{-1}, but was still a record in the open geometry large acceptance CLAS spectrometer. The standard equipment of this

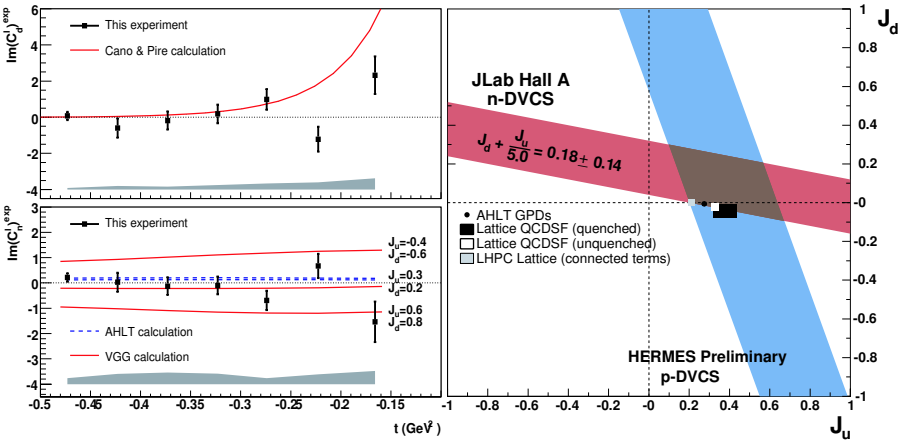

Figure 3: Left top: Coherent deuterium DVCS $\sin\phi$ coefficient as a function of t along with Cano-Pire model [13]. Left bottom: Neutron DVCS $\sin\phi$ coefficient as a function of t along with VGG model. The VGG input parameters for the GPD E are J_u and J_d in this model. Right : Resulting constraint on J_u and J_d. Data and more information can be found in [12].

spectrometer was complemented in this experiment by a new electromagnetic calorimeter (Inner Calorimeter, IC) located 55 cm downstream from the target, in order to detect 1 to 5 GeV photons emitted between 4.5° and 15° with respect to the beam direction. This calorimeter was built of 424 tapered lead tungstate crystals, 16 cm long and with an average cross sectional area of 2.1 cm^2, read out with avalanche photodiodes and associated low-noise preamplifiers.

The analysis of the data consisted in selecting a clean sample of triple coincidence events ($ep\gamma$) and using a set of exclusivity cuts, making sure no other particles were present in the reaction. In spite of this selection, a contamination of events originating from the $ep \to ep\pi^0$ reaction, followed by the subsequent asymmetric decay of the neutral pion, is always possible. It was estimated using π^0 events where both photons are recorded and a Monte-Carlo simulation to correct for the ratio of acceptance for 2-detected photons to 1-detected photons events. The data are then divided into bins in Q^2, x_B, t and ϕ and the beam spin asymmetry is calculated for each bin, plotted as a function of ϕ as shown on Fig. 4 [14], along with the kinematical coverage in Q^2 and x_B. These data represent the largest data set on DVCS to date and they are compared to a number of models and GPD parametrizations such as VGG and others [11, 15, 16, 17, 18].

The only available data on DVCS using a longitudinaly polarized proton target at Jefferson Lab are from non-dedicated data in Hall B [19]. The asymmetry A_{UL} shown in Figure 5 is dominated by the $\sin\phi$ term while the $\sin 2\phi$ term is compatible with zero. As expected, the measured asymmetry is consistent with predictions of a large contribution from the GPD $\widetilde{H}$.

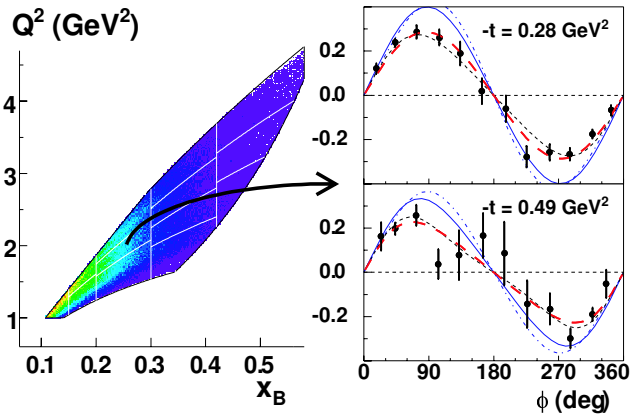

Figure 4: Left: kinematic coverage and binning in the (x_B, Q^2) space. Right: $A(\phi)$ for 2 of the 62 (x_B, Q^2, t) bins, corresponding to $x_B = 0.249$, $Q^2 = 1.95$ GeV^2, and two values of t. Data and more information can be found in [14].

4 The DVCS program at 11 GeV

4.1 The Jefferson Lab 12 GeV Upgrade

The accelerator portion of the Upgrade is straightforward and utilizes the existing tunnel without changing the basic layout of the accelerator. There are four main changes: additional acceleration in the linacs, stronger magnets for the recirculation, an upgraded cryoplant, and the addition of a tenth recirculation arc. The extra arc permits an additional "half pass" through the accelerator to reach the required 12 GeV beam energy, followed by beam transport to Hall D that will be added to support the meson spectroscopy initiative.

The equipment planned for the Upgrade project takes full advantage of apparatus developed for the present program. In two of the existing halls new spectrometers are added and/or present equipment upgraded to meet the demands of the 12 GeV program. Then a new hall, Hall D, will be added to support the meson spectroscopy program. In Hall A, the Upgrade will only add 11 GeV capability to the beamline and will allow for special setup experiments. In Hall B, the CEBAF Large Acceptance Spectrometer (CLAS), which was designed to study multi-particle, exclusive reactions with its combination of large acceptance and moderate momentum resolution, will be upgraded to CLAS12 and optimized for studying exclusive reactions and especially the investigation of GPD's. In Hall C a new, high-momentum spectrometer (the SHMS, Super-High- Momentum Spectrometer) will be constructed to support high-luminosity experiments detecting reaction products with momenta up to the full 11 GeV beam energy. Finally, in Hall D, a tagged coherent bremsstrahlung beam and solenoidal detector will be constructed in support of a program of gluonic spectroscopy.

4.2 The 11 GeV DVCS program in Hall A

The proposal PR12-06-114, accepted by the PAC30 of Jefferson Lab, will measure the $ep \to ep\gamma$ cross sections at fixed x_B for Q^2 up to 9 GeV^2, using a similar (but upgraded) equipment to

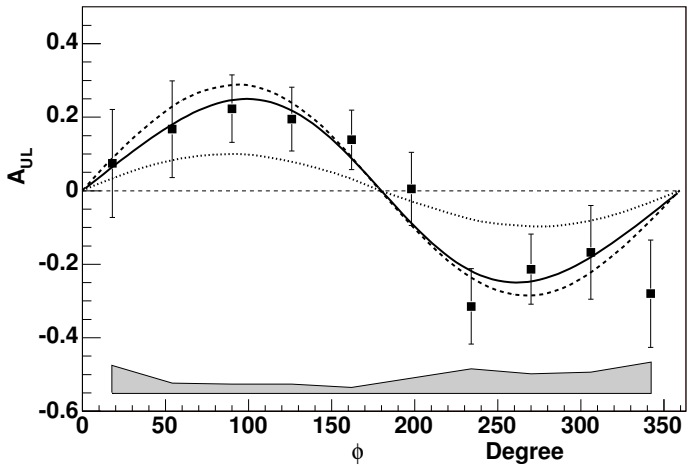

Figure 5: The azimuthal angle ϕ dependence of the target-spin asymmetry for exclusive electroproduction of photons. The dashed curve is the full VGG model prediction. The dotted curve shows the asymmetry when $\widetilde{H}$ =0. The solid curve is a simple fit to the data. Data and more information can be found in [19].

the 6 GeV experiment described earlier. This will determine with what precision the handbag amplitude dominates over the higher twist amplitudes. Using several beam energies, it will be able to fully separate the total cross section among its different contributions, especially DVCS^2, the size of which is mostly unknown. It will also extract superpositions of Compton Form Factors (CFFs). The Q^2 vs x_B domain as well as simulated data for one of the highest Q^2 setting is shown on Fig. 6. In addition, this experiment will measure the $ep \rightarrow ep\pi^0$ cross section in the same kinematics as DVCS and even perform a L-T separation of this cross section for the first time.

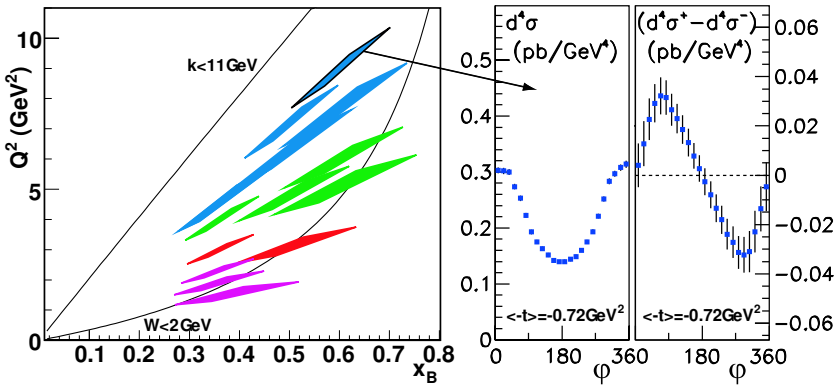

Figure 6: Left: Hall A 11GeV Q^2 vs x_B kinematical coverage: Right: simulated data for the kinematics highlighted on the left.

4.3 The 11 GeV DVCS program in Hall B

The proposal PR12-06-119, accepted by the PAC30 of Jefferson Lab, consists in two separate experiments for a total of 200 days of beam time. The first is a measurement of the DVCS beam spin asymmetries from an unpolarized liquid hydrogen target, and therefore mostly sensitive to the GPD H. The second experiment is dedicated to measuring DVCS target spin asymmetries using a longitudinally polarized target, which is mostly sensitive to the GPD $\widetilde{H}$. These proposals will extend the previous CLAS measurements up to $Q^2 = 9$ GeV^2, using a high 10^{35} cm^{-2}s^{-1} luminosity as well as the augmented CLAS12 detector, including the inner calorimeter already used in the 6 GeV experiment. Simulated data for the beam spin asymmetries are presented on Fig. 7.

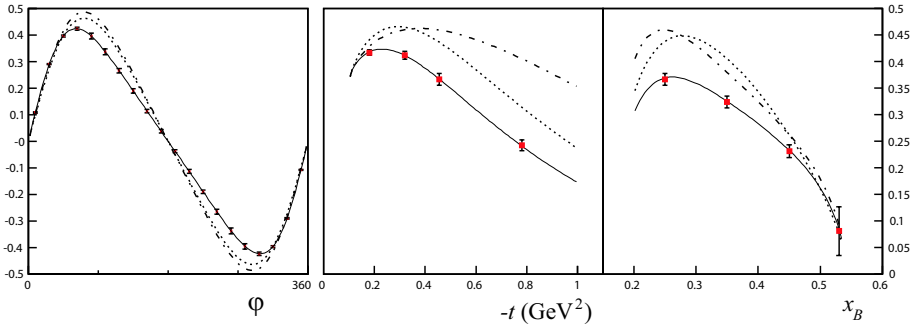

Figure 7: Left : Simulated data for CLAS12 DVCS Beam Spin Asymmetry as a function of ϕ. Middle and right: $A(90°)$ as function of t and x_B as well as curves from [11].

5 Summary

The first 6 GeV dedicated experiments at Jefferson Lab published their data two to three years ago and already, we are challenged to understand their meaning and extract reliable Generalized Parton Distribution information from them. As expected, Deeply Virtual Compton Scattering seems to be scaling early as proved by the Hall A experiment, and constitutes as promised the golden process to access GPD's at moderate energies and Q^2. An enormous amount of data in the valence quark region is now available from Hall B in terms of the A_{LU} asymmetry, soon to be extended to absolute cross section. Along with the very accurate Hall A data, this will constitute a benchmark for GPD parametrization and modelling and keep the community busy until the Jefferson Lab 12 GeV upgrade. The expected data for this second generation of experiments in Halls A and B will undoubtedly unravel for the first time the precise 3-dimensional structure of the nucleon.

References

[1] Matthias Burkardt. Impact parameter space interpretation for generalized parton distributions. *Int. J. Mod. Phys.*, A18:173–208, 2003.

[2] M. Diehl. Generalized parton distributions in impact parameter space. *Eur. Phys. J.*, C25:223–232, 2002.

[3] Andrei V. Belitsky, Xiang-dong Ji, and Feng Yuan. Quark imaging in the proton via quantum phase-space distributions. *Phys. Rev.*, D69:074014, 2004.

[4] Xiang-Dong Ji. Gauge invariant decomposition of nucleon spin. *Phys. Rev. Lett.*, 78:610–613, 1997.

[5] Dieter Mueller, D. Robaschik, B. Geyer, F. M. Dittes, and J. Horejsi. Wave functions, evolution equations and evolution kernels from light-ray operators of QCD. *Fortschr. Phys.*, 42:101, 1994.

[6] Xiang-Dong Ji. Deeply-virtual compton scattering. *Phys. Rev.*, D55:7114–7125, 1997.

[7] A. V. Radyushkin. Scaling limit of deeply virtual compton scattering. *Phys. Lett.*, B380:417–425, 1996.

[8] John C. Collins and Andreas Freund. Proof of factorization for deeply virtual Compton scattering in QCD. *Phys. Rev.*, D59:074009, 1999.

[9] M. Diehl, T. Feldmann, R. Jakob, and P. Kroll. Linking parton distributions to form factors and compton scattering. *Eur. Phys. J.*, C8:409–434, 1999.

[10] C. Munoz Camacho et al. Scaling tests of the cross section for deeply virtual Compton scattering. *Phys. Rev. Lett.*, 97:262002, 2006.

[11] K. Goeke, Maxim V. Polyakov, and M. Vanderhaeghen. Hard exclusive reactions and the structure of hadrons. *Prog. Part. Nucl. Phys.*, 47:401–515, 2001.

[12] M. Mazouz et al. Deeply Virtual Compton Scattering off the neutron. *Phys. Rev. Lett.*, 99:242501, 2007.

[13] F. Cano and B. Pire. Deeply virtual Compton scattering on the deuteron. *Nucl. Phys.*, A711:133–138, 2002.

[14] F. X. Girod et al. Deeply Virtual Compton Scattering Beam-Spin Asymmetries. *Phys. Rev. Lett.*, 100:162002, 2008.

[15] Maxim V. Polyakov and Marc Vanderhaeghen. Taming Deeply Virtual Compton Scattering. 2008.

[16] M. Guidal. A fitter code for Deep Virtual Compton Scattering and Generalized Parton Distributions. *Eur. Phys. J.*, A37:319–332, 2008.

[17] H. Moutarde. Extraction of the Compton Form Factor H from DVCS measurements at Jefferson Lab. *Phys. Rev. D*, 79:094021, 2009.

[18] Kresimir Kumericki and Dieter Muller. Deeply virtual Compton scattering at small x_B and the access to the GPD H. 2009.

[19] S. Chen et al. Measurement of deeply virtual Compton scattering with a polarized proton target. *Phys. Rev. Lett.*, 97:072002, 2006.

DVCS at HERA and at CERN

Laurent Schoeffel

CEA Saclay, Irfu/SPP, 91191 Gif-sur-Yvette Cedex, France

DOI: http://dx.doi.org/10.3204/DESY-PROC-2009-03/Schoeffel

Deeply Virtual Compton Scattering (DVCS) in ep collisions has emerged in recent years as a an essential reaction to obtain information on the correlation of partons in the hadron (proton) or on the transverse distribution of these partons. In these proceedings, we examine the lattest data from HERA (at low $x_{Bj} < 10^{-2}$) and their impact on models. We analyse in detail what these data imply on the spatial structure of the proton. In particular, the most recent measurements of the Beam Charge Asymmetry by the H1 experiment is discussed in this context. Perspectives are presented for further measurements of DVCS cross sections at CERN, within the COMPASS experiment.

1 Introduction

Measurements of the deep-inelastic scattering (DIS) of leptons and nucleons, $e + p \to e + X$, allow the extraction of Parton Distribution Functions (PDFs) which describe the longitudinal momentum carried by the quarks, anti-quarks and gluons that make up the fast-moving nucleons. While PDFs provide crucial input to perturbative Quantum Chromodynamic (QCD) calculations of processes involving hadrons, they do not provide a complete picture of the partonic structure of nucleons. In particular, PDFs contain neither information on the correlations between partons nor on their transverse motion.

Hard exclusive processes, in which the nucleon remains intact, have emerged in recent years as prime candidates to complement this essentially one dimensional picture. The simplest exclusive process is the deeply virtual Compton scattering (DVCS) or exclusive production of real photon, $e + p \to e + \gamma + p$. This process is of particular interest as it has both a clear experimental signature and is calculable in perturbative QCD. The DVCS reaction can be regarded as the elastic scattering of the virtual photon off the proton via a colourless exchange, producing a real photon in the final state [1, 2]. In the Bjorken scaling regime, QCD calculations assume that the exchange involves two partons, having different longitudinal and transverse momenta, in a colourless configuration. These unequal momenta or skewing are a consequence of the mass difference between the incoming virtual photon and the outgoing real photon. This skewedness effect can be interpreted in the context of generalised parton distributions (GPDs) [3] or dipole model [4]. In the following, we examine the most recent data recorded from the DESY ep collider at HERA and their implication on the quarks/gluons imaging of the nucleon [1, 2].

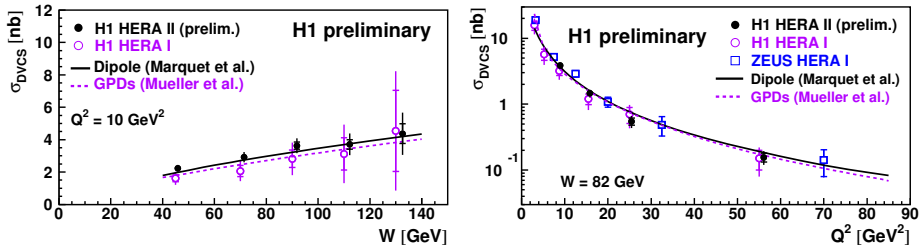

Figure 1: DVCS cross section for the full HERA data as a function of W and Q^2.

2 Latest experimental measurements from HERA

The first measurements of DVCS cross section have been realised at HERA within the H1 and ZEUS experiments [1, 2]. These results are given in the specific kinematic domain of both experiments, at low x_{Bj} ($x_{Bj} < 0.01$) but they take advantage of the large range in Q^2, offered by the HERA kinematics, which covers more than 2 orders of magnitude, from 1 to 100 GeV^2. It makes possible to study the transition from the low Q^2 non-perturbative region (around 1 GeV^2) towards higher values of Q^2 where the higher twists effects are lowered (above 10 GeV^2). The last DVCS cross sections as a function of Q^2 and $W \simeq \sqrt{Q^2/x}$ are presented on Fig. 1. A good agreement with GPDs [3] and dipole [4] models is observed. A very fundamental observation is the steep W dependence in $W^{0.7}$, visible on Fig. 1. This means that DVCS is a hard process. Thus, it is justified to compare DVCS measurements with perturbative QCD calculations, GPDs or dipole approaches, as displayed in Fig. 1.

3 The colour dipole model

Let's discuss in more details the colour dipole model. Indeed, this approach provides a simple unified picture of inclusive and diffractive processes and enables hard and soft physics to be incorporated in a single dynamical framework. At high energies, in the proton's rest frame, the virtual photon fluctuates into a hadronic system (the simplest of which is a $q\bar{q}$ dipole) a long distance upstream of the target proton. The formation time of this hadronic system, and of the subsequent formation of the hadronic final state, is much longer than the interaction time with the target.

DVCS is a good probe of the transition between soft and hard regimes in the dipole model for two reasons. Indeed, the transverse photon wave function can select large dipoles, even for large Q^2, and certainly for the Q^2 range $2 < Q^2 < 20$ GeV^2. Also, because the final photon is real, DVCS is more sensitive to large dipoles than DIS at the same Q^2. Then, in the colour dipole approach, the DIS (or DVCS) process can be seen as a succession in time of three factorisable subprocesses: i) the virtual photon fluctuates in a quark-antiquark pair, ii) this colour dipole interacts with the proton target, iii) the quark pair annihilates into a virtual (or real) photon. The imaginary part of the DIS (or DVCS) amplitude at $t = 0$ is expressed in

the simple way [4, 5]

$$\mathcal{I}m\,\mathcal{A}\,(W,Q_1,Q_2) = \sum_{T,L}\int_0^1 dz \int_0^\infty d^2\boldsymbol{r}\,\Psi^*_{T,L}(z,\,\boldsymbol{r},\,Q_1^2)\,\sigma_{dip}\,(z,\boldsymbol{r})\Psi_{T,L}(z,\,\boldsymbol{r},\,Q_2^2)\,, \qquad (1)$$

where $\Psi(z,\boldsymbol{r},Q_{1,2})$ are the light cone photon wave functions for transverse and longitudinal photons. The quantity Q_1 is the virtuality of the incoming photon, whereas Q_2 is the virtuality of the outgoing photon. In the DIS case, one has $Q_1^2 = Q_2^2 = Q^2$ and for DVCS, $Q_1^2 = Q^2$ and $Q_2^2 = 0$. The relative transverse quark pair (dipole) separation is labeled by $\boldsymbol{r}$ whilst z (respec. $1-z$) labels the quark (antiquark) longitudinal momentum fraction.

It should be noticed that the non-forward kinematics for DVCS is encoded in the colour dipole approach through the different weight coming from the photon wavefunctions in Eq. (1). The off-diagonal effects, which affect the gluon and quark distributions in GPDs models, should be included in the parameterisation of the dipole cross section. At the present stage of the development of the dipole formalism, we have no accurate theoretical arguments on how to compute skewedness effects from first principles. A consistent approach would be to compute the scattering amplitude in the non-forward case [4]. In this case, the dipole cross section, $\sigma_{dip}\,(x_1,x_2,\boldsymbol{r},\vec{\Delta})$, depends on the momenta x_1 and x_2 carried by the exchanged gluons, respectively, and on the total transverse momentum transfer $\vec{\Delta}$. In this case, additional information about the dependence upon $\vec{\Delta}$ is needed for the QCD Pomeron and proton impact factor. A first attempt in this direction is done in [4].

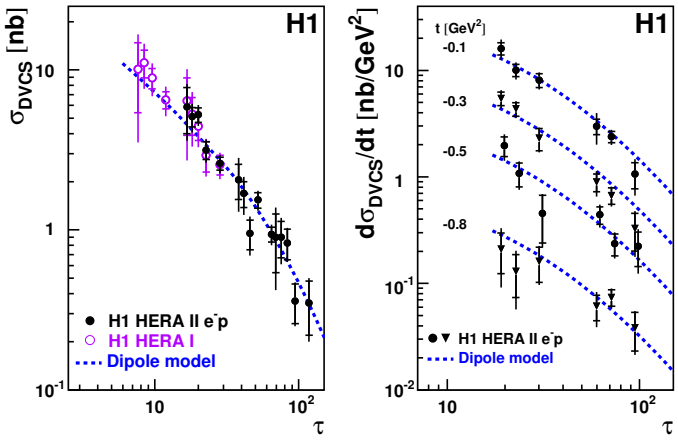

Figure 2: DVCS cross section measurements as a function of the scaling variable $\tau = Q^2/Q_s^2(x)$. Results are shown for the full t range $|t| < 1$ GeV^2 (left) and at four values of t (right). The dashed curves represent the predictions of the dipole model [5].

At very small values of the Bjorken scaling variable x the saturation regime of QCD can be reached. In this domain, the gluon density in the proton is so large that non-linear effects like gluon recombination tame its growth. In the dipole model approach, the transition to the saturation regime is characterised by the so-called saturation scale parametrised here as $Q_s(x) = Q_0(x_0/x)^{-\lambda/2}$, where Q_0, x_0 and λ are parameters. The transition to saturation

occurs when Q becomes comparable to $Q_s(x)$. An important feature of dipole models that incorporate saturation is that the total cross section can be expressed as a function of the single variable τ:

$$\sigma_{tot}^{\gamma^* p}(x, Q^2) = \sigma_{tot}^{\gamma^* p}(\tau), \quad \text{with} \quad \tau = \frac{Q^2}{Q_s^2(x)}. \tag{2}$$

This property, called geometric scaling, has already been observed to hold for the total ep DIS cross section and in diffractive processes [5] (see Fig. 2). It has also recently been addressed in the context of exclusive processes including DVCS and extended to cases with non-zero momentum transfer to the proton [4]. It is therefore interesting to test if the present DVCS measurements obey the geometric scaling laws predicted by such models, as illustraded in Fig. 2 (right plot for non-zero momentum transfer to the proton).

4 Nucleon Tomography and Perspectives at CERN

A major experimental achievement of H1 and ZEUS [1, 2] has been the measurement of DVCS cross sections, differential in $t = (p' - p)^2$, the momentum transfer (squared) at the proton vertex. A good description of $d\sigma_{DVCS}/dt$ by a fit of the form $e^{-b|t|}$ is obtained [1, 2]. Hence, an extraction of the t-slope parameter b is accessible and it can be achieved experimentally for different values of Q^2 and W (see Fig. 3). Again, we observe the good agreement of measurements with GPDs and dipole models.

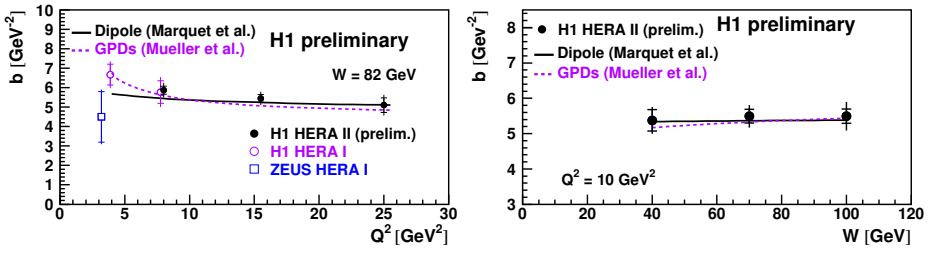

Figure 3: The logarithmic slope of the t dependence for DVCS exclusive production, b as a function of Q^2 and W, extracted from a fit $d\sigma/dt \propto \exp(-b|t|)$ where $t = (p - p')^2$.

Measurements of the t-slope parameters b are key measurements for almost all exclusive processes, in particular DVCS. Indeed, a Fourier transform from momentum to impact parameter space readily shows that the t-slope b is related to the typical transverse distance between the colliding objects [3]. At high scale, the $q\bar{q}$ dipole is almost point-like, and the t dependence of the cross section is given by the transverse extension of the gluons (or sea quarks) in the proton for a given x_{Bj} range. More precisely, from GPDs, we can compute a parton density which also depends on a spatial degree of freedom, the transverse size (or impact parameter), labeled $R_\perp$, in the proton. Both functions are related by a Fourier transform

$$PDF(x, R_\perp; Q^2) \equiv \int \frac{d^2\Delta_\perp}{(2\pi)^2} e^{i(\Delta_\perp R_\perp)} GPD(x, t = -\Delta_\perp^2; Q^2).$$

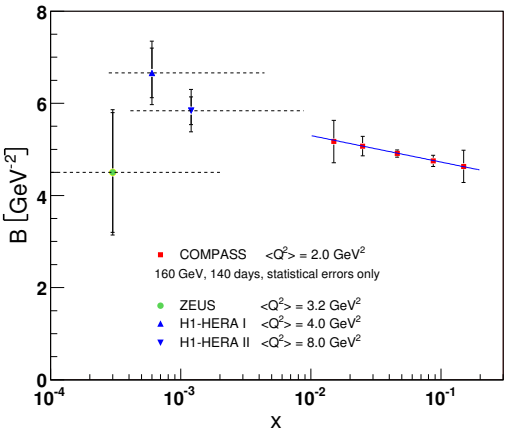

Figure 4: The logarithmic slope of the t dependence for DVCS exclusive production, b as a function of x_{Bj}, extracted from a fit $d\sigma/dt \propto \exp(-b|t|)$ where $t = (p - p')^2$. H1 and ZEUS points are measurements and simulations are displayed for COMPASS (CERN).

Thus, the transverse extension $\langle r_T^2 \rangle$ of gluons (or sea quarks) in the proton can be written as

$$\langle r_T^2 \rangle \equiv \frac{\int d^2R_\perp \, PDF(x,R_\perp) \, R_\perp^2}{\int d^2R_\perp \, PDF(x,R_\perp)} = 4 \, \frac{\partial}{\partial t} \left[\frac{GPD(x,t)}{GPD(x,0)} \right]_{t=0} = 2b$$

where b is the exponential t-slope. Measurements of b presented in Fig. 3 corresponds to $\sqrt{r_T^2} = 0.65 \pm 0.02$ fm at large scale Q^2 for $x_{Bj} < 10^{-2}$. This value is smaller that the size of a single proton, and, in contrast to hadron-hadron scattering, it does not expand as energy W increases. This result is consistent with perturbative QCD calculations in terms of a radiation cloud of gluons and quarks emitted around the incoming virtual photon. The fact the perturbative QCD calculations provide correct descriptions of b measurements (see previous section) is a proof that they deal correctly this this non-trivial aspect of the proton (spatial) structure. As already discussed in the context of dipole models, the modeling of the correlation between the spatial transverse structure and the longitudinal momenta distributions of partons in the proton is one major challenge also for the GPDs approach. In Fig. 4, we present a summary of the measurements of $b(x_{Bj})$ by H1 and ZEUS experiments and simulations for COMPASS at CERN. The importance of such measurements of t-slopes as a function of x_{Bj} at CERN is then obvious.

Another natural way to address the problem of the correlation between x and t kinematical variables proceeds from a determination of a cross section asymmetry with respect to the beam charge. It has been realised recently by the H1 experiment by measuring the ratio $(d\sigma^+ - d\sigma^-)/(d\sigma^+ + d\sigma^-)$ as a function of ϕ, where ϕ is the azimuthal angle between leptons and proton plane. The result is presented on Fig. 5 with a fit in $\cos\phi$. After applying a deconvolution method to account for the resolution on ϕ, the coefficient of the $\cos\phi$ dependence is found to be $p_1 = 0.16 \pm 0.03(stat.) \pm 0.05(sys.)$ (at low $x_{Bj} < 0.01$). This result represents a major experimental progress and is challenging for models (see Fig. 5). Let's note that

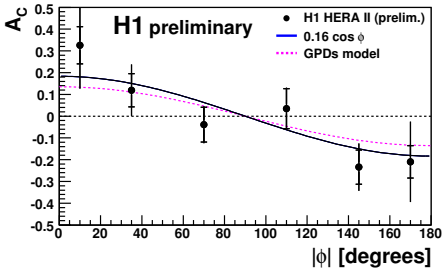

Figure 5: Beam charge asymmetry as a function of ϕ measured by H1. Statistical and systematical uncertainties are shown. Data are corrected from the migrations of events in ϕ. A comparison with the GPDs model described in Ref. [3] is presented. It fits very nicely with the best fit to the data, in $p_1 \cos\phi$ ($p_1 = 0.16$).

models of GPDs can use present HERA data at low x_{Bj}, as well as JLab and HERMES data at larger x_{Bj} ($x_{Bj} > 0.1$), in order to provide a first global understanding of exclusive real photon production [3]. However, as already mentioned above, some efforts have still to be made in the intermediate x_{Bj} domain.

Feasibility for future Beam Charge Asymmetry (BCA) measurements at COMPASS have been studied extensively in the last decade [6]. COMPASS is a fixed target experiment which can use 100 GeV muon beams and hydrogen targets, and then access experimentaly the DVCS process $\mu p \to \mu\gamma p$. The BCA can be determined when using positive and negative muon beams. One major interest is the kinematic coverage from 2 GeV^2 till 6 GeV^2 in Q^2 and x_{Bj} ranging from 0.05 till 0.1. It means that it is possible to avoid the kinematic domain dominated by higher-twists and non-perturbative effects (for $Q^2 < 1$ GeV^2) and keeping a x_{Bj} range which is extending the HERA (H1/ZEUS) domain. As mentioned above, this is obviously an essential measurement to cover the full kinematic range and give some results in the intermediate x_{Bj} range between H1/ZEUS and JLab/HERMES experiments. Simulations done for COMPASS [6, 7] are shown in Fig. 6 for BCA in a setup described in the legend of the figure. Two models of GPDs, with a factorised and non-factorised t dependence, are shown in Fig. 6 and we can observe easily the great discrimination power offered by COMPASS, with the proton recoil detector fully operational. Of course, the discrimination is large in Fig. 6 due to the fact that α' is taken to be large ($\alpha' \sim 0.8$ GeV^{-2}) in simulations. If it happens to be much smaller, as measured at low x_{Bj} by H1 [1], both predictions for BCA in Fig. 6 would be of similar shape, as both curves would converge to the factorised case. This shows clearly the high level of sensitivity of this experimental quantity on the modeling of GPDs. This makes this observable very interesting and challenging for GPDs models in the future, once these measurements at CERN would be realised in 2011/2012.

5 Summary and outlook

DVCS measurements in the HERA kinematics at low x_{Bj} ($x_{Bj} < 0.01$) are well described by recent GPDs models, which also describe correctly measurements at larger values of x_{Bj} in

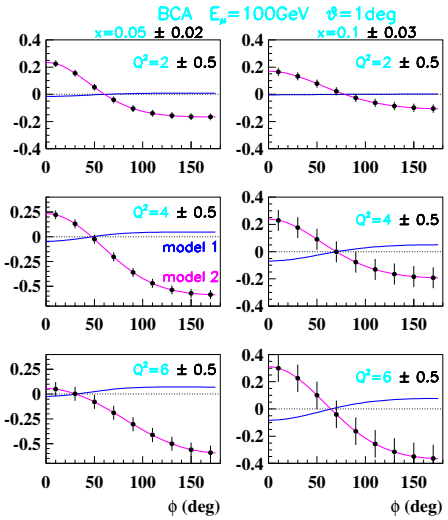

Figure 6: Azimuthal distribution of the beam charge asymmetry measured at COMPASS at E_μ= 100 GeV and $|t| \leq 0.6$ GeV^2 for 2 domains of x_{Bj} ($x_{Bj} = 0.05 \pm 0.02$ and $x_{Bj} = 0.10 \pm 0.03$) and 3 domains of Q^2 ($Q^2 = 2 \pm 0.5$ GeV^2, $Q^2 = 4 \pm 0.5$ GeV^2 and $Q^2 = 6 \pm 0.5$ GeV^2) obtained in 6 months of data taking with a global efficiency of 25% and with $2 \cdot 10^8$ μ per SPS spill ($P_{\mu^+} = -0.8$ and $P_{\mu^-} = +0.8$). More recent simulations are on going which does not change the conclusions of this plot.

the JLab kinematics. DVCS measurements in the HERA kinematics are also nicely described within a dipole approach, which encodes the non-forward kinematics for DVCS only through the different weights coming from the photon wavefunctions. Recently, H1 and ZEUS experiments have also shown that proton tomography at low x_{Bj} enters into the experimental domain of high energy physics, with a first experimental evidence that gluons are located at the periphery of the proton. A new frontier in understanding this structure would be possible at CERN within the COMPASS experimental setup. Major advances have already been done on the design of the project and simulation outputs.

References

[1] F. D. Aaron *et al.* [H1 Collaboration], Phys. Lett. B **659** (2008) 796; A. Aktas *et al.* [H1 Collaboration], Eur. Phys. J. C **44**, 1 (2005); C. Adloff *et al.* [H1 Collaboration], Phys. Lett. B **517** (2001) 47.

[2] S. Chekanov *et al.* [ZEUS Collaboration], JHEP **0905** (2009) 108; S. Chekanov *et al.* [ZEUS Collaboration], Phys. Lett. B **573**, 46 (2003).

[3] K. Kumericki, D. Mueller and K. Passek-Kumericki, Nucl. Phys. B **794** (2008) 244.

[4] C. Marquet, R. B. Peschanski and G. Soyez, Phys. Rev. D **76** (2007) 034011.

[5] C. Marquet and L. Schoeffel, Phys. Lett. B **639** (2006) 471.

[6] N. d'Hose et al., Nucl. Phys. A **711** (2002) 160.

[7] L. Schoeffel, Phys. Lett. B **658** (2007) 33.

On the Physical Relevance of the Study of $\gamma^\star\gamma \to \pi^0\pi^0$ at Small t and Large Q^2

J.P. Lansberg[1], *B. Pire*[2], *L. Szymanowski*[3]

[1]SLAC National Accelerator Laboratory, Theoretical Physics, Stanford University, Menlo Park, CA 94025, USA

[2]Centre de Physique Théorique, École Polytechnique - CNRS, 91128 Palaiseau, France

[3]Soltan Institute for Nuclear Studies, Warsaw, Poland

DOI: http://dx.doi.org/10.3204/DESY-PROC-2009-03/Lansberg

We discuss the relevance of a dedicated measurement of exclusive production of a pair of neutral pions in a hard $\gamma^\star\gamma$ scattering at small momentum transfer. In this case, the virtuality of one photon provides us with a hard scale in the process, enabling us to perform a QCD calculation of this reaction rate using the concept of Transition Distribution Amplitudes (TDA). Those are related by sum rules to the pion axial form factor F_A^π and, as a direct consequence, a cross-section measurement of this process at intense beam electron-positron colliders such as CLEO, KEK-B and PEP-II, or Super-B would provide us with a unique measurement of the neutral pion axial form factor $F_A^{\pi^0}$ at small scale.

1 Introduction

In a series of papers [1, 2, 3, 4, 5, 6, 7, 8], we have advocated that factorisation theorems [9] for exclusive processes may be extended to the case of other reactions such as (M_i stands for a meson and B_i for a baryon) $B_1\,\overline{B}_2 \to \gamma^\star\,\gamma$, $B_1\,\overline{B}_2 \to \gamma^\star\,M_1\;\gamma_T^\star\,B_1 \to B_2\gamma$, $\gamma_T^\star\,B_1 \to B_2 M_1$ or $\gamma_L^\star\,\gamma \to M_1 M_2$, in the kinematical regime where the off-shell photon is highly virtual (Q^2 of the order of the energy squared of the reaction) but the momentum transfer t is small. This enlarges the successful description of deep-exclusive $\gamma\gamma$ reactions in terms of distribution amplitudes [10] and/or generalised distribution amplitudes [11] on the one side and perturbatively calculable coefficient functions describing hard scattering at the partonic level on the other side.

Intense beam electron colliders, such as B factories, are ideal places to study such reactions as

$$\gamma_L^\star\,\gamma \to \rho^\pm\pi^\mp,\ \gamma_L^\star\ \gamma \to \pi^\pm\pi^\mp,\ \gamma_L^\star\gamma \to \pi^0\pi^0,$$

in the near forward region and for large virtual photon invariant mass Q. Recently BaBar reported a new measurement of the reaction $\gamma^\star\gamma \to \pi^0$ up to photon virtualities squared of 40 GeV^2 [12]. In the latter study, the reaction $\gamma^\star\gamma \to \pi^0\pi^0$ was investigated in the $f_2(1270)$ and $f_0(980)$ resonance region as a potential background for the study of the π^0 transition form factor. This low-$W_{\pi\pi}^2$ kinematical region should be analysed in the framework of generalised two-meson distribution amplitudes [11] and in particular should solve the much discussed problem of its phase structure around the f_0 mass [13] which is of crucial importance for the ability to

detect Pomeron-Odderon interference effects in high energy electro-production of meson pairs [14].

We want here to emphasise another kinematical region, namely the small-t large-$W^2_{\pi\pi}$ region at moderate Q^2 (2 GeV^2 and more) which may provide us with unique information on the π^0 axial form factor at small scale which so far has never been experimentally measured. It has been argued that a new duality [15] relates these two factorisation regimes.

In principle, another possibility to study this quantity would be the crossed channel, that is DVCS on a virtual neutral pion along the lines exposed in Ref. [16] for π^+.

2 Pion-pair production in the TDA regime

Let us recall the main ingredients of the analyses developed in [1, 4] focusing on the neutral pion case. With the kinematics described in Fig. 1, we define the axial $\gamma \to \pi$ transition distribution amplitude (TDA) $A(x,\xi,t)$ as the Fourier transform of matrix element $\langle \pi^0(p_\pi)| \mathcal{O}_A |\gamma(p_\gamma)\rangle$ where $\mathcal{O}_A = \bar\psi(\frac{-z}{2})[\frac{-z}{2},\frac{z}{2}]\gamma^\mu\gamma^5\psi(\frac{z}{2})$. The Wilson line $[\frac{-z}{2},\frac{z}{2}]$ ensures the QCD-gauge invariance for non-local operators and equals unity in a light-like (axial) gauge. We do not write the electromagnetic Wilson line, since we choose an electromagnetic axial gauge for the photon. We then factorise the amplitude of the process $\gamma^\star_L\gamma \to \pi^0\pi^0$ as

$$\sum_{q=u,d}\int dxdz\, \Phi^q_\pi(z) M^q_h(z,x,\xi)\frac{A^{\pi^0}_q(x,\xi,t)}{f_\pi}\,, \tag{1}$$

with a hard amplitude $M^q_h(z,x,\xi)$, $\Phi^q_\pi(z)$ the distribution amplitude (DA) for q quark content of the π meson with momentum p'_π and $A^{\pi^0}_q(x,\xi,t)$ the axial $\gamma \to \pi$ TDA for the quark q.

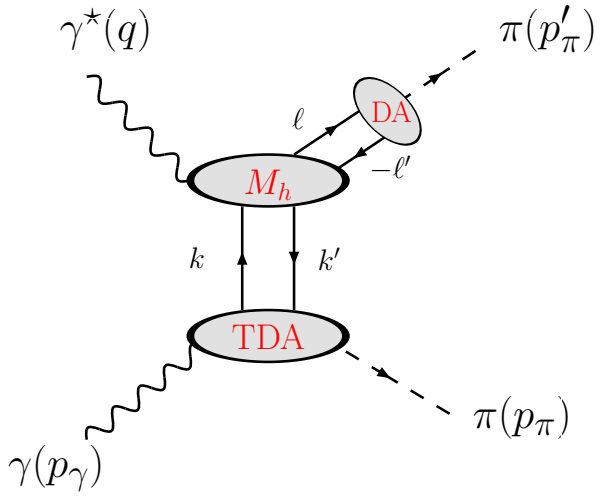

Figure 1: The factorised amplitude for $\gamma^\star\gamma \to \pi^0\pi^0$ at small transfer momentum.

The variable z is as usual the light-cone momentum fraction carried by the quark entering the pion with momentum p'_π, $x+\xi$ (resp. $x-\xi$) is the corresponding one for the quark leaving

(resp. entering) the TDA. The skewness variable ξ describes the loss of light-cone momentum of the incident photon and is connected to the Bjorken variable x_B.

Contrarily to the case of generalised parton distributions (GPD) where the forward limit is related to the conventional parton distributions measured in the deep inelastic scattering (DIS), there is no such interesting constraints for the TDAs. The constraints we have here are sum rules obtained by taking the local limit of the corresponding operators and soft limits when the momentum of the meson in the TDA vanishes.

Let us consider in more detail the $\gamma \to \pi^0$ axial TDAs which is defined by ($P = \frac{p_\pi + p_\gamma}{2}$, $\Delta = p_\pi - p_\gamma$):

$$\int \frac{dz^-}{2\pi} e^{ixP^+z^-} \langle \pi^0 | \bar{q}(\frac{-z}{2}) \Big[\frac{-z}{2}; \frac{z}{2}\Big] \gamma^\mu \gamma^5 q(\frac{z}{2}) | \gamma \rangle = \frac{1}{P^+} \frac{e}{f_\pi} (\varepsilon \cdot \Delta) P^\mu A_q^{\pi^0}(x, \xi, t) \tag{2}$$

A sum rule may be derived for this photon to meson TDA by integrating on x both side of Eq. (2) and we get

$$\frac{e}{f_\pi} (\varepsilon \cdot \Delta) P^\mu \int_{-1}^{1} dx \; A_q^{\pi^0}(x, \xi, t) = \langle \pi^0 | \bar{q}(0) \gamma^\mu \gamma^5 q(0) | \gamma \rangle, \tag{3}$$

The latter matrix element of a local quark–anti-quark operator is directly related to the quark q contribution $F_{A,q}^{\pi^0}$ to the axial form factor of the π^0 meson. Similarly, we have in the vector charged pion case [4]:

$$\int_{-1}^{1} dx \, V^{\pi^\pm}(x, \xi, t) = \frac{f_\pi}{m_\pi} \, F_V^{\pi^\pm}(t), \tag{4}$$

with $F_V^{\pi^\pm} = 0.017 \pm 0.008$ [17].

This sum rule constrains possible parametrisations of the TDAs. Note, in particular, the ξ-independence of the right hand side of the relation.

3 Models and cross section evaluation

3.1 Amplitude

Let us thus consider the $\pi^0\pi^0$ production case when the π^0 with momentum p'_π flies in the direction of the virtual photon and the other π^0 emerges from the TDA. For definiteness, we choose, in the CMS of the meson pair, $p = \frac{Q^2 + W_{\pi\pi}^2}{2(1+\xi) W_{\pi\pi}} (1, 0, 0, -1)$ and $n = \frac{(1+\xi) W_{\pi\pi}}{2(Q^2 + W_{\pi\pi}^2)} (1, 0, 0, 1)$ and we express the momenta through a Sudakov decomposition (with $\Delta_T^2 = \frac{1-\xi}{1+\xi} t$ and neglecting the pion mass):

$$p_\gamma = (1+\xi) p, \quad q = \frac{Q^2 + W_{\pi\pi}^2}{1+\xi} n - \frac{Q^2}{Q^2 + W_{\pi\pi}^2} (1+\xi) p, \quad p_\pi = (1-\xi) p - \frac{\Delta_T^2}{1-\xi} n + \Delta_T. \tag{5}$$

We can see that ξ is determined by the external kinematics through $\xi \simeq \frac{Q^2}{Q^2 + 2W_{\pi\pi}^2}$ – similarly to $x_B = \frac{Q^2}{Q^2 + W_{\pi\pi}^2}$ to which it is linked via the simple relation $\xi \simeq \frac{x_B}{2 - x_B}$.

The hard amplitude amplitude in Eq. (1) thus reads :

$$M_h^q(z, x, \xi) = \frac{4\,\pi^2\,\alpha_{em}\,\alpha_s\,C_F\,Q_q}{N_C\,Q} \frac{1}{z\,\bar{z}} \left(\frac{1}{x - \xi + i\epsilon} + \frac{1}{x + \xi - i\epsilon} \right) \varepsilon \cdot \Delta \,, \tag{6}$$

where $Q_u = 2/3$, $Q_d = -1/3$ and with $\bar{z} = 1 - z$. Note that the factor f_π in the π DA $\Phi^q_\pi(z)$ cancels with the one from the TDA definition and does not appear in Eq. (7). Now, if we choose the asymptotic form for the neutral pion DA, $\Phi^u_{\pi^0}(z) = -\Phi^d_{\pi^0}(z) = \frac{6 f_\pi}{\sqrt{2}} z(1-z)$, the z-integration is readily carried out and after separating the real and imaginary parts of the amplitude, the x-integration gives:

$$\mathcal{I}^A_x = \frac{1}{\sqrt{2}} \sum_{q=u,d} |Q_q| \int_{-1}^{1} dx \left(\frac{1}{x-\xi+i\epsilon} + \frac{1}{x+\xi-i\epsilon} \right) A_q^{\pi^0}(x,\xi,t) = \tag{7}$$

$$\frac{1}{\sqrt{2}} \sum_{q=u,d} |Q_q| \left[\int_{-1}^{1} dx \, \frac{A_q^{\pi^0}(x,\xi,t) - A_q^{\pi^0}(\xi,\xi,t)}{x-\xi} + A_q^{\pi^0}(\xi,\xi,t)(\log\left(\frac{1-\xi}{1+\xi}\right) - i\pi) + \right.$$

$$\left. \int_{-1}^{1} dx \, \frac{A_q^{\pi^0}(x,\xi,t) - A_q^{\pi^0}(-\xi,\xi,t)}{x+\xi} + A_q^{\pi^0}(-\xi,\xi,t)(\log\left(\frac{1+\xi}{1-\xi}\right) + i\pi) \right].$$

The scaling law for the amplitude is

$$\mathcal{M}^{TDA}_{\gamma^\star\gamma}(Q^2,\xi,t) \sim \frac{\alpha_s\sqrt{-t}}{Q}\,, \tag{8}$$

up to logarithmic corrections due to the anomalous dimension of the TDA and the running of α_s.

3.2 Remarks on available models

Lacking any non-perturbative calculations of matrix element defining TDAs, we have initially built a toy model [4] based on double distributions [18] to get estimates for the cross sections, to be compared with experimental data. In [4], we compared the rate obtained with this model with the one from the model built in [19]. Subsequently, a model based on quark spectral representation was developed in [20], another based on NJL model was studied in [21, 22] and lastly the $\pi \to \gamma$ TDAs were studied in a non-local chiral quark model [23]. All the models (see e.g. [24]) used so far for the pion GPDs could be extended to the construction of $\pi \to \gamma$ TDAs. We refer to the different references for details. For illustration, we show here on Fig. 2 the TDA $A(x,\xi,t)$ obtained in Ref. [4] in arbitrary unit; its normalisation would be eventually fixed by the experimental data.

For the purpose of this note, we only need a rough evaluation of the order of magnitude of the cross section and will only use the Model 1 of Ref. [4]. When a dedicated experimental analysis is being carried out, a careful survey of the cross sections obtained from the different theoretical models will be in order. Hence, based on a first experimental study of the ξ dependence and after having checked the scaling in Q^2, we shall be in position to see which model describes best the physics involved. For this best model, we could then obtain by sum rules relations a first measurement of the axial π^0 form factor.

For the following, we shall show results for $\langle \pi^0 | \bar{d}\mathcal{O}_A d|\gamma\rangle = -1/2 \langle \pi^0|\bar{u}\mathcal{O}_A u|\gamma\rangle$ expected from the different charges of the u and d quarks and using (from isospin arguments)

$$\langle \pi^+ | \bar{d}\mathcal{O}_A u|\gamma\rangle = \langle \pi^0|\bar{d}\mathcal{O}_A d|\gamma\rangle - \langle \pi^0|\bar{u}\mathcal{O}_A u|\gamma\rangle. \tag{9}$$

This would give $A_d^{\pi^0} = 1/3 A^{\pi^+}$ and $A_u^{\pi^0} = -2/3 A^{\pi^+}$. Note that more realistic models may give significantly larger rates.

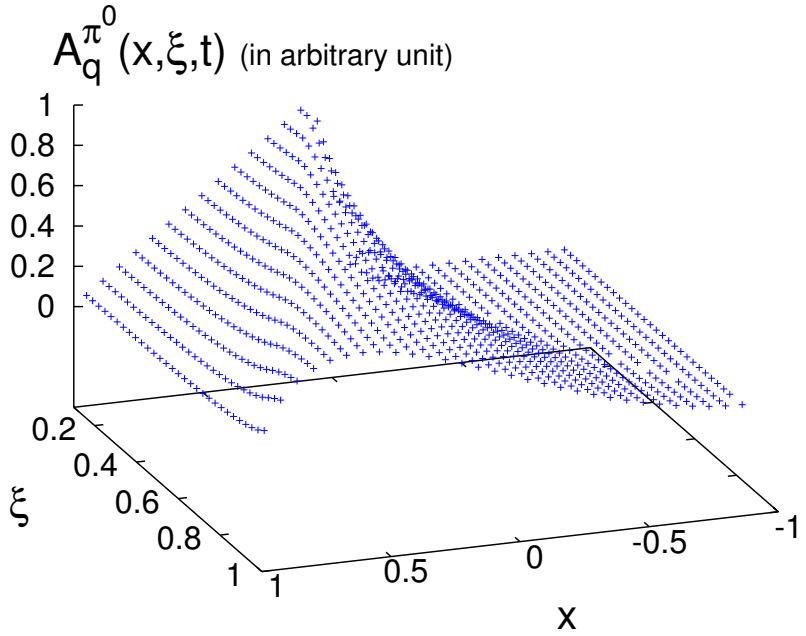

Figure 2: The $\gamma \to \pi^0$ axial transition distribution amplitude $A_q^{\pi^0}(x,\xi,t)$ in Model 1 of Ref. [4] (for $t = -0.5$ GeV^2) in arbitrary unit.

3.3 Cross section

Taking into account the contribution from the fermionic line for the emission by the electron of a longitudinal photon, averaging over the real photon polarisation and integrating over φ thanks to the φ-independence of the TDA process, we eventually obtain the differential cross section[1]:

$$\frac{d\sigma^{TDA}_{e\gamma\to e\pi^0\pi^0}}{dQ^2 dt d\xi} = \frac{64\pi\alpha_{em}^3\alpha_s^2 2\pi}{9(\xi+1)^4 Q^8}(-2\xi t)(1-\xi-(1+\xi)\frac{W^2_{\pi\pi}}{s_{e\gamma}})(\mathrm{Re}^{\,2}(\mathcal{I}^A_x)+\mathrm{Im}^{\,2}(\mathcal{I}^A_x)). \qquad (10)$$

For the hypothesis discussed above, the resulting cross section is roughly one sixth of the one obtained in [4] for the charged case. The evolution as function of ξ is displayed on Fig. 3. Note that for small ξ (particularly $W^2_{\pi\pi} \to Q^2$), the cross section shows a peak.

The Q^2-behaviour is model independent and thus constitutes a crucial test of the validity of our approach.

[1] A factor 1/4 is missing in Eq.(23) of [4].

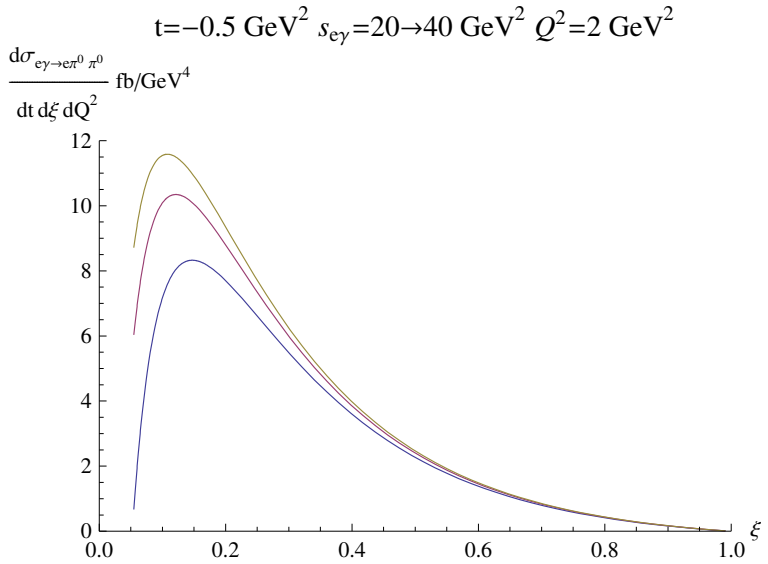

Figure 3: Differential cross sections $\frac{d\sigma_{e\gamma\to e\pi^0\pi^0}}{dQ^2 dt d\xi}$ for the TDA subprocess as a function of ξ for $Q^2 = 2$ GeV^2, $t = -0.5$ GeV^2 and 3 values of $s_{e\gamma}$: 20, 30 and 40 GeV^2 (from bottom to top).

Conclusion

We believe that our models for the photon to meson transition distribution amplitudes are sufficiently constrained to give reasonable orders of magnitude for the estimated cross sections. Cross sections are large enough for quantitative studies to be performed at high luminosity e^+e^- colliders. After verifying the scaling and the φ independence of the cross section, one should be able to measure these new hadronic matrix elements, and thus open a new gate to the understanding of the hadronic structure. In particular, we argued here that the study of $\gamma^\star\gamma \to \pi^0\pi^0$ in the TDA regime could provide with a unique experimental measurement of the π^0 axial form factor.

Acknowledgments

We are thankful to I. Anikin, S.J. Brodsky, M. Davier, S. Li, S. Wallon for useful discussions and correspondence, and the organisers of the Photon 2009 conference for their invitation. This work is supported in part by a Francqui fellowship of the Belgian American Educational Foundation, by the U.S. Department of Energy under contract number DE-AC02-76SF00515, the French-Polish scientific agreement Polonium and the Polish Grant N202 249235.

References

[1] B. Pire and L. Szymanowski, Phys. Rev. D **71** (2005) 111501 [arXiv:hep-ph/0411387].

[2] B. Pire and L. Szymanowski, Phys. Lett. B **622** (2005) 83 [arXiv:hep-ph/0504255].

[3] B. Pire and L. Szymanowski, Acta Phys. Polon. B **37** (2006) 893 [arXiv:hep-ph/0510161].

[4] J. P. Lansberg, B. Pire and L. Szymanowski, Phys. Rev. D **73** (2006) 074014 [arXiv:hep-ph/0602195].

[5] J. P. Lansberg, B. Pire and L. Szymanowski, Nucl. Phys. A **782** (2007) 16 [arXiv:hep-ph/0607130].

[6] J. P. Lansberg, B. Pire and L. Szymanowski, Phys. Rev. D **75**, 074004 (2007) [Erratum-ibid. D **77**, 019902 (2008)] [arXiv:hep-ph/0701125].

[7] J. P. Lansberg, B. Pire and L. Szymanowski, Phys. Rev. D **76**, (2007) 111502R [arXiv:0710.1267 [hep-ph]].

[8] For recent mini-reviews: J. P. Lansberg, B. Pire and L. Szymanowski, In "Exclusive Reactions at High Momentum Transfer" (Singapore, World Scientific, 2008, p. 367) [0709.2567 [hep-ph]]; J. P. Lansberg, B. Pire and L. Szymanowski, Nucl. Phys. Proc. Suppl. **184**, 239 (2008) [arXiv:0710.1294 [hep-ph]].

[9] J. C. Collins, L. Frankfurt and M. Strikman, Phys. Rev. D **56** (1997) 2982.

[10] A. V. Efremov and A. V. Radyushkin, Phys. Lett. B **94** (1980) 245; G. P. Lepage and S. J. Brodsky, Phys. Lett. B **87** (1979) 359.

[11] D. Mueller et al., Fortsch. Phys. **42**, 101 (1994); M. Diehl et al., Phys. Rev. Lett. **81**, 1782 (1998) and Phys. Rev. D **62**, 073014 (2000); B. Pire and L. Szymanowski, Phys. Lett. B **556**, 129 (2003); I. V. Anikin et al., Phys. Rev. D **69**, 014018 (2004) and Phys. Lett. B **626** (2005) 86.

[12] B. Aubert [The BABAR Collaboration], arXiv:0905.4778 [hep-ex].

[13] N. Warkentin, M. Diehl, D. Y. Ivanov and A. Schafer, Eur. Phys. J. A **32**, 273 (2007) [arXiv:hep-ph/0703148].

[14] P. Hagler et al., Phys. Lett. B **535**, 117 (2002) and Eur. Phys. J. C **26**, 261 (2002)

[15] I. V. Anikin, I. O. Cherednikov, N. G. Stefanis and O. V. Teryaev, Eur. Phys. J. C **61**, 357 (2009) and arXiv:0907.2579 [hep-ph].

[16] D. Amrath, M. Diehl and J. P. Lansberg, Eur. Phys. J. C **58** (2008) 179 [arXiv:0807.4474 [hep-ph]].

[17] C. Amsler *et al.* [Particle Data Group], Phys. Lett. B **667** (2008) 1.

[18] A. V. Radyushkin, Phys. Rev. D **59** (1999) 014030.

[19] B. C. Tiburzi, Phys. Rev. D **72** (2005) 094001.

[20] W. Broniowski and E. R. Arriola, Phys. Lett. B **649** (2007) 49;

[21] A. Courtoy and S. Noguera, Phys. Rev. D **76** (2007) 094026 [arXiv:0707.3366 [hep-ph]].

[22] A. Courtoy and S. Noguera, Phys. Lett. B **675** (2009) 38 [arXiv:0811.0550 [hep-ph]].

[23] P. Kotko and M. Praszalowicz, arXiv:0803.2847 [hep-ph].

[24] A. E. Dorokhov and L. Tomio, Phys. Rev. D **62** (2000) 014016; M. Praszalowicz and A. Rostworowski, Acta Phys. Polon. B **34** (2003) 2699; F. Bissey, *et al.* Phys. Lett. B **547** (2002) 210; Phys. Lett. B **587** (2004) 189

Resonance Searches at HERA

Uri Karshon

Weizmann Institute of Science, Rehovot, Israel
On behalf of the H1 and ZEUS Collaborations

DOI: http://dx.doi.org/10.3204/DESY-PROC-2009-03/Karshon

Inclusive production of $K^0_S K^0_S$ in ep collisions was studied with the ZEUS detector. Significant production of $J^{PC} = 2^{++}$ tensor mesons and of the 0^{++} glueball candidate $f_0(1710)$ was seen. Masses and widths were compared with previous experiments. The H1 Collaboration saw a charm pentaquark candidate in the $D^* p$ spectrum at 3.1 GeV, which was not confirmed by a ZEUS higher statistics search. With the full HERA statistics, H1 did not see a signal in this region. Masses, widths and helicity parameters of excited charm and charm-strange mesons were measured by ZEUS. Rates of c quarks hadronising into these mesons were determined and a search for a radially excited charm meson was performed.

1 Introduction

The HERA ep collider operated with electrons or positrons at 27.6 GeV and protons at 820 or 920 GeV. Each of the two general purpose experiments H1 and ZEUS collected during 1995 - 2000 ("HERA I") $\approx 120\ pb^{-1}$ and during 2003 - 2007 ("HERA II") $\approx 370\ pb^{-1}$. Two kinematic regions have been explored: Deep inelastic scattering (DIS) with photon virtuality $Q^2 > 1$ GeV^2, where the scattered electron is visible in the main detector and photoproduction (PHP) with $< Q^2 > \approx 3 \cdot 10^{-4}$ GeV^2, where the virtual photon radiated from the incoming electron is quasi-real. The sample is dominated by PHP events.

2 Glueball search in the $K^0_S K^0_S$ system

Glueballs are predicted by QCD. The lightest glueball is expected to have $J^{PC} = 0^{++}$ and a mass in the range 1550-1750 MeV [1] and can mix with $q\bar{q}$ scalar meson nonet I=0 states of similar mass. There are four such established states: $f_0(980)$, $f_0(1370)$, $f_0(1500)$ and $f_0(1710)$, but only two can fit into the nonet. The $f_0(1710)$ state is considered as a possible glueball candidate. The $K^0_S K^0_S$ system can couple to $J^{PC} = 0^{++}$ and 2^{++}. Therefore, it is a good place to search for the lowest lying 0^{++} glueball.

2.1 Previous results

The e^+e^- experiments TASSO and L3 studied the exclusive reaction $\gamma\gamma \to K^0_S K^0_S$. L3 [2] saw 3 peaks and attributed them to $f_2(1270)/a_2(1320)$, $f_2'(1525)$ and $f_0(1710)$. A maximum likelihood fit with 3 Breit-Wigner (BW) functions plus background yielded $f_2'(1525)$ mass and width values consistent with the Particle Data Group (PDG) [1] and a 4 standard deviation

(s.d.) signal for $f_0(1710)$ with mass and width values above PDG. The TASSO [3] $K^0_S K^0_S$ spectra had no $f_2(1270)/a_2(1320)$ signal and a sizable $f_2^{'}(1525)$ enhancement. The result was interprated by interference effects between the 3 $J^P = 2^+$ resonances $f_2(1270)$, $a_2(1320)$ and $f_2^{'}(1525)$ and the spectra was fitted as a sum of 3 coherent BW functions. Based on SU(3) symmetry arguments [4], the sign of the $a_2(1320)$ term for $K^0_S K^0_S$ is negative and the coefficients of the $f_2(1270)$, $a_2(1320)$ and $f_2^{'}(1525)$ BW amplitudes are +5, -3 and +2, respectively.

2.2 This analysis

The reaction $e^{\pm}p \to K^0_S K^0_S + X$ was studied [5] with the full HERA luminosity of 0.5 fb^{-1}. Both PHP and DIS events were included. No explicit trigger requirement was applied for selecting the above reaction.

K^0_S mesons were identified via their decay mode $K^0_S \to \pi^+\pi^-$. A clean K^0_S signal was seen for events with $\geq 2K^0_S$ candidates. The number of $K^0_S K^0_S$ pairs found in the K^0_S mass range $481 < M(\pi^+\pi^-) < 515$ MeV is $\approx 672,000$.

Figure 1 shows the $K^0_S K^0_S$ mass distribution reconstructed by combining two K^0_S candidates selected in the above mass window. Three peaks are seen around 1.3, 1.5 and 1.7 GeV. No state heavier than 1.7 GeV was observed. The invariant-mass spectrum, m, was fitted as a sum of relativistic Breit-Wigner (RBW) resonances and a smoothly varying background $U(m) = m^A exp(-Bm)$, where A and B are free parameters.

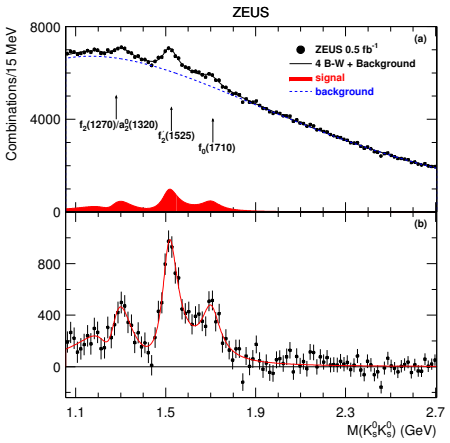

Figure 1: (a)The $K^0_S K^0_S$ distribution (dots). Solid line is the coherent fit (see text); background function is given by the dashed line. (b)Background-subtracted $K^0_S K^0_S$ distribution (dots); solid line is the fit result.

Two types of fit, as performed for the reaction $\gamma\gamma \to K^0_S K^0_S$ by L3 [2] and TASSO [3], respectively, were tried. The first fit (not shown) is an incoherent sum of three modified RBW resonances, R, of the form $F(m) = C_R(\frac{M_R\Gamma_R}{(M_R^2-m^2)^2+M_R^2\Gamma_R^2})$, representing the peaks $f_2(1270)/a_2(1320)$, $f_2^{'}(1525)$ and $f_0(1710)$. Here C_R is the resonance amplitude and M_R and Γ_R are the resonance mass and width, respectively. The goodness of this fit is reasonable ($\chi^2/ndf = 96/95$); however, the dip between the $f_2(1270)/a_2(1320)$ and $f_2^{'}(1525)$ is not well reproduced.

Figure 1 shows a coherent fit motivated by SU(3) predictions[4]. Each resonance amplitude, R, is described by the RBW form [3] $BW(R) = \frac{M_R\sqrt{\Gamma_R}}{M_R^2-m^2-iM_R\Gamma_R}$. The decays of the tensor ($J^P = 2^+$) mesons $f_2(1270)$, $a_2^0(1320)$ and $f_2^{'}(1525)$ into the two pseudoscalar ($J^P = 0^+$) mesons $K^0\bar{K}^0$ are related by SU(3) symmetry with a specific interference pattern. The intensity is the modulus-squared of the sum of these 3 amplitudes plus the incoherent addition of $f_0(1710)$ and a non-resonant background.

Assuming SU(3) symmetry and a direct coupling of the 2^+ states to the exchanged photon, the fitted function to the $m(K^0_S K^0_S)$ spectra is given by $F(m) = a[5 \cdot BW(f_2(1270)) - 3 \cdot BW(a_2(1320)) + 2 \cdot BW(f_2^{'}(1525))]^2 + b[BW(f_0(1710))]^2 + c \cdot U(m)$, where a,b,c as well as the

resonance masses and widths were free parameters in the fit. The background-subtracted mass spectrum is shown in Fig.1(b). The fit quality is good ($\chi^2/ndf = 86/97$). The peak around 1.3 GeV is suppressed due to the destructive interference between $f_2(1270)$ and $a_2(1320)$ and the dip between $f_2(1270)/a_2(1320)$ and $f_2'(1525)$ is well reproduced. The number of fitted $f_0(1710)$ events is 4058 ± 820, which has ≈ 5 s.d. significance. Its mass is consistent with a $J^{PC} = 0^{++}$ glueball candidate, but it cannot be a pure glueball if it is the same state as in $\gamma\gamma \to K^0_S K^0_S$.

Fit	No interference		Interference		PDG 2007 Values	
χ^2/ndf	96/95		86/97			
in MeV	Mass	Width	Mass	Width	Mass	Width
$f_2(1270)$	1304 ± 6	61 ± 11	1268 ± 10	176 ± 17	1275.4 ± 1.1	$185.2^{+3.1}_{-2.5}$
$a_2^0(1320)$			1257 ± 9	114 ± 14	1318.3 ± 0.6	107 ± 5
$f_2'(1525)$	$1523 \pm 3^{+2}_{-8}$	$71 \pm 5^{+17}_{-2}$	$1512 \pm 3^{+2}_{-0.6}$	$83 \pm 9^{+5}_{-4}$	1525 ± 5	73^{+6}_{-5}
$f_0(1710)$	$1692 \pm 6^{+9}_{-3}$	$125 \pm 12^{+19}_{-32}$	$1701 \pm 5^{+5}_{-3}$	$100 \pm 24^{+8}_{-19}$	1724 ± 7	137 ± 8

Table 1: *Fitted masses and widths for $f_2(1270)$, $a_2^0(1320)$, $f_2'(1525)$ and $f_0(1710)$ from the incoherent and coherent fits compared to PDG. The first error is statistical. For $f_2'(1525)$, $f_0(1710)$ the second errors are systematic uncertainties.*

The masses and widths obtained from both fits are shown in Table 1 and compared to PDG [1]. The no-interference fit yields a narrow width for the combined $f_2(1270)/a_2(1320)$ peak, as was also seen by L3 [2]. The fit with interference yields widths close to the PDG values for all observed resonances. The $a_2^0(1320)$ mass is below the PDG value. The $f_2'(1525)$ and $f_0(1710)$ masses are somewhat below PDG with uncertainties comparable with the PDG ones. A fit without $f_0(1710)$ is strongly disfavoured with $\chi^2/ndf = 162/97$.

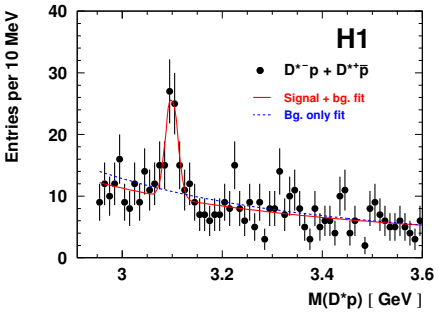

Figure 2: $M(D^{*\pm}p^{\mp})$ from H1 DIS HERA I, compared with fit results where both signal and background components are included and where only background is included.

3 Charm pentaquark search in the D^*p system

A narrow exotic baryon with strangeness +1 around 1530 MeV decaying into K^+n or K^0p was seen by various experiments and attributed to the $\Theta^+ = uudd\bar{s}$ pentaquark state predicted by Diakonov et al.[6]. If a strange pentaquark exists, charmed pentaquarks, $\Theta_c^0 = uudd\bar{c}$, could also exist. If $M(\Theta_c^0) > M(D^*) + M(p) = 2948$ MeV, it can decay to $D^{*\pm}p^{\mp}$.

The H1 Collaboration saw [7] in a DIS HERA I sample of ≈ 3400 $D^{*\pm} \to D^0\pi_S^{\pm} \to K^{\mp}\pi^{\pm}\pi_S^{\pm}$ a narrow signal of 50.6 ± 11.2 events in the $D^{*\pm}p^{\mp}$ invariant mass at 3.1 GeV (Fig.2) with a

width consistent with the mass resolution and a rate of $\approx 1\%$ of the visible D^* production.

ZEUS searched for a Θ_c^0 signal in the $D^{*\pm}p^{\mp}$ mode with the full HERA I PHP + DIS data sample [8]. Clean $D^{*\pm}$ signals were seen in the $\Delta M = M(D^{*\pm}) - M(D^0)$ plots. Two $D^{*\pm} \to D^0\pi_S^{\pm}$ decay channels were used with $D^0 \to K^{\mp}\pi^{\pm}$ and $D^0 \to K^{\mp}\pi^{\pm}\pi^+\pi^-$. The Θ_c^0 search was performed in the kinematic range $|\eta(D^*)| < 1.6$ and $p_T(D^*) > 1.35(2.8)$ GeV and with ΔM values between 0.144 - 0.147 (0.1445 - 0.1465) GeV for the $K\pi\pi$ ($K\pi\pi\pi\pi$) channel. In these bands ≈ 62000 D^*'s were obtained after subtracting wrong-charge combinations with charge ± 2 for the D^0 candidate and ± 1 for the D^* candidate. Selecting DIS events with $Q^2 > 1$ GeV^2 yielded smaller, but cleaner D^* signals with ≈ 13500 D^*'s.

Protons were selected with momentum $P(p) > 0.15$ GeV. To reduce the pion and kaon background, a parameterisation of the expected dE/dx as a function of P/m was obtained using tagged protons from Λ decays and tagged pions from K_S^0 decays. The χ^2 probability of the proton hypothesis was required to be above 0.15.

Figure 3 shows the $M(D^{*\pm}p^{\mp})$ distributions for the $D^0 \to K\pi$ (left) and $D^0 \to K\pi\pi\pi$ (right) channels for the full (up) and the DIS (down) samples. No narrow signal is seen in any of the distributions. 95% C.L. upper limits on the fraction of D^* mesons originating from Θ_c^0 decays, $R(\Theta_c^0 \to D^*p/D^*)$, were calculated in a signal window $3.07 < M(D^*p) < 3.13$ GeV for the $K\pi\pi$ and $K\pi\pi\pi\pi$ channels. The $M(D^*p)$ distributions were fitted to the form $x^a e^{-bx+cx^2}$, where $x = M(D^*p) - M(D^*) - m_p(PDG)$. The number of reconstructed Θ_c^0 baryons was estimated by subtracting the background function from the observed number of events in the signal window, yielding $R(\Theta_c^0 \to D^*p/D^*) < 0.23\%$ and $< 0.35\%$ for the full and DIS combined two channels. A visible rate of 1% for this fraction is excluded by 9 s.d. (5 s.d.) for the full (DIS) combined sample. The acceptance-corrected rates are, respectively, 0.37% and 0.51%. The 95% C.L. upper limit on the fraction of charm quarks fragmenting to Θ_c^0 times the branching ratio $\Theta_c^0 \to D^*p$ for the combined two channels is $f(c \to \Theta_c^0) \cdot B_{\Theta_c^0 \to D^*p} < 0.16\%$ ($< 0.19\%$) for the full (DIS) sample.

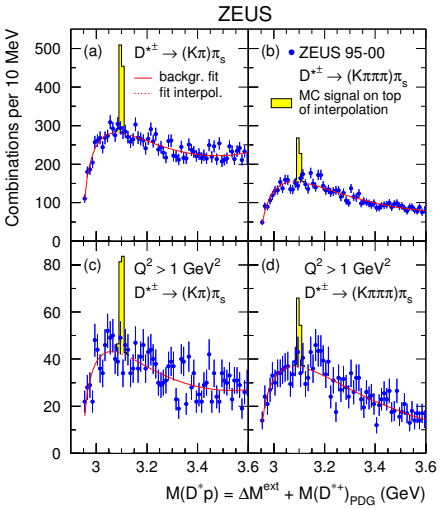

Figure 3: $M(D^{*\pm}p^{\mp})$ from ZEUS HERA I. Solid curves are fits to a background function. Shaded historgams are MC Θ_c^0 signals, normalised to $\Theta_c^0/D^* = 1\%$, on top of the background fit.

In a HERA II DIS data sample that is ≈ 4 times larger than the HERA I sample, H1 does not see any significant peak at 3.1 GeV (Fig.4). A preliminary 95% C.L. for the ratio of D^*p to D^* is 0.1%.

4 Excited charm and charm-strange mesons

The large charm production at HERA allows to search for excited charm states. ZEUS studied the orbitally excited states $D_1(2420)^0 \to D^{*\pm}\pi^{\mp}$ ($J^P = 1^+$), $D_2^*(2460)^0 \to D^{*\pm}\pi^{\mp}, D^{\pm}\pi^{\mp}$

$(J^P = 2^+)$ and $D_{s1}(2536)^\pm \to D^{*\pm}K^0_S, D^{*0}K^\pm$ $(J^P = 1^+)$ and searched for the radially excited state $D^{*'}(2640)^\pm \to D^{*\pm}\pi^+\pi^-$ $(J^P = 1^-\ ?)$ with a HERA I PHP + DIS sample[9].

A large sample of events has been collected with the ground state charm mesons $D^{*\pm}, D^0, D^\pm$. The number of $D^{*\pm}$ mesons was obtained by subtracting the wrong charge background. The number of $D^\pm \to K^\mp\pi^\pm\pi^\pm$ and $D^0(\bar{D}^0) \to K^\mp\pi^\pm$ was extracted from fits to a modified Gauss function, $Gauss^{mod} \sim exp(-0.5x^{1+\frac{1}{(1+0.5x)}})$, where $x = (M - M_D)/\sigma$, plus a background function. For the D^*, both D^0 decay modes to $K\pi$ and $K\pi\pi\pi$ were used.

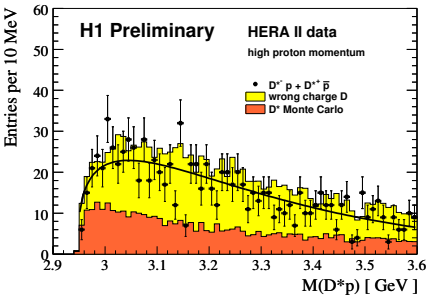

Figure 4: $M(D^{*\pm}p^\mp)$ from H1 DIS HERA II. The solid line is a background parametrisation.

4.1 Excited charm mesons

To reconstruct the excited charm mesons, a $D^{*\pm}$ or $D^\pm$ candidate was combined with a pion of opposite charge, π_a. Figure 5 shows the "extended" mass difference distributions $M(D^{*\pm}\pi_a) - M(D^{*\pm}) + M(D^*)_{PDG}$ (upper plot) and $M(D^\pm\pi_a) - M(D^\pm) + M(D)_{PDG}$ (lower plot). A clear excess is seen in $M(D^{*\pm}\pi_a^\mp)$ around the D_1^0/D_2^{*0} mass region. A small excess near the D_2^{*0} mass is seen in $M(D^\pm\pi_a^\mp)$. No excess is seen for wrong charge combinations, where $D^*(D)$ and π_a have the same charge.

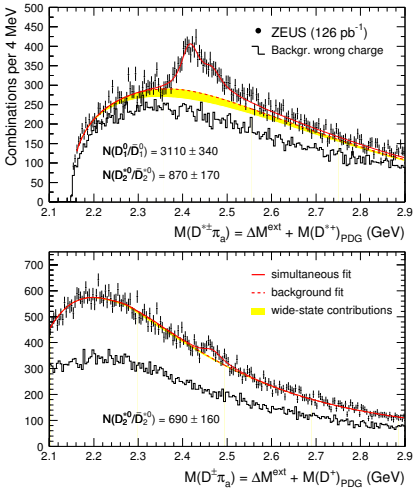

Figure 5: $M(D^{*\pm}\pi_a)$ and $M(D^\pm\pi_a)$ distributions. Solid curves are simultaneous fit; dashed curves are background; histograms are wrong-charge combinations.

To distinguish between the D_1^0 and D_2^{*0}, the helicity angular distribution, parametrised as $dN/d\cos\alpha \approx 1 + h\cos^2\alpha$, was used. Here α is the angle between the π_a and π_S momenta in the D^* rest frame. The helicity parameter h is predicted [10] to be $3(-1)$ for pure D-wave D_1^0 (D_2^{*0}).

Figure 6 shows the $D^{*\pm}\pi_a$ "extended" mass difference in 4 helicity $|\cos\alpha|$ intervals. The D_1^0 contribution increases with $|\cos\alpha|$ and dominates for $|\cos\alpha| > 0.75$. A simultaneous fit was performed to the 4 helicity regions of Fig.6 and to the $M(D\pi)$ distribution of Fig.5. The data is described well with 15 free parameters (signal yields, masses, D_1^0 width and helicity). The fitted masses agree with PDG. The fitted D_1^0 width is $53.2 \pm 7.2(stat.)^{+3.3}_{-4.9}(syst.)$ MeV compared to 20.4 ± 1.7 MeV of PDG. The fitted D_1^0 helicity $(5.9^{+3.0}_{-1.7}(stat.)^{+2.4}_{-1.0}(syst.))$ is consistent with a pure D-wave.

4.2 Excited charm strange mesons

To reconstruct the $D_{s1}^{\pm} \to D^{*\pm}K_S^0$ decays, a $D_{s1}^{\pm}$ candidate was formed by combining a D^* candidate with a reconstructed K_S^0 of the same event. Figure 7 (upper plot) shows the "extended" mass difference distribution $M(D^{*\pm}K_S^0) - M(D^{*\pm}) + M(D^*)_{PDG} + M(K^0)_{PDG}$. A clear $D_{s1}(2536)^{\pm}$ signal is seen. The decay mode $D_{s1}^{\pm} \to D^{*0}K^{\pm}$ is reconstructed from the "extended" mass difference $M(D^0K_a) - M(D^0) + M(D^0)_{PDG}$. A nice $D_{s1}^{\pm}$ signal is seen (Figure 7 lower plot) at a mass shifted down by ≈ 142 MeV from the $D_{s1}^{\pm}$ mass. The signal is a feed-down from $D_{s1}^{\pm} \to D^{*0}K^{\pm}$ with $D^{*0} \to D^0\pi^0, D^0\gamma$. An unbinned likelihood fit was performed using simultaneously values of $M(D^0K_a)$, $M(D^{*\pm}K_S^0)$ and $\cos\alpha$ for the $D^{*\pm}K_S^0$ combinations. Yields and widths of both signals and the $D_{s1}^{\pm}$ mass and helicity parameter were free parameters of the fit. The fitted D_{s1} helicity parameter is $h(D_{s1}^{\pm}) = -0.74^{+0.23}_{-0.17}(stat.)^{+0.06}_{-0.05}(syst.)$. It is inconsistent with a pure $J^P = 1^+$ D-wave and is barely consistent with a pure $J^P = 1^+$ S-wave, indicating a significant $S-D$ mixing.

The helicity angular distribution form of a 1^+ state for any D- and S-wave mixing is: $dN/d\cos\alpha \approx r + (1-r)(1+3\cos^2\alpha)/2 + \sqrt{2r(1-r)}\cos\phi(1-3\cos^2\alpha)$, where $r = \Gamma_S/(\Gamma_S+\Gamma_D)$, $\Gamma_{S/D}$ is the S/D wave partial width and ϕ is relative phase between the 2 amplitudes, $\cos\phi = \frac{(3-h)/(3+h)-r}{2\sqrt{2r(1-r)}}$. Figure 8 shows a range, restricted by the measured $h(D_{s1}^{\pm})$ value and its uncertainties, in a plot of $\cos\phi$ versus r. The measurement suggests a significant contribution of both D- and S-wave amplitudes to the $D_{s1}(2536)^{\pm} \to D^{*\pm}K_S^0$ decay. The ZEUS range agrees nicely with the BELLE result and roughly with the CLEO measurement.

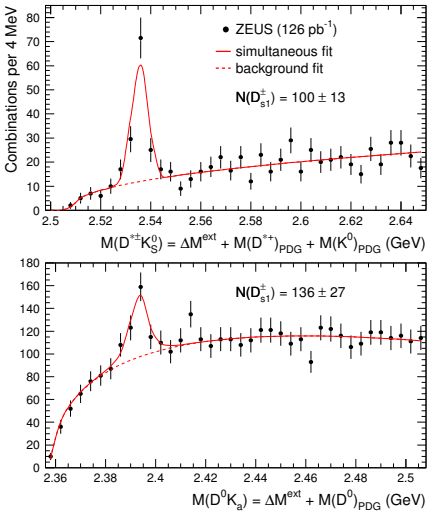

Figure 7: $M(D^{*\pm}K_S^0)$ and $M(D^0K^{\pm})$ distributions. Solid curves are simultaneous fit; dashed curves are background.

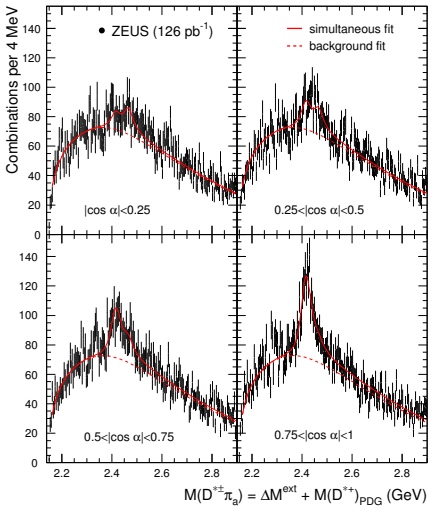

Figure 6: $M(D^{*\pm}\pi_a)$ distributions in 4 helicity intervals.

5 Branching ratios and fragmentation fractions

Using the ZEUS measured fractions $f(c \to D^{*+})$ and $f(c \to D^{+})$[11], the following decay rate ratios were derived: $\frac{B_{D_2^{*0}\to D^+\pi^-}}{B_{D_2^{*0}\to D^{*+}\pi^-}} = 2.8 \pm 0.8^{+0.5}_{-0.6}$ (PDG: 2.3 ± 0.6); $\frac{B_{D_{s1}^+\to D^{*0}K^+}}{B_{D_{s1}^+\to D^{*+}K^0}} = 2.3 \pm 0.6 \pm 0.3$ (PDG: 1.27 ± 0.21).

Assuming isospin conservation for D_1^0 and D_2^{*0} and $B_{D_{s1}^+\to D^{*+}K^0} + B_{D_{s1}^+\to D^{*0}K^+} = 1$ yields a strangeness suppression of excited D mesons $f(c \to D_{s1}^+)/f(c \to D_1^0) = 0.31 \pm 0.06(stat.)^{+0.05}_{-0.04}(syst.)$.

In Table 2 the ZEUS fragmentation fractions of the excited charm mesons are compared with e^+e^- values. The results are consistent within errors.

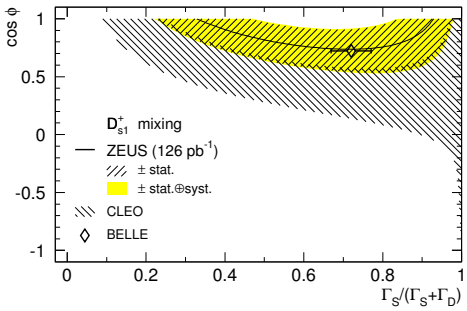

Figure 8: $\cos\phi$ vs. $\Gamma_S/(\Gamma_S + \Gamma_D)$ for $D_{s1}^+ \to D^{*+}K_S^0$ decay.

DELPHI saw a narrow peak in $D^{*\pm}\pi^+\pi^-$ at 2637 MeV [12] and attributed it to a radially excited $D^{*'\pm}$. No signal was seen in ZEUS and a 95% C.L. upper limit of $f(c \to D^{*'\pm}) \cdot B_{D^{*'\pm}\to D^{*+}\pi^+\pi^-} < 0.4\%$ was set, compared to the weaker limit of OPAL (0.9%) [13].

	$f(c \to D_1^0)[\%]$	$f(c \to D_2^{*0})[\%]$	$f(c \to D_{s1}^+)[\%]$
ZEUS	$3.5 \pm 0.4^{+0.4}_{-0.6}$	$3.8 \pm 0.7^{+0.5}_{-0.6}$	$1.11 \pm 0.16^{+0.08}_{-0.10}$
OPAL	2.1 ± 0.8	5.2 ± 2.6	$1.6 \pm 0.4 \pm 0.3$
ALEPH			$0.94 \pm 0.22 \pm 0.07$

Table 2: *The fractions of c quarks hadronising into D_1^0, D_2^{*0} and D_{s1}^+ mesons.*

References

[1] Particle Data Group, W.M. Yao *et al.*, J. Phys. G **C33** 1 (2006). Updated in http://pdg.lbl.gov.
[2] L3 Collaboration, M. Acciarri *et al.*, Phys. Lett. **B501** 173 (2001).
[3] TASSO Collaboration, M. Althoff *et al.*, Phys. Lett. **B121** 216 (1983).
[4] D. Faiman, H.J. Lipkin and H.R. Rubinstein, Phys. Lett. **B59** 269 (1975).
[5] ZEUS Collaboration, S. Chekanov *et al.*, Phys. Rev. Lett. **101** 112003 (2008).
[6] D. Diakonov *et al.*, Z. Phys. **A359** 305 (1997).
[7] H1 Collaboration, A. Aktas *et al.*, Phys. Lett. **B588** 17 (2004).
[8] ZEUS Collaboration, S. Chekanov *et al.*, Eur. Phys. J. **C38** 29 (2004).
[9] ZEUS Collaboration, S. Chekanov *et al.*, Eur. Phys. J. **C60** 25 (2009).
[10] N. Isgur and M.B. Wise, Phys. Lett. **B232** 113 (1989); M. Neubert, Phys. Rep. **245** 259 (1994).
[11] ZEUS Collaboration, S. Chekanov *et al.*, Eur. Phys. J. **C44** 351 (2005).
[12] DELPHI Collaboration, P. Abreu *et al.*, Phys. Lett. **B426** 231 (1998).
[13] OPAL Collaboration, G. Abbiendi *et al.*, Eur. Phys. J. **C20** 445 (2001).

Photon Interactions and Chiral Dynamics

Wojciech Broniowski[1,2], *Alexandr E. Dorokhov*[3], *Enrique Ruiz Arriolo*[4]

[1]Institute of Physics, Jan Kochanowski University, PL-25406 Kielce, Poland
[2]The H. Niewodniczański Institute of Nuclear Physics, Polish Academy of Sciences, PL-31342 Kraków, Poland
[3]Joint Institute for Nuclear Research, Bogoliubov Laboratory of Theoretical Physics, 114980, Moscow region, Dubna, Russia
[4]Departamento de Física Atómica, Molecular y Nuclear, Universidad de Granada, E-18071 Granada, Spain

DOI: http://dx.doi.org/10.3204/DESY-PROC-2009-03/Broniowski

Twist-2 components of the real and virtual photon distribution amplitudes are evaluated in several chiral quark models. The results, obtained at the quark model scale, are then evolved to higher scales, probed in experiments or in lattice QCD. We also analyze the related form factors and coupling constants. Our results are a genuine dynamical prediction, following from the chiral dynamics.

1 Basics

This talk is based on Ref. [1], where more details and results can be found. Our approach is based on the fact that the spontaneously broken chiral symmetry provides the basic dynamics for the evaluation of soft matrix element involving the Goldstone bosons (pion, kaons) and gauge currents (photons, $W^{\pm}$, Z). That way one may evaluate in a genuinely dynamical way the soft quantities appearing in high-energy processes. A detailed presentation of the method and the compilation of predictions for the pion matrix elements can be found in Ref. [2].

A crucial ingredient of the method is the QCD evolution from the a priori unknown *quark model scale* to the scales relevant for the experiments or lattice calculations. Thus the scheme consists of two steps: 1) the evaluation of soft matrix elements in the chiral quark model and 2) the QCD evolution to a higher scale. The quark model scale may be estimated with the help of the momentum sum rule [2], and is found to be low, $Q_0 \simeq 320$ MeV (for the local chiral quark models). After the QCD evolution, a successful description of the available data for the pion is achieved for the parton distribution function (PDF) and the distribution amplitude (DA). There are numerous quark-model studies of these quantities as well as the more general pion generalized parton distributions (GPD's) in the literature [3, 4, 5, 6, 7, 8, 9, 10, 11, 12, 13, 14, 15, 16, 17, 18, 19, 20, 21]. A related quantity, the pion-photon transition distribution amplitude (TDA) [22, 23] has also been evaluated in this framework [24, 25, 26].

The hadronic part of the photon wave-function consists, in the large-N_c limit, of a quark-antiquark pair. Since the chiral dynamics provides the quarks a large (constituent) mass, it influences the photon dynamics. Here we apply the methods developed and tested earlier for the pion to the photon case. We focus on the photon DA's, while the photon structure function

Table 1: The constants obtained in the quark model and evaluated to the reference scale of 1 GeV.

quantity at 1 GeV	non-local	SQM	QCD s.r.	VMD
$(-\langle 0\,\vert\overline{q}q\vert\,0\rangle)^{1/3}$ [GeV]	0.24	0.24	0.24 ± 0.02	-
χ_m [GeV^2]	2.73	1.37	3.15 ± 0.3	3.37
$f_{3\gamma}$ [GeV^{-2}]	-0.0035	-0.0018	-0.0039 ± 0.0020	-0.0046

is left for a separate study. The leading-twist photon distribution amplitudes (DA's) are defined via the matrix elements of quark bilinears delocalized along the light cone [27, 28, 29, 30],

$$\langle 0|\overline{q}(z)\sigma_{\mu\nu}[z,-z]q(-z)|\gamma^\lambda(q)\rangle =$$
$$ie_q\langle\bar{q}q\rangle\chi_{\rm m}f^t_{\perp\gamma}\left(q^2\right)\left(\epsilon^{(\lambda)}_{\perp\mu}p_\nu-\epsilon^{(\lambda)}_{\perp\nu}p_\mu\right)\int_0^1 dx e^{i(2x-1)q\cdot z}\phi_{\perp\gamma}(x,q^2)+h.t.,$$
$$\langle 0|\overline{q}(z)\gamma_\mu[z,-z]q(-z)|\gamma^\lambda(q)\rangle =$$
$$e_qf_{3\gamma}f^v_{\|\gamma}\left(q^2\right)p_\mu\left(\epsilon^{(\lambda)}\cdot n\right)\int_0^1 dx e^{i(2x-1)q\cdot z}\phi_{\|\gamma}(x,q^2)+h.t.,$$

where $\epsilon^{(\lambda)}\cdot q=0$ and $\epsilon^{(\lambda)}\cdot n=0$ (for real photons) and

$$p_\mu=q_\mu-\frac{q^2}{2}n_\mu,\ n_\mu=\frac{z_\mu}{p\cdot z},\ e^{(\lambda)}_\mu=\left(e^{(\lambda)}\cdot n\right)p_\mu+\left(e^{(\lambda)}\cdot p\right)n_\mu+e^{(\lambda)}_{\perp\mu}.$$

The quark magnetic susceptibility, $\chi_{\rm m}$, and $f_{3\gamma}$ are constants, $f^t_{\perp\gamma}(q^2)$ and $f^v_{\|\gamma}(q^2)$ are form factors, $\phi_{\perp\gamma}(x,q^2)$ and $\phi_{\|\gamma}(x,q^2)$ denote the DA's, while *h.t.* stands for the disregarded higher-twist contributions.

The leading-N_c quark model evaluation proceeds according to the one-loop diagram, where one of the vertices corresponds to the photon and the other to the probing operator, in our case $\sigma^{\mu\nu}$ and γ^μ. The quark propagators involve a constituent quark mass, due to spontaneous breaking of the chiral symmetry. We use a few variants of chiral quark models: the Nambu–Jona-Lasinio (NJL) (for reviews see, *e.g.*, [31, 15] and references therein) and the Spectral Quark model (SQM) [11, 32], which incorporates the vector-meson dominance, as well as the instanton-motivated non-local chiral quark model of Ref. [33, 34, 35, 36, 37]. In nonlocal models the quark mass depends on the virtuality, As a consequence, the vertices acquire corrections due to nonlocalities to consistently account for gauge and chiral Ward identities.

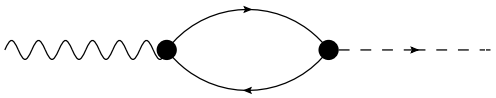

Figure 1: Feynman diagram for the evaluation of the photon DA's in chiral quark models.

2 Results

The result for the constants are presented in Table 1, where we also give the estimates of the QCD sum rules and the Vector Meson Dominance model [30]. QCD predicts the *scale*

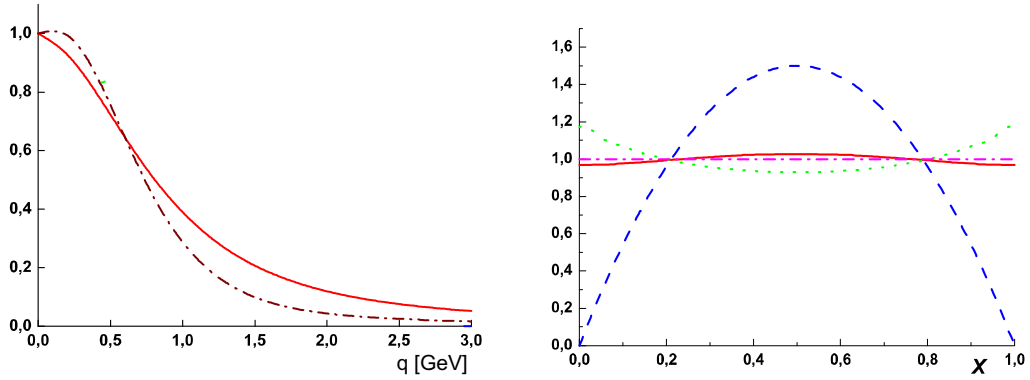

Figure 2: Left: the twist-2 tensor (dashed line) and vector (solid line) form factors in the non-local model. Right: the transverse DA of the photon, $\phi_{\perp\gamma}(x, q^2 = 0)$. Solid – non-local model, dot-dashed – local model, dotted – approximation of Ref. [38], dashed – the asymptotic form $6x(1-x)$.

dependence for the quark condensate $\langle 0\,|\overline{q}q|\,0\rangle$, its magnetic susceptibility $\chi_{\rm m}$, and $f_{3\gamma}$. At the leading order

$$\langle 0\,|\overline{q}q|\,0\rangle|_\mu = L^{-\gamma_{\overline{q}q}/b}\,\langle 0\,|\overline{q}q|\,0\rangle|_{\mu_0}\,,\;\; \chi_m|_\mu = L^{-(\gamma_0-\gamma_{\overline{q}q})/b}\,\chi_m|_{\mu_0}\,,\quad f_{3\gamma}|_\mu = L^{-\gamma_f/b}\,f_{3\gamma}|_{\mu_0}$$

where $r = \alpha_s\left(\mu^2\right)/\alpha_s\left(\mu_0^2\right)$, $b = (11N_c - 2n_f)/3$, is the evolution ratio, with $\gamma_{\overline{q}q} = -3C_F$, $\gamma_0 = C_F$, $\gamma_f = 3C_A - C_F/3$, $C_F = 4/3$, and $C_A = 3$ for $N_c = 3$. We evolve from the quark model scale, $Q_0 = 320$ MeV, to the reference scale of 1 GeV. We note a similar magnitude and signs compared to the QCD sum rules or VMD estimates, with the local model producing smaller values than the nonlocal model.

The form factors from the non-local quark model are shown in the left panel of Fig. 2. For the local models (not displayed) the results are very similar. They exhibit the typical fall-off scale of $\sim m_\rho$ In particular, in SQM we recover the exact VMD formula

$$f_{\perp\gamma}^{t,\rm SQM}(q^2) = \frac{m_\rho^2}{m_\rho^2 + q^2}.$$

We note that the vector DA $\phi_{\perp\gamma}(x, q^2 = 0) = 1$ in local models and is very close to 1 in non-local models. For the virtual photon SQM gives the simple formulas:

$$\phi_{\|\gamma^*}(x, q^2) = \frac{1 + \frac{q^2}{m_\rho^2}}{\left(1 + \frac{4q^2}{m_\rho^2}x(1-x)\right)^{3/2}}.$$

In the limit of $q^2 \to -m_\rho^2$ it becomes $\delta\left(x - \frac{1}{2}\right)$, a quite reasonable result.

One may also study the photon light-cone wave function (a $k_\perp$-unintegrated object). It has a simple form in SQM (at the quark-model scale):

$$\Phi_{\perp\gamma}(x, \boldsymbol{k}_\perp) = \frac{6}{m_\rho^2(1 + 4\boldsymbol{k}_\perp^2/m_\rho^2)^{5/2}}$$

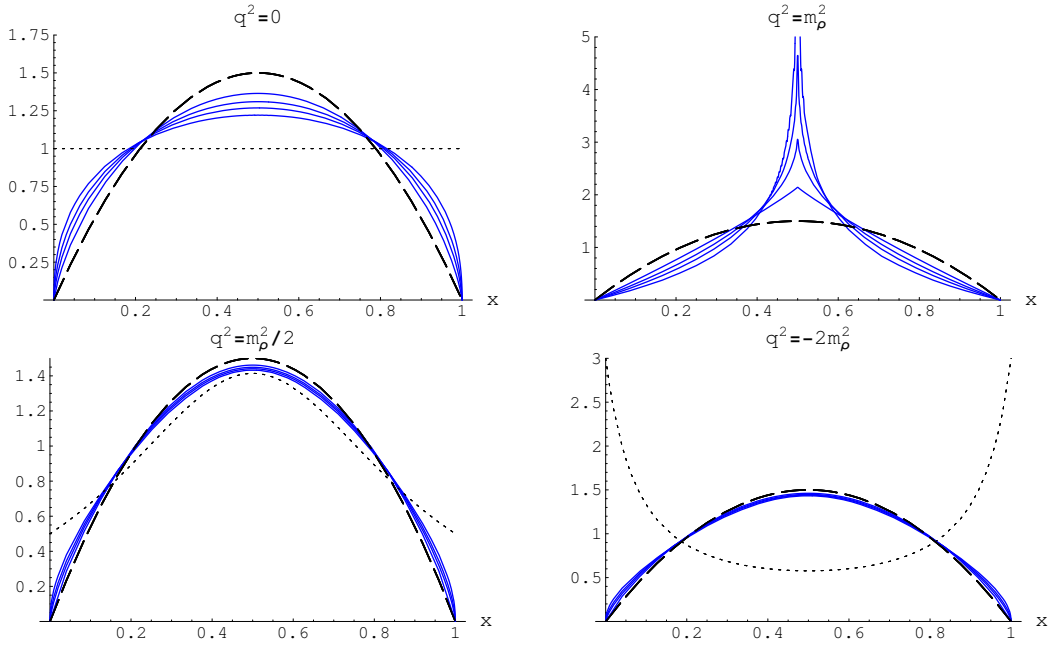

Figure 3: The leading order ERBL evolution of the leading-twist tensor DA, $\phi_{\perp\gamma}(x,q^2)$ evaluated in the local model at various virtualities: real photon (top left), ρ-meson (top right), virtual photon at $q^2=-Q^2=m_\rho^2/2$ (bottom left), and virtual photon at $q^2=-Q^2=-2m_\rho^2$ (bottom right). Initial conditions, indicated by dotted lines, are evaluated in SQM at the initial quark-model scale. The solid lines correspond to LO QCD evolution to the scales $Q=1$, 2.4, 10, and 1000 GeV. With the larger the scale the evolved DA becomes closer to the asymptotic form $6x(1-x)$, plotted with the dashed line. The corresponding values of the evolution ratio r are given in the figures.

Note the power-law fall-off at large transverse momenta, $\Phi_{\perp\gamma}(x,\boldsymbol{k}_\perp)\sim 1/k_\perp^5$. In cross section this leads to tails $\sim 1/k_\perp^{10}$. For the virtual photon

$$\Phi_{\perp\gamma^*}(x,\boldsymbol{k}_\perp)=\frac{6\left(1+\frac{q^2}{m_\rho^2}\right)}{m_\rho^2\left(1+4\frac{\boldsymbol{k}_\perp^2+q^2x(1-x)}{m_\rho^2}\right)^{5/2}}$$

3 QCD evolution of DA's

Now we come to the QCD evolution, which, as already stressed, is crucial in bringing the results to the scales probed in experiments or lattices. We carry out the standard LO ERBL evolution with anomalous dimensions taken for the appropriate channels [39]. The method leads to simple expressions, diagonal in the Gegenbauer moments. In Fig. 3 we show the results for the tensor DA for the real photon, the ρ-meson, and the virtual photon. We note the large change caused by the evolution, which fairly fast brings the model predictions to the vicinity of the asymptotic

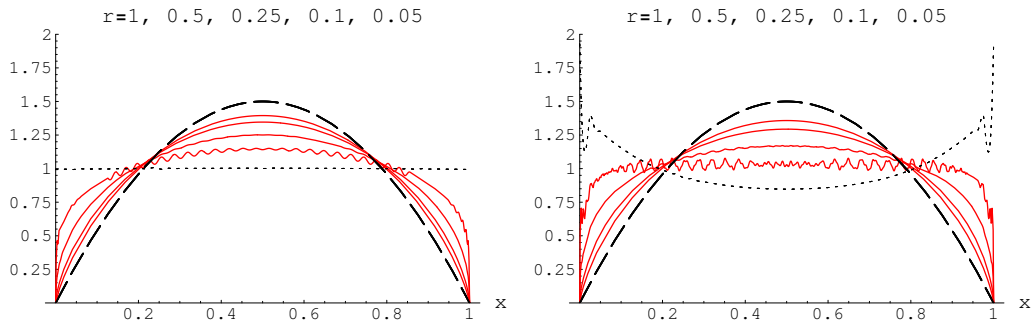

Figure 4: The LO ERBL evolution of the nonlocal model predictions for the leading-twist vector DAs of the photon, $\phi_{\|\gamma}(x,q^2)$. Left: real photon, right: the virtual photon at $q^2 = 0.25$ GeV^2. The dashed lines show the asymptotic DA, $6x(1-x)$. The initial conditions (dotted line) are evaluated in the nonlocal quark model at the initial scale $Q_0^{\rm inst} = 530$ MeV. The solid lines correspond to evolved DA'a at subsequent scales $Q = 1$, 2.4, 10, and 1000 GeV. The corresponding values of the evolution ratio r are given in the figures. Tiny wiggles in the evolved curves is a numerical effect.

limit. Similar results can be done in the nonlocal model, as well as for the vector DA [1]. We show the results in Fig. 4.

4 Conclusion

Chiral quark models provide a link between high- and low-energy analyses, allowing to compute various soft matrix elements for hadronic processes. They yield in a fully dynamical way the initial conditions for the QCD evolution, which is essential to bring the predictions up to the experimental or lattice scales. Numerous predictions for processes involving the Goldstone bosons and photons can be made. The scale in chiral quark models is low, about 320 MeV, hence the QCD evolution is "fast". Simple analytic formulas – useful to understand the general properties, can be obtained in local quark models. For the pion, with the LO QCD evolution the overall agreement with the available data and lattice simulations is very reasonable (PDF, DA, GPD, TDA, generalized form factors [40]). While the presented results for the can be used in phenomenological analyses in high-energy reactions (see, *e.g.*, the recent work of Ref. [41]), the model predictions can be further tested also with future lattice simulations for the photon and ρ-meson.

Acknowledgments

This work has been supported in part by the JINR Bogolyubov-Infeld program, the Scientific School grant 4476.2006.2 the Polish Ministry of Science and Higher Education grants N202 034 32/0918 and N202 249235, and by the Spanish DGI and FEDER funds with grant FIS2008-01143/FIS, Junta de Andalucía grant FQM225-05, and EU Integrated Infrastructure Initiative Hadron Physics Project contract RII3-CT-2004-506078.

References

[1] Alexander E. Dorokhov, Wojciech Broniowski, and Enrique Ruiz Arriola. Photon distribution amplitudes and light-cone wave functions in chiral quark models. *Phys. Rev.*, D74:054023, 2006.

[2] Wojciech Broniowski, Enrique Ruiz Arriola, and Krzysztof Golec-Biernat. Generalized parton distributions of the pion in chiral quark models and their QCD evolution. *Phys. Rev.*, D77:034023, 2008.

[3] R. M. Davidson and E. Ruiz Arriola. Structure functions of pseudoscalar mesons in the su(3) njl model. *Phys. Lett.*, B348:163–169, 1995.

[4] A. E. Dorokhov and Lauro Tomio. Quark distribution function in pion within instanton liquid model. 1998.

[5] Maxim V. Polyakov and C. Weiss. Two-pion light-cone distribution amplitudes from the instanton vacuum. *Phys. Rev.*, D59:091502, 1999.

[6] Maxim V. Polyakov and C. Weiss. Skewed and double distributions in pion and nucleon. *Phys. Rev.*, D60:114017, 1999.

[7] Alexander P. Bakulev, Rusko Ruskov, Klaus Goeke, and N. G. Stefanis. Parton skewed distributions in the pion and quark hadron duality. *Phys. Rev.*, D62:054018, 2000.

[8] A. E. Dorokhov and Lauro Tomio. Pion structure function within the instanton model. *Phys. Rev.*, D62:014016, 2000.

[9] I. V. Anikin, A. E. Dorokhov, A. E. Maksimov, and L. Tomio. Off-diagonal quark distributions in pions in the effective single-instanton approximation. *Phys. Atom. Nucl.*, 63:489–498, 2000.

[10] I. V. Anikin, A. E. Dorokhov, A. E. Maksimov, L. Tomio, and V. Vento. Nonforward parton distributions of the pion within an effective single instanton approximation. *Nucl. Phys.*, A678:175–186, 2000.

[11] E. Ruiz Arriola. Parton distributions for the pion in a chiral quark model. 2001.

[12] R. M. Davidson and E. Ruiz Arriola. Parton distributions functions of pion, kaon and eta pseudoscalar mesons in the njl model. *Acta Phys. Polon.*, B33:1791–1808, 2002.

[13] Michal Praszalowicz and Andrzej Rostworowski. Pion light cone wave function in the non-local NJL model. *Phys. Rev.*, D64:074003, 2001.

[14] Enrique Ruiz Arriola and Wojciech Broniowski. Pion light-cone wave function and pion distribution amplitude in the nambu-jona-lasinio model. *Phys. Rev.*, D66:094016, 2002.

[15] E. Ruiz Arriola. Pion structure at high and low energies in chiral quark models. ((v)). *Acta Phys. Polon.*, B33:4443–4479, 2002.

[16] B. C. Tiburzi and G. A. Miller. Generalized parton distributions for q anti-q pions. *Phys. Rev.*, D67:013010, 2003.

[17] B. C. Tiburzi and G. A. Miller. Generalized parton distributions and double distributions for q anti-q pions. *Phys. Rev.*, D67:113004, 2003.

[18] L. Theussl, S. Noguera, and V. Vento. Generalized parton distributions of the pion in a bethe- salpeter approach. *Eur. Phys. J.*, A20:483–498, 2004.

[19] Michal Praszalowicz and Andrzej Rostworowski. Pion generalized distribution amplitudes in the nonlocal chiral quark model. *Acta Phys. Polon.*, B34:2699–2730, 2003.

[20] Wojciech Broniowski and Enrique Ruiz Arriola. Impact-parameter dependence of the generalized parton distribution of the pion in chiral quark models. *Phys. Lett.*, B574:57–64, 2003.

[21] Adam Bzdak and Michal Praszalowicz. An attempt to construct pion distribution amplitude from the pcac relation in the nonlocal chiral quark model. *Acta Phys. Polon.*, B34:3401–3416, 2003.

[22] B. Pire and L. Szymanowski. Hadron annihilation into two photons and backward vcs in the scaling regime of qcd. *Phys. Rev.*, D71:111501, 2005.

[23] B. Pire and L. Szymanowski. Qcd analysis of anti-p n –¿ gamma* pi in the scaling limit. *Phys. Lett.*, B622:83–92, 2005.

[24] Wojciech Broniowski and Enrique Ruiz Arriola. Pion photon transition distribution amplitudes in the spectral quark model. *Phys. Lett.*, B649:49, 2007.

[25] A. Courtoy and S. Noguera. The Pion-Photon Transition Distribution Amplitudes in the Nambu-Jona Lasinio Model. *Phys. Rev.*, D76:094026, 2007.

[26] Piotr Kotko and Michal Praszalowicz. Pion-to-photon transition distribution amplitudes in the non-local chiral quark model. e-Print: arXiv:0803.2847 [hep-ph].

[27] Ahmed Ali and Vladimir M. Braun. Estimates of the weak annihilation contributions to the decays B → rho + gamma and B → omega + gamma. *Phys. Lett.*, B359:223–235, 1995.

[28] Patricia Ball and Vladimir M. Braun. The ρ Meson Light-Cone Distribution Amplitudes of Leading Twist Revisited. *Phys. Rev.*, D54:2182–2193, 1996.

[29] Patricia Ball, Vladimir M. Braun, Y. Koike, and K. Tanaka. Higher twist distribution amplitudes of vector mesons in QCD: Formalism and twist three distributions. *Nucl. Phys.*, B529:323–382, 1998.

[30] Patricia Ball, V. M. Braun, and N. Kivel. Photon distribution amplitudes in QCD. *Nucl. Phys.*, B649:263–296, 2003.

[31] Chr. V. Christov et al. Baryons as non-topological chiral solitons. *Prog. Part. Nucl. Phys.*, 37:91–191, 1996.

[32] Enrique Ruiz Arriola and Wojciech Broniowski. Spectral quark model and low-energy hadron phenomenology. *Phys. Rev.*, D67:074021, 2003.

[33] John Terning. Gauging nonlocal Lagrangians. *Phys. Rev.*, D44:887–897, 1991.

[34] B. Holdom. Approaching low-energy QCD with a gauged, nonlocal, constituent quark model. *Phys. Rev.*, D45:2534–2541, 1992.

[35] Robert S. Plant and Michael C. Birse. Meson properties in an extended non-local NJL model. *Nucl. Phys.*, A628:607–644, 1998.

[36] Wojciech Broniowski. Gauging non-local quark models. Talk presented at the Miniworkshop on Hadrons as Solitons, Bled, Slovenia, 6-17 Jul 1999. Published in Bled 1999, Hadrons as solitons, p. 17-26, e-print: hep-ph/9909438

[37] I. V. Anikin, A. E. Dorokhov, and L. Tomio. Pion structure in the instanton liquid model. *Phys. Part. Nucl.*, 31:509–537, 2000.

[38] V. Yu. Petrov, Maxim V. Polyakov, R. Ruskov, C. Weiss, and K. Goeke. Pion and photon light-cone wave functions from the instanton vacuum. *Phys. Rev.*, D59:114018, 1999.

[39] A. V. Belitsky and A. V. Radyushkin. Unraveling hadron structure with generalized parton distributions. *Phys. Rept.*, 418:1–387, 2005.

[40] Wojciech Broniowski and Enrique Ruiz Arriola. Gravitational and higher-order form factors of the pion in chiral quark models. *Phys. Rev.*, D78:094011, 2008.

[41] B. Pire and L. Szymanowski. "Probing the nucleon's transversity and the photon's distribution amplitude in lepton pair photoproduction. e-print: arXiv:0905.1258 [hep-ph].

Photon-Photon Collision: Ambiguity and Duality in QCD Factorization Theorem

I. V. Anikin[1], *I. O. Cherednikov*[1,3,4], *N. G. Stefanis*[2], *O. V. Teryaev*[1]

[1]Bogoliubov Laboratory of Theoretical Physics, JINR, 141980 Dubna, Russia
[2] Institut für Theoretische Physik II, Ruhr-Universität Bochum, D-44780 Bochum, Germany
[3] INFN Cosenza, Universitȧ della Calabria, I-87036 Arcavacata di Rende, Italy
[4] ITPM, Moscow State University, RU-119899, Moscow, Russia

DOI: http://dx.doi.org/10.3204/DESY-PROC-2009-03/Anikin

We discuss duality in "two-photon"-like processes in the scalar φ^3_E model and also in the process $\gamma^*\gamma \to \pi\pi$ in QCD. Duality implies the equivalence between two distinct nonperturbative mechanisms. These two mechanisms, one involving a twist-3 Generalized Distribution Amplitude, the other employing a leading-twist Transition Distribution Amplitude, are associated with different regimes of factorization. In the kinematical region, where the two mechanisms overlap, duality is observed for the scalar φ^3_E model, while in the QCD case the appearance of duality turns out to be sensitive to the particular nonperturbative model applied and can, therefore, be used as a tool for selecting the most appropriate one.

1 Introduction

The only known method today to apply QCD in a rigorous way is based on the factorization of the dynamics and the isolation of a short-distance part that becomes this way accessible to perturbative techniques of quantum field theory (see, [1, 2, 3] and for a review, for instance, [4] and references cited therein). Then, the conventional systematic way of dealing with the long-distance part is to parameterize it in terms of matrix elements of quark and gluon operators between hadronic states (or the vacuum). These matrix elements stem from nonperturbative phenomena and have to be either extracted from experiment or be determined on the lattice. In many phenomenological applications they are usually modeled in terms of various nonperturbative methods or models.

Generically, the application of QCD to hadronic processes involves the consideration of hard parton subprocesses and (unknown) nonperturbative functions to describe binding effects. Prominent examples are hard exclusive hadronic processes which involve hadron distribution amplitudes (DAs), generalized distribution amplitudes (GDAs), and generalized parton distributions (GPDs) [5, 6, 7, 8]. Applying such a framework, collisions of a real and a highly-virtual photon provide a useful tool for studying a variety of fundamental aspects of QCD.

Recently, nonperturbative quantities of a new kind were introduced—transition distribution amplitudes (TDAs) [9, 10, 11]—which are closely related to the GPDs. In contrast to the GDAs, the TDAs appear in the factorization procedure when the Mandelstam variable s is of the same order of magnitude as the large photon virtuality Q^2, while t is rather small. Remarkably, there

exists a reaction where both amplitude types, GDAs and TDAs, can overlap. This can happen in the fusion of a real and transversely polarized photon with a highly-virtual longitudinally polarized photon, giving rise to a final state which comprises a pair of pions. The key feature of this reaction is that it can potentially follow either path: proceed via twist-3 GDAs, or go through the leading-twist TDAs, as illustrated in Fig. 1. Such an antagonism of alternative factorization mechanisms in this reaction seems extremely interesting both theoretically and phenomenologically and deserves to be studied in detail.

The intimate relation between these two mechanisms in the production of a vector-meson pair was analyzed in [12] and it was found that these mechanisms can be selected by means of the different polarizations of the initial-state photon. In contrast, for (pseudo)scalar particles, such as the pions, this effect is absent enabling us to access the overlap region of both mechanisms and their duality as opposed to their additivity.

In this talk, we will report on the possibility for duality between these antagonistic mechanisms of factorization, associated either with GDAs or with TDAs, in the regime where *both* Mandelstam variables s and t are rather small compared to the large photon virtuality Q^2.

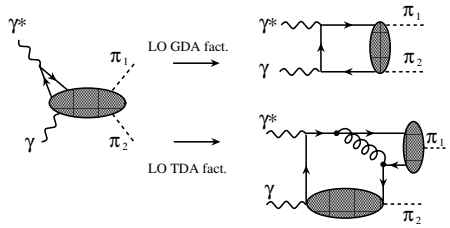

Figure 1: Two ways of factorization: via the GDA mechanism and via the TDA mechanism.

2 Regimes of Factorization within the φ^3_E-model

Consider first the factorization of the scalar φ^3_E model in Euclidean space. To study the four-particle amplitude in detail, it is particularly useful to employ the α-representation—see [7]. Then, the contribution of the leading "box" diagram can be written as (while details can be found in [13])

$$\mathcal{A}(s,t,m^2) = -\frac{g^4}{16\pi^2}\int\limits_0^\infty \frac{\prod\limits_{i=1}^4 d\alpha_i}{D^2}\exp\left[-\frac{1}{D}\left(Q^2\alpha_1\alpha_2 + s\alpha_2\alpha_4 + t\alpha_1\alpha_3 + m^2D^2\right)\right], \qquad (1)$$

where m^2 serves as a infrared (IR) regulator, $s>0$, $t>0$ are the Mandelstam variables in the Euclidean region, and $D=\sum\limits_{i=1}^4 \alpha_i$. Assuming that $q^2=Q^2$ is large compared to the mass scale m^2 (which simulates here the typical scale of soft interactions), the amplitude (1) can indeed be factorized. As regards the other two kinematic variables s and t, one can identify three distinct regimes of factorization: (a) $s \ll Q^2$ while t is of order Q^2; (b) $t \ll Q^2$ while s is of order Q^2; (c) $s,\ t \ll Q^2$.

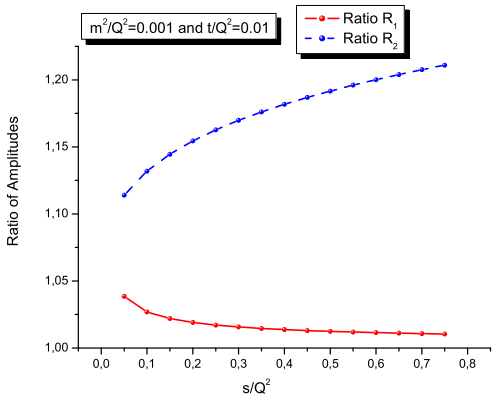

Figure 2: The ratios R_1 and R_2 as functions of s/Q^2.

Regime (a): The process is going through the s-channel. In this regime, the main contribution in the integral in Eq. (1) arises from the integration over α_1 when $\alpha_1 \sim 0$:

$$\mathcal{A}^{\rm as}_{\rm GDA}(s,t,m^2) = -\frac{g^4}{16\pi^2}\int\limits_0^\infty \frac{d\alpha_2\, d\alpha_3\, d\alpha_4}{D_0^2}\ \exp\left(-s\frac{\alpha_2\alpha_4}{D_0} - m^2 D_0\right)\left[Q^2\frac{\alpha_2}{D_0} + t\frac{\alpha_3}{D_0} + m^2\right]^{-1}. \quad (2)$$

Schematically this means that the propagator, parameterized by α_1, can be associated with the partonic (hard) subprocesses, while the remaining propagator constitutes the soft part of the considered amplitude, i.e., the scalar version of the GDA.

Regime (b): Here we have to eliminate from the exponential in Eq. (1) the variables Q^2 and s, which are large. This can be achieved by integrating over the region $\alpha_2 \sim 0$. Performing similar manipulations as in regime (a), we find that the scalar TDA amplitude can be related to the scalar GDA via $\mathcal{A}^{\rm as}_{\rm TDA}(s,t,m^2) = \mathcal{A}^{\rm as}_{\rm GDA}(t,s,m^2)$.

Regime (c): The relevant regime to investigate duality is when it happens that both variables s and t are simultaneously small compared to Q^2, i.e., when $s, t \ll Q^2$. In this case, there are two possibilities to extract the leading Q^2-asymptotics, notably, we can either integrate over the region $\alpha_1 \sim 0$, or integrate instead over the region $\alpha_2 \sim 0$. Clearly, these two options can be associated with (i) the GDA mechanism of factorization with the meson pair scattered at a small angle in its center-of-mass system or, alternatively, (ii) with the TDA mechanism of factorization. We stress that we may face double counting when naively adding these two contributions. We interpret such a behavior as a signal of an ingrained tendency for duality between the GDA(s-channel) and the TDA (t-channel) factorization mechanisms.

In order to verify the appearance of duality we carry out a numerical investigation of the exact and the asymptotic amplitudes. In doing so, we introduce the following ratios $R_1 = \mathcal{A}^{\rm as}_{\rm TDA}/\mathcal{A}$ and $R_2 = \mathcal{A}^{\rm as}_{\rm GDA}/\mathcal{A}$. Appealing to the symmetry of these ratios under the exchange of the variables $s \leftrightarrow t$, we take t/Q^2 to be 0.01 and look for the variation of the ratios with s/Q^2. This variation is illustrated in Fig. 2 from which one sees that in the region where s/Q^2 is rather small, i.e., in the range (0.01, 0.05), both asymptotic formulae are describing the exact amplitude with an accuracy of more than 90%. This behavior supports the conclusion that,

when both Mandelstam variables s/Q^2 and t/Q^2 assume values in the wide interval (0.001, 0.7), duality between the TDA and the GDA factorization mechanisms emerges.

3 TDA- and GDA-Factorizations for $\gamma\gamma^* \to \pi\pi$

Having discussed the appearance of duality between the GDA and the TDA factorization schemes within a toy model, we now turn attention to real QCD. To analyze duality, we consider the exclusive $\pi^+\pi^-$ production in a $\gamma_{\rm T}\gamma_{\rm L}^*$ collision, where the virtual photon with a large virtuality Q^2 is longitudinally polarized, whereas the other one is quasi real and transversely polarized. Notice that the GDA and the TDA regimes correspond to the *same* helicity amplitudes. Given that the considered process involves a longitudinally and a transversally polarized photon, we are actually dealing with twist-3 GDAs [14]. On the other hand, for the twist-2 contribution, related to the meson DA, we use the standard parametrization of the π^+-to-vacuum matrix element which involves a bilocal axial-vector quark operator [1]. Finally, the $\gamma \to \pi^-$ axial-vector matrix elements can be parameterized in the form, cf. [10],

$$\langle \pi^-(p_2)|\bar\psi(-z/2)\gamma_\alpha\gamma_5[-z/2;z/2]\psi(z/2)|\gamma(q',\varepsilon')\rangle \stackrel{\mathcal{F}}{=} \frac{e}{f_\pi}\varepsilon'_T\cdot\Delta_T P_\alpha A_1(x,\xi,t)\,, \tag{3}$$

where $P = (p_2+q')/2$, and $\Delta = p_2 - q'$, and noticing that the symbol $\stackrel{\mathcal{F}}{=}$ means Fourier transformation and that the vector matrix element does not contribute here. To normalize the axial-vector TDA, A_1, we express it in terms of the axial-vector form factor measured in the weak decay $\pi \to l\nu_l\gamma$ [15, 16, 13]. The helicity amplitude associated with the TDA mechanism reads

$$\mathcal{A}^{\rm TDA}_{(0,j)} = \mathcal{F}^{\rm TDA}\frac{\varepsilon'^{\,(j)}\cdot\Delta^T}{Q} \tag{4}$$

with

$$\mathcal{F}^{\rm TDA} = [4\,\pi\,\alpha_s(Q^2)]\frac{C_F}{2\,N_c}\Big({\rm tw{-}2\ \ DA}\Big)\Big({\rm tw{-}2\ \ TDA}\Big), \tag{5}$$

where

$$\begin{aligned}\Big({\rm tw{-}2\ \ DA}\Big) &= \int_0^1 dy\,\phi_\pi(y)\Big(\frac{1}{y}+\frac{1}{\bar y}\Big)\,,\\ \Big({\rm tw{-}2\ \ TDA}\Big) &= \int_{-1}^1 dx\,A_1(x,\xi,t)\,\Big(\frac{e_u}{\xi-x}-\frac{e_d}{\xi+x}\Big),\end{aligned} \tag{6}$$

employing the 1-loop $\alpha_s(Q^2)$ in the $\overline{\rm MS}$-scheme with $\Lambda_{\rm QCD} = 0.312$ GeV for $N_f = 3$ [17]. [Note that there is only a mild dependence on $\Lambda_{\rm QCD}$.]

Turning now to the helicity amplitude, which includes the twist-3 GDA, we anticipate that it can be written as (see, for example, [14])

$$\mathcal{A}^{\rm GDA}_{(0,j)} = \mathcal{F}^{\rm GDA}\frac{\varepsilon'^{\,(j)}\cdot\Delta^T}{Q} \tag{7}$$

with

$$\mathcal{F}^{\rm GDA} = 2\frac{W^2+Q^2}{Q^2}(e_u^2+e_d^2)\bigg(\text{tw}-3\ \text{GDA WW}\bigg), \tag{8}$$

where

$$\bigg(\text{tw}-3\ \text{GDA WW}\bigg) = \int\limits_0^1 dy\,\partial_\zeta \Phi_1(y,\zeta,W^2)\bigg(\frac{\ln\bar{y}}{y}-\frac{\ln y}{\bar{y}}\bigg), \tag{9}$$

with the partial derivative being defined by $\partial_\zeta = \partial/\partial(2\zeta-1)$. In deriving (8), we have used for the twist-3 contribution the Wandzura-Wilczek approximation. Duality between expressions (5) and (8) may occur in that regime, where both variables s and t are simultaneously much smaller in comparison to the large photon virtuality Q^2. More insight into the relative weight of the amplitudes with TDA or GDA contributions can be gained once we have modeled these nonperturbative quantities. We commence our analysis with the TDAs and, assuming a factorizing ansatz for the t-dependence of the TDAs, we write $A_1(x,\xi,t) = 2\frac{f_\pi}{m_\pi}F_A(t)A_1(x,\xi)$, where the t-independent function $A_1(x,\xi)$ is normalized to unity. To satisfy the unity-normalization condition, we introduce a TDA defined by

$$A_1(x,1) = \frac{A_1^{\rm non-norm}(x,1)}{\int\limits_{-1}^{1} dx A_1^{\rm non-norm}(x,1)} \tag{10}$$

and continue with the discussion of the t-independent TDAs. Recalling that we are mainly interested in TDAs in the region $\xi = 1$ [1, 2], it is useful to adopt the following parametrization

$$A_1^{\rm non-norm}(x,1) = (1-x^2)\bigg(1+a_1C_1^{(3/2)}(x)+a_2C_2^{(3/2)}(x)+a_4C_4^{(3/2)}(x)\bigg), \tag{11}$$

where a_1, a_2, a_4 are free adjustable parameters, encoding nonperturbative input, and the standard notations for Gegenbauer polynomials are used. It is not difficult to show that the TDA expressed by Eq. (11) results from summing a D-term, i.e., the term with the coefficient a_1, and meson-DA-like contributions. For our analysis, we suppose that $a_1 \equiv d_0$ [8], which is equal to -0.5 in lattice simulations. With respect to the parameters a_2 and a_4, we allow them to vary in quite broad intervals, notably, $a_2 \in [0.3, 0.6]$ and $a_4 \in [0.4, 0.8]$, that would cover vector-meson DAs with very different profiles at a normalization scale $\mu^2 \sim 1\,GeV^2$ (see, for example, [18]). The function $\Phi_1(z,\zeta)$ is rather standard and well-known (details in [5, 13]).

We close this section by summarizing our numerical analysis presented in [13]. We calculated both functions $\mathcal{F}^{\rm TDA}$ and $\mathcal{F}^{\rm GDA}$, and show the results in Fig. 3. The dashed line corresponds to the function $\mathcal{F}^{\rm TDA}$, where we have adjusted the free parameters to $a_2 = 0.6$, $a_4 = 0.8$. The results, obtained for rather small values of these parameters, are displayed by the broken lines in the same figure. The dotted line denotes the function $\mathcal{F}^{\rm TDA}$ with $a_2 = 0.5$ and $a_4 = 0.6$, whereas the dashed-dotted line employs $a_2 = 0.3$ and $a_4 = 0.4$. For comparison, we also include the results for $\mathcal{F}^{\rm GDA}$. In that latter case, the dense-dotted line corresponds to the GDA amplitude, where the expression for $\tilde{B}_{12}$ has been estimated via Eq. (20) of [13], while the solid line represents the simplest ansatz for $\tilde{B}_{12}$ with $R_\pi = 0.5$. From this figure one may infer that when the parameter $\tilde{B}_{12}$, which parameterizes the GDA contribution, is estimated with the aid

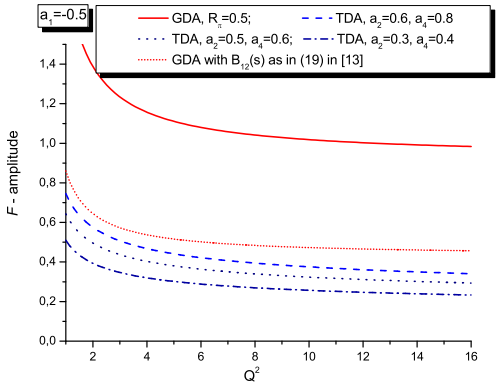

Figure 3: Helicity amplitudes $\mathcal{F}^{\rm TDA}$ and $\mathcal{F}^{\rm GDA}$ as functions of Q^2, using $a_1 = -0.5$ found in lattice simulations. The value of s/Q^2 varies in the interval [0.06, 0.3].

of the Breit-Wigner formula (provided s, $t \ll Q^2$), there is duality between the GDA and the TDA factorization mechanisms. Hence, the model for $\Phi_1(z, \zeta)$, which takes into account the corresponding resonances, can be selected by duality.

4 Conclusions

We have provided evidence that when both Mandelstam variables s and t turn out to be much less than the large momentum scale Q^2, with the variables s/Q^2 and t/Q^2 varying in the interval [0.001, 0.7], the TDA and the GDA factorization mechanisms are equivalent to each other and operate in parallel. We have also demonstrated that duality may serve as a tool for selecting suitable models for the nonperturbative ingredients of various exclusive amplitudes entering QCD factorization. In this context, we observed that twist-3 GDAs appear to be dual to the convolutions of leading-twist TDAs and DAs, multiplied by a QCD effective coupling.

5 Acknowledgments

We would like to thank A. P. Bakulev, A. V. Efremov, N. Kivel, B. Pire, M. V. Polyakov, M. Praszałowicz, L. Szymanowski, and S. Wallon for useful discussions and remarks. This investigation was partially supported by the Heisenberg-Landau Programme (Grant 2008), the Alexander von Humboldt Stiftung, the Deutsche Forschungsgemeinschaft under contract 436RUS113/881/0, the EU-A7 Project *Transversity*, the RFBR (Grants (grants 09-02-01149 and 07-02-91557), the Russian Federation Ministry of Education and Science (Grant MIREA 2.2.2.2.6546), the RF Scientific Schools grant 195.2008.9, and INFN.

References

[1] A. V. Efremov and A. V. Radyushkin, Phys. Lett. B **94**, 245 (1980).

Theor. Math. Phys. **42**, 97 (1980) [Teor. Mat. Fiz. **42**, 147 (1980)].

[2] G. P. Lepage and S. J. Brodsky, Phys. Lett. B **87**, 359 (1979); Phys. Rev. D **22**, 2157 (1980).

[3] J. C. Collins, D. E. Soper and G. Sterman, Adv. Ser. Direct. High Energy Phys. **5**, 1 (1988) [arXiv:hep-ph/0409313].

[4] N. G. Stefanis, Eur. Phys. J. direct C **7**, 1 (1999) [arXiv:hep-ph/9911375].

[5] M. Diehl, Phys. Rept. **388**, 41 (2003) [arXiv:hep-ph/0307382].

[6] A. V. Belitsky and A. V. Radyushkin, Phys. Rept. **418**, 1 (2005) [arXiv:hep-ph/0504030].

[7] A. V. Radyushkin, Phys. Rev. D **56**, 5524 (1997) [arXiv:hep-ph/9704207].

[8] K. Goeke, M. V. Polyakov and M. Vanderhaeghen, Prog. Part. Nucl. Phys. **47**, 401 (2001) [arXiv:hep-ph/0106012].

[9] L. L. Frankfurt, M. V. Polyakov and M. Strikman, arXiv:hep-ph/9808449.

[10] B. Pire and L. Szymanowski, Phys. Rev. D **71**, 111501 (2005) [arXiv:hep-ph/0411387].

[11] J. P. Lansberg, B. Pire and L. Szymanowski, Phys. Rev. D **73**, 074014 (2006) [arXiv:hep-ph/0602195].

[12] B. Pire, M. Segond, L. Szymanowski and S. Wallon, Phys. Lett. B **639**, 642 (2006) [arXiv:hep-ph/0605320].

[13] I. V. Anikin, I. O. Cherednikov, N. G. Stefanis and O. V. Teryaev, Eur. Phys. J. C **61**, 357 (2009) [arXiv:0806.4551 [hep-ph]].

[14] I. V. Anikin and O. V. Teryaev, Phys. Lett. B **509**, 95 (2001) [arXiv:hep-ph/0102209].

[15] W. M. Yao *et al.* [Particle Data Group], J. Phys. G **33**, 1 (2006).

[16] M. Bychkov *et al.*, arXiv:0804.1815 [hep-ex].

[17] A. L. Kataev, G. Parente and A. V. Sidorov, Phys. Part. Nucl. **34**, 20 (2003) [Fiz. Elem. Chast. Atom. Yadra **34**, 43 (2003 ERRAT,38,827-827.2007)] [arXiv:hep-ph/0106221].

[18] A. P. Bakulev, S. V. Mikhailov and R. Ruskov, arXiv:hep-ph/0006216.

Study of Charmonium-like States via ISR at B Factories

X.L. Wang

Institute of High Energy Physics, Chinese Academy of Sciences, Beijing 100049, China

DOI: http://dx.doi.org/10.3204/DESY-PROC-2009-03/Wang

The ISR processes at open charm region studied at the two B factories, BaBar and Belle, are reviewed. The report focuses on charmonium-like states, including the $Y(4008)$ and $Y(4260)$ observed in $e^+e^- \to \pi^+\pi^- J/\psi$, and the $Y(4360)$ and $Y(4660)$ observed in $e^+e^- \to \pi^+\pi^-\psi(2S)$. Measurements of the $e^+e^- \to$ open charm cross sections, including $e^+e^- \to D\overline{D}$, $D^0D^-\pi^+ + c.c.$, $D^*\overline{D} + c.c.$, and $D^*\overline{D}^*$, confirm the excited ψ states $\psi(4040)$, $\psi(4160)$ and $\psi(4415)$, but show no evidence for any of the Y states. The 4 Y states and 3 ψ states between 4.0 and 4.7 GeV/c^2 are too many to be all charmonium states from a point of view of Potential Models, indicates that our understanding of the vector charmonium states above 4 GeV/c^2 is still poor, and one or more of these states may be exotic. Measurement of $e^+e^- \to \Lambda_c^+\overline{\Lambda}_c^-$ shows the existence of an $X(4630)$, which may be the $Y(4660)$ observed in $e^+e^- \to \pi^+\pi^-\psi(2S)$. A $Y(2175)$ is observed in $e^+e^- \to \phi f_0(980)$, this may indicate the existence of the $s\overline{s}$ version of the Y state.

1 Introduction

The Initial State Radiation (ISR) process, shown in Figure 1, is that when e^+e^- collides at $\sqrt{s_0}$, one or several photons (γ_{ISR}) emit from e^+ or e^-, and the left part is still a e^+e^- collision. Because γ_{ISR} takes away some energy, the effective collision energy is lowered down, like a new collider running at new $\sqrt{s}$, which could be much lower than $\sqrt{s_0}$.

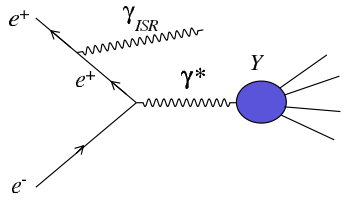

Figure 1: The ISR process at e^+e^- collider. At collision, the emitted photons make the effective $\sqrt{s}$ lower than the original $\sqrt{s_0}$.

The ISR cross section for a particular hadronic final state f (excluding the radiated γ_{ISR})

is related to the corresponding e^+e^- cross section $\sigma_f(s)$ by:

$$\frac{d\sigma_f(s_0,x)}{dx} = W(s_0,x)\cdot\sigma_f(s_0(1-x)) \ , \tag{1}$$

where $x = 2E_\gamma/\sqrt{s_0}$; E_γ is the energy of the γ_{ISR} in the nominal e^+e^- center-of-mass (CM) frame; $\sqrt{s_0}$ is the nominal e^+e^- CM energy; and $\sqrt{s_0(1-x)}$ is the effective CM energy ($\sqrt{s}$) at which the final state f is produced. The invariant mass of the hadronic final state defines the effective e^+e^- CM energy. The function $W(s_0,x)$ is calculated with better than 1% accuracy [1] and describes the probability density function for ISR photon emission, which occurs at all angles. When $\sqrt{s}$ is far from $\sqrt{s_0}$, the effective cross section $\sigma_f(s_0,x)$ is much small. And because the high energy γ_{ISR} is usually along with colliding beams, the detection efficiency is usually very low. So study via ISR needs very large data sample.

The two B factories, BaBar at SLAC and Belle at KEK have collected more than 1 ab^{-1} e^+e^- collision data around $\Upsilon(4S)$. And the designed asymmetric collision increases the detection efficiency. So the B factories become very suitable for the studies via ISR processes, especially at open charm threshold region. At this region, there are just several ψ states established tens of years ago via inclusive production. Here we report the charmonium-like states observed from ISR studies at the B factories, including the $Y(4008)$ and $Y(4260)$ from $e^+e^- \to \pi^+\pi^- J/\psi$, the $Y(4360)$ and $Y(4660)$ from $e^+e^- \to \pi^+\pi^-\psi(2S)$. $e^+e^- \to K^+K^- J/\psi$ is also studied at Belle, no obvious signal of the Y states is observed. Cross sections of $e^+e^- \to D\overline{D}$, $D^0D^-\pi^+ + c.c.$, $D^*\overline{D} + c.c.$, and $D^*\overline{D}^*$ have been measured, $\psi(4040)$, $\psi(4160)$ and $\psi(4415)$ have been confirmed but no obvious Y states signal can be seen. Measurements on $e^+e^- \to \Lambda_c^+\overline{\Lambda}_c^-$ shows a structure at around 4.63 GeV, and in $e^+e^- \to \phi f_0(980)$ the $Y(2175)$ is observed.

2 The Y states via $e^+e^- \to h^+h^-$+charmonium

Three final states are analyzed, including $\pi^+\pi^- J/\psi$, $\pi^+\pi^-\psi(2S)$, and $K^+K^- J/\psi$.

2.1 Measurement on $e^+e^- \to \pi^+\pi^- J/\psi$

BaBar studied $e^+e^- \to \pi^+\pi^- J/\psi$ [2], the data sample used is 232 fb^{-1}. With a J/ψ mass constraint, the $\psi(2S)$ signal is well described by a Cauchy shape function. Figure 2 shows a new structure well above $\psi(2S)$. The new structure is called $Y(4260)$. An unbinned likelihood fit to the $\pi^+\pi^- J/\psi$ mass spectrum is performed using a single relativistic Breit-Wigner signal function and a second-order polynomial background. The fit gives 125±23 events with a mass of $4259 \pm 8^{+2}_{-6}$ MeV/c^2, a width of $88 \pm 23^{+6}_{-4}$ MeV/c^2, and $\Gamma(Y(4260) \to e^+e^-)\cdot\mathcal{B}(Y(4260) \to \pi^+\pi^- J/\psi) = 5.5 \pm 1.0^{+0.8}_{-0.7}$ eV/c^2. The significance is more than 8σ.

Belle studied this channel with about 550 fb^{-1} data [3]. $\psi(2S)$ is used as reference signal. The calculation gives the partial width of $\psi(2S)$ $\Gamma_{e^+e^-} = 2.54 \pm 0.02 \pm 0.15$ keV/c^2, agrees with other experiments very well. The generator used is PHOKHARA. To increase detecting efficiency, the γ_{ISR} is not reconstructed, instead, the recoil mass of the charged track system is required to be agree with a missing massless particle. Figure 3 shows the $\pi^+\pi^- J/\psi$ invariant mass spectrum. Besides the $Y(4260)$ signal, Belle finds a broad enhancement $Y(4008)$ around 4 GeV/s^2. Figure 4 shows the $\pi^+\pi^-$ invariant mass distributions of events for three $m_{\pi^+\pi^- J/\psi}$

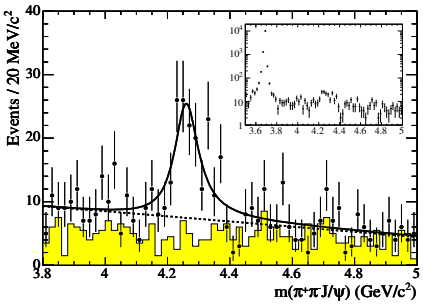

Figure 2: The $\pi^+\pi^- J/\psi$ invariant mass spectrum from BaBar in the range 3.8−5.0 GeV/c^2 and (inset) over a wider range that includes the $\psi(2S)$. The solid curve shows the result of the single-resonance fit.

regions, $[3.8, 4.2]$, $[4.2, 4.4]$, and $[4.4, 4.6]$ (unit in GeV/c^2). The $\pi^+\pi^-$ invariant mass distribution for events around 4.25 GeV/c^2 differs significantly from phase space; for other energy ranges the agreement with phase space is better. And considering the asymmetry shape of the $Y(4260)$, it is reasonable to assume that two coherent structures exist in this channel. An unbinned fit with two coherent resonances is applied to the $\pi^+\pi^- J/\psi$ invariant mass spectrum. There are two solutions with equally good fit quality (see Table 1).

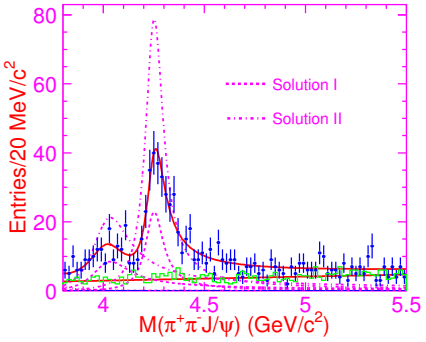

Figure 3: The plot shows the $\pi^+\pi^- J/\psi$ mass spectrum and the fit with two coherent resonances.

2.2 Measurement on $e^+e^- \to \pi^+\pi^-\psi(2S)$

After the discovery of the $Y(4260)$, BaBar searches for it in $e^+e^- \to \pi^+\pi^-\psi(2S)$ with about 300 fb^{-1} data [5]. Figure 5 shows the $\pi^+\pi^-\psi(2S)$ invariant mass spectrum and the $\pi^+\pi^-$ invariant mass distribution. The state $Y(4360)$ was observed around 4.3 GeV/c^2. Fit with one resonance give the mass (4324±24) MeV/c^2 and the width (172±33) MeV/c^2, where systematic errors not included. BaBar tried to fit with a $Y(4260)$, but the conclusion is negative. The statistics didn't allow BaBar fit the spectrum with two resonances.

Belle study this spectrum with a data sample of about 673 fb^{-1} [6]. Figure 6 shows the $\pi^+\pi^-\psi(2S)$ invariant mass spectrum. Belle confirms the $Y(4360)$ and observes the $Y(4660)$ for the first time. Fitting with two coherent resonances gives the results in Table 2, there are

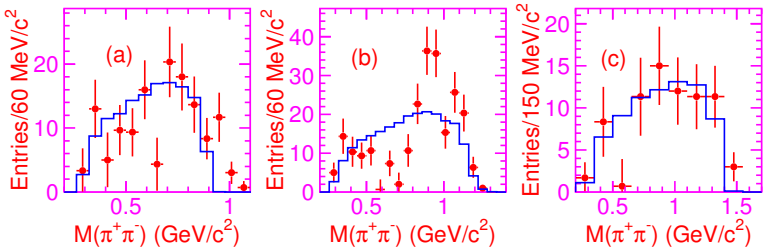

Figure 4: The $\pi^+\pi^-$ invariant mass distribution of events for different $\pi^+\pi^- J/\psi$ mass regions. (a): $m_{\pi^+\pi^- J/\psi} \in [3.8, 4.2]$ GeV/c^2, (b): $m_{\pi^+\pi^- J/\psi} \in [4.2, 4.4]$ GeV/c^2, and (c): $m_{\pi^+\pi^- J/\psi} \in [4.4, 4.6]$ GeV/c^2. The points with errors bars are pure signal events, the histograms are MC simulations made using phase space distributions.

Parameters	Solution I	Solution II
$M(Y(4008))$	$4008 \pm 40^{+114}_{-28}$	
$\Gamma_{\rm tot}(Y(4008))$	$226 \pm 44 \pm 87$	
$\mathcal{B} \cdot \Gamma_{e^+e^-}(Y(4008))$	$5.0 \pm 1.4^{+6.1}_{-0.9}$	$12.4 \pm 2.4^{+14.8}_{-1.1}$
$M(Y(4260))$	$4247 \pm 12^{+17}_{-32}$	
$\Gamma_{\rm tot}(Y(4260))$	$108 \pm 19 \pm 10$	
$\mathcal{B} \cdot \Gamma_{e^+e^-}(Y(4260))$	$6.0 \pm 1.2^{+4.7}_{-0.5}$	$20.6 \pm 2.3^{+9.1}_{-1.7}$
ϕ	$12 \pm 29^{+7}_{-98}$	$-111 \pm 7^{+28}_{-31}$

Table 1: Fit results of the $\pi^+\pi^- J/\psi$ invariant mass spectrum from Belle.

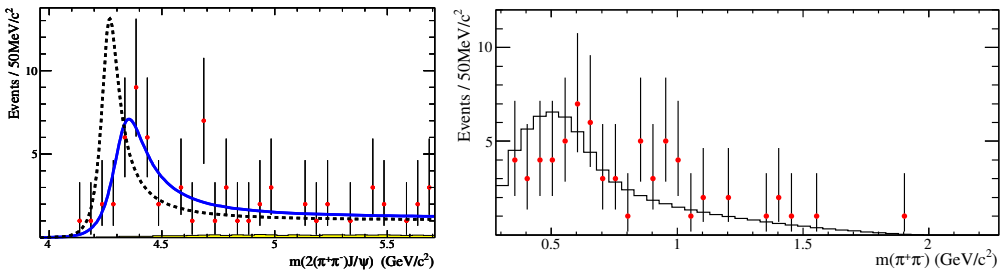

Figure 5: The left plot shows the $\pi^+\pi^-\psi(2S)$ invariant mass spectrum up to 5.7 GeV/c^2 from BaBar. The right plot shows the corresponding $\pi^+\pi^-$ invariant mass distribution.

also two solutions with equal quality and different $\Gamma_{e^+e^-}$. Figure 7 shows the scattering plot of M($\pi^+\pi^-$) versus M($\pi^+\pi^-\psi(2S)$). From the scattering plot, there is a concentration around 1 GeV/c^2 at M($\pi^+\pi^-$). If it is the scalar particle $f_0(980)$, the decay of $Y(4660)$ should be dominated by $\psi(2S) + f_0(980)$. So there is an assumption that $Y(4660)$ is a $\psi(2S)f_0(980)$ bound state [7]. For both $Y(4360)$ and $Y(4660)$, M($\pi^+\pi^-$) distributions tend to be large. And the one of $Y(4360)$ happens to be around 600 MeV/c^2, which looks similar to that from $\psi(2S) \to \pi^+\pi^- J/\psi$. At $\psi(2S)$ decay, an assumption is that $\pi^+\pi^-$ is from scalar particle $\sigma(600)$.

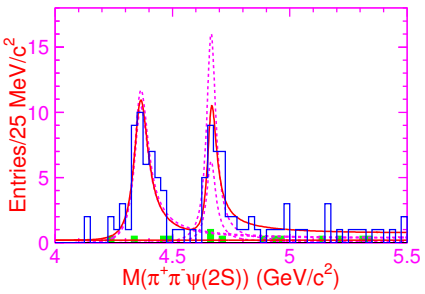

Figure 6: The plot shows the $\pi^+\pi^-\psi(2S)$ invariant mass distribution.

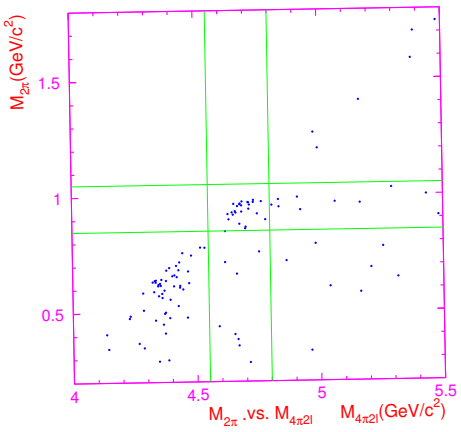

Figure 7: The plot is the scattering plot of M($\pi^+\pi^-$) vs. M($\pi^+\pi^-\psi(2S)$), which indicates a clear signal at M($\pi^+\pi^-$) near 1 GeV/c^2. This structure may be $f_0(980)$.

A combined fit has been performed on BaBar and Belle's measurements, which are also shown in Table 2. From the fits, and the comparison with other vector charomnium(-like) states, the $Y(4660)$ has the highest mass and the narrowest width. This may be because of the narrow width of $f_0(980)$ decays from the $Y(4660)$, or indicates the $Y(4660)$ is a different state.

2.3 $e^+e^- \to K^+K^-J/\psi$

CLEO-c observed 3 K^+K^-J/ψ events at $\sqrt{s} = 4.26$ GeV/c^2, and assumed them from the $Y(4260)$. Limited by statistics, only Belle scans $e^+e^- \to K^+K^-J/\psi$ via ISR [8]. Figure 8

Parameters	Belle fit		Combined fit	
	Solution I	Solution II	Com. Sol.I	Com. Sol.II
$M(Y(4350))$	$4361 \pm 9 \pm 9$		4355^{+9}_{-10}	
$\Gamma_{\rm tot}(Y(4350))$	$74 \pm 15 \pm 10$		103^{+17}_{-15}	
$\mathcal{B} \cdot \Gamma_{e^+e^-}(Y(4350))$	$10.4 \pm 1.7 \pm 1.5$	$11.8 \pm 1.8 \pm 1.4$	$11.1^{+1.3}_{-1.2}$	12.3 ± 1.2
$M(Y(4660))$	$4664 \pm 11 \pm 5$		4661^{+9}_{-8}	
$\Gamma_{\rm tot}(Y(4660))$	$48 \pm 15 \pm 3$		42^{+17}_{-12}	
$\mathcal{B} \cdot \Gamma_{e^+e^-}(Y(4660))$	$3.0 \pm 0.9 \pm 0.3$	$7.6 \pm 1.8 \pm 0.8$	$2.2^{+0.7}_{-0.6}$	5.9 ± 1.6
ϕ	$39 \pm 30 \pm 22$	$-79 \pm 17 \pm 20$	18^{+23}_{-24}	-74^{+16}_{-12}

Table 2: Results of the fits to the $\pi^+\pi^-\psi(2S)$ invariant mass spectrum from Belle's unbinned fit and a combined fit on BaBar and Belle's results.

shows the K^+K^-J/ψ invariant mass distribution, together with the background estimated from the J/ψ mass sidebands. There is a broad enhancement around 4.4-5.5 GeV/c^2. In addition, there are two events near $\sqrt{s} = 4.26$ GeV, where CLEO observes three K^+K^-J/ψ events [4].

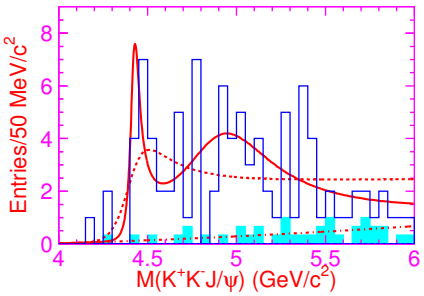

Figure 8: The K^+K^-J/ψ invariant mass distribution from Belle.

Fit the spectrum with a single resonance, The resonance parameters are $M = 4430^{+38}_{-43}$ MeV/c^2, $\Gamma_{\rm tot} = 254^{+55}_{-46}$ MeV/c^2, $\mathcal{B}(R \to K^+K^-J/\psi) \cdot \Gamma_{e^+e^-} = 1.9 \pm 0.3$ eV/c^2, where the errors are statistical only. Since there is a small concentration around 4.4 GeV/c^2, another fit with two resonance has been applied. One resonance is $\psi(4415)$ fixed according to PDG. The fit shows that the other resonance has mass 4875 ± 132 MeV/c^2 and width 630 ± 126 MeV/c^2. The spectrum and fit results are still not very clear. Like previous processes, the K^+K^- invariant mass also tends to be large. No clear $Y(4260)$ signal is observed, and Belle gives an upper limit on $\mathcal{B}(Y(4260) \to K^+K^-J/\psi)\Gamma(Y(4260) \to e^+e^-) < 1.2$ eV/c^2 at the 90% C.L.

3 ψ States at $e^+e^- \to$ Open Charm

Since masses of the Y states are well above the charm threshold, the Y states are expected to decay to open charms easily. Four final states are measured using ISR data, they are $D\overline{D}$ [9, 13], $D\overline{D}\pi + c.c.$ [10], $D\overline{D}^* + c.c.$ [11, 13], and $D^*\overline{D}^*$ [11, 13]. For comparison, cross

sections from Belle of e^+e^- → open charm are shown in Figure 9, as well as the cross sections of e^+e^- →h^+h^- + charmonium. From Belle's results, there are $\psi(4040)$, $\psi(4160)$ and $\psi(4415)$ at open charm final states, and one state could just appear at one or two channel obviously. $D\overline{D}\pi$ is dominated by $D\overline{D}^*(2460)+c.c.$, and $\psi(4415)$ could only decay to $DD(2460)$.

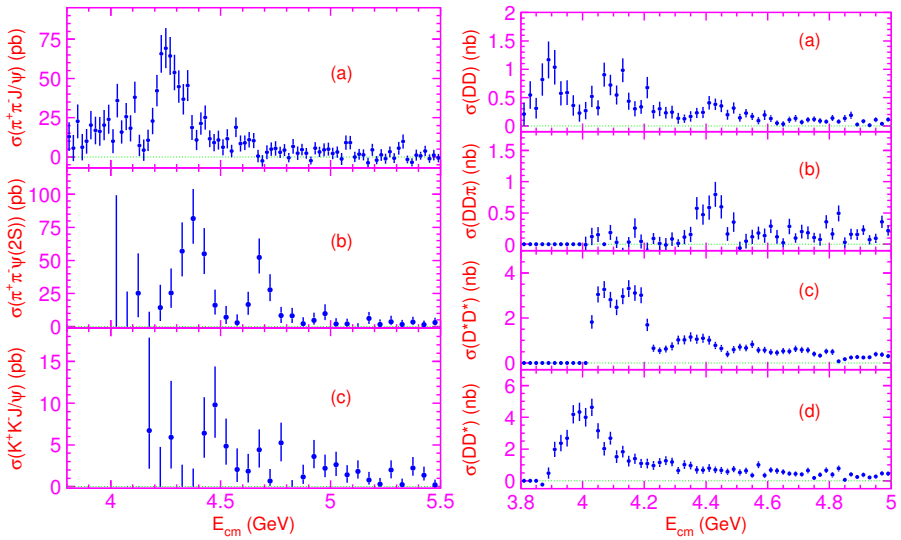

Figure 9: The left plot shows the measured $e^+e^- \to \pi^+\pi^- J/\psi$ (a), $\pi^+\pi^-\psi(2S)$ (b), and K^+K^-J/ψ (c) cross sections. The right plot shows the measured $D\overline{D}$ (a), $D^0D^-\pi^+ + c.c.$ (b), $D^{*+}D^{*-}$ (c), and $D^+D^{*-} + c.c.$ (d) cross sections.

BaBar got similar results on e^+e^- → open charm measurement. Figure 10 shows the sum of the $e^+e^- \to D\overline{D}$, $D\overline{D}^*$, and $D^*\overline{D}^*$ cross sections, the arrow indicates the position of the $Y(4260)$, which falls in a local minimum, in agreement with the cross section measured for hadron production in e^+e^- annihilation [14]. BaBar also obtains $\frac{\mathcal{B}(Y(4260)\to D\overline{D})}{\mathcal{B}(Y(4260)\to J/\psi\pi^+\pi^-)} < 34$ and $\frac{\mathcal{B}(Y(4260)\to D^*\overline{D}^*)}{\mathcal{B}(Y(4260)\to J/\psi\pi^+\pi^-)} < 40$ at the 90% confidence level.

4 $e^+e^- \to \Lambda_c^+\overline{\Lambda}_c^-$ and $\phi\pi^+\pi^-$

It is important to search these exotic Y states in charm baryon-antibaryon pair production. The first study is $e^+e^- \to \Lambda_c^+\overline{\Lambda}_c^-$ from Belle [15]. Figure 11 shows the cross section with statistical uncertainties only. There is a peak slightly above mass threshold. One possible interpretation of it is a new structure, $X(4630)$. Belle gives the mass $M = (4634^{+8+5}_{-7-8})$ MeV/c^2 and the total width $\Gamma_{\rm tot} = (92^{+40+10}_{-24-21})$ MeV/c^2. The significance for this structure is 8.8σ. The $X(4630)$ is close to the $Y(4660)$, and they have the same quantum number, $J^{PC} = 1^{--}$, so it is possible that they are the same structure.

It seems that there exists an $s\overline{s}$ version of the Y states from the study on $e^+e^- \to \phi\pi^+\pi^-$ via ISR. Like $\pi^+\pi^-\psi(2S)$, there are signals $\phi f_0(980)$ in $\phi\pi^+\pi^-$ final state. Figure 12 shows the cross sections on $e^+e^- \to \phi f_0(980)$ from BaBar [16] and Belle [17]. There is a structure

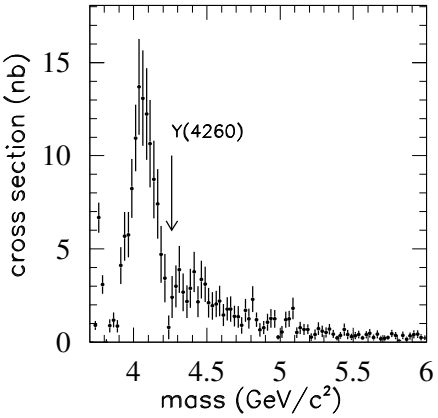

Figure 10: Sum of $e^+e^- \to D\overline{D}$, $D\overline{D}^*$, and $D^*\overline{D}^*$ cross sections. The arrow indicates the position of the $Y(4260)$.

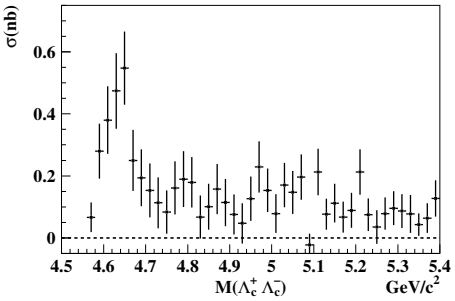

Figure 11: The cross section for the exclusive process $e^+e^- \to \Lambda_c^+\overline{\Lambda}_c^-$.

at 2.17 GeV/c^2. BaBar measures $M = (2175 \pm 10)$ MeV/c^2 and $\Gamma = (58 \pm 16)$ MeV/c^2 with only statistic errors, and Belle obtains $M = (2133^{+69}_{-115})$ MeV/c^2 and $\Gamma = (169^{+105}_{-92})$ MeV/c^2 where the uncertainties include both statistical and systematic errors. BES also confirmed this state in $J/\psi \to \eta\phi f_0(980)$ decay [18], and reports $M = (2186 \pm 10 \pm 6)$ MeV/c^2 and $\Gamma = (65 \pm 23 \pm 17)$ MeV/c^2.

5 Summary

Here we report ISR precesses studied at BaBar and Belle, focusing on charmonium-like states found above 4 GeV/c^2 region. There are four exotic states, $Y(4008)$ and $Y(4260)$ are only observed at $e^+e^- \to \pi^+\pi^- J/\psi$, and $Y(4360)$ and $Y(4660)$ are only observed at $e^+e^- \to \pi^+\pi^-\psi(2S)$. There is no evidence of these state in $e^+e^- \to D\overline{D}$, $D\overline{D}\pi$, $D\overline{D}^*$, and $D^*\overline{D}^*$,

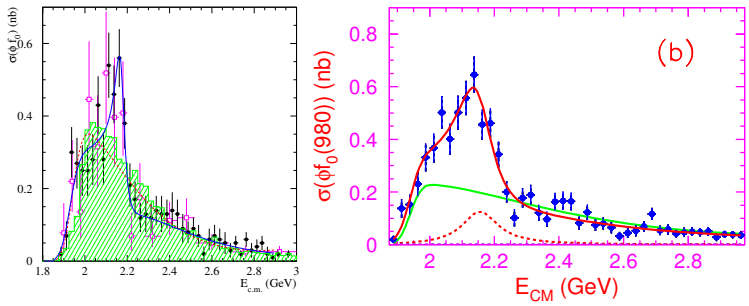

Figure 12: The cross sections of $e^+e^- \to \phi f_0(980)$ from BaBar(left) and Belle(right). Each plot also shows best fit on the spectrum, and give the evidence for Y(2175).

instead, $\psi(4040)$, $\psi(4160)$ and $\psi(4415)$ are confirmed at these channels. The 4 Y states and 3 ψ states too many for the charmonium states predicted in potential models, which may indicate one or several of them are exotic states. Belle observes a structure $X(4630)$ in charm baryon-antibaryon pair $\Lambda_c^+\overline{\Lambda}_c^-$ production. The $X(4630)$ and $Y(4660)$ are consist with each other in mass and width. There looks an $s\overline{s}$ version of the Y state, $Y(2175)$ in $e^+e^- \to \phi f_0(980)$.

6 Acknowledgments

This work is supported in part by NSFC (10825524) and 100 Talents Program of CAS (U-25).

References

[1] M. Benayoun *et al.*, Mod. Phys. Lett. **A14**, 2605 (1999).
[2] Aubert B *et al.* (BaBar Collaboration), Phys. Rev. Lett. (2005) **95**:142001.
[3] Yuan C Z *et al.* (Belle Collaboration), Phys. Rev. Lett. (2007) **99**:182004.
[4] Coan T E *et al.* (CLEO Collaboration). Phys. Rev. Lett. (2006) **96**:162003.
[5] Aubert B *et al.* (BaBar Collaboration), Phys. Rev. Lett. (2007) **98**:212001.
[6] Wang X L *et al.* (Belle Collaboration), Phys. Rev. Lett. (2007) **99**:142002.
[7] Guo F K *et al.*, Phys.Lett.B (2008)665:26-29.
[8] Yuan C Z *et al.* (Belle Collaboration), Phys. Rev. D (2008) **77**:011105(R).
[9] G. Pakhlova *et al.* (Belle Collaboration), Phys. Rev. D (2007) **77**:011103(R).
[10] G. Pakhlova *et al.* (Belle Collaboration), Phys. Rev. Lett. (2008) **100**:062001.
[11] G. Pakhlova *et al.* (Belle Collaboration), Phys. Rev. Lett. (2007) **98**:092001.
[12] Aubert B *et al.* (BaBar Collaboration), Phys. Rev. D (2009) **79**:092001.
[13] Aubert B *et al.* (BaBar Collaboration), arXiv:0607083 [hep-ex].
[14] C. Amsler *et al.*, Review of Particle Physics, Phys. Lett. **B667**, 1 (2008).
[15] G. Pakhlova *et al.* (Belle Collaboration), Phys. Rev. Lett. (2008) **101**:172001.
[16] Aubert B *et al.* (BaBar Collaboration), Phys. Rev. D (2007) **77**:012008.
[17] Shen C P *et al.* (Belle Collaboration), arXiv:0808.0006v1 [hep-ex].
[18] M. Ablikim *et al.* (BES Collaboration), Phys. Rev. Lett. (2008) **100**:102003.

Single- and Two-Photon-Induced Processes at the B Factories

Selina Z. Li

from the BaBar Collaboration
SLAC National Accelerator Laboratory
2575 Sand Hill Road MS61, Menlo Park, CA 94025, U.S.A

DOI: http://dx.doi.org/10.3204/DESY-PROC-2009-03/Li

We discuss single- and two-photon-induced processes in e^+e^- annihilations with center-of-mass energy near 10.58 GeV from the BaBar and Belle experiments. In particular, we present experimental results from two-photon physics of $\gamma\gamma \to \pi^0\pi^0$ and $\gamma\gamma^* \to \pi^0$. We also review the observation of the Two-Virtual-Photon-Annihilation process ($e^+e^- \to \rho^0\rho^0$ and $e^+e^- \to \phi\rho^0$) and the observation of $e^+e^- \to \rho^+\rho^-$, which should be primarily a one virtual photon process, but whose angular distributions may imply potential interference effects.

1 Introduction

Single- and two-photon-induced processes can now be probed at high precision or low cross sections in e^+e^- collisions due to large integrated luminosity at the B factories. The majority of studies has been focused on single-photon-induced processes that produce final states with negative C-parity. The BaBar and Belle experiments are designed to study B physics from $\Upsilon(4S)$ production and its cross section is of the order of nanobarns. In contrast, the exclusive hadron pair production is low multiplicity and produced of the order of femtobarns. The hadron pair production over a wide range of effective center-of-mass (CM) energies via initial state radiation also emerged as an interesting avenue. They provide an excellent testing ground for QCD. On the other hand, two-photon-induced processes have final states with positive C-parity. Two-photon physics and Two-Virtual-Photon-Annihilation (TVPA) fall into this category. In fact the latter has only been first observed [1] in 2006.

In this proceeding, I will present experimental measurements for processes selected from those mentioned above. Results are based on data samples collected by the BaBar and Belle detectors, whose detailed descriptions can be found in Ref. [2] and [3], respectively. In particular, this proceeding will cover results obtained from two-photon physics and other one- or two-photon-induced e^+e^- processes, including $\gamma\gamma \to \pi^0\pi^0$, $\gamma\gamma^* \to \pi^0$, $e^+e^- \to \rho^0\rho^0$, $e^+e^- \to \phi\rho^0$, and $e^+e^- \to \rho^+\rho^-$.

2 Two-photon physics processes

Two-photon physics can be used to study resonance structures, i.e., look for new resonances produced by $\gamma\gamma$ interaction where only $C = +$ can be produced. This is a unique feature because $\gamma\gamma$ gives us extra access to states not produced directly in the beam particle annihilation. Also the $J = 0, 2$ angular momentum of $\gamma\gamma$ nicely complements the $J = 1$ annihilation. An example is the η_c. We can also use two-photon reactions to test the validity of various QCD models that predict the quark and gluon interaction and dynamics.

Two-photon physics can be studied using double-tag, single-tag, and no-tag. In a double-tag mode, the scattered e^+ and e^- are both detected and thus the full kinematic information is available. In a single-tag mode, only one scattered e^+ or e^- is detected while in the no-tag mode neither the e^+ or e^- is detected. There is increasing acceptance going from double-tag to no-tag, but decreasing kinematic information. The next two subsections will describe measurements using no-tag and single-tag analyses.

2.1 An analysis of $\gamma\gamma \to \pi^0\pi^0$

The virtual photon flux falls off rapidly at increasing two-photon CM energy W, so it had been difficult to use the two-photon reaction to study high-mass final states. The high luminosity of the B factories has now made this possible. In a no-tag analysis [4] with quasi-real photons, Belle analyzed a 223 fb^{-1} data sample to study the process $\gamma\gamma \to \pi^0\pi^0$. The production cross section as a function of W is measured from $0.6 - 4.1$ GeV. A partial wave analysis is performed to look at the angular dependence of the differential cross section for different energy bins. The data show a large-scattering-angle enhancement at low energy ($W < 1.9$ GeV) and begin to show a forward angle peak at high energy ($W > 2.0$ GeV). The fits to data in Figure 1 suggest that a G-wave becomes necessary and important at energy greater than 2 GeV.

In the higher energy region, a χ_{c0} charmonium state is observed with a significance of more than seven standard deviations, while χ_{c2} has a significance of about two standard deviations. The products of the two-photon decay width and the branching fraction for the two charmonium states with and without interference between χ_{c0} and continuum are shown in Table 1.

Interference	$\Gamma_{\gamma\gamma}(\chi_{c0})\mathcal{B}(\chi_{c0} \to \pi^0\pi^0)$ **(eV)**	$\Gamma_{\gamma\gamma}(\chi_{c2})\mathcal{B}(\chi_{c2} \to \pi^0\pi^0)$ **(eV)**
Without	$9.7 \pm 1.5 \pm 1.2$	$0.18^{+0.15}_{-0.14} \pm 0.08$
With	$9.9^{+5.8}_{-4.0} \pm 1.6$	$0.48 \pm 0.18 \pm 0.07 \pm 0.14$

Table 1: Products of the two-photon decay width and the branching fraction for the two charmonium states.

The right hand side of Figure 1 shows the W dependence of the cross section at high energy and in the angular region of $|\cos\theta^*| < 0.6$, where θ^* is the CM π^0 scattering angle. The cross section is fit to the power law $\sigma \sim W^{-n}$ for the region $3.1 < W < 4.1$ GeV exclusive of the charmonium region ($3.3 < W < 3.6$ GeV). The power $n = 6.9 \pm 0.6 \pm 0.7$ obtained from the fit for the $\pi^0\pi^0$ mode is compatible with $n = 7.9 \pm 0.4 \pm 1.5$ for the $\pi^+\pi^-$ mode [5]. The leading order pQCD prediction is $\sigma \sim W^{-6}$. The ratio of cross sections for neutral to charged pion-pair production is rapidly falling at low energies, but it is almost constant for $W > 3.1$ GeV. Table 2 compares this ratio with the leading term QCD [6], pQCD [7], and handbag model [8].

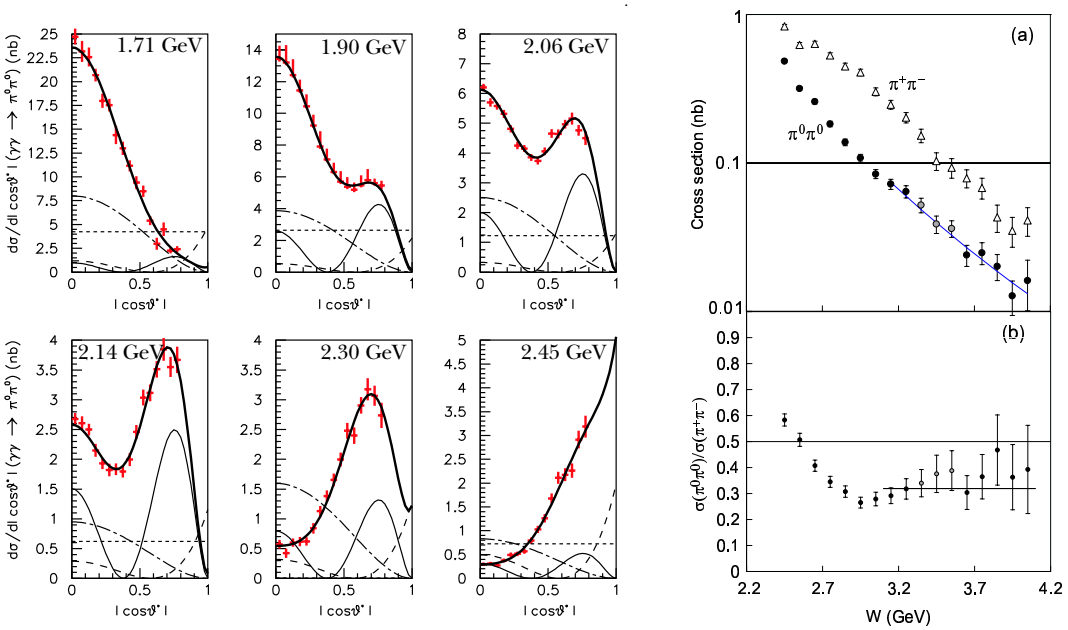

Figure 1: (Left) The angular dependence of the differential cross sections for $\gamma\gamma \to \pi^0\pi^0$ in six different W regions. (right) (a) The cross sections for $\gamma\gamma \to \pi^0\pi^0$ (circles) and $\gamma\gamma \to \pi^+\pi^-$ (triangles) as a function of W. (b) Ratio of the cross section for $\gamma\gamma \to \pi^0\pi^0$ to $\gamma\gamma \to \pi^+\pi^-$.

	Leading term QCD	**pQCD**	**Handbag model**	**Belle**
$\frac{\sigma(\pi^0\pi^0)}{\sigma(\pi^+\pi^-)}$	$0.03 - 0.07$	0.1	0.5	$0.32 \pm 0.03 \pm 0.05$

Table 2: Comparison of the ratio of neutral to charged pion-pair production cross sections.

2.2 A measurement of $\gamma\gamma^* \to \pi^0$ transition form factor

BaBar has made the measurement of $e^+e^- \to e^+e^-\gamma\gamma^*$, where $\gamma\gamma^* \to \pi^0$ in a single-tag analysis [9] based on 442 fb^{-1} of data. The π^0 in the final state is observed through its decay into two photons. The tagged electron must emit a highly virtual photon with a momentum transfer of $Q^2 > 3$ GeV^2 to be accepted by the detector. The momentum transfer to the untagged electron is close to zero. For the $\gamma\gamma^* \to \pi^0$ process, the differential cross section depends on only one form factor $F(Q^2)$. At high Q^2, the form factor can be represented as $F(Q^2) = \int T(x,Q^2)\phi_\pi(x,Q^2)\,\mathrm{d}x$, where x is the fraction of the π^0 momentum carried by one of the quarks, $T(x,Q^2)$ is the calculable hard scattering amplitude for $\gamma\gamma \to q\bar{q}$, and $\phi_\pi(x,Q^2)$ is the pion distribution amplitude for $q\bar{q} \to \pi$. Experimental measurement of the π^0 transition form factor $F(Q^2)$ helps determine the unknown dependence of $\phi_\pi(x,Q^2)$ on x.

To determine the number of events containing a π^0 in data, a binned likelihood fit to the $\gamma\gamma$ mass spectrum is performed in the π^0 region with a sum of signal and background distributions. This fitting procedure is applied in each of the 17 Q^2 intervals to study the Q^2 dependence of the cross section. The detector acceptance limits the detection efficiency at small Q^2. Therefore, to avoid possible systematics due to data-MC simulation differences near detector edges, we measure the cross section and form factor in the region $Q^2 > 4$ GeV^2.

In Figure 2 the measured differential cross section as a function of Q^2 at the Born level is compared to that from the CLEO experiment [10]. In the range $4 < Q^2 < 9$ GeV^2, BaBar results are in a reasonable agreement with CLEO data, but have significantly better precision. A $d\sigma/dQ^2 \sim Q^{-6}$ dependence in the range $12 < Q^2 < 30$ GeV^2 is observed in BaBar data. Also shown in Figure 2 is the π^0 transition form factor extracted from the cross section. At

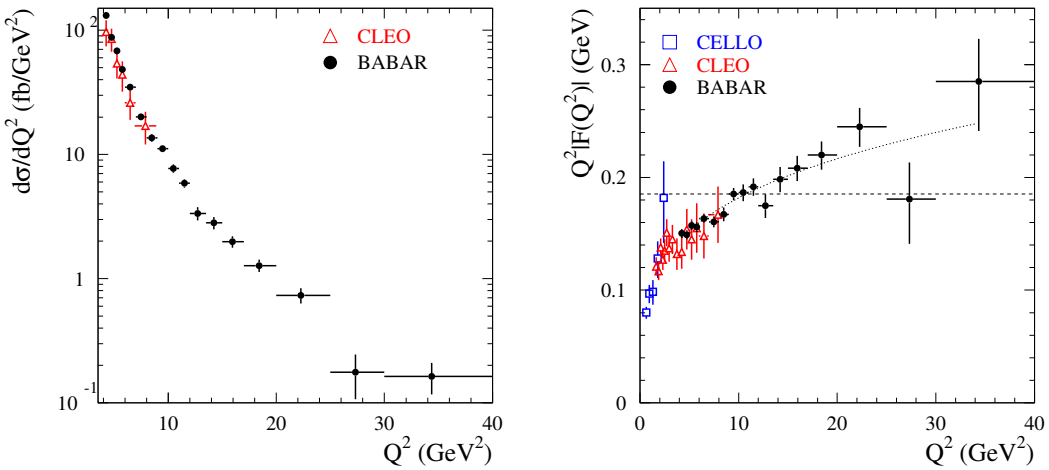

Figure 2: The $e^+e^- \to e^+e^-\pi^0$ differential cross section (left) and the $\gamma\gamma^* \to \pi^0$ transition form factor (right) as a function of Q^2. The dashed line shows the asymptotic limit for the form factor, and the dotted curve is a fit to BaBar data.

$Q^2 > 10$ GeV^2, the product $Q^2F(Q^2)$ exceeds the asymptotic limit of $\sqrt{2}f_\pi = 0.185$ GeV [11] and contradicts most existing theoretical models for the π^0 distribution amplitude [12]-[16]. A

fit to BaBar data in Figure 2 shows that $Q^2F(Q^2)$ is $\sim Q^{1/2}$ while the leading order pQCD predicts it to be constant in the asymptotic limit, thus suggesting that higher-order pQCD and power corrections are needed in the Q^2 region under study.

3 Selected processes from single-photon or two-photon

For a long time, we have understood that the process $e^+e^- \to$ hadrons at CM energy far below the Z mass is dominated by annihilation via a single virtual photon, thus yielding final states with $C = -1$. Very few studies are done for exclusive states with low multiplicity at 10 GeV due to the expectation of low rates, but there can be surprises. With the high luminosity collected at BaBar, TVPA in $e^+e^- \to \rho^0\rho^0$ and $e^+e^- \to \phi\rho^0$ [1] ($C = +1$) has been observed with production cross sections of a few femtobarns. This opens a new avenue for the study of hadron production mechanisms. In the next two subsections, selected results of exclusive hadron production from e^+e^- at 10.58 GeV at BaBar are presented.

3.1 $e^+e^- \to \rho^0\rho^0$ and $e^+e^- \to \phi\rho^0$

The first observation of $e^+e^- \to \rho^0\rho^0$ and $e^+e^- \to \phi\rho^0$ is based on 225 fb^{-1} of BaBar data from which events with exactly four well reconstructed, charged tracks with total charge zero are selected. Two oppositely charged tracks must be identified as pions and the other two as either pions or kaons. The invariant mass of the four charged tracks is required to be near the beam CM energy in order to be selected as $e^+e^- \to \pi^+\pi^-\pi^+\pi^-$ or $e^+e^- \to K^+K^-\pi^+\pi^-$ candidates. The scatter plots for $\pi^+\pi^-$ vs $\pi^+\pi^-$ or K^+K^- show strong signal peaks at the ρ^0 and ϕ mass. A binned log-likelihood fit over nine tiles is performed to extract signal in the $\rho^0\rho^0$ or $\phi\rho^0$ region. The extracted signal yields are 1243 ± 43 and 147 ± 13 for the $\rho^0\rho^0$ and $\phi\rho^0$ modes, respectively. The measured cross sections within the range $\cos\theta^* < 0.8$ are $20.7 \pm 0.7(\text{stat}) \pm 2.7(\text{syst})$ fb and $5.7 \pm 0.5(\text{stat}) \pm 0.8(\text{syst})$ fb for the $\rho^0\rho^0$ and $\phi\rho^0$ respectively, where θ^* is the production angle of ρ or ϕ in the CM frame. These results are consistent with calculations [17][18] from a vector-dominance two-photon exchange model provided after this measurement was released. As a comparison, $e^+e^- \to$ hadrons at 10 GeV is about 3 nb.

The $\rho^0\rho^0$ and $\phi\rho^0$ are final states with positive C-parity, so they cannot be produced via single-photon annihilation from e^+e^- collisions. However, they are allowed in TVPA as illustrated by the Feynman diagram in Figure 3. There are enough signal events to perform an angular analysis to investigate the production mechanism. The production angle θ^* shown in Figure 3 is forward peaking for these two processes, consistent with expectation of $\frac{\mathrm{d}\sigma}{\mathrm{d}\cos\theta^*} \propto \frac{1+\cos^2\theta^*}{1-\cos^2\theta^*}$ for TVPA. As a comparison, the $1 + \cos^2\theta^*$ distribution of single-photon annihilation is also shown. The helicity angles θ_H are also consistent with the $\sin^2\theta_H$ TVPA expectation for quasi-real photons.

3.2 Observation of $e^+e^- \to \rho^+\rho^-$

Given the observation of $e^+e^- \to \rho^0\rho^0$, it is natural to also look for the $\rho^+\rho^-$ final state with negative C-parity, which is expected to be produced dominantly via single-photon annihilation. BaBar has made the first observation of $e^+e^- \to \rho^+\rho^-$ [19] based on 379 fb^{-1} of data from which events with exactly two well reconstructed, oppositely charged tracks and two π^0 candidates are selected. The invariant mass of the four pions is required to be near the beam CM energy. The

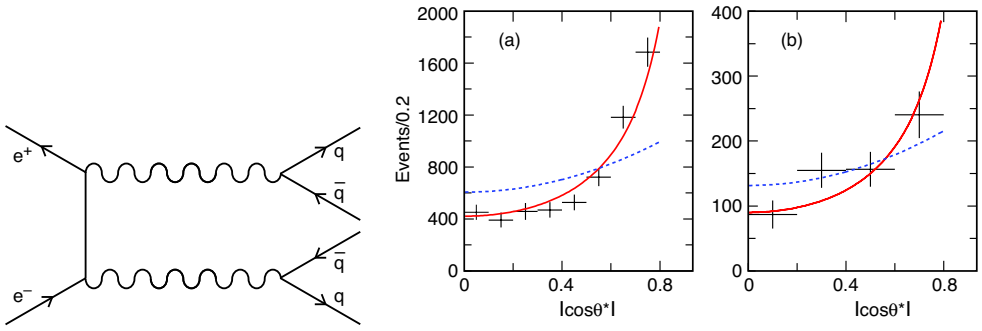

Figure 3: (Left) A Feynman diagram for the two-virtual-photon annihilation. (Right) The production angle distribution after correction for efficiency for (a) $e^+e^- \to \rho^0\rho^0$ and (b) $e^+e^- \to \phi\rho^0$. The solid and dashed curves are the normalized $\frac{1+\cos^2\theta^*}{1-\cos^2\theta^*}$ and $1+\cos^2\theta^*$, respectively.

$\pi\pi$ mass scatter plot shows strong peaks at the ρ mass. A 2D fit yields 357 ± 29 events with the cross section extrapolated to the full angular range measured to be $19.5 \pm 1.6(\text{stat}) \pm 3.2(\text{syst})$ fb. The large, clean sample of signal events allows us to perform an angular analysis to test QCD at the amplitude level.

Assuming a one-photon production mechanism, this vector-vector final state can be described by three independent helicity amplitudes, F_{00}, F_{10}, and F_{11}. The angular distributions for the helicity (azimuthal) angle $\theta_\pm$ ($\varphi_\pm$) of the pion from $\rho^\pm$ decay, and the ρ production angle θ^* are shown in Figure 4. Fits to the angular distributions with the normalization constraint $|F_{00}|^2 + 4|F_{10}|^2 + 2|F_{11}|^2 = 1$ reveal that $|F_{00}|^2 = 0.51 \pm 0.14(\text{stat}) \pm 0.07(\text{syst})$ which deviates from the perturbative QCD prediction of one (i.e., the F_{00} amplitude should dominate at high energy) by more than three standard deviations. This significant disagreement suggests that either the decay is not dominated by single-virtual-photon annihilation as expected, or the QCD prediction does not apply to data in this energy region. Because charged ρ's are involved, $\rho^+\rho^-$ cannot be produced via TVPA unless there is significant final state interaction. Given the possible relevance to potential similar effects in $B^0 \to \rho^+\rho^-$ process, which is crucial for the determination of angle α through CP-violation, understanding the observed $e^+e^- \to \rho^+\rho^-$ decay amplitudes may have broader implications.

4 Conclusion

Over the past nine years of operation, the B factories have integrated very high luminosity and have reopened several interesting areas for hadron physics. Belle provided a high statistics measurement of $\pi^0\pi^0$ production in two-photon physics and measured the cross section and its angular dependence in the kinematic range $0.6 < W < 4.1$ GeV and $|\cos\theta^*| < 0.8$ in a no-tag analysis. BaBar measured the $\gamma\gamma^* \to \pi^0$ transition form factor in a single-tag analysis and provided a gateway to study the pion distribution amplitude. Other single- and two-photon-induced e^+e^- processes are also reviewed. In particular, BaBar explored the cross sections and angular amplitudes of exclusive meson pair productions in e^+e^- annihilations. Studies of low multiplicity final states can provide an excellent testing ground for QCD. The case

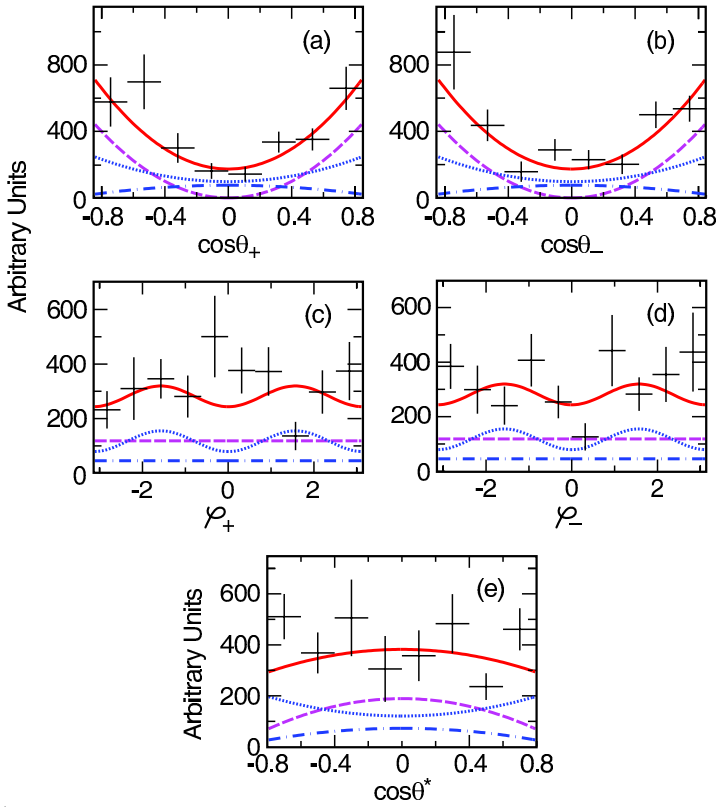

Figure 4: The angle distribution of (a) $\cos\theta_+$, (b) $\cos\theta_-$, (c) φ_+, (d) φ_-, (e) $\cos\theta^*$ after correction for efficiency for $e^+e^- \to \rho^+\rho^-$. See text for definition of the angles. The dashed curves show the contributions from F_{00}, the dotted curves are F_{10}, the dashed-dotted curves are F_{11}, and the solid curve is the total fit result.

of $e^+e^- \to \rho^+\rho^-$ is puzzling since it should be a one virtual photon process, but amplitude results suggest potential interference effects. Other possible final states should be explored to make use of the large datasets available at the B factories. In summary, nearly all of the measurements presented here show some deviations from models and thus are impetus to advance the theoretical front of our understanding.

References

[1] B. Aubert, *et al.*, Phys. Rev. Lett. **97**, 112002 (2006).

[2] B. Aubert, *et al.*, Nucl. Instrum. Methods **A479**, 1 (2002).

[3] A. Abashian, *et al.*, Nucl. Instrum. Methods **A479**, 117 (2002).

[4] S. Uehara, *et al.*, Phys. Rev. **D79**, 052009 (2009).

[5] H. Nakazawa, *et al.*, Phys. Lett. **B615**, 39 (2005).

[6] M. Benayoun and V.L. Chernyak, Nucl. Phys. **B329**, 285 (1990).

[7] S.J. Brodsky and G.P. Lepage, Phys. Rev. **D24**, 1808 (1981).

[8] M. Diehl, P. Kroll and C. Vogt, Phys. Lett. **B532**, 99 (2002).

[9] B. Aubert, *et al.*, arXiv:0905.4778, submitted to Phys. Rev. **D**.

[10] J. Gronberg, *et al.*, Phys. Rev. **D57**,33 (1998).

[11] G.P. Lepage and S.J. Brodsky, Phys. Rev. **D22**,2157 (1980).

[12] N.G. Stefanis, Nucl. Phys. Proc. Suppl. **181-182**, 199 (2008).

[13] A. Khodjamirian, Eur. Phys. J. **C6**, 477 (1999).

[14] V.L. Chernyak and A.R. Zhitnitsky, Nucl. Phys. **B201**, 492 (1982).

[15] G.P. Lepage and S.J. Brodsky, Phys. Lett. **B87**,359 (1979).

[16] A.P. Bakulev, S.V. Mikhailov, and N.G. Stefanis, Phys. Lett. **B508**,279 (2001).

[17] M. Davier, M. Peskin, and A. Snyder, hep-ph/0606155.

[18] G.T. Bodwin, *et al.*, Phys. Rev. **D74**, 074014 (2006).

[19] B. Aubert, *et al.*, Phys. Rev. **D78**, 071103 (2008).

KLOE Results on Light Meson Properties

Camilla Di Donato, On Behalf of The KLOE Coll.

INFN Sez. Napoli, Via Cintia Compl. M.S.A. ed. 6, 80126 Naples, Italy

DOI: http://dx.doi.org/10.3204/DESY-PROC-2009-03/DiDonato

The KLOE experiment operating at the ϕfactory DAϕNE has collected an integrated luminosity of about 2.5 fb^{-1} on the ϕ meson peak. We present recent results achieved from studying properties of light mesons using the full statistic.

1 KLOE at DAϕNE

The KLOE experiment [1] is placed at the Frascati ϕ-factory DAΦNE, an e^+e^- collider running at $\sqrt{s} \simeq$1020 MeV, corresponding to the ϕ meson mass. A ϕ-factory allow to access many of the light mesons via ϕ radiative decay and to study the inner structures of the mesons, in particular the s-quark content via the couplings with the $s\bar{s}$ state. KLOE has collected an integrated luminosity of 2.5 fb^{-1} at the ϕ peak, corresponding to $8 \times 10^9 \phi$ decays, 10 pb^{-1} around the centre of mass energy and 250 pb^{-1} at $\sqrt{s} = 1$ GeV.
The KLOE detector consists of a large cylindrical drift chamber (3.75 m length and 4 m diameter), surrounded by a sampling calorimeter made of lead and scintillating fibers. The detector is inserted in a superconducting coil producing a uniform magnetic field of $\simeq$ 0.52T. Large angle tracks from the origin ($\theta > 45°$) are reconstructed with relative momentum resolution $\sigma_p/p = 0.4\%$. Photon energies and times are measured by the calorimeter with resolutions of $\sigma_E/E = 5.7\%/\sqrt{E(GeV)}$ and $\sigma_t = 57ps/\sqrt{E(GeV)} \oplus 100$ ps.

2 Scalar Mesons

The structure of the scalar mesons (S) with mass below 1 GeV is still an open question. The radiative decays $\phi \to PP'\gamma$ are dominated by the exchange of a S in the intermediate state. Branching ratio and mass spectra of decays are sensitive to the structure of intermediate S and they can clarify whether S are $q\bar{q}$ mesons, tetra-quark state, bound states of $K\bar{K}$ pair or a mix of these configurations. Many approaches have been used to parametrise the production of S in the ϕ radiative decays. We consider the Kaon Loop (KL) model [2] which assumes that the ϕ radiative decay proceeds through a virtual K^+K^- loop, while emitting a photon. Then the K^+K^- annihilate forming a S. The production amplitude of the S depends on the mass and couplings to $\pi\pi$ and KK. The fit parameters are the M_S and the two couplings $g_{SPP'}$, g_{SKK}. An alternative parametrisation of the amplitude is the No Structure (NS) one [3]: a point-like coupling of the scalar to the ϕ meson is assumed; S is parametrised as a Breit-Wigner interfering with a polynomial background. Free parameters are the M_S and the couplings $g_{\phi S\gamma}$, $g_{SPP'}$ and g_{SKK}. In the following we describe how we fit the data using the two approaches described above.

Parameter	Kaon Loop	No Structure
M_{a_0} (MeV)	$982.5 \pm 1.6 \pm 1.1$	982.5 (fixed)
g_{a_0KK} (GeV)	$2.15 \pm 0.06 \pm 0.06$	$2.01 \pm 0.07 \pm 0.28$
$g_{a_0\eta\pi}$ (GeV)	$2.82 \pm 0.03 \pm 0.04$	$2.46 \pm 0.08 \pm 0.11$
$g_{\phi a_0\gamma}$ (GeV^{-1})	$1.58 \pm 0.10 \pm 0.16$	$1.83 \pm 0.03 \pm 0.08$
$BR(\phi \to \rho \to \eta\pi\gamma)\times 10^{-6}$	$0.92 \pm 0.40 \pm 0.15$	-0
$BR(\eta \to \gamma\gamma)/BR(\eta \to \pi\pi\pi)$	$1.70 \pm 0.04 \pm 0.03$	$1.70 \pm 0.03 \pm 0.01$
$P(\chi^2)$	10.4%	30.9%

Table 1: Results from combined fit to $M_{\eta\pi}$ spectra

2.1 Searching for $a_0(980)$ in $e^+e^- \to \eta\pi^0\gamma$

Two independent analyses [4] using $\eta \to \gamma\gamma$ or $\eta \to \pi^+\pi^-\pi^0$ decays are performed from a sample of 450 pb^{-1}. In both analyses there is the requirement of five photons from the interaction point. The selection of also two tracks with balanced charge is required to select the charged final state. The fully neutral chain is characterised by high statistic and large background, while the charged one has small background but lower statistic. Since the interfering $\phi \to \rho\pi^0 \to \eta\pi^0\gamma$ background is small, it is possible to extract the branching ratio (BR) directly from event counting after the residual background subtraction and normalising to $\phi \to \eta\gamma$ decays with the same final state. The two samples lead to consistent branching ratio values, thus a combined fit of the two spectra, is performed to extract relevant parameters of the a_0 scalar meson. The couplings, fitted according to the KL [2] and the NS [3] models, point to a total width in the range $[80 \div 105]$ MeV and to a size-able $s\bar{s}$ content of the $a_0(980)$, see Tab.1.

Recently a new model to describe S has been proposed by t'Hooft et al. [5]. They start from the point that tetra-quarks bound states naturally reproduce the $SU(3)$ nonet structure, with the correct mass ordering and then they add an instaton contribution to induce a mixing between tetra-quarks and diquarks states. The instaton contribution lead to a simple and satisfactory description of light states below 1 GeV and heavier scalar states around 1.5 GeV. The KLOE measurement concerning the f_0 scalar meson has been used as input parameter to evaluate the coefficient in the model and then to compare the effect on the a_0 meson. The results are intriguing [5].

2.2 $\phi \to K^0\bar{K}^0\gamma$

Using 2.18 fb^{-1} of the KLOE data, a search [6] for the decay $\phi \to K^0\bar{K}^0\gamma$ has been performed. This decay is expected to proceed mainly through $\phi \to [a_0(980) + f_0(980)]\gamma \to K^0\bar{K}^0\gamma$. In this decay the $K^0\bar{K}^0$ pair is produced with positive charge conjugation and a limited phase space due to the small mass difference between the ϕ and the production threshold of two neutral kaons (995 MeV). The signature of this decay is provided by the presence of either 2 K_S or 2 K_L and a low energy photon. We select only the K_SK_S component, looking for double $K_S \to \pi^+\pi^-$ decay vertex, because of the clean topology. The main background are the resonant $e^+e^- \to \phi\gamma \to K_SK_L\gamma$ and the continuum $e^+e^- \to \pi^+\pi^-\pi^+\pi^-\gamma$ processes.
After the selection cut we found 5 candidate events in data, whereas 3 events are expected from

Monte Carlo background samples. This leads to: BR($\phi \to K^0\bar{K}^0\gamma$) $< 1.9 \times 10^{-8}$ at the 90% C.L. Theory predictions for the BR spread over several orders of magnitude; several of them are ruled out by our result. Moreover the present upper limit is consistent with the BR($\phi \to K\bar{K}$) prediction computed with $a_0(980)$ [4], $f_0(980)$ [7] couplings measured by KLOE.

3 $\sigma(e^+e^- \to \omega\pi^0)$

We have studied the $e^+e^- \to \omega\pi^0$ cross section in the range $\sqrt{s} \sim 1000-1030$ MeV, on a sample of 600 pb^{-1}, searching for $\pi^+\pi^-\pi^0\pi^0$ and $\pi^0\pi^0\gamma$ final states. At low energy, below 1.4 GeV it is largely dominated by non resonant process. However around the ϕ mass a contribution from the OZI-G parity violating decay $\phi \to \omega\pi^0$ is expected. The strongly suppressed decay can be observed via interference with the non resonant processes, showing as a dip in the total cross section dependence from $\sqrt{s}$, see Fig.1.

The parametrisation for the cross section, that has been convoluted with the radiator function is the following:

$$\begin{aligned} \sigma(\sqrt{s}) &= \sigma_0(\sqrt{s})|1 - Z\frac{M_\phi\Gamma_\phi}{D_\phi}|^2 \\ \sigma_0(\sqrt{s}) &= \sigma_0 + \sigma'(\sqrt{s} - M_\phi) \end{aligned}$$

where the $\sigma_0(\sqrt{s})$ is the bare cross section for the non resonant process, Z is the interference parameter and M_ϕ, Γ_ϕ and D_ϕ are mass, width and inverse propagator of ϕ meson. By fitting the observed interference pattern around ϕ mass for both final states under study we extract the ratio $\Gamma(\omega \to \pi^0\gamma)/\Gamma(\omega \to \pi^+\pi^-\pi^0)$ and combining the result with rare branching fraction and imposing unitarity, we derive the branching fraction:

$$\begin{aligned} BR(\omega \to \pi^0\gamma) &= (8.09 \pm 0.14)\% \\ BR(\omega \to \pi^+\pi^-\pi^0) &= (90.24 \pm 0.19)\% \end{aligned} \quad (1)$$

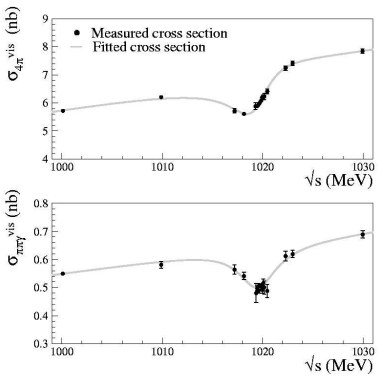

Figure 1: Measured cross section and fitted one. Up: $\pi^+\pi^-\pi^0\pi^0$ final state; down: $\pi^0\pi^0\gamma$ final state.

The interference parameter determined in the $\pi^+\pi^-\pi^0\pi^0$ analysis allow us to determine the branching ratio for the process $\phi \to \omega\pi^0$:

$$\begin{aligned} BR(\phi \to \omega\pi^0) &= \frac{\sigma_0^{\omega\pi}|Z_{4\pi}|^2}{\sigma_\phi} \\ &= (5.63 \pm 0.70) \times 10^{-5} \end{aligned} \quad (2)$$

and the error has been reduced by a factor two with respect to the best previous measurement by SND; the two values are in agreement.

4 $\gamma\gamma$ Fusion at KLOE: $\sigma(600) \to \pi\pi$

The question concerning the $\sigma/f_0(600)$ meson has been debated for a long time.

Evidences come from Dalitz Plot analysis of charged final states from E731, CLEO, Bes, but the values of mass and width are affected by large uncertainties. Indirect evidence comes also from the Dalitz Plot analysis of the $e^+e^- \to \pi^0\pi^0\gamma$ process by KLOE [8].

The preliminary analysis of 11 pb^{-1} at $\sqrt{s} = 1$ GeV, 5 % of the off-peak data sample, has been finalise to search for σ production in $\gamma\gamma$ interaction. An excess of events in the $\pi^0\pi^0$ final state has been observed, when the expected background from Monte Carlo are compared with data, see Fig.2.

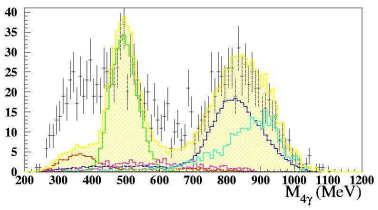

Figure 2: $M_{\gamma\gamma\gamma\gamma}$: data compared with Monte Carlo shows an excess of events compatible σ.

5 Pseudoscalar Mesons

The ϕ-factory DAϕNE can be considered also an η factory. The acquired luminosity of 2.5 fb^{-1} on peak correspond also to $\sim 10^8$ η meson, if we consider the radiative decay of the ϕ meson. The same can be for the η', on peak data furnish a sample of 5×10^5 η', again from radiative decay of the ϕ meson. In the following we describe part of the analysis performed at KLOE.

5.1 $\eta - \eta'$ mixing angle

We have measured the ratio $R_\phi = BR(\phi \to \eta'\gamma)/BR(\phi \to \eta\gamma)$ by looking for the radiative decays $\phi \to \eta'\gamma$ and $\phi \to \eta\gamma$ into the final states $\pi^+\pi^-7\gamma$ and 7γ, respectively, in a sample of $\simeq 1.4 \times 10^9\phi$ mesons. We obtained [9] $R_\phi = (4.77 \pm 0.09 \pm 0.19) \cdot 10^{-3}$, from which we derive BR$(\phi \to \eta'\gamma) = (6.20 \pm 0.11 \pm 0.25) \cdot 10^{-5}$.

The value of R_ϕ can be related to the $\eta - \eta'$ mixing angle in the flavor basis. Using the approach [10] and [11], where the SU(3) breaking is taken into account via constituent quark mass ratio $m_s/\bar{m}$, and the two parameters Z_{NS} and Z_S take into account the effect of the OZI-rule, which reduce the VP wave-function overlaps [12] we have:

$$R = \frac{BR(\phi \to \eta'\gamma)}{BR(\phi \to \eta\gamma)} = cot^2\varphi_P(1 - \frac{m_s}{\bar{m}}\frac{Z_{NS}}{Z_S}\frac{tan\varphi_V}{sin2\varphi_P})^2(\frac{p_{\eta'}}{p_\eta})^3 \qquad (3)$$

Equation 3 combined with our measurement produced the following result: $\varphi_P = (41.4 \pm 0.3_{stat} \pm 0.7_{sys} \pm 0.6_{th})^\circ$.

The η' meson is a good candidate to have a size-able gluonium content, so we can have $|\eta' >= X_{\eta'}|q\bar{q} > +Y_{\eta'}|s\bar{s} > +Z_{\eta'}|gluon >$, where the $Z_{\eta'}$ parameter takes in to account a possible mixing with gluonium. The normalisation implies $X^2_{\eta'} + Y^2_{\eta'} + Z^2_{\eta'} = 1$ with $X_{\eta'} = \cos\phi_G \sin\phi_P$, $Y_{\eta'} = \cos\phi_G \cos\phi_P$ and $Z_{\eta'} = \sin\phi_G$, where ϕ_G is the mixing angle for the gluonium contribution. Possible gluonium content of the η' meson corresponds to non-zero value for $Z^2_{\eta'}$. Introducing other constraints on $X_{\eta'}$ and $Y_{\eta'}$ [11, 12, 13], as: $\Gamma(\eta' \to \gamma\gamma)/\Gamma(\pi^0 \to \gamma\gamma)$; $\Gamma(\eta' \to \rho\gamma)/\Gamma(\omega \to \pi^0\gamma)$; $\Gamma(\eta' \to \omega\gamma)/\Gamma(\omega \to \pi^0\gamma)$, and allowing for gluonium, we built a χ^2, function of (ϕ_P, ϕ_G), to determine $Z^2_{\eta'}$ and ϕ_P. The solution in the hypothesis of no gluonium content, i.e. $Z^2_{\eta'} = 0$ yields $\phi_P = (41.5^{+0.6}_{-0.7})^\circ$; the χ^2 quality is bad, while allowing for gluonium the χ^2 quality is good, $P(\chi^2/N.d.f.) = 0.49$ and the results are $\phi_P = (39.7 \pm 0.7)^\circ$ with $Z^2_{\eta'} = 0.14 \pm 0.04$ showing a 3σ evidence for the η' gluonium content.

Moreover, combining R_ϕ with other constraints [14] and answering in this way to the objections

from [15], [16] to our paper [9], we find $Z^2_{\eta'} = 0.120 \pm 0.035$ and $\phi_P = (40.2 \pm 0.6)^\circ$ in agreement with the previous one.

5.2 $\eta \to \pi^+\pi^- e^+ e^-$

The study of $\eta \to \pi^+\pi^- e^+ e^-$ decay allows to probe the internal structure of the η meson [17] and could be used to compare the predictions based on Vector Meson Dominance (VMD) and Chiral Perturbation Theory (ChPT) [18]. Moreover, it would be possible to study CP violation not predicted by the Standard Model by measuring the angular asymmetry between the decay planes of the electrons and of the pions in the η rest frame.

The experimental scenario is rather poor to investigate the theoretical issue related to this process. Our $\eta \to \pi^+\pi^- e^+ e^-$ analysis [18] is based on a sample of 1.7 fb$^-$1. The event selection is based on the requirement of one photon of $E > 250$ MeV energy, the recoil photon produced in the $\phi \to \eta\gamma$ decay, and four charged tracks coming from the interaction region. Mass assignment for each track is done using time of flight of the charged particles measured in the calorimeter. Background due to γ conversions on the beam pipe has been studied using off-peak data, where ϕ decays are negligible.
The contamination is evaluated by fitting the sidebands of the $M_{\pi\pi ee}$ data spectrum with background components after loose cuts on the kinematic fit χ^2 and on the sum of momenta of the charged particles. Signal events are computed after rejecting γ conversions, and from the fit the branching ratio is evaluated:

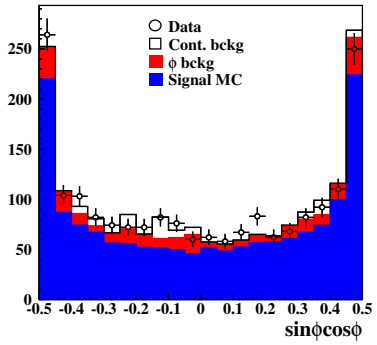

Figure 3: $sin\phi cos\phi$ in the signal region.

$$BR(\eta \to \pi^+\pi^- e^+ e^- \gamma) = (26.8 \pm 0.9_{Stat.} \pm 0.7_{Syst.}) \times 10^{-5}. \quad (4)$$

The decay plane asymmetry is calculated starting from the momenta of the four particles and it is expressed as function of the angle ϕ between the pion and the electron planes in the η rest frame; it has been evaluated for the events in the signal region after background subtraction, see Fig. 3. The result is:

$$\mathcal{A}_\phi = (-0.6 \pm 2.5\ _{Stat.} \pm 1.8\ _{Syst.}) \times 10^{-2} \quad (5)$$

which is the first measurement of this parameter.

5.3 Search for Box Anomaly: $\eta/\eta' \to \pi^+\pi^-\gamma$

Significant contribution from chiral anomaly responsible for $\eta/\eta' \to \gamma\gamma$, which proceed through the triangle anomaly, is expected in $\eta/\eta' \to \pi^+\pi^-\gamma$, called box anomaly. The box anomaly is a higher term of WZW, describing the direct coupling of three pseudoscalar mesons with the photon (Fig. 4). The shapes of the Feynman diagrams representing the WZW gives the names for the anomaly.
The $\eta, \eta' \to \pi^+\pi^-\gamma$ decays provide a good tool to investigate the box anomaly, which describes

a non-resonant coupling. The invariant mass of the pions is a good observable to disentangle this contribution from other possible resonant ones, e.g. from the ρ-meson.

The kinematic range of the decays of η and η' are above the chiral limit where the WZW validity holds, for the η' even the ρ-mass is covered. The $\eta \to \pi^+\pi^-\gamma$ decay has been measured in 1970 by Gormely et al. (7250 events) [20] and in the 1973 by Layter et al. (18150 events) [21]. Theoretical papers trying to combine the two measurements found discrepancies in data treatment and problems in obtaining consistent results [22, 23]. Therefore new experimental results with larger statistics are needed to clarify the scenario. The KLOE data 2.5 fb^{-1}, corresponding to 5×10^6 $\eta \to \pi^+\pi^-\gamma$ decays. This statistics allows a detailed investigation of the di-pion invariant mass distribution. A selection procedure and background rejection criteria are in development.

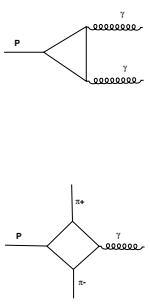

Figure 4: Diagrams for the triangle and box anomalies.

The same framework can be applyed to the η' meson, taking into account that in this case also the ρ-mass is covered. Data related to the $\eta' \to \pi^+\pi^-\gamma$ decays are much more recent: in 1997 the analysis of 7392 events provided by Crystal Barrel gave a box anomaly evidence in the invariant mass of pions [24], while in 1998 the L3 Collaboration found that their data (2123 events) were well described by the resonant contribution [25].
The data already collected at KLOE, 2.5 fb^{-1}, provides 15×10^4 $\eta' \to \pi^+\pi^-\gamma$ decays. Accurate Monte Carlo simulation is under development.

5.4 Conclusions and Outlooks

KLOE has been obtained several important results in hadronic physics, in this paper we descrive some of them. But this is not the end of the story, a new scheme to increase luminosity by a factor 5 is being implemented at DAϕNE, thanks to the *crab weist* and large crossing angle, to open new prospects for KLOE2. In the new data taking scheduled for KLOE, e^+e^- taggers for $\gamma\gamma$ physics will be inserted, to collect 5 fb^{-1}. Another upgrade will be performed in a second phase to insert the inner tracker and new small angle calorimeters. KLOE2 items will be focused on kaon physics and light hadrons, where in particular thanks to the e^+e^- taggers a dedicated data collection will allow us to investigate in a deepper way the $\gamma\gamma$ fusion processes.

References

[1] M. Adinolfi *et al.*, Nucl. Instrum. Meth. **A 461** 25 (2001); Nucl. Instrum. Meth. **A 461** 344 (2001);

[2] N.N. Achasov, V.V. Gubin, Phys. Rev. **D 56** 4084 (1997).

[3] G. Isidori, L. Maiani, M. Nicolaci and S. Pacetti JHEP **0605** 049 (2006).

[4] F. Ambrosino *et al.* [KLOE Coll.], arXiv:hep-ex/0904.2539 (2009), sub. to PLB.

[5] G. 't Hooft, G. Isidori, L. Maiani, A. Polosa, V. Riquer, Phys. Lett. **B662** 424 (2008)

[6] F. Ambrosino *et al.* [KLOE Coll.] arXiv:hep-ex/0903.4115 (2009), accepted by PLB.

[7] F. Ambrosino *et al.* [KLOE Coll.], Phys. Lett. **B634** 148 (2006)

[8] F. Ambrosino *et al.* [KLOE Coll.], Eur. Phys. J. **C49** 473 (2007).

[9] F. Ambrosino *et al.* [KLOE Coll.], Phys. Lett. **B648** 267 (2007)

[10] A. Bramon, R. Escribano, M.D. Scadron, Eur. Phys. J. **C7** 271 (1999)

[11] J.L. Rosner, Phys. Rev. **D27** 1101 (1983)

[12] A. Bramon, R. Escribano, M.D. Scadron, Phys. Lett. **B503** 271 (2001)

[13] E. Kou, Phys. Rev. **D63**, 054027 (2001)

[14] F. Ambrosino *et al.* [KLOE Coll.], arXiv:hep-ph/0906.3819 (2009), sub. to Eur. Phys. J. .

[15] R. Escribano and J. Nadal, JHEP **05** 6 (2007)

[16] C.E. Thomas, JHEP **10** 26 (2007)

[17] L.G. Landsberg, Phys. Rept **128** 301 (1985).

[18] C. Jarlskog and H. Pilkhun, Nucl. Phys. **B 1**264 (1967), A. Faessler *et al.*, Phys. Rev. **C61** 035206 (2000); C. Picciotto, S. Richardson, Phys. Rev.**D48** 3395 (1993); B. Borasoy and R. Nissler, arXiv:hep-ph/07050954 (2007).

[19] F. Ambrosino *et al.* [KLOE Coll.], Phys. Lett. **B675** 283 (2009)

[20] M. Gormley *et al.*, Phys. Rev. **D2** 501 (1970)

[21] J.G. Layter *et al.*, Phys. Rev. Lett. **29** 316 (1972)

[22] M. Benayoun *et al.*, Z. Phys. **C65** 399 (1995)

[23] M. Benayoun *et al.*, Eur. Phys. J. **C31** 525 (2003)

[24] A. Abele *et al.* [Crystal Barrel Coll.], Phys. Lett. **B402** 195 (1997)

[25] M. Acciari *et al.* [L3 Coll.], Phys. Lett. **B418** 399 (1998)

Strong-field effects for lepton and photon production in collisions of relativistic heavy nuclei at RHIC and LHC

Ulrich D. Jentschura[1] *and Valery G. Serbo*[2]

[1]Dept. of Physics, Missouri Univ. of Science and Technology, Rolla, Missouri 65409-0640, USA
[2]Novosibirsk State University, Pirogova 2, 630090 Novosibirsk, Russia,
corresponding author: serbo@math.nsc.ru

DOI: http://dx.doi.org/10.3204/DESY-PROC-2009-03/Serbo

We consider effects of strong electromagnetic fields in collisions of ultra-relativistic nuclei at the RHIC and LHC colliders. Since the parameter $Z\alpha$ is not small ($Z\alpha \approx 0.6$ for Au-Au and Pb-Pb collisions), the whole series in $Z\alpha$ has to be summed in order to obtain the cross section with sufficient accuracy. For the production of lepton pairs we present new results related to the Coulomb corrections (corresponding to multi-photon exchange of the produced leptons with the nuclei) and to the unitarity corrections (corresponding to the exchange of light-by-light blocks between nuclei). For nuclear bremsstrahlung we calculated the unitarity corrections and a special case related to virtual Delbrück scattering.

1 Introduction

Recently, electromagnetic processes in ultra-relativistic nuclear collisions were discussed in numerous papers (see [1, 2, 3] for a review and references therein) which are connected mainly with operation of the RHIC collider and the future LHC lead-lead option. For these colliders, the charge numbers of nuclei $Z_1 = Z_2 \equiv Z$ and their Lorentz factors $\gamma_1 = \gamma_2 \equiv \gamma$ are given in Table 1, together with indicative values for relevant lepton pair production cross sections.

Collider	Z	γ	$\sigma^{e^+e^-}_{\rm Born}$ [kb]	$\sigma^{\mu^+\mu^-}_{\rm Born}$ [b]
RHIC, Au-Au	79	108	36.0	0.213
LHC, Pb-Pb	82	3000	227	2.49

Table 1: Colliders and cross sections for lepton pair production.

Strictly speaking, only a few electromagnetic processes with the production of leptons or photons are related to fundamental physics. Nevertheless, many of electromagnetic processes are of great importance for two reasons: either they are dangerous or they are useful for experiments at the RHIC and LHC colliders. Since the Born cross section $\sigma^{e^+e^-}_{\rm Born}$ is huge (see

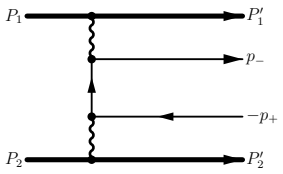

Figure 1: Feynman diagram for lepton pair production in the Born approximation.

Table 1), e^+e^- pair production can be a serious background for many experiments. It is also an important issue for the beam lifetime and luminosity of these colliders [4]. This means that various corrections to the Born cross section are of great importance. The subject is notoriously problematic, and a few controversies have been discussed and clarified in Refs. [1, 5, 6, 7, 8, 9].

A primary reason for the enhanced interest in the nuclear collisions is due to the fact that the typical Lorentz-boosted electric fields of nuclei are immensely strong; they are of the order of

$$\mathcal{E} \sim \frac{Ze}{\rho^2}\,\gamma = \gamma\, Z\alpha\, \mathcal{E}_{\rm Schwinger} \;\; \text{with} \;\; \rho = \frac{\hbar}{m_e c}\,, \;\; \mathcal{E}_{\rm Schwinger} = \frac{m_e^2 c^3}{e\hbar} = 1.3 \cdot 10^{16} \;\; \frac{\rm V}{\rm cm}\,; \qquad (1)$$

therefore,

$$\mathcal{E}/\mathcal{E}_{\rm Schwinger} \;\; \sim 60 \;\; \text{for RHIC and} \;\; \sim 1800 \;\; \text{for the LHC}\,, \qquad (2)$$

but the interaction times are very short, so that only a very small four-dimensional space-time volume is available for pair production. As a result, one can still use perturbation theory in terms of the nuclear interaction, but the perturbation parameter $Z\alpha \approx 0.6$ approaches unity for Au-Au and Pb-Pb collisions.

Throughout the paper we use a system of units in which $c = 1$, $\hbar = 1$, $\alpha = e^2/(\hbar c) \approx 1/137$, and denote the electron, muon and nuclear mass as m, μ and M and $L = \ln(\gamma^2)$.

2 Strong-field effects in the e^+e^- pair production

The cross section of one pair production in the Born approximation (described by the Feynman diagram of Fig. 1) was obtained many years ago [10]. Since the parameter $Z\alpha$ is not small the whole series in $Z\alpha$ has to be summed to obtain the cross section with sufficient accuracy. Fortunately, there is an important small parameter

$$\frac{1}{L} < 0.11\,, \qquad L = \ln\left(\gamma^2\right), \qquad (3)$$

and therefore, in some cases it is sufficient to calculate the corrections in the leading logarithmic approximation (LLA) only.

2.1 Summary of available theoretical results

The exact cross section for one pair production σ_1 can be written in the form

$$\sigma_1 = \sigma_{\rm Born} + \sigma_{\rm Coul} + \sigma_{\rm unit}\,, \qquad (4)$$

where two different types of strong-field corrections have been distinguished. We start our discussion with the production of the lightest lepton pairs, electrons and positrons. The *Coulomb*

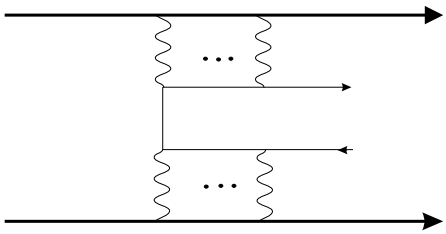

Figure 2: Feynman diagram for the Coulomb correction to the lepton pair production.

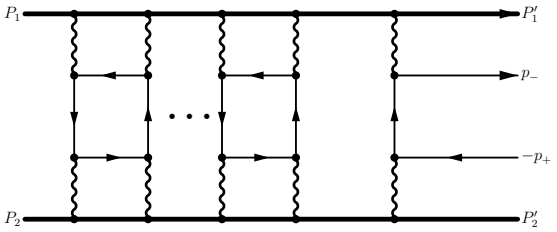

Figure 3: Feynman diagram for the unitarity correction to the lepton pair production

corrections $\sigma_{\rm Coul}$ to electron-positron pair production correspond to multi-photon exchanges of the produced $e^{\pm}$ with the nuclei (Fig. 2),

$$\sigma_{\rm Coul} = -A(Z\alpha)\,[L^2 - B(Z\alpha)\,L]\,\frac{28}{27\pi}\,\frac{(Z\alpha)^4}{m^2}\,, \tag{5}$$

where the leading coefficient

$$A(Z\alpha) = 6f(Z\alpha) = 6\,(Z\alpha)^2\sum_{n=1}^{\infty}\frac{1}{n(n^2+(Z\alpha)^2)} \approx 1.9 \tag{6}$$

was calculated ten years ago in Ref. [5] and next-to-leading coefficient

$$B(Z\alpha) \approx 5.5 \tag{7}$$

was calculated only recently [9]. It was also shown in Ref. [5] that the Coulomb corrections disappear for large transverse momenta of the produced leptons, at $p_{\pm\,\perp} \gg m$.

Collider	$\frac{\sigma_{\rm Coul}}{\sigma_{\rm Born}}$	$\frac{\sigma_{\rm unit}}{\sigma_{\rm Born}}$	$\frac{\sigma_{\rm Coul}}{\sigma_{\rm Born}}$ (Ref. [11])
RHIC, Au-Au	-10%	-5.0%	-17%
LHC, Pb-Pb	-9.4%	-4.0%	-11%

Table 2: Coulomb and unitarity corrections to the e^+e^- pair production.

The unitarity corrections $\sigma_{\rm unit}$ which are due to the unitarity requirement of the scattering matrix, correspond to the exchange of the virtual light-by-light blocks between the nuclei (Fig. 3). They were calculated in Ref. [7] and updated in Ref. [8].

It was found that the Coulomb corrections are about 10 % while the unitarity corrections are about two times smaller (see Table 2). In the last column of Table 2 we display the result of Baltz [11] obtained by numerical calculations using a formula for the cross section resulting from "exact solution of the semiclassical Dirac equations". In fact, this formula allows one to calculate the Coulomb correction in the leading logarithmic approximation only which is insufficient in this very case.

2.2 Probabilities for e^+e^- pair production at a given impact parameter between nuclei

Due to the fact that $Z_1 Z_2 \alpha \gg 1$ for modern heavy-ion colliders, it is possible for $\gamma \gg 1$ to treat the nuclei as sources of the external field and calculate the probability of n-pair production $P_n(\rho)$ in the collision of two nuclei at a given impact parameter ρ. The cross section is then found to be

$$\sigma_n = \int P_n(\rho)\, d^2\rho\,. \tag{8}$$

What do we know about the function $P_n(\rho)$?

It was realized many years ago that in the Born approximation

$$P_1(\rho) \sim (Z\alpha)^4 L \quad \text{at } \rho \sim 1/m \tag{9}$$

and, therefore, this probability can be greater than 1 (see Ref. [12]). It means *(i)* that one should take into account the unitarity corrections, which come from the unitarity requirement for the S-matrix and *(ii)* that the cross section for multiple pair production should be quite large.

It was argued in [13] that the factorization of the multiple pair production probability is described with good accuracy by the Poisson distribution:

$$P_n(\rho) = \frac{[\bar{n}_e(\rho)]^n}{n!} \mathrm{e}^{-\bar{n}_e(\rho)}\,, \tag{10}$$

where $\bar{n}_e(\rho)$ is *the average number of produced e^+e^- pairs*. It is evident that the unitarity requirement is fulfilled by the Poisson distribution, whose sum over n gives one.

The probability for producing one pair, given in perturbation theory by $\bar{n}_e(\rho)$, should be modified to read $\bar{n}_e(\rho)\,\exp[-\bar{n}_e(\rho)]$. For the one-pair production it corresponds to replacement:

$$\sigma_{e^+e^-} = \int \bar{n}_e(\rho)\, d^2\rho \quad \to \quad \sigma_{e^+e^-} + \sigma^{\rm unit}_{e^+e^-} = \int \bar{n}_e(\rho)\, \mathrm{e}^{-\bar{n}_e(\rho)}\, d^2\rho\,, \tag{11}$$

where

$$\sigma^{\rm unit}_{e^+e^-} = -\int \bar{n}_e(\rho)\, \left[1 - \mathrm{e}^{-\bar{n}_e(\rho)}\right]\, d^2\rho \tag{12}$$

is the unitarity correction. It should be noted that the main contribution to $\sigma_{e^+e^-}$ comes from $\rho \gg 1/m$, while the main contribution to $\sigma^{\rm unit}_{e^+e^-}$ comes from $\rho \sim 1/m$.

The function $\bar{n}_e(\rho)$ is a very important quantity for the evaluation of unitarity corrections. It was found for $\gamma \gg 1$ in closed form (taken into account $(Z\alpha)^n$ terms exactly) in Ref. [14]

and the problem of its proper regularization was solved in [6]. But the obtained close form for $\bar{n}_e(\rho)$ is, in fact, a nine-fold integral and its calculation is very laborious.

A simpler approximate expression for $\bar{n}_e(\rho)$ is very desirable. The functional form of this function in the region of interest reads

$$\bar{n}_e(\rho,\gamma,Z) = (Z\alpha)^4\, F(x,Z)\, [L - G(x,Z)]\ , \quad L = \ln(\gamma^2)\,,\ x = m\,\rho\,. \tag{13}$$

The simple analytical expressions for functions $F(x,Z)$ and $G(x,Z)$ is obtained in [7] only at large values of the impact parameters, $\rho \gg 1/m$. On the other hand, for the calculation of the unitarity corrections we need $F(x,Z)$ and $G(x,Z)$ in the range $\rho \sim 1/m$.

In the paper [15] the authors gave a detailed consideration of the function $F(x,Z)$ including tables and compact integral presentation in the form of an "only" five-dimensional integral. Using some numerical calculations for the function $\bar{n}_e(\rho,\gamma,Z)$, a simple approximation for $G(x,Z)$ has been found in [8]:

$$G(x,Z) \approx 1.5\,\ln(x+1.4) + 1.9\,. \tag{14}$$

As a result, the approximate expression

$$\bar{n}_e(\rho,\gamma,Z) = (Z\alpha)^4\, F(x,Z)\, [L - 1.5\,\ln(x+1.4) - 1.9]\ , \quad L = \ln(\gamma^2)\,, \quad x = m\,\rho \tag{15}$$

with the function $F(x,Z)$ from [15] can be used for calculation of unitarity corrections with an accuracy on the order of 5 %.

3 Strong-field effects in $\mu^+\mu^-$ pair production

The motivation for the consideration of processes involving heavier lepton pairs is given by the fact that they may be easier to observe experimentally than e^+e^- pair production. This process was recently considered in detail in Refs. [16, 8]. It was found that: *(i)* the Coulomb corrections are small, while unitarity corrections are large; *(ii)* the exclusive cross section differs considerable from its Born value, but its experimental observation is difficult; *(iii)* the inclusive cross section coincides with the Born cross section; *(iv)* the Born contribution can be easily calculated using the equivalent photon approximation (EPA) which has a very good accuracy in this particular case.

3.1 Born cross section for $\mu^+\mu^-$ pair production

Let us consider the production of a $\mu^+\mu^-$ pair,

$$Z_1 + Z_2 \to Z_1 + Z_2 + \mu^+\mu^-\,, \tag{16}$$

using the EPA, but taking into account nuclear electromagnetic form factors. The Born differential cross section $d\sigma_{\rm B}$ for the considered process is related to the cross section $\sigma_{\gamma\gamma}$ for the real $\gamma\gamma \to \mu^+\mu^-$ process by the equation

$$d\sigma_{\rm B} = dn_1 dn_2\, d\sigma_{\gamma\gamma}\,, \tag{17}$$

where dn_i is the number of equivalent photons. A further simple integration leads to the result shown in Table 1. The accuracy of this calculation is of the order of a few percent.

In the impact parameter representation, the probability of muon pair production $P_{\rm B}(\rho)$ in the Born approximation is given as follows (in the LLA),

$$P_{\rm B}(\rho) = \int dn_1 dn_2\, \delta(\boldsymbol{\rho}_1 - \boldsymbol{\rho}_2 - \boldsymbol{\rho})\, \sigma_{\gamma\gamma} = \frac{28}{9\pi^2}\, \frac{(Z_1\alpha Z_2\alpha)^2}{(\mu\rho)^2}\, \Phi(\rho)\,, \tag{18}$$

where μ is the muon mass. There are two scales in dependence of function $\Phi(\rho)$ on ρ:

$$\Phi(\rho) = \left(4\ln\frac{\gamma}{\mu\rho} + \ln\frac{\rho}{R}\right)\ln\frac{\rho}{R} \quad \text{at} \quad R \ll \rho \leq \gamma/\mu\,,$$
$$\Phi(\rho) = \left(\ln\frac{\gamma^2}{\mu^2\rho R}\right)^2 \quad \text{at} \quad \gamma/\mu \leq \rho \ll \gamma^2/(\mu^2 R)$$

(here R is the nuclear radius). Reassuringly, when we compare the expression for $\Phi(\rho)$ with numerical calculations based on the exact matrix element, we find good agreement for Pb-Pb collisions: the discrepancy is less then 10 % for $\mu\rho > 10$, so that $\Phi(\rho)$ can be used with good effect for the calculation of unitarity corrections below.

3.2 Coulomb and unitarity corrections

For the Coulomb correction, the following simple estimate can be obtained. Due to the nuclear form factor, there is restriction of transverse momenta of additional exchange photons on the level of $1/R$ and the effective parameter of the perturbation series is not $(Z\alpha)^2$, but $(Z\alpha)^2/(R\mu)^2$. Besides, there is an additional logarithmic suppression because the Coulomb corrections lack the large Weizsäcker–Williams logarithm L. As a consequence, the real suppression parameter is of the order of

$$\eta_2 = \frac{(Z\alpha)^2}{(R\mu)^2 L}\,, \quad L = \ln\left(\gamma^2\right), \tag{19}$$

which corresponds to the Coulomb correction $\sim 1\,\%$. We have recently carried out a calculation, based on the asymptotic limit of the Coulomb corrections for the muon pair photo-prodution by Ivanov and Melnikov [5]. The results of this investigation, whose details will be published

Collider	$\frac{\sigma_{\rm Coul}}{\sigma_{\rm Born}}$	$\frac{\sigma_{\rm Coul}}{\sigma_{\rm Born}}$ (Ref. [17])
RHIC, Au-Au	-3.7%	-22%
LHC, Pb-Pb	-1.3%	-14%

Table 3: Coulomb corrections to the $\mu^+\mu^-$ pair production.

elsewhere, are in agreement with (19) and they are given in Table 3. In the last column we display the recent results of Baltz [17], which are in strong disagreement with the results in the second column obtained by us. Because the simple estimate (19) corresponds to a decrease of the Coulomb corrections with the growth of the lepton mass, it seems questionable that the

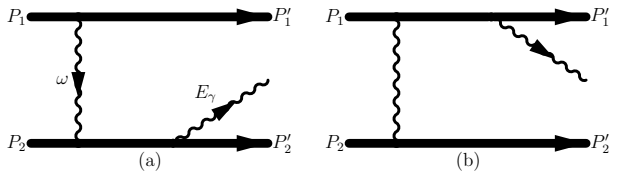

Figure 4: Ordinary nuclear bremsstrahlung via a virtual Compton scattering.

Coulomb corrections for the muon pair production, according to Ref. [17], might be larger that those for the e^+e^- pair production.

The unitarity correction $\sigma_{\rm unit}$ to muon pair production is described by the exchange of blocks, corresponding to light-by-light scattering via a virtual *electron* loop, between the nuclei (see Fig. 3). As usual,

$$\sigma_{\rm B} = \int_{2R}^{\infty} P_{\rm B}(\rho)\; d^2\rho \to \sigma_{\rm B} + \sigma_{\rm unit} = \int_{2R}^{\infty} P_{\rm B}(\rho)\, {\rm e}^{-\bar{n}_e(\rho)}\, d^2\rho \tag{20}$$

and

$$\sigma_{\rm unit} = -\int_{2R}^{\infty} \left[1 - {\rm e}^{-\bar{n}_e(\rho)}\right]\; P_{\rm B}(\rho)\, d^2\rho \tag{21}$$

is the unitarity correction for the exclusive production of one muon pair. In LLA we find

$$\delta_{\rm unit} = \frac{\sigma_{\rm unit}}{\sigma_{\rm B}} = -49\ \% \text{ for the Pb-Pb collisions at LHC.} \tag{22}$$

It is seen that unitarity corrections are large, in other words, the exclusive production of one muon pair differs considerable from its Born value.

However, the experimental study of the exclusive muon pair production seems to be a very difficult task. Indeed, this process requires that the muon pair should be registered without any electron–positron pair production, including $e^{\pm}$ emitted at very small angles. Otherwise, the corresponding inclusive cross section will be inclusive and close to the Born cross section (for details see Ref. [8]).

4 Strong-field effects for the nuclear bremsstrahlung

Ordinary nuclear bremsstrahlung without excitation of the final nuclei is given by the Feynman diagrams of Fig. 4 and was known in detail many years ago. It can be described as the Compton scattering of the equivalent photon off the incoming nucleus:

$$d\sigma_{\rm br} = d\sigma^a_{\rm br} + d\sigma^b_{\rm br}\,, \tag{23}$$

and

$$d\sigma^a_{\rm br} = dn_1(\omega)\; d\sigma_{\rm C}(\omega, E_\gamma, E_2, Z_2)\,. \tag{24}$$

Here, dn_1 is the number of equivalent photons emitted by the nucleus Z_1 and $d\sigma_{\rm C}(\omega, E_\gamma, E_2, Z_2)$ is the differential cross section for the Compton scattering off nucleus Z_2. We can rewrite these equations as

$$d\sigma^a_{\rm br} = dP_a(\rho)\, d^2\rho\,, \tag{25}$$

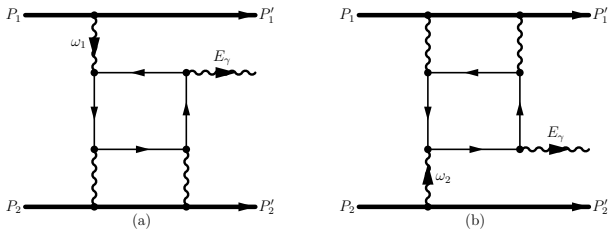

Figure 5: Nuclear bremsstrahlung via the virtual Delbrück scattering.

where the differential probability $\mathrm{d}P_a(\rho)$ assumes the form

$$\mathrm{d}P_a(\rho) = \frac{Z_1^2\alpha}{\pi^2}\,\frac{\sigma_{\mathrm{T}}(Z_2)}{\rho^2}\left(1 - x_\gamma + \frac{3}{4}\,x_\gamma^2\right)\frac{\mathrm{d}E_\gamma}{E_\gamma}\,,\quad x_\gamma = \frac{E_\gamma}{E_2} \tag{26}$$

with the Thomson cross section (M is the mass of nucleus)

$$\sigma_{\mathrm{T}}(Z_2) = \frac{8\pi}{3}\,\frac{Z_2^4\alpha^2}{M^2}\,. \tag{27}$$

Now we calculate the unitarity correction [8].

$$\delta_{\mathrm{unit}} = \frac{\mathrm{d}\sigma^a_{\mathrm{unit}}}{\mathrm{d}\sigma^a_{\mathrm{br}}}\,. \tag{28}$$

In our case it reads

$$\delta_{\mathrm{unit}} = -\frac{1}{L_\gamma}\int_{2R}^{\infty}\frac{\mathrm{d}\rho}{\rho}\,\left[1 - \mathrm{e}^{-\bar{n}_e(\rho)}\right]\,,\quad L_\gamma = \ln\left(\frac{2\gamma_1\,\gamma_2^2\,(1-x_\gamma)}{R\,E_\gamma}\right). \tag{29}$$

An evaluation of this integral gives the following result for a photon energy $E_\gamma = 1$ GeV:

$$\delta_{\mathrm{unit}} = -19\,\%\ \text{for the RHIC}\,,\quad \delta_{\mathrm{unit}} = -15\,\%\ \text{for the LHC}\,. \tag{30}$$

5 Large contribution of the virtual Delbrück scattering into nuclear bremsstrahlung

Recently, in Ref. [18], we have considered the emission of photons not via the virtual Compton subprocess, but via another one – the virtual Delbrück scattering subprocess of Fig. 5 (the first results were presented at the PHOTON-2007 conference in Paris). Nuclear bremsstrahlung via virtual Delbrück scattering in the lowest order of quantum electrodynamics is described by Feynman diagram of Fig. 5. A first note about this process was given in Ref. [19].

At first sight, this is a process of a very small cross section since $\sigma \propto \alpha^7$. But at second sight, we should add a very large factor $Z^6 \sim 10^{11}$ and take into account that the cross section scale $1/m^2$ is determined not by the nucleon mass, but the electron mass. And last, but not least, we found that this cross section has an additional logarithmic enhancement of the order of

$$L^2 \gtrsim 100\,,\quad L = \ln\left(\gamma^2\right). \tag{31}$$

Thus, the estimate is

$$\sigma \sim \frac{(Z\alpha)^6\,\alpha}{m^2}\,L^2\,. \tag{32}$$

Our analytical result (see for detail Refs. [18]) is

$$\sigma = C\frac{(Z\alpha)^6\,\alpha}{m^2}\,L^2 \tag{33}$$

with $C \approx 0.4$. This cross sections is considerably larger than that for ordinary nuclear bremsstrahlung in the photon energy range:

$$m \ll E_\gamma \ll m\,\gamma\,. \tag{34}$$

Thus, the discussed cross section is

$$\sigma = 14 \text{ barn for RHIC}, \quad \sigma = 50 \text{ barn for LHC}\,. \tag{35}$$

That is quite a serious number! Note for comparison, that the last cross section is 6 times larger than the total hadronic/nuclear cross section in Pb–Pb collisions, which is roughly 8 barn. The energy and angular distribution of photons is also calculated in [18].

We conclude this brief report by emphasizing that Coulomb and unitarity corrections, and loop effects (virtual Delbrück scattering) are essential for an accurate quantitative understanding of photon and lepton production cross sections in ultrarelativistic heavy-ion collisions. The extremely strong fields encountered in these processes lead to a physical situation not encountered anywhere else in nature, and thus, surprising effects like loop-dominance over the tree-level graphs for photon production or a 50 % decrease of an exclusive over an inclusive muon pair production cross section due to unitarity represent testimonies of the extreme state of matter and radiation at the RHIC and LHC colliders.

Acknowledgments

U.D.J. acknowledges support from the National Science Foundation and from the Missouri Research Board. V.G.S. is supported by grants of RFBR 08-02-00334-a and NSh-1027.2008.2 and acknowledges support from GSI Darmstadt (project HD–JENT).

References

[1] G. Baur, K. Hencken, D. Trautmann, S. Sadovsky and Yu. Kharlov, Phys. Rep. **364** 359 (2002).

[2] G. Baur, K. Hencken and D. Trautmann, Phys. Rep. **453** 1 (2007).

[3] A. Baltz et al., Phys. Rep. **458** 1 (2008).

[4] S.R. Klein, Nucl. Instrum. Meth. **A459** 51 (2001).

[5] D.Yu. Ivanov, A. Schiller and V.G. Serbo, Phys. Lett. **B454** 155 (1999).

[6] R.N. Lee and A.I. Milstein, Phys. Rev. **A61** 032103 (2000).

[7] R.N. Lee, A.I. Milstein and V.G. Serbo, Phys. Rev. **A65** 022102 (2002).

[8] U.D. Jentschura, K. Hencken and V.G. Serbo, Eur. Phys. J. **C58** 281 (2008).

[9] R.N. Lee and A.I. Milstein, arXiv:hep-ph/0903.0235 (2009).

[10] L.D. Landauand E.M. Lifshitz, Phys. Z. Sowjet. **6** 244 (1934);
G. Racah, Nuovo Cimento **14** 93 (1937).

[11] A. Baltz, Phys. Rev. **C71** 024901 (2005) and arXive:nucl-th/0409044 (2004).

[12] G. Baur, Phys. Rev. **A42** 5736 (1990).

[13] G. Baur, Phys. Rev. **D41** 3535 (1990);
M. J. Rhoades-Brown and J. Weneser, Phys. Rev. **A44** 330 (1991);
C. Best, W. Greiner and G. Soff, Phys. Rev **A46** 261 (1992);
K. Henken, D. Trautman and G. Baur, Phys. Rev. **A51** 998 (1995);
E. Bartoš, S.G. Gevorkyan, E.A. Kuraev and N.N. Nikolaev, Phys. Lett. **B538** 45 (2002).

[14] A. Baltz and L. McLerran, Phys. Rev. **C58** 1679 (1998);
B. Segev and J.C. Wells, Phys. Rev. **A57** 1849 (1998);
A. Baltz, F. Gelis, L. McLerran and A. Peshier, Nucl. Phys. **A695** 395 (2001).

[15] R. N. Lee and A. I. Milstein, arXive:nucl-th/0610008 (2006).

[16] K. Hencken, E. A. Kuraev and V. G. Serbo. Phys. Rev. **C75** 034903 (2007).

[17] A. Baltz, arXiv:0901.0891 [nucl-th] (2009).

[18] I. F. Ginzburg, U. D. Jentschura and V. G. Serbo, Phys. Lett. **B658** 125 (2008);
I. F. Ginzburg, U. D. Jentschura and V. G. Serbo, Eur. Phys. J. **C54** 267 (2008).

[19] G. Baur and C. Bertulany, Z. f. Phys. **A330** 77 (1988).

Chapter 10

Photons in Astroparticle Physics

Convenor:

A. Ringwald (DESY)

Implications of the Electron/Positron Excesses on Astrophysics and Particle Physics

Alejandro Ibarra

Physik-Department T30d, Technische Universität München,
James-Franck-Straße, 85748 Garching, Germany.

DOI: http://dx.doi.org/10.3204/DESY-PROC-2009-03/Ibarra

A series of experiments measuring high energy cosmic rays have recently reported strong indications for the existence of an exotic source of high energy electrons and positrons. We review the implications of this result for astrophysics and particle physics with special emphasis on decaying dark matter as the origin of the PAMELA and Fermi anomalies.

1 Introduction

Different experiments measuring high energy cosmic rays have reported over the last months a wealth of new results pointing to the existence of an exotic source of electrons and positrons. The PAMELA collaboration reported evidence for a sharp rise of the positron fraction at energies $7 - 100$ GeV [1], possibly extending towards higher energies, compared to the expectations from spallation of primary cosmic-rays on the interstellar medium [2]. This result confirmed previous hints on the existence of a positron excess from HEAT [3], CAPRICE [4] and AMS-01 [5]. Almost at the same time, the balloon-borne experiments ATIC [6] and PPB-BETS [7] reported the discovery of a peak in the total electron plus positron flux at energies 600-700 GeV, while the H.E.S.S. collaboration [8] reported a substantial steepening in the high energy electron plus positron spectrum above 600 GeV compared to low energies. More recently, the Fermi LAT collaboration has published measurements of the electron plus positron flux from 20 GeV to 1 TeV with unprecedented accuracy [9], revealing an energy spectrum that roughly follows a power law $E^{-3.0}$ without prominent spectral features. Simultaneously, the H.E.S.S. collaboration reported a measurement of the cosmic ray electron plus positron spectrum at energies larger than 340 GeV, confirming the Fermi result of a power-law spectrum with spectral index of $3.0 \pm 0.1(\text{stat.}) \pm 0.3(\text{syst.})$, which furthermore steepens at about 1 TeV [10]. The measured energy spectrum is much harder than the expectations of conventional diffusive models, suggesting the existence of additional sources of high energy electrons and positrons in the Galaxy.

One of the most popular astrophysical interpretations of the electron/positron excesses are the electron-positron pairs produced by the interactions of high energy photons in the strong magnetic field of nearby pulsars, such as Geminga or Monogem [11, 12, 13]. This interpretation requires, though, a rather large percentage of the total spin-down power injected in the form of electron-positron pairs, about 40%, and a large cut-off of the electron/positron energy spectrum, about 1 TeV. Alternatively, the electron/positron excesses could be explained by the combined emission of both nearby and distant pulsars, this solution requiring a percentage of spin-down

power ranging between 10-30% and again a large cut-off in the energy spectrum, 800-1400 GeV [14].

A more exciting explanation of the cosmic ray electron/positron excesses is the possibility that the electrons and positrons are produced in the annihilation or the decay of dark matter particles. Would this interpretation be confirmed by future experiments, the electron/positron excesses would constitute the first non-gravitational evidence for the existence of dark matter in our Galaxy. The interpretation of the PAMELA and Fermi results in terms of dark matter is subject to constraints from the flux measurements of other cosmic ray species. A very important constraint arises from the measurements of the antiproton flux by PAMELA [15], BESS95 [16], BESS95/97 [17], CAPRICE94 [18], CAPRICE98 [19] and IMAX [20], which are hitherto consistent with the expectations from conventional propagation models, thus excluding the possibility of a large antiproton flux from dark matter annihilation or decay [21].

The steep rise in the positron fraction observed by PAMELA and the Fermi results on the total electron plus positron flux can be explained by dark matter annihilations in the center of the Milky Way, provided the dark matter particle has a mass in the TeV range and annihilates preferentially into $\tau^+\tau^-$ or 4μ [22]. This interpretation of the positron excess, however, typically requires the *ad hoc* introduction of large boost factors. Furthermore, it has been argued that if dark matter annihilations are the origin of the PAMELA anomaly, the predicted gamma-ray emission from the center of the Galaxy is in conflict with the H.E.S.S. observations for typical cuspy halo profiles [23].

In the remainder, we will discuss the possibility that dark matter decay could be the origin of the PAMELA and Fermi excesses. We will show that there exist a number of decay channels which can accommodate simultaneously the PAMELA data on the positron fraction and the Fermi data on the total electron plus positron flux, while being at the same time consistent with present measurements of the antiproton flux and the diffuse extragalactic gamma-ray flux [24, 25]. This explanation to the cosmic ray anomalies requires that the dark matter particle should have a mass of a few TeV and a lifetime around 10^{26} s. In this framework, no boost factors are required and the gamma-ray emission from the center of the Galaxy is consistent with present measurements [26].

In Section 2 we will present some motivations to consider the scenario of decaying dark matter, in Section 3 we will show our results for the high-energy cosmic rays from dark matter decay and lastly, in Section 4, we will present our conclusions.

2 Decaying Dark Matter

One of the necessary requirements for the viability of a dark matter candidate is to have a lifetime longer than the age of the Universe. However, present observations do not require absolute stability of the dark matter particles, as is implicitly assumed in most studies of the indirect detection of dark matter. Most of these analyses focus on the possibility that the dark matter is constituted by weakly interacting massive particles (WIMPs) which annihilate in the center of the Milky Way, producing an exotic contribution to the positron flux observed at Earth. It is interesting to note that, being weakly interacting, these particles are typically very short-lived. To be more precise, a WIMP with a mass of $\mathcal{O}(100$ GeV) will generically decay into Standard Model particles with a lifetime of $\mathcal{O}(10^{-25}$ s), which is obviously too short to constitute a viable dark matter candidate. In particular, this is the case for the lightest neutralino in the Minimal Supersymmetric Standard Model (MSSM), which in general decays

too fast into Standard Model particles, for instance via $\chi_1^0 \to \gamma\nu$. Then, in order to obtain a lifetime longer than the age of the Universe, the dangerous WIMP couplings to Standard Model particles have to be suppressed by at least 22 orders of magnitude, which may be justified in some particular frameworks but which is nonetheless dubious. Therefore, in the absence of a compelling explanation for this extreme suppression of the coupling, the simplest possibility to guarantee the longevity of a WIMP is to *impose* a symmetry which prevents the fast decays into Standard Model particles. In the case of the MSSM this symmetry is R-parity, which guarantees that the neutralino is absolutely stable.

However, WIMPs only correspond to a subclass of all dark matter candidates; the dark matter particle could also have interactions with ordinary matter much weaker than the weak interactions. If the dark matter particle is superweakly interacting, the decay rate into Standard Model particles is naturally suppressed, thus yielding lifetimes which can be larger than the age of the Universe or perhaps a few orders of magnitude smaller. In the latter case, to obtain a sufficiently long lifetime, a suppression of the coupling by just a few orders of magnitude suffices, which can be justified in simple models. These dark matter candidates eventually decay into Standard Model particles, producing an exotic contribution to the cosmic-ray fluxes which may be detected at Earth. In the next section, the possible signatures of decaying dark matter in the cosmic-ray fluxes will be discussed in detail.

In fact, many superweakly interacting dark matter candidates have been recently proposed which decay into Standard Model particles with lifetimes longer than the age of the Universe. A very interesting candidate is the gravitino in R-parity breaking vacua [27, 28, 29], which is motivated by the requirement of a consistent thermal history of the Universe with supersymmetric dark matter, baryogenesis through leptogenesis and successful primordial nucleosynthesis. Other candidates for decaying dark matter recently proposed are hidden sector gauge bosons or gauginos [30, 31], where the decay rate is suppressed by a small kinetic mixing between a hidden $U(1)$ gauge group and the $U(1)$ of hypercharge, right-handed sneutrinos in scenarios with Dirac neutrino masses [32], where the decay rate is suppressed by the tiny neutrino Yukawa couplings, or hidden sector fermions [33] and bound states of strongly interacting particles [34, 26], where the decay rate is suppressed by the scale of grand unification.

Instead of analyzing the cosmic-ray signatures for each of these scenarios, we will present here the results of a model-independent approach which encompasses the main features of all the scenarios listed above [24, 25].

3 High-energy cosmic rays from dark matter decay

We will assume that the Milky way halo is populated with dark matter particles with mass $M_{\rm DM}$ and lifetime $\tau_{\rm DM}$ which are distributed following a Navarro-Frenk-White density profile [35]. In order to keep the analysis as model-independent as possible, we have considered the predictions for the positron fraction and the total electron plus positron flux for various decay channels and different dark matter masses and lifetimes [24, 25]. Namely, in the case of a fermionic dark matter particle $\psi_{\rm DM}$, we have considered that the dark matter particle decays exclusively via the two-body decay channels $\psi_{\rm DM} \to Z^0\nu$, $\psi_{\rm DM} \to W^\pm\ell^\mp$, as well as the three-body decay channel mediated by a heavy scalar $\psi_{\rm DM} \to \ell^+\ell^-\nu$, with $\ell = e,\ \mu,\ \tau$ being the charged leptons. On the other hand, for a scalar dark matter particle $\phi_{\rm DM}$, we have considered the two-body decay channels $\phi_{\rm DM} \to Z^0Z^0$, $\phi_{\rm DM} \to W^+W^-$, $\phi_{\rm DM} \to \ell^+\ell^-$. The fragmentation of the weak gauge bosons produces a continuous spectrum of positrons (mainly from π^+ decay) that we

have obtained using the event generator PYTHIA 6.4 [36]. Then, with the energy spectrum of positrons being calculable, the only free parameters from the particle physics point of view are the dark matter mass and lifetime.

Antimatter particles propagate through the halo in a complicated way that we describe by means of a stationary two zone diffusion model with cylindrical boundary conditions [37]. For the positron propagation we will adopt the MED propagation model defined in [38], although our conclusions for the electron/positron fluxes are rather insensitive to the choice of propagation parameters or to the choice of dark matter halo profile.

We show in Fig. 1, top-left plot, the predicted positron fraction for a dark matter particle which decays as $\psi_{\rm DM} \to Z^0 \nu$, compared to the PAMELA, HEAT, CAPRICE and AMS-01 data for dark matter masses $M_{\rm DM} = 5$ and 100 TeV. We also show, in the top-right plot, the corresponding total electron plus positron flux compared to the Fermi, HESS, PPB-BETS, ATIC, AMS-01, BETS and HEAT data. For each mass, the dark matter lifetime and the normalization of the background flux of electrons have been left as free parameters which have been determined to provide a qualitatively good fit to the PAMELA and Fermi measurements. In this decay channel, the only source of electrons and positrons is the fragmentation of the Z^0 boson, which produces relatively soft particles. As a result, even though this decay mode can produce a visible excess in the positron fraction, the energy spectrum is in general too flat to explain the high rise observed by PAMELA. An exception occurs if the dark matter mass is very large, $M_{\rm DM} \gtrsim 50$TeV. In this case, the electrons and positrons from dark matter decay are boosted to high enough energies to produce the steep rise in the positron fraction. However, these high dark matter masses seem to be in conflict with the H.E.S.S. observations, which require a fall-off in the total electron plus positron spectrum at ~ 1TeV.

More promising is the case when the dark matter particle decays as $\psi_{\rm DM} \to W^\pm \ell^\mp$. In this case, the positrons created in the fragmentation of the $W^\pm$ gauge bosons again produces a rather flat contribution to the positron fraction. However, the hard electrons and positrons resulting from the decay of the $\mu^\pm$ and $\tau^\pm$ leptons or directly from the dark matter decay into $e^\pm$ produce a rise in the total energy spectrum and in the positron fraction. The decay mode $\psi_{\rm DM} \to W^\pm e^\mp$ which can produce a steep rise in the positron fraction and is thus consistent with the PAMELA observations, produces also a steep rise and a sharp fall-off in the total electron plus positron flux, which is not observed by Fermi. Thus, the possibility that the dark matter particle decays preferentially in this decay mode, which was favored by the PAMELA observations, is now excluded in the light of the Fermi results on the total electron plus positron flux. On the other hand, the positrons produced in the decay mode $\psi_{\rm DM} \to W^\pm \tau^\mp$ induce a contribution to the positron fraction and the electron plus positron flux which is too flat to explain the anomalies observed by PAMELA and Fermi. Lastly, as shown in Fig. 1, second panel from the top, the decay mode $\psi_{\rm DM} \to W^\pm \mu^\mp$ can nicely accommodate the PAMELA and Fermi observations when the dark matter mass is $M_{\rm DM} \simeq 3\,{\rm TeV}$ and the lifetime is $\tau_{\rm DM} \simeq 2.1 \times 10^{26}\,{\rm s}$.

Similar conclusions hold when the dark matter particle decays into a lepton-antilepton pair and a neutrino. In this case many possibilities can arise depending on the specific particle physics scenario. We will just concentrate on the case where the lepton and the antilepton carry the same flavor and the decay is mediated by a heavy scalar. In this case, the spectrum produced is flatter than in the two body decay $\psi_{\rm DM} \to W^\pm \ell^\mp$ discussed above, but the same conclusions hold: the decay mode $\psi_{\rm DM} \to e^- e^+ \nu$ predicts a peak in the total electron plus positron spectrum which is not observed by Fermi, and the decay mode $\psi_{\rm DM} \to \tau^- \tau^+ \nu$ produces an electron plus positron spectrum with an energy dependence much steeper than $E^{-3.0}$ at high energies, in conflict with the Fermi measurements. However, the decay channel $\psi_{\rm DM} \to \mu^- \mu^+ \nu$

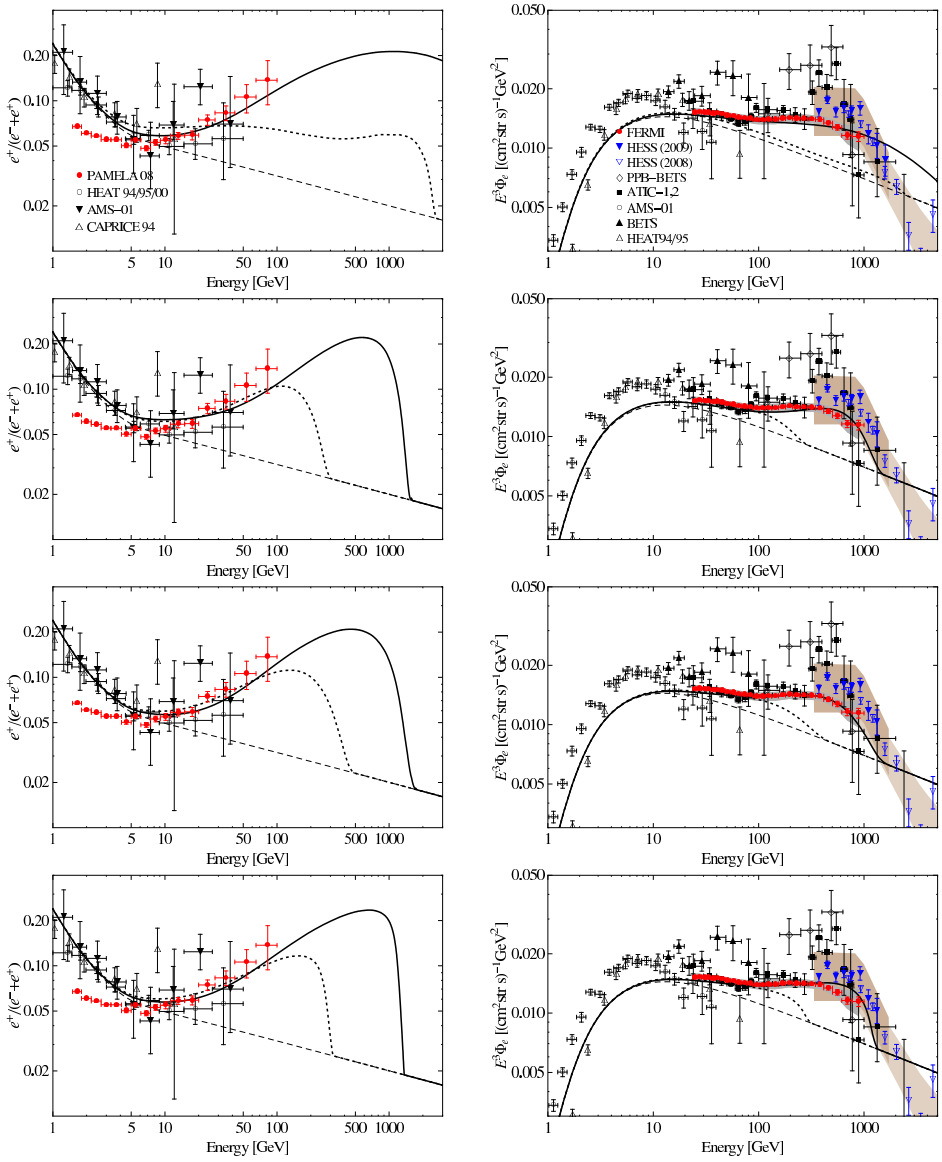

Figure 1: Positron fraction (left panel) and total electron plus positron flux (right panel) for various dark matter decay channels and masses. The dashed line shows the background fluxes as discussed in Ref. [25]. Solar modulation is taken into account using the force field approximation with $\phi = 550\,\mathrm{MV}$. From top to bottom, we show $\psi_{\mathrm{DM}} \to Z^0\nu$ with $M_{\mathrm{DM}} = 100\,\mathrm{TeV}$ (solid) and $5\,\mathrm{TeV}$ (dotted); $\psi_{\mathrm{DM}} \to W^{\pm}\mu^{\mp}$ with $M_{\mathrm{DM}} = 3000\,\mathrm{GeV}$ (solid) and $600\,\mathrm{GeV}$ (dotted); $\psi_{\mathrm{DM}} \to \mu^-\mu^+\nu$ with $M_{\mathrm{DM}} = 3500\,\mathrm{GeV}$ (solid) and $1000\,\mathrm{GeV}$ (dotted); $\psi_{\mathrm{DM}} \to \ell^{\pm}\ell^{\mp}\nu$ with equal branching ratio into the three charged lepton flavors, with $M_{\mathrm{DM}} = 600\,\mathrm{GeV}$ (dotted) and $2500\,\mathrm{GeV}$ (solid). The last three cases can accommodate reasonably well the energy spectra of the positron fraction and the total flux.

can reproduce quite nicely the Fermi electron plus positron spectrum and the steep rise in the positron fraction observed by PAMELA when the dark matter mass is $M_{\rm DM} \simeq 3500$GeV and the lifetime is $\tau_{\rm DM} \simeq 1.1 \times 10^{26}$ s, as shown in Fig. 1, third panel from the top.

In some decaying dark matter scenarios, the dark matter particle decays into charged leptons of different flavors and not exclusively in just one channel. As an illustration of the predictions of this class of scenarios, we show in Fig. 1, bottom panel, the positron fraction and the total electron plus positron flux for a dark matter particle which decays $\psi_{\rm DM} \to \ell^+\ell^-\nu$ with identical branching ratio into the three flavors, for dark matter masses $M_{\rm DM} = 600\,{\rm GeV}$ (dotted) and $2500\,{\rm GeV}$ (solid), inspired in the particularly interesting case where dark matter neutralinos decay into light hidden gauginos via kinetic mixing, or vice-versa [31]. It is interesting that this possibility is also in agreement with the PAMELA and Fermi data, as is apparent from the plot.

The most promising decay channels for a fermionic or a scalar dark matter particle are listed in Tab. 1, where we also show the approximate mass and lifetime which provide the best fit to the data. It should be borne in mind that the astrophysical uncertainties in the propagation of cosmic rays and in the determination of the background fluxes of electrons and positrons are still large. Besides, the existence of a possibly large primary component of electrons/positrons from astrophysical sources, such as pulsars, cannot be precluded. Therefore, the precise values of the dark matter parameters can vary. These results can nevertheless be used as a guidance for building models with decaying dark matter as an explanation of the PAMELA and Fermi anomalies.

Decay Channel	$M_{\rm DM}$ [GeV]	$\tau_{\rm DM}$ [10^{26}s]
$\psi_{\rm DM} \to \mu^+\mu^-\nu$	3500	1.1
$\psi_{\rm DM} \to \ell^+\ell^-\nu$	2500	1.5
$\psi_{\rm DM} \to W^\pm\mu^\mp$	3000	2.1
$\phi_{\rm DM} \to \mu^+\mu^-$	2500	1.8
$\phi_{\rm DM} \to \tau^+\tau^-$	5000	0.9

Table 1: Decay channels for fermionic and scalar dark matter, $\psi_{\rm DM}$ and $\phi_{\rm DM}$ respectively, that best fit the Fermi and PAMELA data.

Decay modes into weak gauge bosons produce an associated antiproton flux, which is severely constrained by present experiments [15, 16, 17, 18, 19, 20]. Indeed, the measurements of the antiproton flux do not show any deviation with respect to the theoretical expectations from spallation of cosmic rays on the interstellar medium, thus constraining the size of any exotic contribution. Therefore, purely leptonic dark matter decays are favored over the decays into weak gauge bosons. Nevertheless, as discussed in [39, 25], the antiproton flux produced by the dark matter decay into weak gauge bosons can be consistent with present measurements for certain choices of propagation parameters, especially when the dark matter mass is large. It is interesting to note that an antiproton flux from dark matter decay is necessarily accompanied by an antideuteron flux which could be observed in future experiments [39].

A very important constraint on the decaying dark matter scenario stems from observations of the diffuse extragalactic gamma-ray flux. The scenario of decaying dark matter predicts a well-defined angular map of gamma rays in the diffuse extragalactic background [40]. Furthermore, decay modes which can successfully reproduce the PAMELA and Fermi results lead to different signatures in the diffuse extragalactic gamma-ray flux. Therefore, future observations by the

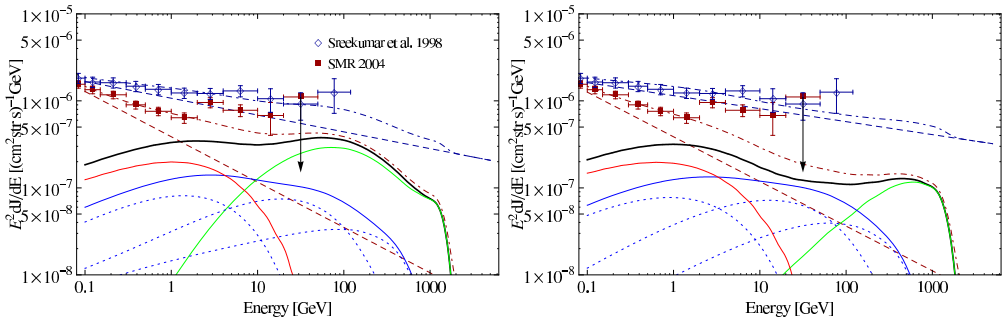

Figure 2: Extragalactic diffuse gamma-ray flux for $\psi_{\rm DM} \to W^{\pm}\mu^{\mp}$ (left panel) and $\psi_{\rm DM} \to \mu^{-}\mu^{+}\nu$ (right panel) for the dark matter mass and lifetime that can reproduce the observed positron fraction and total electron plus positron flux. We included gamma-rays produced directly in the final state radiation of the muons and the fragmentation of $W^{\pm}$ (green line), gamma-rays from inverse Compton scattering of dark matter electrons and positrons on the interstellar radiation field (solid blue line; the dotted blue lines show the fluxes that come from scattering on the cosmic microwave background, on the thermal radiation of dust and on star light from left to right) and gamma-rays from inverse Compton scattering outside of our galaxy (red). The black solid line shows the overall flux. The dark red and dark blue lines show the total flux (dash-dotted) adding an isotropic extragalactic background (dashed) with a power-law spectrum. Normalization and power index are chosen to fit one of the two shown data sets [42, 43].

Fermi Large Area Telescope (LAT) may exclude or give support to the paradigm of decaying dark matter and could exclude some decay channels, thus giving invaluable constraints on the properties of the dark matter particles.

The total extragalactic diffuse gamma-ray flux receives several contributions. The first one stems from the photons produced directly in the dark matter decay (mainly via π^0 decay) or final state radiation of the final particles. The second one is produced during the propagation of the electrons and positrons in the Galaxy, through the inverse Compton scattering on the interstellar radiation field, which includes the cosmic microwave background, thermal dust radiation and starlight [41]. Lastly, there exists a background contribution, presumably originating in Active Galactic Nuclei (AGNs), which is perfectly isotropic and which has an energy spectrum which is assumed to follow a simple power law; the normalization and index will be treated as free parameters to be determined by requiring a good fit of the total flux to the data.

We show in Fig.2 the predictions for the total diffuse extragalactic diffuse gamma ray background for the two promising decay modes $\psi_{\rm DM} \to W^{\pm}\mu^{\mp}$ (left panel) and $\psi_{\rm DM} \to \mu^{-}\mu^{+}\nu$ (right panel). We show the gamma-ray fluxes from final state radiation and $W^{\pm}$ fragmentation (green) and from galactic (blue) and extragalactic (red) inverse Compton scattering of dark matter electrons and positrons. We also show the total flux compared to the extraction of the extragalactic diffuse gamma-ray flux by Sreekumar et al. [42] and by Strong, Moskalenko and Reimer [43], averaging over the whole sky excluding the region of the galactic plane with latitudes $|b| < 10^{\circ}$ and assuming a power law for the genuinely extragalactic component. In both cases, they are consistent with the present data and show a deviation from the putative power

law of the astrophysical background, which could be observed by the Fermi LAT, depending on the precise spectrum of the genuinely extragalactic contribution to the flux. Furthermore, this deviation is more prominent in the decay mode $\psi_{\rm DM} \to W^{\pm}\mu^{\mp}$, due to the gamma rays produced in the fragmentation of the W boson, thus offering a way of discriminating between these two decay channels.

4 Conclusions

Astrophysical and cosmological observations do not require the dark matter particles to be absolutely stable. If they are indeed unstable, their decay into electrons and positrons might occur at a sufficiently large rate to allow the indirect detection of dark matter through an anomalous contribution to the cosmic electron/positron fluxes. In this work we have investigated whether the anomalies in the positron fraction and the total electron plus positron flux reported by the PAMELA and the Fermi LAT collaborations, respectively, could be interpreted as a signature of the decay of dark matter particles. We have shown that indeed some decaying dark matter scenarios can reproduce reasonably well the energy spectra of the positron fraction and the total flux, while being at the same time consistent with present measurements of the antiproton flux and the radio and gamma-ray fluxes. We have also discussed the expectations from the scenario of dark matter decay for the diffuse extragalactic gamma-ray flux, which will be tested in the near future by the Fermi LAT.

Acknowledgements

The author would like to thank Wilfried Buchmüller, Gianfranco Bertone, Laura Covi, Michael Grefe, Koichi Hamaguchi, Tetsuo Shindou, Fumihiro Takayama, Andreas Ringwald, Christoph Weniger, Tsutomu Yanagida and very especially David Tran for very pleasant collaborations. This work was partially supported by the DFG Cluster of Excellence "Origin and Structure of the Universe."

References

[1] O. Adriani *et al.*, (2008), 0810.4995.

[2] I. V. Moskalenko and A. W. Strong, Astrophys. J. **493**, 694 (1998), astro-ph/9710124.

[3] S. W. Barwick *et al.* [HEAT Collaboration], Astrophys. J. **482** (1997) L191, arXiv:astro-ph/9703192.

[4] M. Boezio *et al.* [CAPRICE Collaboration], Astrophys. J. **532** (2000) 653.

[5] AMS-01, M. Aguilar *et al.*, Phys. Lett. **B646**, 145 (2007), astro-ph/0703154.

[6] J. Chang *et al.*, Nature (London) **456**, 362 (2008).

[7] S. Torii *et al.* [PPB-BETS Collaboration], arXiv:0809.0760 [astro-ph].

[8] F. Aharonian *et al.* [H.E.S.S. Collaboration], Phys. Rev. Lett. **101** (2008) 261104, arXiv:0811.3894 [astro-ph]

[9] A. A. Abdo *et al.* [The Fermi LAT Collaboration], arXiv:0905.0025 [astro-ph.HE].

[10] F. Aharonian *et al.* [H.E.S.S. Collaboration] arXiv:0905.0105 [astro-ph.HE].

[11] A. K. Harding and R. Ramaty, Proc. 20th ICRC, Moscow **2**, 92-95 (1987); A. M. Atoian, F. A. Aharonian and H. J. Volk, Phys. Rev. D **52** (1995) 3265; X. Chi, E. C. M. Young and K. S. Cheng, Astrophys. J. **459** (1995) L83.

[12] D. Hooper, P. Blasi and P. D. Serpico, arXiv:0810.1527 [astro-ph].

[13] C. Grimani, Astron. Astrophys. **418**, 649 (2004)

[14] D. Grasso *et al.* [FERMI-LAT Collaboration], arXiv:0905.0636 [astro-ph.HE].

[15] O. Adriani *et al.*, Phys. Rev. Lett. **102** (2009) 051101.

[16] H. Matsunaga *et al.*, Phys. Rev. Lett. **81** (1998) 4052.

[17] S. Orito *et al.* [BESS Collaboration], Phys. Rev. Lett. **84** (2000) 1078.

[18] M. Boezio *et al.* [WIZARD Collaboration], Astrophys. J. **487** (1997) 415.

[19] M. Boezio *et al.* [WiZard/CAPRICE Collaboration], Astrophys. J. **561** (2001) 787.

[20] J. W. Mitchell *et al.*, Phys. Rev. Lett. **76** (1996) 3057.

[21] L. Bergstrom, J. Edsjo and P. Ullio, Astrophys. J. **526** (1999) 215; F. Donato, D. Maurin, P. Salati, A. Barrau, G. Boudoul and R. Taillet, Astrophys. J. **563** (2001) 172.

[22] P. Meade, M. Papucci, A. Strumia and T. Volansky, arXiv:0905.0480 [hep-ph].

[23] G. Bertone, M. Cirelli, A. Strumia and M. Taoso, JCAP **0903** (2009) 009, arXiv:0811.3744 [astro-ph].

[24] A. Ibarra and D. Tran, JCAP **0902**, 021 (2009), arXiv:0811.1555 [hep-ph].

[25] A. Ibarra, D. Tran and C. Weniger, arXiv:0906.1571 [hep-ph].

[26] E. Nardi, F. Sannino and A. Strumia, JCAP **0901** (2009) 043.

[27] F. Takayama and M. Yamaguchi, Phys. Lett. B **485**, 388 (2000).

[28] W. Buchmüller, L. Covi, K. Hamaguchi, A. Ibarra and T. Yanagida, JHEP **0703**, 037 (2007).

[29] A. Ibarra and D. Tran, Phys. Rev. Lett. **100**, 061301 (2008); JCAP **0807** (2008) 002; K. Ishiwata, S. Matsumoto and T. Moroi, Phys. Rev. D **78** (2008) 063505, Phys. Lett. B **675** (2009) 446; L. Covi, M. Grefe, A. Ibarra and D. Tran, JCAP **0901** (2009) 029; S. L. Chen, R. N. Mohapatra, S. Nussinov and Y. Zhang, Phys. Lett. B **677** (2009) 311; W. Buchmüller *et al.* arXiv:0906.1187 [hep-ph];

[30] C. R. Chen, F. Takahashi and T. T. Yanagida, Phys. Lett. B **671** (2009) 71, C. R. Chen, F. Takahashi and T. T. Yanagida, Phys. Lett. B **673** (2009) 255.

[31] A. Ibarra, A. Ringwald and C. Weniger, JCAP **0901** (2009) 003, A. Ibarra, A. Ringwald, D. Tran and C. Weniger, arXiv:0903.3625 [hep-ph]; S. Shirai, F. Takahashi and T. T. Yanagida, arXiv:0902.4770 [hep-ph].

[32] M. Pospelov and M. Trott, JHEP **0904** (2009) 044.

[33] K. Hamaguchi, S. Shirai and T. T. Yanagida, Phys. Lett. B **673**, 247 (2009); A. Arvanitaki *et al.*, arXiv:0812.2075 [hep-ph].

[34] K. Hamaguchi, E. Nakamura, S. Shirai and T. T. Yanagida, Phys. Lett. B **674**, 299 (2009).

[35] J. F. Navarro, C. S. Frenk and S. D. M. White, Astrophys. J. **462** (1996) 563.

[36] T. Sjöstrand, S. Mrenna and P. Skands, JHEP **0605** (2006) 026.

[37] See for example V. S. Berezinskii, S. V. Buolanov, V. A. Dogiel, V. L. Ginzburg, V. S. Ptuskin, Astrophysics of Cosmic Rays (Amsterdam: North–Holland, 1990).

[38] D. Maurin, F. Donato, R. Taillet and P. Salati, Astrophys. J. **555** (2001) 585.

[39] A. Ibarra and D. Tran, JCAP **0906** (2009) 004.

[40] G. Bertone, W. Buchmüller, L. Covi and A. Ibarra, JCAP **0711** (2007) 003.

[41] M. Cirelli and P. Panci, arXiv:0904.3830 [astro-ph.CO]; K. Ishiwata, S. Matsumoto and T. Moroi, arXiv:0905.4593 [astro-ph.CO].

[42] P. Sreekumar *et al.* [EGRET Collaboration], Astrophys. J. **494** (1998) 523.

[43] A. W. Strong, I. V. Moskalenko and O. Reimer, Astrophys. J. **613**, 956 (2004); Astrophys. J. **613** (2004) 962.

Chapter 11

Invited Presentations and Summaries

The Structure of the Proton and HERA

Max Klein

University of Liverpool, Physics Department, Oxford Street, L69 7ZE Liverpool, UK

DOI: http://dx.doi.org/10.3204/DESY-PROC-2009-03/Klein

A brief summary is given on what we have learnt from inclusive DIS measurements with HERA on the structure of the proton, recalling some experimental results available twenty years ago, and presenting some HERA milestones up to most recent results.

1 Introduction

This paper summarises a seminar given at the PHOTON09 conference. It therefore is not a typical conference contribution. The seminar title was "What have we learned on proton structure from HERA?" devoted to the collider experiments H1 and ZEUS. This subject is difficult to discuss on a few proceedings pages. Before HERA, and following the seminal discovery of pointlike constitutents of the proton at SLAC, now 40 years ago, a series of neutrino and muon deep inelastic scattering (DIS) experiments was performed in order to study the partonic structure of nucleons further and to also develop and test Quantum Chromodynamics (QCD), which had been put forward as the gauge field theory of the strong interaction of confined quarks and gluons. Some of the findings of these fixed target experiments are recalled here in order to understand better the new developments which HERA brought. The kinematic range of these experiments was determined by the cms energy squared, $s = 2M_pE_l$, i.e. by the lepton beam energy E_l, typically 200 GeV, and the mass of the proton M_p as the fixed target energy.

HERA collided electrons (and positrons) of 27.5 GeV energy with protons of 820/920 GeV energy. There were three main reasons for HERA to provide a much deeper understanding of proton's structure than the fixed target experiments of the eighties: i) The energy s was much increased with the now moving proton "target", to values of $s = 4E_eE_p \simeq 10^5\,\mathrm{GeV}^2$, more than two orders of magnitude higher than before; ii) At the collider, the scattering kinematics is determined from the scattered electron angle and energy, from the hadronic final state or/and from a combination of the electron and hadron momenta. The redundancy of the kinematics was at the origin of the reliability and large kinematic range of the HERA measurements; iii) The two collider experiments H1 and ZEUS had a nearly 4π acceptance which enabled the radiative corrections to be much suppressed by establishing the energy-momentum balance of each event.

In this very brief summary a few developments may be recalled only, and the discussion is restricted to inclusive scattering. A detailed overview on experimentation at HERA and the results achieved with the data taken until 2000, in period I, can be found in these proceedings and in [1]. The slides of this talk are available from the PHOTON09 web site.

Section 2 presents a reminder on experimental results on DIS available before HERA. Section 3 recalls the first two major observations, made by H1 and ZEUS, the rise of the proton structure

function $F_2(x, Q^2)$ towards low x and the existence of a significant fraction of events, in which the proton remained intact, a process then termed deep inelastic diffractive scattering. It also reminds of ideas, discussed in 1994, on the increase of the luminosity and future measurements, in particular of the longitudinal structure function F_L, which eventually was pursued prior to the termination of HERA's operation in 2007. Section 4 presents most recent results which have allowed completing the analysis of the HERA I data, a combination of H1 and ZEUS measurements and a joint QCD analysis. Section 5 presents some recent preliminary results, based on the full HERA statistics, completion of which will end the analysis of the inclusive cross section data in the not far future. A short summary is presented in Section 6.

2 Experiments before HERA

Twenty years ago, seven major experiments on deep inelastic scattering (DIS) were analysing data, the BCDMS, BFP and EMC muon experiments and the BEBC, CCFRR, CDHSW and CHARM neutrino experiments. These experiments measured neutral (NC) and charged current (CC) scattering, respectively, at values of momentum transfer squared Q^2 up to some $100\,\mathrm{GeV}^2$ and Bjorken x values above 0.01, as is summarised in [2].

The inclusive DIS cross section, at lower Q^2, is determined by the two proton structure functions F_2 and F_L as

$$\frac{d^2\sigma}{dxdQ^2} = \frac{2\pi\alpha^2}{Q^4 x}[(Y_+ + \frac{M_p^2 x^2}{Q^2}y^2)F_2 - y^2 \cdot F_L] \simeq \frac{2\pi\alpha^2}{Q^4 x}Y_+[F_2 - \frac{y^2}{Y_+}F_L], \qquad (1)$$

where $y = Q^2/sx$ is the inelasticity of the process, or the relative energy transfer in the fixed target configuration, and $Y_+ = 1+(1-y)^2$. The structure function expression $F_2 - y^2/Y_+ \cdot F_L$ is referred to as the reduced DIS cross section σ_r. In the Quark Parton Model (QPM) for photon exchange, F_2 is determined by the sum of quark and anti-quark distributions weighted by the electric quark charges squared $F_2 = x\sum e_q^2(q + \overline{q})$, and $F_L = 0$.

Figure 1 shows one of the salient measurements of that time, the structure function $F_2(x, Q^2)$, for different x between 0.07 and 0.75 as a function of Q^2, from 9 to $220\,\mathrm{GeV}^2$, as obtained by the BCDMS Collaboration in μp scattering [3]. This data set, a combination of data from four different muon beam settings, has been crucial input for most of the subsequent extractions of parton density functions (pdf) until today. With an accuracy of up to about 2%, the data are rather precise, with good coverage of the large x region. The plot illustrates that the BCDMS data continue the behaviour of the historic SLAC ep data, obtained at lower Q^2, albeit some trend is visible of F_2 being a bit flatter at larger x in the BCDMS measurement. The tendency of the BCDMS data to be 'flat' leads to a rather small value of the strong coupling constant α_s, of about 0.11 at $Q^2 = M_Z^2$ when using the BCDMS data alone. There is also a clear deviation visible of the EMC data from the BCDMS result, in particular at lower x (left part of the plot). It was realised subsequently that the EMC analysis was incomplete at low x, and the BCDMS result was supported by the CDHSW data. The BCDMS Collaboration had also deuteron data taken, as did many other DIS fixed target experiments, unlike HERA, which was not given the time to study the structure of the neutron in the much extended range.

Using the variation of the muon beam energy, the BCDMS collaboration determined the ratio of the cross sections of longitudinally and transversely polarised virtual photon-proton interactions, $R = \sigma_L/\sigma_T = F_L/[(1 + M_p^2 x^2/Q^2)F_2 - F_L] \simeq F_L/[F_2 - F_L]$. The result, as shown in Figure 2, covers an x range from about 0.1 to 0.65 with a tendency to larger R values of

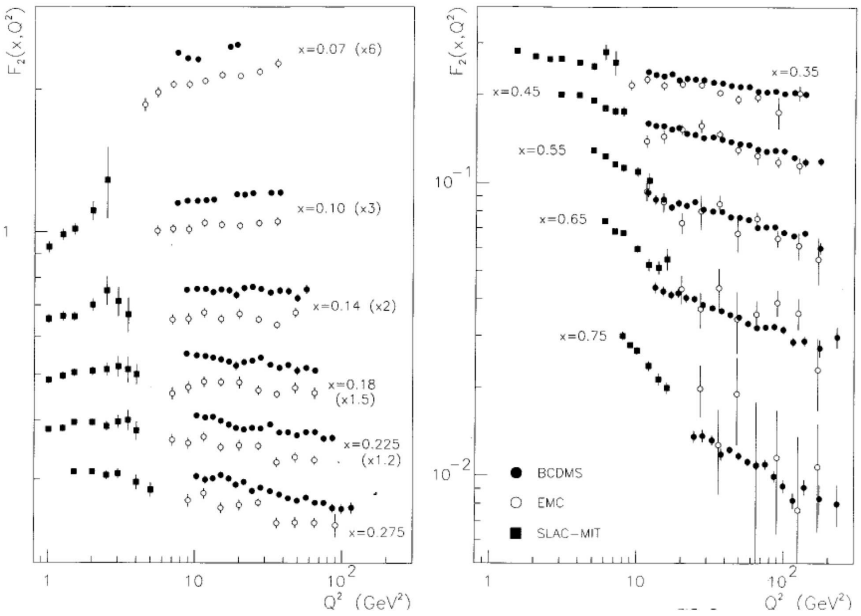

Figure 1: Solid points: Combined measurement of F_2 by BCDMS at low x (left) and large x (right). Open points: Corresponding data from EMC. Squares at lower Q^2: F_2 measured in ep scattering at SLAC.

about 0.15 towards smaller x values. Since F_L is sensitive to the gluon distribution xg [4], an increase of R may be caused by an enlarged xg. The information on xg available from the fixed target DIS experiments had yet been sparse. The gluon distribution cannot be measured directly but is deduced from QCD analyses. Since it does not enter the non-singlet evolution equations, obeyed by the valence quarks which dominate at high x, it is difficult to extract xg accurately from large x DIS data alone. An attempt to determine xg was performed by the BCDMS Collaboration [5]. Using the momentum sum rule and fixing α_s, the result of Figure 2 was obtained for a few x bins around $x \sim 0.1$. The solid overall curve describes the NLO QCD fit result [5] giving $xg = 4.93(1-x)^{8.3}$ at $Q^2 = 5\,\mathrm{GeV}^2$.

A series of DIS neutrino and anti-neutrino scattering experiments provided complementary information to the muon experiments. These experiments, by the nature of the W exchange, are sensitive to the flavour decomposition of proton structure. An example is given in Figure 3, which shows the simultaneous measurement by CDHSW [6] of the sum of the anti-quark distributions and of F_L, expressed as R, in the range of x between 0.015 and 0.65 and of Q^2 from about 0.5 to 200 GeV^2. This decomposition relies on the different y dependence, at large y, of the anti-neutrino and neutrino-nucleon scattering cross section difference on $\overline{q}$ and F_L

$$\frac{1}{\sigma_0}\left[\frac{d^2\sigma^{\overline{\nu}N}}{dxdy} - (1-y)^2\frac{d^2\sigma^{\nu N}}{dxdy}\right] = [1-(1-y)^4]\overline{q}^{\overline{\nu}} + [(1-y)-(1-y)^3]F_L. \qquad (2)$$

The result on R is very similar to the one from BCDMS. One also notices the result from the electron scattering experiment at SLAC and the strong Q^2 dependence of R at fixed, large x as shown in Figure 3. The result on the anti-quark distribution exhibits strong positive scaling

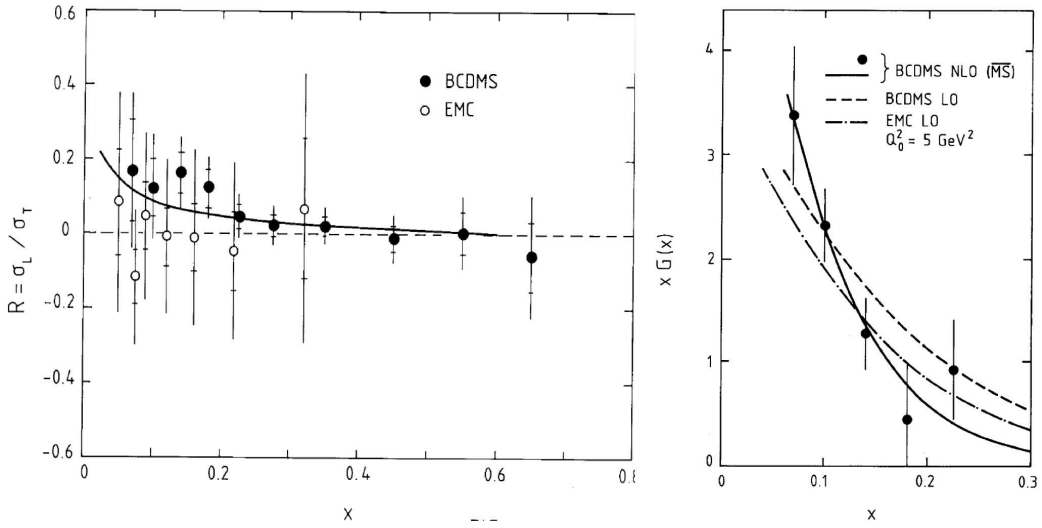

Figure 2: Measurements of $R \simeq F_L/(F_2 - F_L)$ by the muon DIS experiments BCDMS and EMC (left). Determination of the gluon distribution in NLO QCD by BCDMS (points and solid line) compared with LO determinations by BCDMS and EMC, at $Q_0^2 = 5\,\mathrm{GeV}^2$ (right).

violations at small x, down to 0.01. From the νN and $\overline{\nu} N$ cross sections it was also possible to disentangle the x behaviour of the sum of quark and anti-quark distributions, $q + \overline{q}$, and their difference, which in the QPM was assumed to be equal to the valence quarks $q - \overline{q} = u_v + d_v$. As Figure 3 illustrates, it was found that above $x \simeq 0.3$ the proton structure was dominated by valence quarks. QCD analyses showed that at low x the gluon distribution was exceeding the quark distributions.

The determination of parton distributions twenty years ago had already reached a certain state of art [7, 8]. Based on the Buras-Gaemers type of parameterisation [9], $xP \propto x^{\lambda}(1-x)^{c}$, fits were performed up to next to leading order (NLO), using global data sets, including systematic errors and renormalisation scheme effects. The predictions for HERA were of wide range, as is illustrated in Figure 4. The low x behaviour was determined by the parameter λ which was predicted to change rapidly with Q^2. The value of λ was not fixed. In an alternative approach [10], parton distributions were radiatively generated, assuming that at a very small initial scale $Q_0^2 \sim 0.3\,\mathrm{GeV}^2$ both xg and $\overline{q}$ are zero and the renormalisation group equation would still hold. This allowed predictions to be made for the behaviour of F_2 in the so far unexplored range of very small Bjorken x, down to 10^{-4}. Results from HERA were eagerly awaited.

3 First Results

The first years at HERA were particularly exciting and lead to a very large number of first observations and non-observations, as of lepto-quarks, which are reviewed in [1]. For the subject of proton structure two observations were probably of key importance, the rise of F_2 at low x

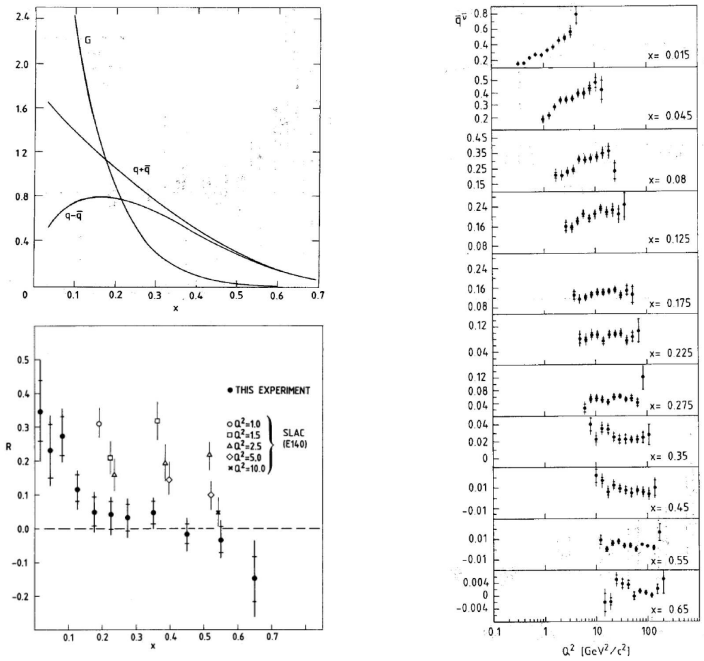

Figure 3: Right: Measurement of the total anti-quark distribution as a function of Q^2 for different x by CDHS. Left bottom: Measurement of R derived from the y distribution, compared with SLAC data at different Q^2 (open points). Left top: Determination of the sum and differences of the the total quark and total anti-quark distributions and also of the gluon distribution as a function of x, at $Q^2 = 20\,\mathrm{GeV}^2$.

and diffractive DIS.

The first measurements of the proton structure function F_2, shown in Figure 5, were based on only $0.03\,\mathrm{pb}^{-1}$ of data, taken in 1992. With these first measurements the rise of F_2 towards low x was discovered. This rise is in agreement with general expectations on the low x (large $\omega = 1/x$) asymptotic limit of QCD [11]; however, the actual scale (Q^2), at which the limit would be applicable, was not predicted. The dynamical parton model approach, termed GRV91 in Figure 5, was rather successful.

A second surprise came when an excess was observed of events with a much reduced activity in forward direction, usually populated by the remnants of the proton being in colour connection with the struck quark fragments. In 1993 an about 10% fraction of events was observed, see Figure 6, in which apparently the proton yet stayed intact. The interpretation is that of a diffractive exchange, often termed the Pomeron, which carries a fraction x_{IP} of the proton momentum. A parton of momentum fraction $\beta = x_{IP}/x$ interacts with the exchanged photon of virtual mass squared Q^2. The salient feature of these events is the absence of forward particle production, near the proton beam pipe, which is measured as an activity gap in polar angle, or equivalently rapidity, from the proton beam axis to the more centrally produced particles which stem from the struck parton in the diffractive exchange. Factorising out the Pomeron flux, the hard γIP scattering part can be treated as in conventional DIS. This allowed QCD

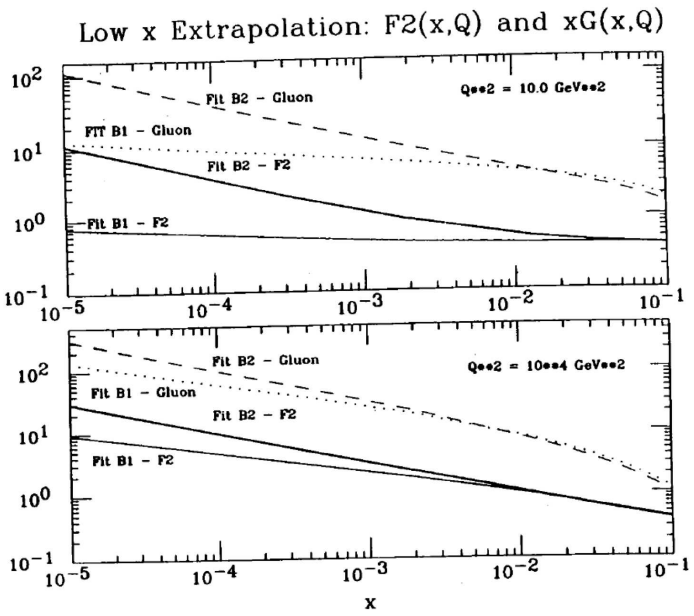

Figure 4: Extrapolation of the behaviour of F_2 and the gluon distribution xg towards low x at $Q^2 = 10$ (top) and $Q^2 = 10^4\,\mathrm{GeV}^2$ (bottom) within the framework of the 1991 global pdf analysis [7]. The low x behaviour was phenomenologically determined by the term x^B, which could be large or small. Both fits described the data which extended down to x about 0.01 at a few GeV^2. From the measurements of HERA one now knows that F_2 at $Q^2 = 10\,\mathrm{GeV}^2$ and $x = 10^{-4}$ is about 1.7 and $xg \simeq 13$, thus somewhat closer to the B_1 curves.

analyses to be performed in order to derive the quark and gluon distributions of the diffractive exchange. Such analyses are based on the diffractive cross section $\sigma^{D(3)}$

$$\frac{\mathrm{d}^3\sigma^{ep\to eXY}}{dx_{IP}dxdQ^2} = \frac{2\pi\alpha^2}{xQ^4}\cdot Y_+ \cdot [F_2^{D(3)} - \frac{y^2}{Y_+}F_L^{D(3)}], \tag{3}$$

which is integrated over the ranges of four-momentum transfer from the incoming to the outgoing proton and the dissociation mass. Similarly to inclusive DIS, the reduced ep cross section depends on the diffractive structure functions $F_2^{D(3)}$ and $F_L^{D(3)}$. For y not too close to unity, $\sigma_r^{D(3)} = F_2^{D(3)}$ holds to very good approximation. The field of diffractive DIS has developed very much as the comparison of the first observations with a recent measurement of $\sigma^{D(3)}$ illustrates, Figure 6. The major result of detailed QCD analyses has been that the diffractive interaction dynamics, or the partonic contents of the diffractive exchange, for all β below about 0.3, is dominantly due to gluons, in line with the view of the Pomeron representing a colourless exchange of two gluons.

In September 1994 a first meeting was held between the collider experiments and the HERA machine experts in order to discuss the future. The luminosity development until then was steady, as is illustrated in Figure 7, but the expectations had been on about $100\,\mathrm{pb}^{-1}$ annually while by then only about $5\,\mathrm{pb}^{-1}$ had been collected. It was obvious that for the physics at high Q^2 a much higher integrated luminosity was required. The machine was achieving an annual

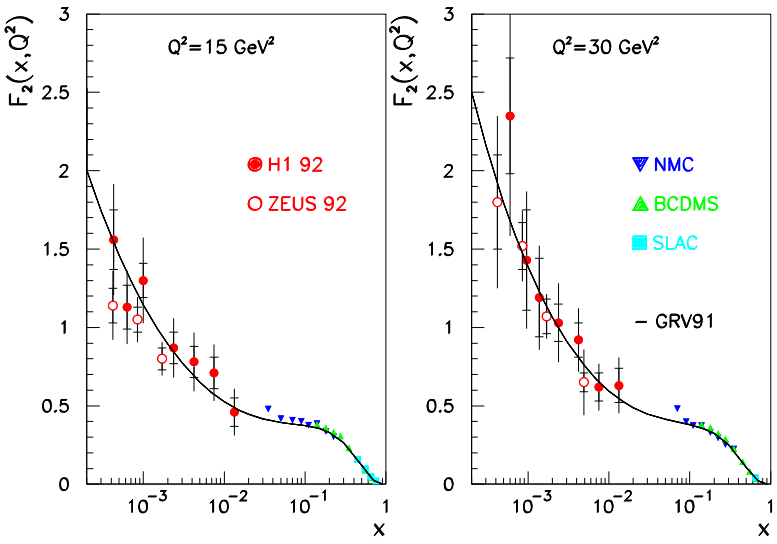

Figure 5: The first measurements of H1 (solid points) and ZEUS (open points) of the proton structure function $F_2(x, Q^2)$ based on the data taken in 1992 shown as a function of Bjorken x. The HERA experiments were able to extend the kinematic range of the F_2 data provided by the fixed target electron (SLAC) and muon (BCDMS, NMC) proton experiments by two orders of magnitude into the then-unknown domain of low x. For GRV91 see text.

luminosity close to the expectations by summer 2000 when phase I was terminated and a major upgrade began, in particular of the interaction regions. The result of placing focussing magnets close to the vertex was an increase of the specific luminosity by a factor of 4 which lead to a large increase of the luminosity when HERA had overcome initial problems due to synchrotron radiation initiated background.

At the 1994 meeting a further 'first result' was discussed. Besides a measurement of the structure functions F_2 and F_2^D there was an obvious interest in the measurement of the longitudinal structure functions, F_L and F_L^D, because these would allow a non-trivial test of QCD at higher orders and provide independent information on the gluon density at low x. Figure 8 presents the expectation on the measurement of R and the recently released, still preliminary, measurement of F_L. The result is interesting: at Q^2 lower than about 10 GeV^2, a region accessed with the upgraded backward apparatus of H1, the data tend to exceed the NLO QCD fit prediction which essentially is derived from the $\ln Q^2$ derivative of F_2. The definition of F_L to NLO and the exact treatment of the charm contribution near threshold are theoretical issues under discussion. The data analysis is being finalised to accomplish publication of this first observation [12], relying on the last data taken at HERA. Further interesting results on F_L have also been obtained by ZEUS [13] while H1 has also measured F_L^D for the first time [14].

4 Precision Results

Since the first results on F_2 in the DIS region of Q^2 of O(10) GeV^2, obtained with the initial data, the accuracy of this measurement was constantly improved. The most accurate measurement

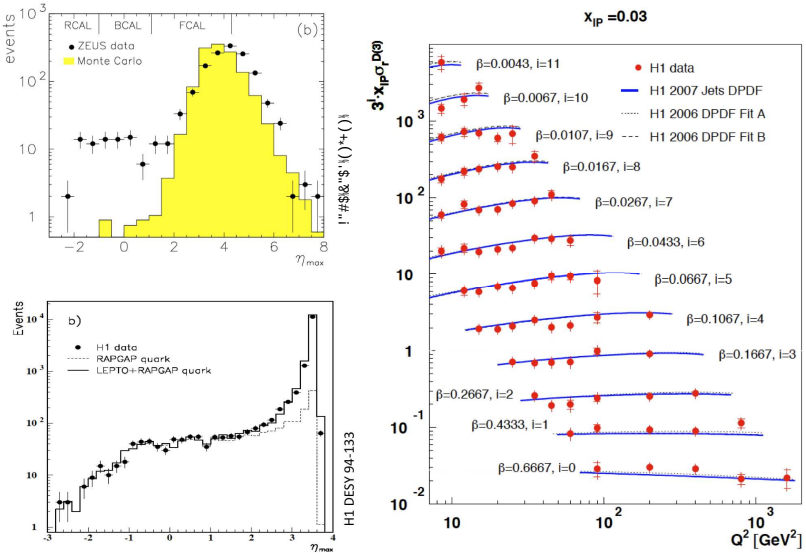

Figure 6: Left: The first observations of hard diffraction - top left: Distribution in DIS events of η_{max}, the maximum pseudorapidity of a cluster of energy larger than 400 MeV, in the ZEUS calorimeters; bottom left: Similar observation in the H1 DIS η_{max} distribution compared with a simulation which included diffractive and genuine DIS events. Right: An example for a recent measurement of the diffractive DIS cross section as a function of Q^2 for different β at $x_{IP} = 0.01$. The data are well described by a theoretical model based on QCD evolution of diffractive parton densities using a Regge factorisation ansatz.

of F_2 at HERA is shown in Figure 9 and may be compared for curiosity with Figure 5. Based on H1 detector upgrades in the mid nineties, a huge step of improvement could be realised [15] and F_2 is now known to nearly 1 % accuracy. The structure function rises approximately as x^{λ} towards low x. There is no sign of saturation of this behaviour at lowest x in the DIS region observed. Using the 1997 H1 data the power was determined [16] as $\lambda = -0.05\ln(Q^2/0.3^2)$ with Q^2 in GeV^2. Together with a variety of measurements on neutral (NC) and charged current (CC) scattering by H1 and ZEUS, a first inclusive cross section combination was recently published [17] of all HERA I data, which covers the wide kinematic range of $6 \cdot 10^{-7} \leq x \leq 0.65$ and $0.045 \leq Q^2 \leq 30000\,\text{GeV}^2$. Due to the independence of the H1 and ZEUS results and the use of complementary methods of kinematic reconstruction, the accuracy of the combined data set is better than that of a simple mean.

The combined data set was used for an updated QCD analysis at NLO [17] following the approach introduced in [15] by H1, regarding in particular the parameterisation of the parton distributions and the treatment of uncertainties. As compared to the QCD fits prior to HERA, mentioned above, quite some substantial improvements to the art of extracting parton information from DIS cross sections have been introduced over the years. These rely on experimental progress as summarised in [1] and theoretical developments, especially the challenging calculations of QCD to higher orders which reached the NNLO level [18]. These improvements are: i) a refined treatment of experimental uncertainties in terms of their uncorrelated and correlated error contributions; ii) a choice of parameters based on χ^2 saturation criteria supplemented

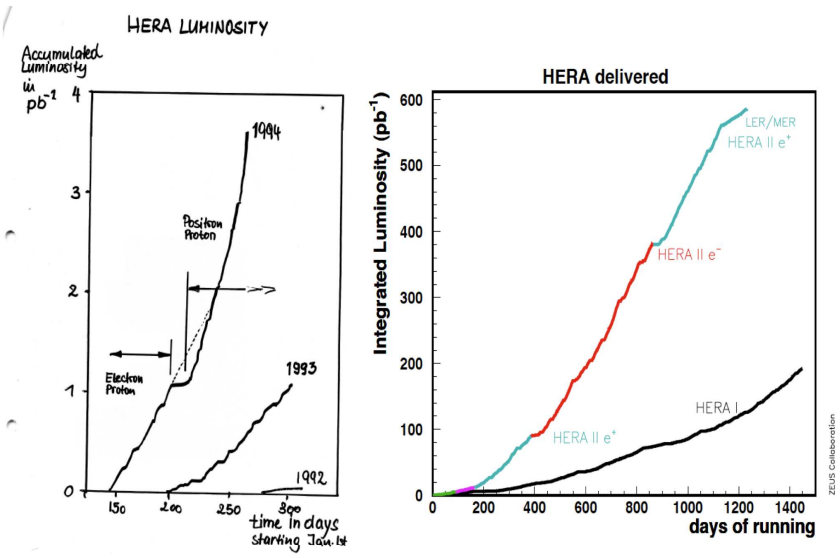

Figure 7: Development of the integrated luminosity at HERA over time. Left: Status in September 1994 as presented by Ferdinand Willeke at an upgrade meeting; right: The luminosity delivered by HERA in the first phase (1992-2000) and the upgrade phase (2003-2007). The last four months were devoted to the lower proton beam energy runs. The trend resembled HERA I as the luminosity is proportional to E_p^{-2}, i.e. the factor 3-4 loss due to the reduction of E_p at the end of HERA's operation brought the luminosity back to HERA I values of about $10^{-31}\,\mathrm{cm}^{-2}\,\mathrm{s}^{-1}$.

by in depth investigations of possible and inacceptable fit solutions; iii) attempts to consider such parameterisation uncertainties in the final error bands; iv) following the measurements of charm and beauty densities by H1 and ZEUS and theoretical prescriptions, still developing, a simulation of the threshold effects of c and b density contributions; v) a consideration of the effect of parameters such as cut or mass values. The results therefore are more reliable, not only due to the improved experimental input. There remains an element of subjectivity in performing such analyses, which underlines the importance of having several approaches, some of which are cited below [19]. There are yet some common observations associated to HERA data which may be illustrated well with the recent HERAPDF1.0 fit result [17] in Figure 10. The apparent structure of the proton depends on the resolution $\propto 1/\sqrt{Q^2}$, with which it is probed. At Q^2 of about $1\,\mathrm{GeV}^2$, corresponding to $0.2\,\mathrm{fm}$, the proton structure may be decomposed as is shown in Figure 10 top. The gluon distribution has a valence like shape, i.e. at very low x the momentum is carried by sea quarks. At medium $x \sim 0.05$ the gluon dominates over all quarks. At largest x, above 0.3, the proton structure is dominated by the up and down valence quarks. This picture evolves such that below $10^{-16}\,\mathrm{m}$ for $x \leq 0.1$ the gluon density dominates also over the sea quark density, see Figure 10 c,d). One may compare this HERA result with the early determination of xg by BCDMS, as shown in Figure 2, or the pdf determination by CDHS, Figure 3, to judge upon the immense progress achieved. The valence quarks are rather insensitive to the resolution, i.e. for any Q^2 a rather constant behaviour of the valence quarks is observed which is a feature of their non-singlet transformation behaviour in QCD.

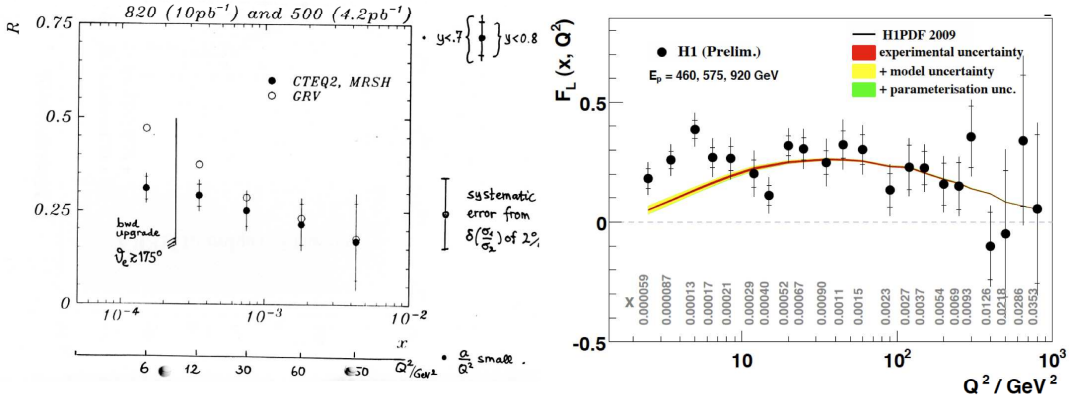

Figure 8: Left: Projected measurement of $R = F_L/(F_2 - F_L)$ as presented to the upgrade meeting in September 1994. The plot indicates the need for an upgrade of the backward region for accessing the region below Q^2 of about $10\,\mathrm{GeV}^2$. Right: Measurement of F_L with data taken 15 years later. In the low Q^2 region the predictions from various fits differ most, and the H1PDF2009 calculation tends to be below the still preliminary data.

5 Outlook

In the second phase of beam operation, HERA II, a much increased integrated luminosity was taken. For e^-p, a tenfold increase was achieved because in HERA I, due to lifetime limitations from trapped dust particles, only $15\,\mathrm{pb}^{-1}$ could be registered. Figure 12 shows the so far most accurate data on the inclusive CC scattering[1], $e^-p \to \nu X$, provided by ZEUS. One sees that the striking characteristics of CC, the missing transverse momentum, is well understood. The Figure also illustrates the confirmation of the linear dependence of the CC cross section on the lepton beam helicity. Unlike NC, the CC cross section is sensitive to the flavour contents of the proton. This is shown in Figure 12 with the decomposition of the cross section into the up quark part, $u+c$, and the down quark part $\overline{d}+\overline{s}$, weighted by $(1-y)^2$. At highest Q^2 the data extend to $x = 0.65$, albeit with limited accuracy. Currently the H1 experiment is completing a similar analysis. It then is intended to combine the H1 and ZEUS HERA II measurements, which will improve the accuracy obtained from the combination, illustrated in Figure 11, especially in the high Q^2 domain.

Deep inelastic scattering is the cleanest method to search for sub-substructure effects in the proton. The results from HERA, based on the total data statistics, limit a possible quark substructure, within the most simple form factor approach, to a dimension below $6 \cdot 10^{-19}\,\mathrm{m}$, which is about a factor of 100 below where quarks appeared and a factor of 1000 below the radius of the proton. This is deduced by both H1 and ZEUS from the Q^2 behaviour of the inclusive NC cross section. This and a number of further results are being finalised by the collaborations.

[1] A salient feature of HERA was that it measured simultaneously the NC and the CC scattering processes. Thus H1 and ZEUS were the equivalent, at much increased kinematic range, of both the charged lepton (e, μ) and the neutrino fixed target scattering experiments of the past. Loosely speaking, H1 for example was BCDMS and CDHS in one apparatus, and it also combined many physicists from these and similar experiments.

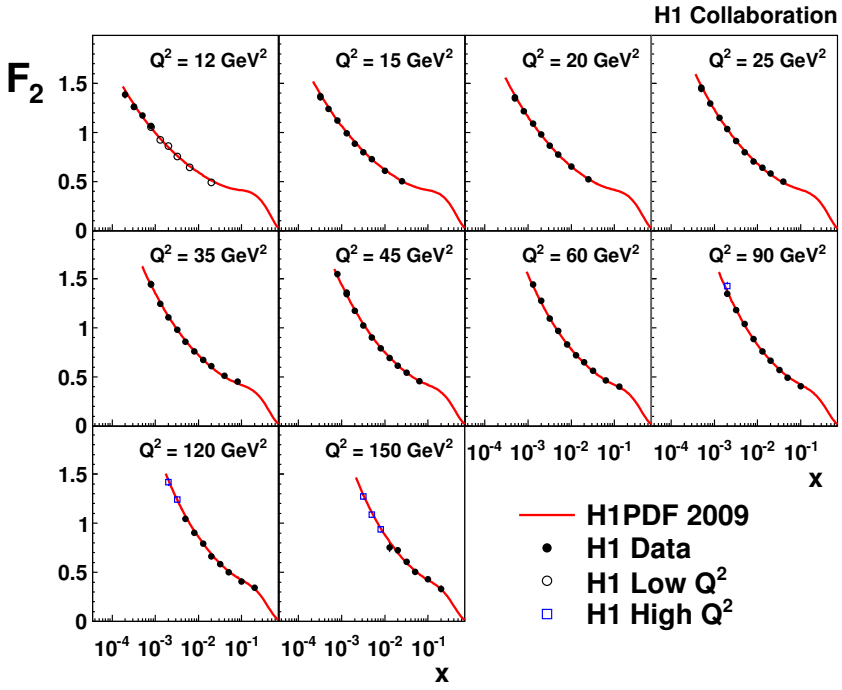

Figure 9: Recent precision measurement [15] of F_2 based on the H1 data taken in 2000.

6 Summary

So, what has been learned with HERA on the proton structure? This is not easily summarised in a few statements because H1 and ZEUS found a new world of parton dynamics inside the proton. Major observations which were not known before are: i) there is no substructure of quarks down to $6 \cdot 10^{-19}$ m; ii) the gluon momentum distribution, for $x \lesssim 0.1$, dominates the proton structure having evolved from very small values at low x and $Q^2 \simeq 1\,\mathrm{GeV}^2$; iii) QCD at higher orders is able to describe the dynamic change of partonic momentum distributions with linear evolution over more than four orders of magnitude in Q^2, with suitable parameterisations of the x dependence and question marks regarding the low Q^2, x domain as accessed with joint F_2 and F_L measurements; iv) HERA discovered diffractive DIS at the level of 10 % of the inclusive cross section. There has also been made major progress in the understanding of the hadronic final state, in the formulation of parton amplitudes from deeply virtual Compton scattering, in the measurement of the heavy quark contents of the proton including its theoretical description, and further areas of lepton-nucleon scattering not covered here.

HERA has been a major and extremely successful milestone in the development of particle physics. Ahead are still a large number of problems, some raised by HERA, to be solved for an understanding of nucleon's structure. These, for example, are: i) why are leptons and quarks different in the strong interactions; ii) is the gluon density saturating at low x, as unitarity requires, and is it equally distributed over the proton or concentrated in so-called hot spots; iii) what is the exact momentum distribution of all quarks and anti-quarks in the proton,

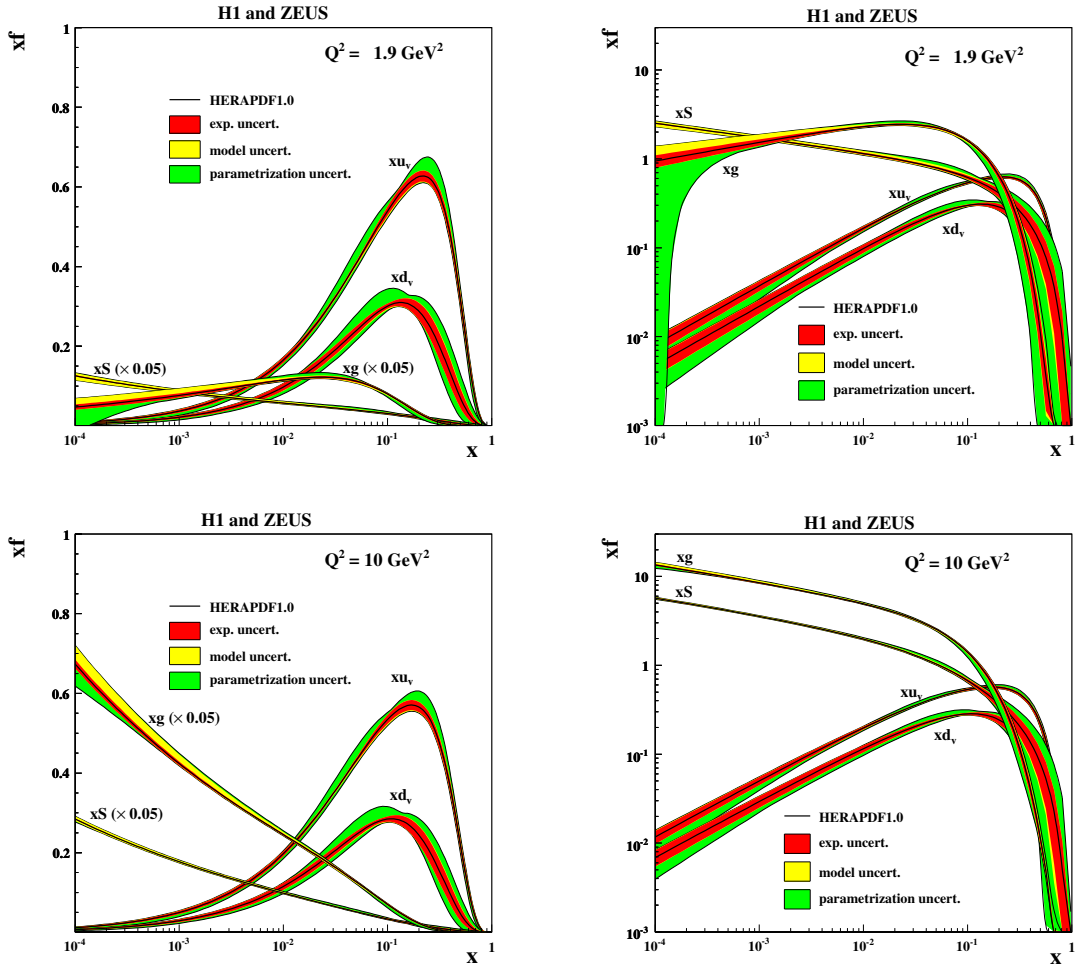

Figure 10: Parton distributions as determined by the QCD fit to the combined HERA I data at $Q^2 = 1.9$ GeV^2 (top) and at $Q^2 = 10$ GeV^2 (bottom). The inner error bands show the experimental uncertainty, the middle error bands include the theoretical model uncertainties of the fit assumptions, and the outer error band represents the total uncertainty including the parameterisation uncertainty. Here $xS = 2x(\overline{U} + \overline{D})$ denotes the total sea quark density.

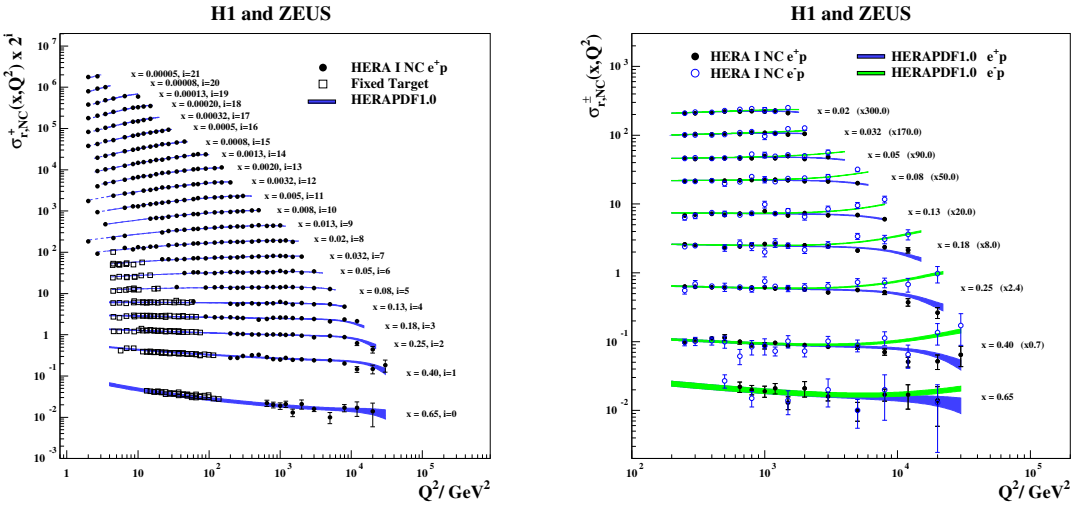

Figure 11: Combined H1-ZEUS HERA I measurement of the reduced neutral current cross section σ_r, which at lower Q^2 and y is a direct measure of the proton structure function F_2. On the right side the e^-p and e^+p cross sections are shown as open and closed symbols. The lines are from an NLO QCD fit to these data, from which at high Q^2 charge asymmetry effects are clearly visible which result from the charge dependent γZ interference cross section term.

regarding for example the strange quark density and the u/d ratio at low and at large x; iv) is there a sub-substructure at smaller dimensions than accessed by HERA; v) what is the parton dynamics and structure inside the neutron and nuclei. Searches for instantons and odderons, two peculiarities of QCD, have been unsuccessful so far. These and many further fundamental questions require a higher energy ep and eA collider to be built, which is currently under study at CERN [20] with the aim to further extend the Q^2 and x range and to increase the luminosity, both by a factor of about hundred as compared to HERA.

Acknowledgments

The invitation to this seminar turned out to be a particular event in my life for which I wish to thank Olaf Behnke, Tobias Haas and Thomas Schörner-Sadenius very warmly.

References

[1] M. Klein and R. Yoshida, Prog. Part. Nucl. Phys. **61** (2008) 343 [arXiv:0805.3334 [hep-ex]]

[2] W.-K. Tung *et al.*, Structure Functions and Parton Distributions, Fermilab Conf 89/26 (1989), Proceedings of the Snowmass Summer Study, 1988.

[3] A. Benvenuti *et al.*, BCDMS Collaboration, Phys. Lett. B **223** (1989) 485.

[4] G. Altarelli and G. Martinelli, Phys. Lett. B **76** (1978) 89.

[5] A. Benvenuti *et al.*, BCDMS Collaboration, Phys. Lett. B **223** (1989) 490.

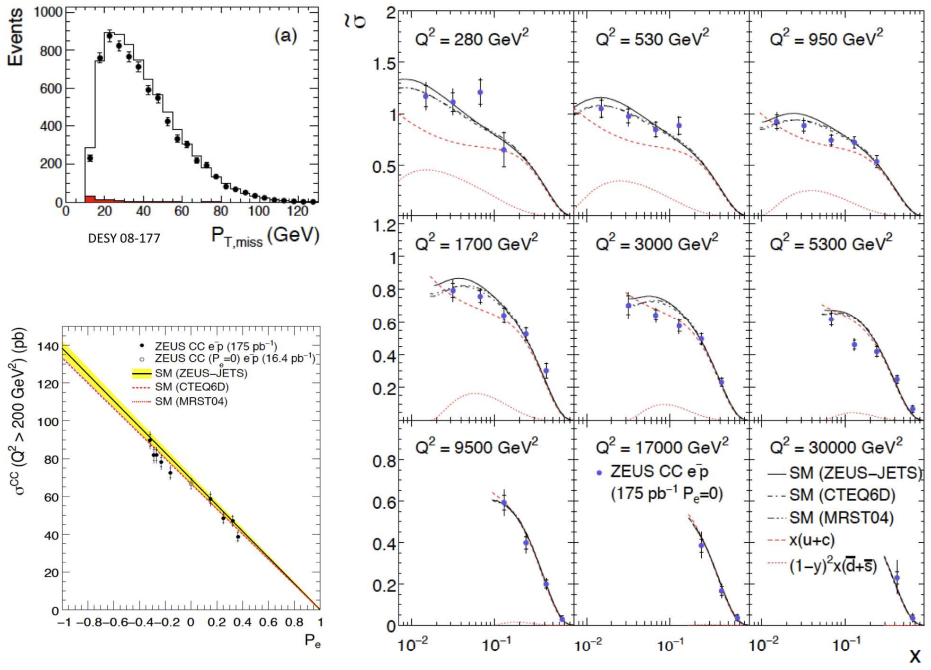

Figure 12: Measurements of CC scattering in e^-p by ZEUS. Left top: missing p_T distribution in data and simulation; left bottom: dependence of the reduced cross section on the longitudinal e^- beam polarisation; right: cross section measurement compared to various NLO QCD parameterisations.

[6] P. Berge *et al.*, CDHSW Collaboration, Z. Phys. C **49** (1991) 187.

[7] J.G. Morfin and W.K. Tung, Z. Phys. C **52** (1991) 13.

[8] P. Harriman, A.D. Martin, R.G. Roberts and W.J. Stirling, Phys. Rev. D **42** (1990) 798.

[9] A.J. Buras and K.J.F. Gaemers, Nucl. Phys. B **132** (1978) 249.

[10] M. Glück, E. Reya and A. Vogt, Z. Phys. C **48** (1990) 471.

[11] A. De Rujula et al, Phys. Rev. D **10** (1974) 1649.

[12] H1 Collaboration, Measurement of the Longitudinal Structure Function F_L of the Proton at Low x in an extended Q^2 range, H1prelim-09-044 (2009) submitted to DIS09, Madrid.

[13] S. Chekanov et al., ZEUS Collaboration, Phys. Lett. B **682** (2009) 8.

[14] H1 Collaboration, Measurement of the diffractive longitudinal structure function F_L^D, H1prelim-09-011 (2009) submitted to DIS09, Madrid.

[15] F.D. Aaron et al., H1 Collaboration, Eur. Phys. J. C **64** (2009) 56, arXiv:0904.3513 [hep-ex].

[16] C. Adloff et al., H1 Collaboration, Phys. Lett. B **520** (2001) 183 [arXiv:hep-ex/0108035].

[17] F.D. Aaron et al, H1 and ZEUS Collaborations, DESY 09-158, submitted to EPJ, arXiv:0911.0884 [hep-ex].

[18] J.A.M. Vermaseren, A. Vogt and S. Moch, Nucl. Phys. B **724** (2005) 3 [hep-ph/0504242].

[19] A.D. Martin, W.J. Stirling, R.S. Thorne and G. Watt, Eur. Phys. J. C **63** (2009) 189 [arXiv:0901.0002];
P.M. Nadolsky et al., Phys. Rev. D **78** (2008) 013004 [arXiv:0802.0007];
S. Alekhin, J. Blumlein, S. Klein and S. Moch, DESY 09-102, arXiv:0908.2766(2009).

[20] M. Klein, The LHeC Project, arXiv0908.2877, Proceedings DIS09, Madrid, 2009;
http://www.lhec/cern.ch

Experimental Summary

Peter Bussey

Department of Physics and Astronomy, Faculty of Physical Sciences,
University of Glasgow, Glasgow G12 8QQ, U.K.

DOI: http://dx.doi.org/10.3204/DESY-PROC-2009-03/Summary.Bussey

I summarise the content of the experimental talks of the conference.

1 Introduction

In this account, I am attempting to summarise a substantial collection of very diverse experimental talks, all of which carry some kind of association with the physics of photons. This was of course a particle physics conference, and so we are dealing with photons that in some sense behave as elementary particles. However this does not necessarily mean that the photons treated in a given context were always of high energy. It is part of the richness of the subject that the photons in the experiments presented here could vary in energy by orders of magnitude, and yet still maintain the connection with elementary particle physics. I intend to depart from the presentational order of the talks and start with those that involved photons of lowest energy, finishing with those of the highest. Much material has had to be omitted, but it can be found in the respective single-topic talks. These should in any case be consulted for more details and for references to the published work. The following sections, therefore, are very much an "invitation to further reading".

2 Axions and their relatives

Axions and their relatives constitute a wide class of hypothetical neutral particles that couple to photons. They have been proposed in different contexts, and in his talk Joerg Jaeckel presented the motivations for looking for these various objects. There is a theoretical problem with explaining why CP is conserved in QCD, the so-called "strong CP problem", since the theory's vacuum structure permits a CP violation. The axion is a proposed particle whose presence prevents this from happening. It must be very light and very weakly interacting, but it should couple to two photons. It is an example of a more generic class of "WISPs" –

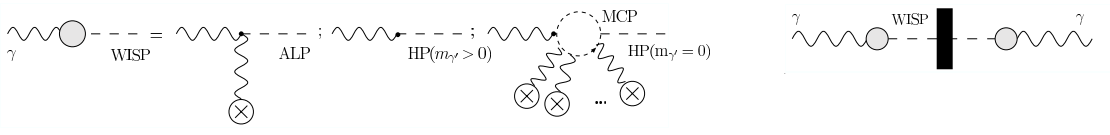

Figure 1: Schematic production and detection of WISPs (Lindner).

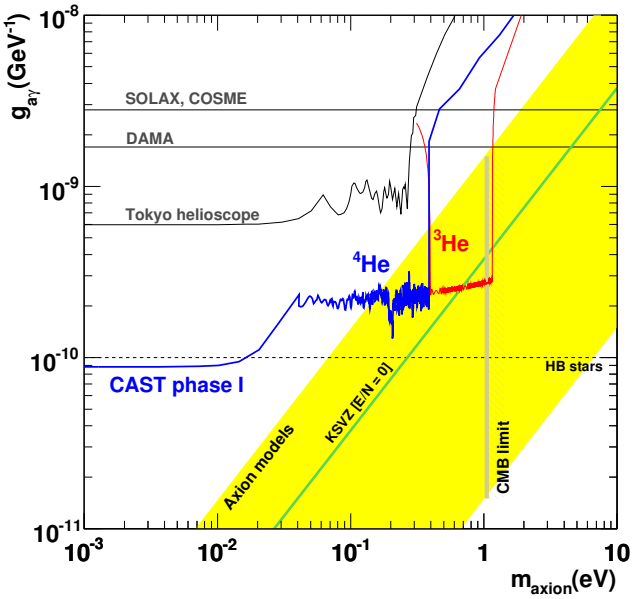

Figure 2: Present limits from ALP experiments (Cantatore).

Weakly Interacting Sub-eV Particles. In the case of axion searches, one approach is to use a strong magnetic field to supply a virtual photon, with which photons from a strong laser beam interact, hopefully generating some axions. A barrier then absorbs the remaining laser beam and everything else except the axions, which proceed through the barrier into a further region of magnetic field, where they regenerate a photon that may be observed. Thus "light shines through a wall" (Fig. 1).

Giovanni Cantatore provided a comprehensive review of a diversity of attempts to discover WISPs: in general the search is for ALPs, "Axion-Like Particles". The lowest energy photons featuring in this conference were those of the ADMX collaboration, in which cosmological relic axions are invited to interact with microwaves in a cavity. Within a relatively narrow band of axion masses in the micro-eV region, this experiment is currently unique in actually reaching the sensitivity of the theories; however no signal was found. The CERN axion search CAST points a powerful magnet at the sun to detect ALPS in the meV energy range, as does the Tokyo Helioscope (Fig. 2). PVLAS approaches the problem by using an intense laser beam to look for an effective vacuum dichroism in a magnetic field. Its former claimed result has now been disconfirmed. So no signal has been found yet, but the searches go on since the sensitivity in most cases still needs to be improved substantially. Axel Lindner described a far-ranging collection of further proposed theoretical end experimental ideas for improved ALP and WISP searches of various kinds. There are hypothetical "Mini-Charged Particles" and even a class of "Hidden Photons" that do not need a magnetic field but will just appear in a vacuum tube! Clearly this area is proving an immensely fertile ground for theoretical imagination as well as experimental ingenuity.

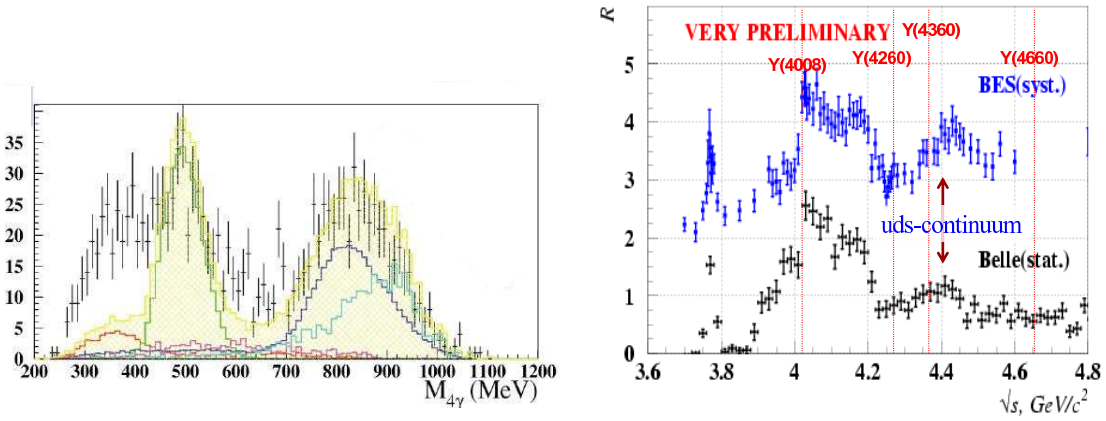

Figure 3: (a) 4-photon mass spectrum showing a low-mass excess at KLOE (Di Donato); (b) R ratio of hadrons to muon pairs in e^+e^- collider data showing the charm threshold and resonances (Wang).

3 Photons at electron-positron colliders

The electron-positron colliders from which results were presented at this conference were DAΦNE, BaBar and Belle. Data taking at DAΦNE ended in 2006, with 2.5 fb^{-1} of data at the ϕ mass, and BaBar have finished with 553 fb^{-1} of data. Many results on radiative ϕ decays and photon-photon processes are now becoming available, a selection of which was presented by Camilla Di Donato. The radiative ϕ decays that were studied include those in which a single light meson is accompanied by a photon, and those where two mesons are produced. There are open questions here regarding the existence and properties of scalar mesons below 1 GeV in mass, which these data are uniquely posed to answer. In particular, there is the long-standing question of whether a $\sigma(600)$ meson exists. Production of a $2\pi^0$ final state shows an anomaly that could indicate the presence of a new effect in this channel, but apparently at a lower energy than 600 GeV (Fig. 3(a)). A gluonium content within the η' is indicated, and analyses have been started on the decay of the η and η' into $\pi^+\pi^-\gamma$.

Initial-state photon radiation is able to make a number of resonant states available for study at the B factories. A wide range of masses is scanned in this way, and the high statistics available are generating some interesting results. Xiao Long Wang showed how exotic charm structures referred to as $Y(4008)$, $Y(4260)$, $Y(4360)$, $Y(4660)$ are now under study. They are formed from charmonium plus hadron pairs and are not yet all fully understood – a topic of considerable interest in the context of the quark model of mesons (Fig. 3(b)). It is interesting that when two charm mesons are observed in the final state, no evidence of the Y states is seen. There is also the $Y(2175)$, which may be an excited strange quark state, and its presence has been confirmed at BES. Here are some ongoing investigations where Belle is best placed to give further answers.

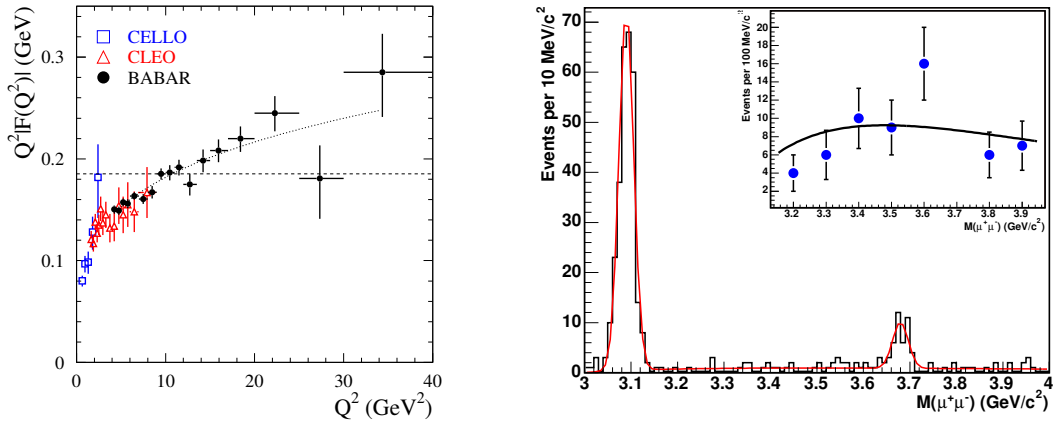

Figure 4: (a) Transition form factor of π^0 with latest BaBar measurements (Li); (b) Exclusive dimuon spectrum in CDF, with diffractive peaks on $\gamma\gamma \to \mu^+\mu^-$ background (Nystrand).

4 Two-photon processes

Selina Li presented some major new photon-photon studies at BaBar and Belle, reminding us again of the original subject-matter of the Photon series of conferences! The process $\gamma\gamma \to \pi^0\pi^0$ has been accurately measured by Belle for dipion masses above 0.6 GeV, and BaBar have measured the π^0 transition form factor in a single-tagged analysis, matching up with data from CLEO and also CELLO at DESY's PETRA collider (Fig. 4(a)). These are just a few topics, and there remains a rich field of work here to be continued by Belle.

Klaus Dehmelt reminded us of the photon leptonic structure function, as measured by L3. More results are coming out in this area, in particular determinations of the structure functions as a function of both photon virtualities; unsurprisingly, the results are in good agreement with the QED calculation. Richard Nisius surveyed the current state of play with the hadronic photon structure function. There are many contributions to an overall fit, but most of the precision points are provided by LEP, especially by OPAL. Although the low-x reach of the measurements is limited, so that the predicted low-x rise is not yet experimentally established, a charm contribution is evident. We keenly await further results from BaBar and Belle, which should soon appear.

Two-photon collisions have now been observed at hadron colliders! Joakim Nystrand showed how CDF have events of the type $\gamma\gamma \to \mu^+\mu^-$ (Fig. 4(b)) and PHENIX have $\gamma\gamma \to e^+e^-$, seen in their studies of diffractive photoproduction of the J/ψ and ψ'. So here, the background is almost as interesting as the signal.

5 Diffraction

A number of new results were presented on diffraction in photoproduction. At STAR at RHIC, again a hadron collider experiment, photoproduced ρ mesons have been observed and their angular distribution measured. Andrzej Sandacz showed results from the COMPASS experiment at CERN, using a 160 GeV muon beam on a polarised ammonia target. In addition to a strong muoproduction programme, the experiment has measured a variety of asymmetry parameters

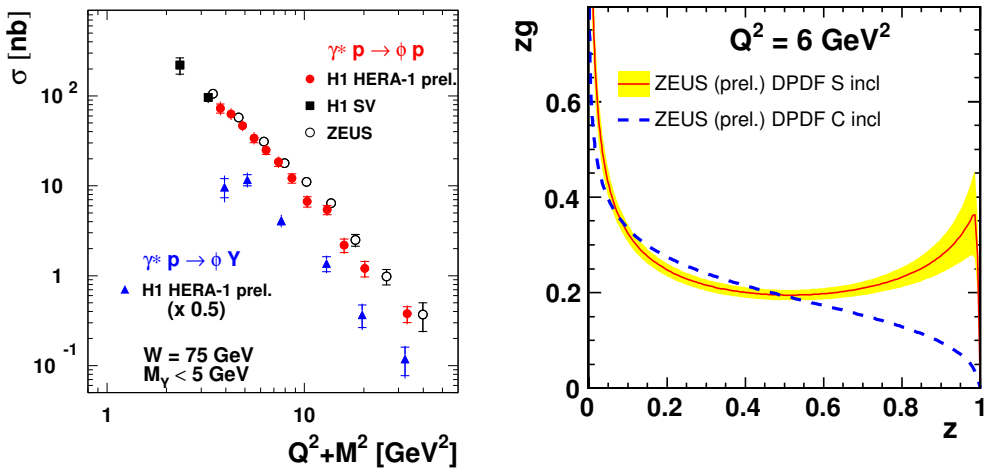

Figure 5: (a) Cross sections for exclusive ϕ production at HERA (Kananov); (b) Gluon density function in pomeron (Newman).

in ρ photoproduction from both protons and deuterons, and have proceeded to extract spin density matrix elements. Results for ϕ production are expected and there are plans for further measurements concentrating on Deeply Virtual Compton Scattering (DVCS).

Most of the work in diffractive physics in recent years has come from HERA. Sergey Kananov presented a general survey of what we have learnt on vector meson photoproduction. There is now an impressive collection of results from H1 and ZEUS on this subject, and he made a comparison of vector meson production without and with a hard scale in the process. Elastic photoproduction of light mesons, namely the ρ, ω and ϕ shows the normal properties of soft diffraction, with parameters gently varying with the centre of mass energy W. The same also holds in electroproduction measured as a function of W. However when a hard scale is present, typified by a heavy quark or large value of Q^2, the cross sections rise with W while falling with $Q^2 + M^2$ (Fig. 5(a)). These features are compatible with hard diffraction as evaluated within the framework of perturbative QCD.

One of HERA's major achievements, of course, has been the study of diffractive physics from the point of view of the pomeron as a hadronic object with a partonic substructure. Paul Newman presented a broad overview of the extensive H1 and ZEUS analyses in this area. Diffractive structure functions have been measured with precision, as illustrated by recent ZEUS results (Fig. 5(b)), and a variety of detailed ideas can be tested, such as the factorisation properties of the proton vertex as the diffractive process at higher Q^2 looks more and more like a kind of hard gluon exchange. Different analysis approaches give consistent results, and a pure DIS or rapidity-gap approach can be successfully compared with the ZEUS data with forward proton or neutron detection. H1 have presented the first diffractive F_L determination. For the future, the full HERA II data need to be analysed, and the H1 and ZEUS data combined for overall measurements.

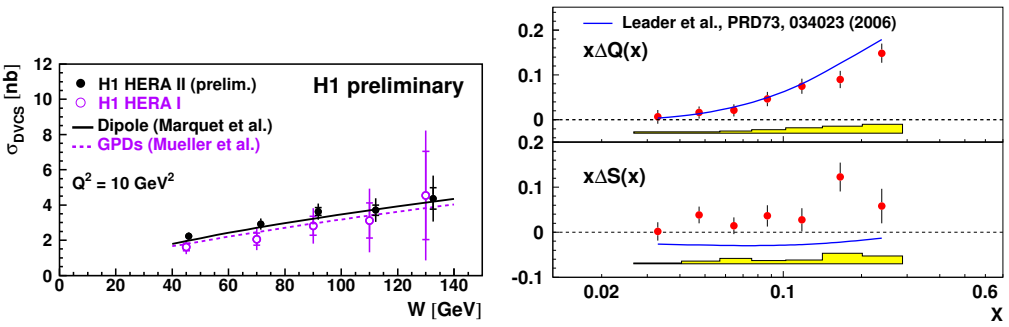

Figure 6: (a) DVCS cross sections at H1 (Schoeffel); (b) Nucleon quark helicity distributions at HERMES (Hillenbrand).

6 DVCS and proton structure

Several results on Deeply Inelastic Compton Scattering were presented, a topic that requires fairly high integrated luminosities in order to obtain useful statistics. Photons are scattering off protons – this is high energy photon microscopy! Laurent Schoeffel described results from H1 and ZEUS. At these low x values, for $x < 0.01$ in the proton, the relevant gluon density is high and one might need to think about saturation effects. Direct DVCS can be measured and the Q^2 and W dependence analysed. However there is an irreducible Bethe-Heitler background of a similar magnitude. Both HERA experiments have presented new cross sections and H1 show that both a dipole model and a Generalised PDF model can fit the data. Are GPDFs as opposed to simple PDFs needed? H1 present clear evidence that argues for a skewing effect, in support of the idea of GPDFs. In their upgrade, COMPASS are making DVCS a major focus and will continue these investigations. Measurements of the Beam Charge Asymmetry will provide an important tool for more detailed studies, and first measurements of this quantity have already been made by H1.

Frank Sabatié gave a dedicated talk on DVCS measurements at JLAB. High statistics are available making use of intense electron beams, enabling several angular correlations to be measured and asymmetries to be determined, together with detailed determinations of the amplitude properties evaluated from suitable cross section differences. It is found that the data are badly described by several of the simpler models, suggesting the presence of more complex or higher order effects.

A further perspective on DVCS was given by Achim Hillenbrand in a presentation of a variety of highlights from the HERMES experiment. HERMES have measured many aspects of nucleon structure using hydrogen targets as well as different atomic nuclei. A particular emphasis has been on spin structures (Fig. 6(b)), a topic also taken up by Joerg Pretz in a discussion of the helicity contribution of gluons to the proton spin structure, measured by means of charmed meson distributions in the COMPASS experiment. Max Klein discussed one of HERA's major showpieces, the DIS study of the PDFs of the proton, using combined H1 and ZEUS data. A new fit has been made to these results, confirming the global utility of perturbative QCD, and comparisons are being made to data from the Tevatron. Specific proton structure functions are being evaluated for charm and beauty production. More will come at higher values of Q^2 and y as well as for the heavy flavours, together with more on F_L, which has now been measured by

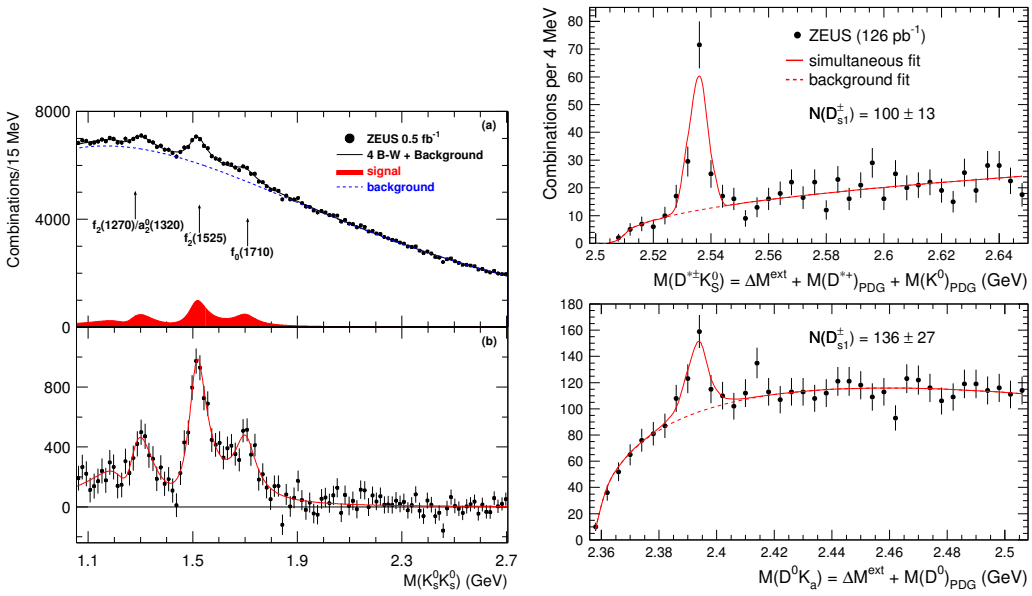

Figure 7: (a) Structure in K^0K^0 spectrum at ZEUS; (b) $D(2536)$ signal in mass difference spectrum (Karshon).

H1 and ZEUS. It can be said that quarks are pointlike down to 0.7×10^{-18} m, making HERA also the world's best electron microscope.

7 Resonance production

As a high energy collider, HERA produced final states containing the usual variety of hadronic resonances. This has provided the opportunity to search for new or exotic resonances that had in some cases been reported at other colliders. Uri Karshon presented results on several such searches, one being for glueballs in the $K^0_sK^0_s$ system. The scalar meson sector contains too many 0++ states to fit into the normal quark model, and it is natural to investigate these as possible glueballs, the lightest of which is predicted by lattice gauge calculations to have a mass in the range 1550-1750 MeV. The state $f_0(1710)$ is an interesting glueball candidate, for several reasons including an apparently high decay BR into strange quarks. The $K^0_sK^0_s$ system is therefore an attractive area to look for confirmation of these ideas. ZEUS have observed evidence for several $K^0_sK^0_s$ resonances in this mass region and the $f_0(1710)$ is present with good statistical significance. It is argued, however, that the state is not a pure glueball.

H1 had earlier proposed a charm pentaquark signal at 3.1 GeV. However ZEUS did not see this, and with more HERA II statistics this peak has gone away and presumably must be treated as a statistical fluctuation, albeit a rather enigmatic one.

ZEUS are studying excited charm states, which are well observed even in the HERA I data set. A variety of states are observed, and the availability of the HERA II data with a better vertex detector makes this a very promising prospect for the future.

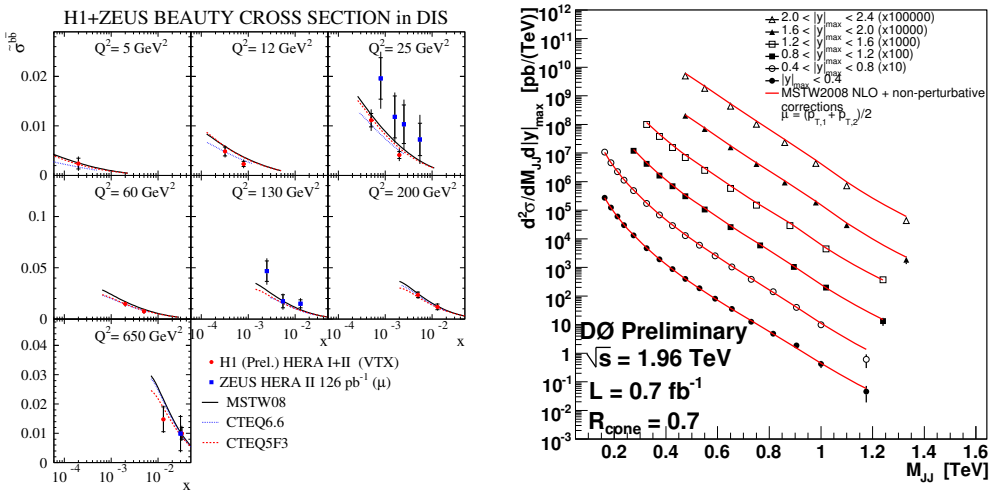

Figure 8: (a) Combined HERA beauty DIS data (Grindhammer); (b) D0 dijet mass spectrum (Yu).

8 Jet physics

The theme of heavy flavours formed a major aspect of Günter Grindhammer's discussion of the physics at different hard scales. Both in photoproduction and in DIS, the presence of a heavy quark facilitates the use of perturbative QCD and encourages the calculation of theoretical models. It is found that the HVQDIS model describes charm production in DIS well, but predicts too low cross sections for beauty. Overall, however, NLO and NNLO calculations do a good job at describing the features of the data (Fig. 8(a)). Results from the final HERA data sets are very eagerly anticipated. In another part of this talk, the evaluation of α_S from jet measurements at HERA was surveyed. H1 and ZEUS are able to do this in various ways and many of the measurements are very competitive on a world basis. It remains the case that with the increasing experimental precision, theoretical uncertainties dominate most of these determinations.

The story is continued with the study of jets at the Tevatron, presented by Shin-Shan Yu. Both CDF and D0 have accumulated in their data very large samples of jets, produced up to transverse momentum values above 600 GeV/c. At one time, high-p_T anomalies were suggested but at present everything is well described by the latest fits to the proton structure which are based on lower-p_T data. Everything about inclusive jets and dijets currently looks very satisfactory (Fig. 8(b)). Studies of W and Z accompanied by jets and, specifically, by heavy flavours have been carried out. These will be of particular relevance in connection with Higgs searches. Anne-Marie Magnan took the view to a higher energy level, presenting projected jet features at LHC. Not only are the extensive studies being performed here important with regard to understanding QCD and the proton structure in more depth, they will be esssential in understanding the backgrounds to searches for exotics and Higgs at LHC.

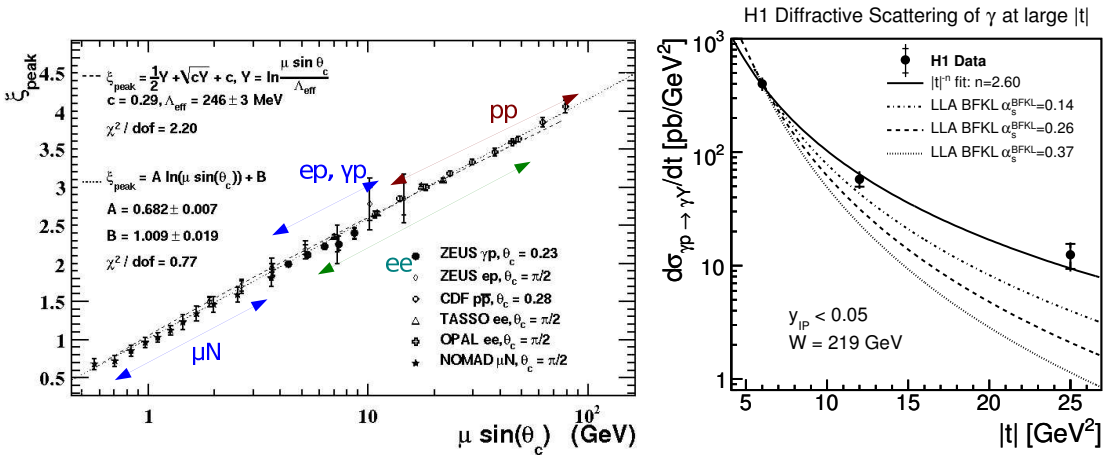

Figure 9: (a) Universal properties of scaled momentum in fragmentation; (b) high-t photon distribution (Müller).

9 Photoproduction

Most of the events recorded in the two larger HERA experiments lie in the category of photoproduction, in which the virtuality of the exchanged proton is very much lower than 1 GeV^2. A thorough survey of many aspects of these processes was given by Katherina Müller. Hard photoproduction may be specified as comprising processes in which either the photon itself or a parton within it undergoes hard scattering, commonly giving rise to jets in the final state. The photon in this way often behaves as if it has a hadronic parton structure. Inclusive jets, dijets and the properties of dijets have been measured and show no unusual properties; neither does the topology of the jets nor the fraction of the photon momentum that is taken up in the jet formation.

In a recent analysis, ZEUS have given measurements of scaled momentum distributions in photoproduced jets, testing our understanding of fragmentation and its universality when this is compared with appropriately scaled measurements from other regimes; again, all is in order (Fig. 11(a)). However the diffractive scattering of high-t photons was found by H1 to be higher than expected and the topic well merits further study (Fig. 9(b)).

10 Prompt photons

In the study of high energy collisions involving hadrons, events in which an isolated high-energy photon is observed provide a direct probe of the underlying parton process, since the emission of these photons is largely unaffected by parton hadronisation. The study of such "prompt" photons gives new perspectives on QCD processes, allowing the theory to be tested from new viewpoints. Prompt photons may be emitted in hard partonic interactions, and were the subject of part of the talk on photoproduction. H1 have measured prompt photons in photoproduction accompanied by a jet, giving cross sections and distributions in the azimuthal separation of the photon and the jet (Fig. 10(a). These distributions are compared with models of the photon,

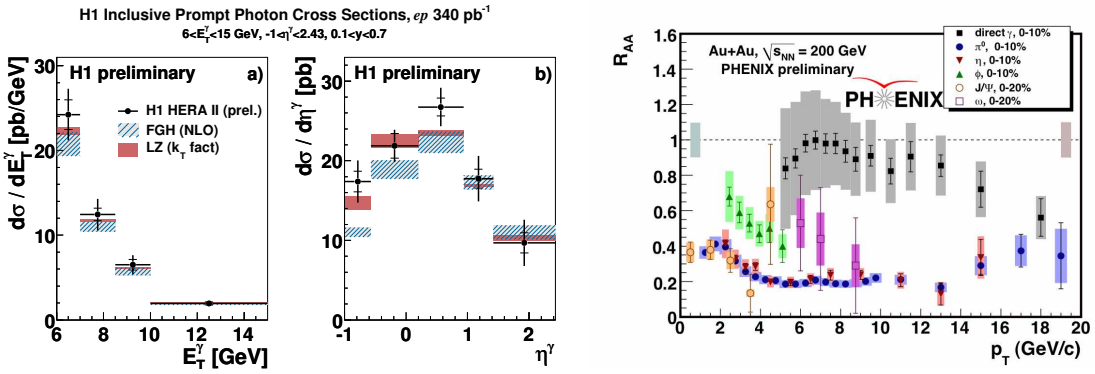

Figure 10: (a) H1 prompt photon + jet in photoproduction (Müller)); (b) PHENIX enhanced prompt photon ratio, compared to other emitted particles (Reygers).

with fair but not perfect agreement.

Recent results on prompt photons in DIS in ZEUS were presented by myself. In this process, attention must be paid to the radiation of the photon by either the incoming or outgoing lepton. Agreement with theoretical models is fair but shows some serious disagreements in some kinematic regions.

At the Tevatron, the story was continued by Ashish Kumar. Both CDF and D0 are active in the prompt photon area. This process is sensitive to the structure of the proton, as well as to the possibility of new physics. CDF and D0 find good agreement with theory, to within some fairly substantial theoretical uncertainties, for prompt photons at transverse momenta above 50 GeV. Below this CDF see a discrepancy while with D0 the situation is suggestive but a little ambiguous – this region clearly merits further study. Measuring a jet as well as the photon does not bring the situation fully under control, as measured by D0. Demanding a b-jet does achieve agreement with theory, but there are serious disagreements if the photon is accompanied by a c-jet. Again, more study is indicated.

Prompt photons also form an important topic of investigation at the RHIC collider, as reported by Klaus Reygers. The PHENIX results in proton-proton collisions are consistent with a large collection of results from other colliders. However, in nucleus-nucleus collisions, it is understood that the colliding nuclei are likely to form a quark-gluon plasma or fireball, out of which prompt photons can emerge. At photon energies of a few GeV this effect has apparently been observed by PHENIX using gold-gold collisions. There is indeed an enhancement of these photons compared to the distributions observed in proton-proton collisions (Fig. 10(b)), confirming the idea that a quark-gluon plasma is being formed.

11 The present high energy frontier

As energies rise, we enter the realm of electroweak physics, and of many possibilities of new physics. Luca Stanco presented some updated HERA cross sections comparing neutral current and charged current exchange. The already classic HERA I results are now augmented by preliminary HERA II measurements, giving further accuracy, and we see how pure photon exchange merges into Z exchange at the same level as W exchange, with differences between

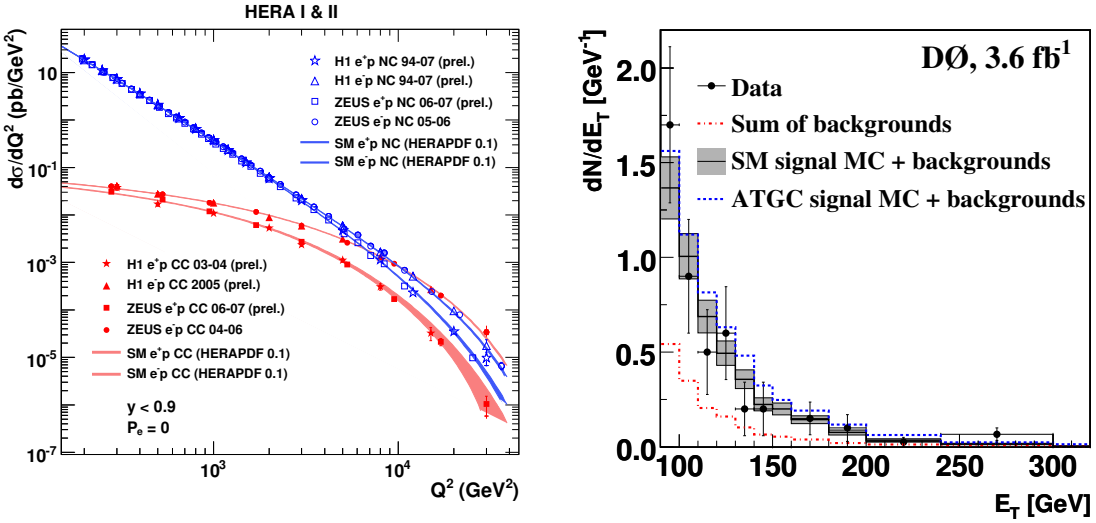

Figure 11: (a) H1 + ZEUS electroweak DIS cross sections (Stanco); (b) D0 data showing no evidence for anomalous triple gauge couplings (Krop).

electron and positron cross sections (Fig. 11(a)). The beam polarisation asymmetries illustrate the physics equally powerfully.

At the Tevatron, Dan Krop pointed out the plethora of theoretically proposed new processes that involve photons. These range from the familiar area of Higgs physics, through SUSY models and extra dimensions, to Compositeness, new generation(s) and Technicolor. All these areas are the subject of searches at the Tevatron and all the searches have so far proved unsuccessful. The anomalous coupling of the photon to the Z is one such example (Fig. 11(b)), although the search has given the first observation (by D0) of the production of $Z\gamma \to \nu\nu\gamma$ at the Tevatron. There has also been an unsuccessful search for "dark photons" that might explain certain excesses seen in astroparticle physics experiments. No Higgs signal, which would be non-SM under present conditions in the photon-photon channel, has been observed. There are many other possibilities, limited only by the imagination of theorists, for anomalous physics to be observed in conjunction with photons. These searches will continue until the Tevatron terminates and LHC takes over the baton.

At LHC, as explained by Suen Hou, there will be a lot of work to do in connection with photons. There are many Standard Model processes that involve high energy photons, all of which should be studied. Some of these are standard processes, such as W and Z production, in which a photon is radiated by an incoming quark line: a correct understanding of this kind of process will help ensure that we understand the basic W and Z production correctly. Of course, the search for anomalous couplings will be extended. The decay of the Higgs into two photons will be a major focus of LHC work, as elaborated by David Joffe in a talk that presented much information on the techniques of photon detection at ATLAS and CMS. While we are waiting for the Higgs to be discovered, it will be interesting to measure the proton-proton total cross section (Hasko Stenzel).

Finally, there are interesting prospects for photoproduction physics at the LHC, since the high energy protons are quite efficient at radiating photons. Vincent Lemaître outlined this photoproduction programme, concentrating on the possibility of single top production via an incoming photon. The process will be tagged, it is hoped, by installing forward silicon detectors close to the beamline downstream of the detectors. Nicolas Schul extended this discussion to a programme of photon-photon physics at the LHC, epitomised by SUSY searches which can be performed in a very effective way using this approach.

12 A high energy photon collider?

For the far future, plans have been under development for many years to construct a high energy photon photon collider as a part of the International Linear Collider project. Talks by Valery Telnov and Tohru Takahashi presented some technical ideas that might be able to turn this project from aspiration into reality, while Jeff Gronberg discussed the possible benefits of constructing an "early photon collider" that could, for example, become a kind of Higgs factory by manufacturing the Higgs out of pairs of photons, the converse of the decay process that will be eagerly sought at the LHC. Unfortunately, these are financially very difficult times, and the present climate of opinion is unfavourable to the pursuance of this option.

13 Final remarks

In this overview I have attempted to give an impression of the remarkable range of talks given at the Photon 2009 conference. There is an enormous diversity of particle physics processes in which photons, whether incoming or outgoing, real or virtual, play an important role. The fact that a particle is ubiquitous does not make it less interesting than those that are rarer; quite on the contrary, the humble photon provides a key to the deeper understanding of many things. From low energies to high, from the firmly established to the speculatively hypothetical, we have seen how important photon physics is to all aspects of our subject. It seems that there is no other particle in the universe that serves us in so many ways.

I must express regrets with respect to those topics which this review has had to omit. These include the DESY laboratory's extensive programme of "low-energy" photon research, and the entire area of new developments in photon detectors. I have also not been able to cover the subject of photons in astroparticle physics. These topics are treated in their own papers in this volume.

Above all, I would like to thank the organisers of the conference for their dedication in making possible such an excellent week of presentations and discussions, in which an outstanding breadth of fascinating physics was presented. We all look forward keenly to the next conference in the Photon series.

Photon 2009: Summary of Theory Talks

Hubert Spiesberger

Institut für Physik - Johannes-Gutenberg-Universität
Staudinger Weg 7, D-55099 Mainz, Germany

DOI: http://dx.doi.org/10.3204/DESY-PROC-2009-03/Spiesberger

The conference *Photon 2009* on the structure and the interactions of the photon included sessions on photon-photon collisions and a future high-energy photon linear collider. This summary of theoretical contributions to the conference therefore has two parts. I will discuss the physics potential of photon colliders with an emphasis on the study of electroweak physics and the search for physics beyond the standard model. Secondly, I will describe a few highlights in recent progress in the understanding of the properties and the interaction of the photon, comprising the production of prompt photons, the photon structure and exclusive hadron production, small-x and total cross sections of deep inelastic scattering. Finally, I will review the status of the comparison of measurement and theory for the muon anomalous magnetic moment $g-2$.

1 Introduction

The photon, the leitmotif of the conference *Photon 2009*, has appeared in the various talks in two different roles. First, the photon is an ideal tool to probe new physics in high-energy photon-photon or photon-electron collisions. During recent years a lot of work has been devoted to the study of the prospects of photon colliders in the search for physics beyond the standard model or to perform precision measurements of standard model phenomena. It was also suggested that a photon collider would be the suitable place to study the properties of a Higgs boson, if it had a mass of about 120 GeV. In particular, the possibility to build a photon-collider as a precursor of an electron-positron linear collider has been discussed, but was not supported by the International Linear Collider Steering Committee [1] and the construction of such a facility will have to wait for its turn, maybe as an extension of an e^+e^- linear collider. Corresponding plans will have a chance to be revived only, if results of forthcoming experiments at the LHC would require new theoretical ideas whose further scrutiny at a photon collider can be expected to considerably improve our knowledge. Till then, it may be worthwhile to study the feasibility of experimentation with $\gamma\gamma$ and γp collisions at the LHC.

Secondly, as the main and traditional subject of this series of conferences, the photon has appeared as a research object on its own right. The study of the photon and its properties, described in terms of structure functions that are measured first of all in virtual-photon scattering (i.e., in deep-inelastic lepton-nucleon scattering), and its generalizations needed for a description of exclusive processes, opens a wide field of research topics in QCD, located at the border-line of perturbative and non-perturbative phenomena. There is a wealth of experimental data not yet understood at a quantitative level and more theoretical work is needed. The photon as a theory laboratory, as an object to gain a deeper understanding of theoretical concepts,

as for example factorization in exclusive processes, is often helpful. Recent progress in this field of research is highlighted in a second part of this summary.

A topic of special importance where aspects of both electroweak and strong interactions play a crucial role, is the measurement of the anomalous magnetic moment of the muon and the comparison with theoretical predictions. A short status review is presented at the end of this article.

This printed version of the summary talk includes only a tiny portion of the figures that have been shown at the conference. The text should therefore be read together with the slides [2].

2 Physics potential of a photon collider

2.1 Motivation

A first motivation for the study of scattering processes with one or two photons in the initial state comes from a naive evaluation of typical cross sections for standard model processes. These cross sections are often comparable, in some cases even larger, than for corresponding processes in e^+e^- annihilation. From a quick look at Fig. 1 it should be obvious that detailed studies including experimental conditions are worthwhile being performed. In particular one may expect that through studies of the W^+W^- final state one can obtain information on 3- and 4-boson interactions. A crucial question is, however, whether photon collisions can be realized with high enough luminosity and present technical design studies indicate that this would indeed be the main limitation. It is therefore important to identify possible measurements at a photon collider that provide information complementary to what can be found at an e^+e^- linear collider. It was argued that in particular with respect to the determination of properties of standard model or supersymmetric Higgs bosons a photon collider may be advantageous in comparison with e^+e^- collisions[1].

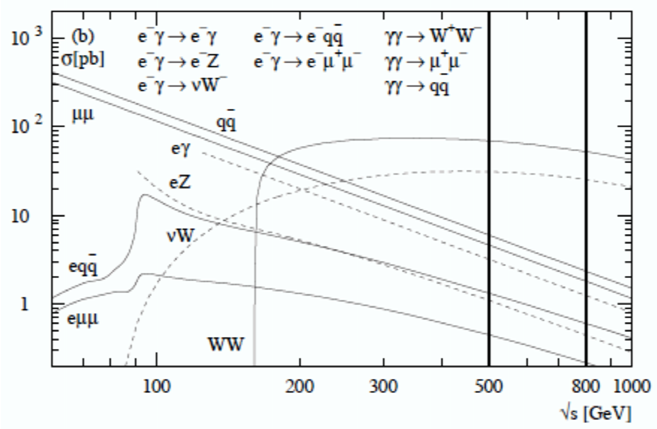

Figure 1: Typical cross sections at $e\gamma$ and $\gamma\gamma$ colliders [3].

For a meaningful assessment of the possible reach of high energy experiments in the seach for new phenomena, it is an important prerequisite to know the constraints on model parameters imposed by present day's experiments, including those at low energies. A new tool has been presented [5] that allows to obtain allowed parameter ranges for supersymmetric models and

[1] For more details and for phenomenological aspects of QCD and hadron physics at photon colliders, see Refs. [3, 4].

general 2-Higgs-doublet models. Flavor physics observables like rare B decays are viewed as most promising for this purpose.

2.2 Higgs bosons at a photon collider

It is a common belief that a Higgs boson, if it exists, cannot be missed at the forthcoming experiments at the LHC. The question whether an observed Higgs boson fits into a supersymmetric model will then be of utmost importance. In the minimal supersymmetric standard model (MSSM), there is a large region in parameter space where the LHC will not be able to distinguish a SM from a MSSM Higgs boson. This 'blind wedge' covers values above $m_A \simeq 200$ GeV, the mass of the CP-odd Higgs particle, and a region around $\tan\beta \simeq 5$ increasing in size with increasing m_A. Precise measurements of the decay branching ratios will then be needed. In particular if CP-violating interactions are present in the Higgs sector, a potential photon collider will provide additional help to identify the correct underlying theory.

In $\gamma\gamma$ collisions, s-channel production of the electrically neutral SM Higgs boson proceeds via a triangle loop of the heaviest SM particles, mainly top and W. A measurement of the production cross section will provide a determination of the 2-photon decay width $\Gamma(H \to \gamma\gamma)$ [6]. Realistic studies have shown that a statistical precision of roughly 2 % can be reached for a light Higgs boson in the interesting mass range of $M_H = 120$ GeV with a total luminosity of 410 fb^{-1} in the decay channel $H \to b\bar{b}$. For a heavy CP-even or CP-odd MSSM Higgs boson, the precision is worse, ranging between 10 and 20 % [7]. If the energy of $\gamma\gamma$ collisions is high enough, the production of two Higgs bosons will be observable and cross section measurements will allow one to determine also the values of the Higgs boson self couplings. Corresponding information will be crucial to an analysis of the Higgs sector. At an e^+e^- linear collider, a precision between 10 and 20 % for a measurement of the three-Higgs coupling λ_{HHH} can be reached, provided the center-of-mass energy is $\sqrt{s} = 1$ TeV and M_H in the range between 100 and 200 GeV. At lower $\sqrt{s} = 500$ GeV, $\Delta\lambda_{HHH}/\lambda_{HHH}$ will degrade quickly, in particular for larger M_H. For larger values of the Higgs mass up to $M_H \simeq 200$ GeV, measurements of the process $\gamma\gamma \to HH$ are expected to provide a determination of $\Delta\lambda_{HHH}/\lambda_{HHH}$ with a statistical precision of about 20 %, even in the energy range between $\sqrt{s} \simeq 520 - 650$ GeV, assuming 100 % tagging efficiency (see Fig. 2).

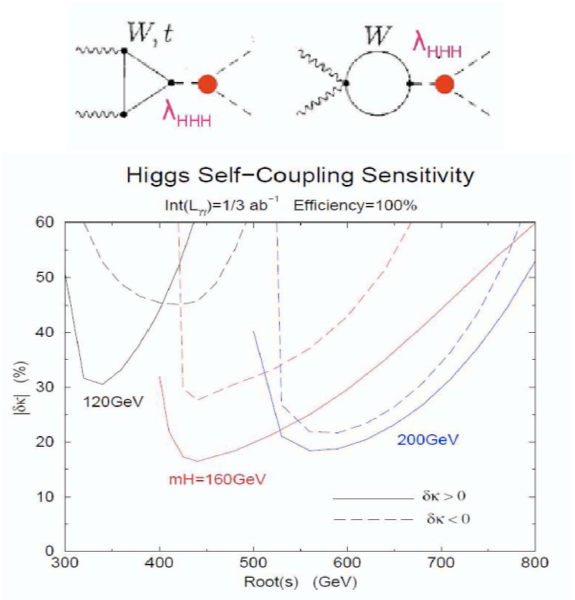

Figure 2: Higgs boson self coupling: sensitivity at a $\gamma\gamma$ collider [8].

In models which implement CP violation in the Higgs sector, a photon collider will play a crucial role [9]. In the presence of CP violation, the three neutral states in the SUSY Higgs sector may mix with no fixed CP property. The coupling to the Z boson, relevant for

the dominating discovery channel $e^+e^- \to Z\phi_1$ may be reduced for the lightest scalar mass eigenstate ϕ_1. In fact, the search at LEP may have missed such Higgs bosons and existing limits, for example from OPAL, cannot exclude the full range of $\tan\beta$ even for masses in the range below 50 GeV. It may also be missed at the Tevatron and at the LHC if the coupling to top quarks is also reduced. A photon collider would be the place for a discovery since there these states can always be produced. The possibility to control the polarization of the back-scattered photons will be an important prerequisite for a study of the CP properties of Higgs bosons; an analysis of WW and ZZ final states in combination with information obtained from top (and τ) polarization observables may then provide access to regions in the parameter space of CP-violating scenarios which are unreachable by the LHC. Also mixed polarization-charge asymmetries in $e\gamma$ collisions with a polarized electron beam have been studied as a means to enhance the signal of heavy CP-even or CP-odd Higgs production [9].

In the MSSM or in general 2-Higgs-doublet models, violation of CP can occur via different mechanisms. As is well-known in the case of CP violation in the quark sector of the standard model, a careful definition of parameters is needed, even more so in the Higgs sector in order to identify the specific mechanism. Reparametrization invariants, similar to the Jarlskog determinant, can be defined and allow to distinguish CP violation through mixing of states or through direct CP-violating interactions at tree level [10].

A characteristic feature of the MSSM is that there is decoupling of the heavy states in the Higgs sector, i.e. the MSSM becomes indistinguishable from the SM if the masses of the heavier Higgs bosons (and of the superpartner particles, of course) become large. In a general 2-Higgs doublet model this is not necessarily the case. Even if the model parameters are chosen such that all tree-level couplings to fermions and gauge bosons are the same as in the standard model, differences may enter through one-loop contributions. The production of a pair of the lightest CP-even Higgs boson h^0 in $\gamma\gamma$ collisions proceeds both in the standard model and in its extensions with two Higgs doublets via one-loop diagrams and is therefore an ideal place to look for differences. An important contribution to this process comes from one-loop corrections to the $h^0h^0h^0$ vertex which is affected by non-decoupling effects: after renormalization, quartic mass terms of the heavier Higgs bosons remain and lead to enhancements with respect to the tree-level coupling. These non-decoupling effects may be visible in the production cross section $\sigma(\gamma\gamma \to h^0h^0)$. Also diagrams with the charged Higgs boson contribute here and depending on its mass $m_{H^\pm}$, cross sections can be orders of magnitudes above the (MS)SM prediction [11, 12]. More exotic extensions of the Higgs sector may predict the existence of doubly charged Higgs bosons. The production process $\gamma\gamma \to H^{++}H^{--}$ is enhanced by the square of the charge as compared to production in e^+e^- annihilation and provides another example of the complementarity in searches for physics beyond the standard model that a photon collider may provide.

2.3 Non-standard gauge boson couplings at photon colliders

One of the less well-studied properties of the SM are the gauge boson self-interactions. Precise measurements would require high enough energies to produce at least a pair of W or Z bosons with large cross sections. At a photon-photon collider such processes, and even three- and four-boson production, could be studied. It is conceivable that the processes $\gamma\gamma \to W^+W^-$ or $e\gamma \to \nu W$ could be measured with a precision high enough to be sensitive to two-loop contributions. From the theoretical point of view, a full understanding of these processes is difficult since it involves the yet unsolved problem of a consistent definition of scattering

amplitudes for unstable particles [13].

The main motivation for a study of multiple boson production consists in the possibility to observe deviations from standard model predictions. Many speculative models of physics beyond the standard model (from more conventional extensions of the underlying gauge group to models with extra dimensions) lead to effective three- and four-gauge boson vertices with couplings that deviate from the standard model prediction. There are various parametrizations of these couplings that are conventionally used to perform model-independent studies. As a minimal requirement, anomalous couplings have to be defined in such a way that the electromagnetic $U(1)$ gauge invariance is respected. However, for realistic underlying theories that are compatible with existing data, one should base studies on an effective Lagrangean that takes also $SU(2)$ invariance into account. Limits on anomalous gauge-boson couplings have been determined by the LEP experiments and could be considerably improved at a linear collider based on measurements of the process $e^+e^- \to W^+W^-$. Also the LHC is expected to contribute to this kind of analyses since there protons can be used as a source of photons and anomalous gauge boson couplings could be studied in processes like $pp \to pp + W^+W^-$ and $pp \to pp + ZZ$ (the latter is forbidden at tree-level in the standard model). For the LHC, studies taking into account a realistic detector environment have obtained limits that improve those obtained by the LEP experiments by a factor of up to 10^3, but these studies assume independent variations of coupling parameters not respecting $SU(2)$ symmetry [14]. A study based on a $SU(2)$-invariant effective Lagrangean [15] has revealed strong correlations and smaller sensitivities. Limits that could be obtained at a photon collider are comparable with those from an e^+e^- linear collider, but better than those from photon-photon collisions at the LHC by a factor of roughly 10^2.

3 Direct photons

The study of direct photon production as a testing ground for QCD has a long tradition, also as a topic at this series of conferences. A considerable amount of experimental and theoretical work was reported already at *Photon 2007* [16]. A very good description by QCD predictions at NLO has been obtained for inclusive prompt photon production in hadronic collisions from the majority of experiments (i.e., with the exception of E706) for energies ranging from about 20 GeV up to 1.96 TeV and up to transverse momenta slightly above 200 GeV. Recent improved measurements of prompt photon + jet production by D0 show a slight disagreement of the predicted p_T-slope. Data for photoproduction from H1 and ZEUS are underestimated by present NLO calculations if one considers inclusive prompt photon production, even at the largest measured values of the photon transverse momentum of $p_T = 10$ GeV [17]. In the presence of an accompanying jet, however, there appears to be good agreement if the photon p_T is large, i.e. for $p_T > 7$ GeV. The presence of a second hard scale, provided by the jet-p_T, seems to make predictions of a perturbative calculation more reliable. The rapidity distribution is usually not described as good, but this is simply so because corresponding data are dominated by small values of p_T. There are now also data for prompt photon production in the deep-inelastic kinematic regime from both experiments at HERA. These data, however, can at present be compared with leading-order predictions only and it is not surprising that no agreement of data with theory can be obtained.

It is interesting to note that an alternative approach based on the so-called quasi-multi-Regge-kinematics [18] describes both inclusive photon production and the associated production of a photon and a jet in deep inelastic scattering at HERA. Moreover, it was successfully applied

to heavy quark production. In this approach, a class of corrections beyond the collinear parton model is resummed in the framework of an effective theory and only tree-level calculations are needed to obtain predictions. It remains to be studied how this approach could be extended to the next-to-leading order level, so that a reliable estimation of scale uncertainties can be obtained.

It would be very interesting if additional direct photon data for more exclusive measurements could be made available, as for example $\gamma+c/b$-tagged jets, or γ plus a rapidity gap. Also in this case, more theoretical work is needed. The recent work on photon + jet associated production in pp collisions [19] has shown that forthcoming measurements at the LHC are promising and may provide sensitivity on parton distribution and fragmentation functions.

Prompt photon production in nuclear collisions at RHIC is believed to be a crucial measurement since it might provide a reference process to be compared with jet quenching. Since photons, once produced, do not interact strongly with the nuclear medium in heavy-ion collisions, a comparison of both processes should help in understanding the dynamics of the quark-gluon plasma. The essential object needed for reliable predictions of photon production is the gluon density in nuclei, but it is poorly constrained by present fixed-target data. This lack of precise knowledge leads to huge uncertainties at low x and low scales. In addition, effects like jet-photon conversion, medium-induced photon emission, or photon quenching may be important. Data from PHENIX at RHIC on the nuclear production ratio R_{AA} for photons produced in $Au + Au$ collisions are consistent with various models predicting almost no suppression (see Fig. 3). Certainly, more precise data are needed; but it seems that also the observed problems in the description of other prompt photon data, in particular from photoproduction, have to be resolved before firm conclusions can be drawn with confidence.

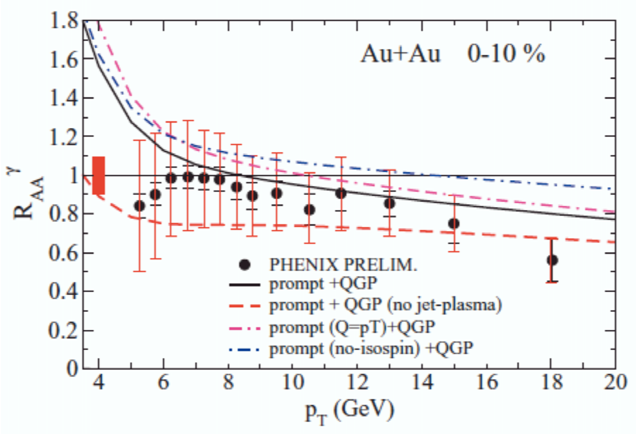

Figure 3: Prompt photon production in $Au + Au$ collisions at PHENIX [20].

4 Photon structure and exclusive hadron production

Since its first measurement by PLUTO in 1981, the analysis of the photon structure function F_2^γ has been a fruitful laboratory of perturbative QCD. The corresponding final LEP2 results published in 2005 have provided us with very precise data spanning two orders of magnitude in Q^2, and more improved data may be expected from Belle and BaBar, or possibly from the ILC. Most of the data come from deep inelastic scattering off a photon target with negligibly small virtuality P^2. At large P^2, the photon structure function $F_2^\gamma(x, Q^2, P^2)$ is suppressed; however, in the kinematic range $Q^2 \gg P^2 \gg \Lambda^2_{\rm QCD}$ perturbative QCD provides a definite prediction,

both for the shape and the magnitude of $F_2^\gamma(x, Q^2, P^2)$ since no separate non-perturbative hadronic input is needed as for the case of $P^2 \simeq 0$. In [21], heavy quark effects at NLO and target mass corrections have been studied for the structure function of a highly virtual photon, with the conclusion that PLUTO data at $Q^2 = 5$ GeV^2, $P^2 = 0.35$ GeV^2 are better described with 3 massless quarks + massive charm than with 4 massless quarks. For L3 data at higher Q^2 and P^2 where b quarks contribute, the comparison is not conclusive, both due to the smaller b-quark charge and the less precise measurements.

The hadronic properties of the electromagnetic current measured in deep-inelastic scattering and described with the help of structure functions can be studied in the framework of perturbative QCD since the factorization theorem allows one to separate structure functions into hard parton scattering cross sections and non-perturbative hadronic matrix elements of certain operators constructed from quark and gluon fields. In the case of inclusive deep-inelastic scattering, these matrix elements correspond to the kinematics of γ^*-hadron forward scattering and are called parton distribution functions (PDF). In the case of non-forward scattering, as for virtual Compton scattering $\gamma^* + p \to \gamma + p$, the necessary matrix elements correspond to so-called generalized parton distribution (GPD) functions. If the photon in the final state of virtual Compton scattering is replaced by a hadron, so that exclusive forward-production of hadrons is described, one has to introduce in addition distribution amplitudes (DA) or, for backward-production after $t \to u$-channel crossing, transition distribution amplitudes (TDA). Finally, $s \to t$ crossing leads from GPDs to generalized distribution amplitudes (GDA) needed to describe hadron production in two-photon processes. The diagrams shown in Figure 4 illustrate how the various hard exclusive processes and the objects required for their description are related to each other.

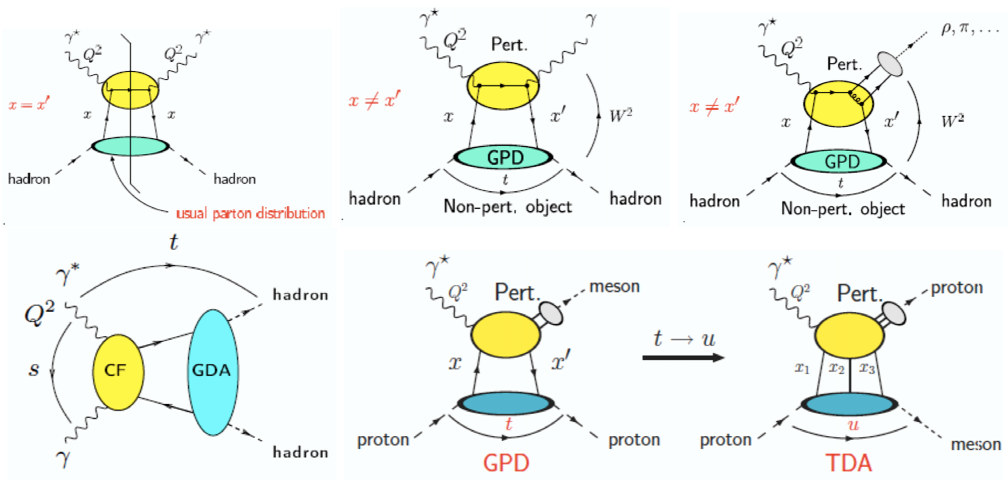

Figure 4: Basics of hard exclusive processes [22].

Measurements of exclusive processes like deeply virtual Compton scattering and meson production, also for experiments with polarized beams, are being performed at moderate and high energies and the amount and precision of corresponding data require corresponding efforts towards an improved theoretical understanding. Considerable work in this direction has been done in the recent years and a framework has been developed to describe a large number

of processes. However, factorization has been shown to work only for very few cases (e.g. $\gamma^* p \to \gamma p$), for others a prove at any order is not yet available, but factorization is plausible (e.g. for processes involving TDAs). Some studies have revealed explicit factorization breaking (e.g. $\gamma_T^* p \to \rho_T p$ with a transversely polarized photon and ρ) [22].

Corresponding calculations are complicated and the study of simplified situations may often be helpful. For example, the process $\gamma\gamma \to \gamma\gamma$ is considered as a theory playground to study factorization in GPDs close to threshold kinematics [23]. No phenomenological application for this process is visible, but apart from insight into the way how factorization works, one may also obtain hints for a reasonable choice of parametrizations of GPDs in more realistic cases. Similarly, calculations for $\gamma\gamma^* \to \pi\pi$ in the framework of a euclidean ϕ_E^3 model have been used to study the duality between factorization into GDAs and TDAs [24]. In the overlap region, when both s and t are small compared to Q^2, there is an ambiguity since both factorization into GDAs and TDAs can operate and it is not clear whether the two descriptions are equivalent to each other on a quantitative level, or whether the predictions based on both mechanisms should be added. In the scalar ϕ_E^3 model, duality between the two mechanisms has been demonstrated. If this property also holds for the case of QCD, then it would pose strong restrictions on the allowed non-perturbative ingredients needed for the description of various exclusive processes.

The framework for backward production of mesons was described in [25]. The kinematics with small u forces one to consider matrix elements that describe the exchange of three quarks and factorization leads to TDAs, i.e. probability amplitudes to find a meson inside a nucleon. The non-perturbative TDAs have to be modeled by a comparison with measurements, e.g. with existing data for $\gamma^* p \to \pi p$ or $\gamma^* p \to \eta p$, or based on measurements of related processes like $p\bar{p} \to \gamma^* \pi^0 \to \ell^+\ell^-\pi^0$ or $\gamma^* p \to J/\Psi p$, which may be accessible by future experiments, for example at GSI/FAIR, at JLAB or at B-factories.

GDAs are needed to describe hadron-pair production in 2-photon processes and can be used also to describe the production of two pairs of mesons, e.g. in $\gamma\gamma \to \pi^+\pi^-\pi^+\pi^-$. This process was identified as a candidate for the observation of the perturbative odderon. In the language of perturbative QCD, the odderon is described by the exchange of three gluons in the color singlet state. A suitably defined angular asymmetry for 2π-pair production is sensitive to the interference of the odderon and the Pomeron. The 2π GDAs are unknown and have to be modeled; reasonable choices for them predict asymmetries that rise above the level of 10 % only at very low or very large 2π invariant masses. The event rates in 2-photon scattering at the LHC may be large enough, but background from hadronic interactions will most likely prevent a corresponding analysis [26].

Similarly to conventional parton distribution functions, also DAs and their generalizations, the transverse-momentum unintegrated light-cone wave functions obey simple evolution equations derived in perturbative QCD, at leading order so-called Efremov-Radyushkin-Brodsky-Lepage evolution equations. The DAs reach an ultraviolet fixed-point at large scales and are, consequently, uniquely defined by perturbative QCD; however, scales that are accessible by present experiments are low and corresponding predictions are sensitive to the non-perturbative initial conditions. Therefore, a comparison with data is mainly a test of various model assumptions used to obtain these initial conditions, as for example models based on QCD sum rules, relativistic quark models, instanton liquid models, or effective chiral quark models. The case of pion or photon DAs is particularly interesting. From lattice QCD there are results for the pion DAs available. Experimental information is obtained indirectly from hard di-jet production by incident pions or real photons as well as from the electromagnetic pion form factor and from the $\gamma\pi$ transition form factor. In the case of pions, the DAs (and corresponding generalized form

factors) obtained from a chiral quark model and evolved at leading order [27] are in reasonable overall agreement with the available data and results from lattice simulations.

The classical area for the study of GPDs is deeply virtual Compton scattering (DVCS), i.e. the process $e^{\pm}N \to e^{\pm}N\gamma$. Other related processes are the production of lepton pairs, e.g. $e^{\pm}N \to e^{\pm}N\mu^+\mu^-$ or $\gamma N \to N'e^+e^-$ and hard exclusive meson production, e.g. $ep \to ep\pi^0$, $ep \to ep\rho$, $ep \to en\pi^+$, $ep \to en\rho^+$. There is a considerable amount of data available now, for example from H1, ZEUS and HERMES at HERA, or from the CEBAF Large Acceptance Spectrometer (CLAS) and Hall A (CEBAF Experiment 91-010) collaborations at JLAB. Moreover, measurements are expected to provide more data from COMPASS, or from experiments at JLAB with a future 12 GeV beam upgrade.

Before fitting GPDs to data, their functional form has to be carefully modeled. GPDs are intricate functions with a non-trivial interplay of the dependence of various kinematic variables and subject to constraints in a number of limiting cases. For example, they have to reduce to the conventional PDFs in the limit of forward scattering, there are various sum rules, and at LO they have to obey a positivity constraint. Moreover, their evolution at next-to-leading order has to be described properly. Because of their relation with conventional PDFs, it seems reasonable to perform a simultaneous fit of inclusive DIS and DVCS data. If based on a flexible ansatz for the GPDs, good fits to DVCS data can be obtained [28]. The complicated structure of GPDs make them a promising tool to reveal the transverse distribution of partons in a nucleon, or to address the spin content of the nucleon. It will be interesting to perform at more detail comparisons with non-perturbative methods, as for example lattice simulations.

5 Small-x and total cross sections

At small Bjorken-x, the behavior of structure functions in deep inelastic scattering is most conveniently studied in terms of color dipoles, the pair of color charges carried by quark-anti-quark pairs into which the virtual photon splits during its interaction with a nucleon. At high energies, these color charges propagate along straight lines separated by a transverse distance that remains unchanged, and the associated color dipole is described by a two-Wilson-line operator. The low-x evolution of the structure functions is then governed by the rapidity evolution of the color dipoles. At leading order in the leading logarithmic approximation, the rapidity evolution can be determined by the non-linear Balitsky-Kovchegov (BK) equation. The BK equation extends the BFKL equation by a non-linear term which describes parton annihilation and predicts saturation at low x. The leading-order BK equation is conformally invariant, however, at next-to-leading order, conformal invariance is broken in QCD by the running of the strong coupling constant.

It should be instructive to consider the evolution of color dipoles in a $\mathcal{N} = 4$ supersymmetric Yang-Mills theory. The $\mathcal{N} = 4$ SYM theory has received a lot of interest recently as it is conjectured to be dual, at strong coupling, to a type IIB string theory in 5-dimensional Anti-de-Sitter space-time. Its β-function vanishes and one can hope that its conformal invariance provides strong restrictions on the correct effective action of QCD at high energies. At LO, the color dipole evolution equation has the same form as in QCD and it has been demonstrated [29] that with suitably defined "composite conformal dipole operators", the conformally invariant analytic part of the QCD evolution equation at NLO can be obtained in that theory. It has also been shown that the resulting evolution equation agrees with the forward BFKL equation at next-to-leading order.

The complicated physics of the deep inelastic structure functions results from the cooperation of weak coupling due to the asymptotic freedom of QCD at high energies and the high density of gluons inside the nucleus. The gluon density increases towards lower Bjorken-x since at weak coupling, soft and collinear gluon emission is favored. Ultimately, this would break unitarity. However, gluon bremsstrahlung is limited by recombination effects, an effect which restores unitarity and leads to saturation at a limit depending on x and Q^2 given by $Q_s^2(x) \propto 1/x^\lambda$ with $\lambda \simeq 0.2 - 0.3$.

The situation may change dramatically in heavy-ion collisions where data indicate the presence of strong coupling effects. According to the famous conjecture by Maldacena, there is a correspondence between a strongly coupled gauge theory and a string theory at weak coupling. If this conjecture is right, it would be possible to infer from the study of the classical dynamics of a black hole in AdS_5-supergravity properties of photon interactions with a strongly coupled quark-gluon plasma. Corresponding investigations [30] lead to the conclusion that saturation should set in faster and the behavior of $Q_s^2(x)$ would be changed to $Q_s^2(x) \propto 1/x$. As an important consequence, since strong coupling would lead to unlimited, quasi-democratic parton branchings, one would expect to observe no collimated jets in e^+e^- annihilation, and no large-x partons in the hadron wave functions, i.e. no jets in the forward or backward direction of hadron-hadron collisions. It has to be seen whether future data from RHIC can contribute to a clarification of these concepts.

6 Vacuum polarization and $g-2$

The comparison of experimental data with theoretical predictions for the anomalous magnetic moment of the muon has received considerable interest in the past years, after the experiment E821 at Brookhaven has published the most precise measurement of $a_\mu^{\rm exp} = (g_\mu - 2)/2 = (11659208.0 \pm 6.3) \times 10^{-10}$. Since then a discrepancy of about 3σ has been observed. It is an open question whether this is a sign of new physics, or of an incomplete understanding of photon-hadron interactions contributing to a_μ.

At present, the precision of theoretical calculations nicely match the size of the experimental uncertainty, but for a conclusive comparison of theory with results of future experiments aiming at an accuracy of $\pm 1.5 \times 10^{-10}$, considerable improvements in the theoretical understanding will be necessary. The present theoretical uncertainty is dominated by the precision with which hadronic contributions to a_μ can be calculated.

Hadronic contributions enter at the two-loop level via the hadronic vacuum polarization (the two-point correlator of the electromagnetic current) and at the three-loop level via light-by-light scattering (a certain component of the four-point correlator of the electromagnetic current). The

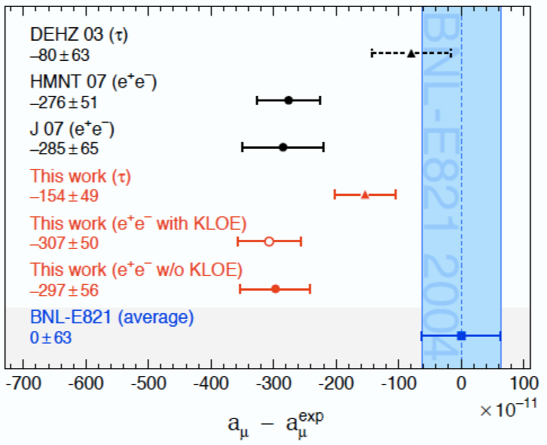

Figure 5: Status of $g-2$ [31].

former contribution, denoted $a_\mu^{\rm had,LO}$, was traditionally calculated, by using a dispersion relation, from data of the total hadronic cross section for e^+e^- annihilation and its accuracy is limited by those data. Improvements in the measurement of e^+e^- cross section data by the CMD-2, SND and KLOE collaborations have reduced the accuracy of $a_\mu^{\rm had,LO}$ to $\pm 5.0 \times 10^{-10}$ [31]. On the other hand, with the increasing precision of LEP data for the decay spectrum of the τ, it became possible to use, instead of e^+e^- data, the τ spectral functions in the calculation of $a_\mu^{\rm had,LO}$. The most recent analyses [31] based on τ data reports a precision of $\pm 4.9 \times 10^{-10}$, very similar to the e^+e^--based calculations. The new analysis takes into account recent high-precision data from the Belle collaboration on the decay $\tau^- \to \pi^-\pi^0\nu_\tau$ and is based on a new analysis of isospin-violating corrections. Interestingly, this analysis results in a better agreement with e^+e^--based calculations than previously, but is shifted away from $a_\mu^{\rm exp}$ by -15.4×10^{-10}. The long-standing discrepancy between spectral functions for $e^+e^- \to \pi^+\pi^-$ and $\tau^- \to \pi^-\pi^0\nu_\tau$ is reduced, but still present, in particular for data from KLOE. It will be interesting to see whether the inconclusive situation persists when preliminary data from BaBar on $e^+e^- \to \pi^+\pi^-(\gamma)$ using the ISR-method are finalized so that they can be used for an updated calculation of $a_\mu^{\rm had,LO}$.

The hadronic contribution to a_μ from light-by-light scattering, $a_\mu^{\rm hLbL}$, cannot be directly related to experimental data and there is at present no complete calculation from first principles. A counting of various contributions can be based on the $1/N_c$ expansion and power-counting of chiral perturbation theory. At order $O(N_c)$, one-particle-reducible exchange diagrams involving Goldstone bosons (at $O(p^6)$) and non-Goldstone bosons (at $O(p^8)$) dominate, whereas loop-diagrams start at order $O(1/N_c)$. Various model calculations are in fair agreement with each other, resulting in the dominating contribution $a_\mu^{\rm hLbL}(\pi^0,\eta,\eta') = (11.4 \pm 1.3) \times 10^{-10}$ [32] from Goldstone-boson exchange. Contributions due to the exchange of pseudo-vector and scalar resonances, heavy quark loops and π loops are less well-known and cancel each other to some extent. A conservative estimate of their precision, but adding theoretical errors from different contributions in quadrature, results in $a_\mu^{\rm hLbL} = (10.5 \pm 2.6) \times 10^{-10}$ [32]. Improvements will be difficult to achieve, but may be expected by a more refined consideration of short-distance QCD constraints and by utilizing experimental information on the properties of the off-shell $\pi\gamma\gamma$ and $\pi\pi\gamma\gamma$ form factors. Data from BaBar, KLOE-2 and DAΦNE on radiative decays of pions and pseudo-vector resonances and other 2-photon processes will play an important role in this respect.

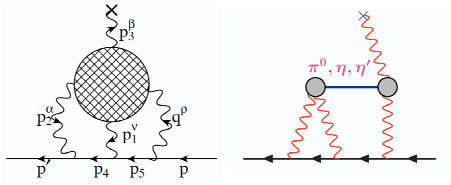

Figure 6: Hadronic light-by-light scattering and the dominating π^0, η, η' exchange diagram [32].

7 Acknowledgments

I thank the speakers of the conference for help in preparing this summary talk and the organizers for their kind invitation.

References

[1] V. Telnov, this conference.

[2] https://indico.desy.de/contributionDisplay.py?contribId=59&sessionId=19&confId=1407

[3] ECFA/DESY LC Physics Working Group, E. Accomando et al., Phys. Rept. 299 (1998) 1 [hep-ph/9705442].

[4] TESLA Technical Design Report, Part VI, Chapter 1: The Photon Collider at TESLA, B. Badelek et al., Int. J. Mod. Phys. A19 (2004) 5097 [hep-ex/0108012].

[5] F. N. Mahmoudi, this conference; http://superiso.in2p3.fr/.

[6] M. Spira, this conference.

[7] P. Niezurawski, A. F. Zarnecki, M. Krawczyk, hep-ph/0507006; P. Niezurawski, hep-ph/0507004.

[8] E. Asakawa, D. Harada, S. Kanemura, Y. Okada, K. Tsumura, Int. Linear Collider Workshop (LCWS08 and ILC08), Chicago, Illinois, 16-20 Nov 2008 [arXiv:0902.2458]; Phys. Lett. B672 (2009) 354.

[9] R. M. Godbole, this conference; R. M. Godbole, S. Kraml, S. D. Rindani, R. K. Singh, Pramana 69 (2007) 771; see also: Report of the Workshop on CP Studies and Non-Standard Higgs Physics, hep-ph/0608079.

[10] M. Krawczyk, this conference; D. Sokolowska, K. A. Kanishev, M. Krawczyk, arXiv:0812.0296; E. E. Jenkins, A. V. Manohar, arXiv:0907.4763.

[11] R. Santos, this conference; A. Ahrhib, R. Benbrick, C.-H. Chen, R. Santos, arXiv:0901.3380.

[12] F. Cornet, W. Hollik, Phys. Lett. B669 (2008) 58.

[13] I. Ginzburg, this conference.

[14] E. Chapon, this conference; O. Kepka, C. Royon, Phys. Rev. D78 (2008) 073005; E. Chapon, C. Royon, O. Kepka, arXiv:0908.1061.

[15] A. von Manteuffel, this conference; M. Maniatis, A. von Manteuffel, O. Nachtmann, Nucl. Phys. B – Proc. Suppl. 179 (2008) 104.

[16] G. Heinrich, Nucl. Phys. B – Proc. Suppl. 184 (2008) 121 [arXiv:0711.2464].

[17] F. Arleo, this conference.

[18] V. Saleev, this conference; Phys. Rev. D78 (2008) 114031; Phys. Rev. D78 (2008) 034033.

[19] Z. Belghobsi, M. Fontannaz, J.-Ph. Guillet, G. Heinrich, E. Pilon, M. Werlen, Phys. Rev. D79 (2009) 114024.

[20] S. Turbide, C. Gale, E. Frodermann, U. Heinz, Phys. Rev. C77 (2008) 024909.

[21] K. Sasaki, this conference; Y. Kitadono, K. Sasaki, T. Ueda, T. Uematsu, Phys. Rev. D77 (2008) 054019; Progr. Theor. Phys. 121 (2009) 495; T. Ueda, K. Sasaki, T. Uematsu, Eur. Phys. J. C62 (2009) 467.

[22] S. Wallon, this conference.

[23] L. Szymanowski, this conference.

[24] I. V. Anikin, this conference; I. V. Anikin, N. G. Stefanis, O. V. Teryaev, arXiv:0806.4551.

[25] J. P. Lansberg, this conference.

[26] F. Schwennsen, this conference; F. Schwennsen, L. Szymanowski, S. Wallon, Phys. Rev. D78 (2008) 094009; arXiv:0906.5512.

[27] W. Broniowski, this conference; W. Broniowski, E. Ruiz Arriola, K. Golec-Biernat, Phys. Rev. D77 (2008) 034023; A. E. Dorokhov, W. Brioniowski, E. Ruiz Arriola, Phys. Rev. D74 (2006) 054023.

[28] D. Müller, this conference; K. Kumericki, D. Müller, K. Passek-Kumericki, Nucl. Phys. B794 (2008) 244; Eur. Phys. J. C58 (2008) 193; arXiv:0807.0159; K. Kumericki, D. Müller, arXiv:0904.0458.

[29] G. Chirilli, this conference; I. Balitsky, G. Chirilli, Phys. Rev. D77 (2008) 014019; arXiv:0903.5326.

[30] E. Iancu, this conference.

[31] G. López Castro, this conference; M. Davier et al., arXiv:0906.5443 [hep-ph].

[32] J. Prades, arXiv:0907.2938; J. Prades, E. de Rafael, A. Vainshtein, in *Lepton Dipole Moments*, eds. B. L. Roberts and W. J. Marciano, World Scientific (Singapore) 2009 [arXiv:0901.0306].